(NASA-CR-161198) AERODYNAMIC HEATING TO REPRESENTATIVE SRB AND ET PROTUBERANCES Final Report (Remtech, Inc., Huntsville, Ala.) 388 p HC A17/MF A01 CSCL 01A

N79-21004

Unclas
G3/02 14710

MAY 1979
RECEIVED
NASA STI FACILITY
ACCESS DEPT.

REMTECH inc.

Huntsville, Alabama

REMTECH INC.
2603 Artie Street, Suite 21
Huntsville, Alabama 35805

RTR 029-1

AERODYNAMIC HEATING TO
REPRESENTATIVE SRB AND ET
PROTUBERANCES

February, 1979

by

Dr. Carl D. Engel

and

Judy K. Lapointe

Prepared under contract NAS8-32585

for

George C. Marshall Space Flight Center
Marshall Space Flight Center, Alabama 35812

FOREWORD

This is the final report presenting work which was conducted for Marshall Space Flight Center (MSFC) in response to requirements of Contract NAS8-32585. The work presented was performed at REMTECH's Huntsville office and is entitled "Aerodynamic Heating to Representative SRB and ET Protuberances."

The NASA Technical coordination for this study was provided by Mr. Lee Foster and Mr. John Warmbrod of the Thermal Environment Branch of the Systems Dynamics Laboratory.

TABLE OF CONTENTS

TABLE OF CONTENTS (cont.)

Section 1

INTRODUCTION

This report describes heating data and data scaling methods which can be used on representative Solid Rocket Booster (SRB) and External Tank (ET) protuberances. Each of the following sections can be used as a stand alone document of a particular aspect of protuberance heating. However, taken together the sections complement each other. The following section titles are:

2. ET Geometry and Heating Body Points
3. IH-51A Data
4. FH-15 and FH-16 Data
5. Individual Protuberance Data
6. IH-42 Paint Data

All of the protuberances found on the ET are shown pictorially in Section 2. Data and correlative procedures for a large set of protuberance shapes are given in Sections 3 and 4 for ET protuberances and Section 5 for SRB protuberances. Section 6 provides protuberance data in the context of the complete ET geometry.

Section 2

ET GEOMETRY AND HEATING BODY POINTS

The purpose of this section is to provide the handbook user a set of drawings of the ET moldline and protuberances and to define where thermal environment body points are located. This is accomplished by presenting figures and tables that define body point numbers and locations on each component surface of the external tank. The figures show design body point locations on views of each component. Supporting tables specify the location (i.e. X_T and Θ_T) and give surface identifications (e.g. aft face). Preceding each subsection a list is given of the surface areas and protuberances included in the subsection. The listing is in order in which the item appears.

2.1 FORWARD CONES AND OGIVE

This subsection contains geometry and body point information for the 10 degree cone, 40 degree cone and LO_2 tank ogive ($322.5 \leq X_T \leq 852.8$).

2.1.1 Acreage Definition

This subsection gives the moldline geometry and related body points for the 10°/40° cone and ogive. The information sequence is as follows:

- 10°/40° cone and ogive projections
- 10° and 40° cone unrolled views
- Acreage body point table

Several additional blank columns are given for user convenience in the acreage body point tables throughout this section.

Note: A = Division 2.1.1 on figures and tables.

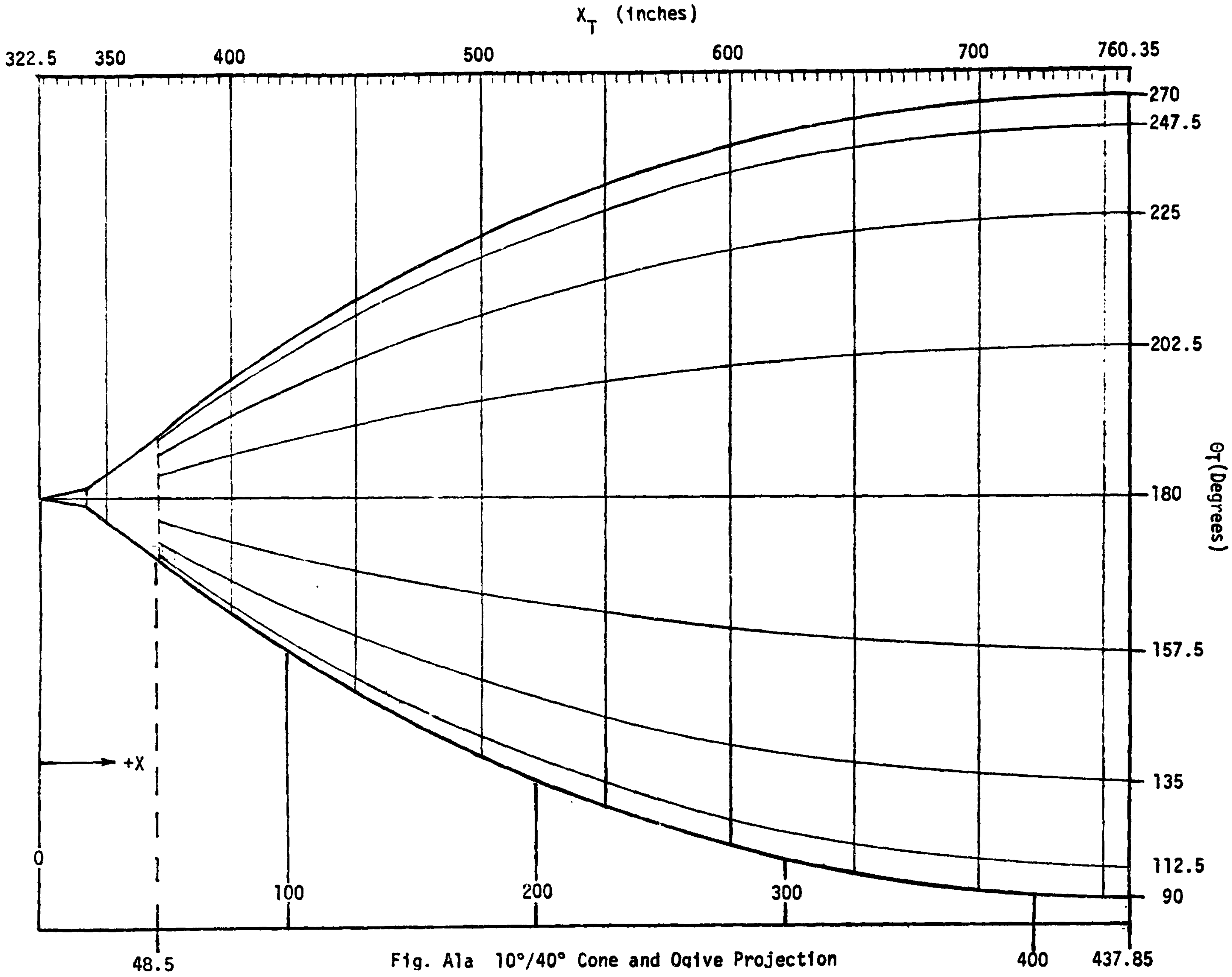

Fig. A1a 10°/40° Cone and Ogive Projection

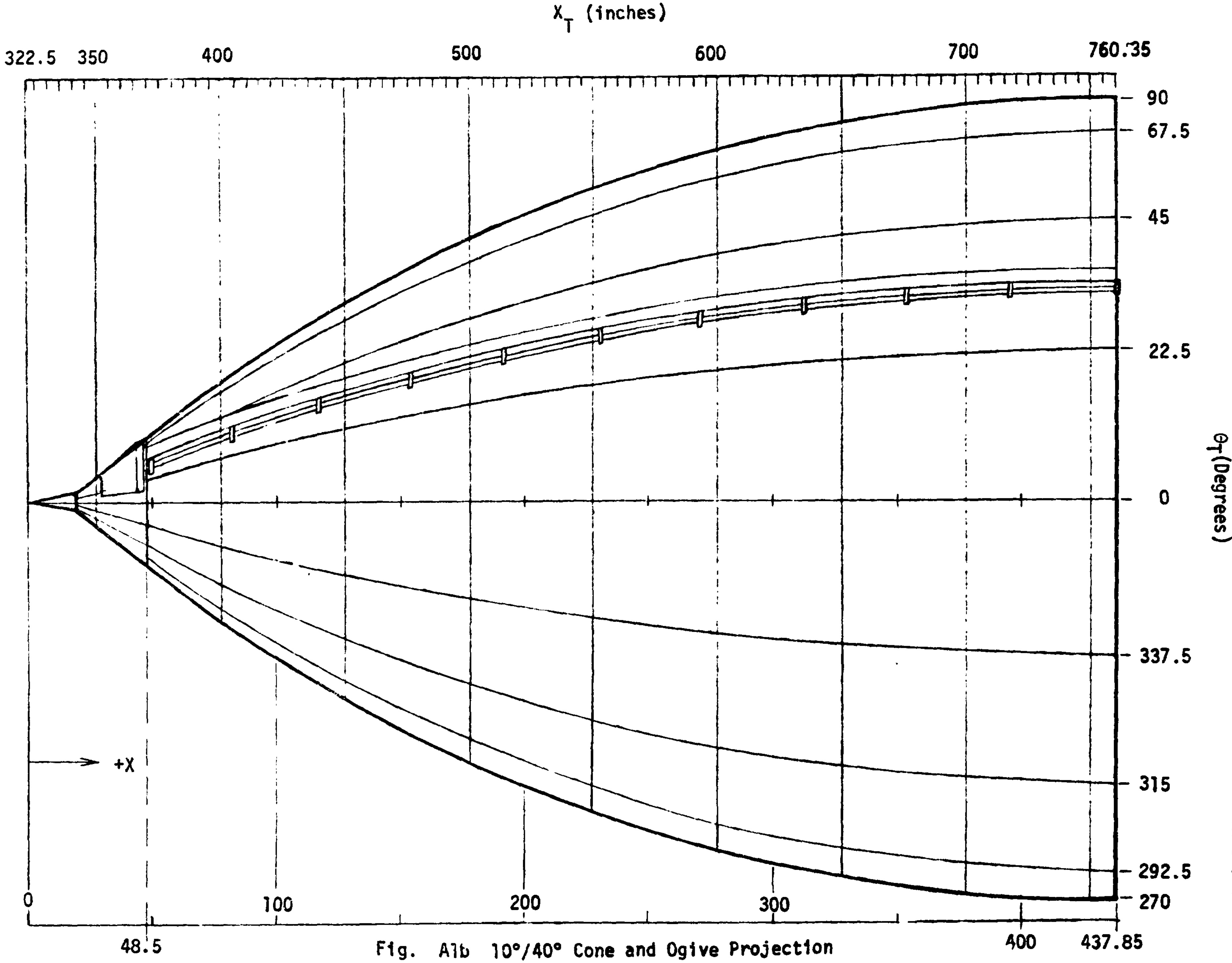

Fig. A1b 10°/40° Cone and Ogive Projection

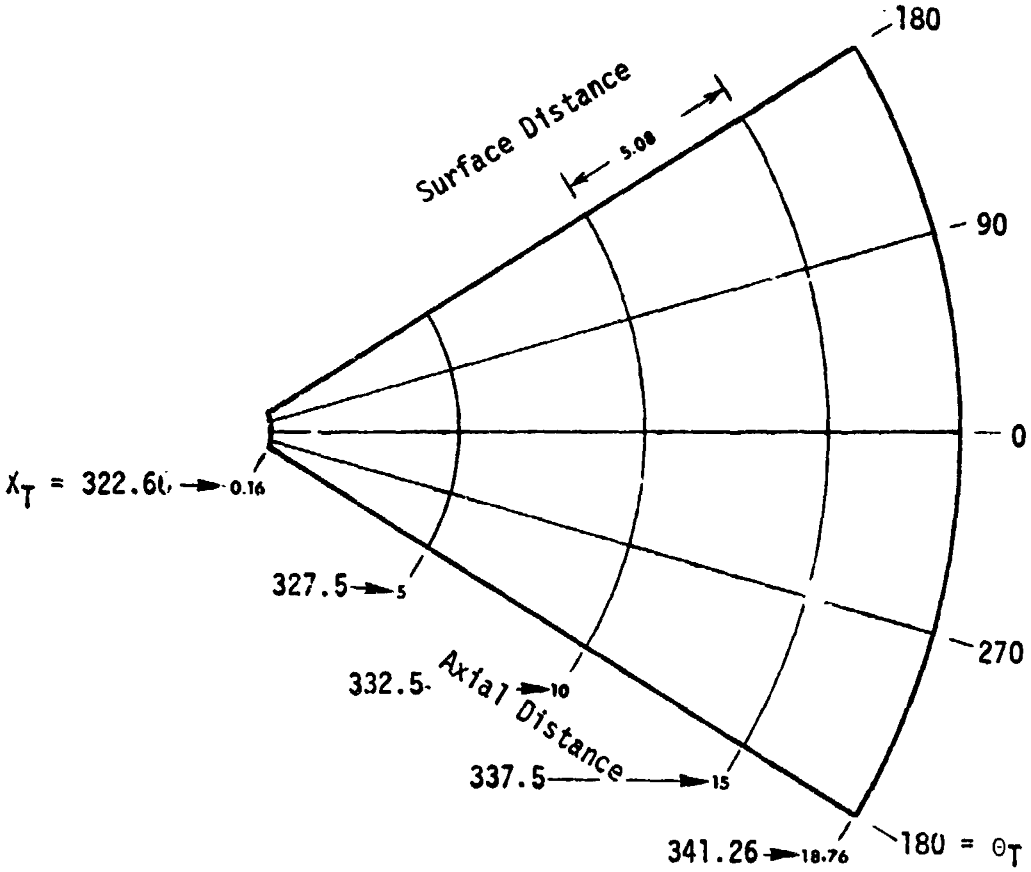

Fig. A2 Unrolled View of 10 Degree Cone

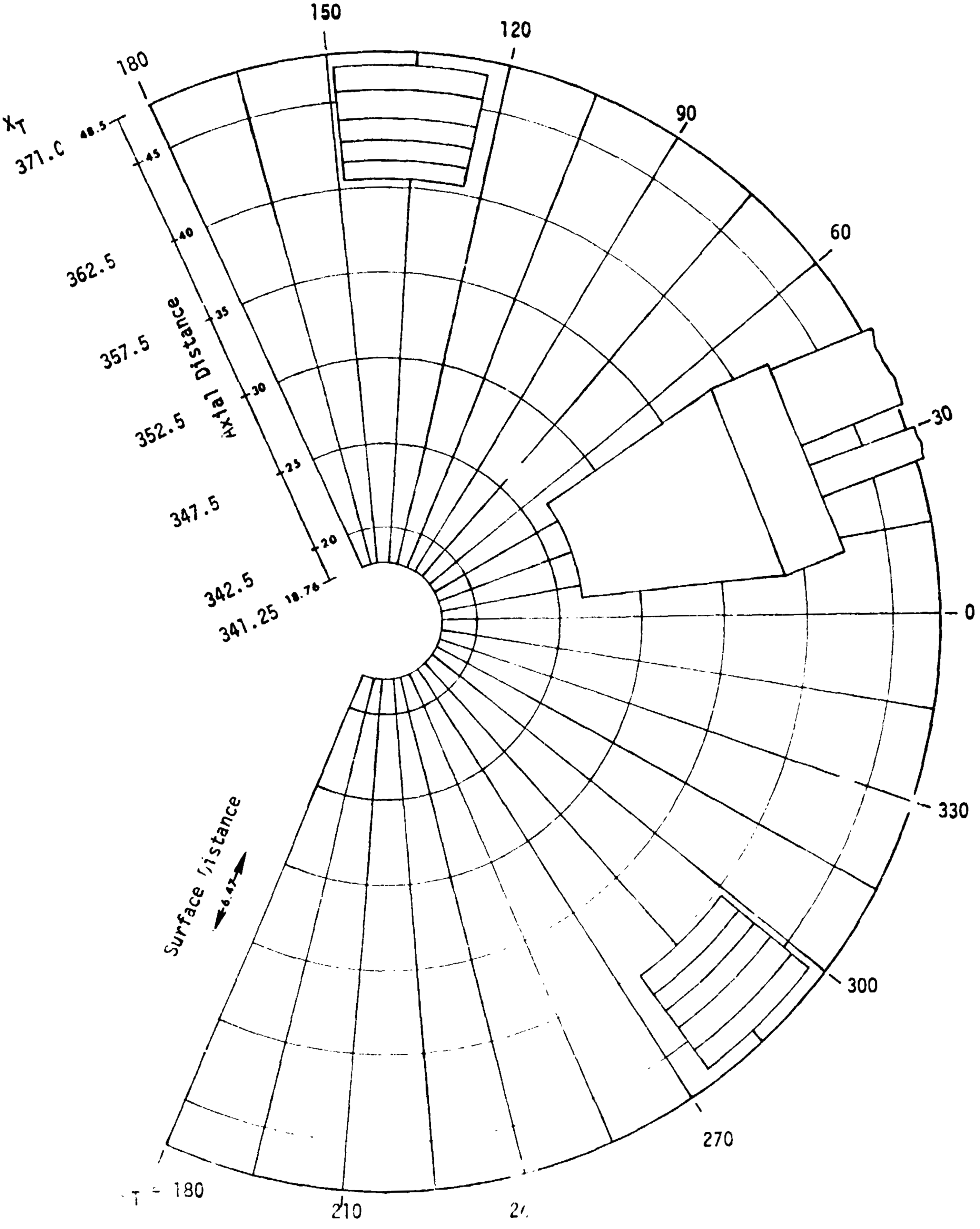

Fig. A3 Unrolled View of 40° Cone (Actual Cone Angle = 39.38°)

TABLE A4

CONE OGIVE ACREAGE BODY POINT DEFINITIONS

B. P. No.	X_T (in.)	Θ_T (deg.)					
70100	322.5	0					
70200	323.0	0.0					
70250	↓	180.0					
70275		270.0					
70300	329.0	0.0					
70350	↓	180.0					
70375		270.0					
70400	335.0	0.0					
70450	↓	180.0					
70475		270.0					
70500	342.24	0.0					
70550	↓	180.0					
70563		225.0					
70575		270.0					
70588		315.0					
70600	345.5	0.0					
70650	↓	180.0					
70663		225.0					
70675		270.0					
70688		315.0					
70700	354.5	0.0					
70750	↓	180.0					
70763		225.0					
70775		270.0					
70788		315.0					
70800	364.5	0.0					
70850	↓	180.0					
70863		225.0					
70875		270.0					
70888		315.0					
70900	375.1	0.0					
70950	↓	180.0					
70956		202.5					
70963		225.0					
70969		247.5					

Table A4 (Cont. 1)

CONE OGIVE ACREAGE BODY POINT DEFINITIONS

B. P. No.	X_T (in.)	Θ_T (deg.)					
70975	375.1	270.0					
70981		292.5					
70988		315.0					
*70994	↓	337.5					
71000	421.3	0.0					
71050		180.0					
71056		202.5					
71063		225.0					
71069		247.5					
71075		270.0					
71081		292.5					
71088		315.0					
*71094	↓	337.5					
71100	453.6	0.0					
71150		180.0					
71156		202.5					
71163		225.0					
71169		247.5					
71175		270.0					
71181		292.5					
71188		315.0					
*71194	↓	337.5					
71200	467.4	0.0					
71250		0.0					
71256		202.5					
71263		225.0					
71269		247.5					
71275		270.0					
71281		292.5					
71288		315.0					
*71294	↓	337.5					
71300	513.6	0.0					
71350		180.0					
71356		202.5					
71363		225.0					
71369		247.5					
71375		270.0					
71381		292.5					
71388		315.0					
*71394	↓	337.5					

Table A4 (Cont. 2)

CONE OGIVE ACREAGE BODY POINT DEFINITIONS

B. P. No.	X_T (in.)	Θ_T (deg.)					
71400	606.0	0.0					
71450		180.0					
71456		202.5					
71463		225.0					
71469		247.5					
71475		270.0					
71481		292.5					
71488		315.0					
*71494		337.5					
71500	698.0	0.0					
71550		180.0					
71556		202.5					
71563		225.0					
71569		247.5					
71575		270.0					
71581		292.5					
71588		315.0					
*71594		337.5					
71600	751.5	0.0					
71650		180.0					
71656		202.5					
71663		225.0					
71669		247.5					
71675		270.0					
71681		292.5					
71688		315.0					
*71694		337.5					
71700	796.5	0.0					
71750		180.0					
71756		202.5					
71763		225.0					
71769		247.5					
71775		270.0					
71781		292.5					
71788		315.0					
*71794		337.5					

TABLE A4 (Cont. 3)

CONE OGIVE ACREAGE BODY POINT DEFINITIONS

B. P. No.	X_T (in.)	Θ_T (deg.)					
71800	841.5	0.0					
71850	↓	180.0					
71856		202.5					
71863		225.0					
71869		247.5					
71875	841.5	270.0					
71881	↓	292.5					
71888		315.0					
*71894		337.5					

* B.P.s with asterisk indicates skin points used as reference for top of Electrical Conduit and GO_2 pressure line. In 1977 RI environment, these B.P. were multiplied by 1.5.

2.1.2 Protuberance Definition

This subsection contains all the protuberance geometries and body points on the 10°/40° cone and ogive. The information sequence is as follows:

- Louver Vent
- Tumble Valve Pipe
- Forward Electrical Conduit
  - Forward Fairing
  - Attachment Fittings
- GO_2 Pressure Line
  - Flanges
  - Attachment Fittings
- Skin Points Influenced by Protuberances

Note: B = Division 2.1.2 on figures and tables

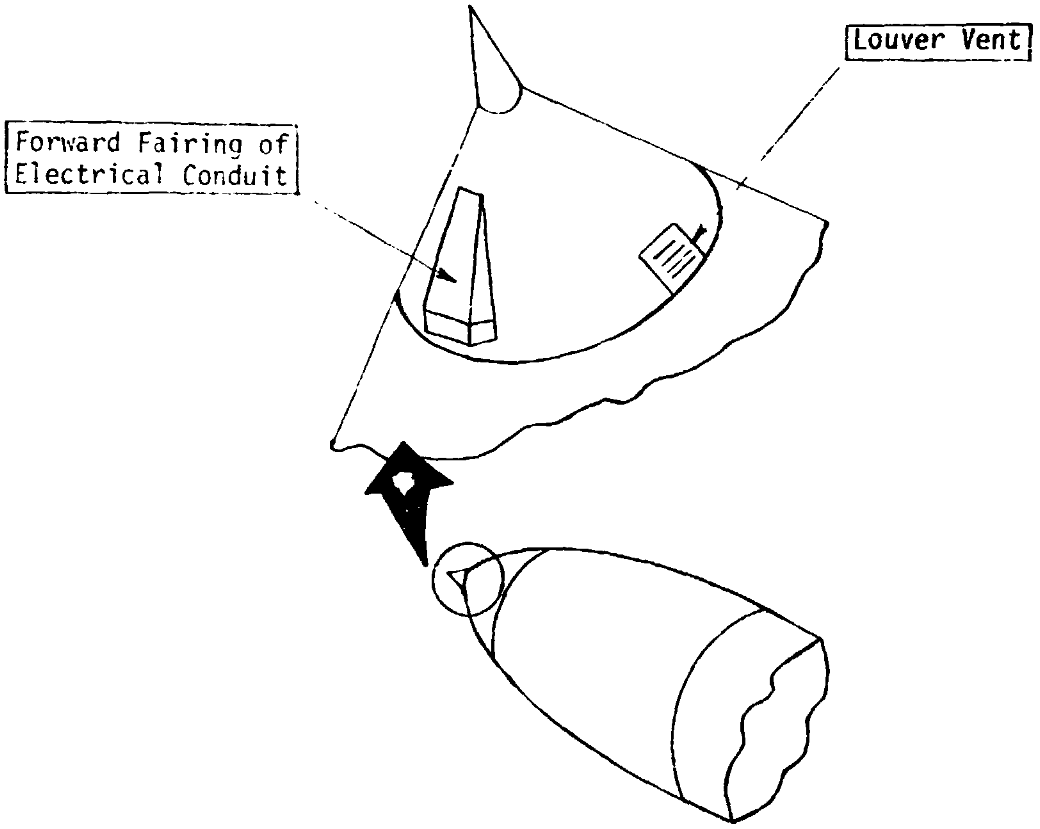

Fig. B1 40° Cone Protuberances

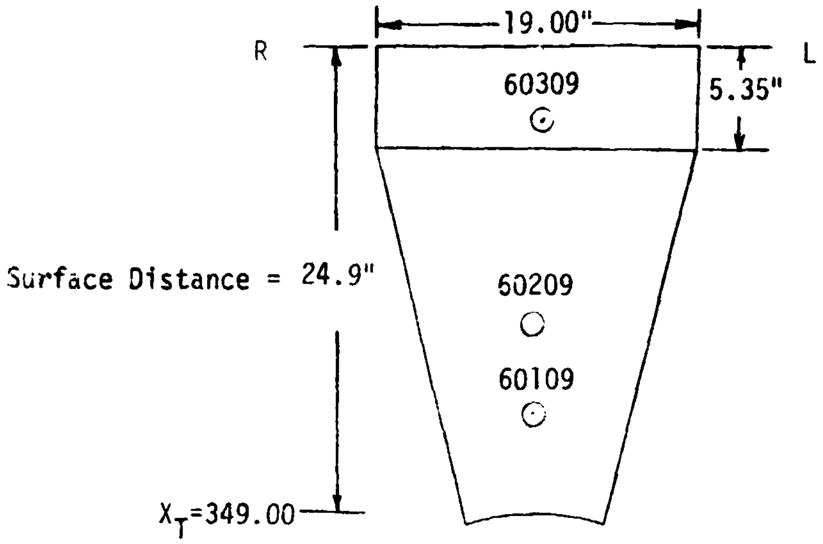

TOP VIEW

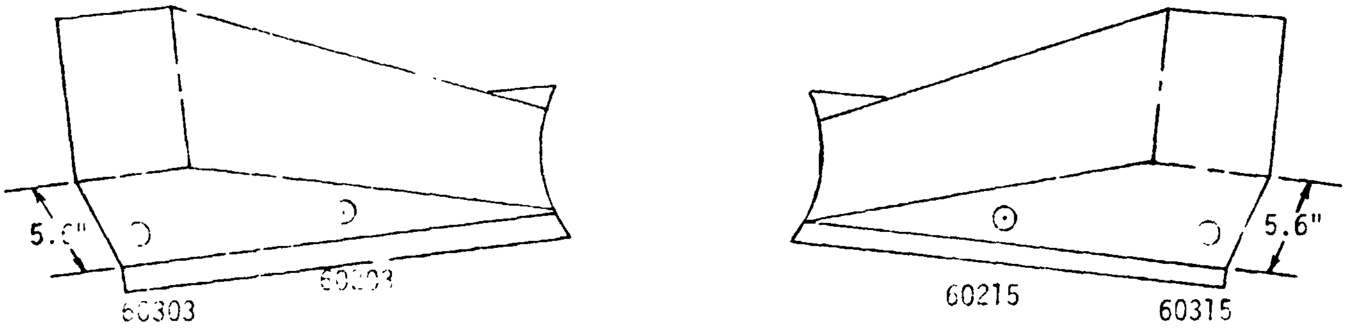

RIGHT SIDE VIEW

LEFT SIDE VIEW

Fig. B2 Forward Fairing of the Forward Electrical Conduit
Body Point Definition

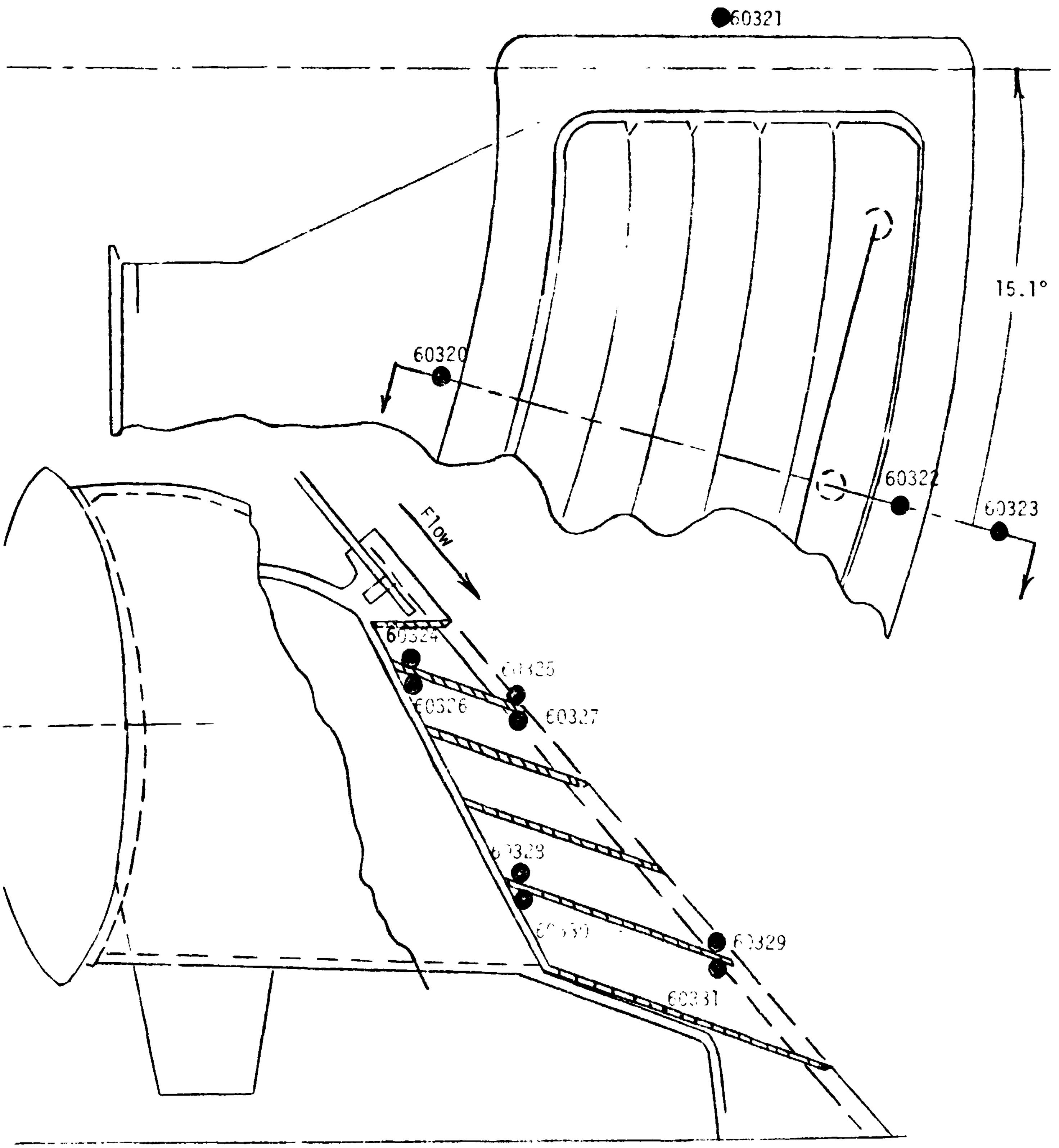

Fig. 83 O Tank Vent Louver Gage Point Definition

Table B4

	Protuberance Body Point Definitions			
	Body Points	X_T (In.)	θ_T (Deg.)	Location
LO_2 Tank Vent Louver	60320	364.0	313.5	Forward Centerline
	60321	368.0	328.6	Side
	60322	371.0	313.5	Aft Centerline
	60323	372.0	313.5	Aft Centerline
	60324	365.0	313.5	Bottom Forward
	60325	366.0	313.5	Top Front
	60326	365.0	313.5	Bottom Back Face
	60327	366.0	313.5	Top Back Face
	60328	368.0	313.5	Bottom Forward
	60329	369.0	313.5	Top Forward
	60330	368.0	313.5	Bottom Back Face
	60331	369.0	313.5	Top Back Face
Fwd. Fair Electrical Conduit	60109	353.0	31.5	Top of Cable Tray Fairing
	60209	357.0	31.5	Top of Cable Tray Fairing
	60309	364.0	31.5	Top of Cable Tray Fairing
	60203	357.0	9.5	Side of Cable Tray Fairing
	60303	364.0	9.5	Side of Cable Tray Fairing
	60215	357.0	53.5	Side of Cable Tray Fairing
	60315	364.0	53.5	Side of Cable Tray Fairing

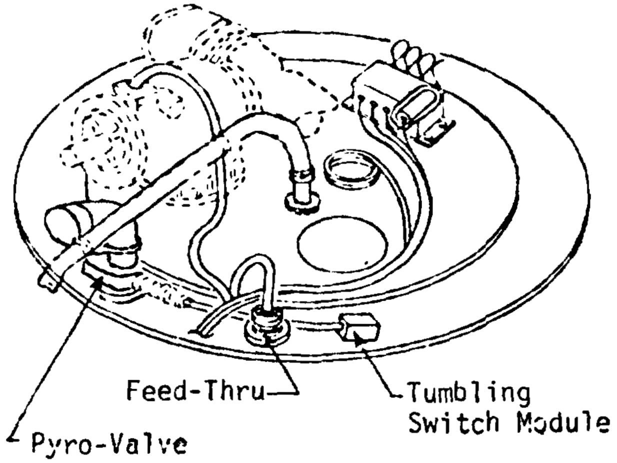

LO$_2$ Upper Tank Sensor Mounting

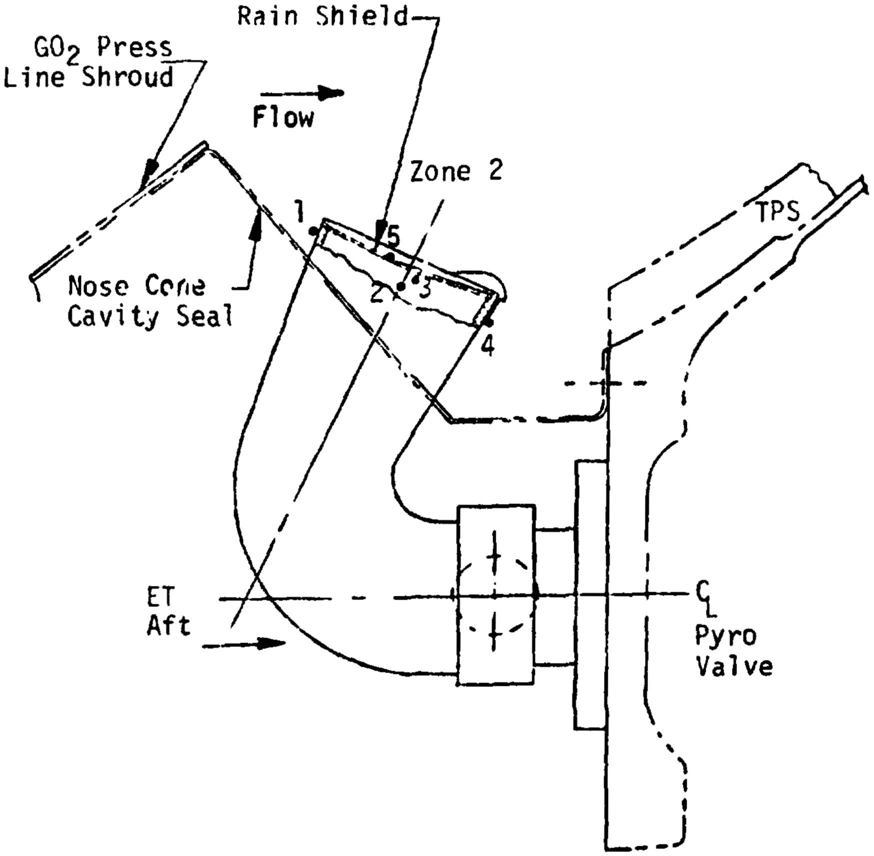

Reference Body Point	Comment
60309 ↓	1. Pipe Top 2. Pipe Side 3. Pipe Inside 4. Pipe Bottom 5. Rain Shield

Fig. B5 Tumble Valve Pipe

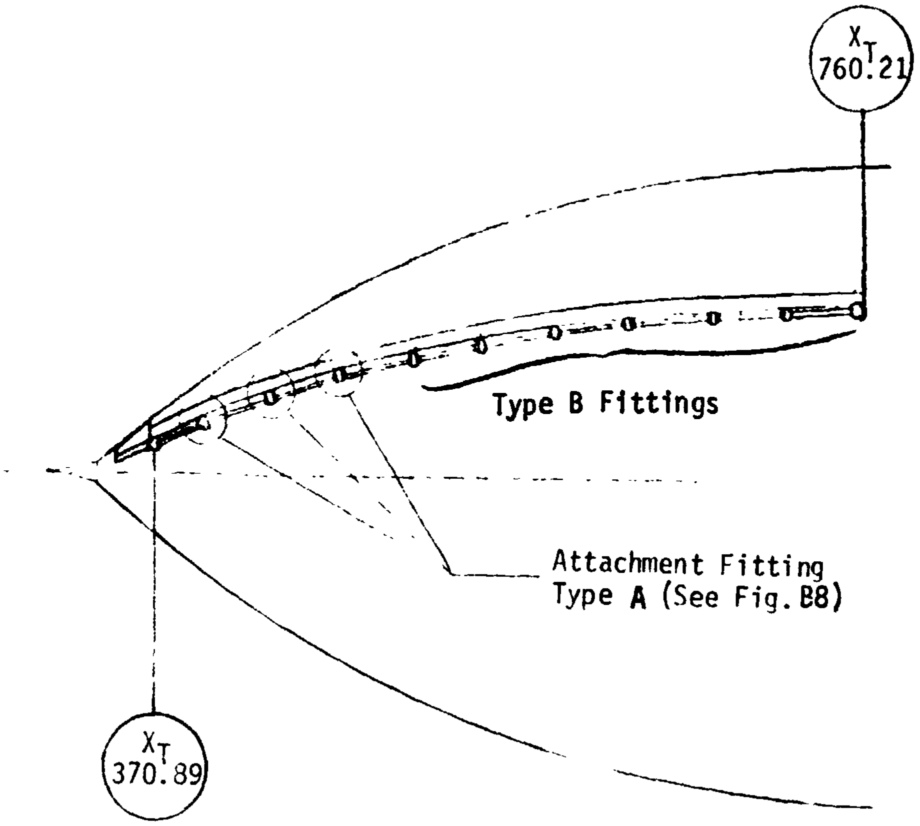

FORWARD FACE BODY POINT DEFINITIONS	
Body Points	Attachment Fitting Station X_T (In.)
60310	370.89
60420	404.34
60820	439.49
60920	476.16
61020	514.12
61120	553.37
61220	593.54
61320	634.51
61420	676.03
61520	718.04
61620	760.21

Fig. B6 GO_2 Pressure Line - Electrical Conduit Attachment Fitting Forward Face Body Points

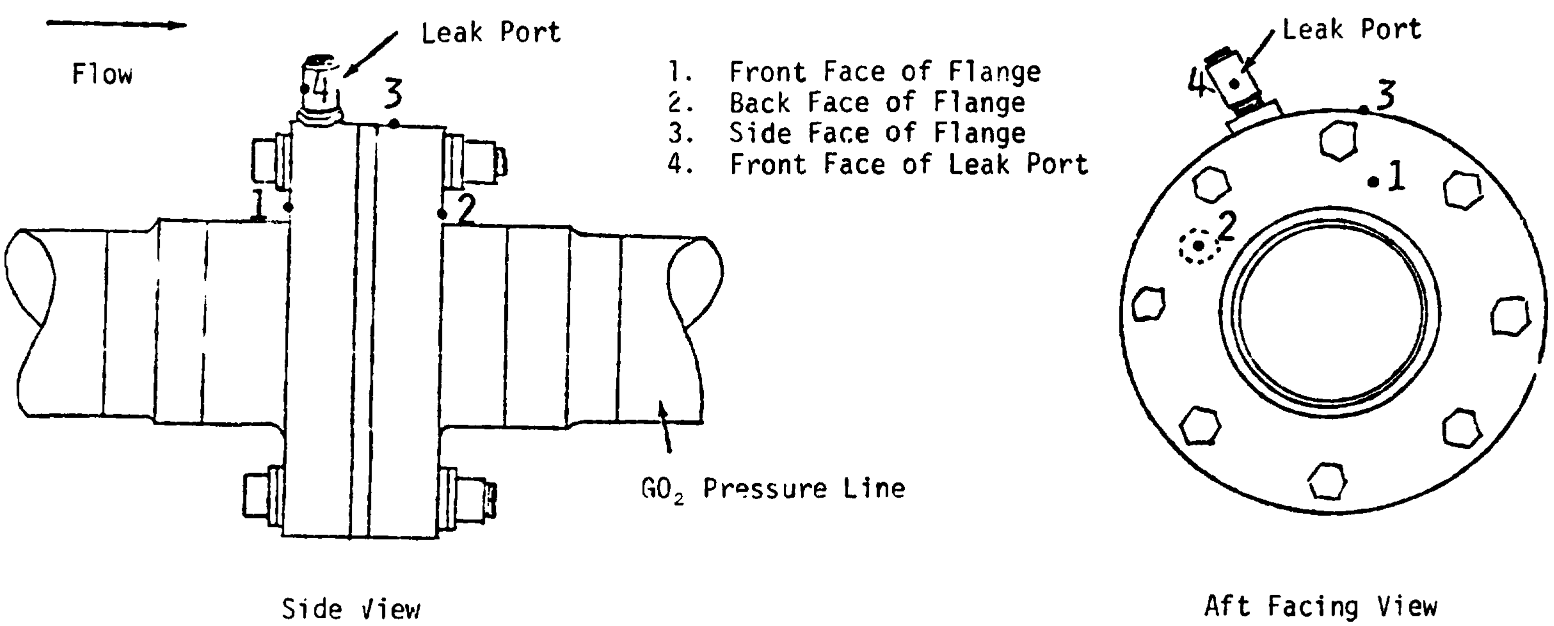

STA.	1	2	3	4
394.745	[1560]	[1564]	[1561]	1*
610.51	↓	↓	↓	↓
849.0	↓	↓	↓	↓
1088.0	80127	80128	80129	80130
1327.0	80131	80132	80133	80134
1566.0	80135	80136	80137	80138
1805.0	80139	80140	80141	80142
2044.0	80143	80144	80145	80146

* Stagnation Line Heating
[ ] Reference Body Point

Fig. B7 GO_2 Pressure Line Flanges Body Point Locations at Fitting Stations

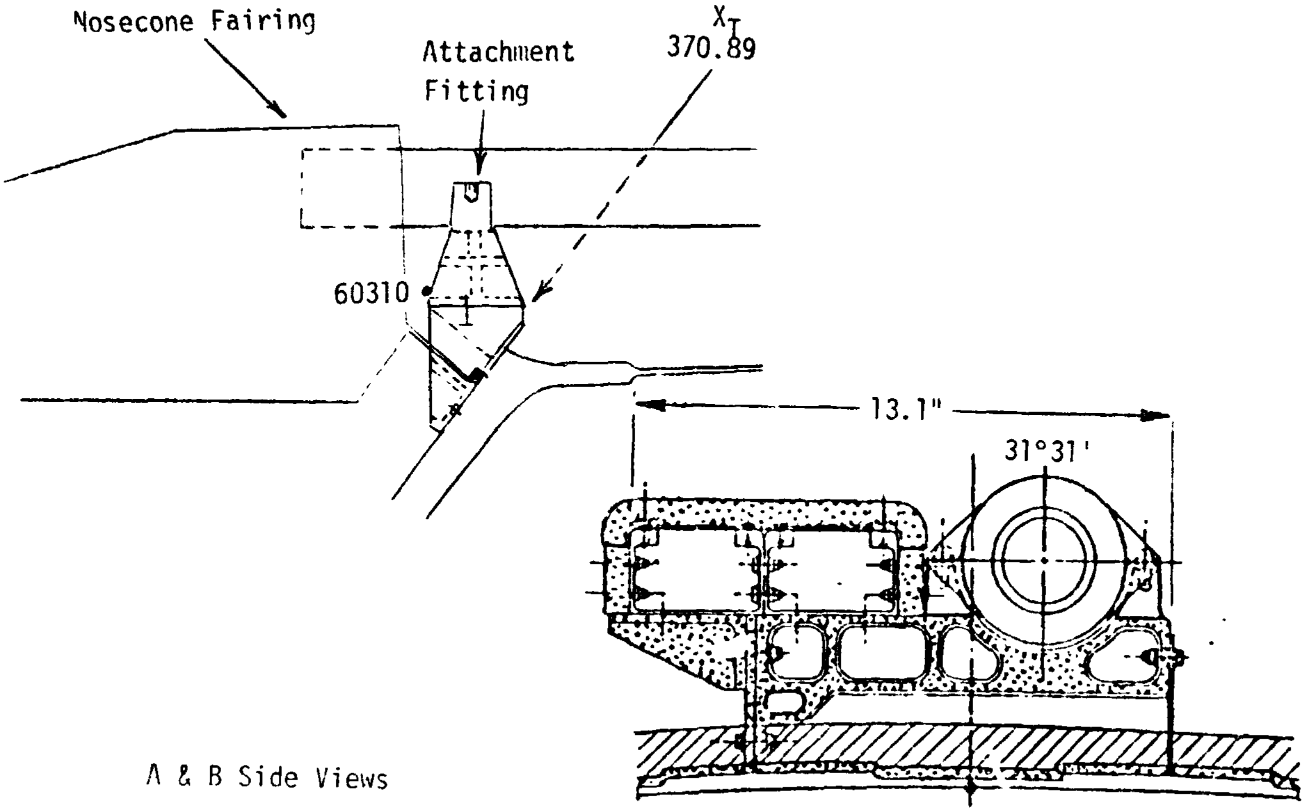

A & B Side Views

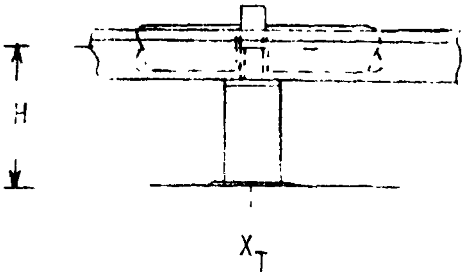

X_T	H
370.89	-
404.34	5.37
439.49	
476.16	
514.12	
553.37	
593.54	
634.51	
676.08	
718.04	
760.21	5.69

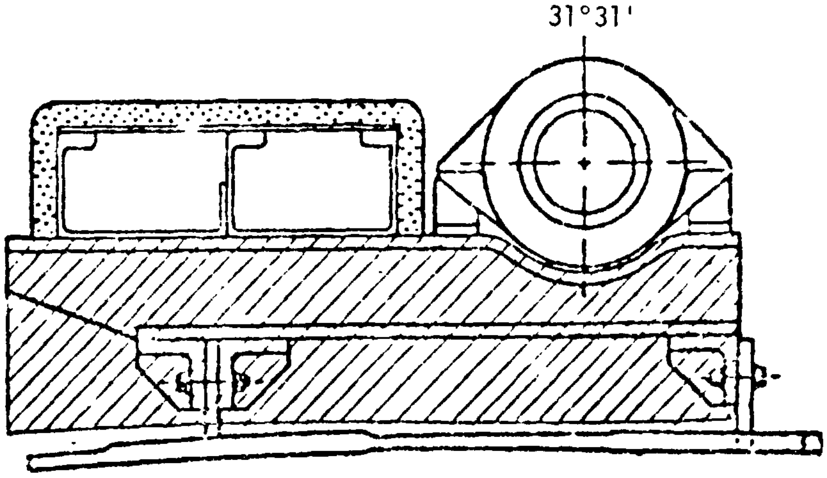

Fig. B8 GO_2 Pressure Line - Electrical Conduit Attachment Fittings Type A and Type B and Cross-Sectional Views

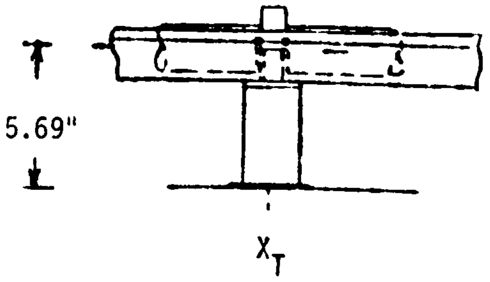

Side View of Attachment Fitting

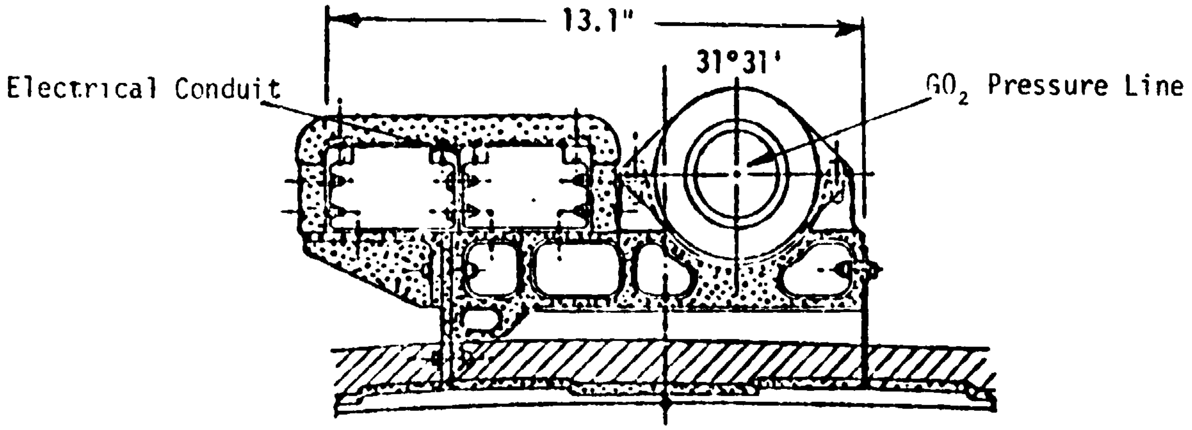

Cross-Sectional View of Attachment Fitting

Protuberance Body Point Definitions		
X_T (In.)	Body Point	Location
794.13	62020	Forward Face on Fitting
828.06	62120	Forward Face on Fitting

Fig. B9 GO_2 Pressure Line - Electrical Conduit Attachment Fittings (Type B)

Table B10

CONE OGIVE PROTUBERANCE BODY POINT DEFINITIONS

B. P. No.	X_T (in.)	θ_T (deg.)					Location
60320	364.0	313.5					Vent Louver Forward ℄
60321	368.0	328.6					Side
60322	371.0	313.5					Aft ℄
60323	372.0	↓					℄
60324	365.0	↓					[illegible]om Fwd.
60325	366.0	↓					Front
60326	365.0	↓					[illegible]
60327	366.0	↓					TBF[2]
60328	368.0	↓					Bottom Fwd.
60329	369.0	↓					Top Fwd.
60330	368.0	↓					BBF
60331	369.0	↓					TBF
60109	353.0	31.5					Top of Conduit Fairing
60209	357.0	↓					↓
60309	364.0	↓					↓
60203	357.0	9.5					Side of Conduit Fairing
60303	364.0	9.5					↓
60215	357.0	53.5					↓
60315	364.0	53.5					↓
60400	402.5	357.4					Skin Points below & near GO_2 Line & Electrical Conduit
60405	↓	16.9					↓
60407	↓	24.3					↓
• 60409	↓	31.5					↓
60411	↓	38.7					↓
60413	↓	46.1					↓
60418		65.6					↓
60500	409.9	0.1					↓
60503	↓	11.4					↓
60506	↓	21.6					↓
60507	↓	24.9					↓
60509	↓	31.5					↓
60510	↓	38.1					↓
60511	↓	41.4					↓
60514	↓	51.6					↓
60517		62.9					

[1] Bottom Back Face

[2] Top Back Face

Table B10 (Cont. 1)

CONE OGIVE PROTUBERANCE BODY POINT DEFINITIONS

B. P. No.	X_T (in.)	θ_T (deg.)					Location
60601	422.3	3.2					Skin Points below & near GO$_2$ Line and Electrical Conduit
60604		14.1					
60606		22.9					
60607		25.8					
*60609		31.5					
60610		37.2					
60611		40.1					
60614		46.9					
60617		59.8					
60701	432.1	5.0					
60704		15.7					
60707		23.7					
60709		31.5					
60711		39.4					
60713		47.3					
60716		58.0					
60802	437.6	5.9					
60806		21.5					
60807		26.5					
*60809		31.5					
60810		36.5					
60812		41.5					
60816		57.1					
60903	474.2	9.5					
60907		23.7					
60908		27.6					
*60909		31.5					
60910		35.4					
60911		39.3					
60915		53.5					
61003	512.1	11.8					
61007		24.9					
61008		28.2					
*61009		31.5					
61010		34.8					
61011		38.1					
61014		51.2					

Table B10 (Cont. 2)

CONE OGIVE PROTUBERANCE BODY POINT DEFINITIONS

B. P. No.	X_T (in.)	Θ_T (deg.)					Location
61104	551.3	14.0					Skin Points Below and Near GO_2 Line and Electrical Conduit
61107	↓	25.7					↓
61108	↓	28.6					↓
*61109	↓	31.5					↓
61110	↓	34.4					↓
61111	↓	37.3					↓
61114	↓	49.0					↓
61204	591.4	15.6					↓
61207	↓	26.3					↓
61208	↓	28.9					↓
*61209	↓	31.5					↓
61210	↓	34.1					↓
61211	↓	36.7					↓
61313	↓	47.4					↓
61305	632.3	16.7					↓
61307	↓	26.6					↓
61308	↓	29.1					↓
*61309	↓	31.5					↓
61310	↓	33.9					↓
61311	↓	36.4					↓
61313	↓	46.3					↓
61405	673.9	17.4					↓
61407	↓	26.8					↓
61408	↓	29.2					↓
*61409	↓	31.5					↓
61410	↓	33.8					↓
61411	↓	36.2					↓
61413	↓	45.6					↓
61505	715.8	17.9					↓
61507	↓	27.0					↓
61508	↓	29.3					↓
*61509	↓	31.5					↓
61510	↓	33.7					↓
61511	↓	36.0					↓
61513	↓	45.1					↓
61605	759.2	17.9					↓
61607	↓	27.0					↓
61608	↓	29.3					↓

Table B10 (Cont. 3)

CONE OGIVE PROTUBERANCE BODY POINT DEFINITION

B. P. No.	X_T (in.)	Θ_T (deg.)					Location
*61609	759.2	31.5					Skin Points Below and Near GO_2 Line and Electrical Conduit
61610		33.8					
61611	↓	36.0					
61613		45.1					↓
61705	762.2	17.9					
61706		24.8					
61707		28.1					
61708		29.3					
61709		31.5					
61710		33.7					
61711		34.9					
61712		38.3					
61713	↓	45.1					
61805	773.7	17.9					
61806		24.8					
61807		28.1					
61808		29.3					
61809		31.5					
61810		33.7					
61811		34.9					
61812		38.3					
61813	↓	45.1					
61905	786.2	17.9					
61907		24.8					
61908		28.1					
61909		31.5					
61910		34.9					
61911	↓	38.3					
61913		45.1					
62005	793.1	17.9					
62007		27.0					
62008		29.3					
*62009		31.5					
62010		33.8					
62011		36.0					
62013	↓	45.1					↓

Table P10 (Cont. 4)

CONE OGIVE PROTUBERANCE BODY POINT DEFINITION

B. P. No.	X_T (in.)	θ_T (deg.)					Location
62105	827.1	17.9					Skin Points Below and Near GO_2 Line and Electrical Conduit
62107	↓	27.0					
62108		29.3					↓
62109		31.5					
62110		33.8					
62111		36.0					
62113		45.1					

*B.P. with asterisk indicates skin points used as reference for bottom of electrical conduit and GO_2 pressure line. In 1977 RI environment, these B.P.s were multiplied by 1.0.

2.2. ET BARREL

This subsection contains geometry and body point information for the cylindrical section of the tank under five divisions.

2.2.1 Acreage Definition

This subsection gives the moldline geometry and related body points for the cylindrical section of the tank. Unrolled views of the surface are given showing the top view of protuberances. The information sequences is as follows:

- Intertank Region Views
- LH_2 Barrel Mid-section Views
- LH_2 Barrel Aft section Views
- Tabulated Body Points

Note: C = Division 2.2.1 on figures and tables

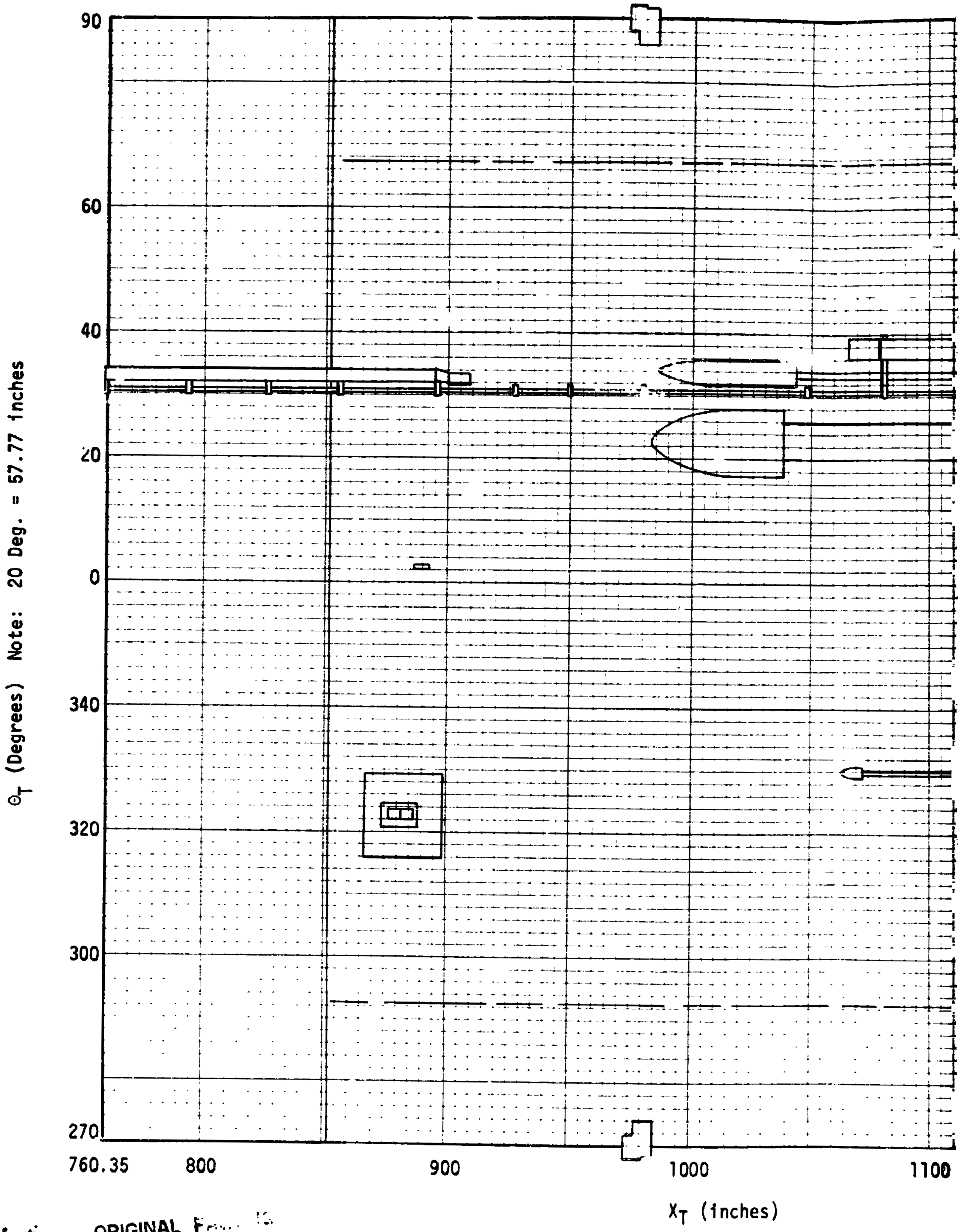

Fig. C1a Intertank and Near Region Section

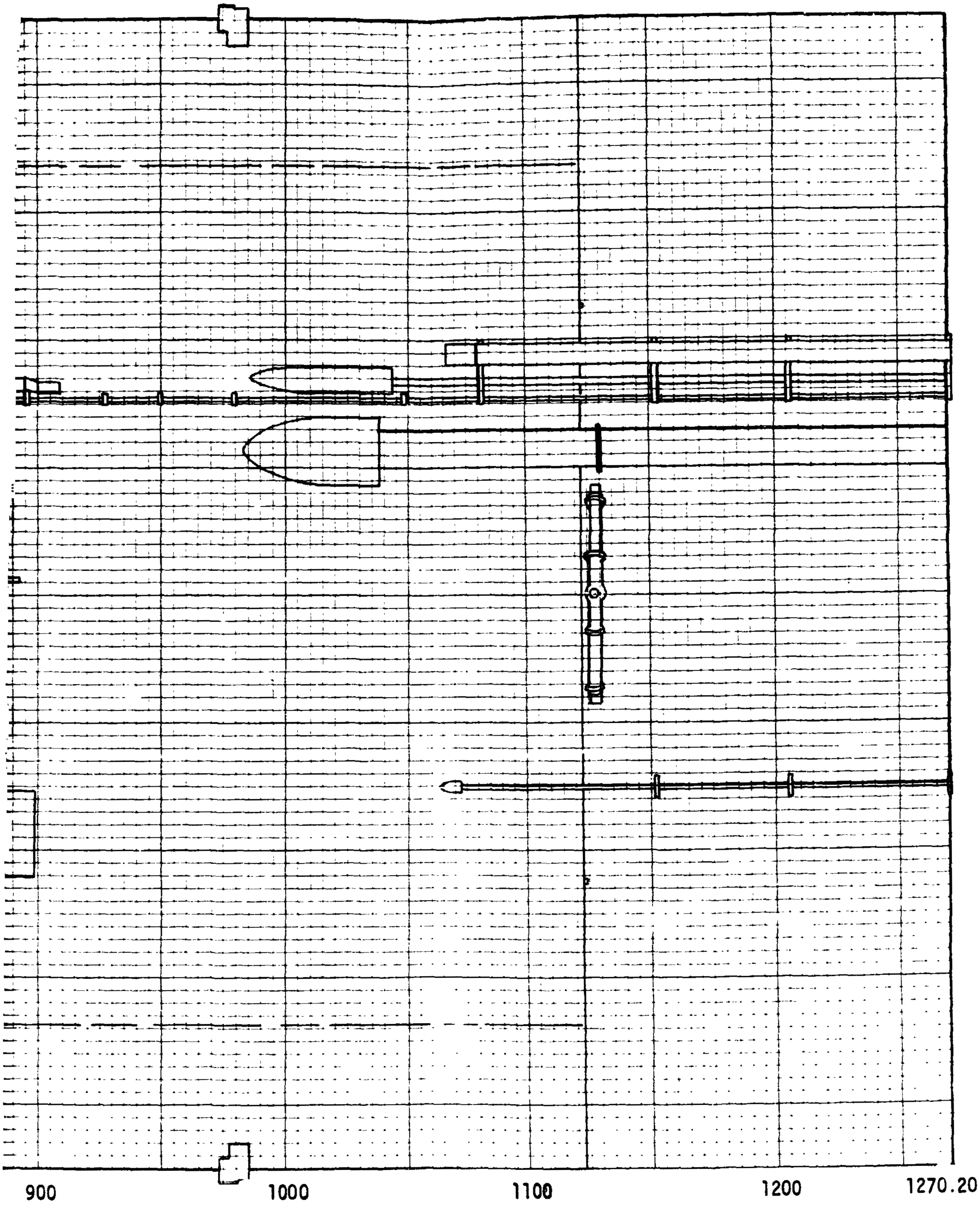

Fig. C1a Intertank and Near Region Section

ORIGINAL PAGE IS OF POOR QUALITY

2 FOLDOUT FRAME

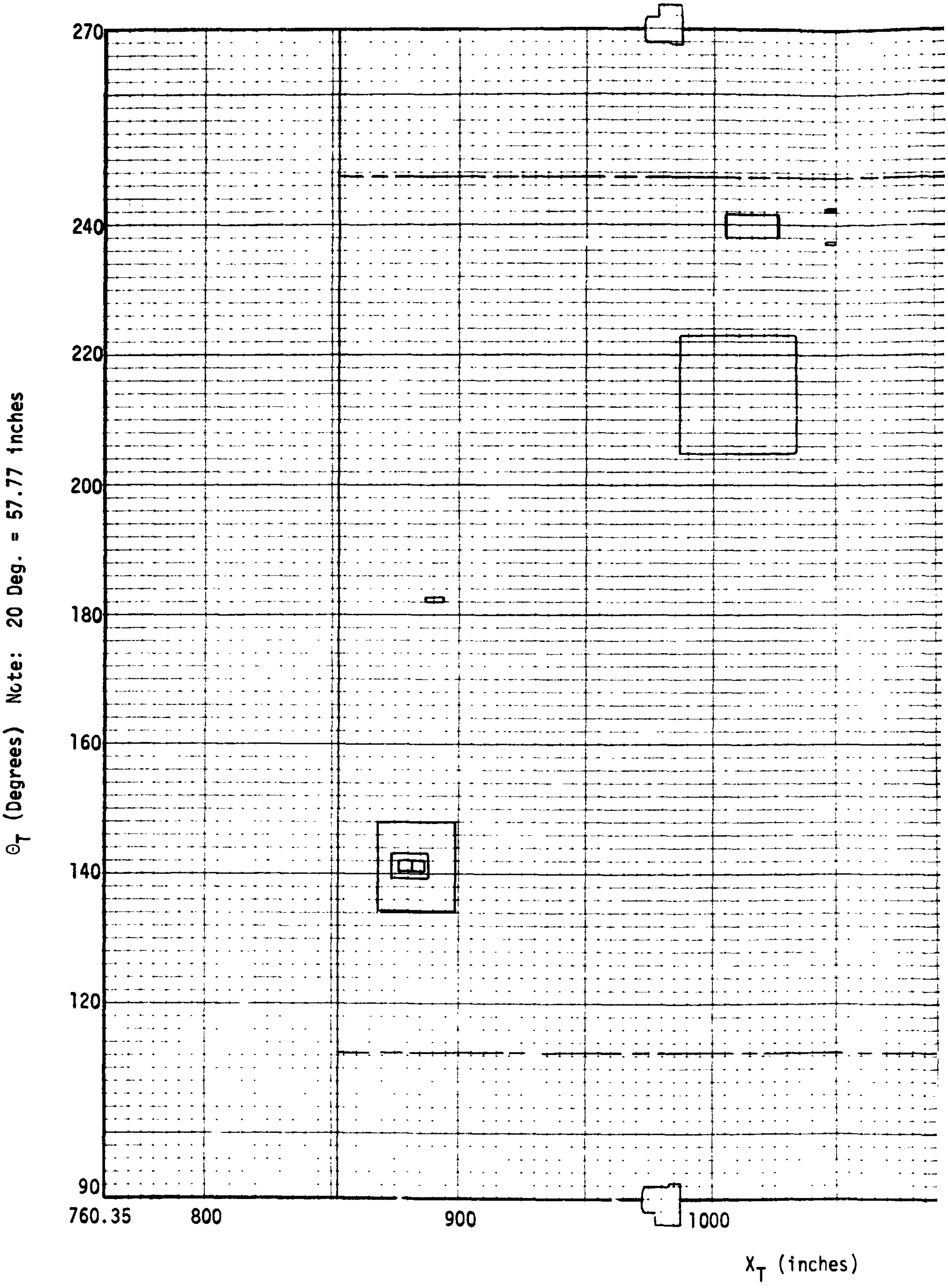

Fig. C1b Intertank and Near Regions

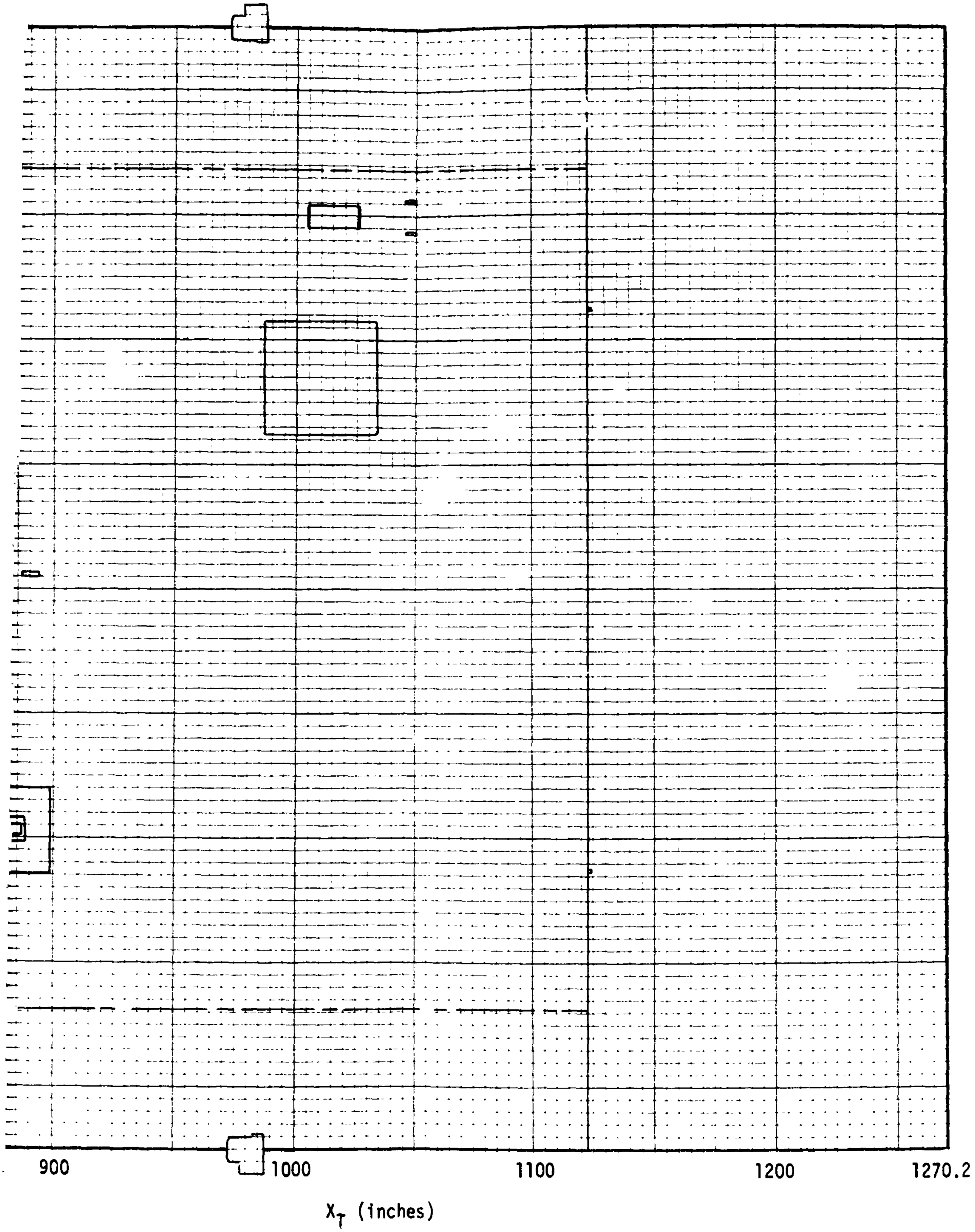

Fig. C1b Intertank and Near Regions Section

FOLDC

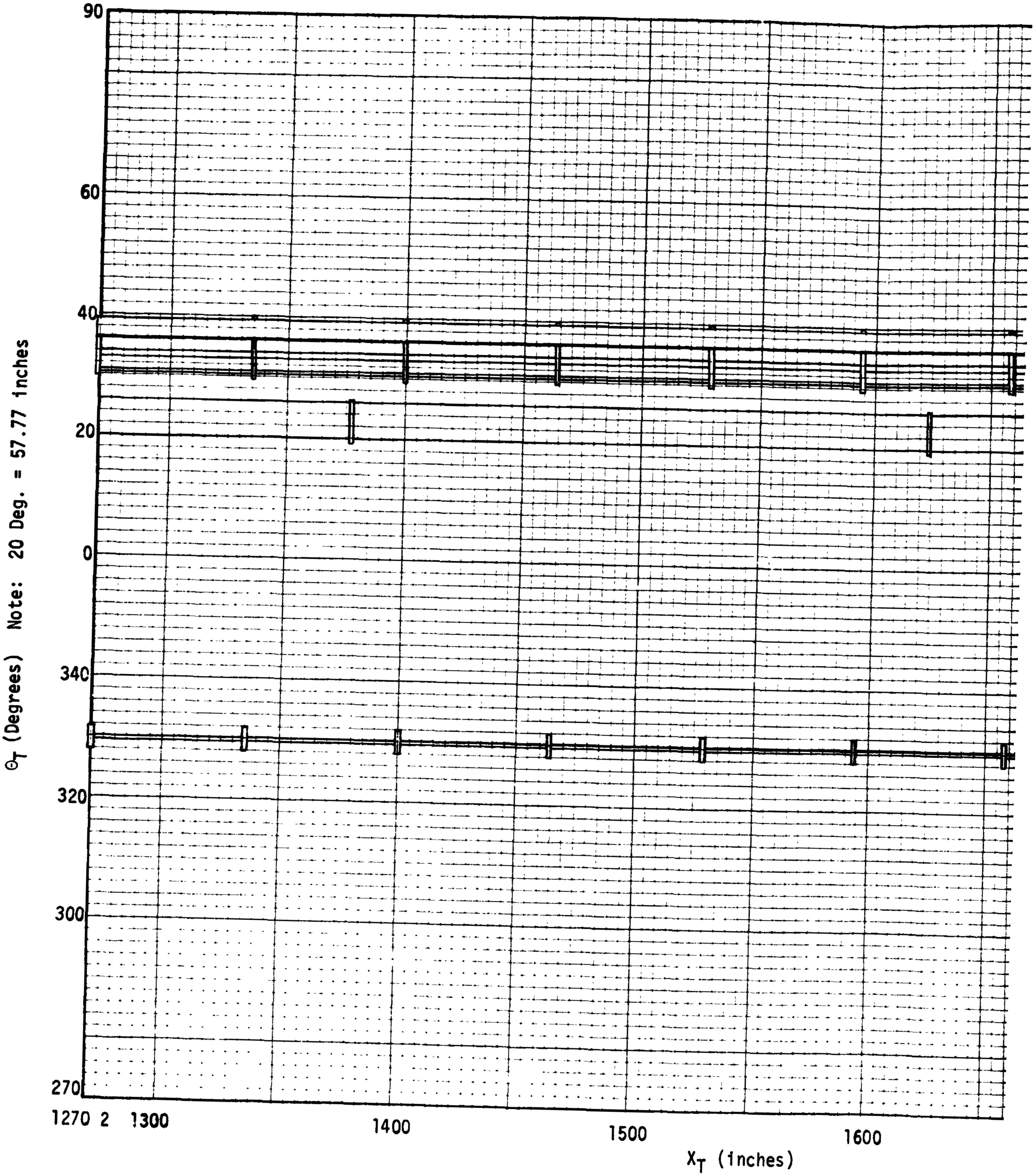

FOLDOUT FRAME

Fig. C2a LH_2 Tank Mid-Section

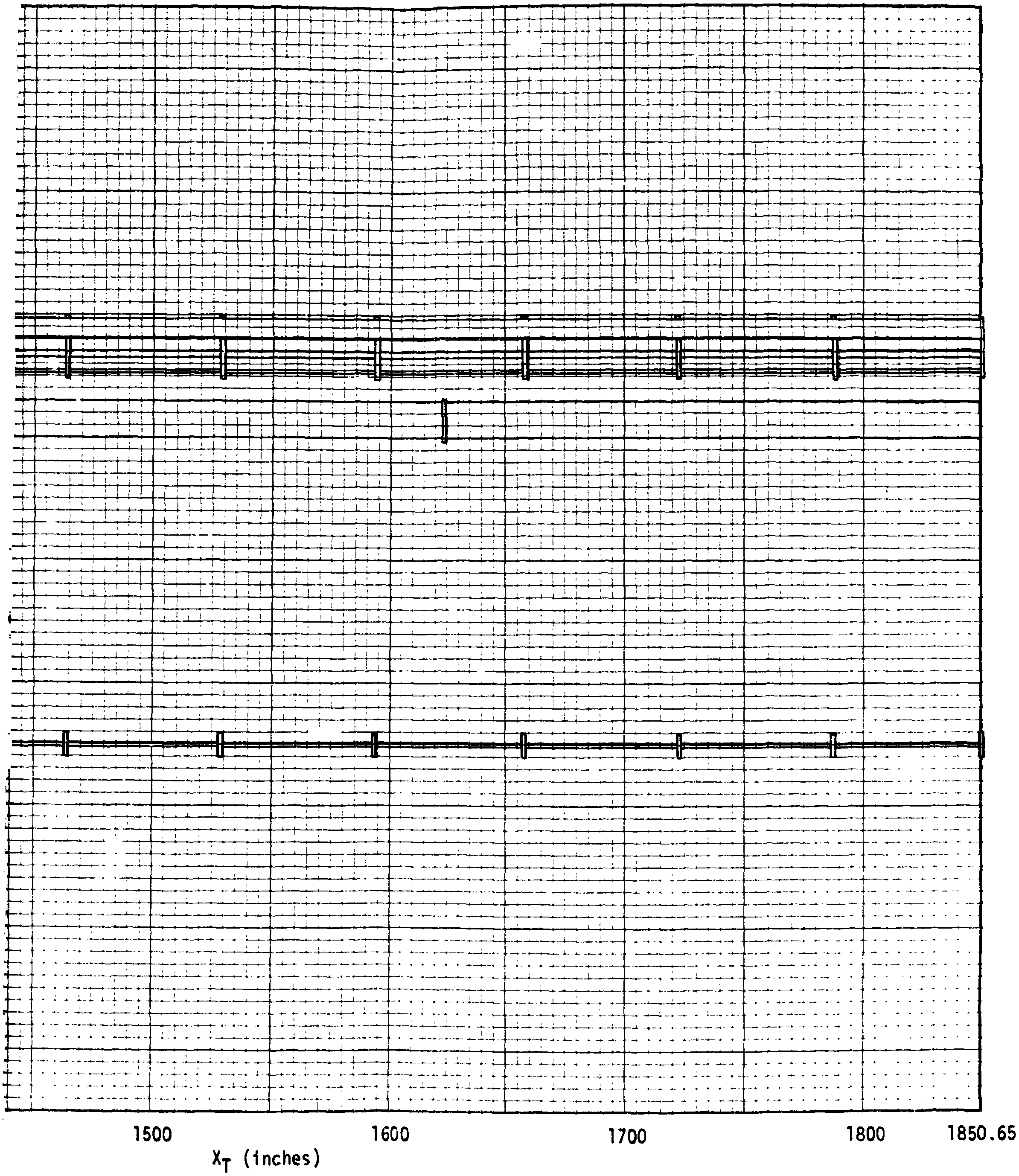

Fig. C2a LH_2 Tank Mid-Section

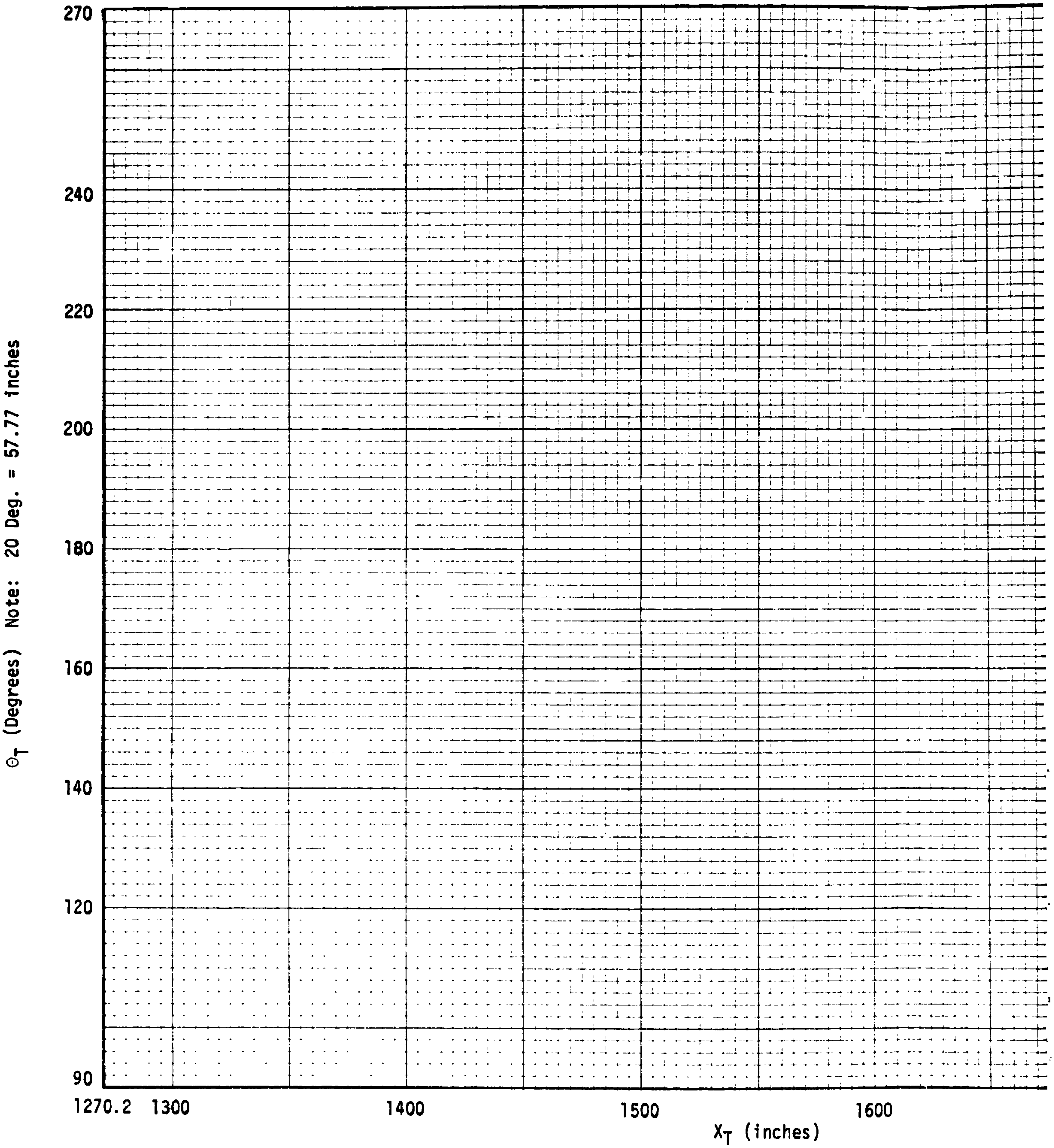

FOLDOUT FRAME

Fig. C2b LH_2 Tank Mid-Section

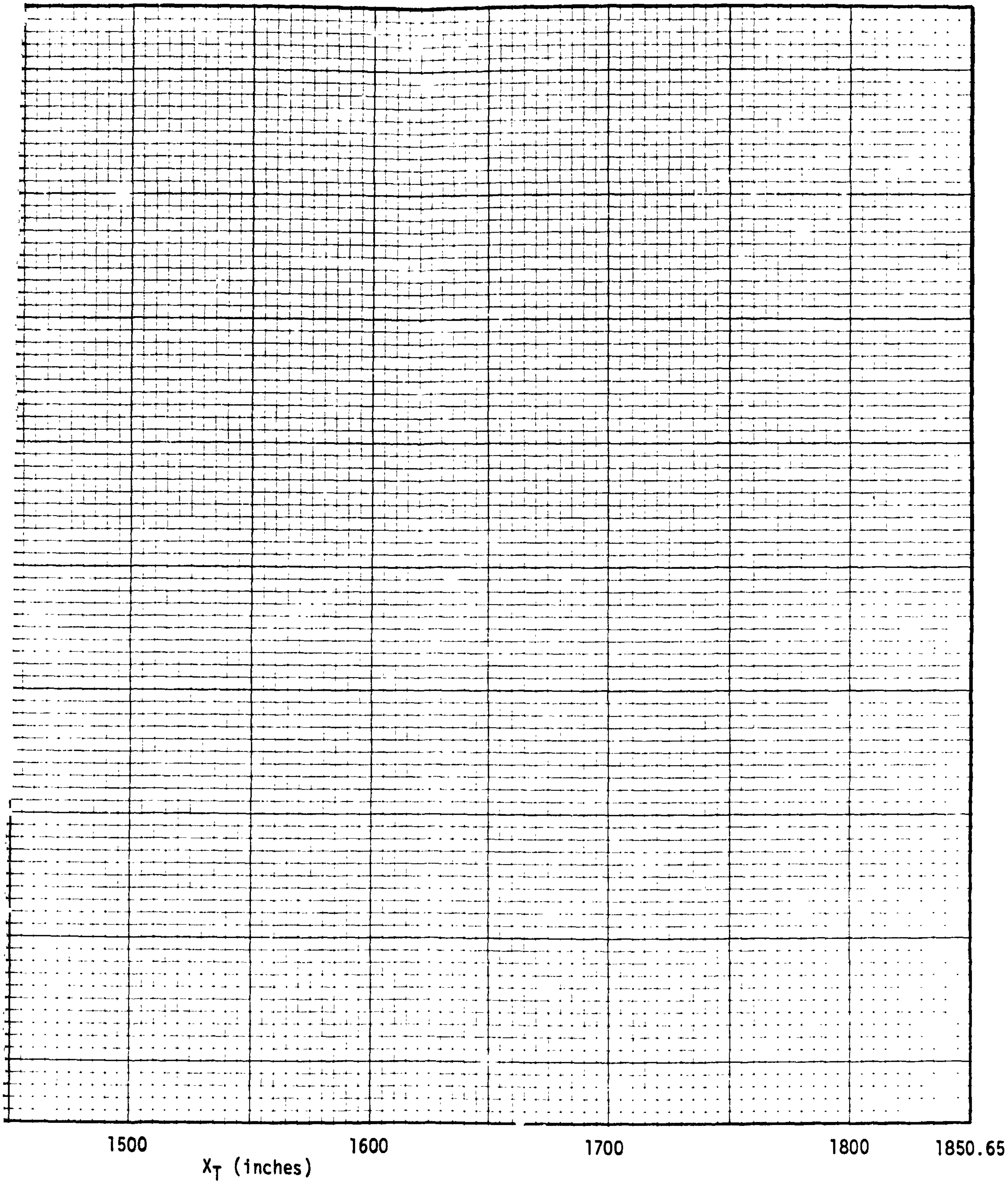

Fig. C2b LH_2 Tank Mid-Section

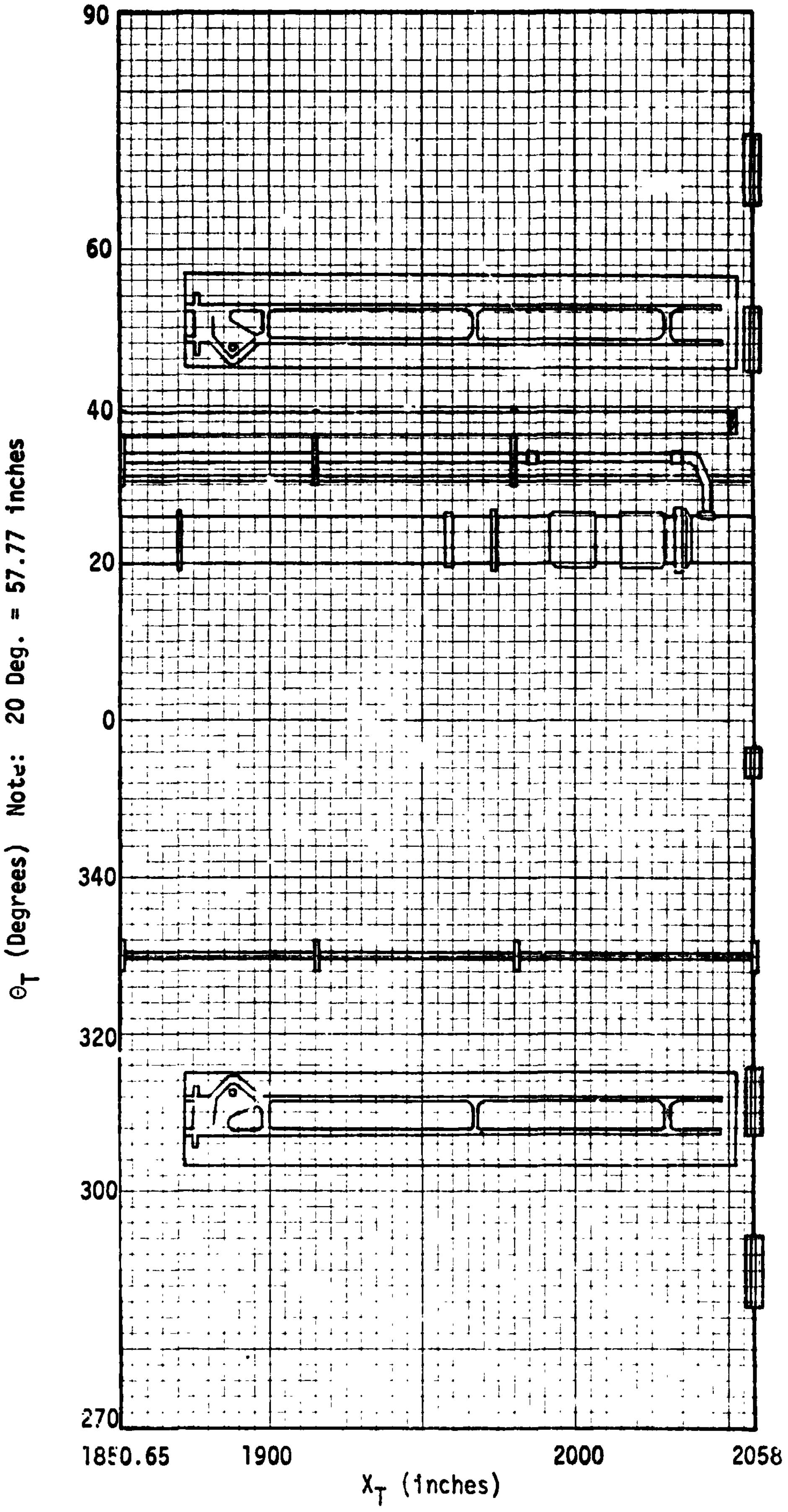

Fig. C3a LH_2 Barrel Aft Section

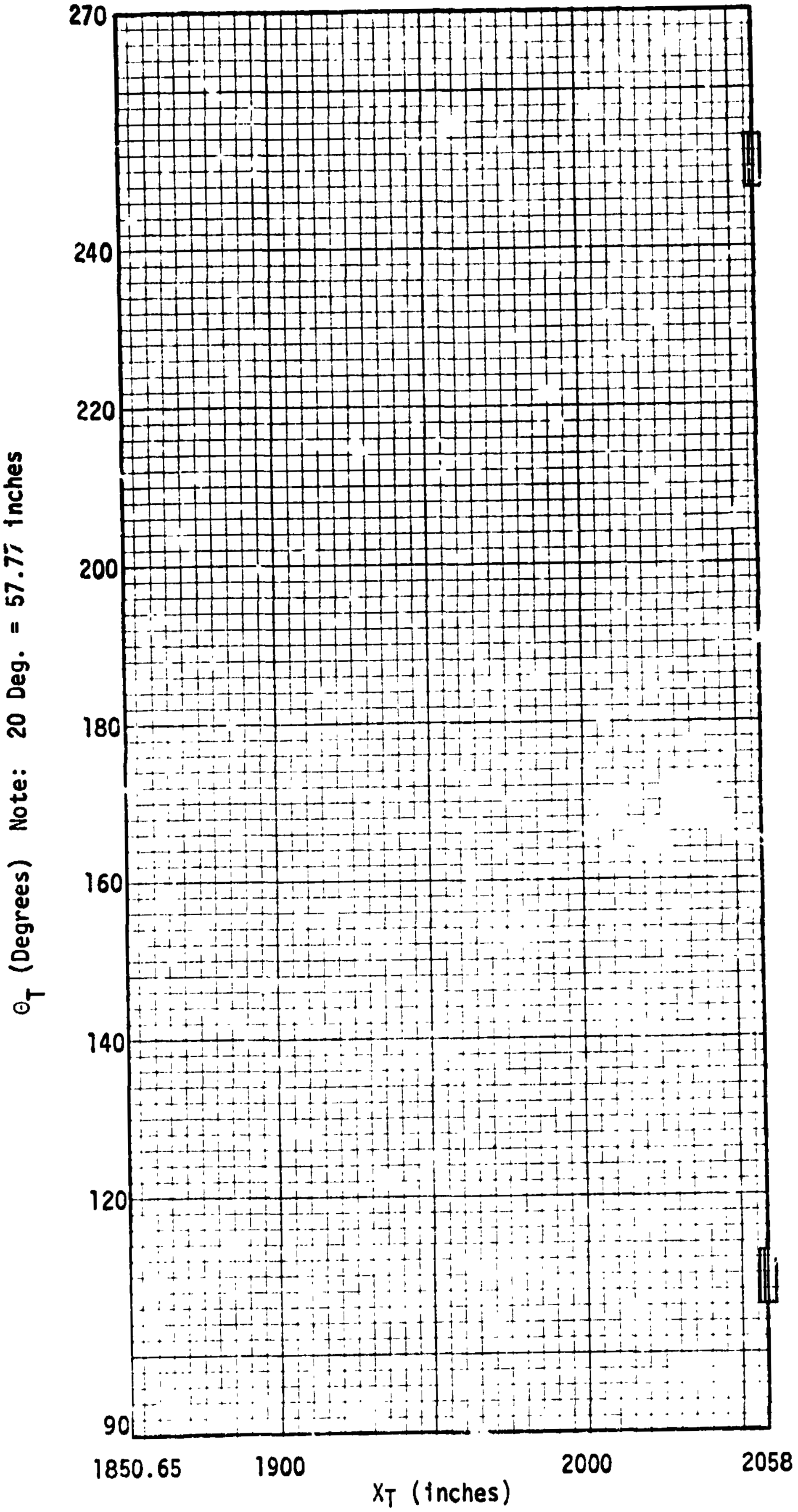

Fig. C3b [illegible] Barrel Aft Section

Table C4

BARREL ACREAGE BODY POINT DEFINITIONS

B. P. No.	X_T (in.)	Θ_T (deg.)					
7280	852.80	0					
7300	884.85	↓					
7320	929.14						
7350	973.43						
7360	1006.65						
1747	1021.7	1.5					
7380	1038.03	0					
7400	1069.40	↓					
7420	1102.62						
7430	1123.15						
7440	1137.29						
7450	1167.21	0					
7470	1201.51	↓					
7480	1229.96						
7520	1297.83						
7550	1359.15						
7590	1426.26	0					
7620	1486.49	↓					
7660	1554.69						
7690	1615.67						
7760	1743.[illegible]2						
7830	1872.20	0					
7850	1898.04	↓					
7870	1936.79						
7900	1999.54						
7920	2036.46						
7930	2058.0						
1307	2058.0	357.1					
1308	↓	358.14					
1309		358.32					
1310		3.67					
6366	1006.65	11.25					
1746	1021.7	13.5					
6386	1038.03	11.25					
6406	1069.40	↓					
6426	1102.62						

Table C4 (Cont. 1)

BARREL ACREAGE BODY POINT DEFINITIONS

B. P. No.	X_T (in.)	Θ_T (deg.)					
1112	1111.85	12.0					
1113	1121.08	12.0					
6436	1123.15	11.25					
1114	1130.30	12.0					
1115	1139.53	12.0					
1116	1148.76	12.0					
6486	1229.96	11.25					
6556	1359.15	↓					
6626	1486.49	↓					
6696	1615.67	↓					
6766	1743.02	↓					
6836	1872.20	11.25					
6906	1999.54	↓					
6926	2036.45	↓					
6368	1006.65	15.0					
6369	1006.65	19.0					
1745	1021.7	17.0					
1744	↓	17.5					
1743	↓	18.5					
1742	1021.7	19.5					
6388	1038.03	15.0					
6389	1038.03	19.0					
6408	1069.40	15.0					
6409	1069.40	19.0					
6428	1102.62	15.0					
6429	1102.62	19.0					
1117	1111.85	17.0					
1118	1121.08	17.0					
1119	1121.08	17.0					
6438	1123.15	15.0					
6439	1123.15	19.0					
1120	1126.90	17.0					
1121	1132.90	↓					
1122	1139.53	↓					
1123	1148.76	17.0					
6488	1229.96	15.0					
6489	1229.96	19.0					

Table C4 (Cont. .

BARREL ACREAGE BODY POINT DEFINITIONS

B. P. No.	X_T (in.)	θ_T (deg.)					
6558	1359.15	15.0					
6559	1359.15	19.0					
6628	1486.49	15.0					
6629	1486.49	19.0					
6698	1615.67	15.0					
6699	1615.67	19.0					
6768	1743.02	15.0					
6769	1743.02	19.0					
6838	1872.20	15.0					
6839	1872.20	19.0					
6908	1999.54	15.0					
6909	1999.54	19.0					
6928	2036.45	15.0					
6929	2036.45	19.0					
1730	885.7	23.5					
1731	987.7	↓					
1732	996.2	↓					
1733	1004.7	↓					
6361	1006.65	↓					
1734	1013.2	23.5					
1735	1017.45	↓					
6285	1086.66	↓					
6286	1111.20	↓					
6287	1118.68	↓					
6579	1124.29	23.5					
6580	1125.60	↓					
6581	1127.10	↓					
6582	1127.56	↓					
6583	1132.71	↓					
6584	1136.21	23.5					
6585	1139.95	↓					
6586	1153.30	↓					
6587	1334.37	↓					
6588	1358.90	↓					

Table C4 (Cont. 3)

BARREL ACREAGE BODY POINT DEFINITIONS

B. P. No.	X_T (in.)	Θ_T (deg.)					
6589	1366.38	23.5					
6590	1371.99	↓					
6591	1373.3	↓					
6592	1374.80	↓					
6593	1375.26	↓					
6594	1380.41	23.5					
6595	1383.91	↓					
6596	1387.65	↓					
6597	1401.0	↓					
6598	1434.36	↓					
6599	1581.06	23.5					
6601	1605.60	↓					
6602	1613.08	↓					
6603	1618.69	↓					
6604	1620.0	↓					
6605	1621.50	23.5					
6606	1621.96	↓					
6607	1627.11	↓					
6608	1630.61	↓					
6609	1634.35	↓					
6610	1647.70	23.5					
6611	1827.76	↓					
6612	1852.30	↓					
6613	1859.78	↓					
6614	1865.39	↓					
6615	1866.70	23.5					
6616	1868.20	↓					
6617	1868.66	↓					
6618	1873.81	↓					
6619	1877.31	↓					
6620	1881.05	23.5					
6621	1486.49	↓					
6630	1894.40	↓					
6631	1930.76	↓					
6632	1955.30	↓					

Table C4 (Cont. 4)

BARREL ACREAGE BODY POINT DEFINITIONS

B. P. No.	X_T (in.)	Θ_T (deg.)					
6633	1962.78	23.5					
6634	1968.39	↓					
6635	1969.70	↓					
6636	1971.20	↓					
6637	1971.66	↓					
6638	1976.81	23.5					
6639	1980.31	↓					
6640	1984.05	↓					
6641	1997.40	↓					
6642	2016.61	↓					
6643	2024.09	23.5					
6644	2029.70	↓					
6645	2031.01	↓					
6646	2032.51	↓					
6647	2032.97	↓					
6648	2038.12	23.5					
6649	2041.62	↓					
6650	2045.36	↓					
6651	2058.71	↓					
6367	1006.65	29.0					
1738	1021.70	29.25					
1739	↓	28.25					
1740	↓	27.50					
1741	↓	26.75					
6387	1038.03	29.0					
6407	1069.40	↓					
6427	1102.62	↓					
6437	1123.15	↓					
6487	1229.96	↓					
6557	1359.15	29.0					
6627	1486.49	↓					
6697	1615.67	↓					
6767	1743.02	↓					
6837	1872.20	↓					
6907	1999.54	29.0					
6927	2036.45	↓					

Table C4 (Cont. 5)

BARREL ACREAGE BODY POINT DEFINITIONS

B. P. No.	X_T (in.)	Θ_T (deg.)					
1737	1021.7	32.5					
6288	1056.15	34.0					
6282	1069.4	↓					
6283	1113.85						
6284	1123.15						
6501	1123.15						
6502	1127.55	34.0					
6503	1132.09	↓					
6504	1136.61						
6505	1139.34						
6506	1140.24						
6507	1145.69	34.0					
6508	1150.21	↓					
6509	1154.75						
6510	1178.35						
6511	1192.05						
6512	1196.59	34.0					
6513	1201.11	↓					
6514	1203.84						
6515	1204.74						
6516	1210.19						
6517	1214.71	34.0					
6518	1219.25	↓					
6519	1229.96						
6520	1242.85						
6521	1256.55						
6522	1261.09	34.0					
6523	1265.61	↓					
6524	1268.34						
6525	1269.24						
6526	1274.69						
6527	1279.21	34.0					
6528	1283.75	↓					
6529	1565.35						
6530	1579.05						
6531	1583.59						

Table C4 (Cont. 6)

BARREL ACREAGE BODY POINT DEFINITIONS

B. P. No.	X_T (in.)	Θ_T (deg.)					
6532	1588.11	34.0					
6533	1590.84	↓					
6534	1591.74	↓					
6535	1597.19	↓					
6536	1601.71	↓					
6537	1606.25	34.0					
6538	1615.67	↓					
6539	1823.35	↓					
6540	1837.05	↓					
6541	1841.59	↓					
6542	1846.11	34.0					
6543	1848.84	↓					
6544	1849.74	↓					
6545	1855.19	↓					
6546	1859.71	↓					
6547	1864.25	34.0					
6548	1872.2	↓					
6549	1887.85	↓					
6561	1901.55	↓					
6562	1906.09	↓					
6563	1910.61	34.0					
6564	1913.34	↓					
6565	1914.24	↓					
6566	1919.69	↓					
6567	1924.21	↓					
6568	1928.75	34.0					
6569	1952.35	↓					
6571	1966.05	↓					
6572	1970.59	↓					
6573	1975.11	↓					
6574	1977.84	34.0					
6575	1978.74	↓					
6576	1984.19	↓					
6577	1988.71	↓					
6578	1993.25	↓					
6570	1999.54	↓					

Table C4 (Cont. 7)

BARREL ACREAGE BODY POINT DEFINITIONS

B. P. No.	X_T (in.)	Θ_T (deg.)					
6365	1006.65	40.0					
6385	1038.03	↓					
6405	1069.40	↓					
6424	1102.62	37.7					
6425	1102.62	40.0					
6422	1118.15	37.7					
6435	1123.15	40.0					
6485	1229.96	↓					
6555	1359.15	↓					
6625	1486.49	↓					
6695	1615.67	↓					
6765	1743.02	40.0					
6835	1872.20	↓					
6905	1999.54	↓					
6925	2036.45	↓					
1736	1021.7	44.0					
7289	852.80	180.0					
7309	884.85	↓					
7329	929.14	↓					
7359	973.43	↓					
7369	1006.65	↓					
7389	1038.03	180.0					
7409	1069.40	↓					
7429	1102.62	↓					
7439	1123.15	↓					
7449	1137.29	↓					
7459	1167.21	180.0					
7479	1209.51	↓					
7489	1229.96	↓					
7529	1297.83	↓					
7559	1359.15	↓					
7599	1426.26	180.0					
7629	1486.49	↓					
7669	1554.69	↓					
7699	1615.67	↓					
7769	1743.02	↓					

Table C4 (Cont. 8)

BARREL ACREAGE BODY POINT DEFINITIONS

B. P. No.	X_T (in.)	Θ_T (deg.)					
7839	1872.20	180.0					
7859	1898.04	↓					
7879	1936.79						
7909	1999.54						
7929	2036.46						
7939	2058.0						
7287	852.80	225.0					
7307	884.85	↓					
7327	929.14						
7357	973.43						
7367	1006.65						
7387	1038.03	225.0					
7407	1069.40	↓					
7427	1102.62						
7437	1123.15						
7447	1137.29						
7457	1167.21	225.0					
7477	1201.51	↓					
7487	1229.96						
7527	1297.83						
7557	1359.15						
7597	1426.26	225.0					
7627	1486.49	↓					
7667	1554.69						
7697	1615.67						
7767	1743.02						
7837	1872.20	225.0					
7857	1898.04	↓					
7877	1936.79						
7907	1999.54						
7927	2036.46						
7937	2058.0						
7286	852.80	247.5					
7306	884.86	↓					
7326	929.14						
7356	973.43						
7366	1006.65						

Table C4 (Cont. 9)

BARREL ACREAGE BODY POINT DEFINITIONS

B. P. No.	X_T (in.)	Θ_T (deg.)					
7386	1038.03	247.5					
7406	1069.40	↓					
7426	1102.62						
7436	1123.15						
7446	1137.29						
7456	1167.21	247.5					
7476	1201.51	↓					
7486	1229.96						
7526	1297.83						
7556	1359.15						
7596	1426.26	247.5					
7626	1486.49	↓					
7666	1554.69						
7696	1615.67						
7766	1743.02						
7836	1872.20	247.5					
7856	1898.04	↓					
7876	1936.79						
7906	1999.54						
1040	2006.75	250.5					
7926	2036.46	247.6					
1041	2040.75	250.5					
1042	2046.75	250.5					
1051	2048.75	247.4					
1043	2048.75	250.5					
1044	2050.75	250.5					
1052	2052.75	247.4					
1045	2052.75	250.5					
1053	2053.75	247.4					
1046	2053.75	250.5					
1055	2058.0	246.39					
1054	2058.0	247.0					

Table C4 (Cont. 10)

BARREL ACREAGE BODY POINT DEFINITIONS

B. P. No.	X_T (in.)	Θ_T (deg.)					
7285	852.80	270.0					
7305	884.85	↓					
7325	929.14	↓					
1000	952.83	↓					
1001	971.48	↓					
7355	973.43	270.0					
1002	977.43	↓					
1003	981.43	↓					
1006	981.43	270.52					
1004	982.43	270.0					
1007	982.43	270.52					
1009	982.43	|					
1005	983.43	270.0					
1008	983.43	270.52					
1010	983.43	271.04					
1011	983.43	271.56					
1012	1003.28	270.0					
1013	1004.73	↓					
7365	1006.65	↓					
7385	1038.03	↓					
7405	1069.40	↓					
7425	1102.62	270.0					
7435	1123.15	↓					
7445	1137.29	↓					
7455	1167.21	↓					
7475	1201.51	↓					
7485	1229.96	270.0					
7525	1277.83	↓					
7555	1359.15	↓					
7595	1426.26	↓					
7625	1486.49	↓					
7665	1554.69	270.0					
7695	1615.67	↓					
7765	1763.02	↓					
7835	1872.20	↓					
7855	1898.04	↓					

Table C4 (Cont. 11)

BARREL ACREAGE BODY POINT DEFINITIONS

B. P. No.	X_T (in.)	Θ_T (deg.)					
7875	1936.79	270.0					
7905	1999.54	↓					
7925	2036.46	↓					
7935	2058.0	↓					
1029	2044.25	284.65					
1030	2043.45	↓					
1031	2052.65	↓					
1033	2058.0	281.74					
1032	2058.0	283.92					
7284	852.80	292.5					
7304	884.85	↓					
7324	929.14	↓					
7354	973.43	↓					
7364	1006.65	↓					
7384	1038.03	292.5					
7404	1069.40	↓					
7424	1102.62	↓					
7434	1123.15	↓					
7444	1137.29	↓					
7454	1167.21	292.5					
7474	1201.51	↓					
7484	1229.96	↓					
7524	1297.83	↓					
7554	1359.15	↓					
7594	1426.26	292.5					
7624	1486.49	↓					
7664	1554.69	↓					
7694	1615.67	↓					
7764	1743.02	↓					
7834	1872.20	292.5					
7854	1898.04	↓					
7874	1936.79	↓					
1020	1968.65	289.5					
7904	1999.54	292.5					
1021	2031.65	289.5					
7924	2036.46	292.5					

Table C4 (Cont. 12)

BARREL ACREAGE BODY POINT DEFINITIONS

B. P. No.	X_T (in.)	Θ_T (deg.)					
1022	2044.25	289.5					
1023	2048.45	↓					
1024	2050.55						
1025	2052.65						
1405	1877.74	304.0					
1406	1914.65	↓					
1407	1951.56						
1400	1803.92	309.38					
1401	1822.38	↓					
1402	1840.83						
1403	1859.29						
1404	1868.51						
1200	2038.5	312.58					
1201	2042.5	↓					
1202	2046.5						
1203	2050.5						
1204	2052.5						
1205	2053.5						
7282	852.80	315.0					
7302	884.85	↓					
7322	929.14						
7352	973.43						
7362	1003.65						
7382	1038.03	315.0					
7402	1069.40	↓					
7422	1102.62						
7432	1123.15						
7442	1137.29						
7452	1167.21	315.0					
7472	1201.51	↓					
7482	1229.96						
7522	1297.83						
7552	1359.15						
7592	1426.26	315.0					
7622	1486.49	↓					
7662	1554.69						

Table C4 (Cont. 13)

BARREL ACREAGE BODY POINT DEFINITIONS

B. P. No.	X_T (in.)	Θ_T (deg.)					
7692	1615.67	315.0					
7762	1743.02	↓					
7832	1872.20	315.0					
1408	1877.74	↓					
7852	1898.04						
1409	1914.65						
7872	1936.79						
1410	1951.56	315.0					
1411	1970.02	↓					
1412	1988.47						
7902	1999.54						
7922	2036.46						
1209	2058.0	316.78					
1210	↓	317.93					
1211		319.38					
6280	1060.65	330.0					
6403	1069.40	327.0					
6401	1069.40	333.0					
6423	1102.62	327.0					
6421	1102.62	333.0					
6281	1107.65	330.0					
6433	1123.15	327.0					
6431	1123.15	333.0					
6430	1131.15	330.0					
6432	1139.29	↓					
6434	1139.65						
6440	1147.75						
6441	1149.58						
6442	1151.85	330.0					
6443	1172.65	↓					
6445	1196.15						
6446	1203.29						
6447	1204.65						
6448	1212.75	330.0					
6449	1214.58	↓					
6450	1216.85						

Table C4 (Cont. 14)

BARREL ACREAGE BODY POINT DEFINITIONS

B. P. No.	X_T (in.)	θ_T (deg.)					
6483	1229.96	327.0					
6481	1229.96	333.0					
6451	1237.65	.0					
6452	1302.65	↓					
6453	1326.15	↓					
6454	1333.29	↓					
6455	1334.65	↓					
6456	1342.75	330.0					
6457	1344.58	↓					
6458	1346.85	↓					
6553	1359.15	327.0					
6551	1359.15	333.0					
6459	1367.65	330.0					
6623	1486.49	327.0					
6621	1486.49	333.0					
6693	1615.67	327.0					
6691	1615.67	333.0					
6763	1743.02	327.0					
6761	1743.02	333.0					
6833	1872.20	327.0					
6831	1872.20	333.0					
6460	1887.65	330.0					
6461	1911.15	↓					
6462	1918.29	↓					
6463	1919.65	↓					
6464	1927.75	↓					
6465	1929.58	330.0					
6466	1931.85	↓					
1413	1936.79	322.3					
1414	1936.79	330.2					
6467	1952.65	330.0					
6468	1976.15	↓					
6469	1983.29	↓					
6470	1984.65	↓					
6471	1992.75	↓					

Table C4 (Cont. 15)

BARREL ACREAGE BODY POINT DEFINITIONS

B. P. No.	X_T (in.)	Θ_T (deg.)					
6472	1994.58	330.0					
6473	1996.85	330.0					
6903	1999.54	327.0					
6901	1999.54	333.0					
6474	2017.65	330.0					
6923	2036.45	327.0					
6921	2036.45	333.0					
6475	2041.15	330.0					
6476	2048.29	↓					
6477	2049.65						
1212	2058.0	322.16					
6478	2057.75	330.0					
7281	852.80	337.5					
7301	884.85	↓					
7321	929.14						
7351	973.43						
7361	1006.65						
7381	1038.03	337.5					
7401	1069.40	↓					
7421	1102.62						
7431	1123.15						
7441	1137.29						
7451	1167.21	337.5					
7471	1201.51	↓					
7481	1229.96						
7521	1297.83						
7551	1359.15						
7591	1426.26	337.5					
7621	1486.49	↓					
7661	1554.69						
7691	1615.67						
7761	1743.02						
7831	1872.20	337.5					
7851	1898.04	337.5					
1700	1908.6	340.0					
7871	1936.79	337.5					
7901	1999.54	337.5					

Table C4 (Cont. 16)

BARREL ACREAGE BODY POINT DEFINITIONS

B. P. No.	X_T (in.)	θ_T (deg.)					
1701	2028.6	340.0					
7921	2036.46	337.5					
1702	2038.6	340.0					
1703	2048.6	340.0					
7931	2058.0	337.5					
1704	2058.6	340.0					
1705	2063.6	↓					
1100	1111.85	343.0					
1101	1121.08	↓					
1102	1124.90	↓					
1103	1126.90	343.0					
1104	1132.90	↓					
1105	1139.53	↓					
1106	1148.76	↓					
1107	1111.85	348.0					
1108	1121.08	↓					
1109	1130.30	↓					
1110	1139.53	↓					
1111	1148.76	↓					
1300	2032.0	355.0					
1301	2046.5	↓					
1302	2051.5	↓					
1303	2053.5	↓					
1304	2054.5	↓					

2.2.2 Protuberance on Intertank

This subsection contains geometry and body point information for all protuberances located on the intertank ($852.8 \leq X_T \leq 1123.15$). The information sequence is as follows:

- Thrust and stringer panels
- Access door
- Forward ET/SRB Attachment
- Area influenced by bolt catcher
- Umbilical disconnect
- LH_2 Sidewall body point adjacent to RSS Electrical connector
- Range safety antenna

Note: D = Division 2.2.2 in figures and tables

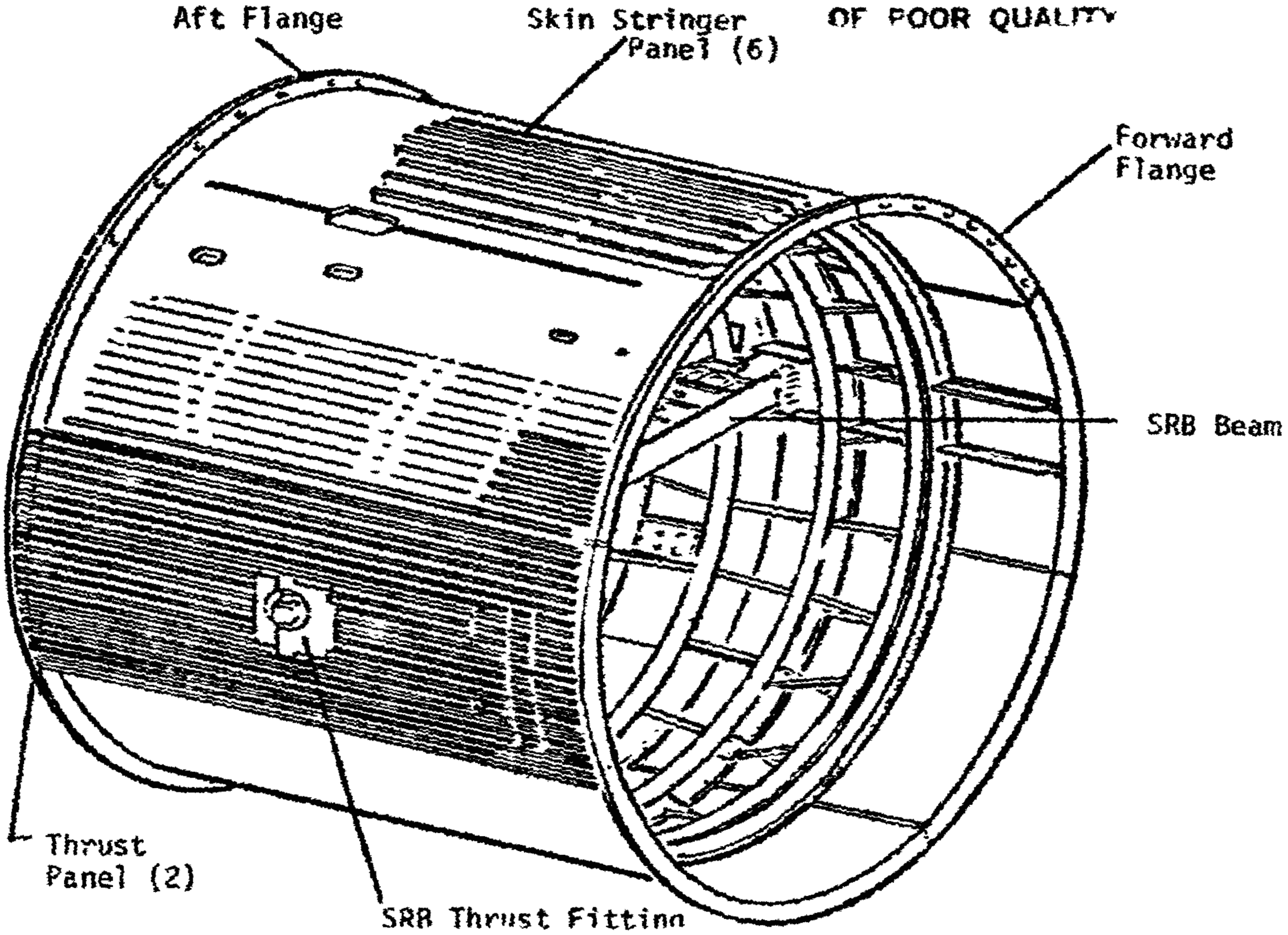

Fig. D1 Thrust Panel and Skin Stringer Panel Located on Intertank (X_T = 852.8 to 1123.15)

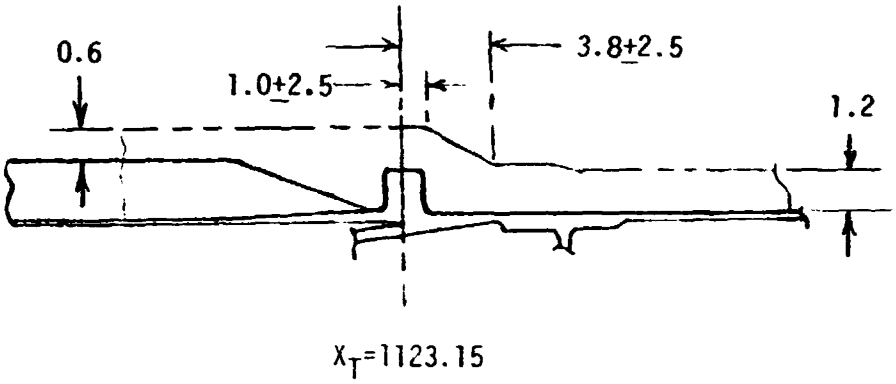

Side View of Aft End of Intertank

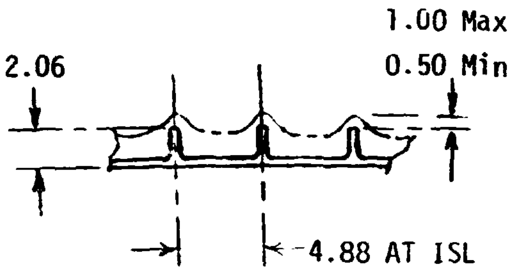

Cross-Sectional View
(Looking Forward)

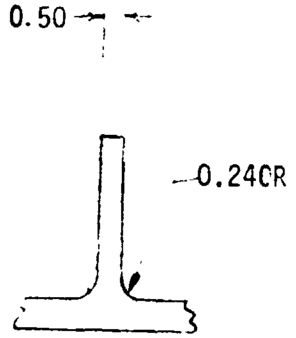

Typical Thrust Panel Stringer

Fig. D2 Thrust Panel Stringer Views
(2 panels at $67.5° \leq \theta_T \leq 112.5°$ and $247.5° \leq \theta_T \leq 292.5°$)

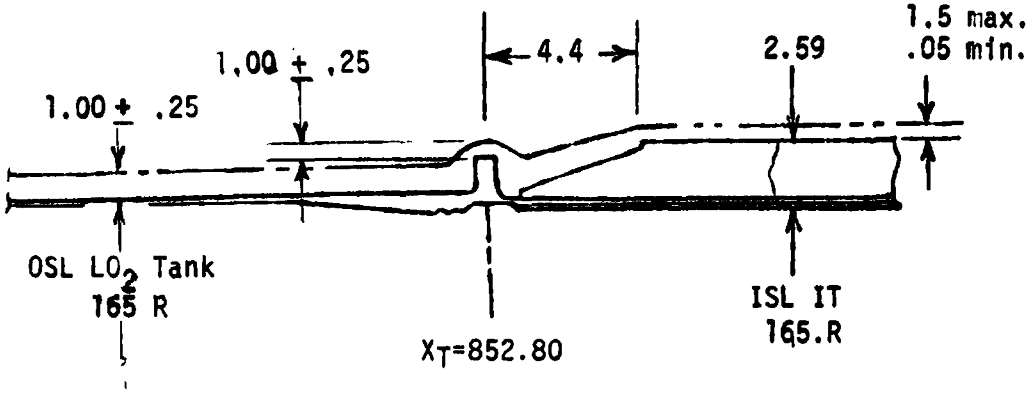

Side View of Forward End of Intertank

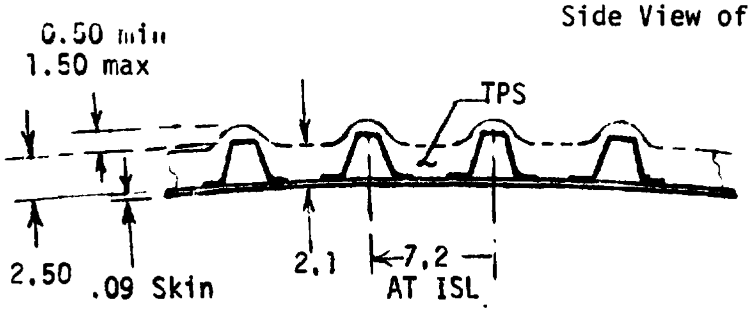

Cross-Sectional View
(Looking Forward)

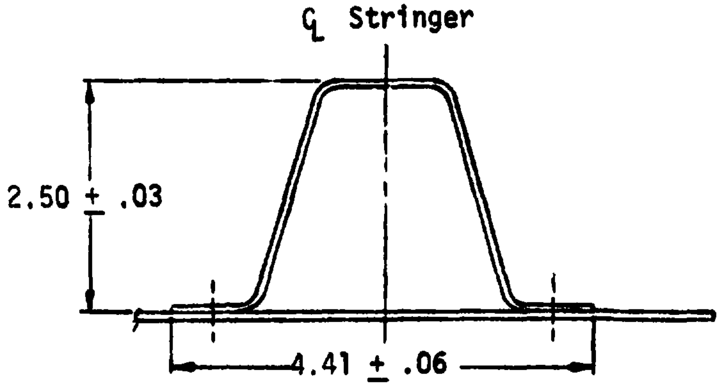

Typical Skin Stringer

Six Skin Stringer Panels θ Locations
$337.5° \le \theta_T \le 22.5°$
$22.5° \le \theta_T \le 67.5°$
$112.5° \le \theta_T \le 157.5°$
$157.5° \le \theta_T \le 202.5°$
$202.5° \le \theta_T \le 247.5°$
$292.5° \le \theta_T \le 337.5°$

Fig. D3 Skin Stringer Panel Views

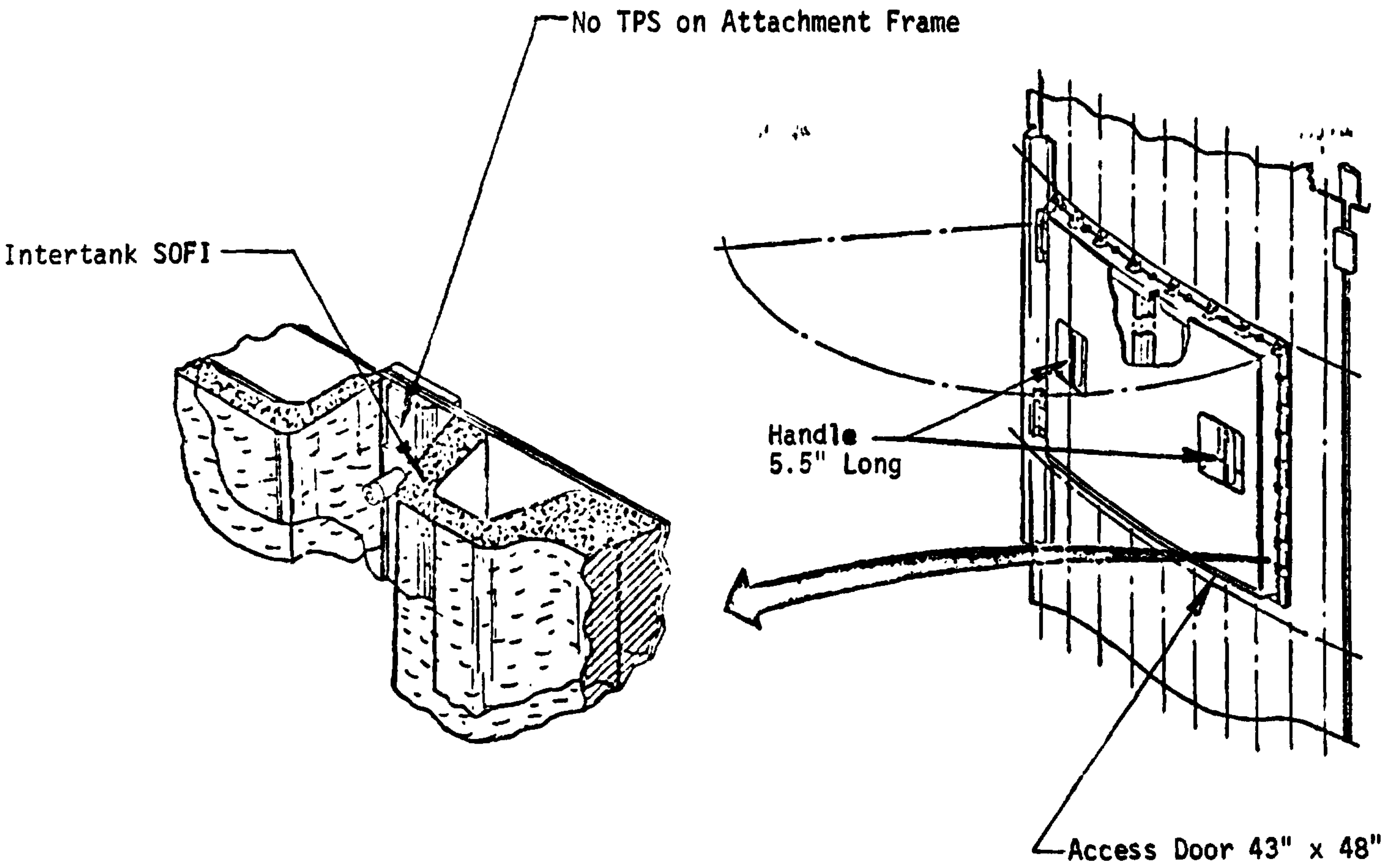

Fig. D4 Access Door

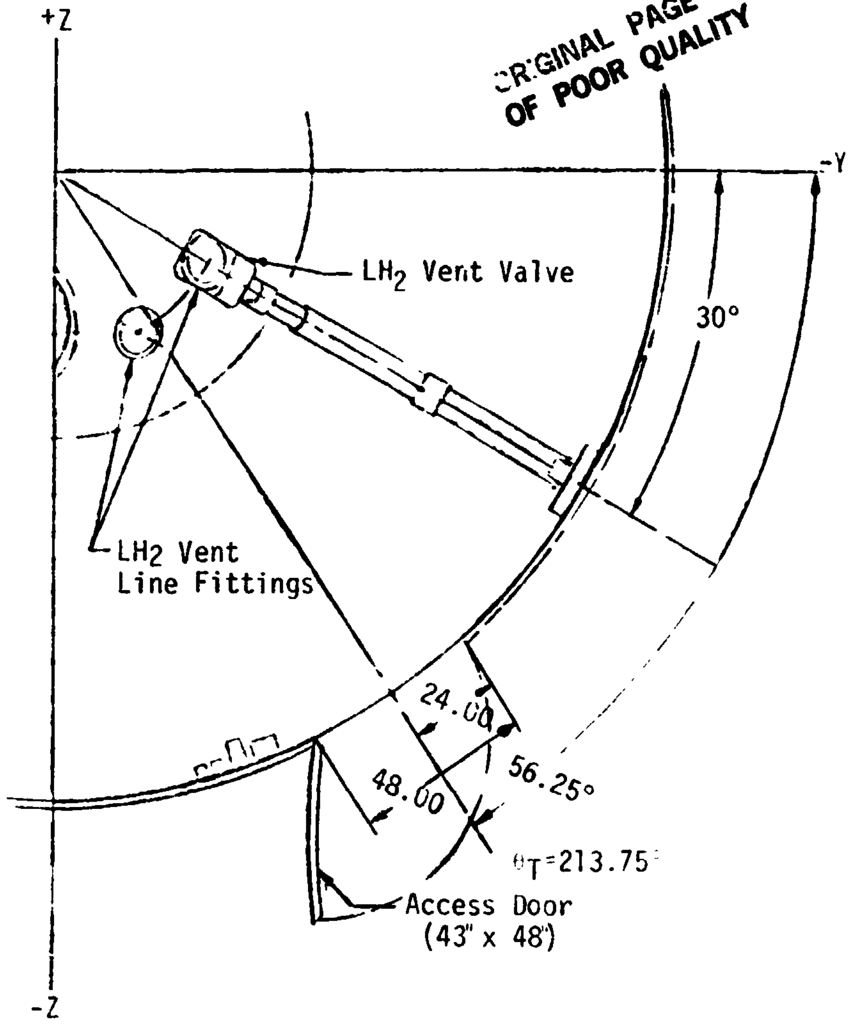

Fig. D5 Intertank Section Showing Access Door

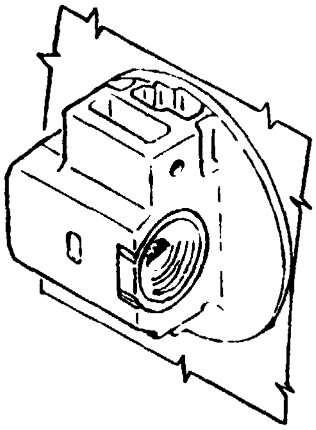

Second Stage Configuration

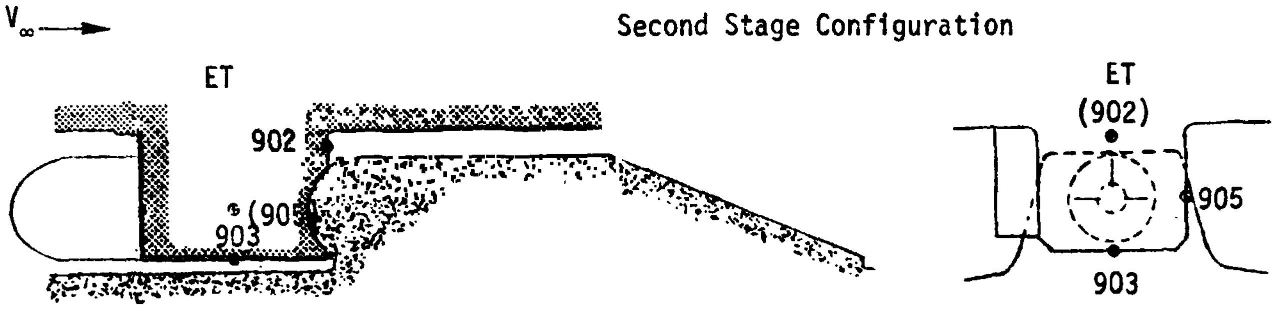

Planform View (Left Attachment) First Stage Configuration

Forward Facing View

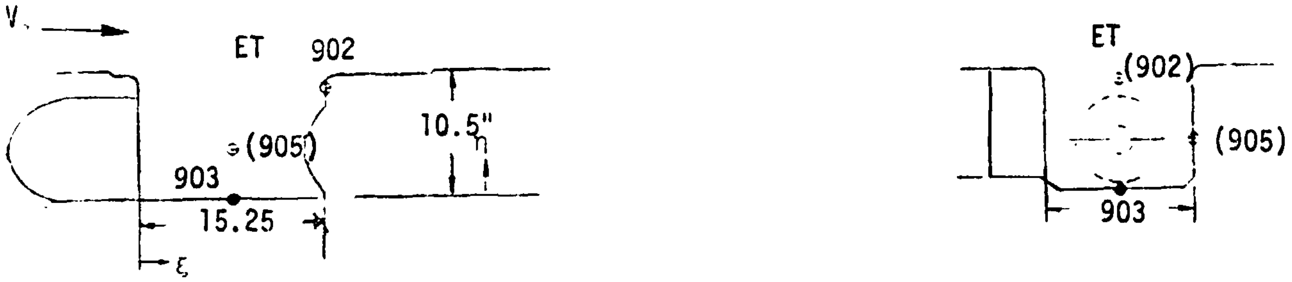

Second Stage Configuration

Body Point	Location	ξ (In.)	η (In.)
*901	Side Face		
902	Aft Face	15.25	9.0
903	Outboard Face	7.625	0.0
*904	Forward Face		
305	Side Face	7.625	4.0

*Removed due to Bolt Catcher addition

Fig. D6 Forward ET/SRB Attachment Structure Design Body Point Definition

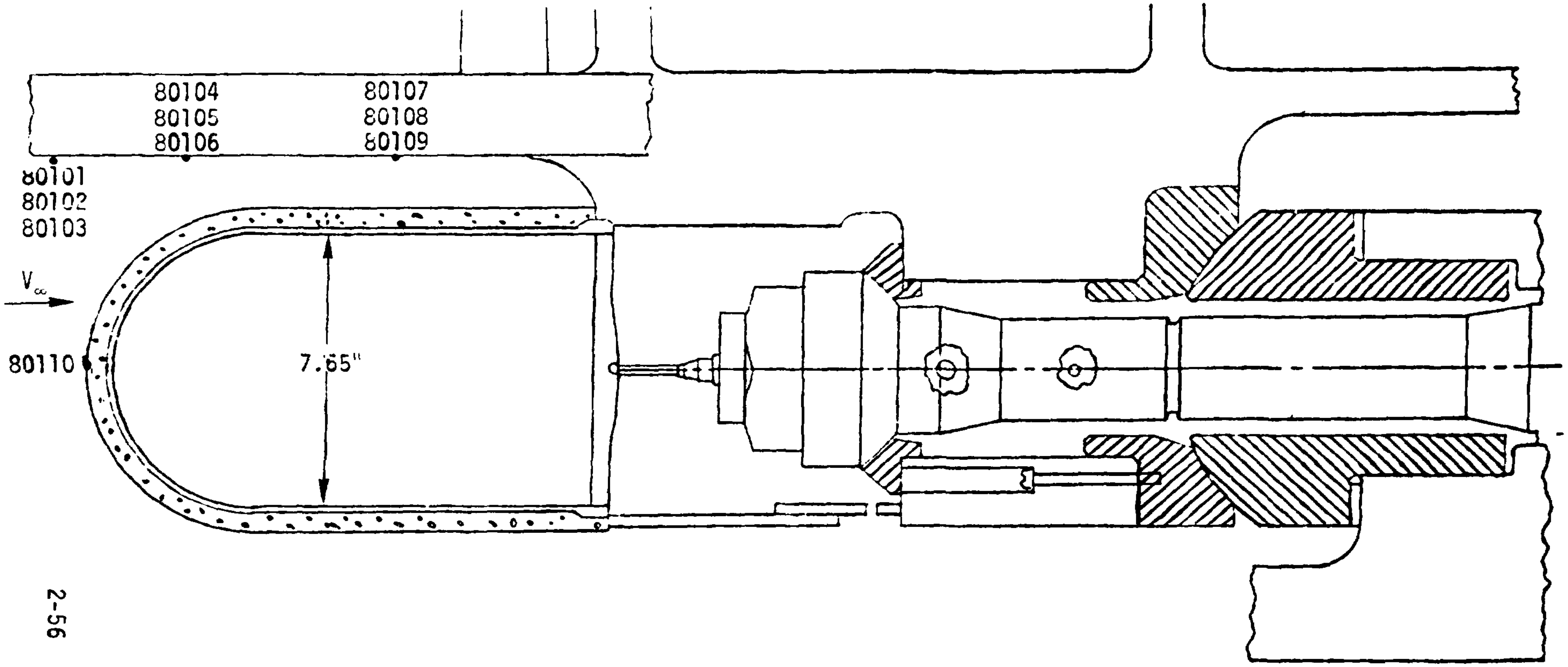

Body Point	STA.	θ_T
80101	959	274
80102	959	270
80103	959	266
80104	963	274
80105	963	270
80106	963	266
80107	967	274
80108	967	270
80109	967	266
80110	959.26	270

Fig. D7 Intertank Area Influenced By Bolt Catcher

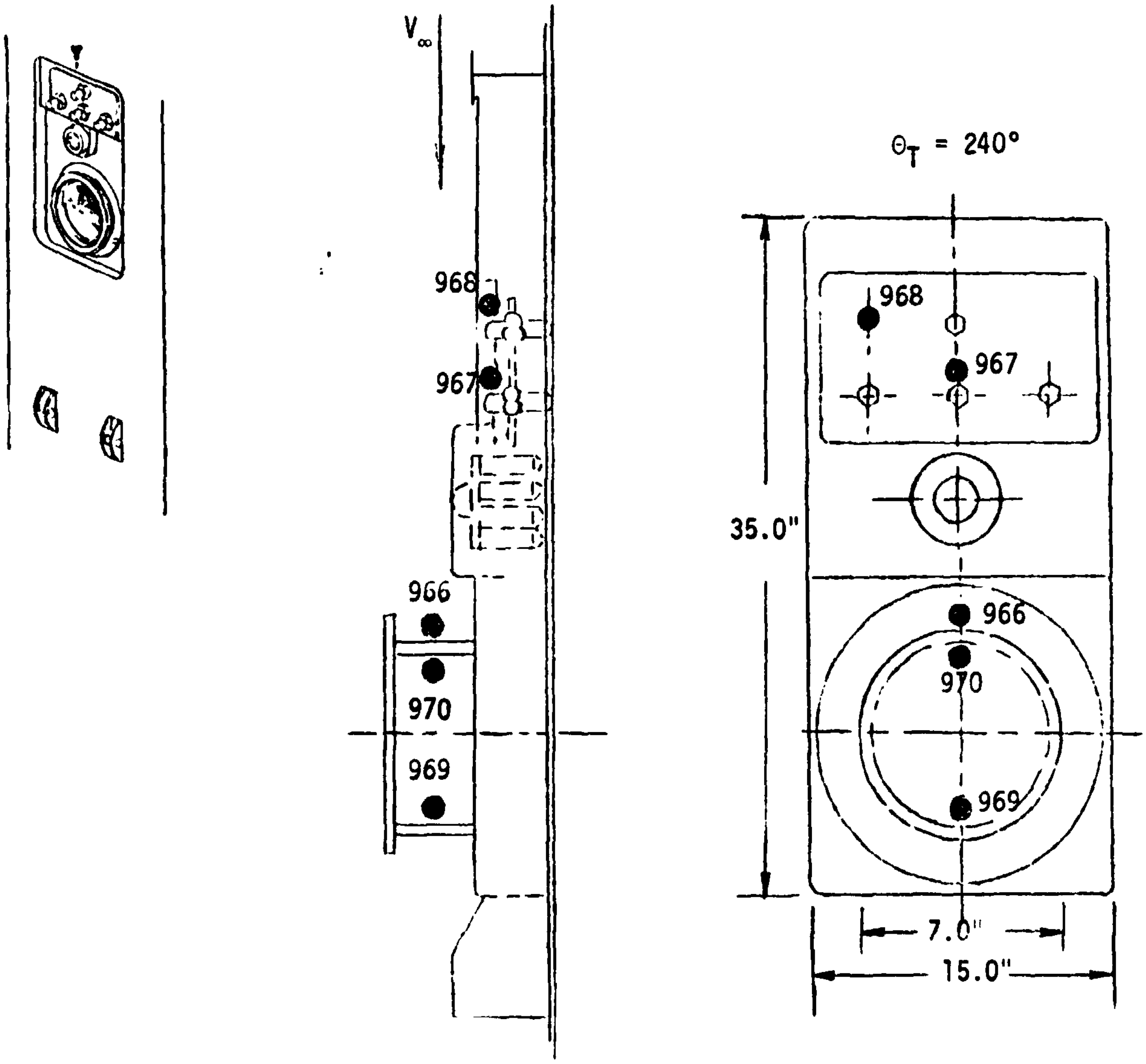

Body Point	Location
966	GH_2 Vent Line Disconnect Forward Stagnation Line
967	GH_2 Purge Disconnect
968	Carrier Plate
969	GH_2 Vent Line Disconnect Downstream Wall (Internal)
970	GH_2 Vent Line Disconnect Upstream Wall (Internal)

Fig. D8 Intertank Umbilical Disconnect Body Point Definition

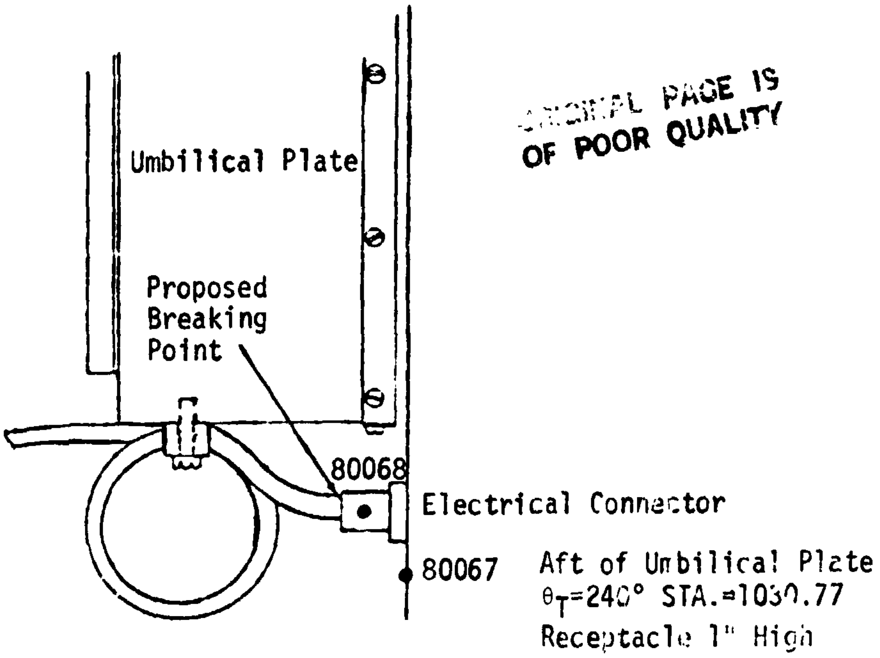

Body Point	Location
80067	Intertank Area Aft of RSS Electrical Connector
80068	Heating to the RSS Electrical Connector

Fig. D9 LH_2 Sidewall Body Points Adjacent to the RSS Electrical Connector

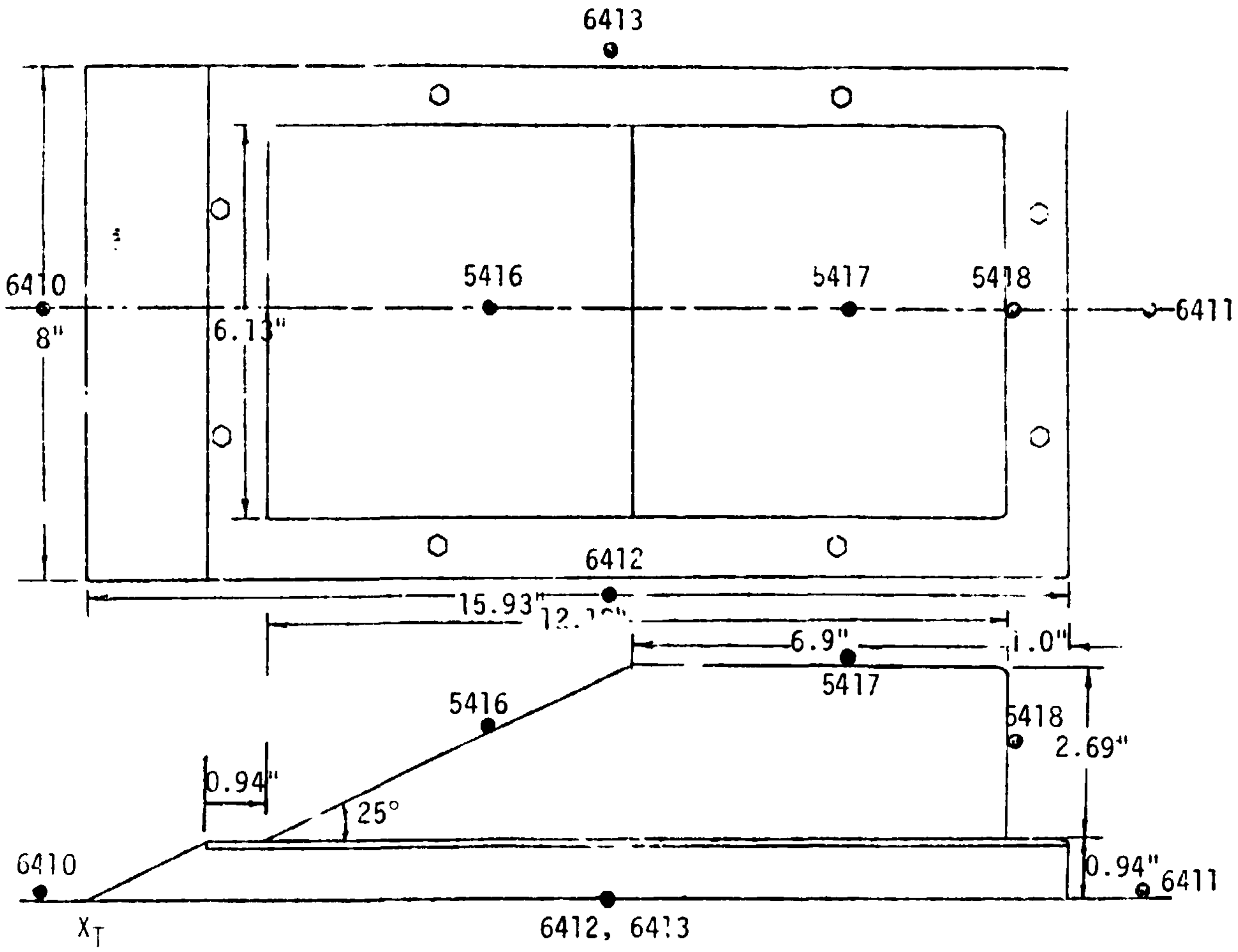

Body Point	Location	X_T (In.)
5416	Forward Face	879.0
5417	Upper Face	884.0
5418	Back Face	887.0
6410	Forward of Antenna on Intertank	870.0
6411	Aft of Antenna on Intertank	888.0
6412	Left Side of Antenna on Intertank	880.0
6413	Right Side of Antenna on Intertank	880.0

Fig. D10 Range Safety Antennae Body Point Definition (θ_T=141.25 and 321.25°)

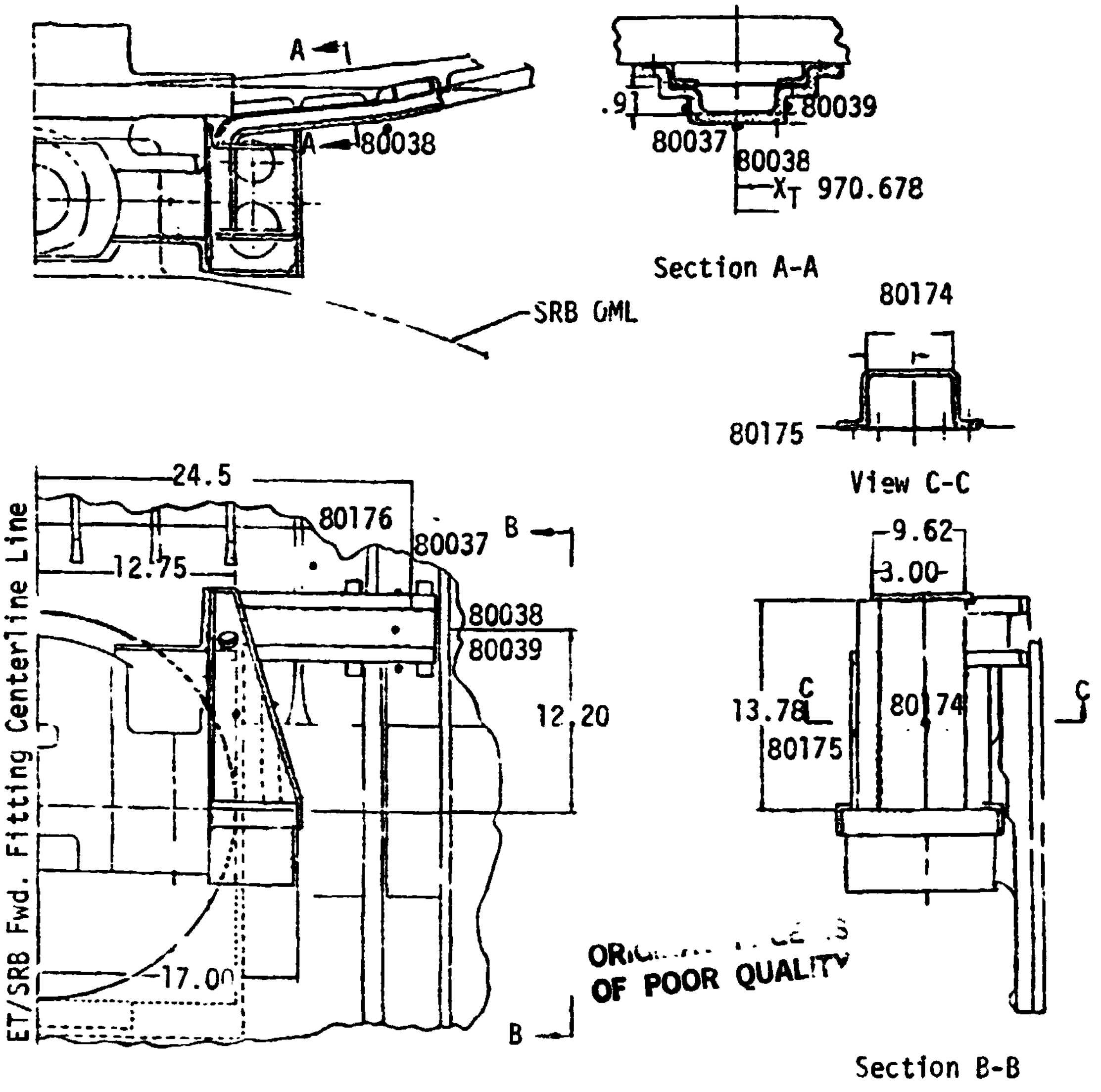

Body Point	STA.	Location	ϴ(Deg.)
80037	971.928	Cable Tray Front Face	279
80038	970.678	Cable Tray Top	279
80039	969.428	Cable Tray Aft Face	279
80174		Fairing Forward Face	
80175		Fairing Side Face	
80176		On ET Machine Panel Forward of Cable Tray	

Fig. D11 RSS ET/SRB Cable Tray and Fairing Design Body Point Definition

2.2.3 Protuberances that start on the Intertank

This subsection contains geometry and body point information for protuberances which begin on the intertank. Information is given for all X_T if the protuberance starts on the intertank. One exception is the electrical conduit and GO_2 pressure line. This section contains all the information for these two protuberances starting at the shoulder of the ET. The other exception is the forward attach strut, which is just aft of the intertank. The sequence of information is given in ascending order of Θ_T as follows:

- ET/Orbiter forward attach strut
- LO_2 feed line
  - Fairing
  - Attachment fittings
- GO_2 pressure line
  - Attachment fittings
  - Flanges
- Forward Electrical Conduit/GO_2 pressure line attachment fitting
- GO_2,Antigeyser line, Electrical conduit attachment fitting
- LO_2 Antigeyser Line
  - Fairing
  - Flanges
  - Fitting shield
- Electrical Conduit
  - Forward aft fairing
  - Aft fairing
- GH_2 pressure line
  - Fairing

- Attachment fitting and Barry mount
- Flanges grounding strap and Barry mount

Note: E = Division 2.2.3 on figures and tables

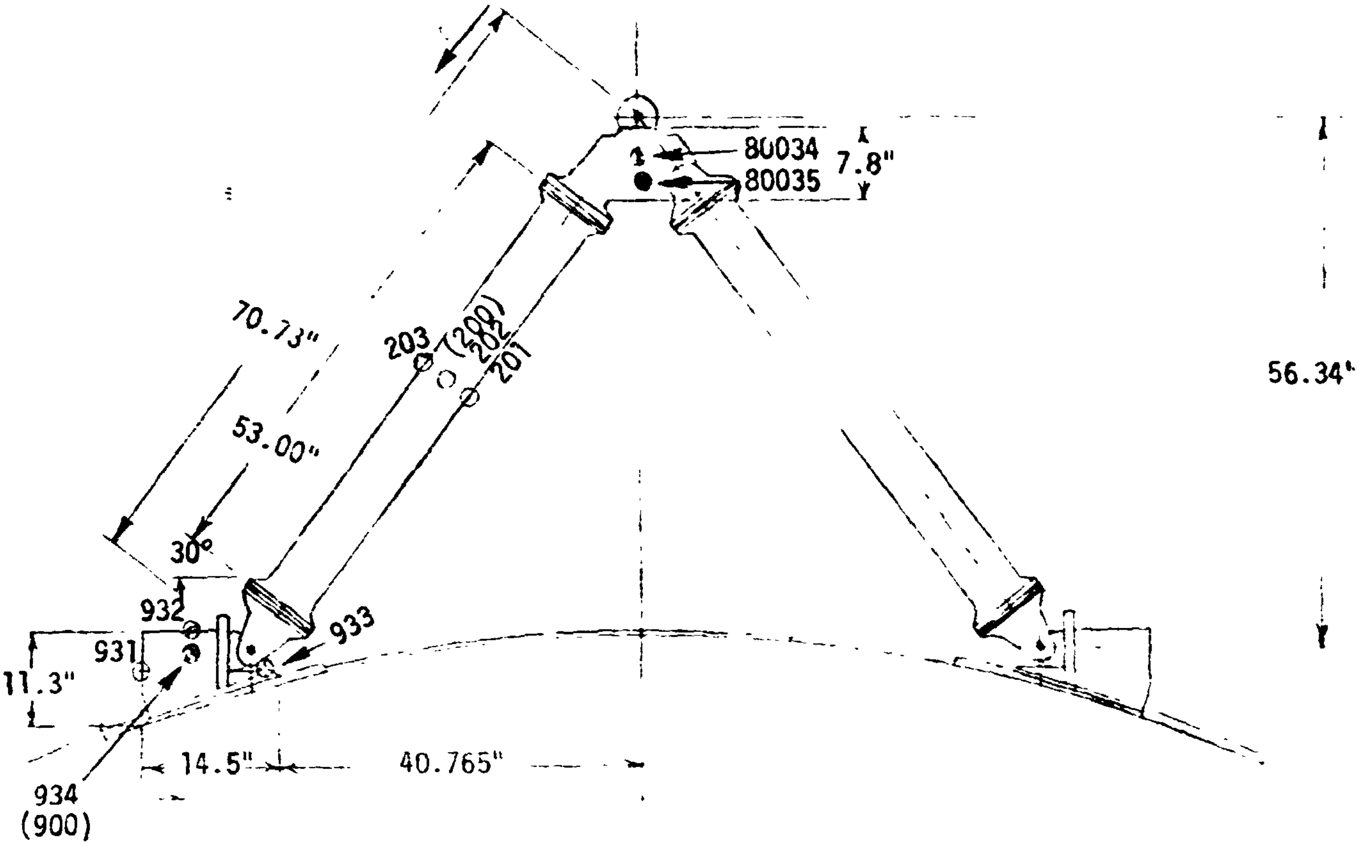

Aft View (Looking Forward)

Body Point	Description	ξ (In.)	φ (Deg.)
200	ET/Orbiter Forward Attachment Strut	35.5	0
201	↓	↓	[illegible]
202			[illegible]
203		35 5	270
900	Fitting Forward Face	8.5	
931	Fitting Outboard Side	2.75	
932	Fitting Top	8.5	
933	Fitting Inboard Side	12.85	
934	Fitting Aft Face	8.5	
80034	Yoke Fitting Front Face		
80035	Yoke Fitting Back Face		

Fig. E1 ET/Orbiter Forward Attachment Strut and Fitting Body Point Definition

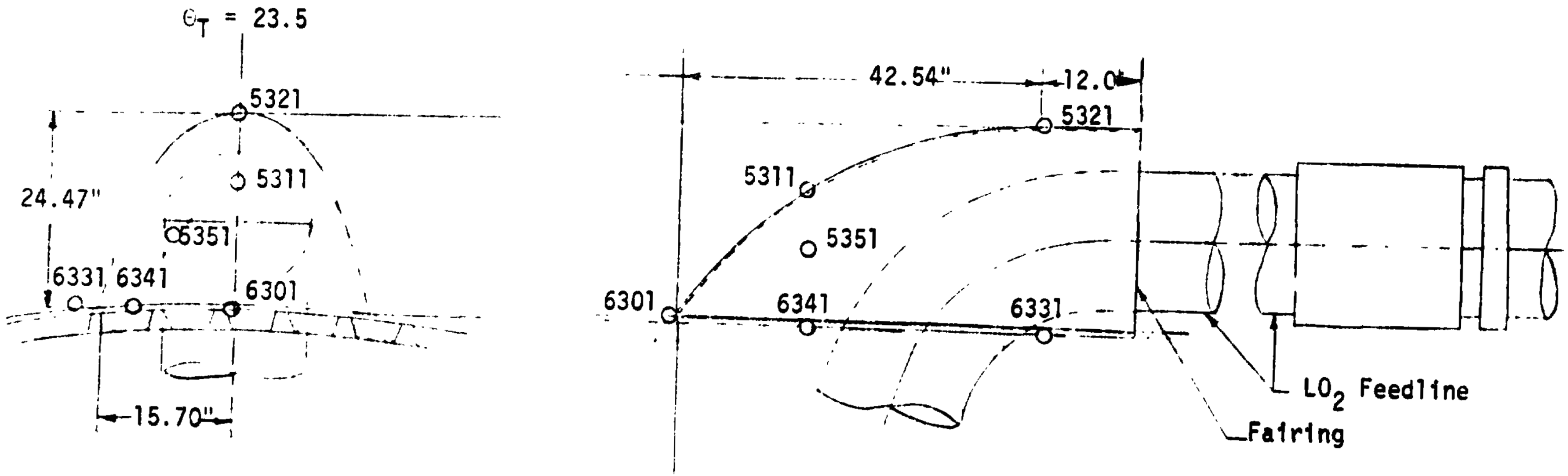

Cross-Sectional View

Side View

ORIGINAL PAGE IS
OF POOR QUALITY

X_T (In.)	Body Points	Description
983.46	6301	Intertank Sidewall Near Fairing
999.46	5311	Fairing Forebody
1026.0	5321	Fairing Afterbody
1026.0	6331	Intertank Sidewall Near Fairing
999.46	5351	Fairing Side
999.46	6341	Intertank Sidewall Near Fairing

Fig. E2 LO_2 Feedline Fairing Body Point Definition

Table E3

LO_2 Feedline Body Point Definitions O_T=23.5°

X_T (In.)	Body Point	Location
1038.03	5381	Upper Centerline of Feedline
1069.4	5401	
1102.62	5421	
1123.15	5431	
1229.96	5481	
1359.15	5551	
1486.49	5621	
1615.67	5691	
1743.02	5761	
1872.20	5831	
1999.54	5901	
2036.45	5921	Upper Centerline of Feedline
1111.20	5001	Adjacent to Attachment Fittings
1118.68	5002	
1124.29	5003	
1125.60	5004	
1127.095	5005	
1127.56	5006	
1086.657	5007	
1111.20	5008	
1118.68	5009	
1124.29	5010	
1125.60	5011	
1127.095	5012	
1127.56	5015	
1132.705	5016	
1136.21	5017	
1139.95	5018	
1153.30	5019	
1086.657	5020	
1111.20	5021	
1118.68	5022	
1124.29	5025	
1125.60	5026	
1127.095	5027	
1127.56	5028	
1358.90	5029	
1366.38	5030	
1371.99	5031	
1373.30	5032	
1374.795	5035	
1375.26	5036	
1334.357	5037	
1358.90	5551	
1366.38	5039	
1371.99	5040	
1373.30	5041	
1374.795	5042	
1375.26	5045	
1380.405	5046	

Table E3 (Cont, 1)

LO_2 Feedline Body Point Definition		
X_T (In.)	Body Point	Location
1383.91	5047	Adjacent to Attachment Fittings
1387.65	5048	
1401.0	5049	
1334.357	5050	
1358.90	5051	
1366.38	5052	
1371.99	5055	
1373.30	5056	
1374.795	5057	
1375.26	5058	
1605.60	5059	
1613.08	5060	
1618.69	5061	
1620.0	5062	
1621.495	5065	
1621.960	5066	
1581.057	5067	
1605.60	5068	
1613.08	5069	
1618.69	5070	
1620.0	5071	
1621.495	5072	Adjacent to Attachment Fittings
1621.96	5075	
1627.105	5076	
1630.61	5077	
1634.35	5078	
1647.70	5079	
1581.057	5080	
1605.60	5081	
1613.08	5082	
1618.69	5085	
1620.0	5086	
1621.495	5087	
1621.96	5088	
1852.30	5089	
1859.78	5090	
1865.39	5091	
1866.70	5092	
1868.195	5095	
1868.66	5096	
1827.757	5097	
1852.30	5098	
1859.78	5099	
1865.39	5101	
1866.70	5102	
1868.195	5103	
1868.66	5105	
1873.805	5106	
1877.31	5107	
1881.05	5108	
1894.40	5109	

Table E3 (Cont. 2)

LO_2 Feedline Body Point Definition		
X_T (In.)	Body Point	Location
1827.757	5110	Adjacent to Attachment Fittings
1852.30	5111	
1859.78	5112	
1865.39	5115	
1866.70	5116	
1868.195	5117	
1868.66	5118	
1955.30	5119	
1962.78	5120	
1968.39	5121	
1969.70	5122	
1971.195	5125	
1971.66	5126	
1930.757	5127	
1955.30	5128	
1962.78	5129	
1968,39	5130	
1969.70	5131	
1971.195	5132	
1971.66	5135	
1976.805	5136	
1980.31	5137	
1984.05	5138	
1997.4	5139	
1930.757	5140	
1955.30	5141	
1962.78	5142	
1968.39	5145	
1969.70	5146	
1971.195	5147	
1971.66	5148	
2016.61	5149	Adjacent to Attachment Fittings
2024.09	5150	
2029.70	5151	
2031.01	5152	
2032.505	5155	
2032.97	5156	
2016.61	5157	
2024.09	5158	
2029.7	5159	
2031.01	5160	
2032.505	5161	
2032.97	5162	
2038.115	5165	
2041.62	5166	
2045.36	5167	
2058.71	5168	
2016.61	5169	
2024.09	5170	
2029.7	5171	
2031.01	5172	
2032.505	5175	
2032.97	5176	

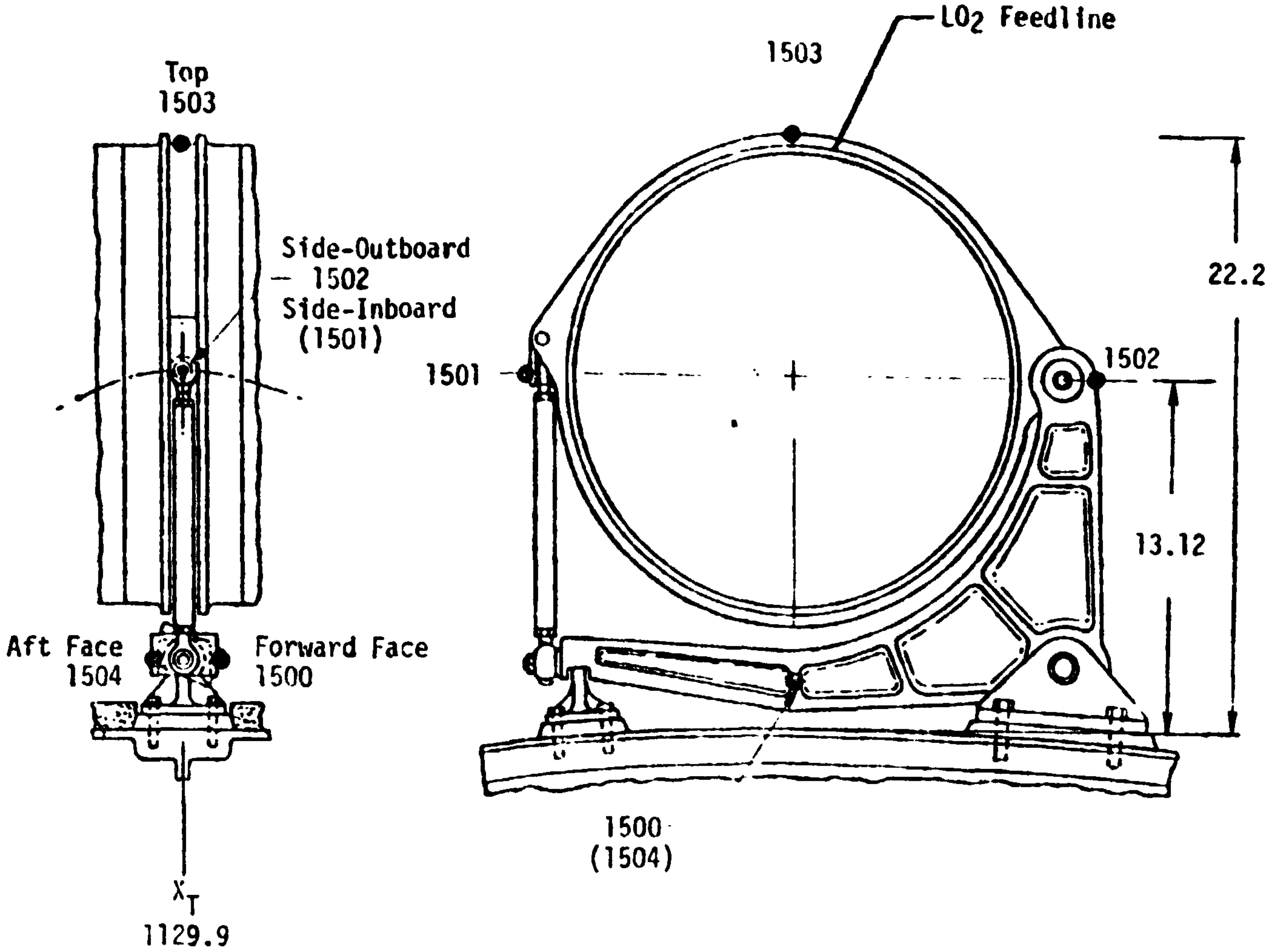

Aft Facing View

Typical at Stations:

Top Face X_T	B.P.	B.P.	B.P.	B.P.	B.P.
1129.9	1500	1501	1502	1503	1504
1377.6	1510	1511	1512	1513	1514
1623.8	1520	1521	1522	1523	1524
1871.0	1530	1531	1532	1533	1534
*1973.5	1540	1541	1542	1543	1544

*Similar to the other fittings with changes as increased pin size, new bearings and hardware, and an increase in webs and flanges.

Fig. E4 LO_2 Feedline Attachment Fitting Design Body Points for a Typical Fitting Station

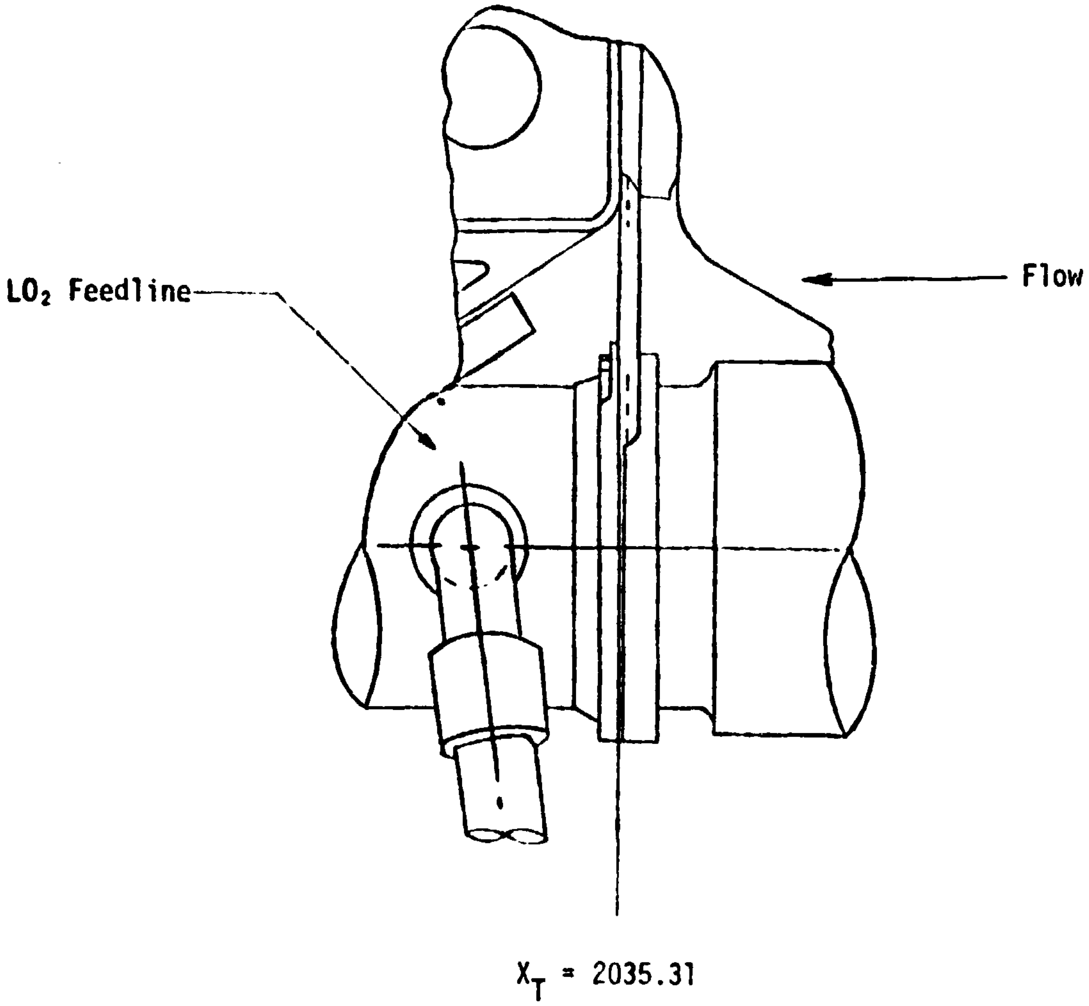

	Forward Face	Side-Inboard	Side-Outboard	Top	Aft Face
X_T	B.P.	B.P.	B.P.	B.P.	B.P.
2035.31	1550	1551	1552	1553	1554

Note See Fig. F29 for surrounding geometry.

Fig. E5 LO_2 Feedline Attachment Fitting for Fitting Station X_T = 2035.31

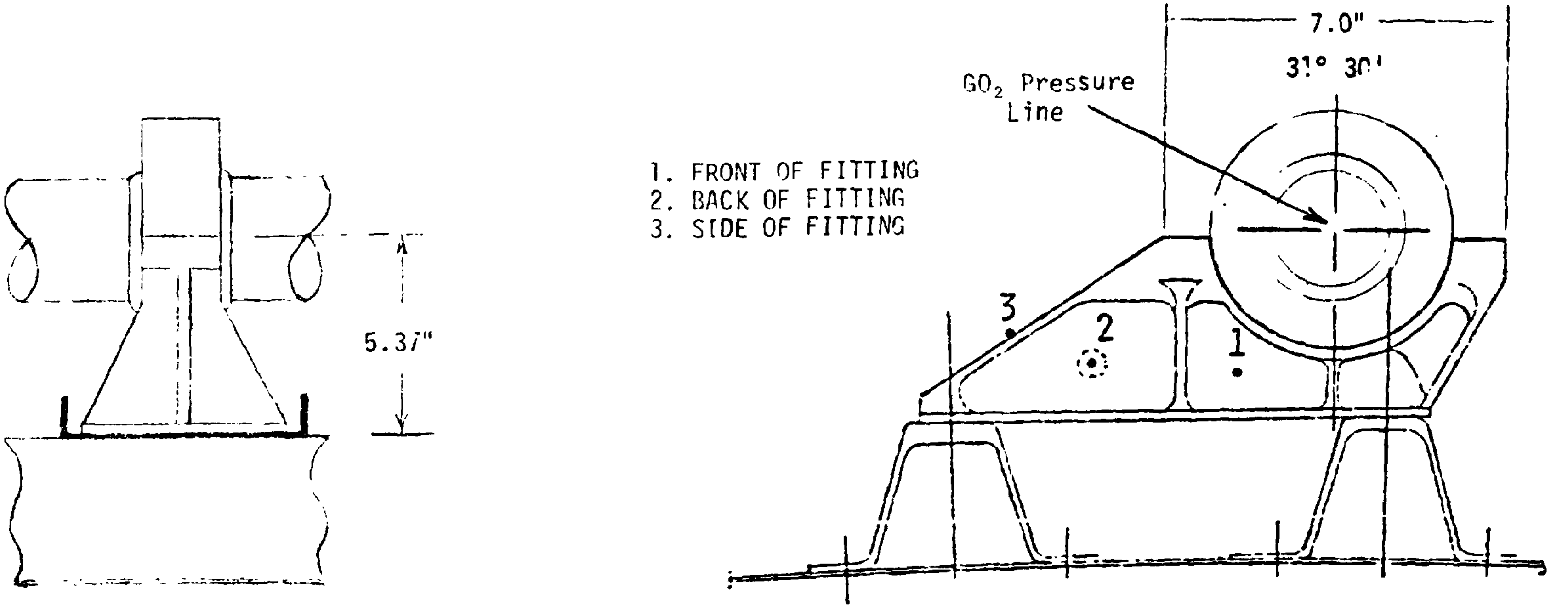

Side View of Attachment Fitting

Cross-Sectional View of Attachment Fitting

Protuberance Body Point Definitions		
X_T (In.)	Body Point	Location
922.75	80147	Front of GO_2 Pressline Fitting
	80148	Back ↓
	80149	Side
949.75	80150	Front of GO_2 Pressline Fitting
	80151	Back ↓
	80152	Side
980.00	80153	Front of GO_2 Pressline Fitting
	80154	Back ↓
	80155	Side
1049.00	80156	Front of GO_2 Pressline Fitting
	80157	Back ↓
	80158	Side

Fig. E6 GO_2 Pressure Line Attachment Fittings

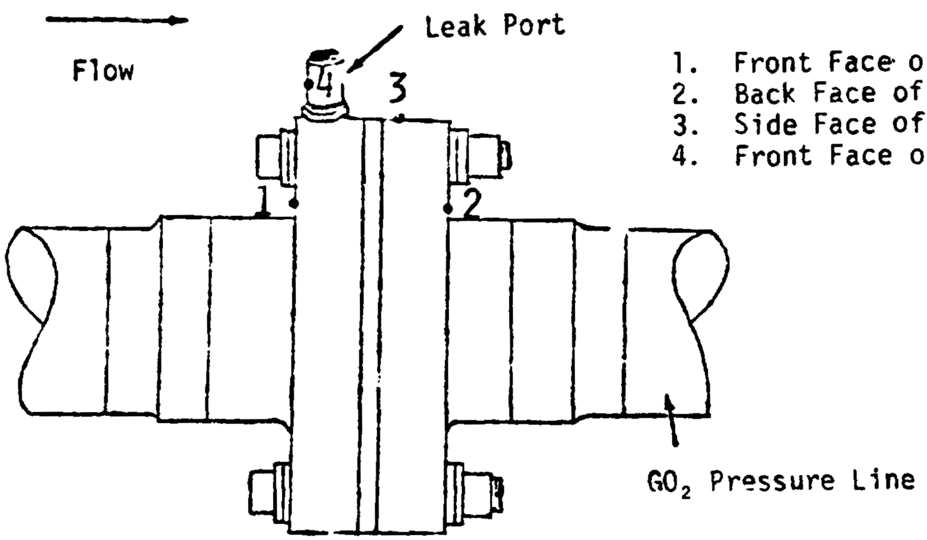

S.ue View

1. Front Face of Flange
2. Back Face of Flange
3. Side Face of Flange
4. Front Face of Leak Port

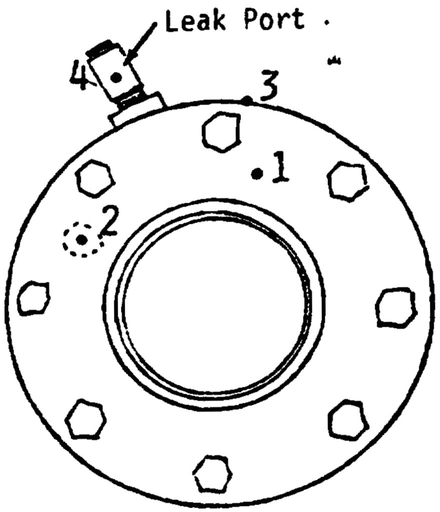

Aft Facing View

STA.	1	2	3	4
394.745	[1560]	[1564]	[1561]	1*
610.51	↓	↓	↓	↓
849.0	↓	↓	↓	↓
1088.0	80127	80128	80129	80130
1327.0	80131	80132	80133	80134
1566.0	80135	80136	80137	80138
1805.0	80139	80140	80141	80142
2044.0	80143	80144	80145	80146

* Stagnation Line Heating
[ ] Reference Body Point

Fig. E7 GO_2 Pressure Line Flanges Body Point Locations at Fitting Stations

Table E8.

GO$_2$ Pressure Line Design Body Point Definitions

X_T (In.)	Body Point	Location
852.8	5282	Upper Centerline of Press. Line
884.848	5302	
929.14	5322	
973.43	5352	
1006.65	5362	
1038.03	5382	
1080.05	5402	
1102.62	5422	
1133.80	5432	
1229.96	5482	
1359.15	5552	
1486.49	5622	
1615.67	5692	
1743.02	5762	
1872.20	5832	
1999.54	5902	
2036.45	5922	Upper Centerline of Press. Line
1080.05	5402	Adjacent to Line Attachment Fittings
1113.27	5422	
1124.50	5292	
1133.80	5432	
1138.20	5312	
1142.74	5332	
1147.26	5342	
1139.985	5372	
1150.89	5392	
1178.35	5412	
1192.05	5442	
1196.59	5452	
1201.11	5462	
1203.84	5472	
1204.74	5492	
1229.96	5482	
1242.85	5502	
1256.55	5512	
1261.09	5522	
1265.61	5532	
1268.335	5542	
1269.24	5506	
1565.35	5562	
1579.05	5572	
1583.59	5582	
1588.11	5592	
1590.835	5602	
1591.74	5612	
1615.67	5692	

Table 28 (Cont.)

GO_2 Pressure Line Design Body Point Definitions

X_T (In.)	Body Point	Location
1823.35	5632	Adjacent to Line Attachment Fittings
1837.05	5642	
1841.59	5652	
1846.11	5662	
1848.835	5672	
1849.74	5682	
1872.20	5832	
1887.85	5702	
1901.55	5712	
1906.09	5722	
1910.61	5732	
1913.335	5742	
1914.24	5752	
1952.35	5772	
1966.05	5782	
1970.59	5792	
1975.11	5802	
1977.835	5812	
1978.74	5822	
1999.54	5902	↓

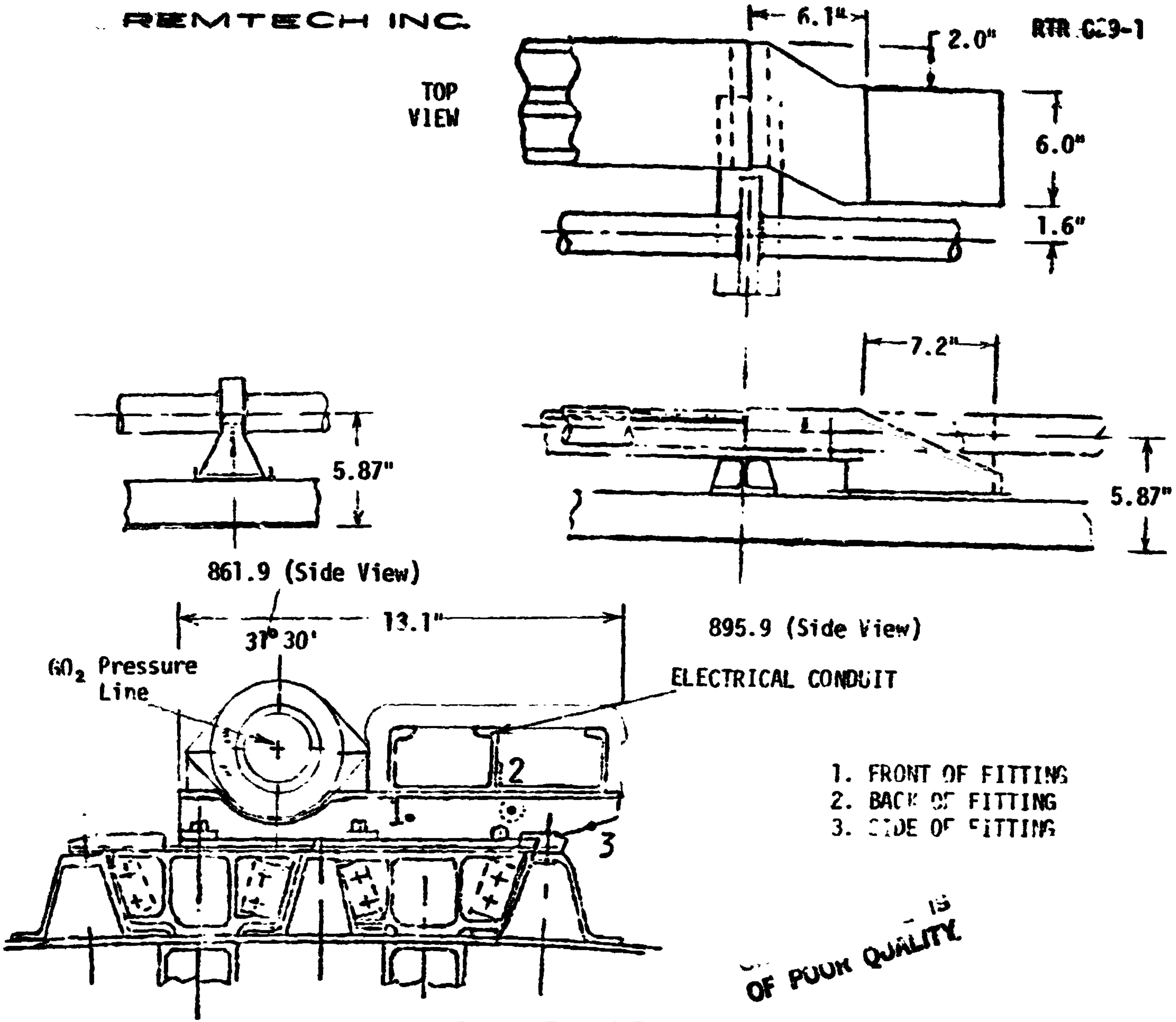

Cross-Sectional View Type C Fitting

Protuberance Body Point Definitions		
X_T (In.)	Body Point	Location
861.9	80155 80166 80167	(1) Front of GO_2 Pressline/Electrical Conduit Fitting (2) back ↓ (3) Side
895.9	80168 80169 80170	(1) Front of GO_2 Pressline/Electrical Conduit Fitting (2) Back ↓ (3) Side

Fig. C9 GO_2 Pressure Line/Electrical Conduit Attachment Fitting Type C (Located on LO_2 Panel)

GO_2 Pressure Line/Antigeyser Fitting

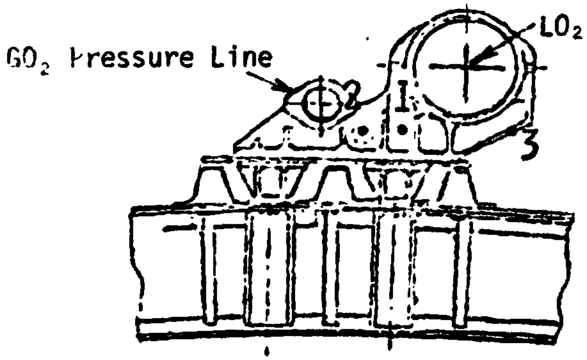

1. FRONT OF FITTING
2. BACK OF FITTING
3. SIDE OF FITTING

Cross-Sectional View at Sta. 1082.0

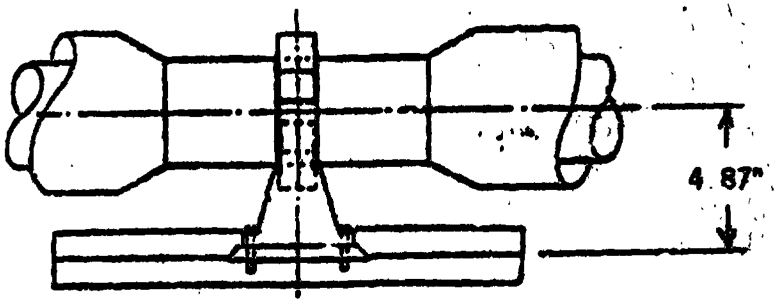

Side View of All Station Fittings in Table E11

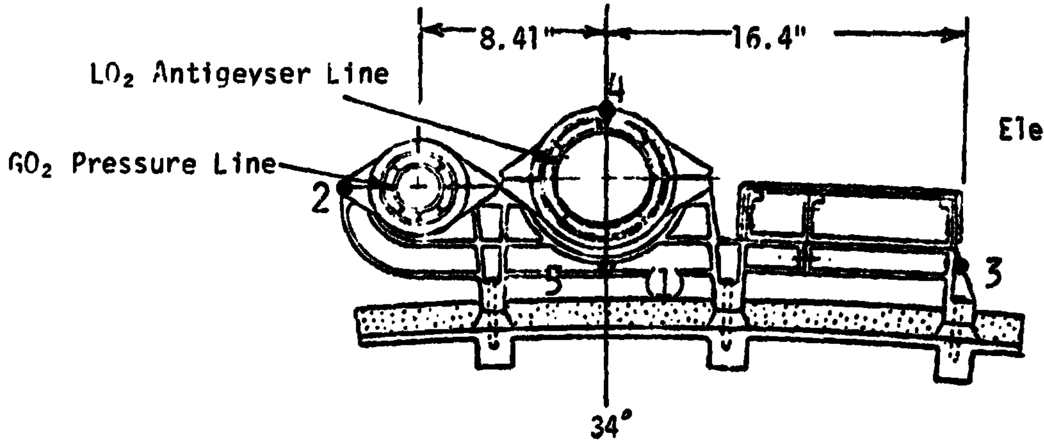

Cross-Sectional View For All Other Fitting Stations in Table E11

1. FORWARD FACE
2. SIDE FACE-INBOARD
3. SIDE FACE-OUTBOARD
4. TOP FACE
5. AFT FACE

Fig. E10 GO_2 Pressure Line/Antigeyser Line/Electrical Conduit Attachment Fitting Body Point Definition

Table E11

Antigeyser Line/Electrical Conduit/GO$_2$ Pressure Line Attachment Fitting Body Point Definitions		
X_T (In.)	Body Point	Location
1082.0	80162	Front of Fitting
↓	80163	Back of Fitting
	80164	Side of Fitting
1150.8	1560	Forward Face
1151.8	1561	Side Face-Inboard*
↓	1562	Side Face-Outboard**
	1563	Top Face
1152.8	1564	Aft Face
1204.6	1570	Forward Face
1205.6	1571	Side Face-Inboard
↓	1572	Side Face-Outboard
	1573	Top Face
1206.6	1574	Aft Face
1269.3	1580	Forward Face
1270.3	1581	Side Face-Inboard
↓	1582	Side Face-Outboard
	1583	Top Face
1271.3	1584	Aft Face
1334.8	No B. P.	
1399.4	↓	
1464.0		
1528.6		
1592.2	1590	Forward Face
1593.2	1591	Side Face-Inboard
↓	1592	Side Face-Outboard
	1593	Top Face
1594.2	1594	Aft Face
1657.8	No B. P.	
1722.4	↓	
1787.0		

*Towards θ_T=0°

**Away from θ_T=0°

Table E11 (Cont.)

Antigeyser Line/Electrical Conduit/GO_2 Pressure Line Attachment Fitting Body Point Definitions

X_T (In.)	Body Point	Location
1850.6	1600	Forward Face
1851.6	1601	Side Face-Inboard
↓	1602	Side Face-Outboard
	1603	Top Face
1852.6	1604	Aft Face
1915.2	1610	Forward Face
1916.2	1611	Side Face-Inboard
↓	1612	Side Face-Outboard
	1613	Top Face
1917.2	1614	Aft Face
1978.7	1620	Forward Face
1979.7	1621	Side Face-Inboard
↓	1622	Side Face-Outboard
	1623	Top Face
1980.7	1624	Aft Face

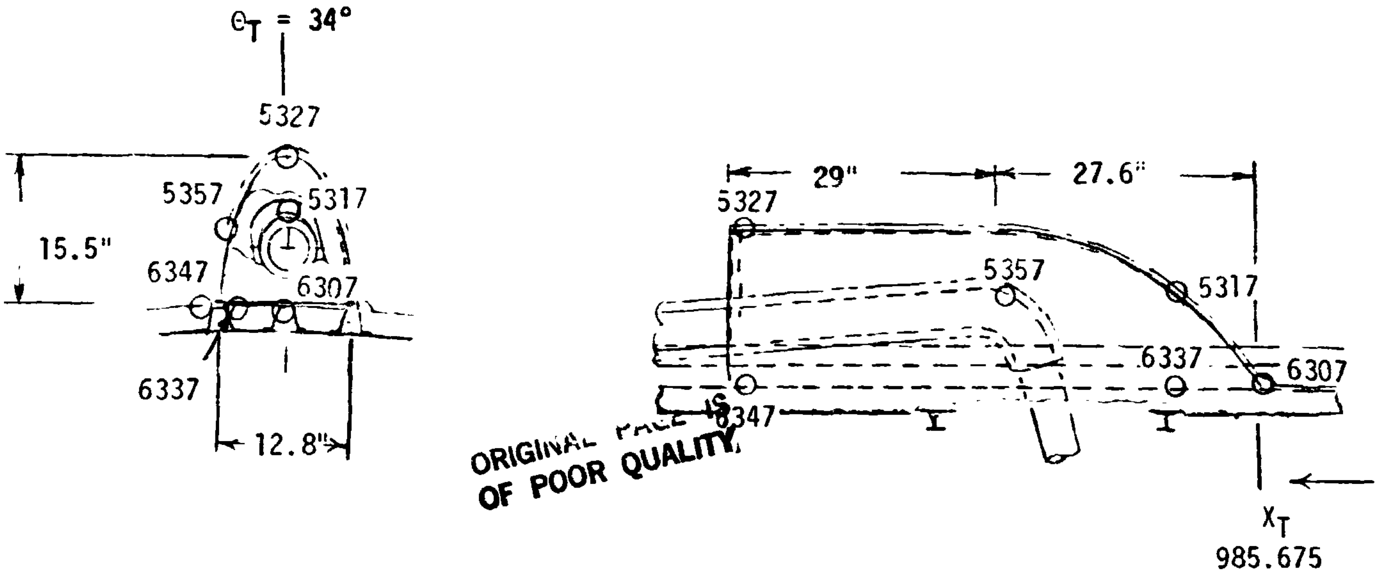

X_T (In.)	Body Points	Surface
985.675	6367	On Intertank Sidewall Near Fairing
994.645	5317	Fairing Forebody
994.645	6337	On Intertank Sidewall Near Fairing
1040.875	5327	Fairing Afterbody
1013.275	5357	Fairing Side
1013.275	6347	On Intertank Sidewall Near Fairing

Fig. E12 LO_2 Antigeyser Line Fairing Body Point Definition

Table E13

LO_2 Antigeyser Line Design Body Point Definition θ_T=34°

X_T (In.)	Body Point	Location
1080.05	5403	Upper Centerline of Antigeyser Line
1113.27	5423	
1138.80	5433	
1229.96	5483	
1359.1[illegible]	5553	
1486.49	5623	
1615.67	5693	
1743.02	5763	
1872.20	5833	
1999.54	5903	
2036.45	5923	Upper Centerline of Antigeyser Line
1080.05	5403	LO_2 Antigeyser Line Adjacent to Line Attachment Fittings
1113.27	5423	
1124.5	5013	
1133.8	5433	
1138.2	5023	
1142.74	5033	
1147.26	5043	
1149.985	5053	
1150.89	5063	
1156.34	5073	
1160.86	5083	
1165.4	5093	
1178.35	5103	
1192.05	5113	
1196.59	5123	
1201.11	5133	
1203.84	5143	
1204.74	5153	
1210.19	5163	
1214.71	5173	
1219.25	5183	
1229.96	5483	
1242.85	5203	
1256.55	5213	
1261.09	5223	
1265.61	5233	
1268.335	5243	
1269.24	5253	
1274.69	5263	
1279.21	5273	
1283.75	5283	
1565.35	5303	
1579.05	5313	
1583.59	5323	
1588.11	5333	
1590.835	5343	
1591.74	5353	

Table E13 (Cont.)

LO_2 Antigeyser Line Design Body Point Definitions (Continued)		
X_T (In.)	Body Point	Location
1597.19	5363	LO_2 Antigeyser Line Adjacent to Line Attachment Fittings
1601.71	5373	↓
1606.25	5383	↓
1615.67	5693	↓
1823.35	5406	↓
1837.05	5413	↓
1841.59	5407	↓
1846.11	5408	↓
1848.835	5443	↓
1849.74	5453	↓
1855.19	5463	↓
1859.71	5473	↓
1864.25	5409	↓
1872.20	5833	↓
1887.85	5503	↓
1901.55	5513	↓
190[illegible].09	5523	↓
191[illegible].61	5533	↓
1913.335	5543	↓
1914.24	5504	↓
1919.69	5563	↓
1924.21	5573	↓
19[illegible]8.75	5583	↓
1952.35	5603	↓
1966.05	5613	↓
1970.59	5606	↓
1975.11	5633	↓
1977.835	5643	↓
1978.74	5653	↓
1984.19	5663	↓
1988.71	5673	↓
1993.25	5683	↓
1999.54	5903	↓

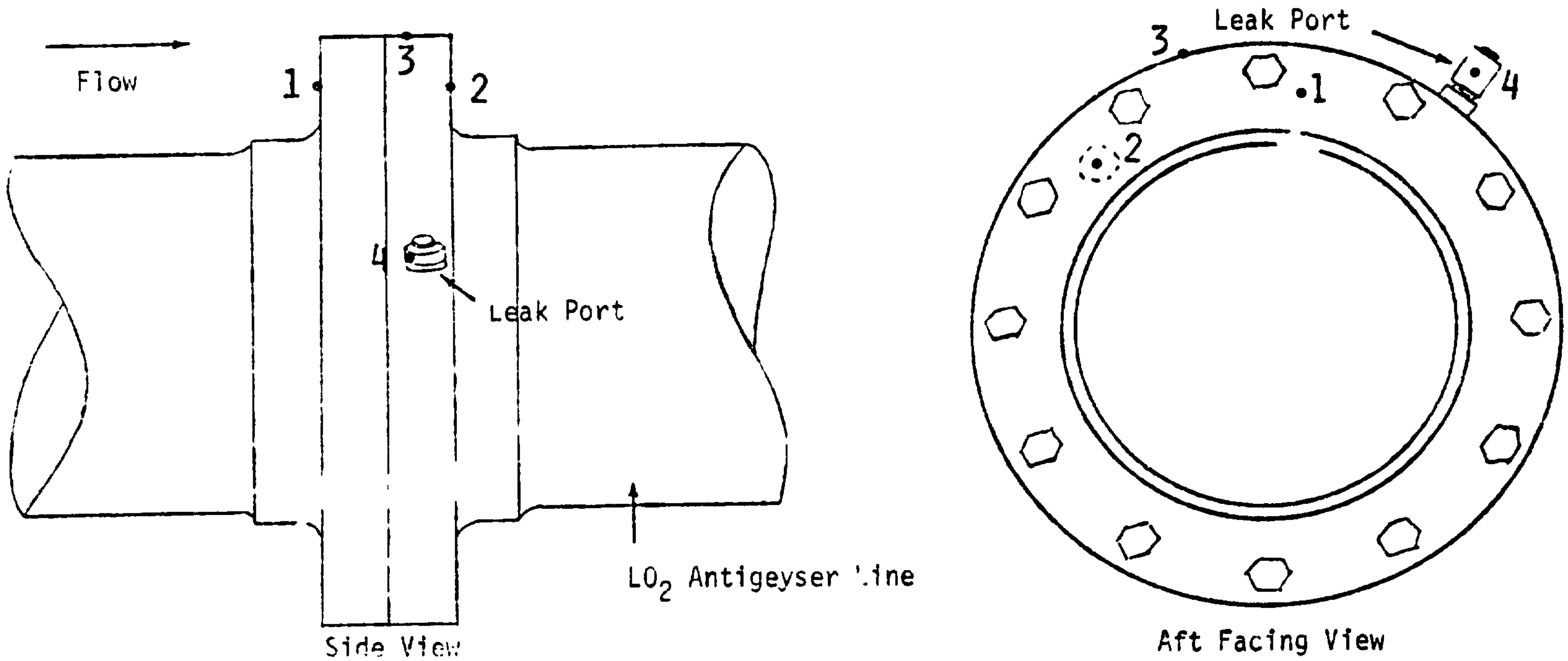

Body Point I.D. and Location				
	Front Face	Back Face	Side Face	Leak Port
STA	1	2	3	4
1075	80070	80071	80072	80073
1253	80074	80075	80076	80077
1494	80078	80079	80080	80081
1734	80082	80083	30084	80085
1974	80086	80087	80088	80089

Fig. E14 LO_2 Antigeyser Line Flanges Body Point Definition

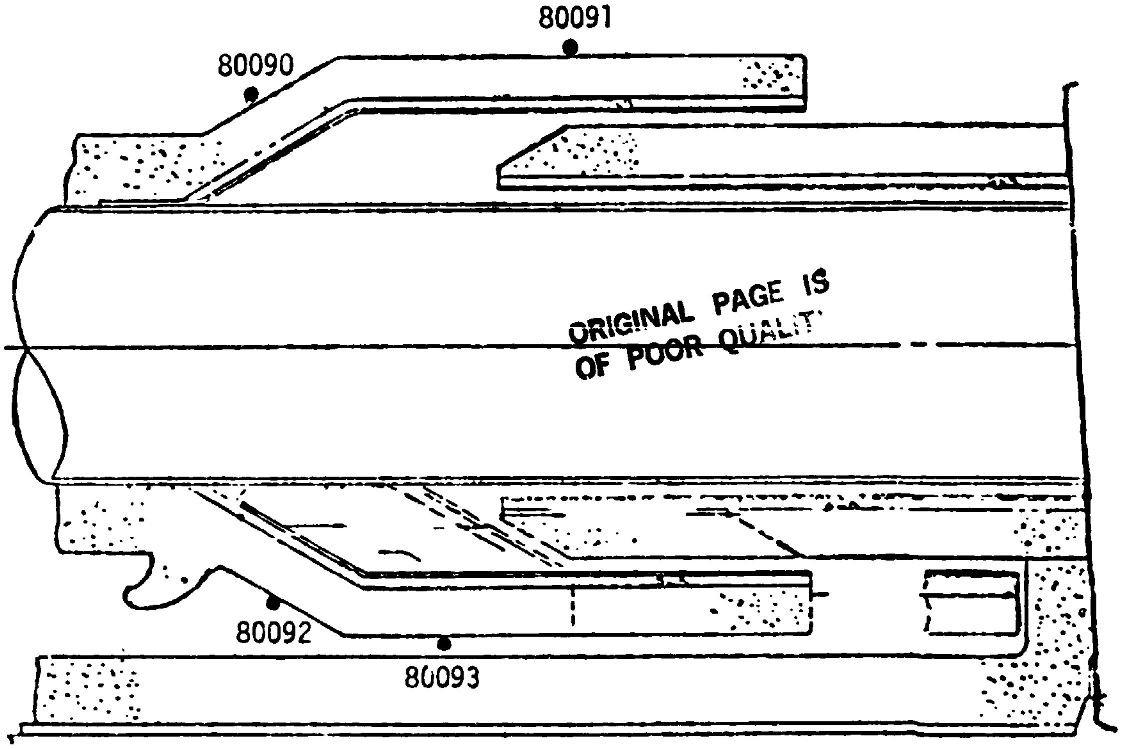

Body Point	Location
80090	Top of Shield Front Step
80091	Top of Shield Flat Section
80092	Bottom of Shield Front Step
80093	Bottom of Shield in Gap Between Shield and Tank TPS

Fig. E15 Typical LO_2 Antigeyser Line Shield Forward of Each Fitting Location (X_T=1850.60)

Note: Body Point 6394 is located on the Intertank sidewall near the fairing.

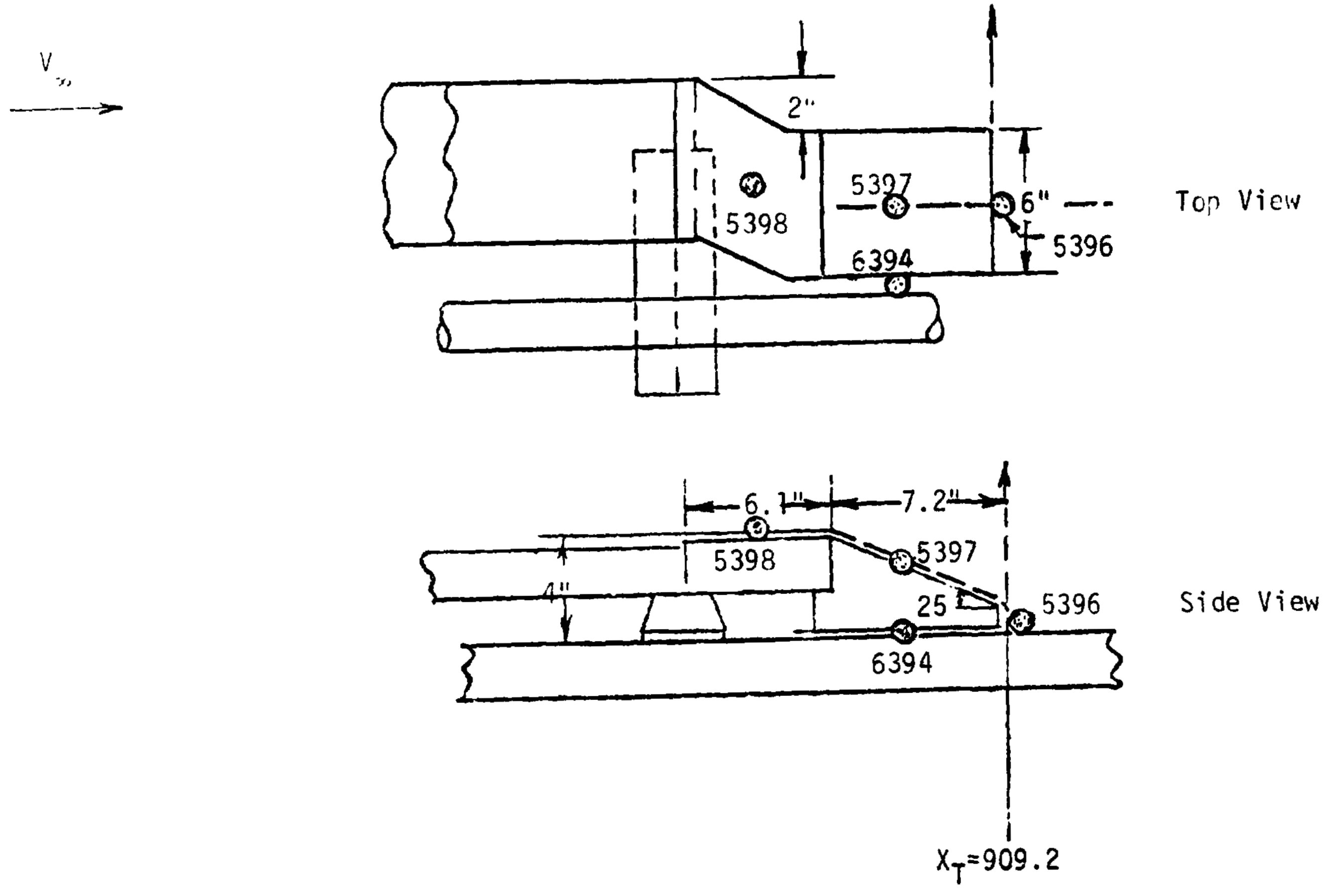

Fig. E16 Forward Electrical Conduit Aft Fairing Body Point Definition

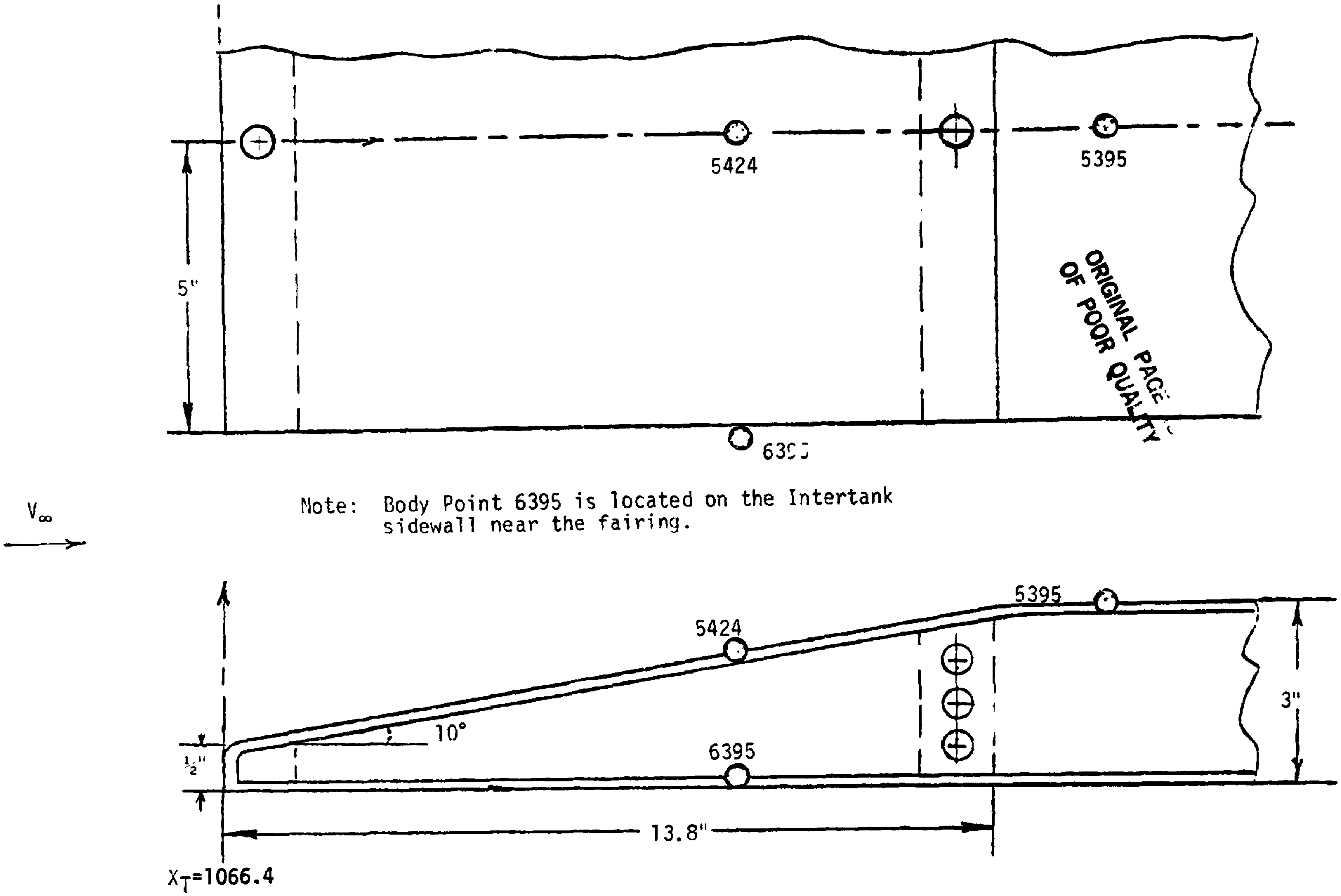

Note: Body Point 6395 is located on the Intertank sidewall near the fairing.

Fig. E17Aft Electrical Conduit Fairing Body Point Definition

Table E18

Electrical Conduit Centerline And Forward And Aft Fairing Design Body Point Definitions		
X_T (In.)	Body Point	Location
899.0	5398	Forward Conduit Aft Fairing Upper Surface
905.0	5397	Forward Conduit Aft Fairing Aft Face
905.0	6394	Located on Intertank Sidewall Near the Fairing
909.2	5396	Conduit Aft Fairing Aft Face
1074.4	5424	Conduit Aft Fairing Afterbody
1074.4	6395	On Intertank Sidewall Near Fairing
1081.4	5395	Aft Conduit Forward Fairing Forebody
1133.8	5434	Upper Centerline of Conduit θ_T=37.7°
1229.96	5484	↓
1359.15	5554	
1486.49	5624	
1615.67	5694	
1743.02	5764	
1872.20	5834	
1999.54	5904	
2036.45	5924	Upper Centerline of Conduit
1133.8	5434	Upper Centerline (Attachment No. 1)
1138.2	5014	↓
1142.74	5024	
1147.26	5034	
1149.985	5044	
1150.89	5054	Upper Centerline (Attachment No. 1)
1178.35	5064	Upper Centerline (Attachment No. 2)
1192.05	5074	↓
1196.59	5084	
1201.11	5094	
1203.84	5104	
1204.74	5114	
1229.96	5484	Upper Centerline (Attachment No. 2)
1242.85	5124	Upper Centerline (Attachment No. 3)
1256.55	5134	↓
1261.09	5144	
1265.61	5154	
1268.335	5164	
1269.24	5174	Upper Centerline (Attachment No. 3)

Table E18 (Cont.)

Electrical Conduit Centerline And Forward And Aft Fairing Design Body Point Definitions		
X_T (In.)	Body Point	Location
1565.35	5184	Upper Centerline (Attachment No. 8)
1579.05	5194	
1583.59	5204	
1588.11	5214	
1590.835	5224	
1591.74	5234	
1615.67	5694	Upper Centerline (Attachment No. 8)
1823.35	5244	Upper Centerline (Attachment No. 12)
1837.05	5254	
1841.59	5264	
1846.11	5274	
1848.835	5284	
1849.74	5294	
1872.20	5834	Upper Centerline (Attachment No. 12)
1887.85	5304	Upper Centerline (Attachment No. 13)
1901.55	5314	
1906.09	5324	
1910.61	5334	
1913 335	5344	
1914.24	5354	Upper Centerline (Attachment No. 13)
1952.35	5364	Upper Centerline (Attachment No. 14)
1966.05	5374	
1970.59	5384	
1975.11	5394	
1977.835	5404	
1978.74	5414	
1999.54	5904	Upper Centerline (Attachment No. 14)

GH$_2$ Pressure Line Fairing

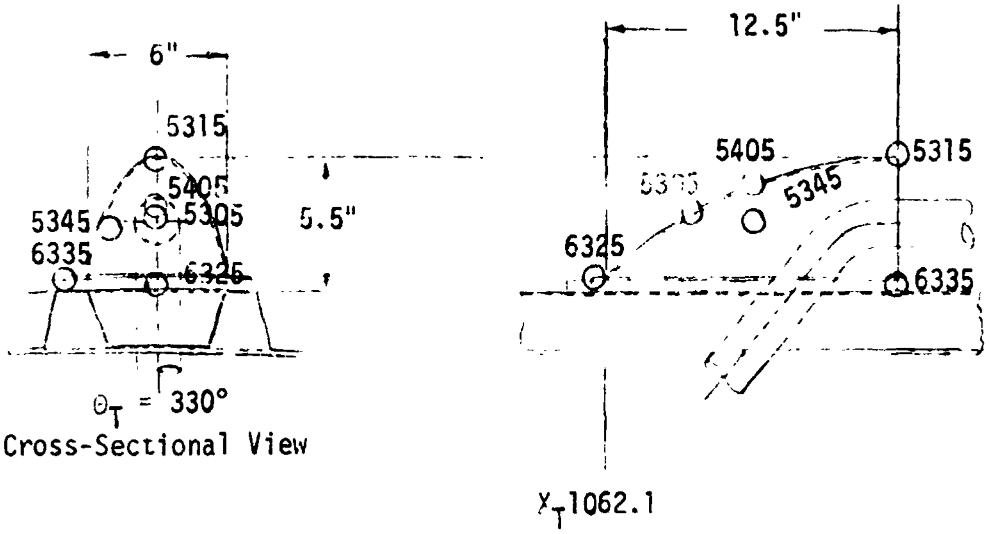

Cross-Sectional View

Side View

X_T (In.)	Body Points	Surface
1062.1	6325	Forward of Fairing
1066.1	5305	Fairing Forebody
1069.40	5405	Fairing Centerline
1074.6	5315	Fairing Afterbody
1074.6	6335	Outboard of Faring
1069.35	5345	Fairing Side

Note: Body Points 6325 and 6335 are located on the Intertank Adjacent to the GH$_2$ Pressure Line Fairing.

Fig. E19 GH$_2$ Pressure Line Fairing Body Point Definition

Table E20

GH_2 Pressure Line Body Point Definition Θ_T=330°		
X_T (In.)	Body Point	Location
1[illegible].09	5425	Upper Centerline Press. Line
1133.84	5435	
1229.96	5485	
1359.15	5555	
1486.49	5625	
1615.67	5695	
1743.02	5765	
1872.20	5835	
1994.19	5905	
2036.45	5925	Upper Centerline Press. Line
1113.31	5415	Adjacent to Attachment Fitting No. 1
1141.84	5445	
1148.98	5455	
1150.34	5465	
1158.44	5475	
1160.27	5495	
1162.54	5505	
1172.65	5515	Adjacent to Attachment Fitting No. 1
1196.15	5535	Adjacent to Attachment Fitting No. 2
1203.29	5545	
1204.65	5565	
1212.75	5575	
1214.58	5585	
1216.85	5595	
1237.65	5605	Adjacent to Attachment Fitting No. 2
1302.65	5615	Adjacent to Attachment Fitting No. 4
1326.15	5635	
1333.29	5645	
1334.65	5655	
1342.75	5665	
1344.58	5675	
1346.85	5685	
1367.65	5705	Adjacent to Attachment Fitting No. 4
1887.65	5715	Adjacent to Attachment Figgint No. 13
1911.15	5725	
1918.29	5735	
1919.65	5745	
1927.75	5755	Adjacent to Attachment Fitting No. 13

Table E20 (Cont'd)

GH$_2$ Pressure Line Body Point Definition		
X$_T$ (In.)	Body Point	Line Upper Centerline Surface
1924.6	5775	Adjacent to Attachment Fitting No. 13
1926.9	5785	Adjacent to Attachment Fitting No. 13
1947.3	5795	Adjacent to Attachment Fitting No. 14
1970.8	5805	↓
1977.94	5815	↓
1979.3	5825	↓
1987.4	5845	↓
1989.23	5855	↓
1991.5	5865	Adjacent to Attachment Fitting No. 14
2024.5	5875	Adjacent to Attachment Fitting No. 15
2048.0	5885	↓
2055.14	5895	↓
2056.5	5915	↓
2064.6	5935	Adjacent to Attachment Fitting No. 15

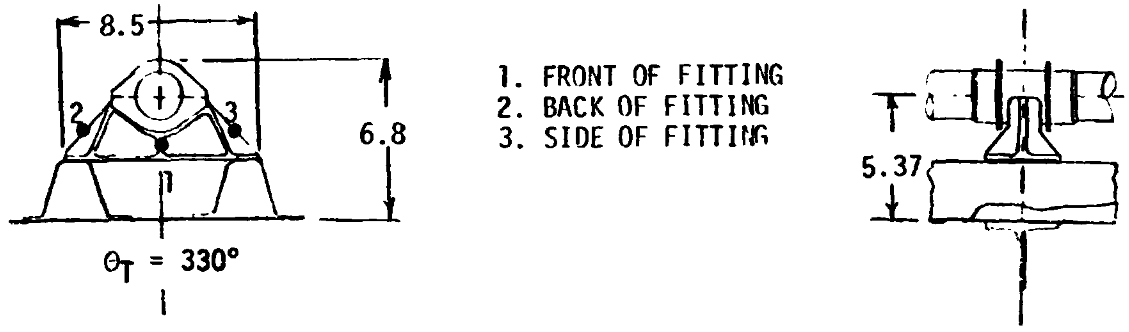

Sta. 1082
Cross-Sectional View

Sta. 1082
Side View

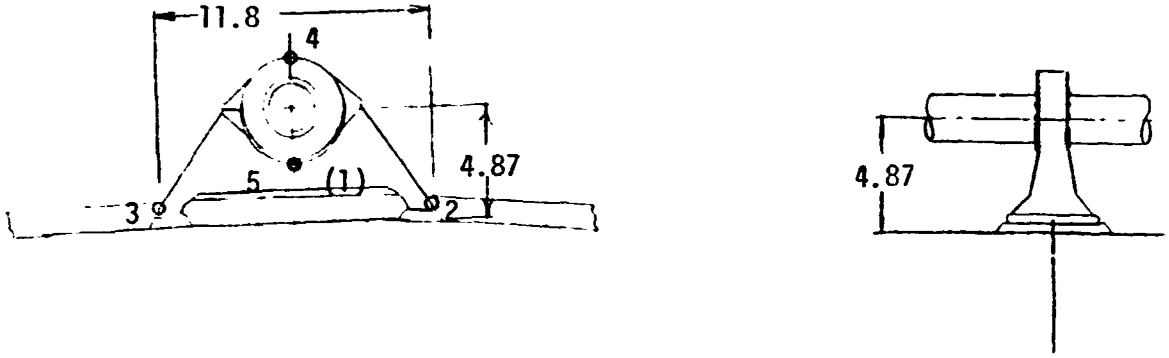

All Other Stations
Cross-Sectional View

Side View

1. FORWARD FACE
2. SIDE-INBOARD
3. SIDE-OUTBOARD
4. TOP FACE
5. AFT FACE

Fig. E21 GH_2 Pressure Line Attachment Fitting Design Body Points For Typical Fitting Stations

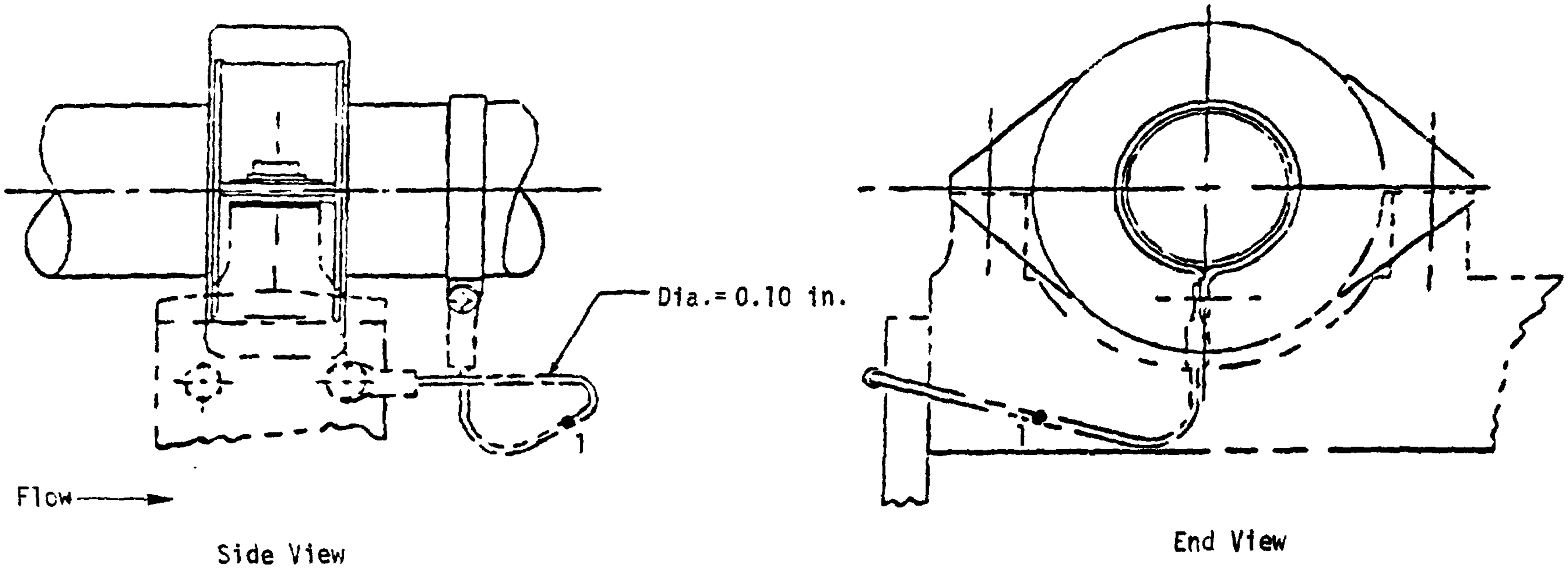

Body Points for Position 1	Comment
80096	Strap Heating Typical at all LO_2 Feedline Fitting Locations
80097	Strap Heating Typical at all GO_2 Line and Cable Tray Fitting Locations
80098	Strap Heating Typical at all GH_2 Pressure Line Fitting Locations

Fig. E22 Typical Barry Mount to Fitting Grounding Strap

Table E23

GH_2 Pressure Line Attachment Fitting Body Point Definitions

X_T (In.)	Body Point	Location
1082.0	80063	Front Face
	80064	Side Face
	80065	Aft Face
1150.8	1630	Forward Face
1151.8	1631	Side-Inboard (Towards θ_T=0)
↓	1632	Side-Outboard (Away from θ_T=0)
1151.8	1633	Top Face
1152.8	1634	Aft Face
1204.6	1640	Forward Face
1205.6	1641	Side-Inboard
↓	1642	Side-Outboard
1205.6	1643	Top Face
1206.6	1644	Aft Face
	No B.P.	Top Centerline
1270.2		
1333.8	1650	Forward Face
1334.8	1651	Side-Inboard
↓	1652	Side-Outboard
1334.8	1653	Top Face
1335.8	1654	Aft Face
	No B.P.	Top Centerline
1399.4	↓	↓
1464.0		
1528.6		
1593.2		
1657.8		
1722.4		
1787.0		
1851.6		
1918.8	1660	Forward Face
1919.8	1661	Side-Inboard
↓	1662	Side-Outboard
1919.8	1663	Top Face
1920.8	1664	Aft Face

Table E23 (Cont.)

GH$_2$ Pressure Line Attachment Fitting Body Point Definitions		
X_T (In.)	Body Point	Location
1979.8	1670	Forward Face
1980.8	1671	Side-Inboard
↓	1672	Side-Outboard
1980.8	1673	Top Face
1981.8	1674	Aft Face
2057.0	1680	Forward Face
2058.0	1681	Side-Inboard
↓	1682	Side-Outboard
2058.0	1683	Top Face
2059.0	1684	Aft Face

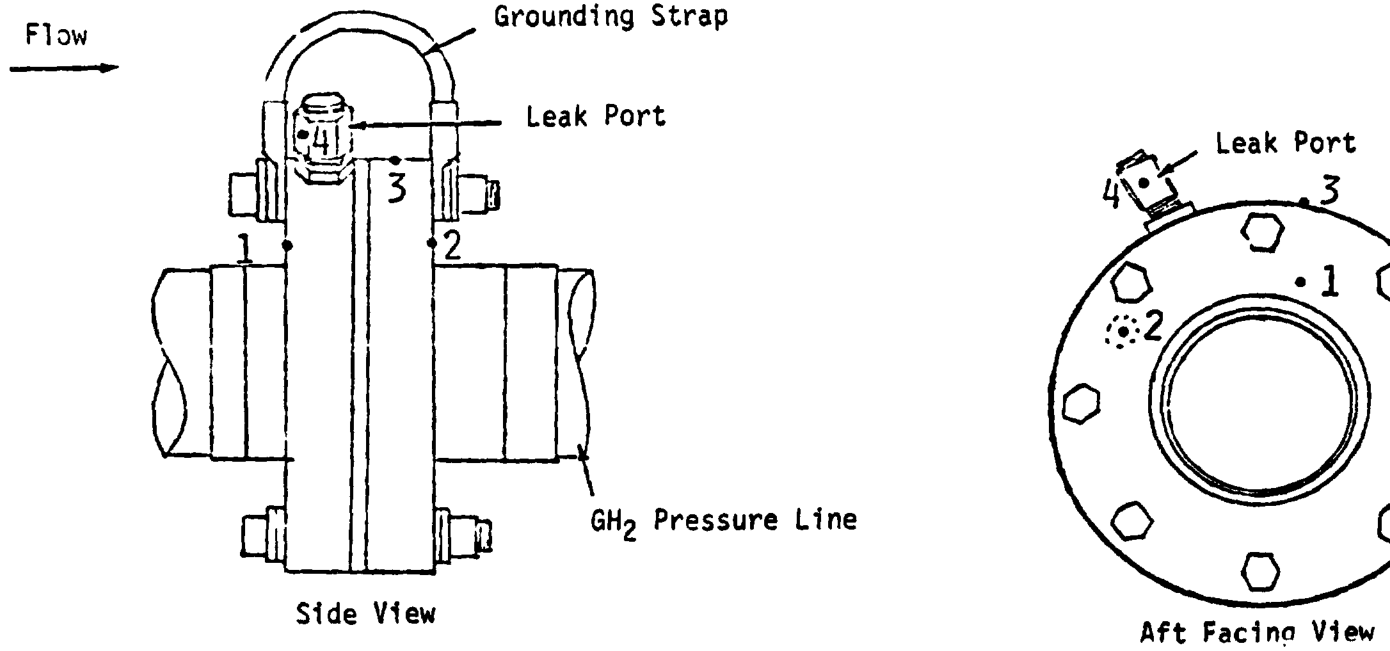

	Body Point I.D. and Location			
	Front Face	Back Face	Side Face	Leak Port
STA	1	2	3	4
1088	80045	80046	80047	80048
1327	80049	80050	80051	80052
1566	80053	80054	80055	80056
1805	80057	80058	80059	80042
2044	80043	80060	80061	80062

Fig. E24 GH_2 Pressure Line Flanges Body Point Definition **at Fitting Stations**

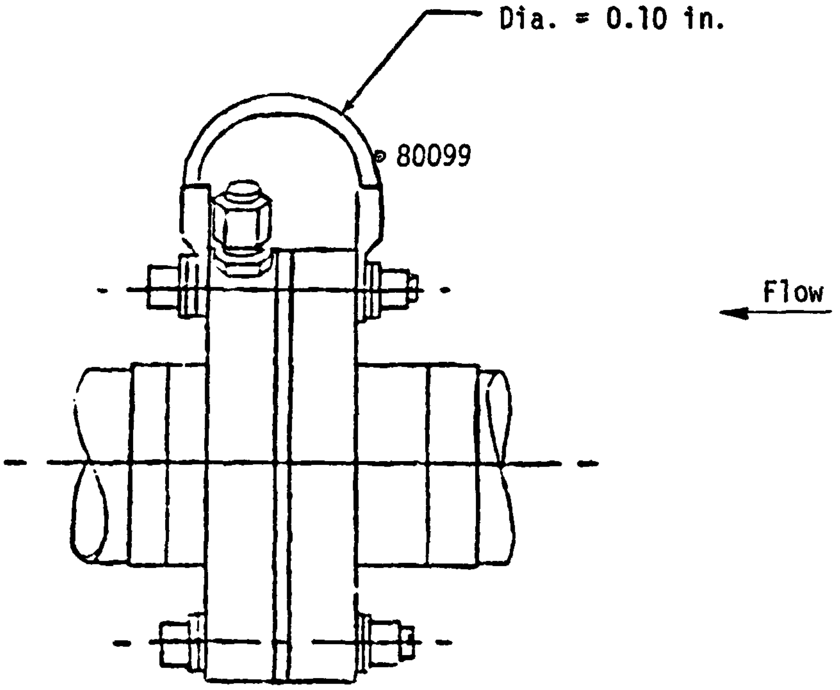

Body Point	Locations	
	θ_T	STA. No. Strap Heating
80099	330 ↓	2044 1805 1566 1327 1088

Fig. E25 Typical GH_2 Pressure Line Flange Grounding Strap

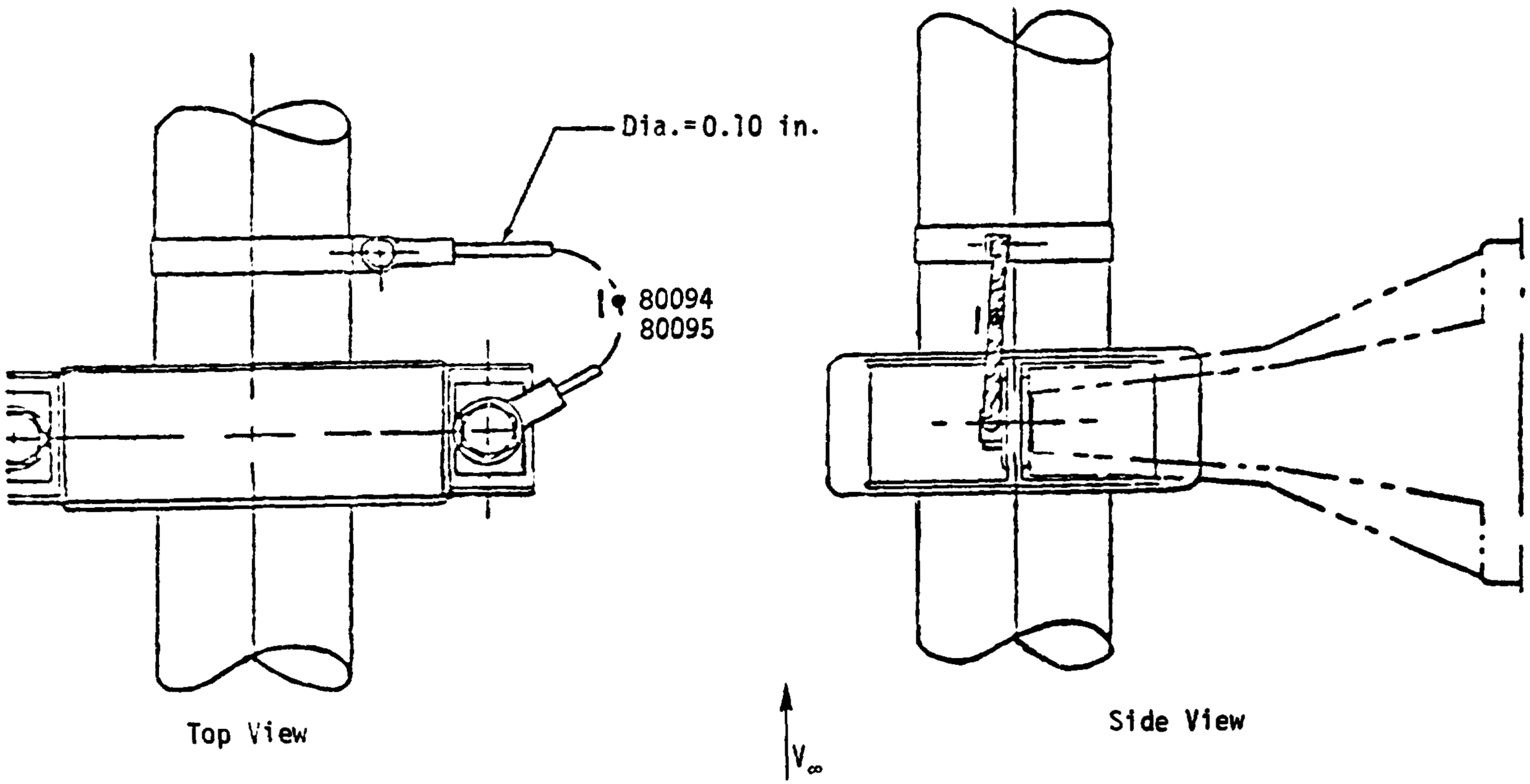

Body Point	Location
80094	Strap Heating Typical at all GH_2 Pressure Line Fitting Locations
80095	Strap Heating Typical at all GO_2 Pressure Line Fitting Locations

Fig. E26 Typical Barry Mount to Pressure Line Grounding Strap

2.2.4 ET/Orbiter Aft Interface Structure

This subsection contains geometry and body point information for all protuberances located at the aft end of the LH_2 tank. The information sequence is as follows:

- Electrical conduit
- Aft thrust strut
- Aft thrust strut attachment longeron
- Vertical strut
- Sway strut
- Aft support beam
- Ball fitting
- LO_2 feedline, Antigeyser line, and GO_2 pressure line
- LH_2 feedline, Recirculation, and GH_2 pressure line
- LO_2 and LH_2 Umbilical plates
- LO_2 and LH_2 feedline brackets
- He injection system line

Note: F = Division 2.2.4 in figures and tables

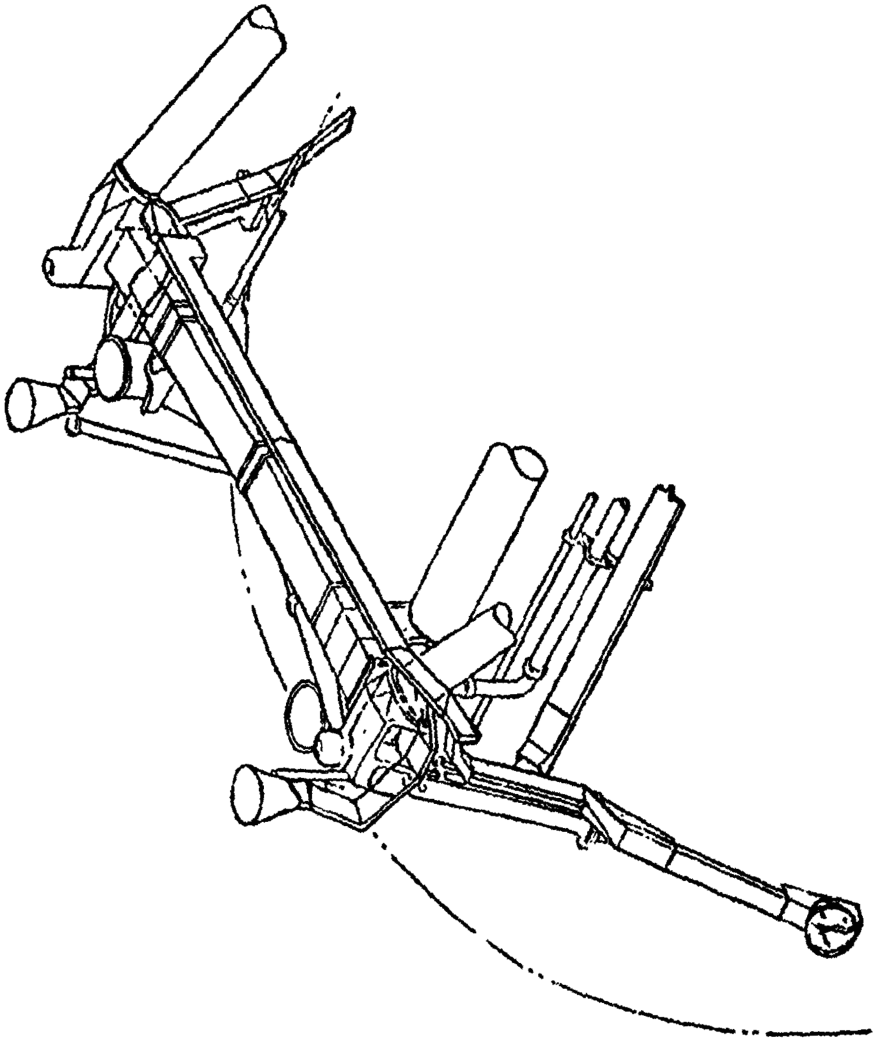

Fig. F1 ET/Orbiter Aft Interface Structure

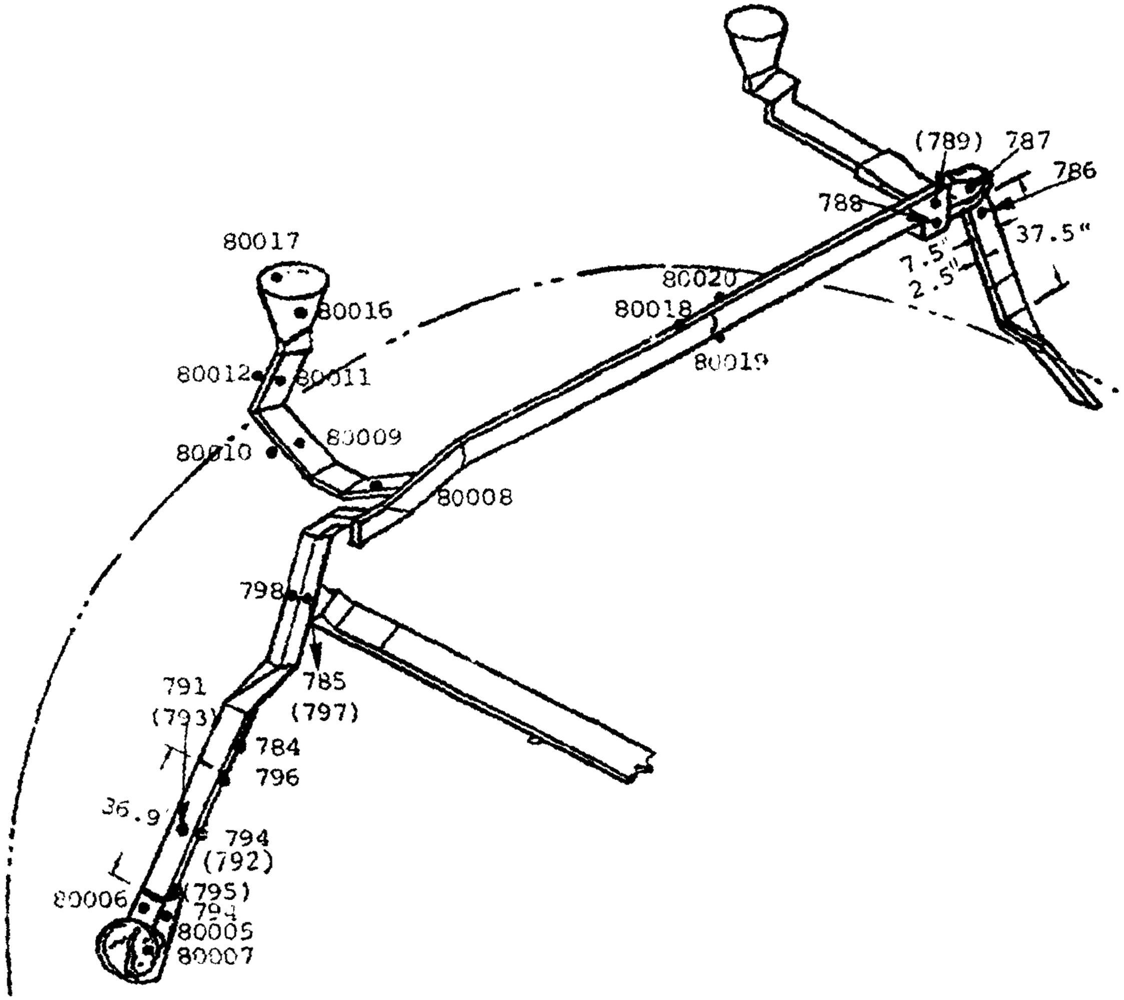

Fig. **F2** ET/Orbiter Electrical Interface Cable and Conduit Design Body Point Definition

Table F3

ET/Orbiter Electrical Interface Cable and Conduit Design Body Point Definition	
Body Point	Component Surface
785	Cable Tray - Forward Face
786	Cable - Forward Face
787	↓
788	↓
789	Cable - Umbilical Cavity
790	Conduit - Forward Face
791	Conduit - Outboard Face
792	Conduit - Aft Face
793	Conduit - Inboard Face
794	Cable - Forward Face
795	Cable - Aft Face
796	Cable - Aft Face
797	Cable Tray - Aft Face
798	Cable Tray - Side Face
[910] 80005	ET/SRB Fitting Fairing Front Face
80006	ET/SRB Fitting Fairing Top
80007	ET/SRB Fitting Fairing Inside
80008	Cable Tray Top
80009	Cable Tray Top
80010	Cable Tray Bottom
80011	Cable Tray Front
80012	Cable Tray Back
80016	ET/Orb Disconnect Fairing Front
80017	ET/Orb Disconnect Fairing Back
80018	Crossbeam Cable Tray Top
80019	Crossbeam Cable Tray Bottom
80020	Crossbeam Cable Tray Back

[ ] Reference Body Point

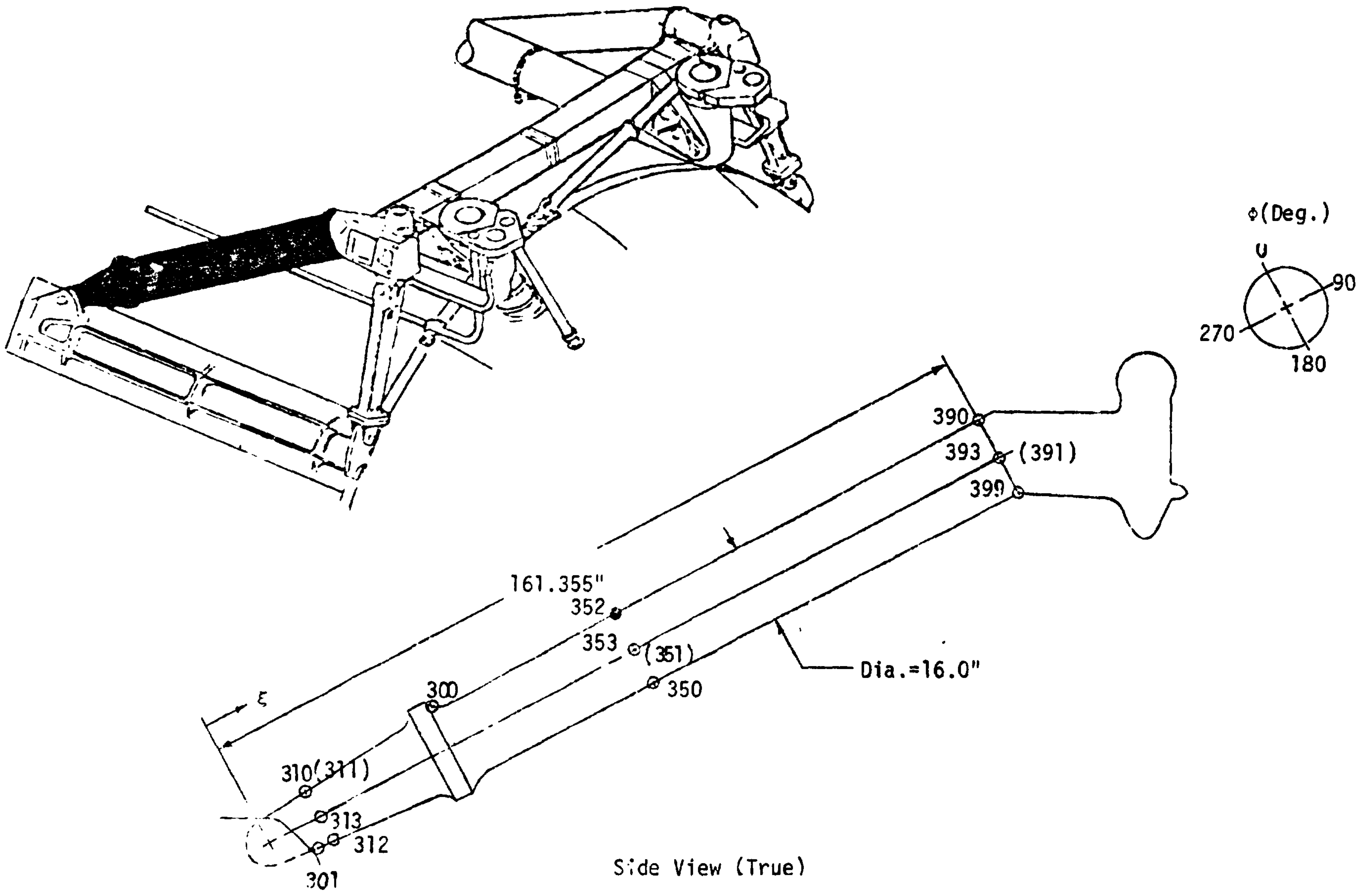

Note. Body points enclosed in parentheses are for φ = 90 degrees.

Fig. F4 ET/Orbiter Aft Thrust Strut Design Body Point Definition

Table F5

ET/Orbiter Aft Thrust Strut Design Body Point Definition			
Body Point	Location	ξ (in.)	Φ (deg.)
300	ET/Orbiter Aft Thrust Strut	40.34	0
301	↓	8.0	180
310	↓	11.0	0
311	↓	↓	90
312	↓	↓	180
313	↓	↓	270
352	↓	80.67	0
351	↓	↓	90
350	↓	↓	180
353	↓	↓	270
390	↓	161.355	0
391	↓	↓	90
399	↓	↓	180
393	↓	↓	270

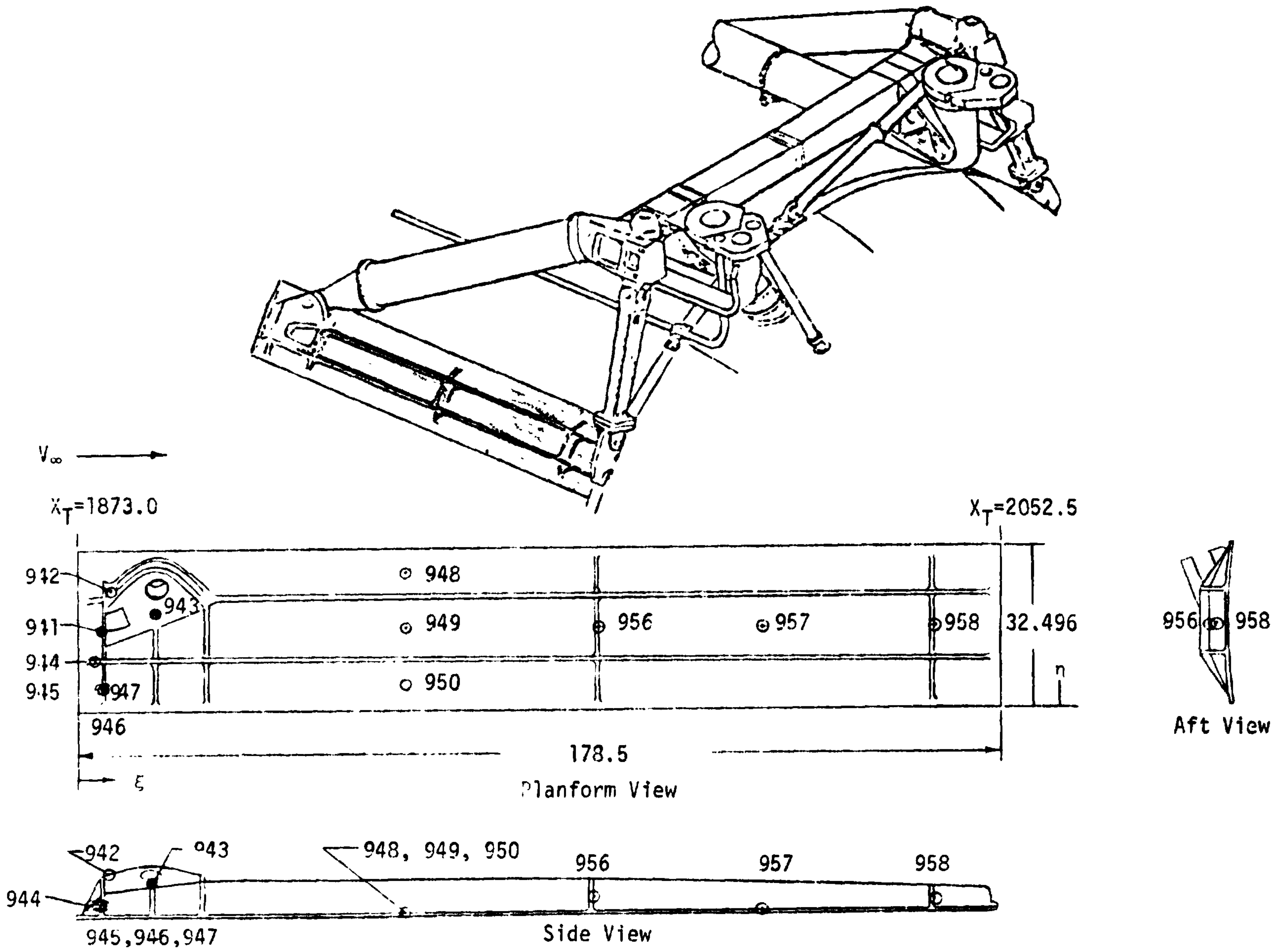

Fig. F6 ET/Orbiter Thrust Strut Attachment Longeron Design Body Point Definition

Table F7

Thrust Strut Attachment Longeron Design Body Point Definition

Body Point	Location	ξ (in.)	η (in.)
941	Forward Face	4.5	16.25
942	Upper Face	6.5	24.3
943	Side Face	15.0	20.0
944	Forward Face	3.0	10.5
945	Forward Face	4.5	5.0
946	Upper Face	4.75	5.0
947	Aft Face	5.0	5.0
948	Upper Face	63.5	27.496
949	Upper Face	63.5	16.25
950	Upper Face	63.5	5.0
956	Aft Face	101.0	16.25
957	Upper Face	133.0	16.25
958	Aft Face	166.5	16.25

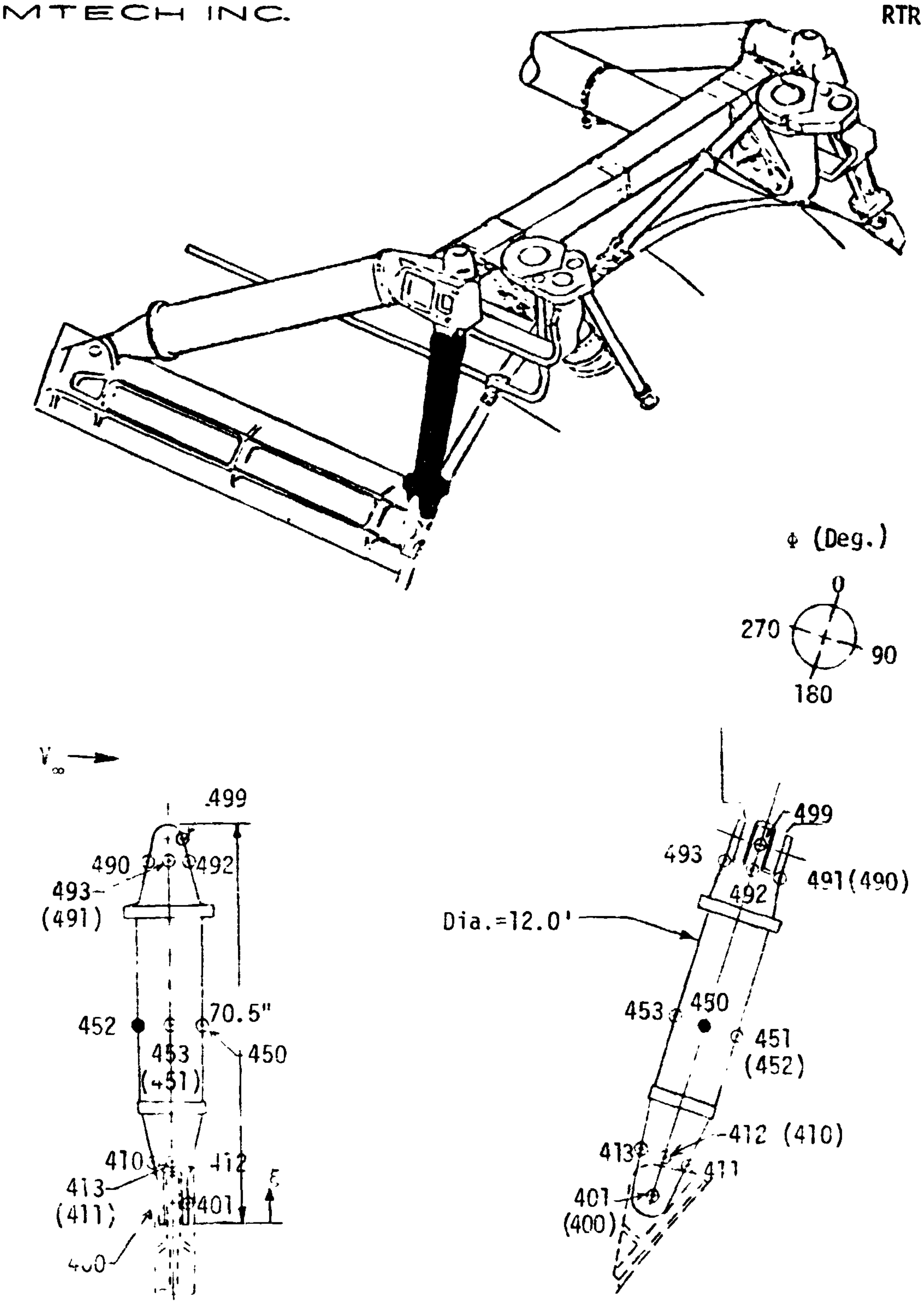

Side View (True)

Aft View

Note: The body points enclosed in parentheses are oriented 180 degrees from the location shown in the respective view.

Fig. F8 ET/Orbiter Aft Vertical Strut Design Body Point Definition

Table F9

ET/Orbiter Aft Vertical Strut Design Body Point Definition

Body Point	Location	ξ (in.)	ϕ (deg.)
400	ET/Orbiter Aft Vertical Strut	4.0	0
401	↓	4.0	180
410		11.0	0
411		↓	90
412			180
413			270
462		35.25	0
451		↓	90
450			180
453			270
490		64.0	0
491		↓	90
492			180
493			270
499		67.0	180

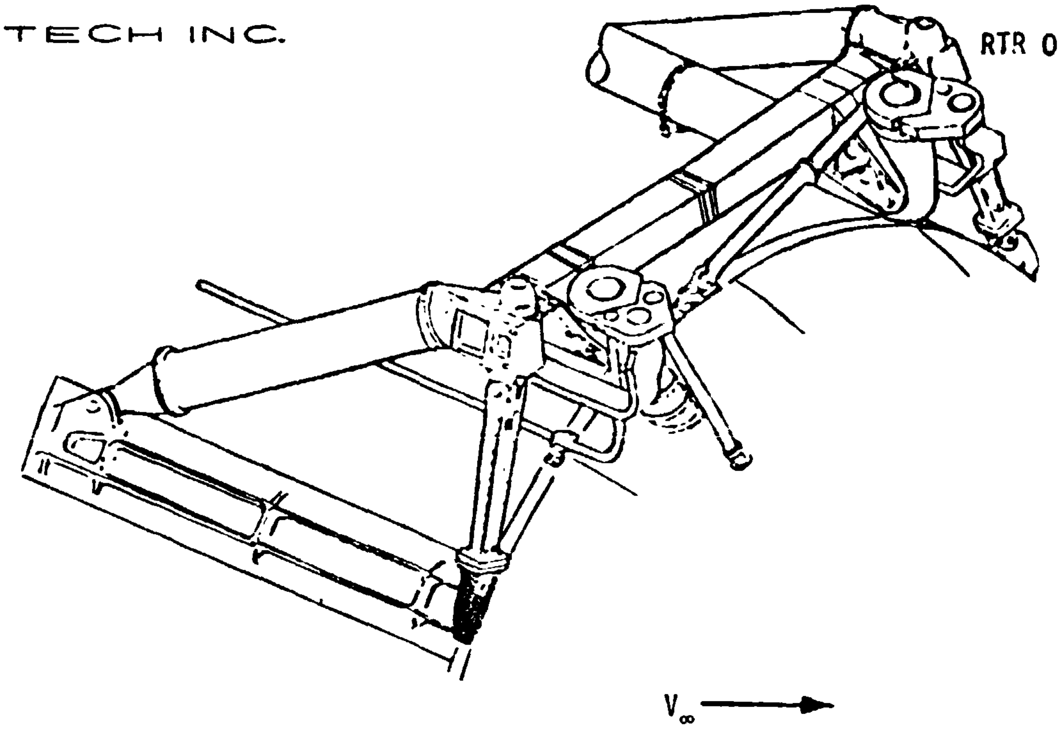

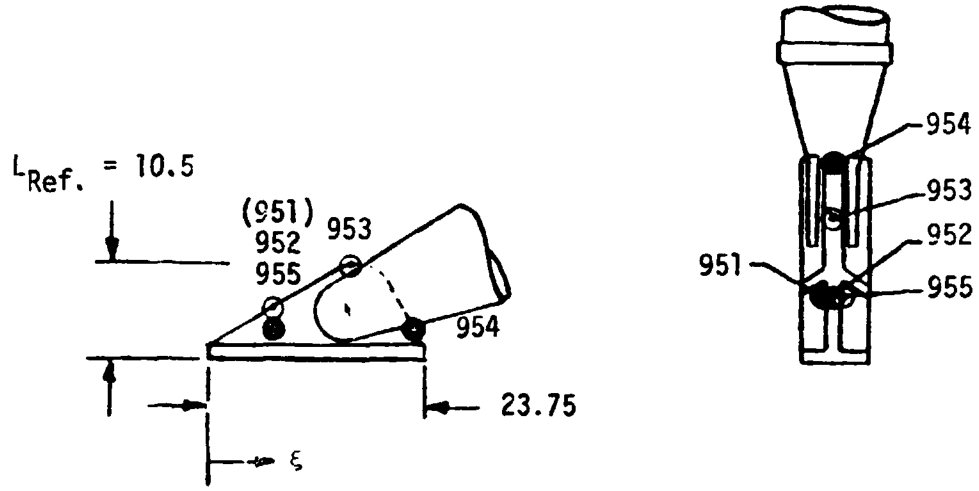

Left Aft View

Planform View

Body Point	Location	ξ (In.)
951	Forward Face	7.2
952	Side Face	7.2
953	Upper Face	15.5
954	Side Face	23.0
955	Aft Face	7.2

Fig.F10 ET/Orbiter Vertical Strut Fitting Design Body Point Definition

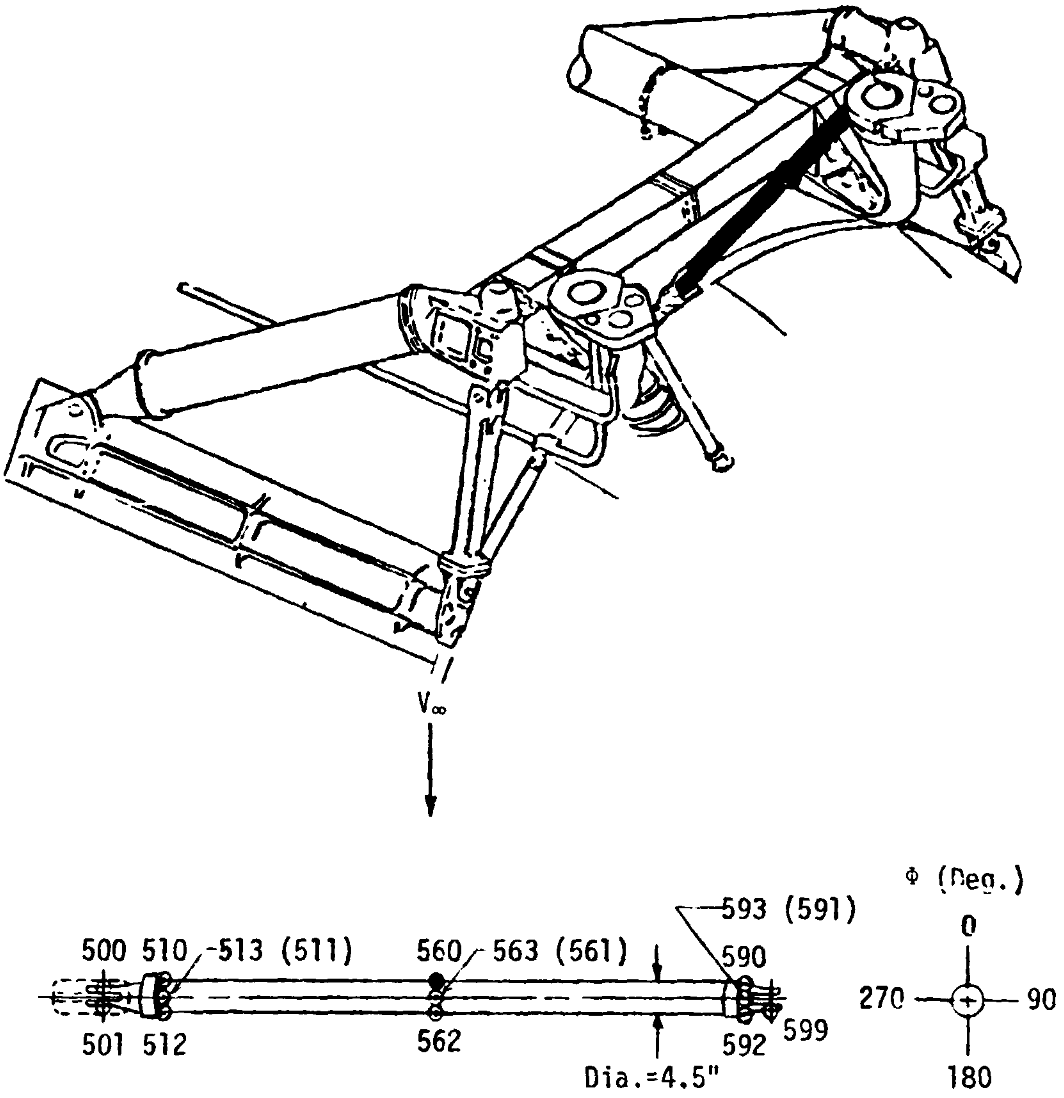

Planform View

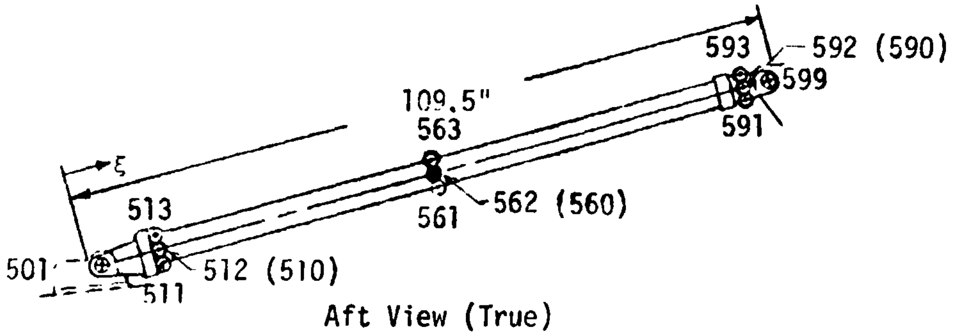

Aft View (True)

Note: The body points enclosed in parentheses are oriented 180 degrees from the location shown in the respective view.

Fig. F11 ET/Orbiter Aft Sway Strut Design Body Point Definition

Table F12

ET/Orbiter Aft Sway Strut Design Body Point Definition

Body Point	Location	ξ (in.)	Φ (deg.)
500	ET/Orbiter Aft Sway	0	0
501	↓	0	180
510	↓	11.0	0
511	↓	↓	90
512	↓	↓	180
513	↓	↓	270
560	↓	54.75	0
561	↓	↓	90
562	↓	↓	180
563	↓	↓	270
590	↓	104.0	0
591	↓	↓	90
592	↓	↓	180
593	↓	↓	270
599	↓	109.5	180

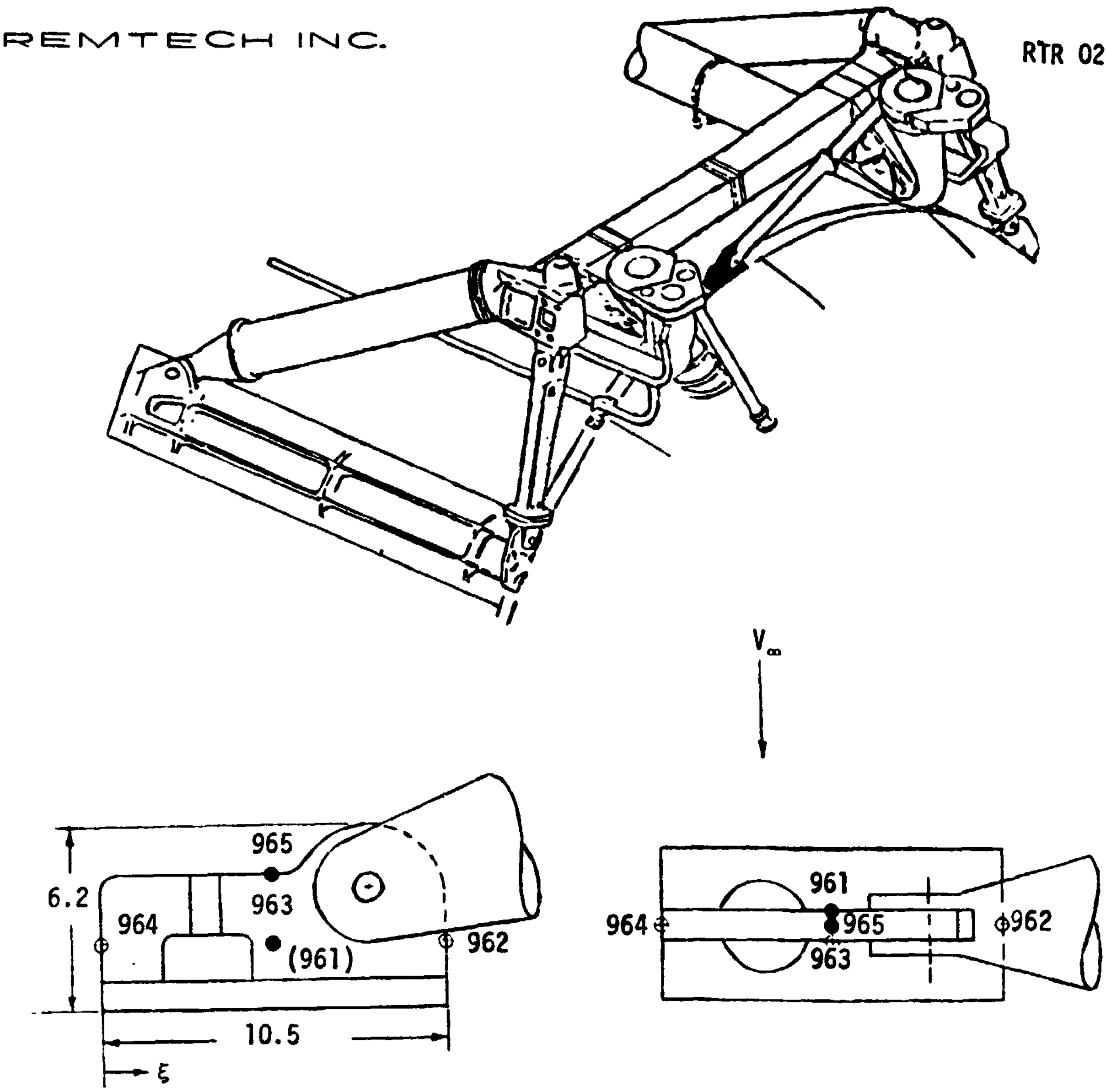

Aft View

Planform View

Body Point	Location	ξ(In.)
961	Forward Face	5.75
962	Side Face	10.5
963	Aft Face	5.75
964	Side Face	0
965	Top Face	5.75

Fig. F13 ET/Orbiter Sway Strut Fitting Design Body Point Definition

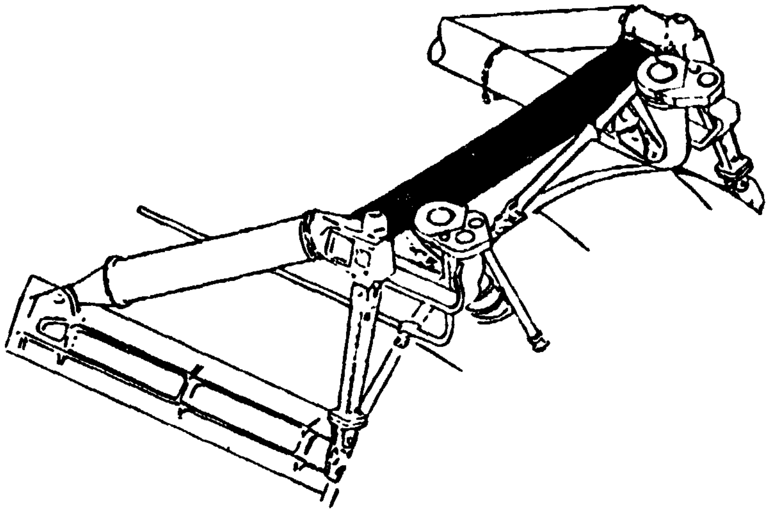

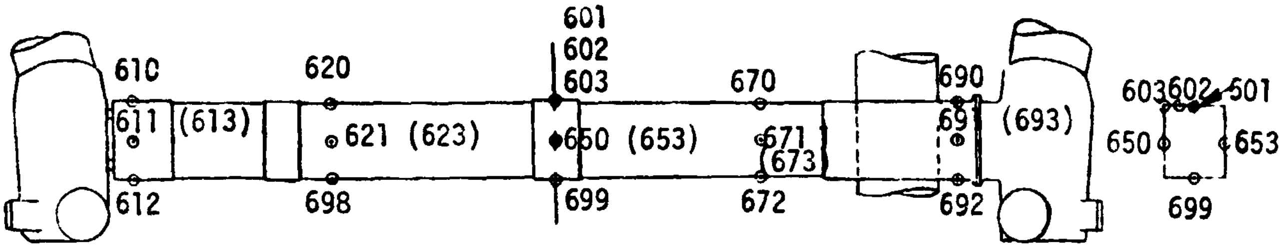

Planform View

Typical Cross-Section

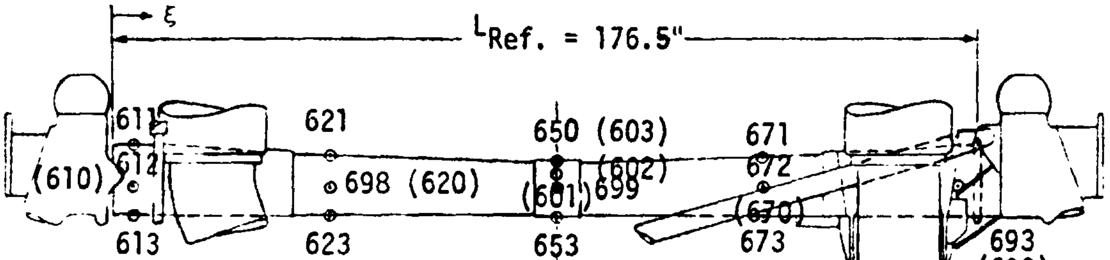

Aft View

Fig. F14 ET Aft Support Beam Design Body Point Definition

Table F15

ET Aft Cross Beam Design Body Point Definition		
Body Point	Location	ε (In.)
610	Forward Face	4.0
611	Upper Face	↓
612	Aft Face	↓
613	Lower Face	↓
620	Forward Face	44.2
621	Upper Face	↓
698	Aft Face	↓
623	Lower Face	↓
601	Forward Face	90.5
602	↓	↓
603	↓	↓
650	Upper Face	↓
653	Lower Face	90.5
670	Forward Face	132.0
671	Upper Face	↓
672	Aft Face	↓
673	Lower Face	↓
690	Forward Face	172.5
691	Upper Face	↓
692	Aft Face	↓
693	Lower Face	↓
699	Aft Face	40.5

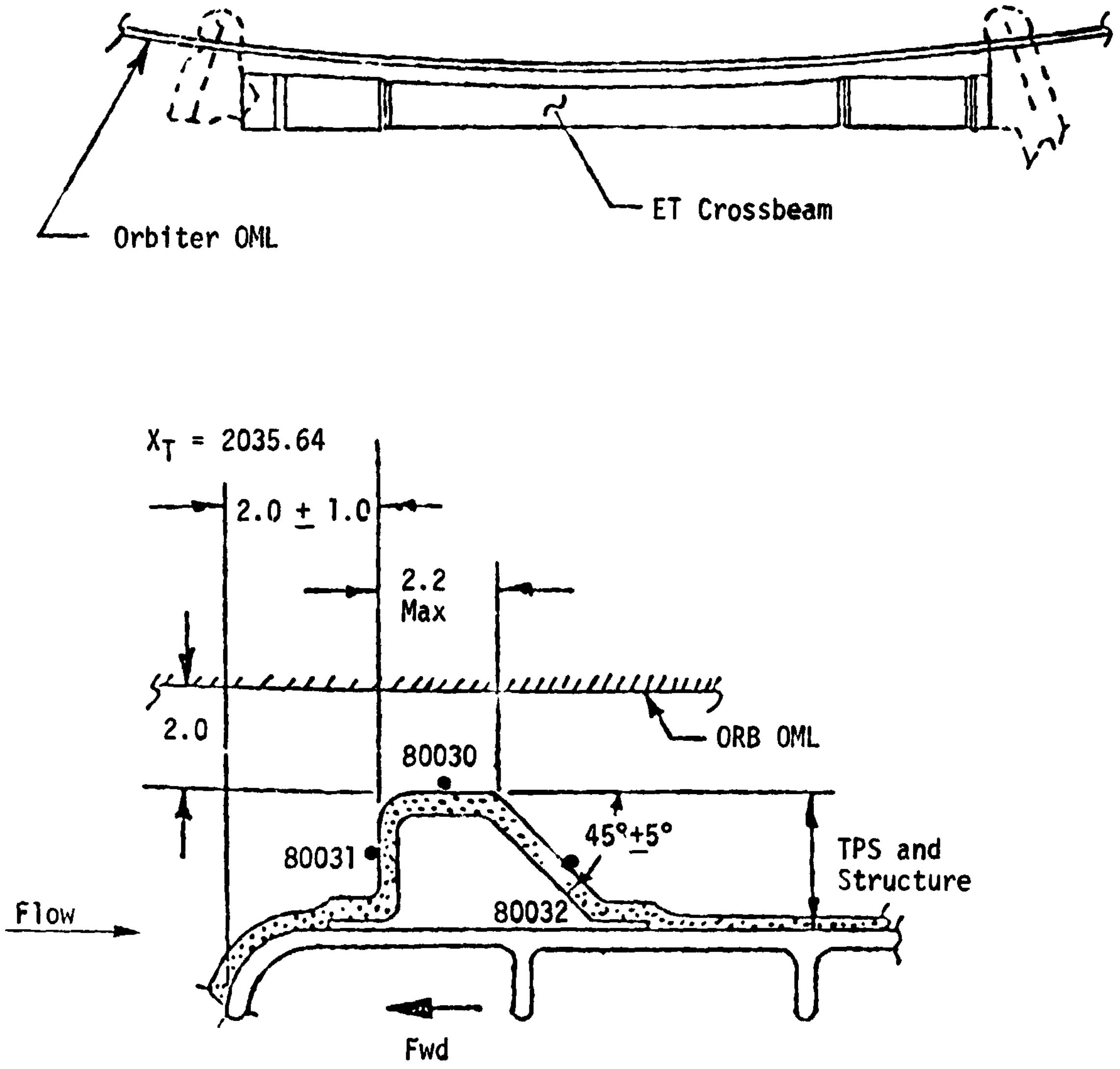

Body Point	Comment
80030	Heating to Top of Gap Control Spacer
80031	Heating to Front of Gap Control Spacer
80032	Heating to Aft Face of Gap Control Spacer

Fig.F16 ET/Orbiter Gap Control Spacer

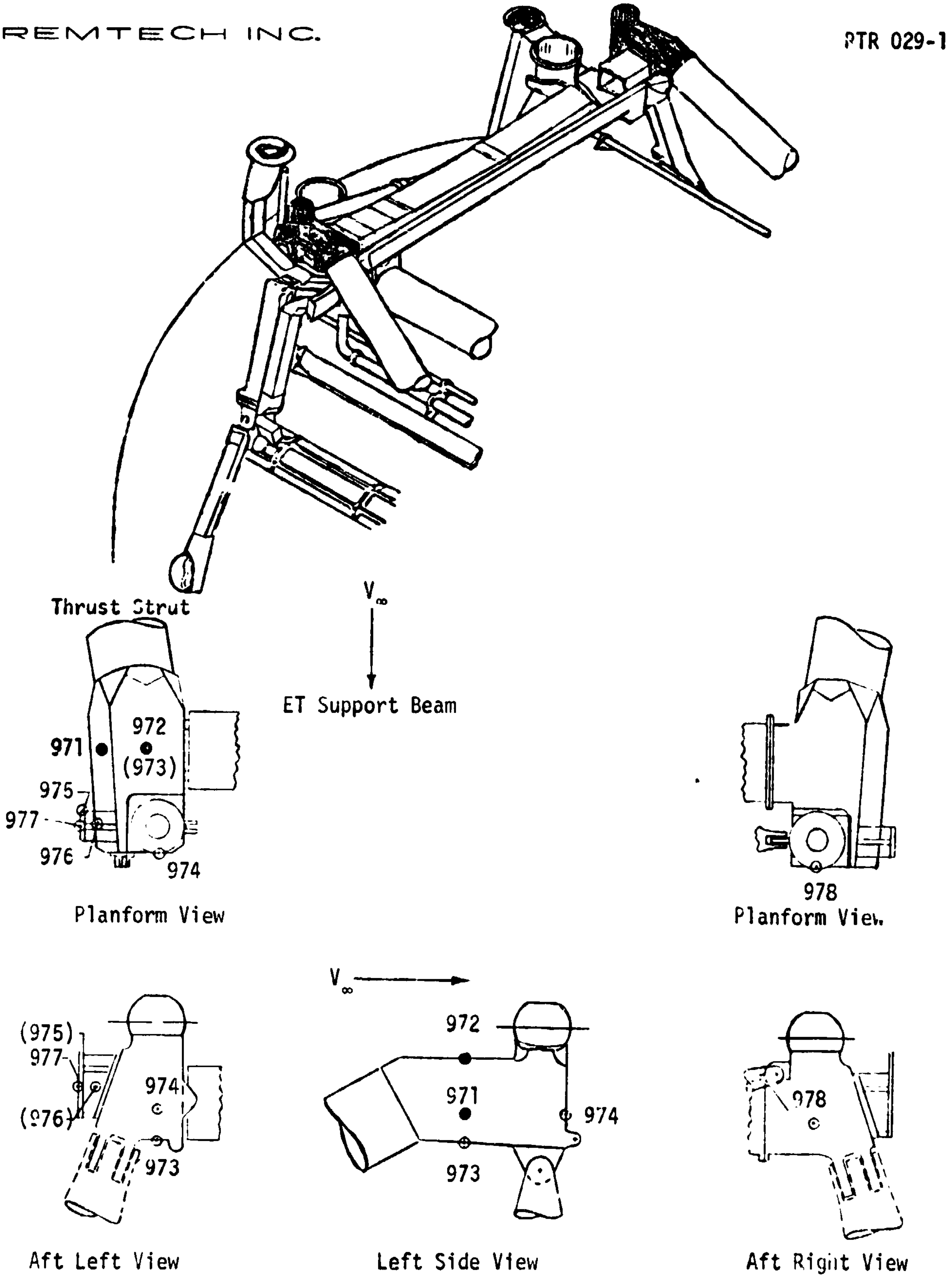

Fig. F17 ET/Orbiter Aft Ball Fitting Design Body Point Definition

Table F18

ET/Orbiter Aft Ball Fitting Design Body Point Definition		
Body Point	Location	
971	Outboard Side	
972	Upper Surface	
973	Lower Surface	
974	Aft Face	
975	Forward Face	
976	Forward Face	
977	Outboard Face	
978	Aft Face (Right Component)	

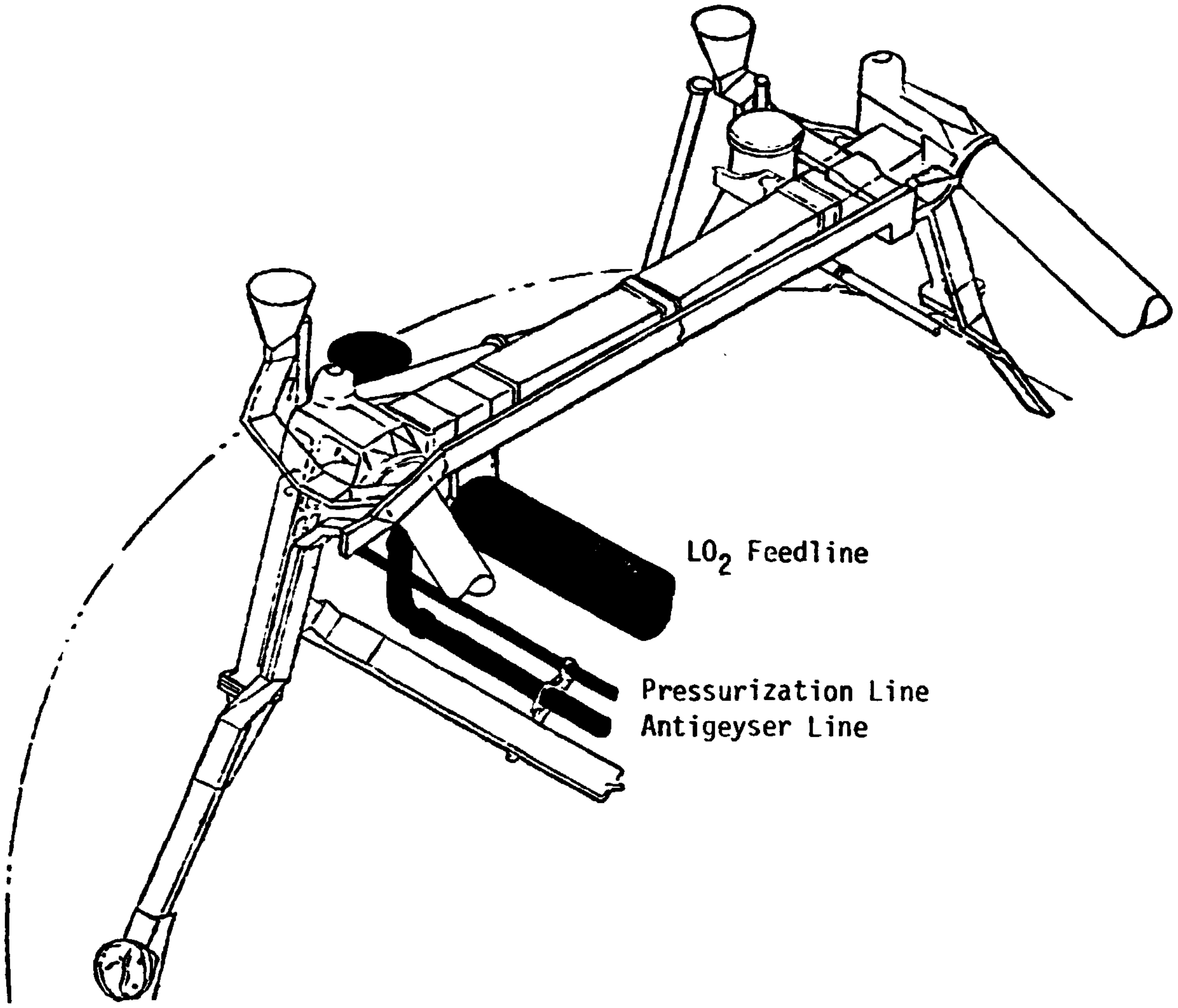

Fig. F19 LO_2 Feedline, Antigeyser, and Pressurization Line Definition

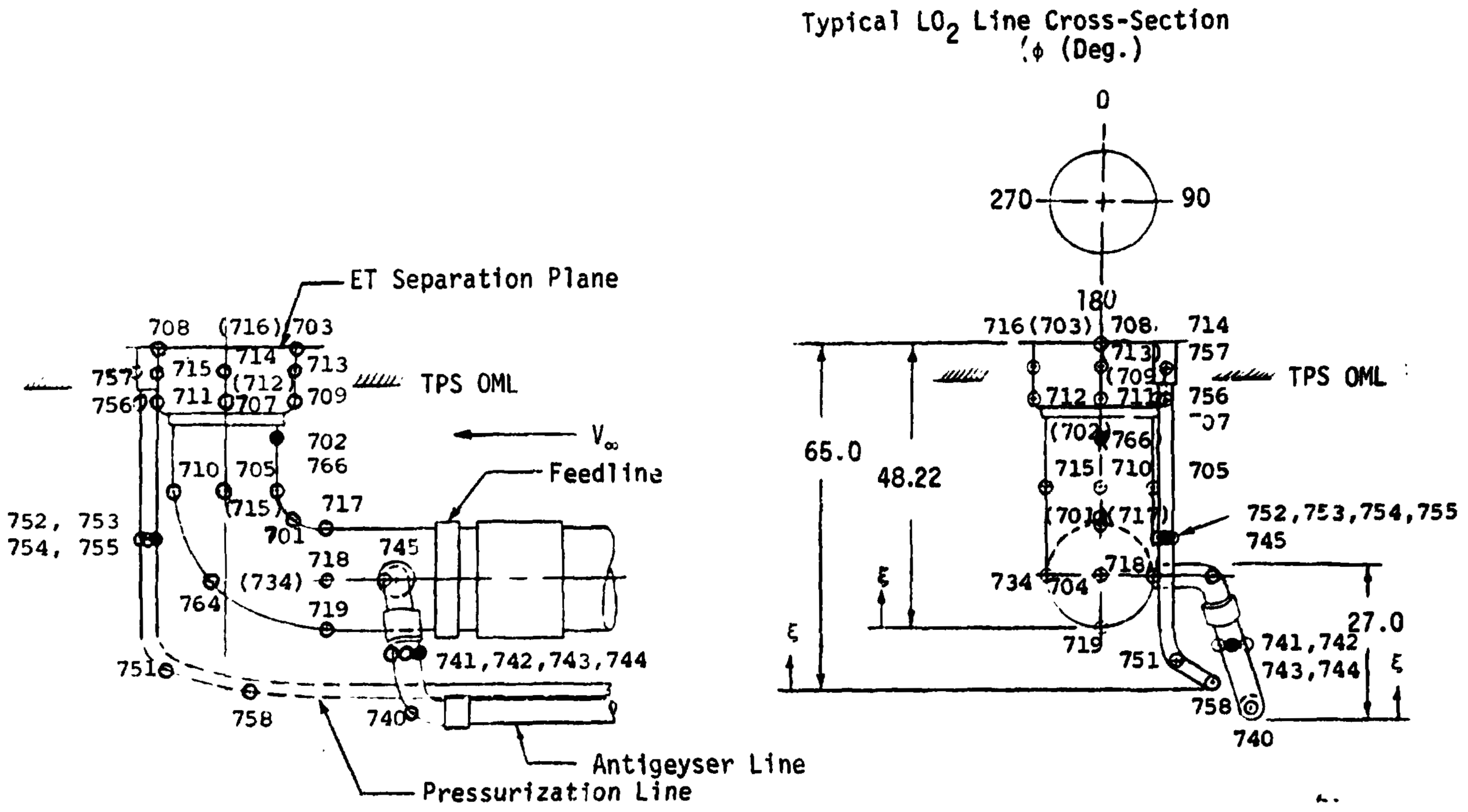

Note: The body points enclosed in parentheses are located on the opposite side of the component

Fig. F20 LO_2 Feedline, Antigeyser, and Pressurization Line Design Body Point Definition

Table F21

LO_2 Feedline, Antigeyser, and Pressurization Line Design Body Point Definition			
Body Point	Location	ξ (In.)	φ (Deg.)
719	LO_2 Feedline	0	180
717		17.0	0
702		32.3	0
703		48.22	0
718		8.5	90
704		8.5	180
734		8.5	270
705		24.11	90
706			0
710			180
715		24.11	270
709		38.22	0
707			90
711			180
712		38.22	270
713		44.22	0
714			90
708			180
716		44.22	270
740	LO_2 Antigeyser Line	2.0	180
741		13.5	0
742			90
743			180
744		13.5	270
745		25.0	180
751	LO_2 Pressurization Line	10.5	180
752		32.5	0
753			90
754			180
755		32.5	270
756		55.0	180
757		61.0	180
758		1.0	180

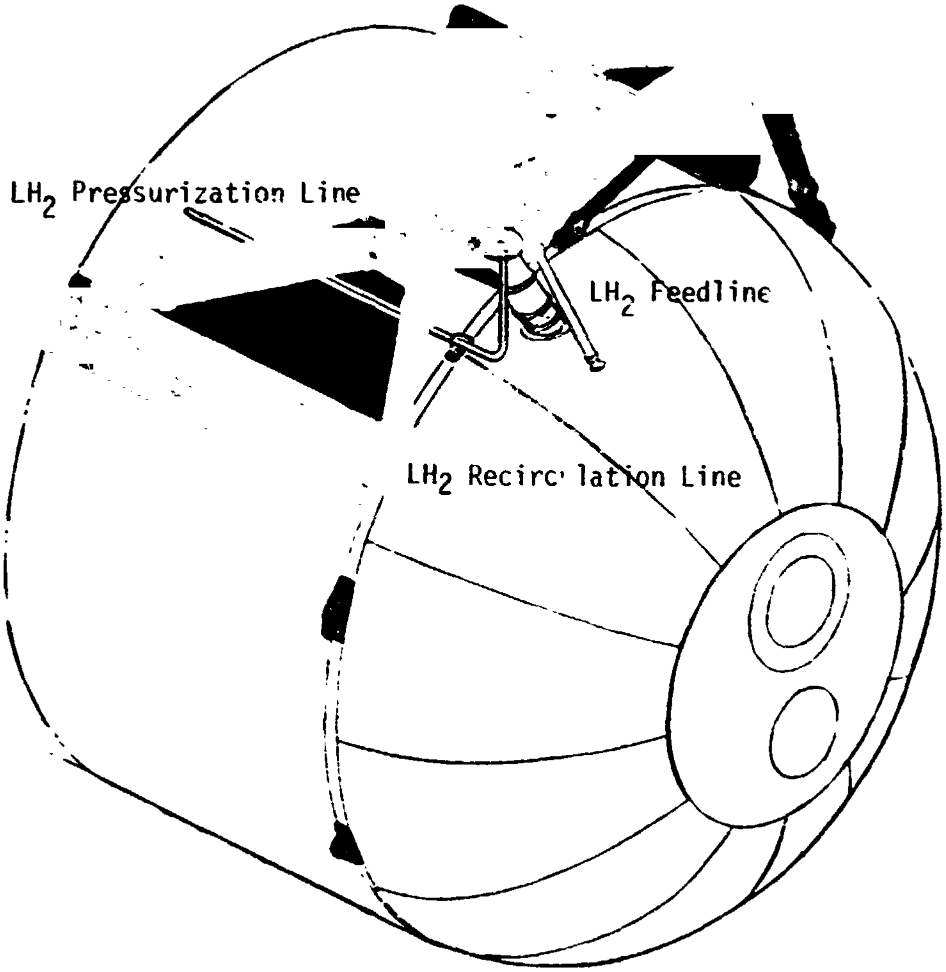

Fig. F22 LH$_2$ Feedline, Recirculation, and Pressurization Line Definition

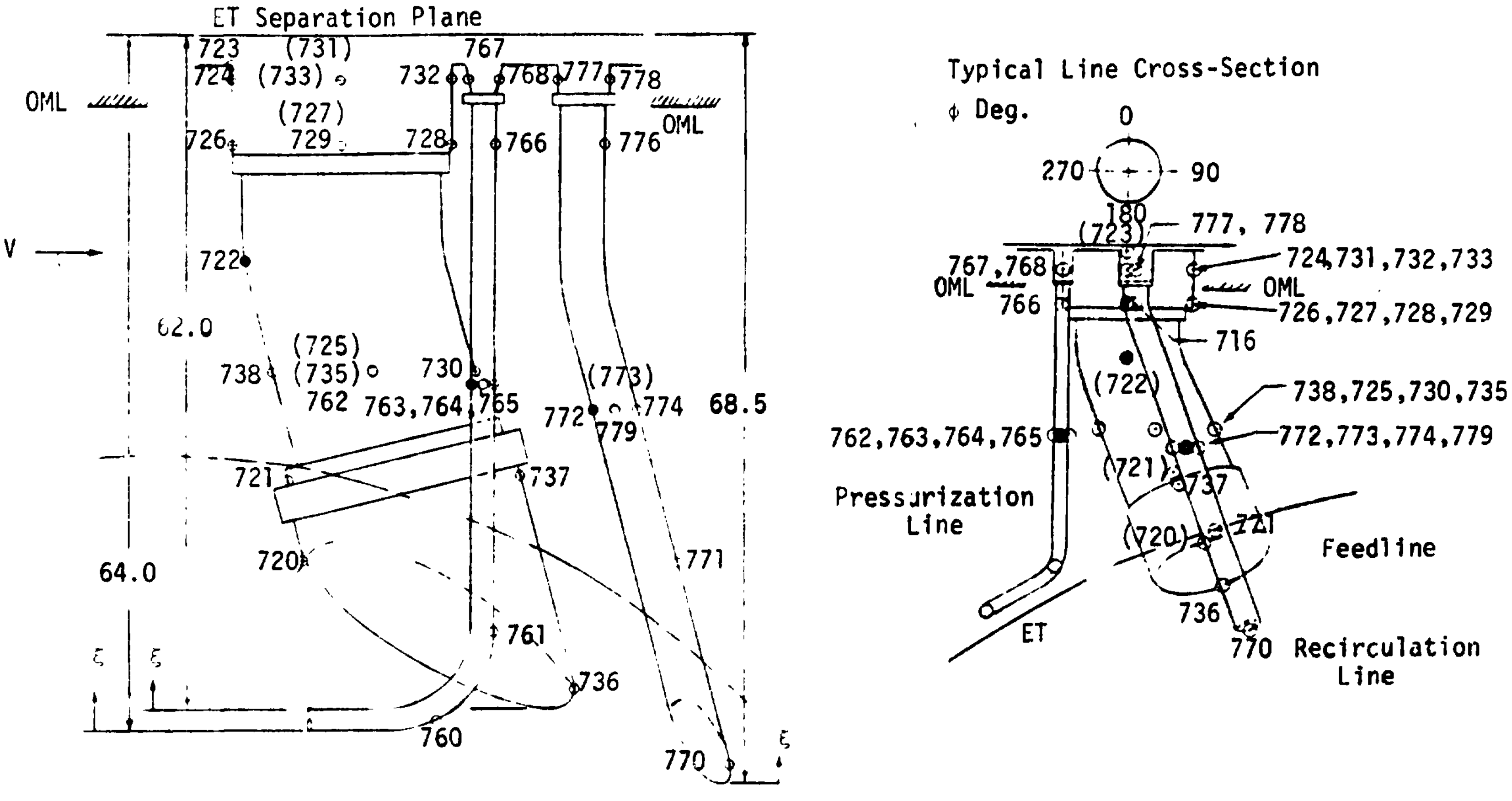

Side View

Aft View

Note: The body points shown in parentheses are oriented 180 degrees from the location shown in the respective view.

Fig. F23 LH_2 Feedline, Recirculation, and Pressurization Line Design Body Point Definition

Table F24

LH_2 Feedline, Recirculation, and Pressurization Line Design Body Point Definition

Body Point	Location	ξ (In.)	ϕ (Deg.)
720	LH_2 Feedline	0	0
721		20.45	
722		41.5	
723		62.0	
738		31.0	0
725			90
730			180
735		31.0	270
726		52.0	0
727			90
728			180
729		52.0	270
724		58.0	0
731			90
732			180
733		58.0	270
736		1.6	180
737		21.4	180
760	LH_2 Pressurization Line	1.0	180
761		9.1	180
762		32.0	0
763			90
764			180
765		32.0	270
766		54.0	180
767		60.0	0
768		60.0	180
770	LH_2 Recirculation Line	1.7	180
771		20.2	180
772		34.25	0
773			90
774			180
779		34.25	270
776		58.5	180
777		64.5	0
778		64.5	180

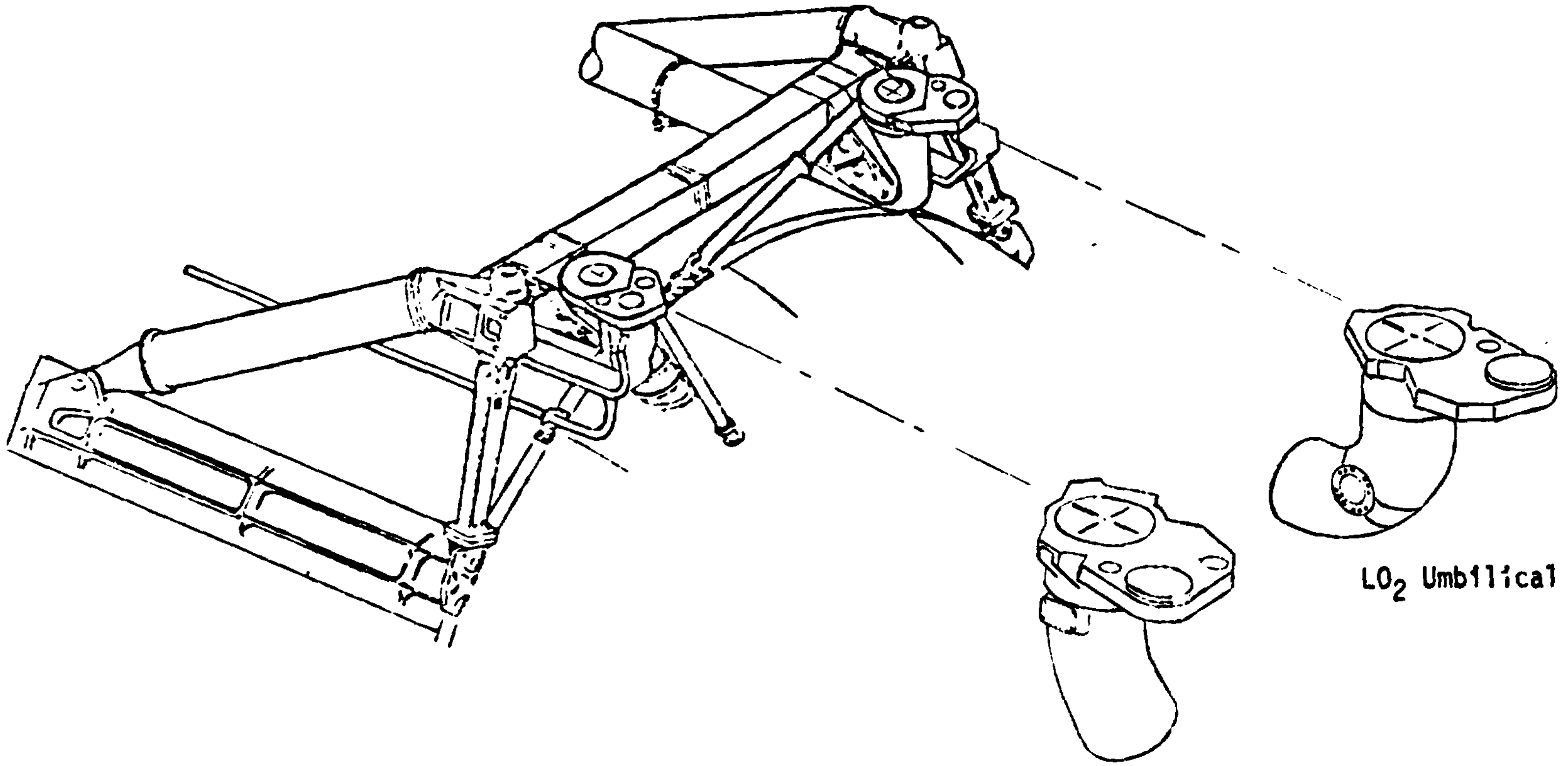

Fig. F25 LO$_2$ and LH$_2$ Umbilical Plate Design Body Point Definition

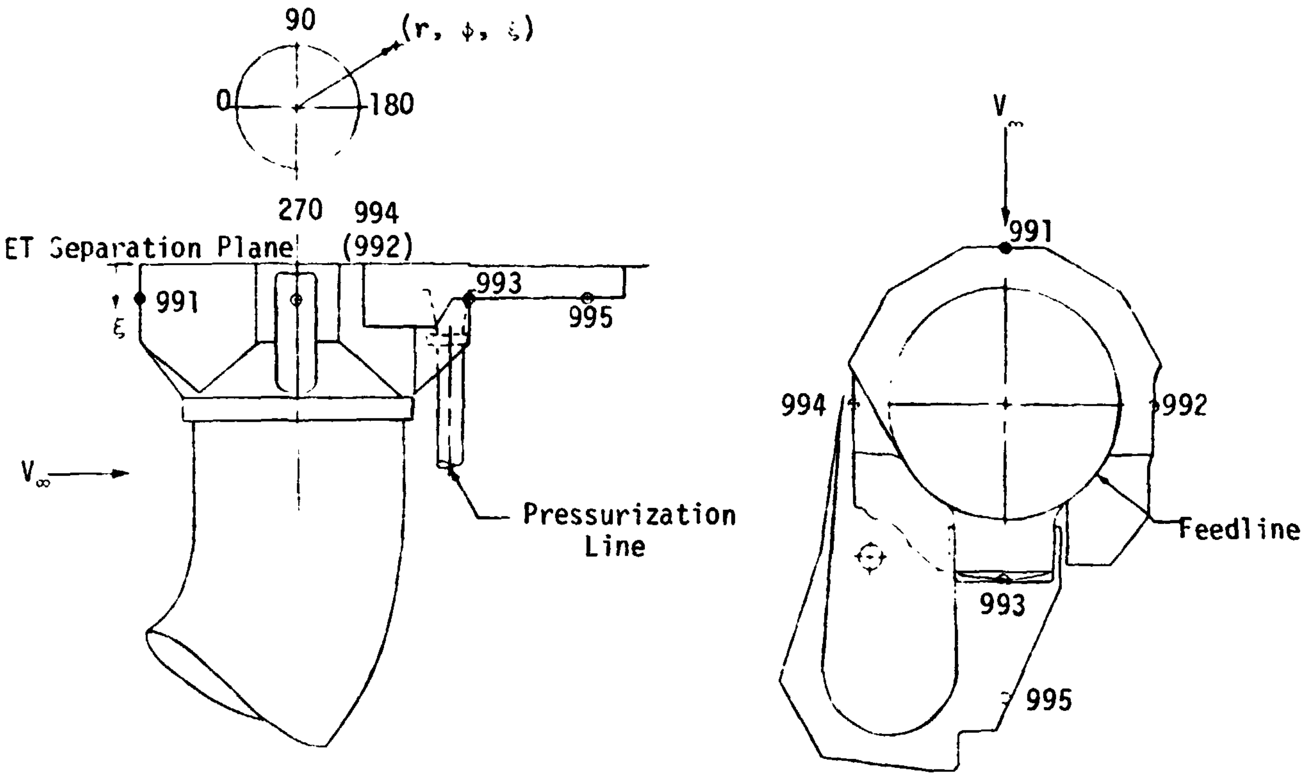

Side View

Planform View
(Looking From ET into Cavity)

Note: The body point shown in parentheses is oriented 180 degrees from the location shown in the respective view.

Body Point	Location	r (In.)	φ (Deg.)	ξ (In.)
991		13.0	0	2.8
992		12.3	90	
993		14.2	180	
994		12.3	270	
995		24.0	180	2.8

Fig. F26 LO_2 Umbilical Plate Design Body Point Definition

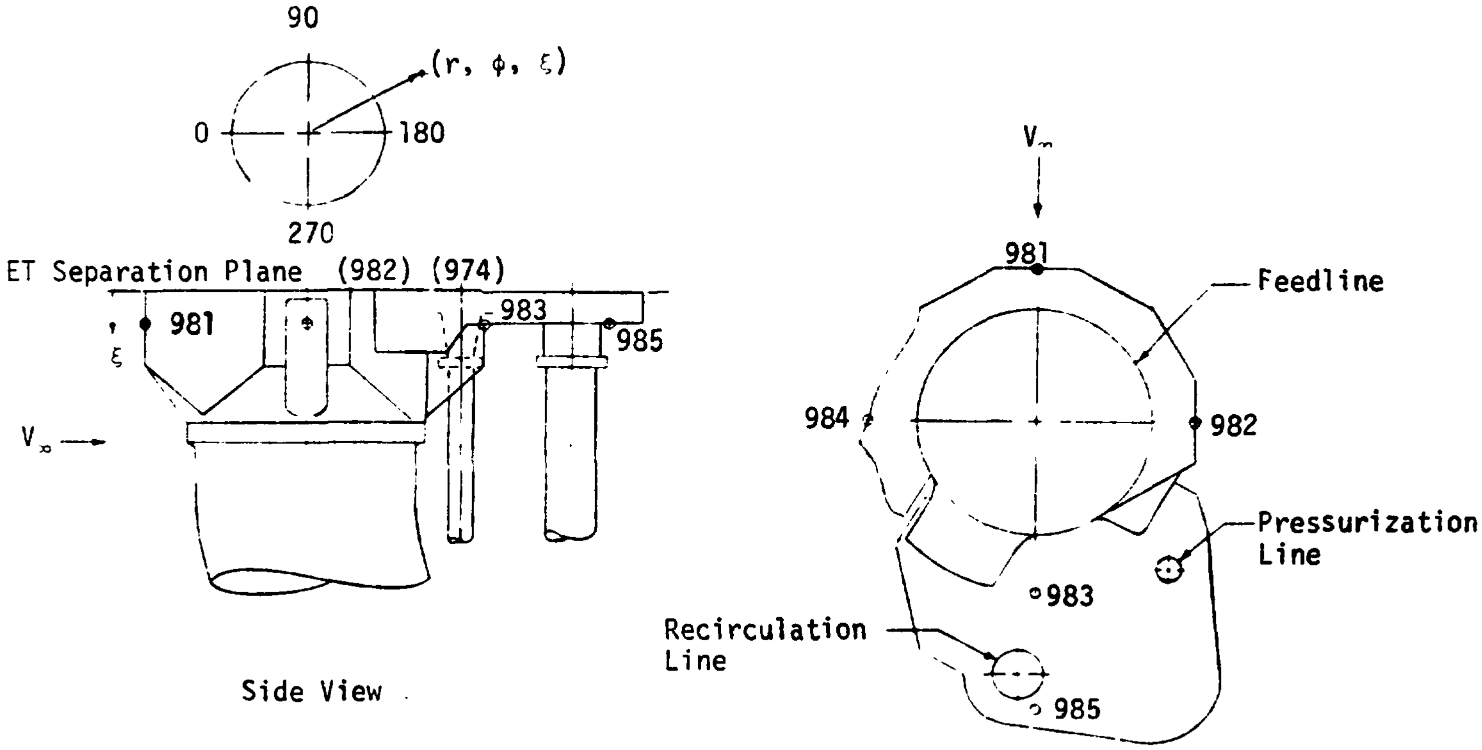

Note: The body point shown in parentheses is oriented 180 degrees from the location shown in the respective view.

Body Point	Location	r (In.)	ξ (In.)	ϕ (Deg.)
981	LH$_2$ Umbilical Plate	12.8	2.8	0
982	↓	13.0	↓	90
983		14.2		180
984		13.4		270
985		24.0	2.8	180

Fig. F27 LH$_2$ Umbilical Plate Design Body Point Definition

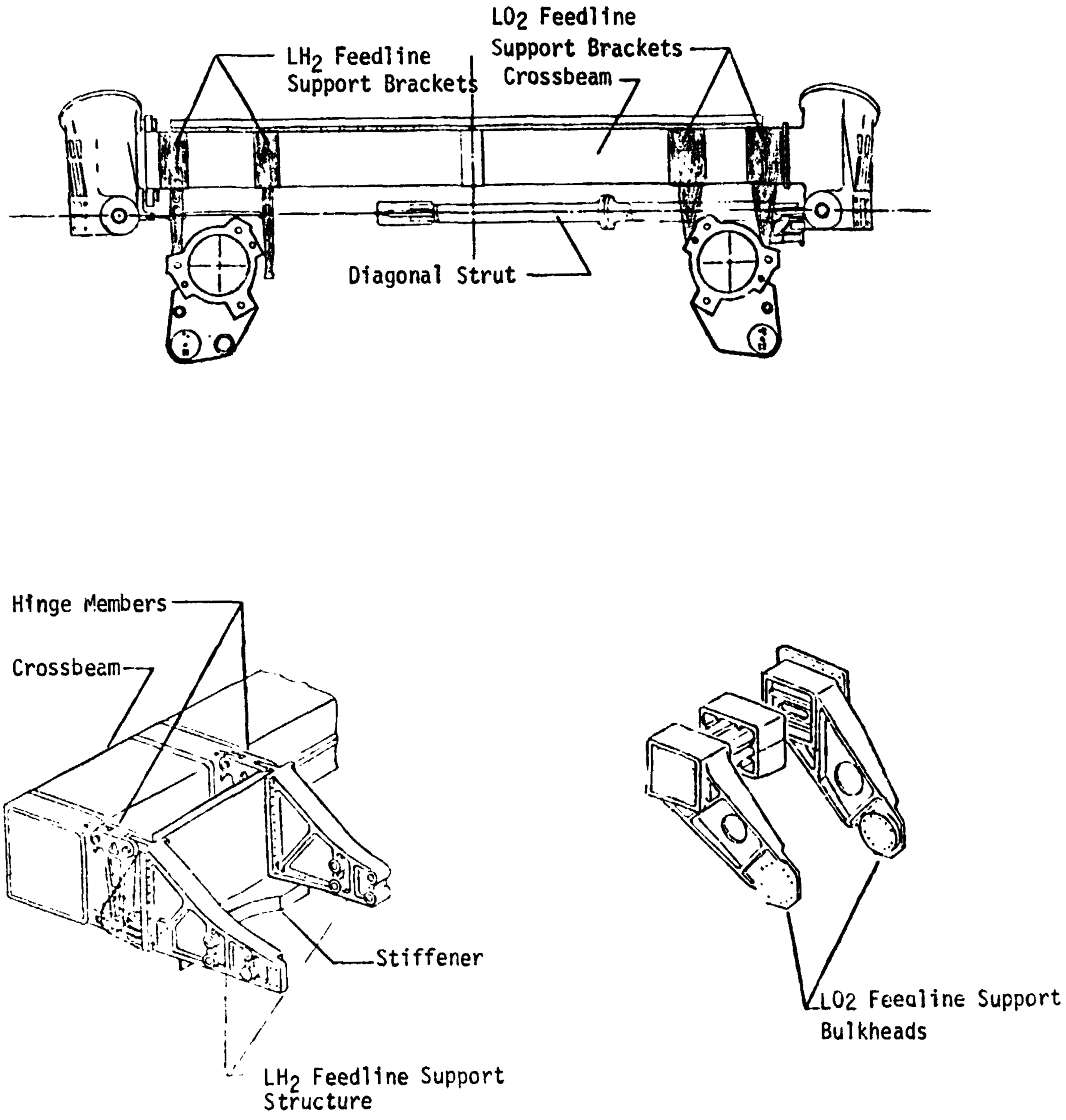

Fig. F28 LH_2 and LO_2 Feedline Bracket Body Point Definition

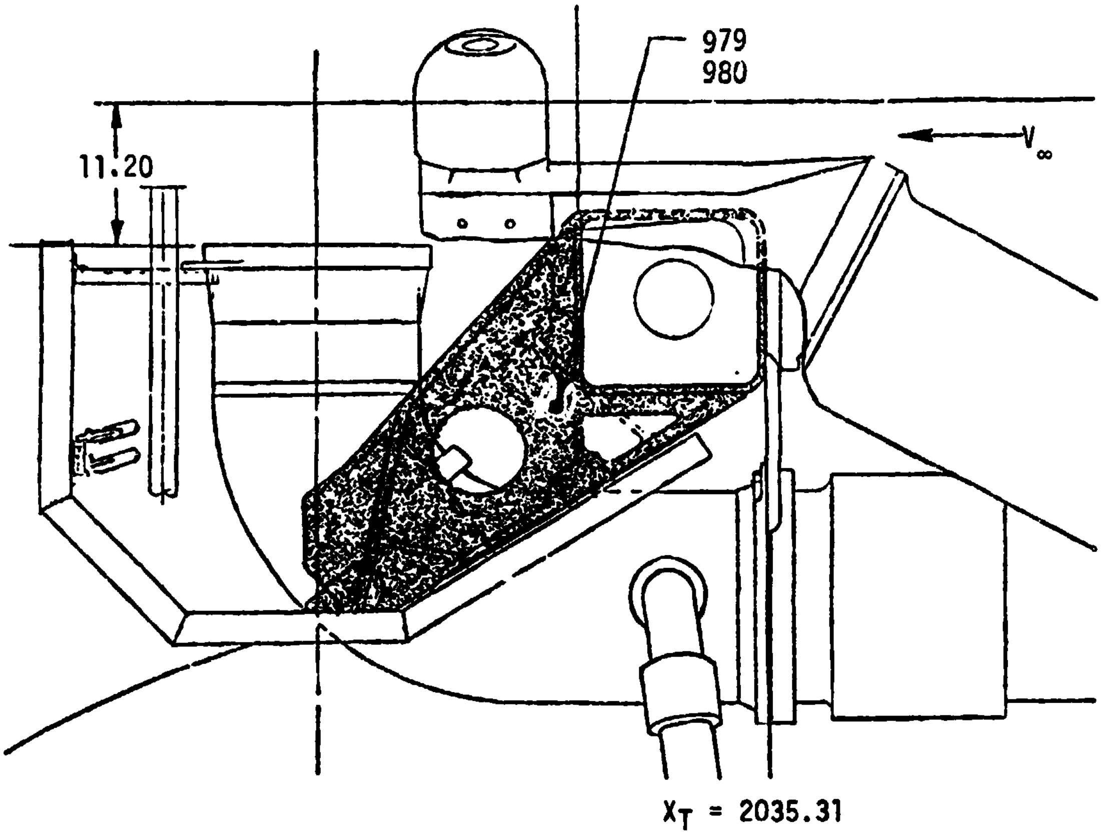

Body Point	Location
979	Outboard Support Bracket
980	Inboard Support Bracket

Fig. F29 LO_2 Feedline Fitting Body Point Definition

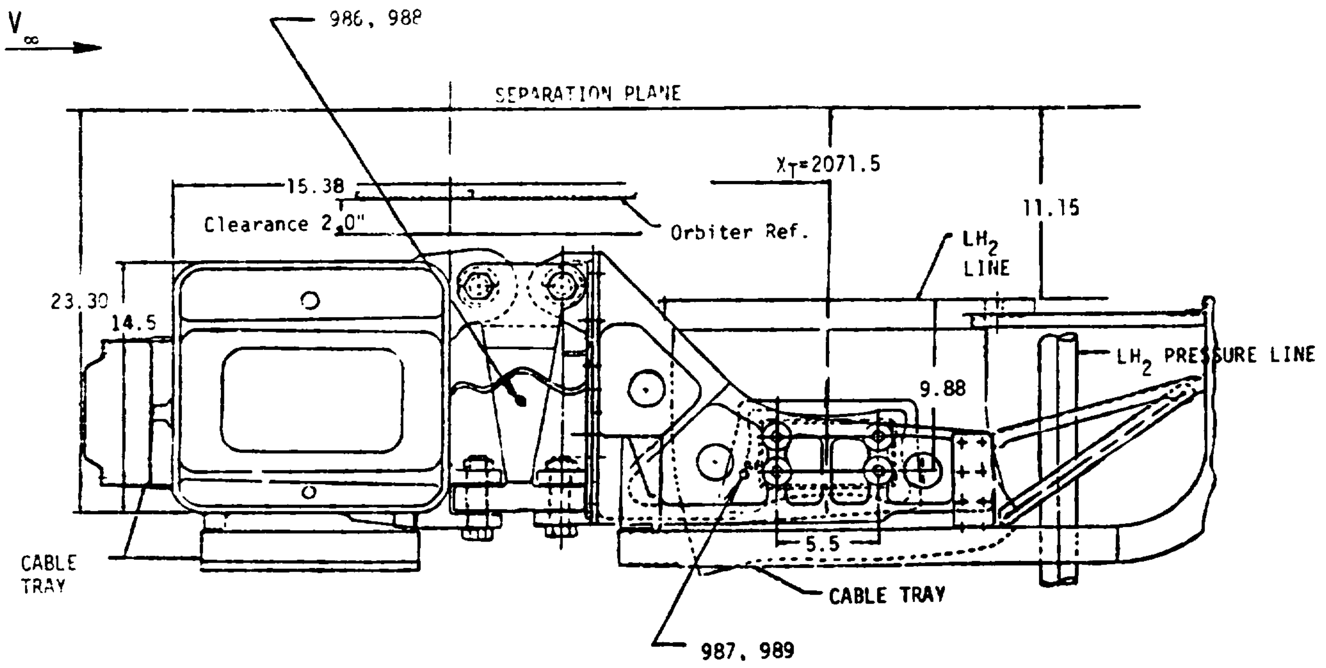

Body Point	Location
986	Outboard Hinge Bracket
987	Outboard Support Bracket
988	Inboard Hinge Bracket
989	Inboard Support Bracket

Fig. F30 LH_2 Feedline Fitting Body Point Definition

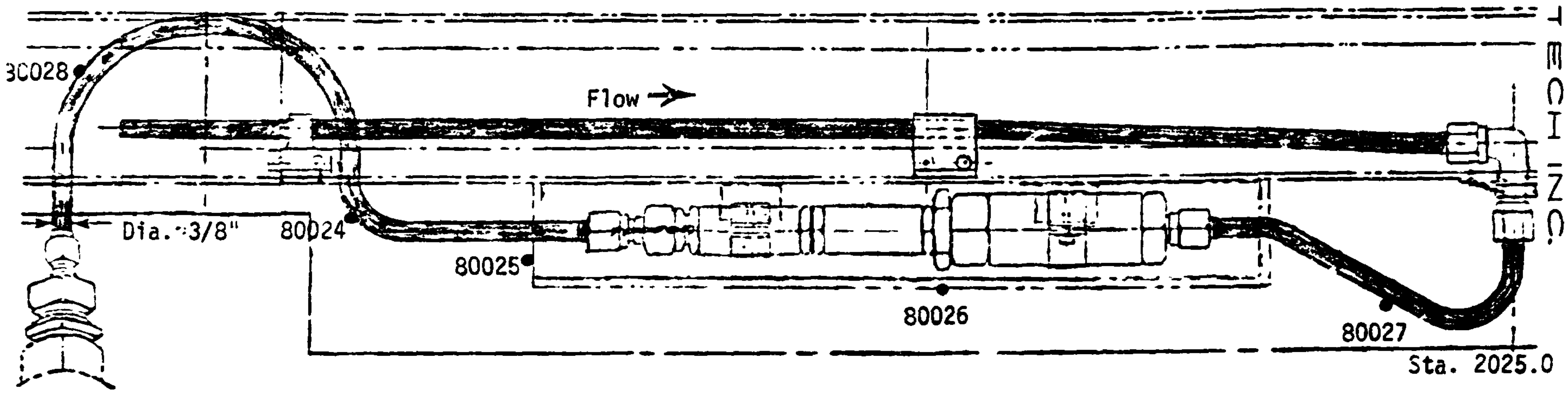

Body Point	Location
80024	He Line
80025	Check Valve Fairing Front
80026	Check Valve Fairing Top
80027	He Line
80028	He Line

Fig. E31 He Injection System Lines and Components Outside of the Cable Tray

2.2.5 ET/SRB Aft Interface Structure

This subsection contains geometry and body point information for the ET/SRB aft interface structure. The information sequence is as follows:

- Upper aft strut fitting
- Lower aft strut fitting
- Upper and diagonal struts
- Lower strut

Note: G = Division 2.2.5 in figures and tables

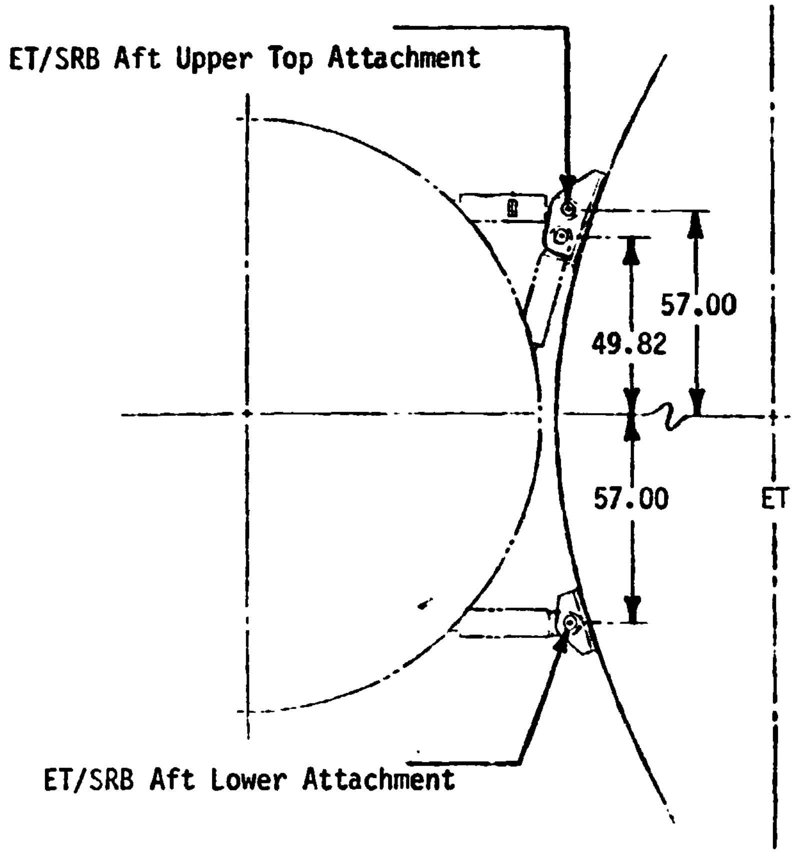

Fig. G1 Aft ET/SRB Orientation (Looking Forward)

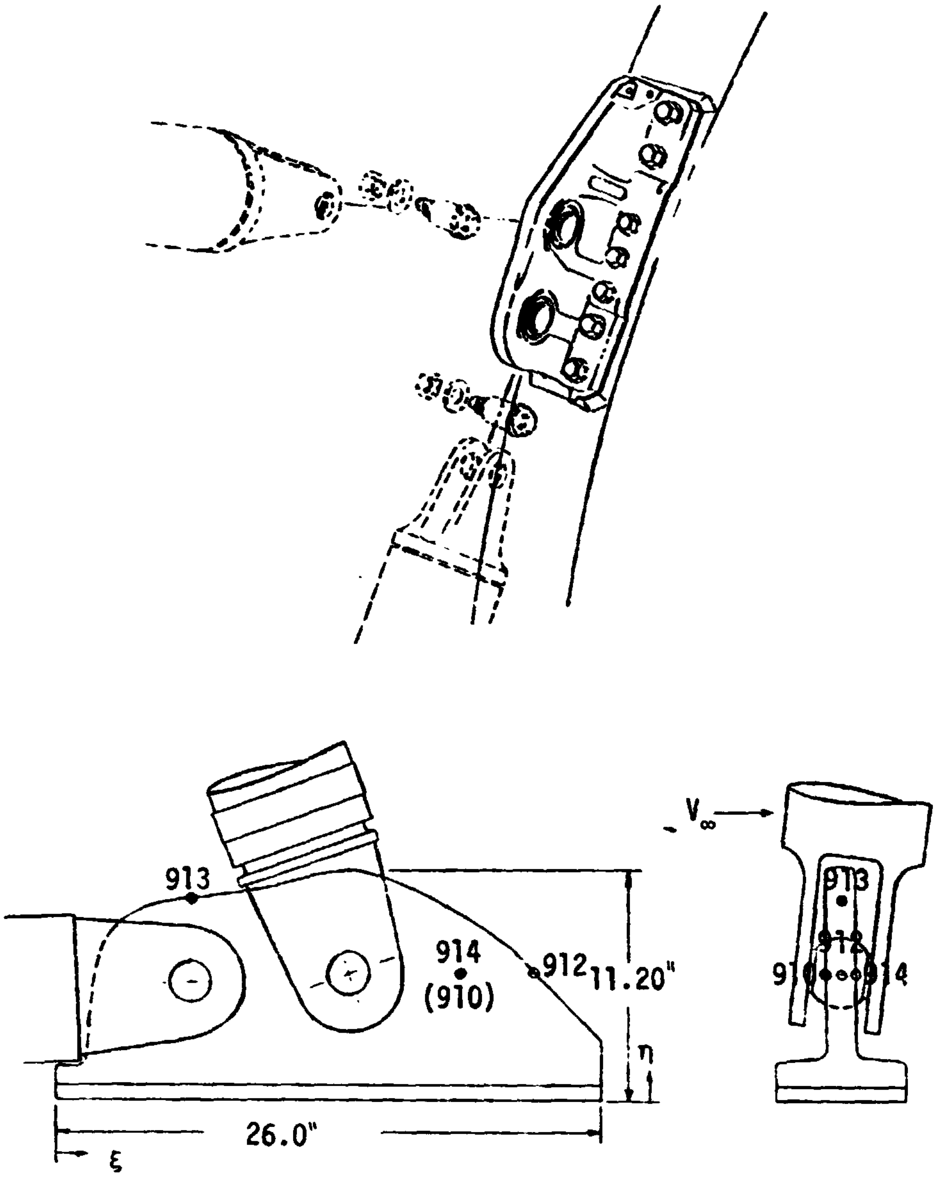

Left Aft View

Side View

Body Point	Location	ξ (In.)	η (In.)
910	Forward Face	19.1	6.0
912	Side Face	22.6	6.0
913	Upper Face	6.4	9.4
914	Aft Face	19.1	6.0

Fig. G2 ET/SRB Upper Aft Strut Fitting Design Body Point Definition

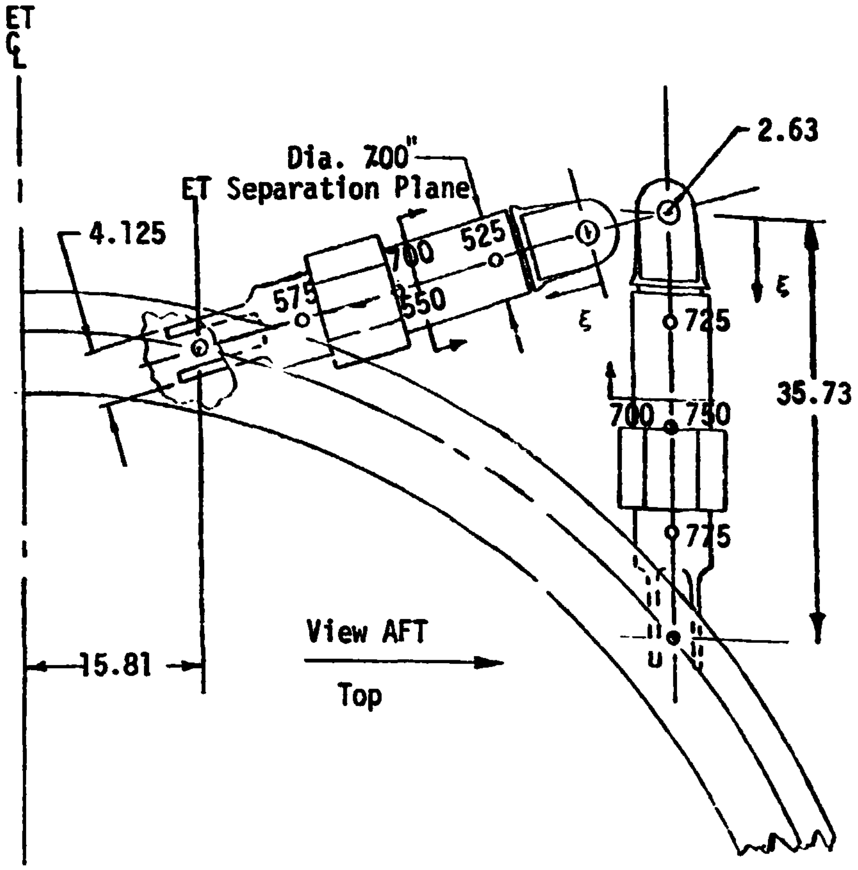

Body Point	Location	ξ (In.)	ϕ (Deg.)
525	Diagonal Strut Aft Stagnation Line	8.9325	180
550		17.865	180
575		26.7975	180
700	Upper and Diagonal Strut	-	0
701	Forward Stagnation Line	0	180
725	Upper Strut Aft Stagnation Line	8.9325	
750		17.865	
775		26.7975	
799		35.73	180

Fig. G3 ET/SRB Aft Upper and Diagonal Strut Design Body Point Definition

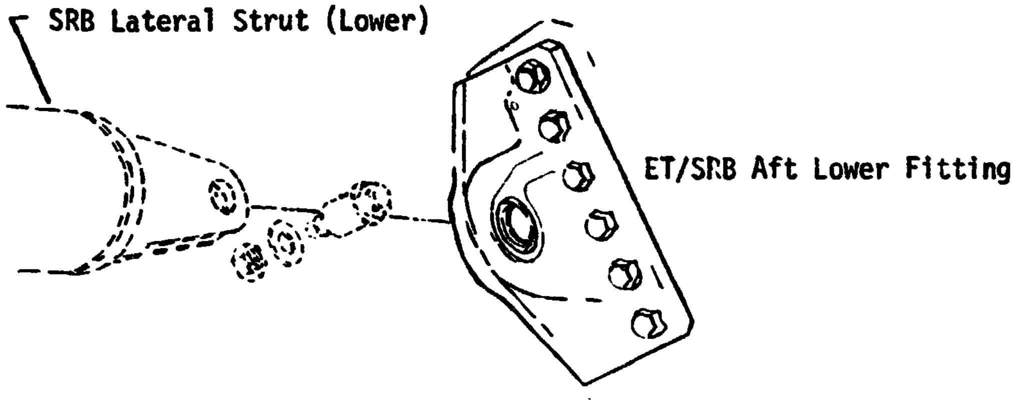

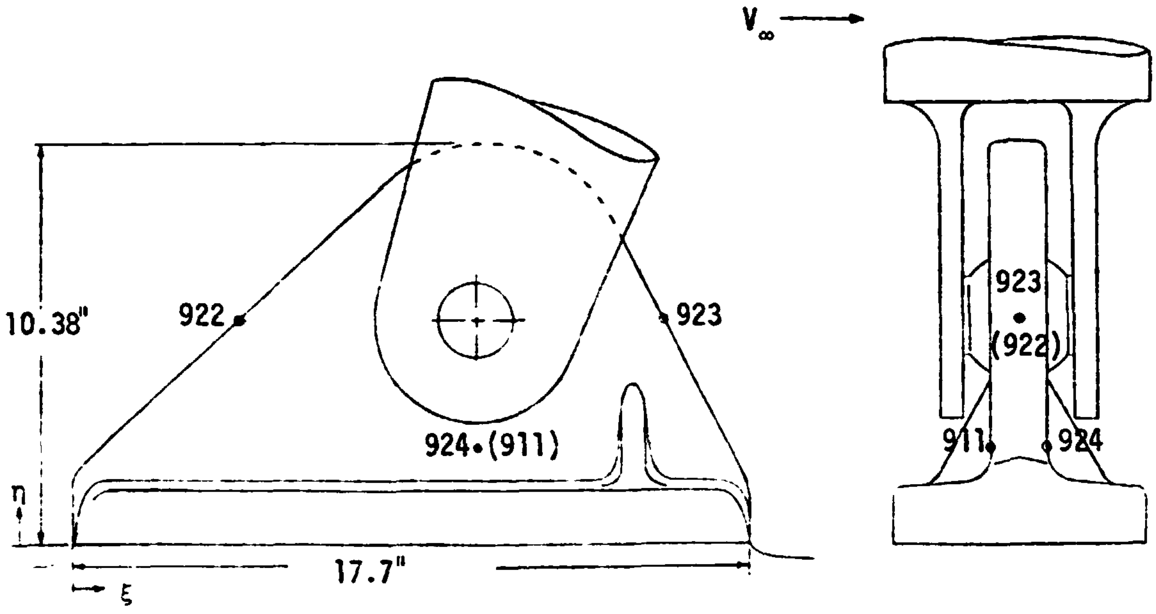

Left Aft View

Side View

Body Point	Location	ξ (In.)	η (In.)
911	Forward Face	10.50	2.48
922	Side Face	4.475	5.8
923	Side Face	15.40	5.8
924	Aft Face	10.50	2.48

Fig. G4 ET/SRB Lower Aft Attachment Strut Fitting Design Body Point Definition

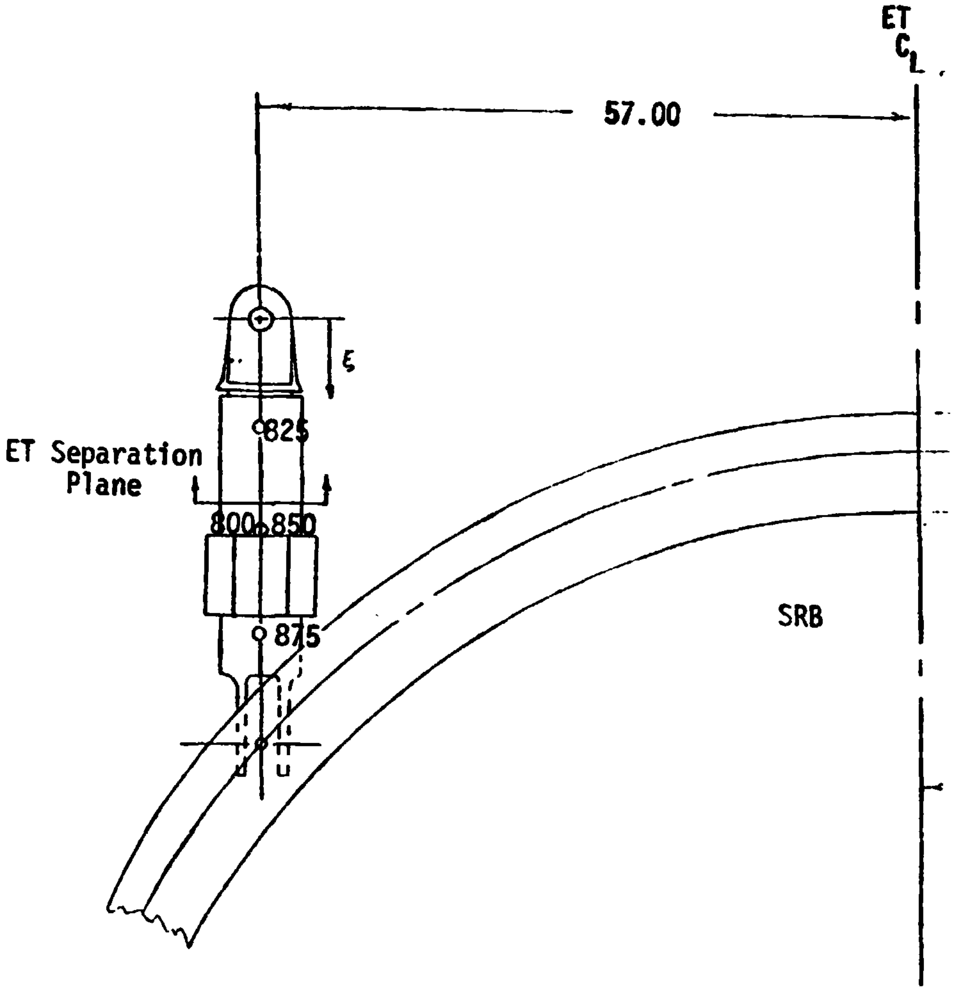

Body Point	Location	ξ (In.)	φ (Deg.)
800	Forward Stagnation Line	--	0
801	Aft Stagnation Line	0	180
825	↓	8.9325	↓
850		17.865	
875		26.7975	
899		35.73	180
851		17.865	45
852		17.865	90

Fig. G5 ET/SRB Aft Lower Strut Design Body Point Definition

SECTION 3

IH-51A DATA

This section describes the data obtained in a test conducted at the NASA/ARC 3.5 Foot Hypersonic Wind Tunnel using a simulated external tank (ET) and orbiter forebody (Ref. 1). The ET was simulated by a flat plat with the protuberances located as if the cylinder section was unrolled. The data used in this analysis was obtained from a facility printout. This section provides a test description, reduced data, a comparison of additive and multiplicative methods, and methods for application to flight.

3.1 Test Description

The IH-51A test was conducted using a 0.04-scale thin skin thermocouple instrumented Model 58-0. The model consists of a 0.04-scale SSV orbiter forebody mounted above a flat plate representing a rolled out upper section of the ET. The flat plate inserts and attached scaled ET protuberances contained 325 thermoccuples. The objective of the test was to investigate interference heating effects on the upper portion of the ET in the proximity of the external hardware at Mach 5.3.

The following nominal operating conditions were used during the test.

M_∞	$R_e/ft \times 10^{-6}$	P_0(psia)	T_0(°R)
5.3	5.0	400	1300
5.3	1.0	100	1300

The test configurations used during each of these operating conditions are shown in Fig. 3.1. These configurations are described as follows:

5 Undisturbed, clean skin

4 Oribter interference, proximity

3 Tiedown interference, forward attach strut interference

2 Tunnel interference; cable tray, LO_2 feedline, GO_2 pressure line interference, LO_2 antigeyser line

1 Total interference, total geometry

The thermocouple locations on plate XI are shown in Fig. 3.2. This plate has been divided into regions A to G for ease of analysis and presentation. Thermocouple locations on protuberances are shown in Fig. 3.3.

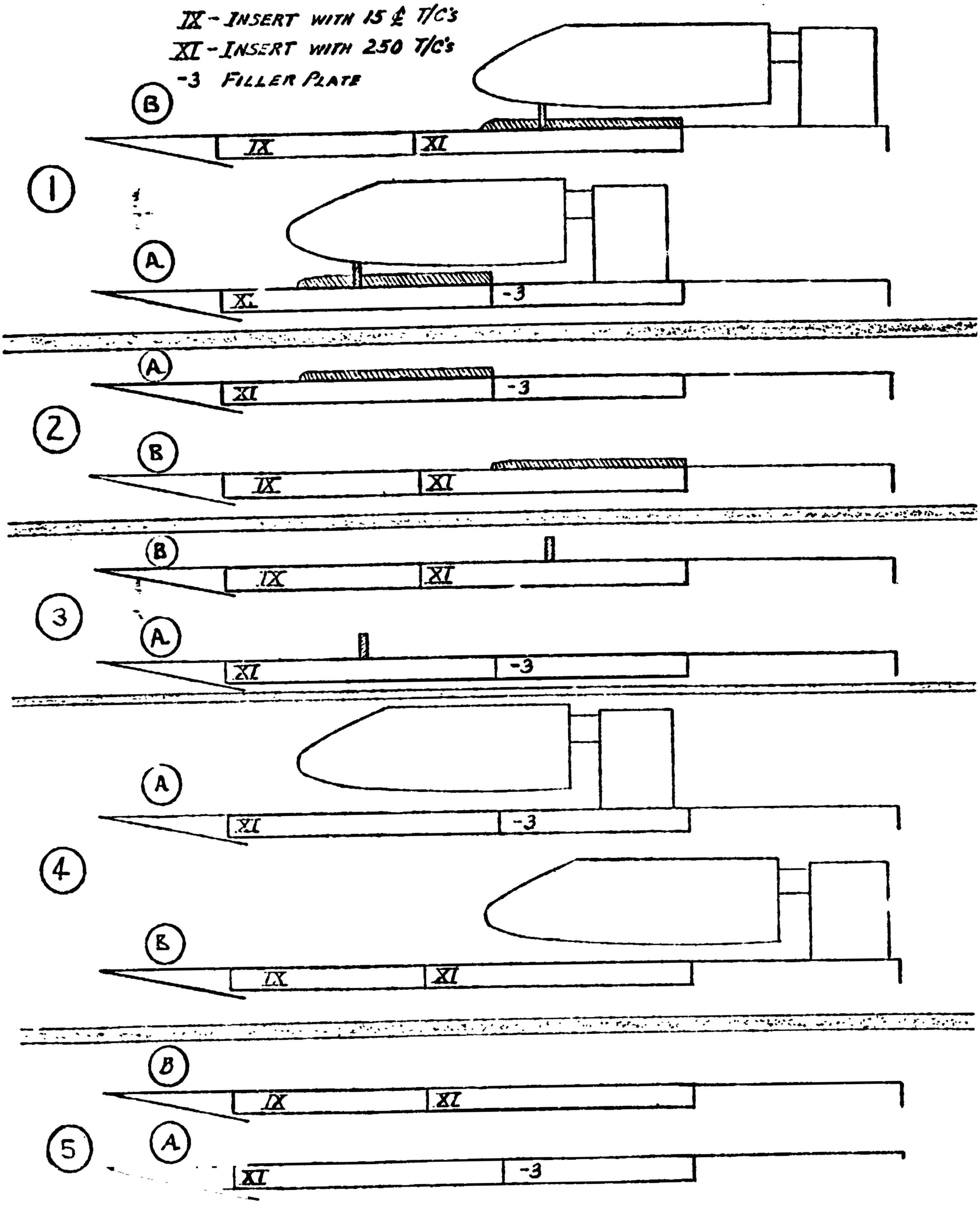

Fig. 3.1 TH-51A Test Configurations

3.2 Reduced Data

The heating data was reduced by nondimensionalizing the heat transfer coefficient data with the undisturbed flat plate heat transfer coefficient in the following manner:

$$(h_i/h_{ref})/(h_u/h_{ref})$$

The value of h_u/h_{ref} was evaluated from experimental data of configuration 5. Figure 3.4 shows the measured values of h/h_{ref} for configuration 5. The turbulent theory of Dirling (Ref. 3.2) agrees with the high Reynolds number data. The data for the low Reynolds number is transitional over almost the entire plate. Consequently, the low Reynolds number data was dropped from consideration.

For nondimensionalization purposes a smaller range in axial distance than shown in Fig. 3.4 was all that was required. As a result, the data fairing shown in Fig. 3.5 was used throughout this work to nondimensionalize the data for all five configurations.

The data for the skin is presented according to the regions defined in Fig. 3.2. For each region a table of thermocouple locations are given. The table consists of thermocouple number, station number, B. P. number, equivalent full scale axial distance, equivalent tank axial coordinant and equivalent circumferential coordinant. The transformations from model to full scale ET is

$$X_T = 25 \text{ (STA number)} \qquad \text{(inches)}$$

$$\theta_T = 8.3836 \text{ (B. P. number)} \qquad \text{(Deg.)}$$

except for T/C's near and on the LO_2 feedline

where $\theta_T = 8.0176$ (B. P. number) (Deg.)

In addition to the tables, the thermocouple locations for each region are shown pictorially. The interference factors for each configuration is then given sequentially

5 Clean skin
4 Orbiter interference
3 Tiedown interference
2 Tunnel interference
1 Total interference

after the thermocouple pictorial.

Table 3.1 and Figs. 3.6 to 3.11 present the information for region A. Figures 3.8 and 3.9 show that neither the orbiter or tiedown influences region A. Thus, the total interference effects in region A shown in Fig. 3.11 are due to the fairing and tunnels.

Table 3.2 and Figs. 3.12 to 3.17 present the information for region B. Figure 3.14 shows the effect of the orbiter shock crossing the tunnel locations. The tiedown shock interference shown in Fig. 3.15 occurs in nearly the same locations as the orbiter shock. The peak factors due tunnels alone are smaller, as shown in Fig. 3.16, than the orbiter or tiedown peak factors. Total interference factors for region B are given in Fig. 3.17.

Table 3.3 and Figs. 3.18 to 3.23 present the information for region C. The orbiter significantly influences the heating over the entire region C as shown in Fig. 3.20. The tiedown has a less significant effect than the orbiter as shown in Fig. 3.21. The tunnels create even a smaller effect than the tiedown as illustrated in Fig. 3.21. The total interference effects are quite severe in region C as shown in Fig. 3.23.

Table 3.4 and Figs. 3.24 to 3.29 present the information for region D which is around the tiedown. The orbiter shock impingement interference begins slightly ahead of the tiedown as shown in Fig. 3.26. The peak heating occurs a significant distance behind the primary shock impingement location. The tiedowns region of influence and amplification factors are about the same as the orbiters as shown in Fig. 3.27. The shock off of the LO_2 feedline fairing produces low level heating amplification over most of this region (Fig. 3.28). Total factors for this region are given in Fig. 3.29.

Table 3.5 and Figs. 3.30 to 3.35 present the information for region E around the LH_2 pressure line forward end. The orbiter influences only the upper right corner of region D as shown in Fig. 3.32. The tiedown influences the same area (Fig. 3.33). The tunnel amplifies the heating in a small area near it (Fig. 3.34). The total interference pattern is much more severe than the combination of components would indicate as shown in Fig. 3.35.

Table 3.6 and Figs. 3.36 to 3.41 present the information for region F around the midsection of the LH_2 pressure line. The orbiter interference effects are quite significant in this region as shown in Fig. 3.38. The tiedown interference is less significant than for the orbiter as illustrated in Fig. 3.39. The tunnel interference is ab the same magnitude as for the tiedown around the tunnel as shown in Fig. 3.40. The total interference is given in Fig. 3.41.

Table 3.7 and Figs. 3.42 to 3.47 present the information for region G around the LH_2 pressure line. Figure 3.44 shows a radial increase in heating from near the top centerline moving outward. The tiedown shock sweeps this ray line giving the increased heating shown in Fig. 3.45. The tunnel and tiedown interference factors are nearly the same as shown in Fig. 3.46. Total interference factors for this region are given in Fig. 3.47.

The interference factors on the protuberances are given in tabular form in Table 3.8. The total interference factors for both the A and B configurations (short and long plates respectively). The components of the total are given fo the B configuration only. The percent change of the A configuration data from the B configuration data was calculated for each T/C. The mean of this percentage was 0.51%. Thus, on the average there was no difference in the heating amplification in the A or B configuration. One standard deviation of the percent change of the two data sets was 13.85 percent. Thus, there are individual data differences as can be seen in Table 3.8 but on the whole the sets are the same.

Some of the protuberance data are presented in the next section along with an analysis of the additive and multiplicative combination methods for predicting protuberance heating.

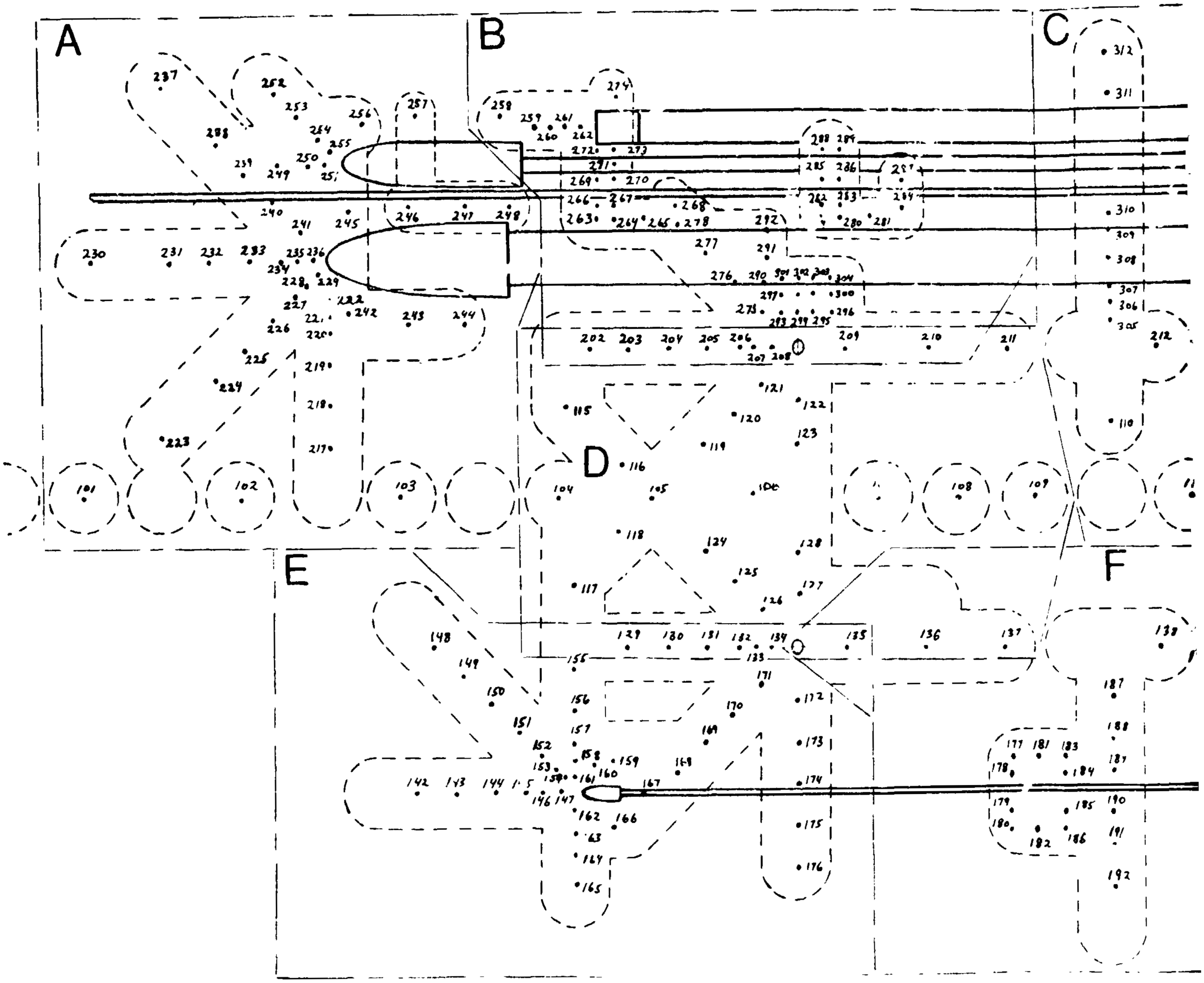

Fig. 3.2 Skin Thermocouple Configuration Drawing for IH-51A Te

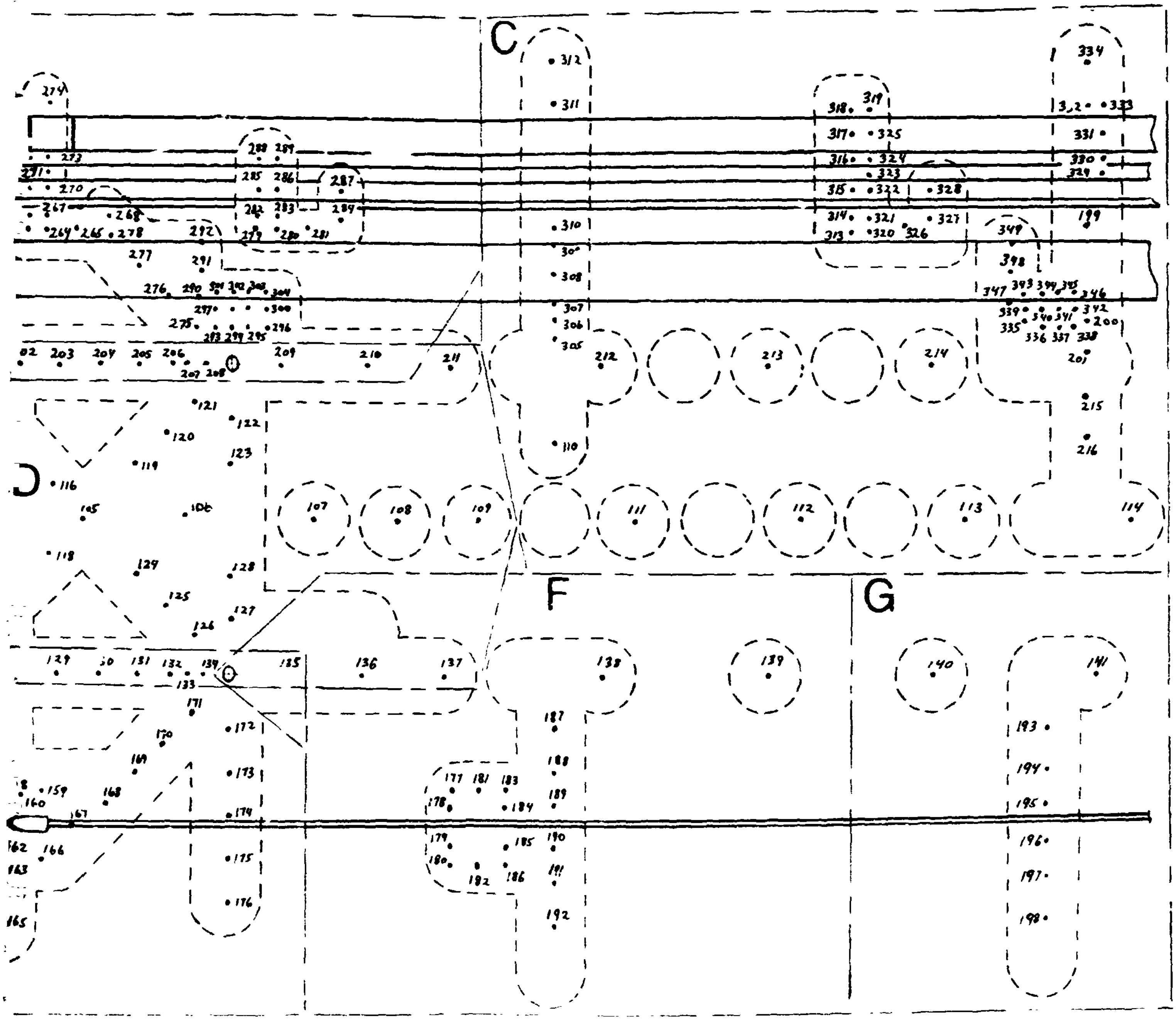

Skin Thermocouple Configuration Drawing for IH-51A Test

2 FOLDOUT FRAME

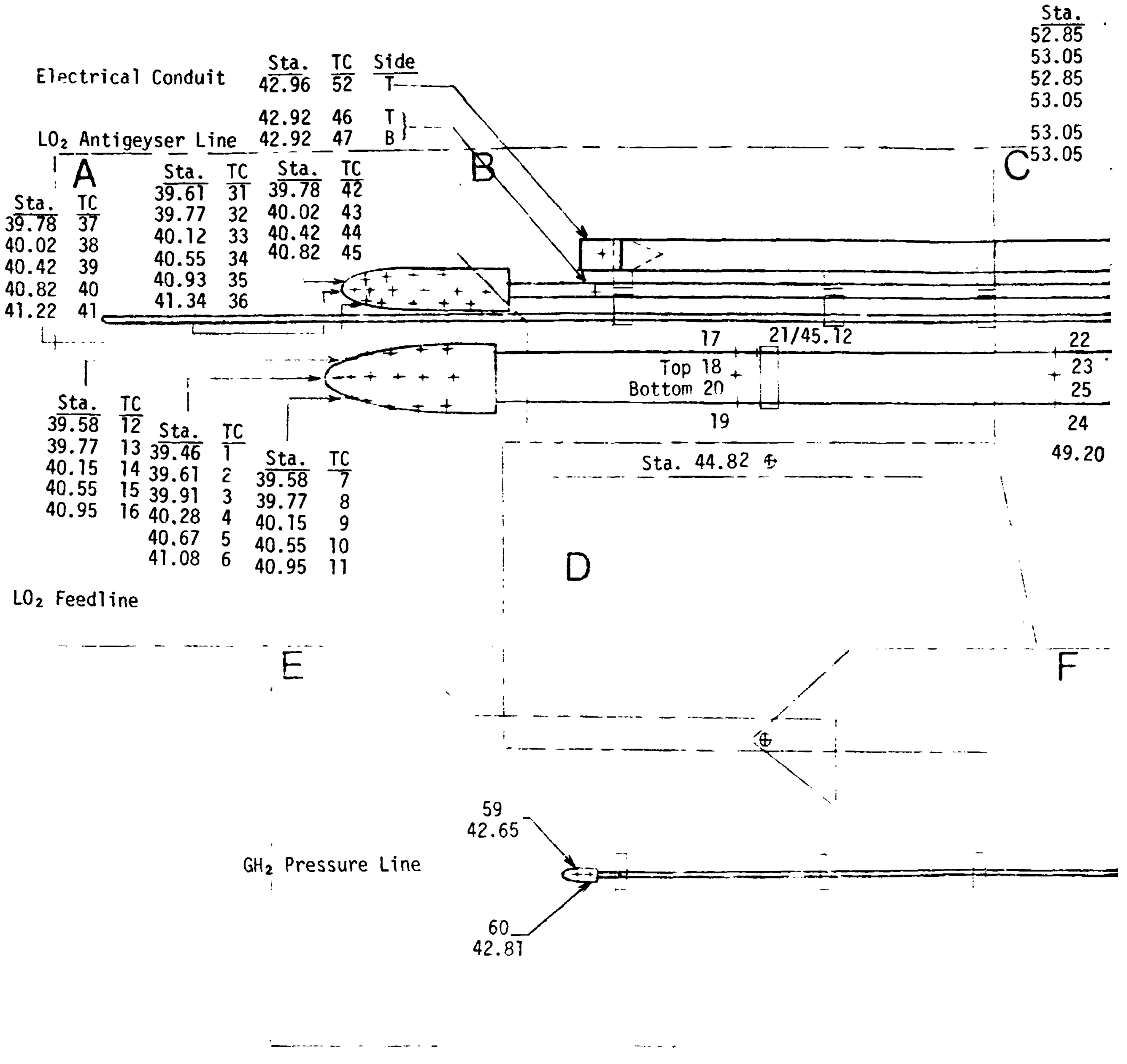

Fig. 3.2 IH-51A Thermocouple Locations on Protuberanc

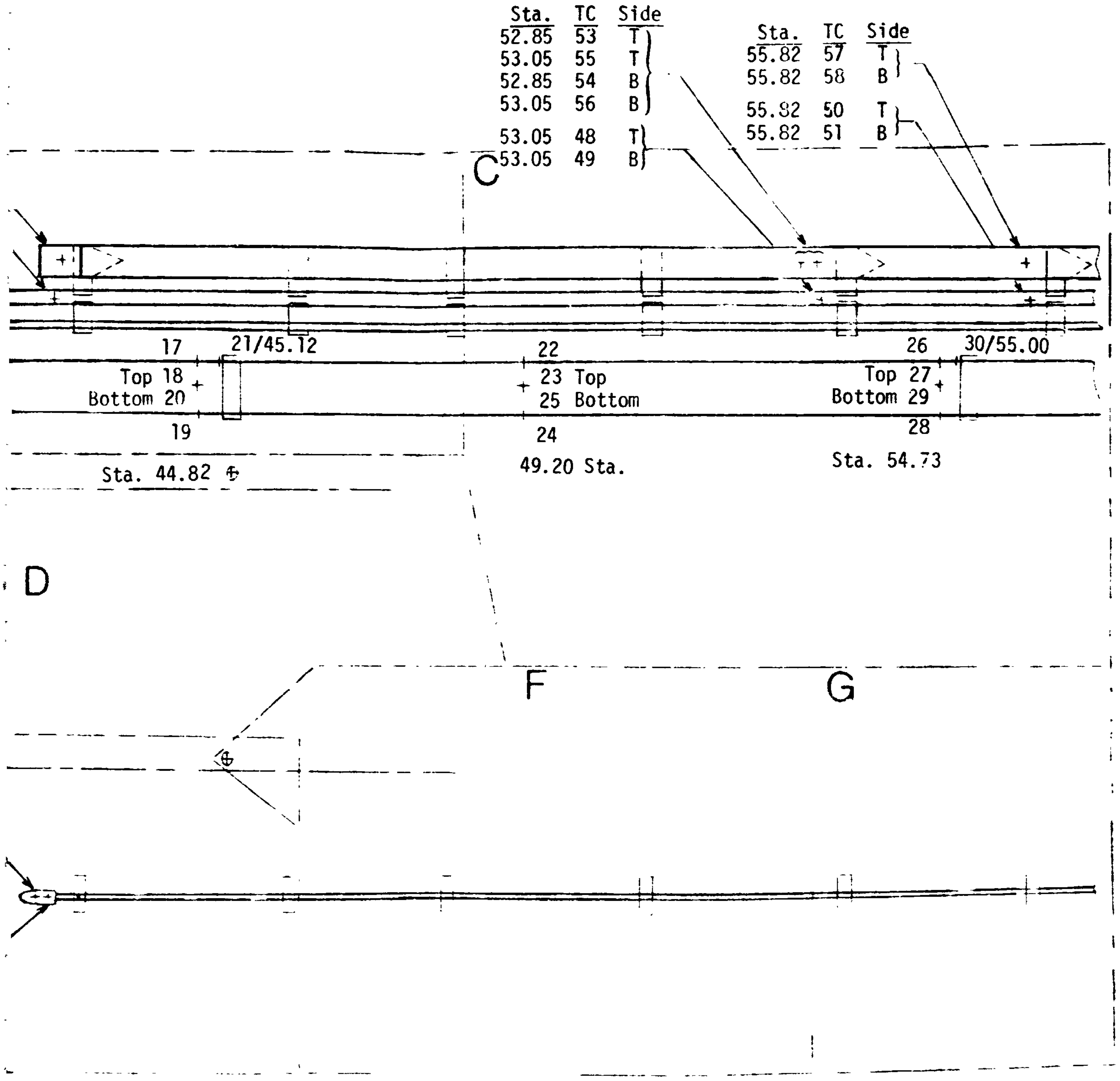

. 3.3 IH-51A Thermocouple Locations on Protuberances

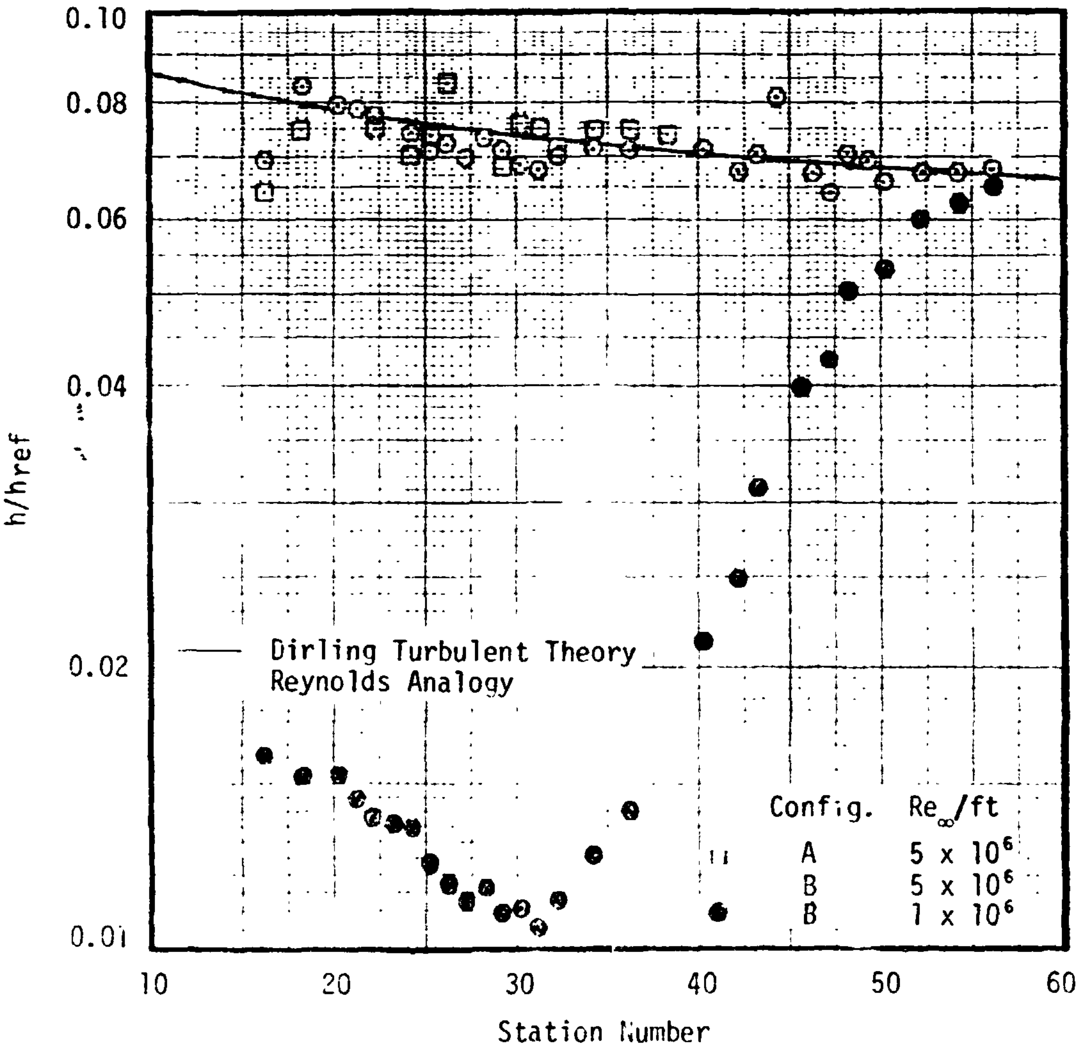

Fig. 3.4 Centerline Undisturbed Heat Transfer Coefficient Ratio Data from IH-51A

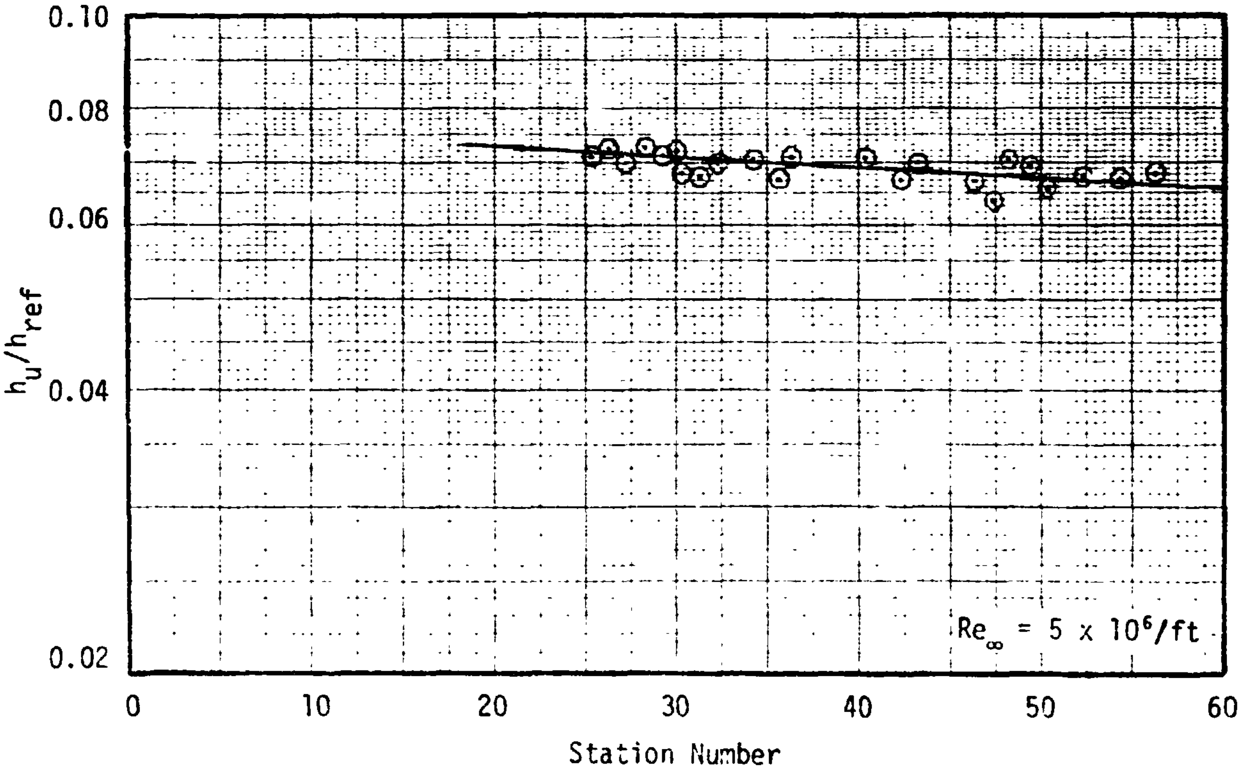

Fig. 3.5 Flat Plate Centerline Data and Reference Line for Interference Heating Calculations (B Configuration)

TABLE 3.1
T/C LOCATION TABLE
REGION A

T/C #	STA No.	B. P.	X (Inches)*	X_T (Inches)	θ (Deg.)
101	36.196	0	582.40	904.90	0
102	38.196	↓	632.40	954.90	↓
103	40.196	↓	682.40	1004.90	↓
217	39.296	0.60	659.90	982.40	5.03
218	↓	1.10	↓	↓	9.22
219	↓	1.60	↓	↓	13.40
220	↓	2.00	↓	↓	16.04
221	39.296	2.20	659.90	982.40	17.64
222	↓	2.40	↓	↓	19.24
223	37.196	0.74	607.40	929.90	6.20
224	37.896	1.44	624.90	947.40	12.07
225	38.246	1.80	633.65	956.15	15.09
226	38.596	2.16	642.40	964.90	17.32
227	38.896	2.43	649.90	972.40	19.48
228	39.016	2.57	652.90	975.40	20.61
229	39.156	2.72	656.40	978.90	21.81
230	36.296	2.87	584.90	907.40	23.01
231	37.296	2.87	609.90	932.40	23.01
232	37.796	↓	622.40	944.90	↓
233	38.296	↓	634.90	957.40	↓
234	38.696	↓	644.90	967.40	↓
235	38.896	↓	649.90	972.40	↓
236	39.096	2.87	654.90	977.40	23.01
237	37.196	4.98	607.40	929.90	41.75
238	37.896	4.27	624.90	947.40	35.80
239	38.246	3.91	633.65	956.15	[illegible].78
240	38.596	3.56	642.40	964.90	2[illegible].85
241	38.946	3.21	651.15	973.60	25.74
242	39.546	2.22	666.15	988.65	17.80
243	40.296	2.10	684.90	1007.40	16.84
244	41.026	2.10	703.15	1025.65	↓
245	39.546	3.46	666.15	988.65	27.74

*X = X_T-322.5 Equivalent Full Scale Axial Distance

TABLE 3.1
T/C LOCATION TABLE
REGION A (Cont.)

T/C	STA No.	B. P.	X (Inches)*	X_T (Inches)	θ (Deg.)
246	40.296	3.50	684.90	1007.40	28.06
247	41.016	↓	702.90	1025.40	↓
248	41.566	↓	716.65	1039.15	↓
249	38.656	4.02	643.90	966.40	33.70
250	39.046	↓	653.65	976.15	↓
251	39.246	4.02	658.65	981.15	33.70
252	38.596	4.88	642.40	964.90	40.91
253	38.896	4.60	649.90	972.40	38.56
254	39.196	4.30	657.40	979.90	36.05
255	39.316	4.18	660.40	982.90	35.04
256	39.696	4.50	669.90	992.40	37.73
257	40.396	4.60	687.40	1009.90	38.56

* $X = X_T - 322.5$ Equivalent Full Scale Axial Distance

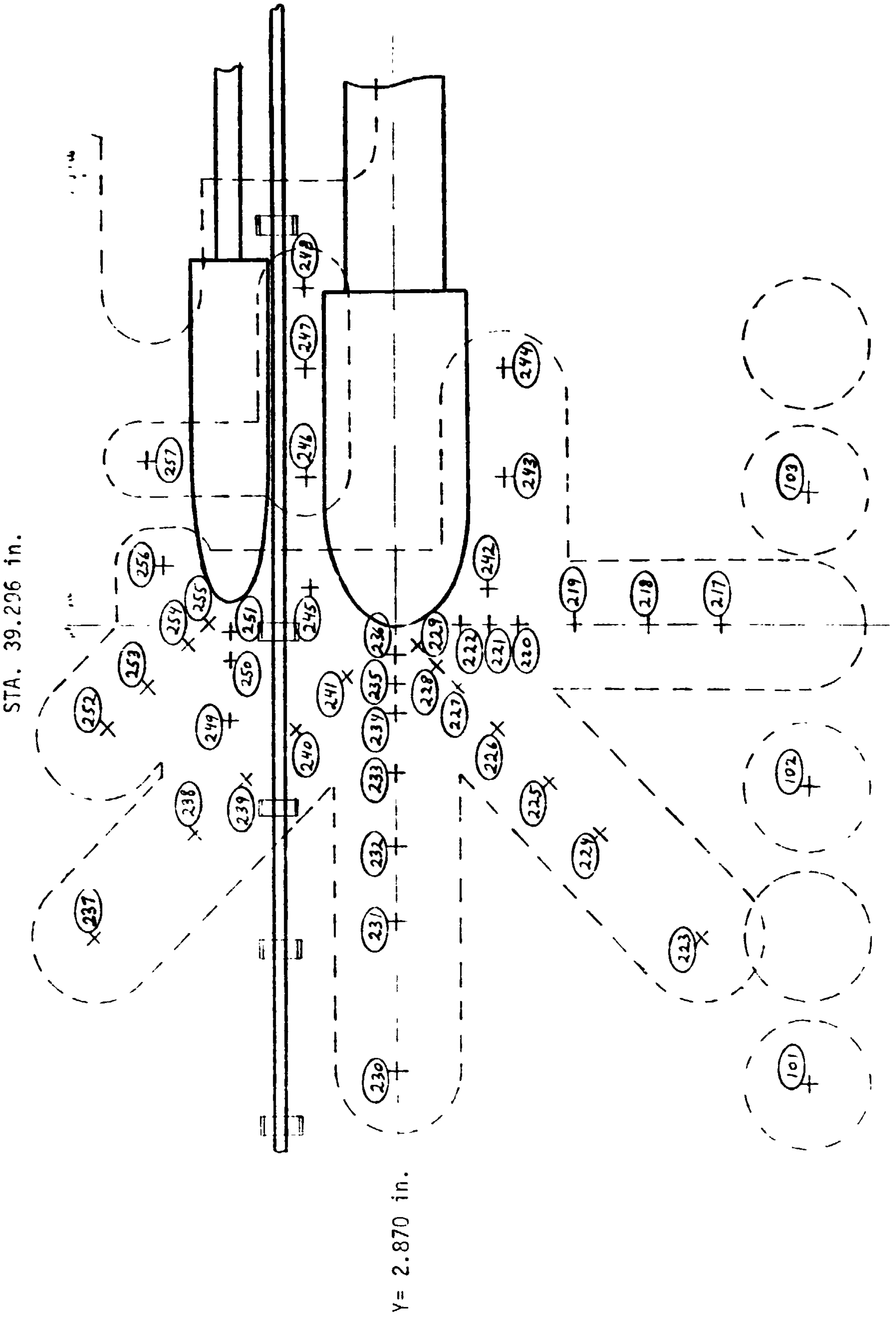

Fig. 3.6 Region A Skin Thermocouple Locations

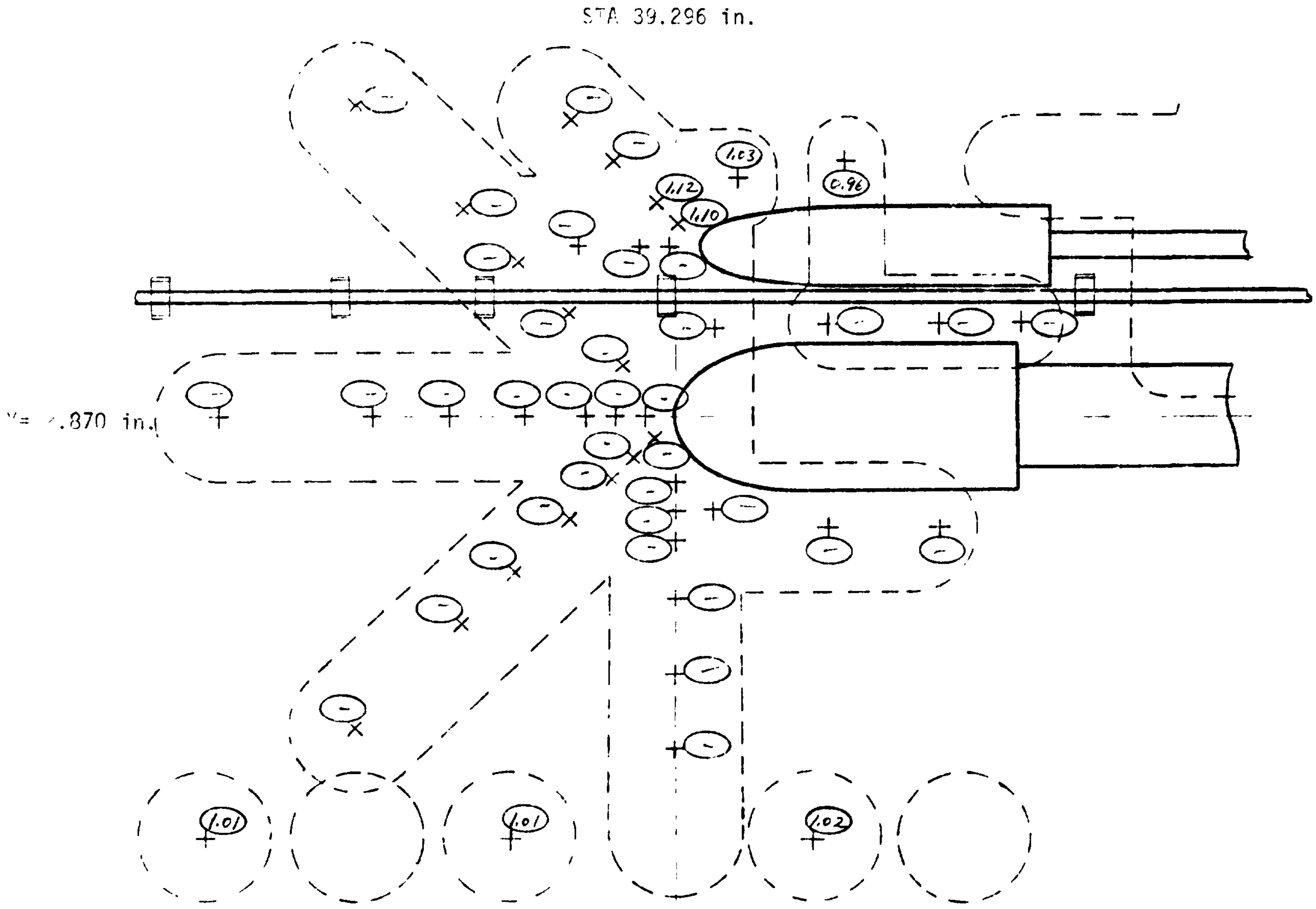

Fig. 3.7 Region A Clean Skin Factors (Flat Plate, B Config.)

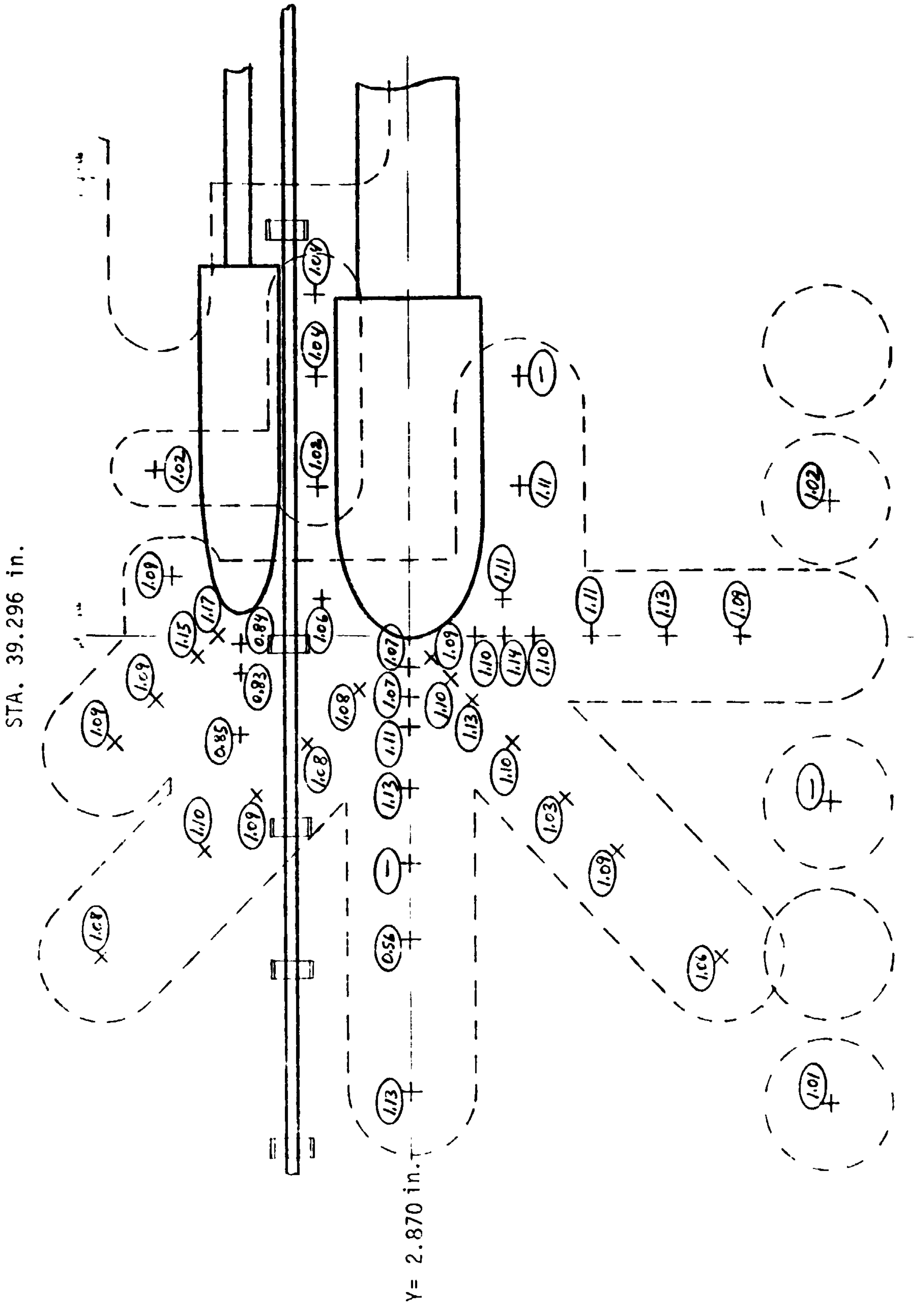

Fig. 3.8 Region A Orbiter Interference Factors (B Config.)

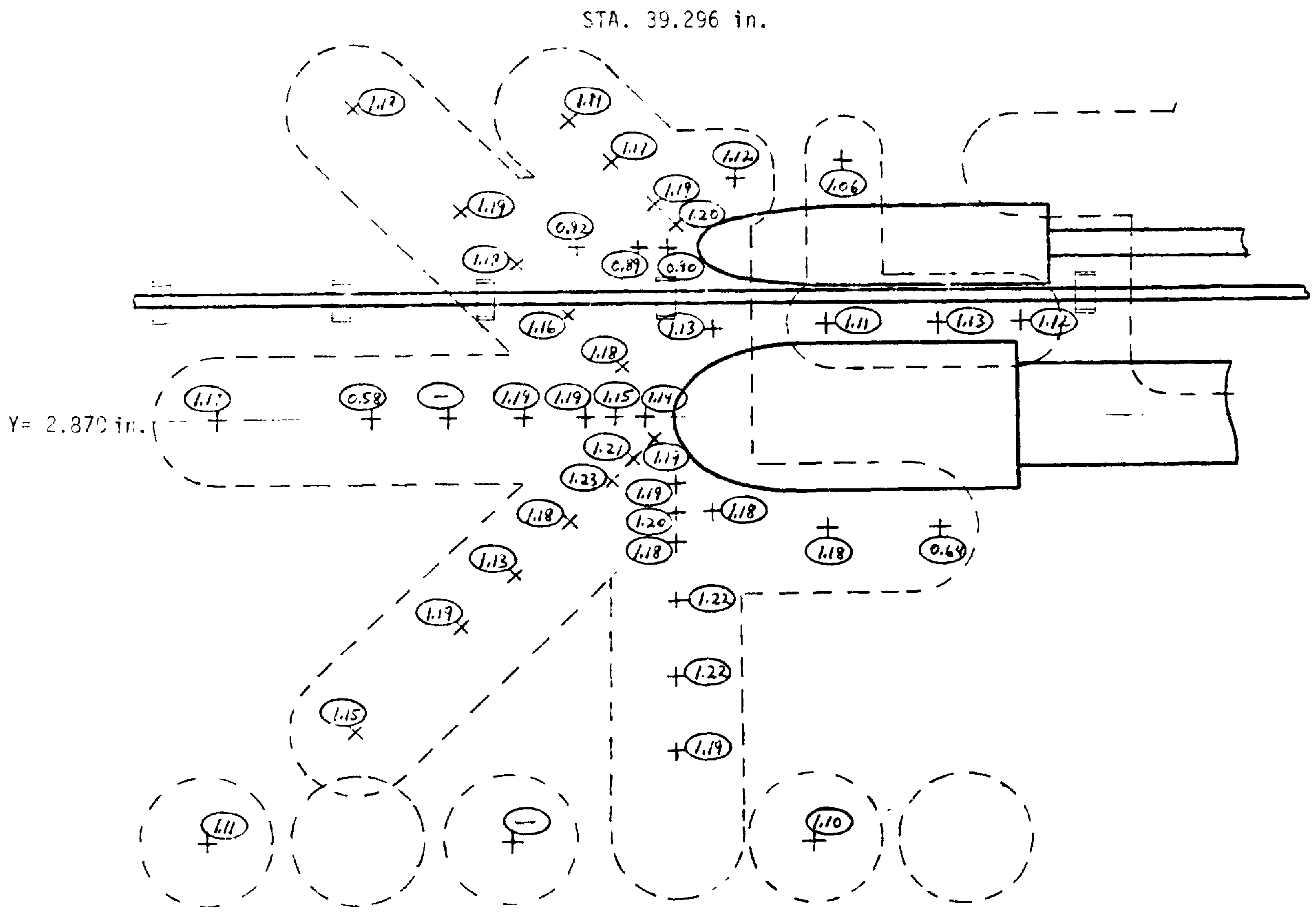

Fig. 3.9 Region A Tiedown Interference Factors (B Config.)

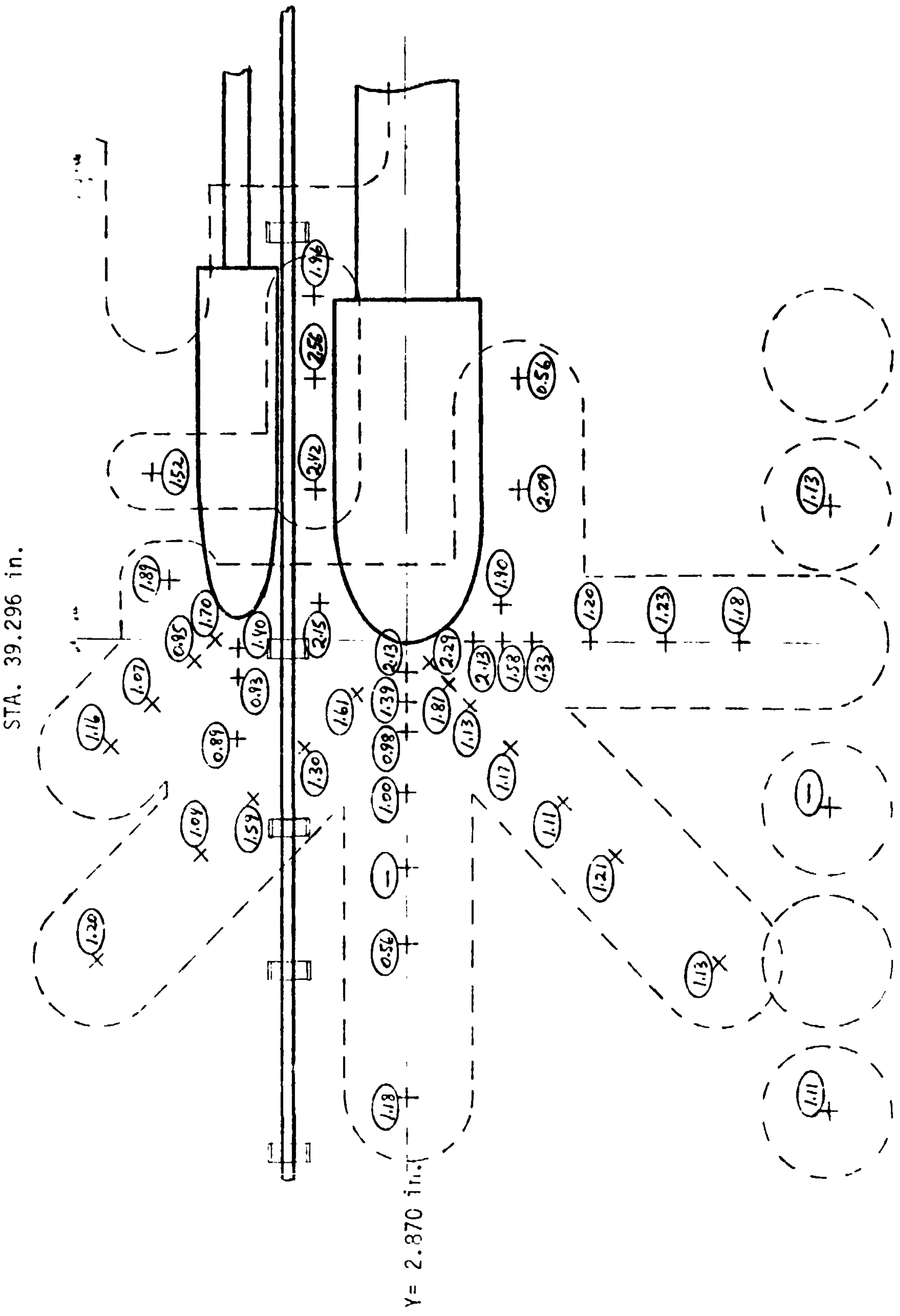

Fig. 3.10 Region A Tunnel Interference Factors (B Config.)

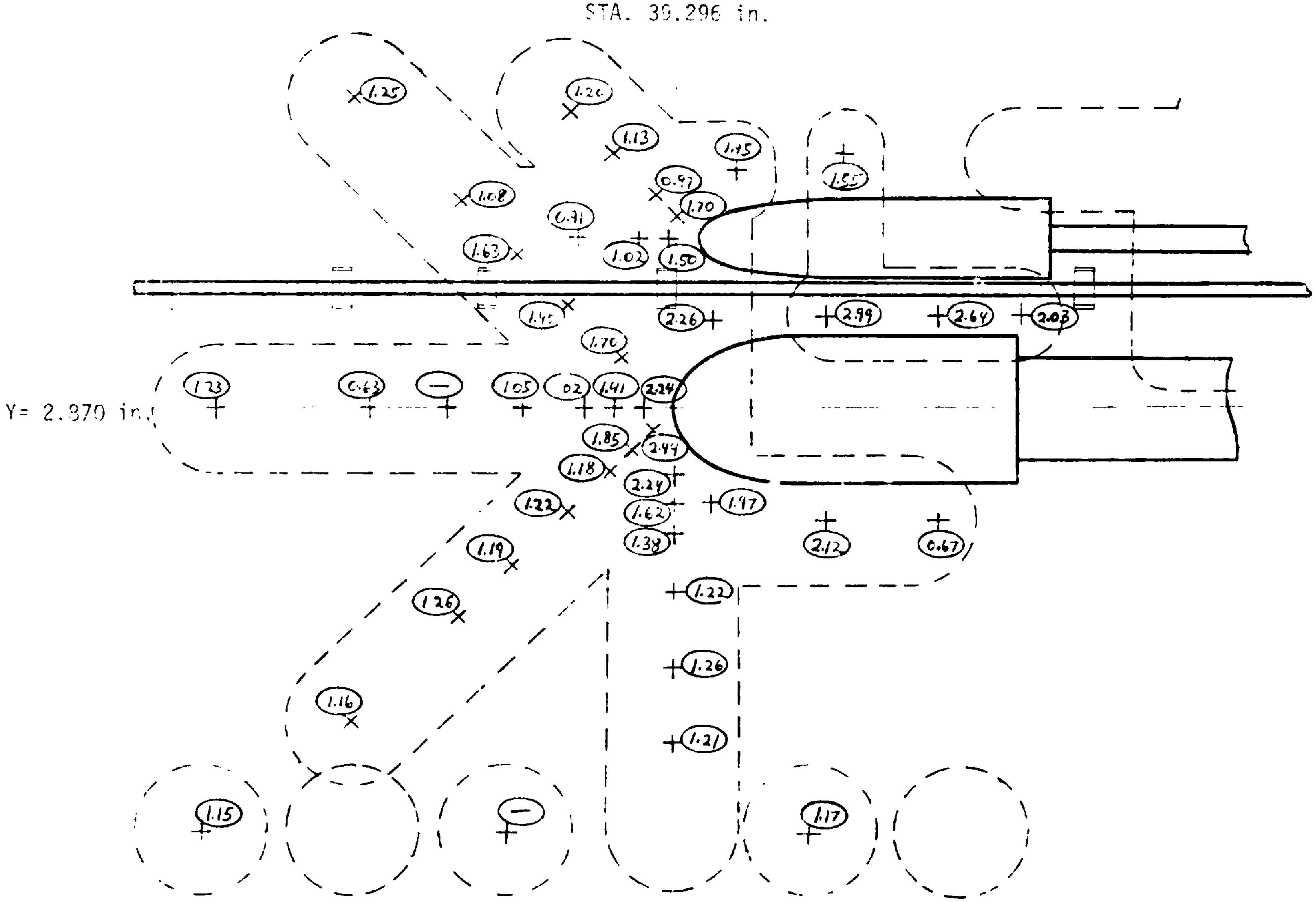

Fig. 3.11 Region A Total Interference Factors, Orbiter, Tiedown and Tunnels (B Config.)

TABLE 3.2
T/C LOCATION TABLE
REGION B

T/C	STA No.	B. P.	X (Inches)*	X_T (Inches)	0 (Deg.)
202	42.596	1.80	742.40	1064.90	15.09
203	43.096	↓	754.90	1077.40	↓
204	43.596	↓	767.40	1089.90	↓
205	44.076	↓	779.40	1101.90	↓
206	44.496	1.80	789.90	1112.40	15.09
207	44.696	↓	794.90	1117.40	↓
208	44.896	↓	799.90	1122.40	↓
209	45.796	↓	822.40	1144.90	↓
210	46.796	↓	847.40	1169.90	↓
258	41.446	4.60	713.65	1036.15	38.565
259	41.896	4.48	724.90	1047.40	37.556
260	42.096	4.48	729.90	1052.40	↓
261	42.296	4.48	734.90	1057.40	37.556
262	42.496	↓	739.90	1062.40	↓
263	42.696	3.35	744.90	1067.40	26.859
264	42.896	↓	749.90	1072.40	↓
265	43.296	↓	759.90	1082.40	↓
266	42.696	3.50	744.90	1067.40	29.34
267	42.896	↓	749.90	1072.40	↓
268	43.676	↓	769.40	1091.90	↓
269	42.696	3.82	744.90	1067.40	32.026
270	42.896	↓	749.90	1072.40	↓
271	42.896	4.02	749.90	1072.40	33.70
272	42.696	4.20	744.90	1067.40	35.21
273	42.916	4.20	750.40	1072.90	35.211
274	42.916	5.84	750.40	1072.90	48.96
275	44.746	2.25	796.15	1118.65	18.86
276	44.396	2.60	787.40	1109.90	20.846
277	44.066	2.95	779.15	1101.65	23.652
278	43.696	3.30	769.90	1092.40	26.458
279	45.496	3.35	814.90	1137.40	26.859
280	45.696	3.35	819.90	1142.40	↓

* $X = X_T - 322.5$ Equivalent Full Scale ET Axial Distance

TABLE 3.2
T/C LOCATION TABLE
REGION B

T/C	STA No.	B. P.	X (Inches)*	X_T (Inches)	θ (Deg.)
281	46.076	3.35	829.40	1151.90	26.859
282	45.496	3.50	814.90	1137.40	29.34
283	45.696	↓	819.90	1142.40	↓
284	46.446	↓	838.65	1161.15	↓
285	45.496	3.83	814.90	1137.40	32.11
286	45.696	3.83	819.90	1142.40	32.11
287	46.446	↓	838.65	1161.15	↓
288	45.496	4.18	814.90	1137.40	35.044
289	45.696	↓	819.90	1142.40	↓
290	44.816	2.52	797.90	1120.40	20.204
291	44.816	2.88	797.90	1120.40	23.09
292	44.816	3.20	797.90	1120.40	25.656
293	44.996	2.23	802.40	1124.90	17.88
294	45.196	↓	807.40	1129.90	↓
295	45.396	↓	812.40	1134.90	↓
296	45.596	2.23	817.40	1139.90	17.88
297	44.996	2.43	802.40	1124.90	19.483
298	45.196	↓	807.40	1129.90	↓
299	45.396	↓	812.40	1134.90	↓
300	45.596	↓	817.40	1139.90	↓
301	44.99	2.63	802.40	1124.90	21.086
302	45.196	↓	807.40	1129.90	↓
303	45.396	↓	812.40	1134.90	↓
304	45.596	↓	817.40	1139.90	↓

* $X = X_T - 322.5$ Equivalent Full Scale ET Axial Distance

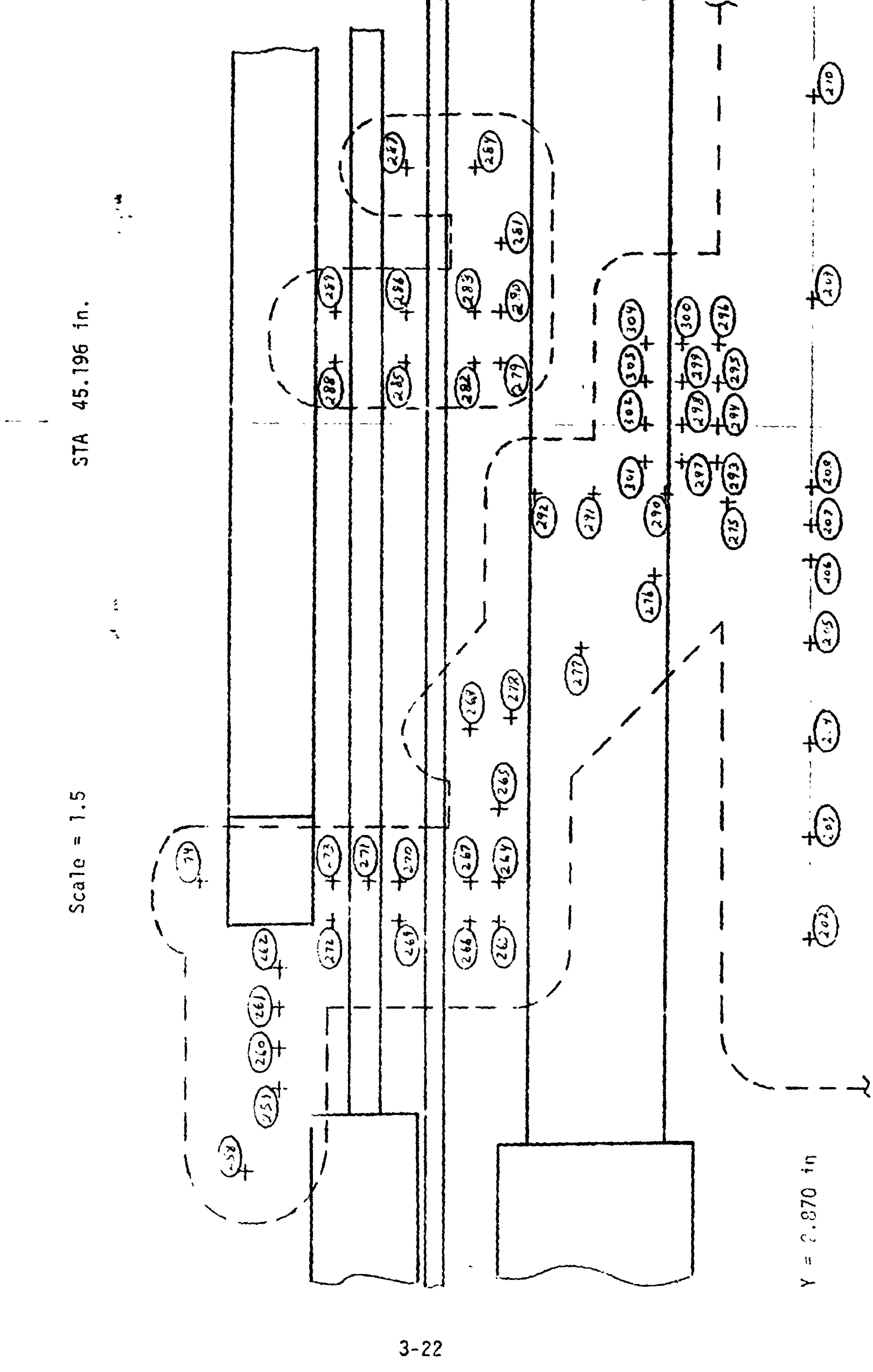

Fig. 3.12 Thermocouple Locations on the Skin Aft of Tunnel Fairings

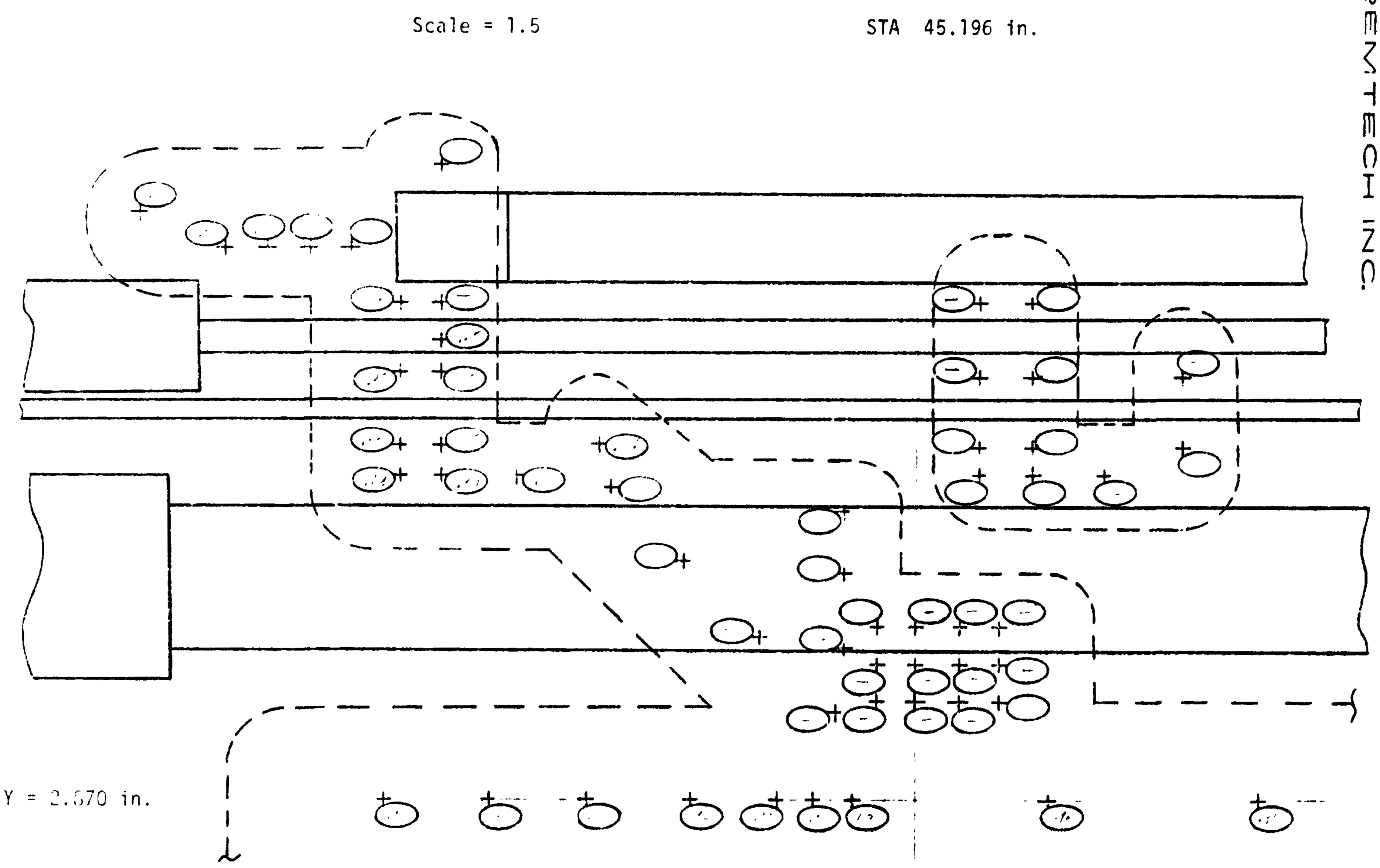

Fig. 3.[illegible]3 Clean Skin Factors (Plate Alone)

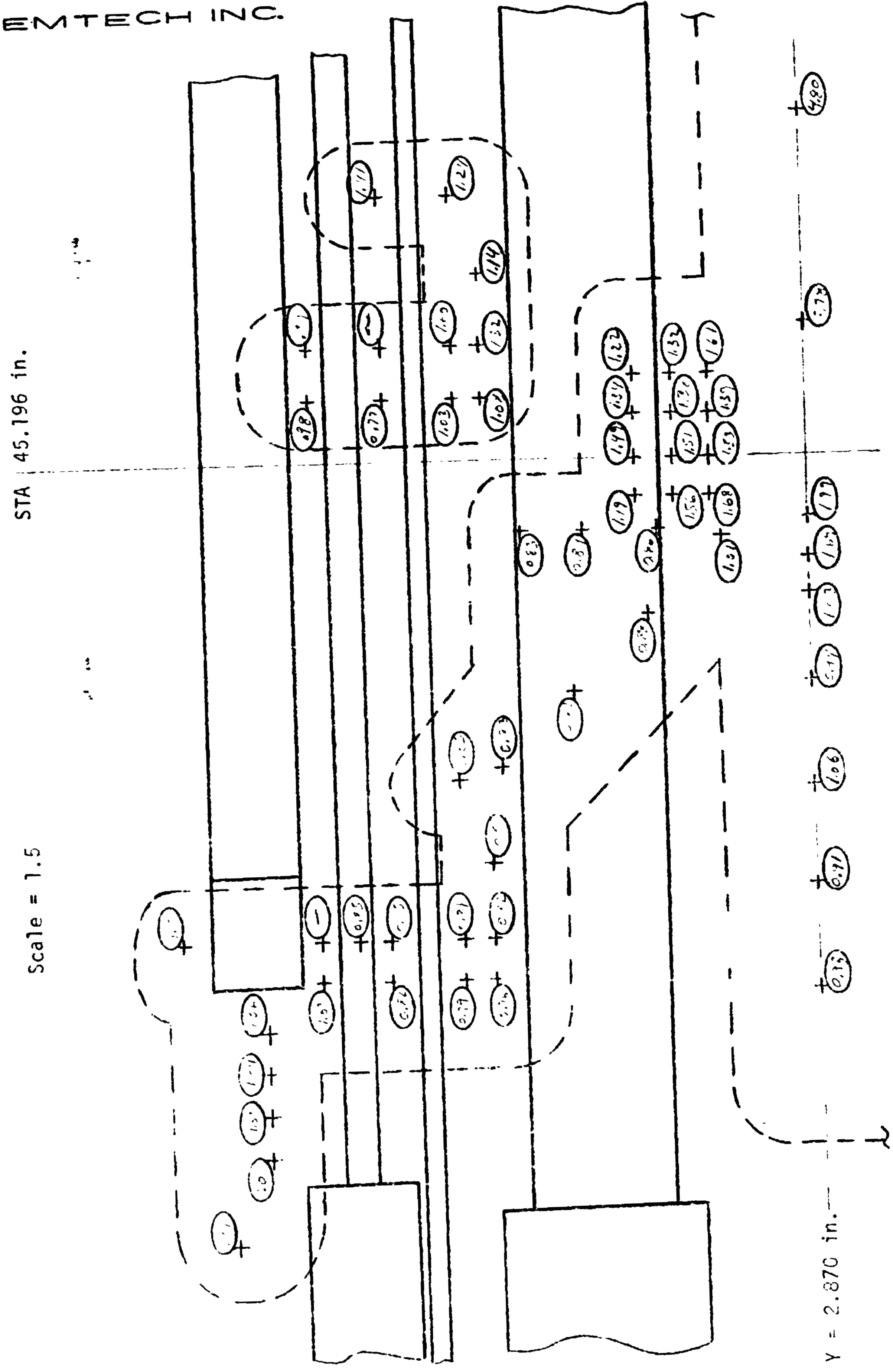

Fig. 3.14 Orbiter Interference Factors on the Skin (B Configuration)

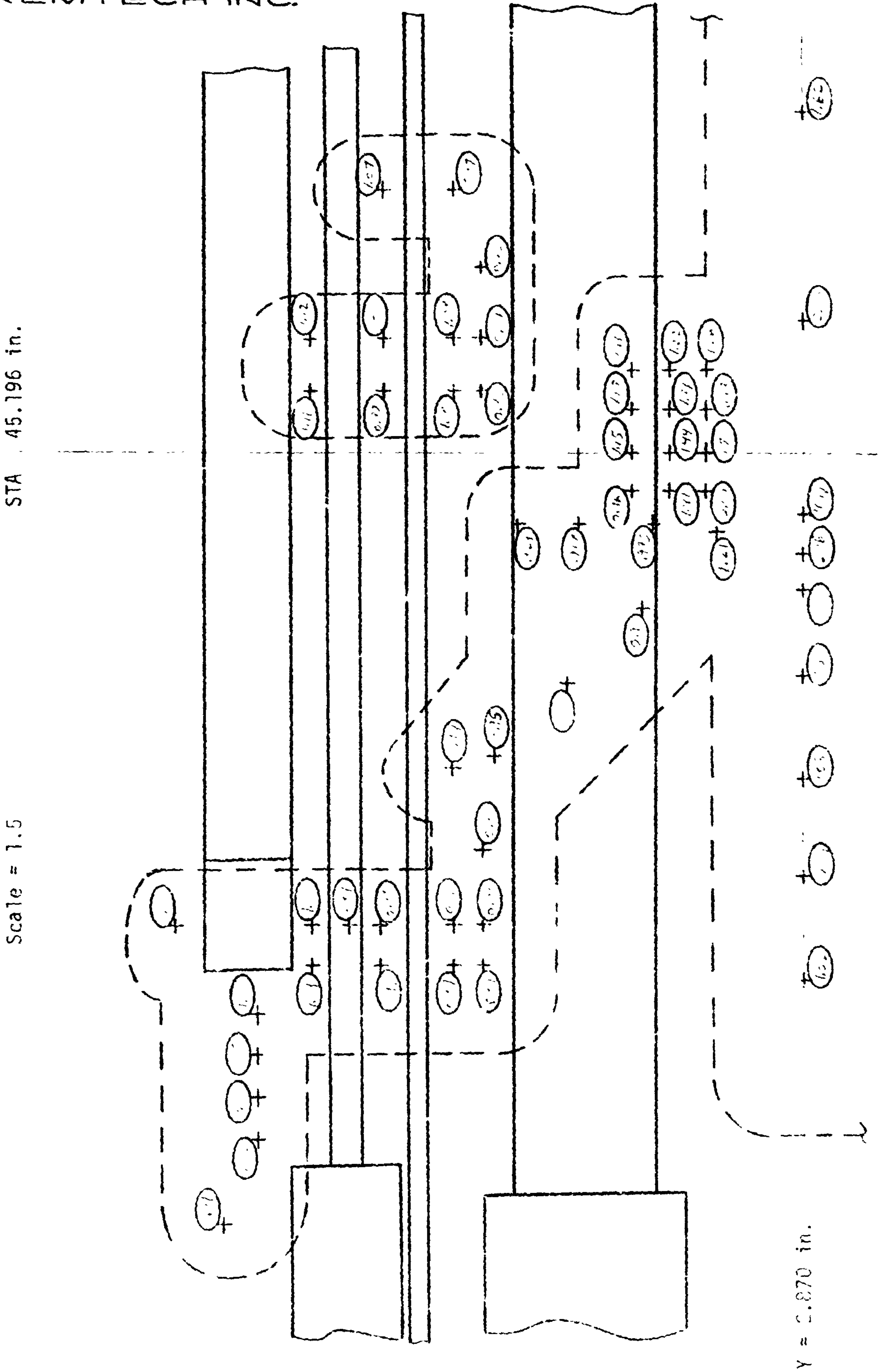

Fig.3.15 Tiedown Interference Factors on the Skin (B Configuration)

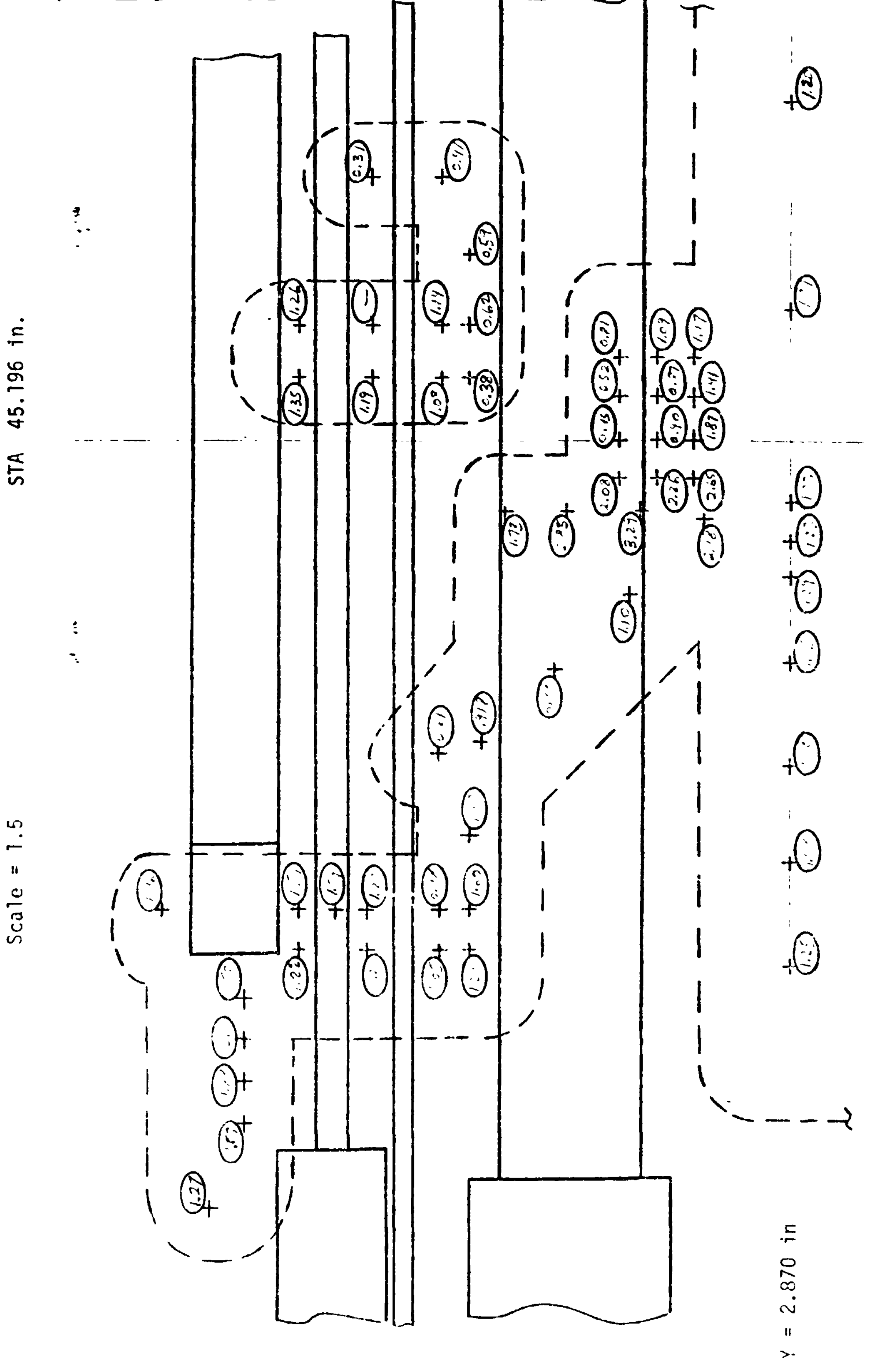

Fig. 3.16 Tunnel Interference Factors on the Skin (B Configuration)

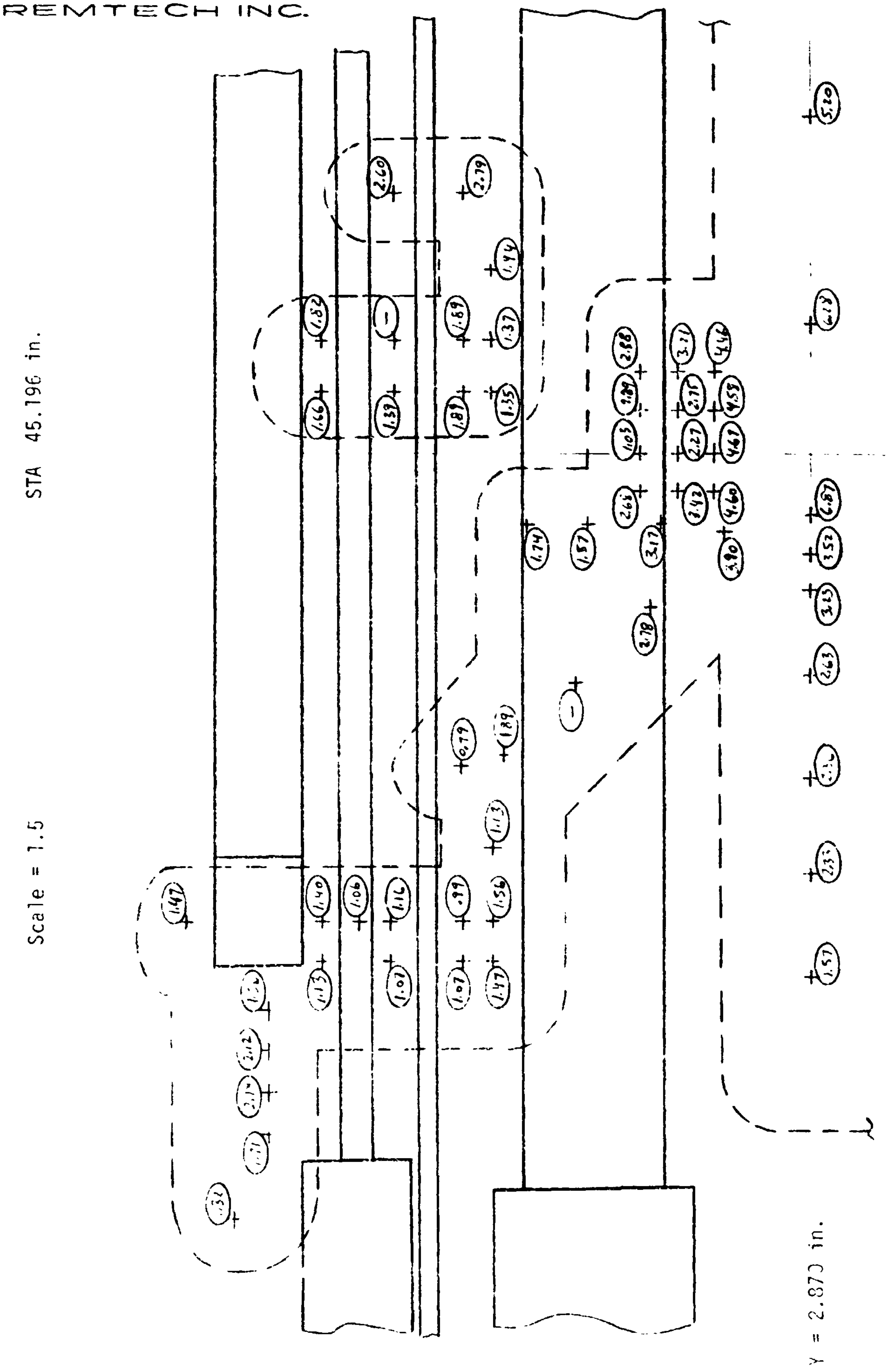

Fig. 3.17 Total Interference Factors on the Skin Near the Tunnels (Orbiter, Tunnels & Tiedown) B Configuration

TABLE 3.3
T/C LOCATION TABLE
REGION C

T/C #	STA No.	B. P.	X (Inches)*	X_T (Inches)	Θ (Deg.)
110	49.196	0.93	907.4	1229.9	7.80
111	50.196	0	932.4	1254.9	0
112	52.196	↓	982.4	1304.9	↓
113	54.196	↓	1032.4	1354.9	↓
114	56.196	↓	1082.4	1404.9	↓
199	55.646	3.43	1068.6	1391.2	27.50
200	↓	2.33	↓	↓	18.68
201	↓	1.93	↓	↓	16.18
212	49.796	1.80	922.4	1244.9	15.10
213	51.796	↓	972.4	1294.9	↓
214	53.796	↓	1022.4	1344.9	↓
215	55.646	1.43	1068.6	1391.2	11.99
216	↓	0.93	↓	↓	7.80
305	49.196	2.12	907.4	1229.9	17.00
306	↓	2.32	↓	↓	18.60
307	↓	2.52	↓	↓	20.20
308	↓	2.87	↓	↓	23.01
309	↓	3.20	↓	↓	25.66
310	↓	3.40	↓	↓	27.26
311	49.196	4.80	907.4	1229.9	40.24
312	↓	5.30	↓	↓	44.43
313	52.816	3.35	997.9	1320.4	28.09
314	↓	3.50	↓	↓	29.34
315	↓	3.82	↓	↓	32.03
316	52.816	4.18	997.9	1320.4	35.04
317	↓	4.48	↓	↓	37.56
318	↓	4.76	↓	↓	39.91
319	53.016	↓	1002.9	1325.4	↓
320	↓	3.35	↓	↓	28.09
321	53.016	3.50	1002.9	1325.4	29.34
322	↓	3.82	↓	↓	32.03
323	↓	4.02	↓	↓	33.70
324	↓	4.18	↓	↓	35.04
325	53.016	4.48	↓	↓	37.56

* $X = X_T - 322.5$ Equivalent Full Scale Axial Distance

TABLE 3.3
T/C LOCATION TABLE
REGION C (Cont.)

T/C	STA No.	B. P.	X (Inches)*	X_T (Inches)	Θ (Deg.)
326	53.376	3.35	1011.9	1334.4	28.09
327	53.746	3.50	1021.2	1343.6	29.34
328	↓	3.82	↓	↓	32.03
329	55.796	4.02	1072.4	↓	33.70
330	↓	4.18	↓	1394.9	35.04
331	55.796	4.48	1072.4	1394.9	37.56
332	55.636	4.82	1068.4	1390.9	40.41
333	55.796	↓	1072.4	1394.9	↓
334	55.636	5.30	1068.4	1390.9	44.43
335	54.896	2.24	1049.9	1372.4	17.96
336	55.096	2.24	1054.9	1377.4	17.96
337	55.296	↓	1059.9	1382.4	↓
338	55.496	↓	1064.9	1387.4	↓
339	54.896	2.43	1049.9	1372.4	19.48
340	55.096	↓	1054.9	1377.4	↓
341	55.296	2.43	1059.9	1382.4	19.48
342	55.496	↓	1064.9	1387.4	↓
343	54.896	2.63	1049.9	1372.4	21.09
344	55.096	↓	1054.9	1377.4	↓
345	55.296	↓	1059.9	1382.4	↓
346	55.496	↓	1064.9	1387.4	↓
347	54.716	2.52	1045.4	1367.9	20.20
348	↓	2.87	↓	↓	23.01
349	↓	3.20	↓	↓	25.66

* X = X_T-322.5 Equivalent Full Scale Axial Distance

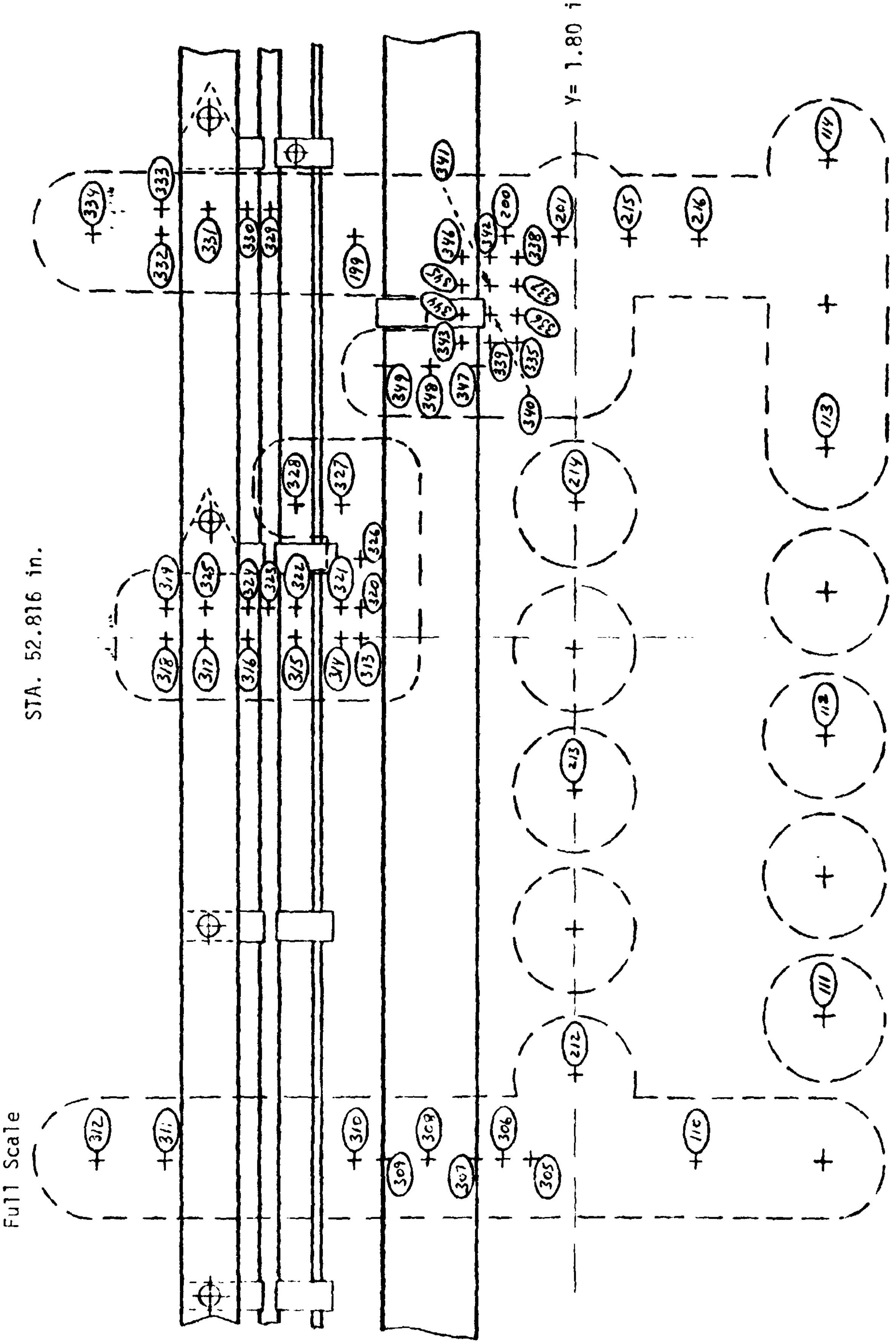

Fig. 3.18 Region C Skin Thermocouple Locations

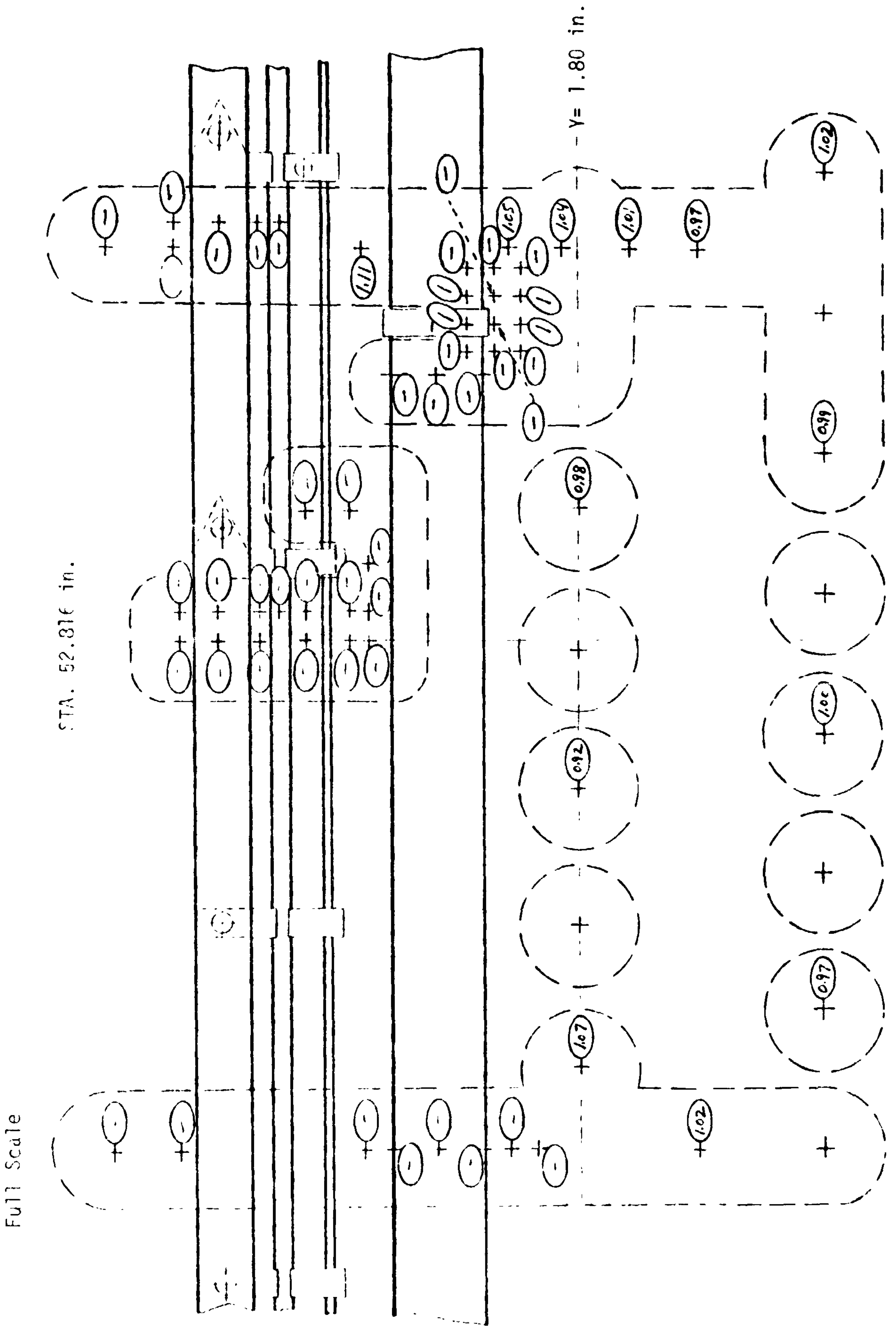

Fig. 3.19 Region C Clean Skin Factors (Flat Plate, B Config.)

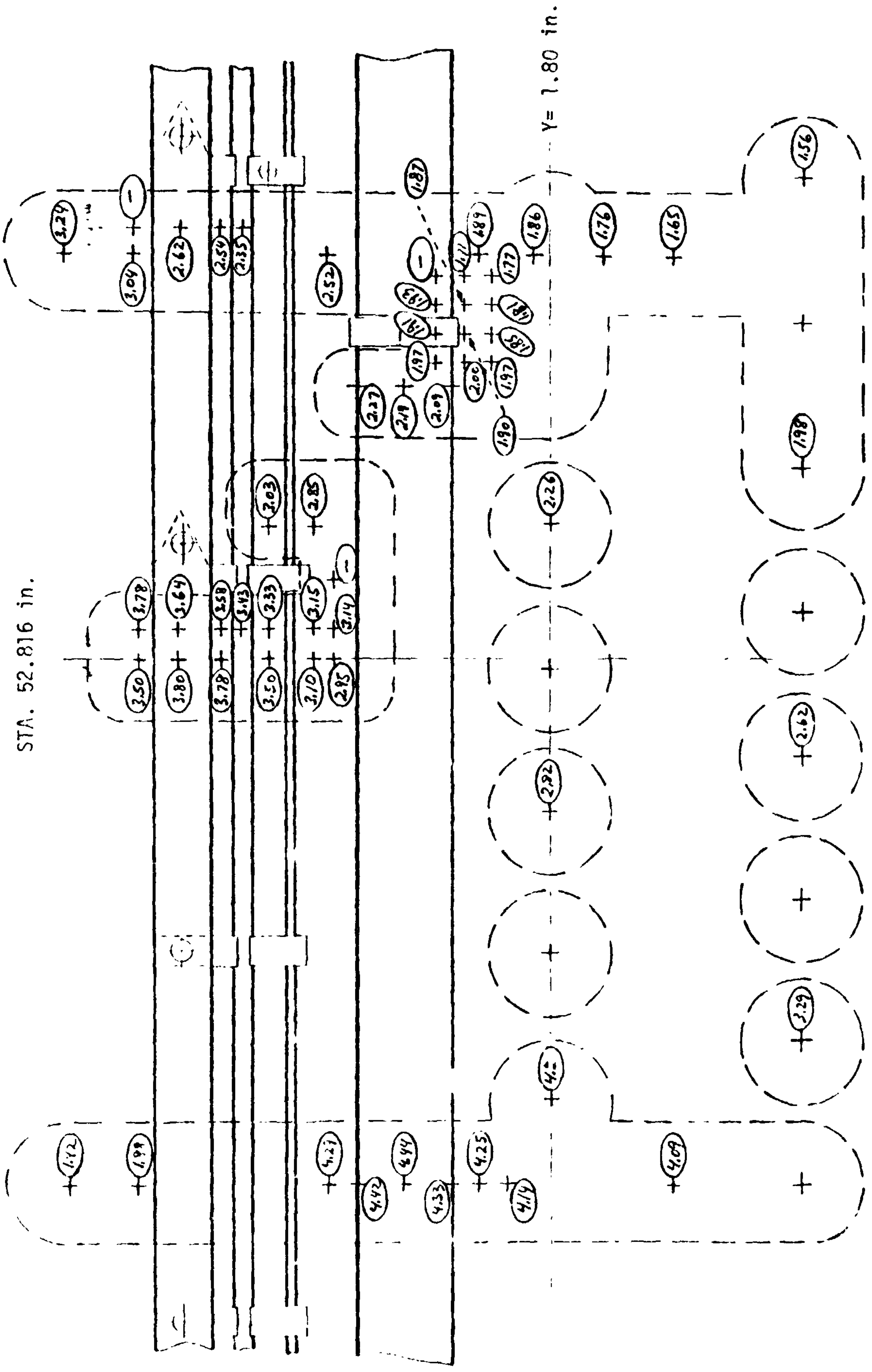

Fig. 3.20 Region C Orbiter Interference Factors (B Config.)

Full Scale

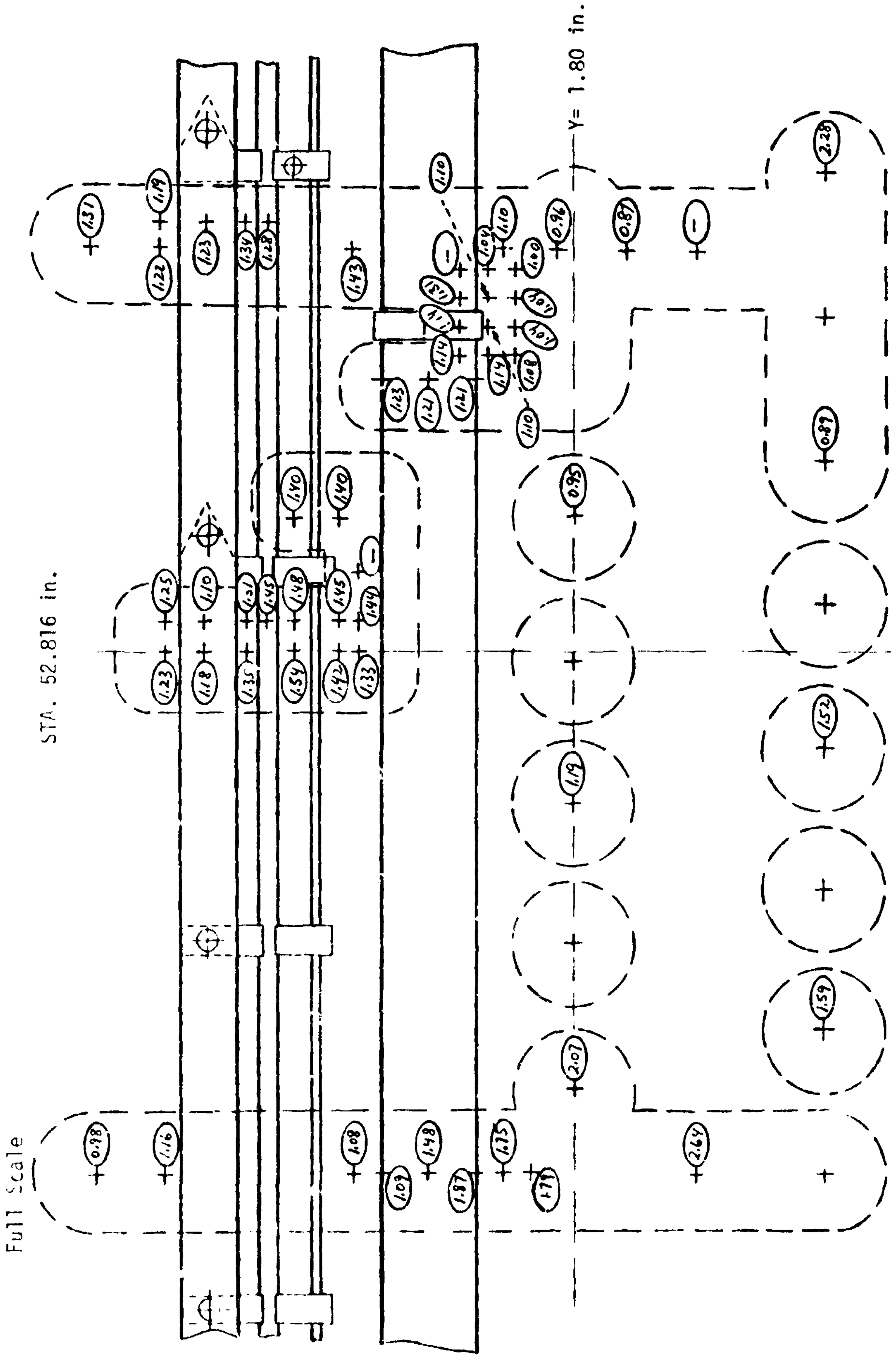

Fig. 3.21 Region C Tiedown Interference Factors (B Config.)

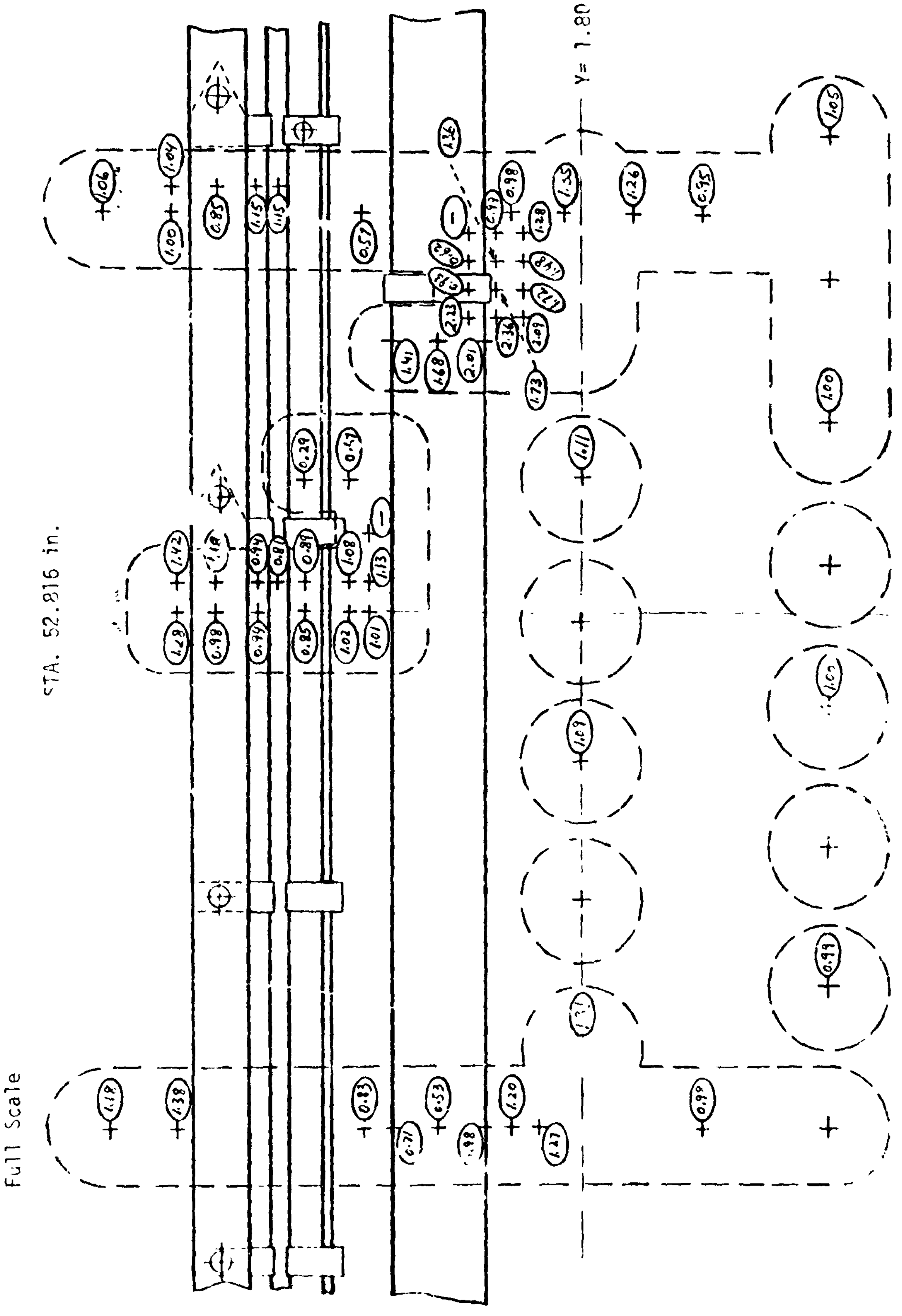

Fig. Region C Tunnel Interference Factors (B Config.)

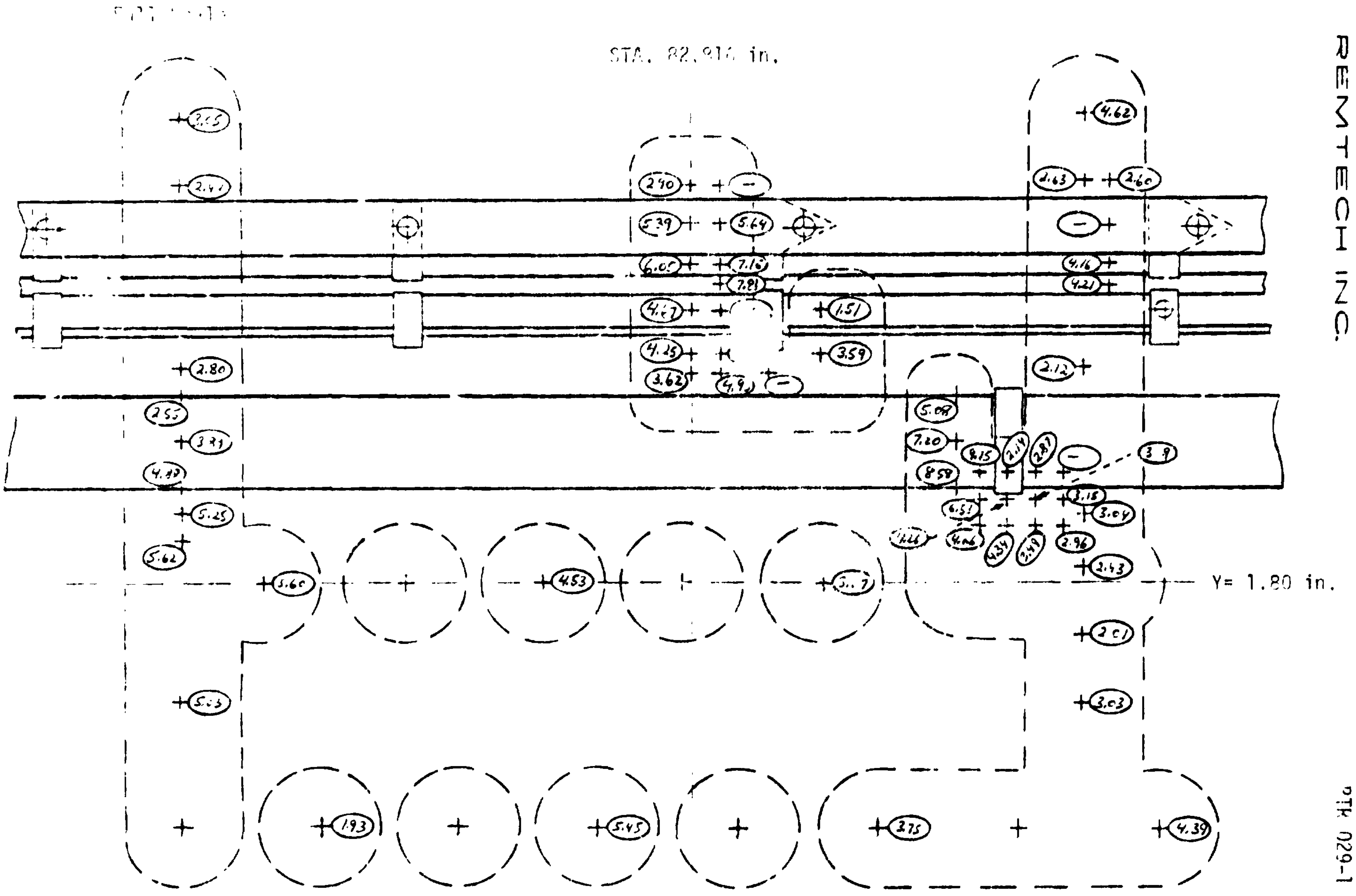

Fig. 3.23 Region C Total Interference Factors, Orbiter, Tiedown and Tunnels (B Config.)

TABLE 3.4

T/C LOCATION TABLE

REGION D

T/C #	STA No.	B. P.	X (Inches)*	X_T (Inches)	Θ (Deg.)
104	42.196	0.0	732.4	1054.9	0
105	43.196		757.4	1079.9	
106	44.196		782.4	1104.9	
107	46.196		832.4	1154.9	
108	47.196		857.4	1179.9	
109	48.196	↓	882.4	1204.9	↓
115	42.296	1.10	734.9	1057.4	9.22
116	43.016	0.38	752.9	1075.4	3.19
117	42.396	-1.06	737.4	1059.9	351.11
118	42.996	-0.40	752.4	1074.9	356.65
119	44.056	0.64	778.9	1101.4	5.37
120	44.396	1.00	787.4	1109.9	8.38
121	44.756	1.35	796.4	1118.9	11.32
122	45.196	1.16	807.4	1129.9	9.72
123	↓	0.64	807.4	1129.9	5.37
124	44.056	-0.64	778.9	1101.4	354.63
125	44.396	-1.02	787.4	1109.9	351.45
126	44.746	-1.35	796.15	1118.65	343.68
127	45.196	-1.16	807.4	1129.9	350.28
128	↓	-0.67	807.4	1129.9	354.38
129	43.096	-1.80	754.9	1077.4	344.91
130	43.596	↓	767.4	1089.9	↓
131	44.096	-1.80	779.9	1102.4	344.91
132	44.496		789.9	1112.4	
133	44.696		794.9	1117.4	
134	44.896		799.9	1122.4	
135	45.796	↓	822.4	1144.9	↓
136	46.796	-1.80	847.4	1169.9	344.91
137	47.796	↓	872.4	1194.9	↓
202	42.596	1.80	742.4	1064.9	15.09
203	43.096		754.9	1077.4	
204	43.596		767.4	1089.9	
205	44.076	↓	789.9	1112.4	↓

* $X = X_T - 322.5$ Equivalent Full Scale Axial Distance

TABLE 3.4
T/C LOCATION TABLE
REGION D (Cont.)

T/C	STA No.	B. P.	X (Inches)*	X_T (Inches)	θ (Deg.)
206	44.496	1.80	789.9	1112.4	15.09
207	44.696	1.80	794.9	1117.4	15.09
208	44.896	↓	799.9	1122.4	↓
209	45.796		822.4	1144.9	
210	46.796		847.4	1169.9	
211	47.796		872.4	1194.9	

* $X = X_T - 322.5$ Equivalent Full Scale Axial Distance

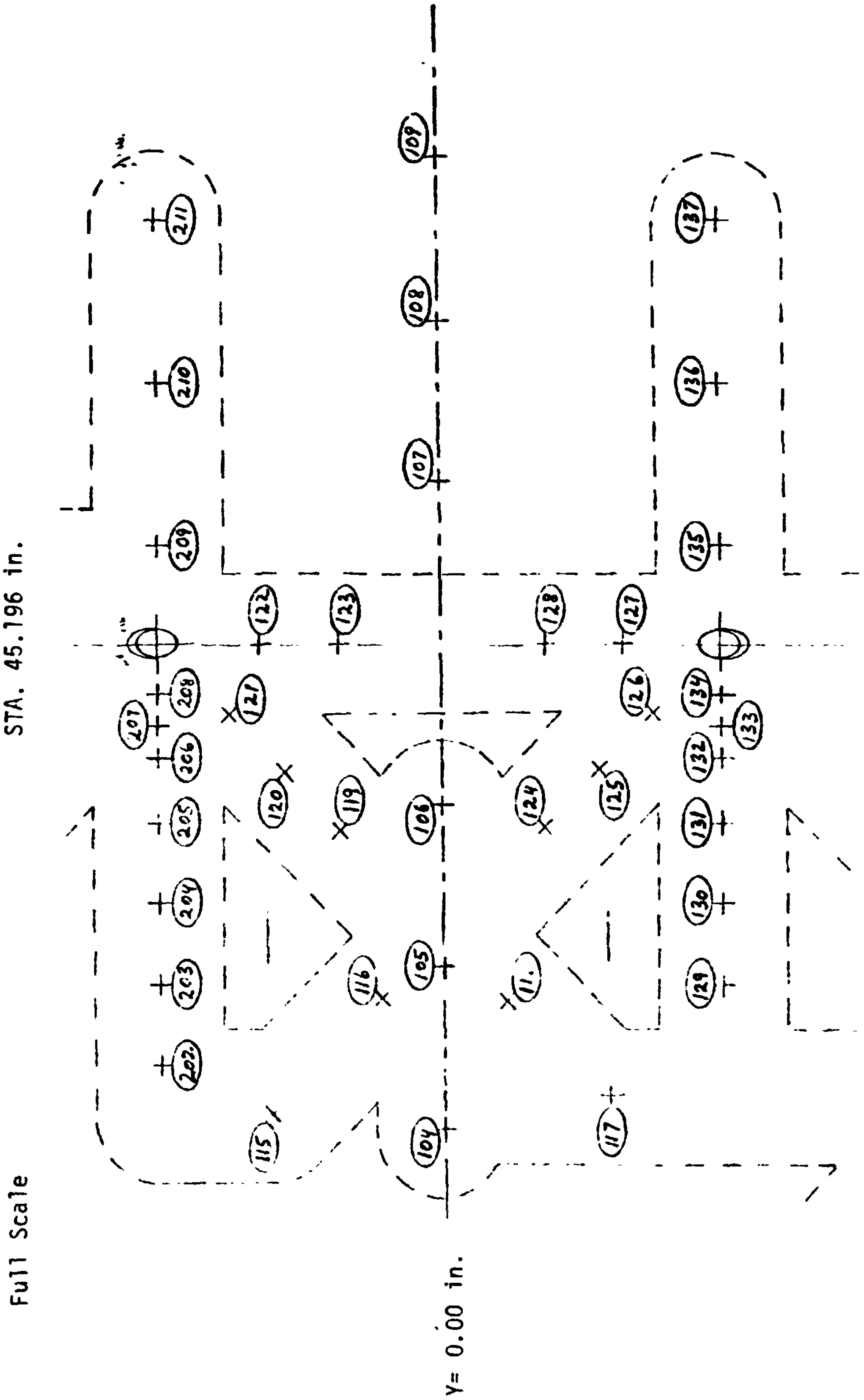

Fig. 3.24 Region D Skin Thermocouple Locations

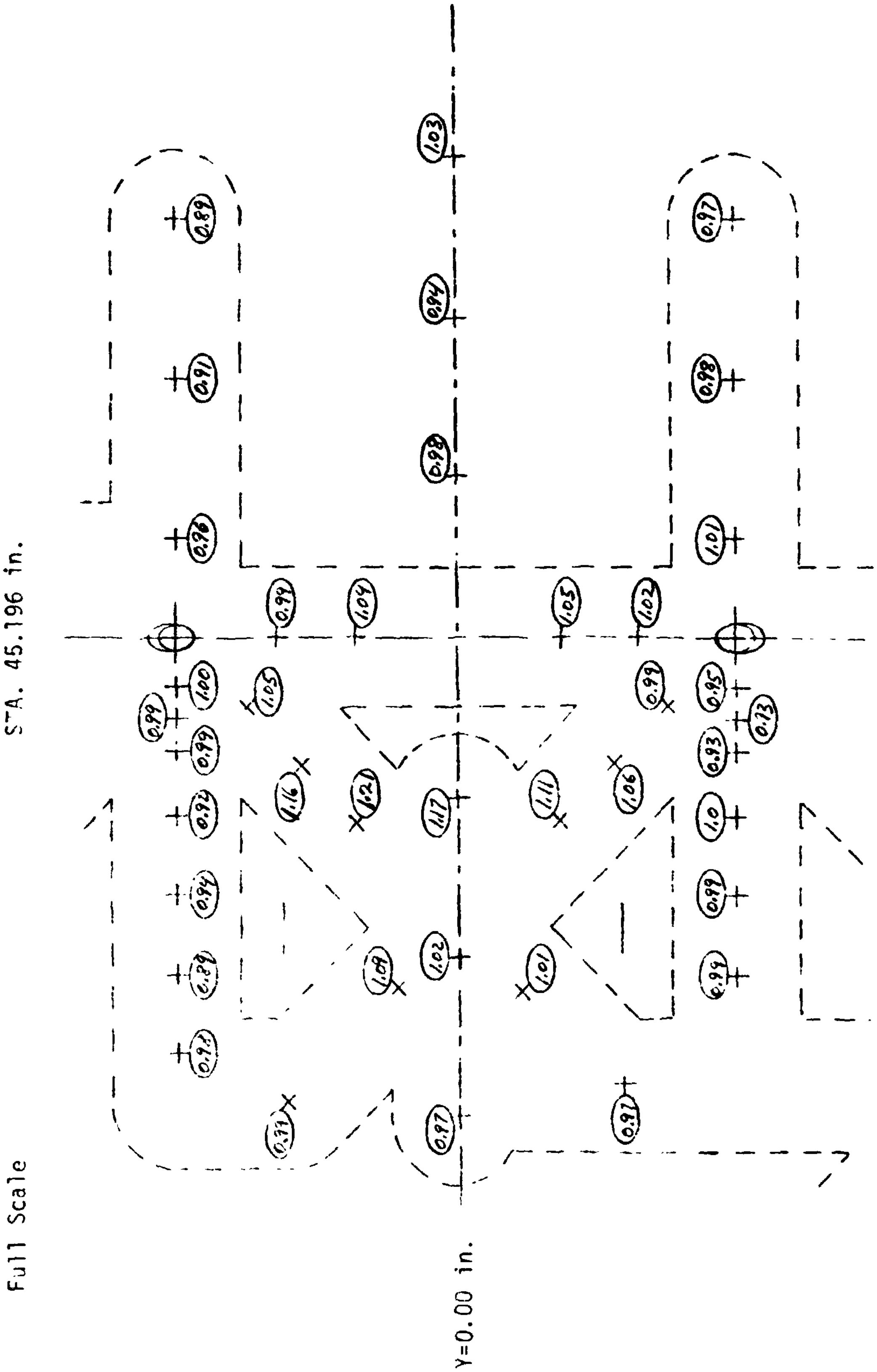

Fig. 3.25 Region D Clean Skin Factors (Flat Plate, B Config.)

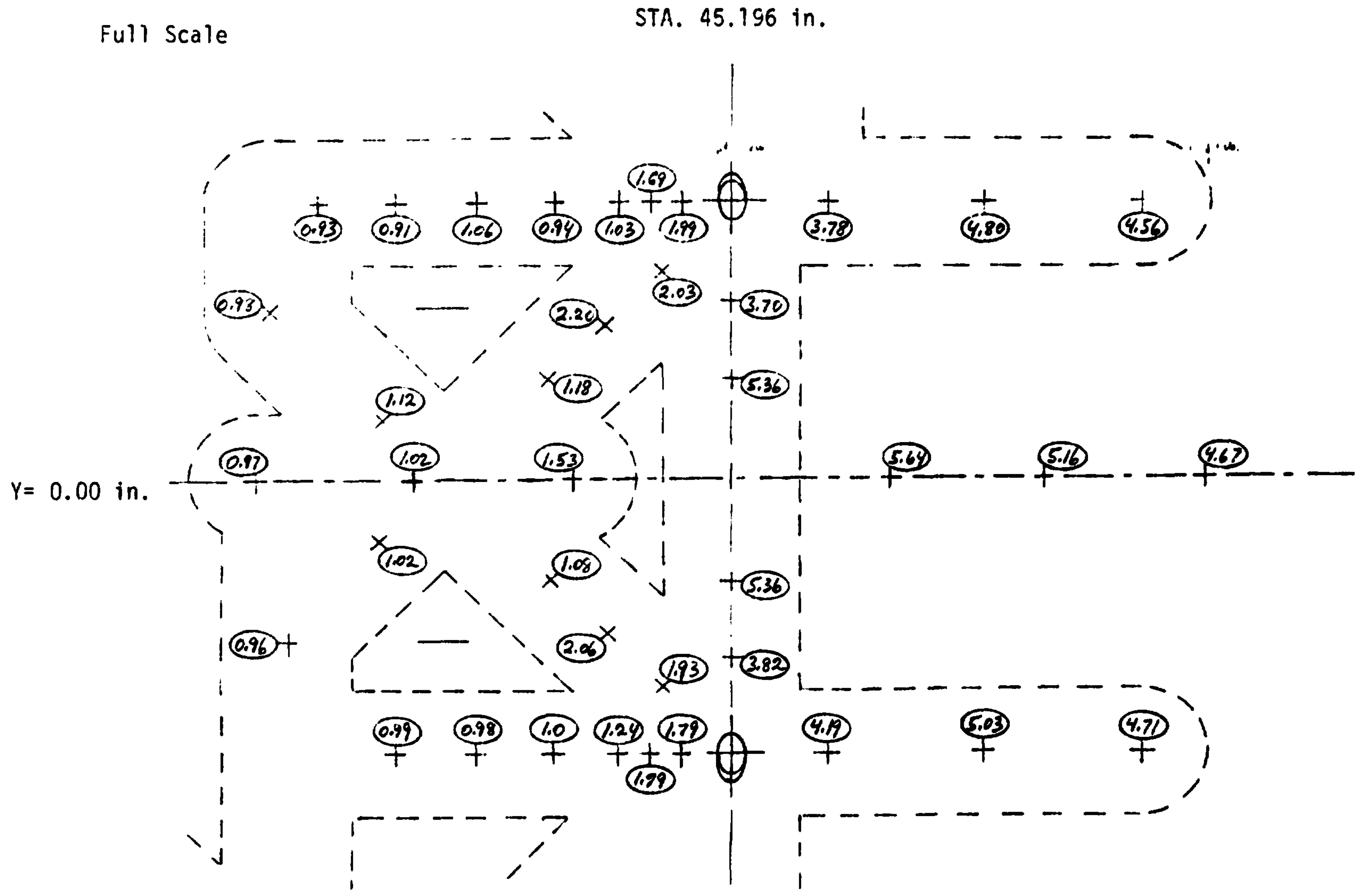

Fig. 3.26 Region D Orbiter Interference Factors (B Config.)

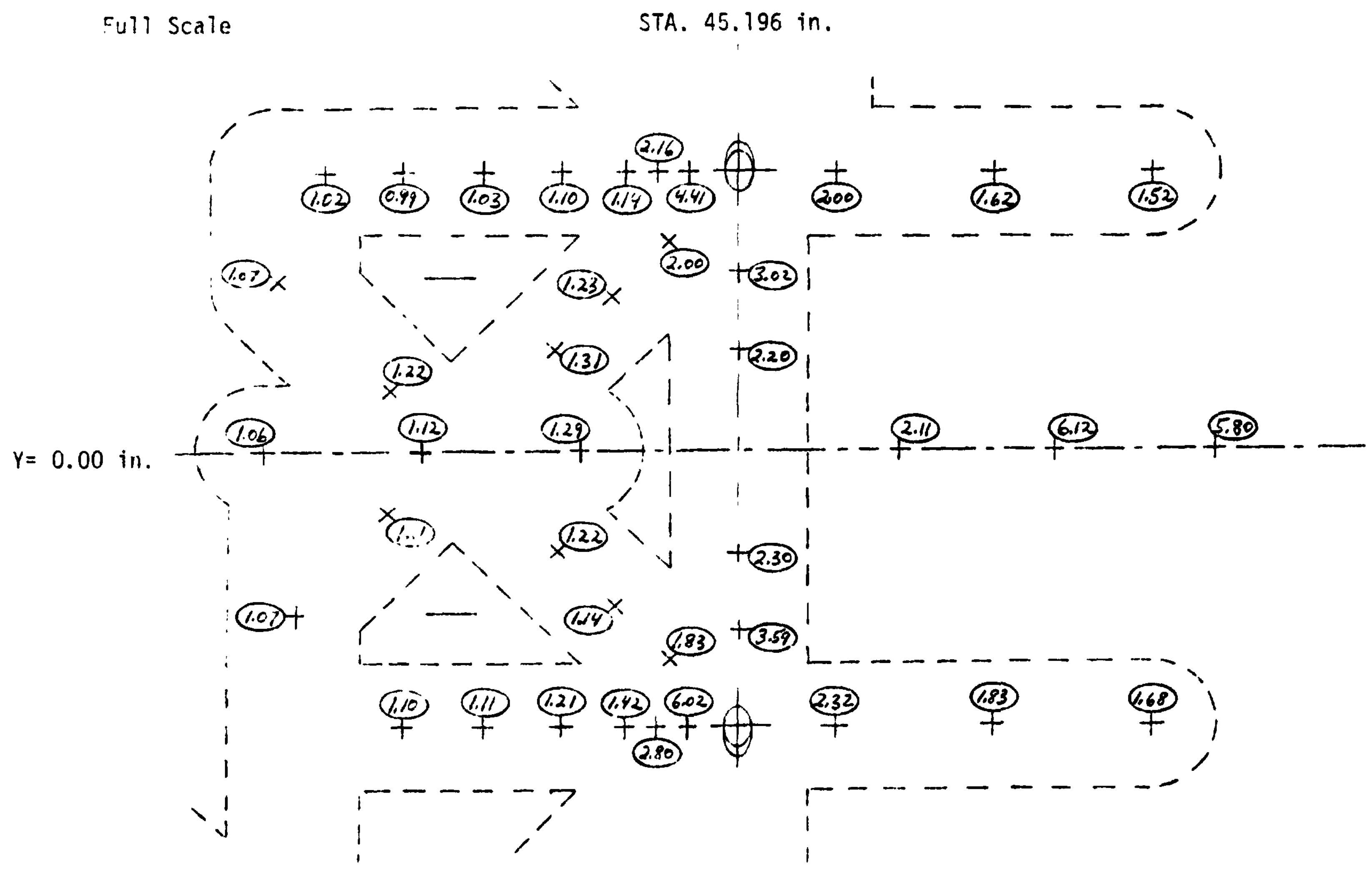

Fig. 3.27 Region D Tiedown Interference Factors (B Config.)

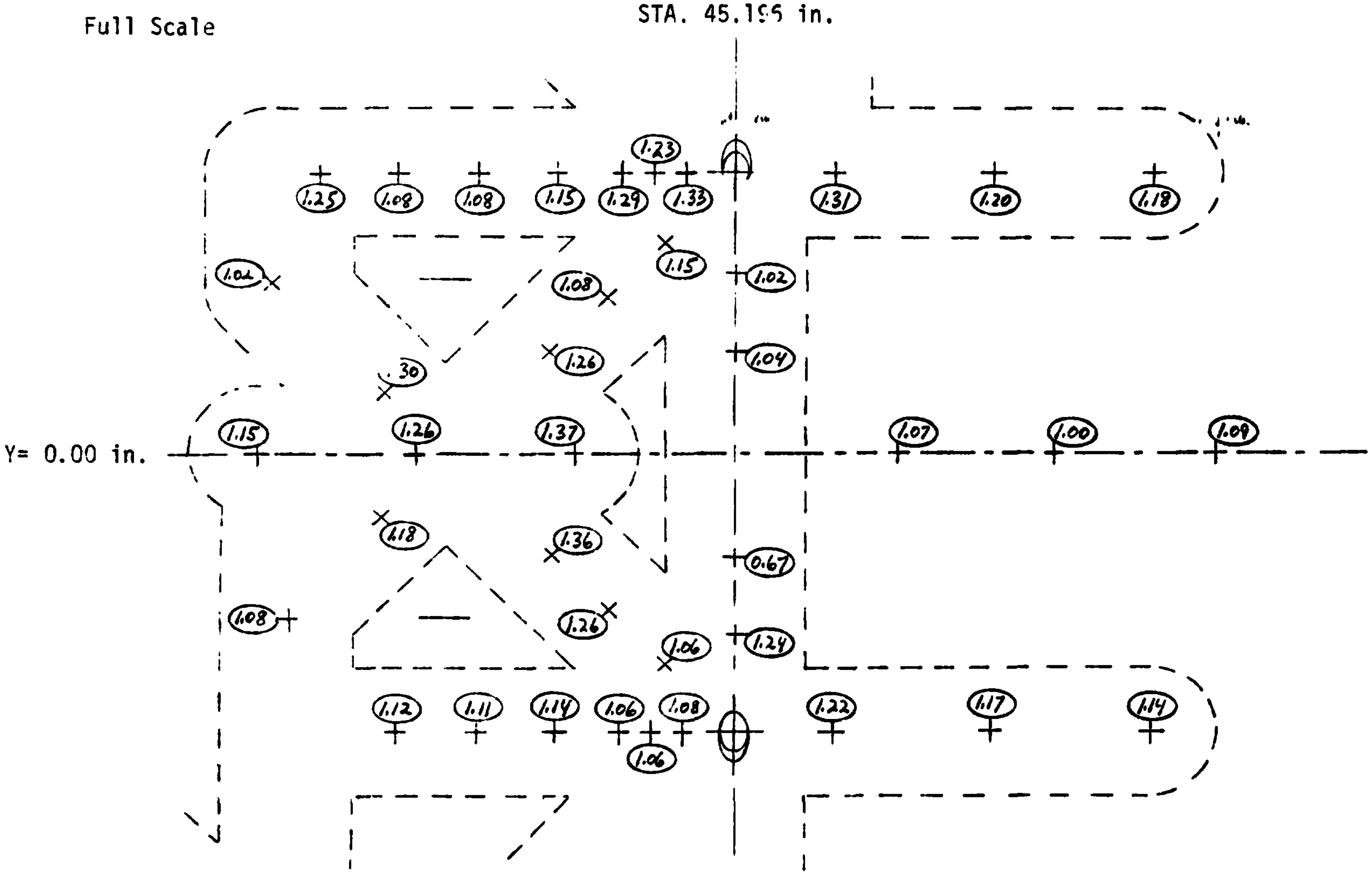

Fig. 3.28 Region D Tunnel Interference Factors (B Config.)

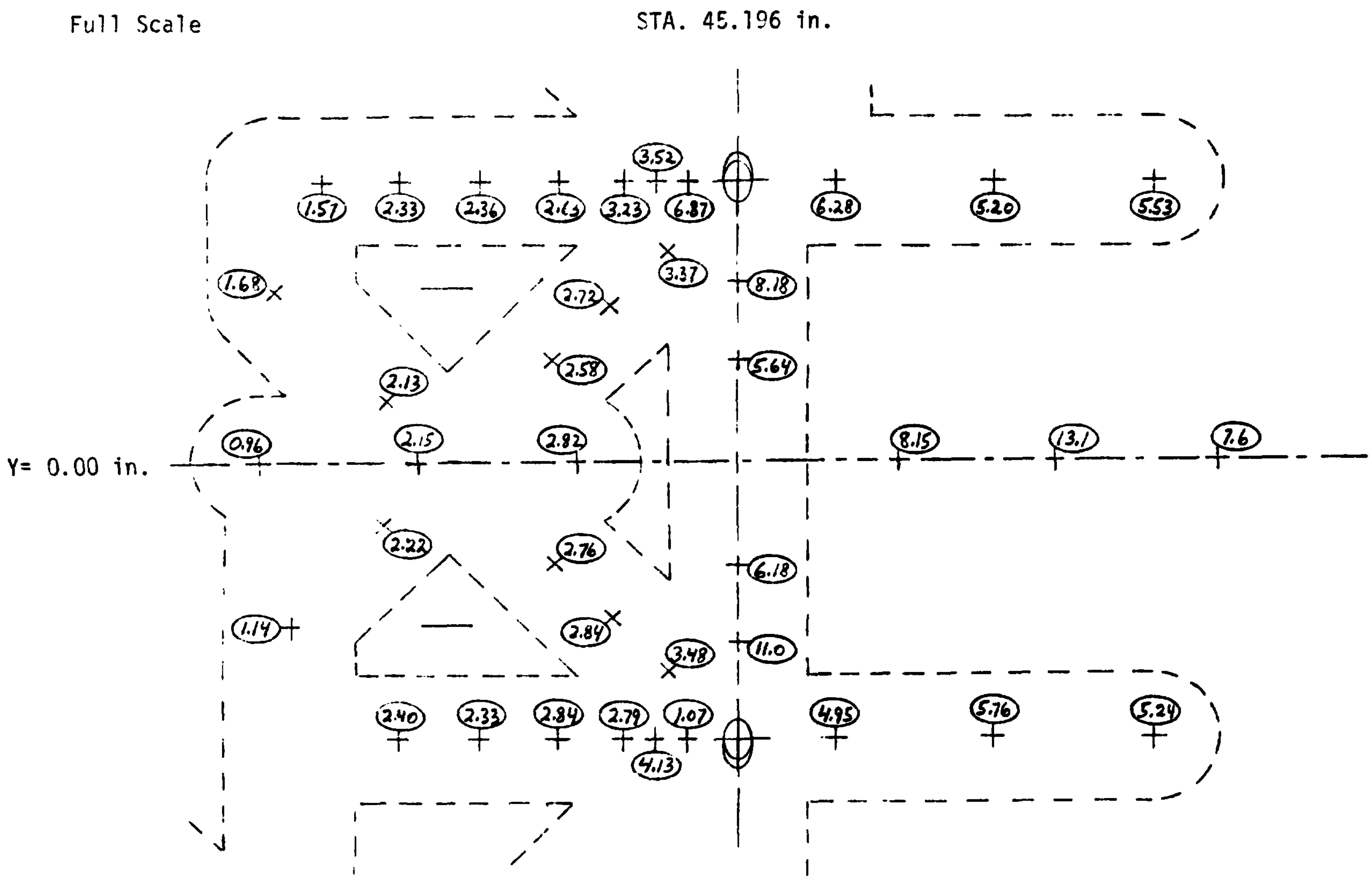

Fig. 3.29 Region D Total Interference Factors, Orbiter, Tiedown and Tunnels (B Config.)

TABLE 3.5
T/C LOCATION TABLE
REGION E

T/C #	STA No.	B. P.	X (Inches)*	X_T (Inches)	Θ (Deg.)
129	43.096	-1.80	754.90	1077.40	344.91
130	43.596	↓	767.40	1089.90	↓
131	44.096	-1.80	779.90	1102.40	344.91
132	44.496	↓	814.90	1137.40	↓
133	44.696	↓	794.90	1117.40	↓
134	44.896	↓	799.90	1122.40	↓
135	45.796		822.40	1140.90	↓
142	40.396	-3.57	687.40	1009.90	330.07
143	40.896	↓	699.90	1022.40	↓
144	41.396	↓	712.40	1034.90	↓
145	41.796		722.40	1044.90	↓
146	41.996	-3.57	727.40	1049.90	330.07
147	42.196	↓	732.40	1054.90	↓
148	40.646	-1.80	693.65	1016.15	344.91
149	40.996	-2.15	702.40	1024.90	341.98
150	41.346	-2.50	711.15	1033.65	339.04
151	41.696	-2.86	719.90	1042.40	336.02
152	41.996	-3.14	727.40	1049.90	333.68
153	42.126	-3.28	730.65	1053.15	332.50
154	42.266	-3.42	734.15	1056.65	331.33
155	42.396	-2.06	737.40	1059.90	342.73
156	42.396	-2.57	737.40	1059.90	338.45
157	↓	-2.97	↓	↓	335.10
158	↓	-3.17	↓	↓	333.42
159	42.896	↓	749.90	1072.40	↓
160	42.646	-3.23	743.65	1066.15	332.92
161	42.396	-3.37	737.40	1059.90	331.75
162	↓	-3.77	↓	↓	328.39
163	↓	-4.07	↓	↓	325.88
164	↓	-4.35	↓	↓	323.53
165	↓	-4.69	↓	↓	320.68

* X = X_T-322.5 Equivalent Full Scale Axial Distance

TABLE 3.5
T/C LOCATION TABLE
REGION E (Cont.)

T/C	STA No.	B. P.	X (Inches)*	X_T (Inches)	Θ (Deg.)
166	42.896	-3.97	749.90	1072.40	326.72
167	43.296	-3.25	759.90	1082.40	332.75
168	43.696	-3.32	769.90	1092.40	332.17
169	44.046	-2.97	778.65	1101.15	335.10
170	44.396	-2.62	787.40	1109.90	338.03
171	44.756	-2.27	796.40	1118.90	340.97
172	45.196	-2.47	807.40	1129.90	339.29
173	↓	-2.97	↓	↓	335.10
174		-3.47			330.91
175		-3.97			326.72
176		-4.47			322.53

* $X = X_T - 322.5$ Equivalent Full Scale Axial Distance

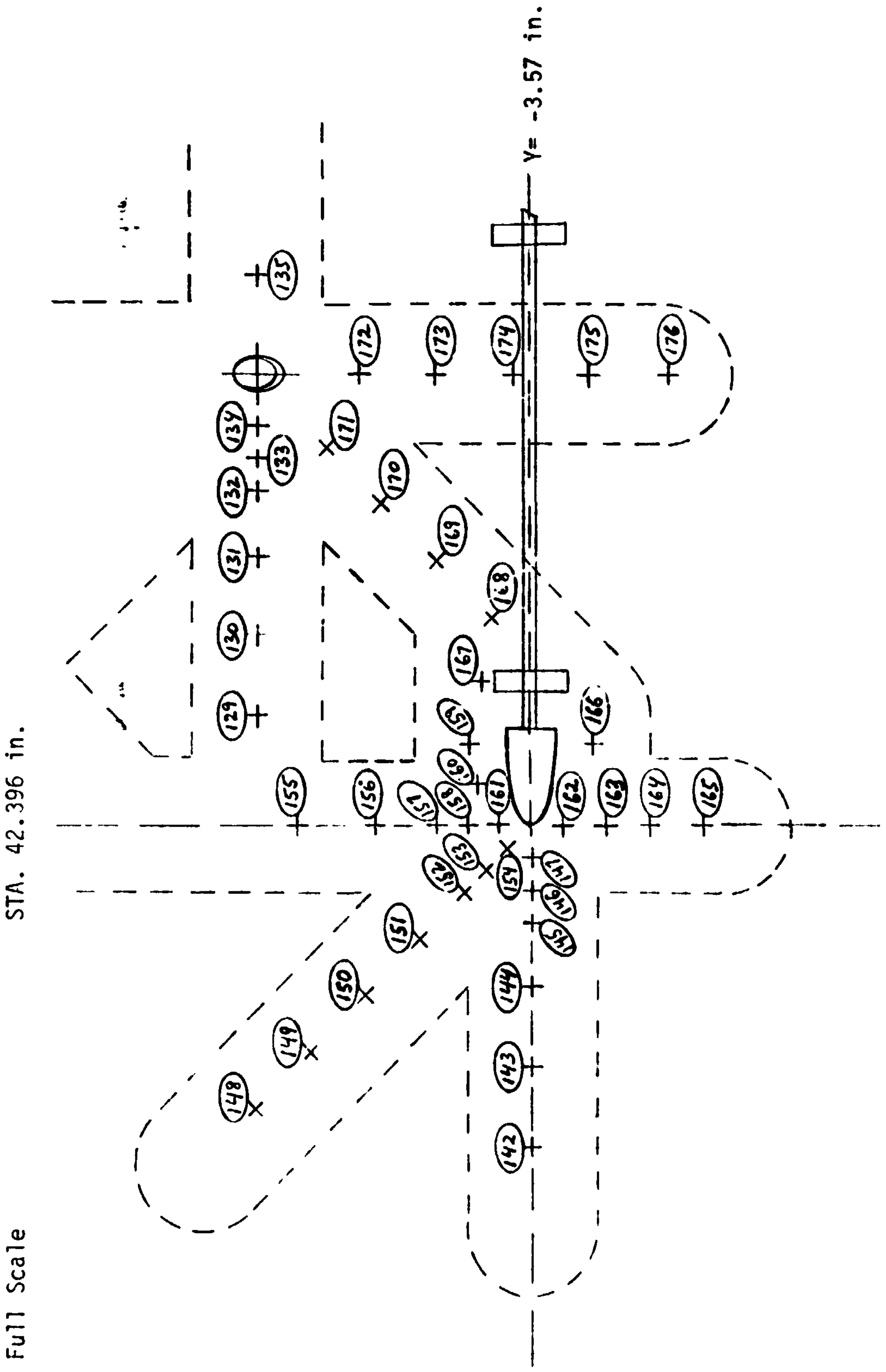

Fig. 3.30 Region E Skin Thermocouple Locations

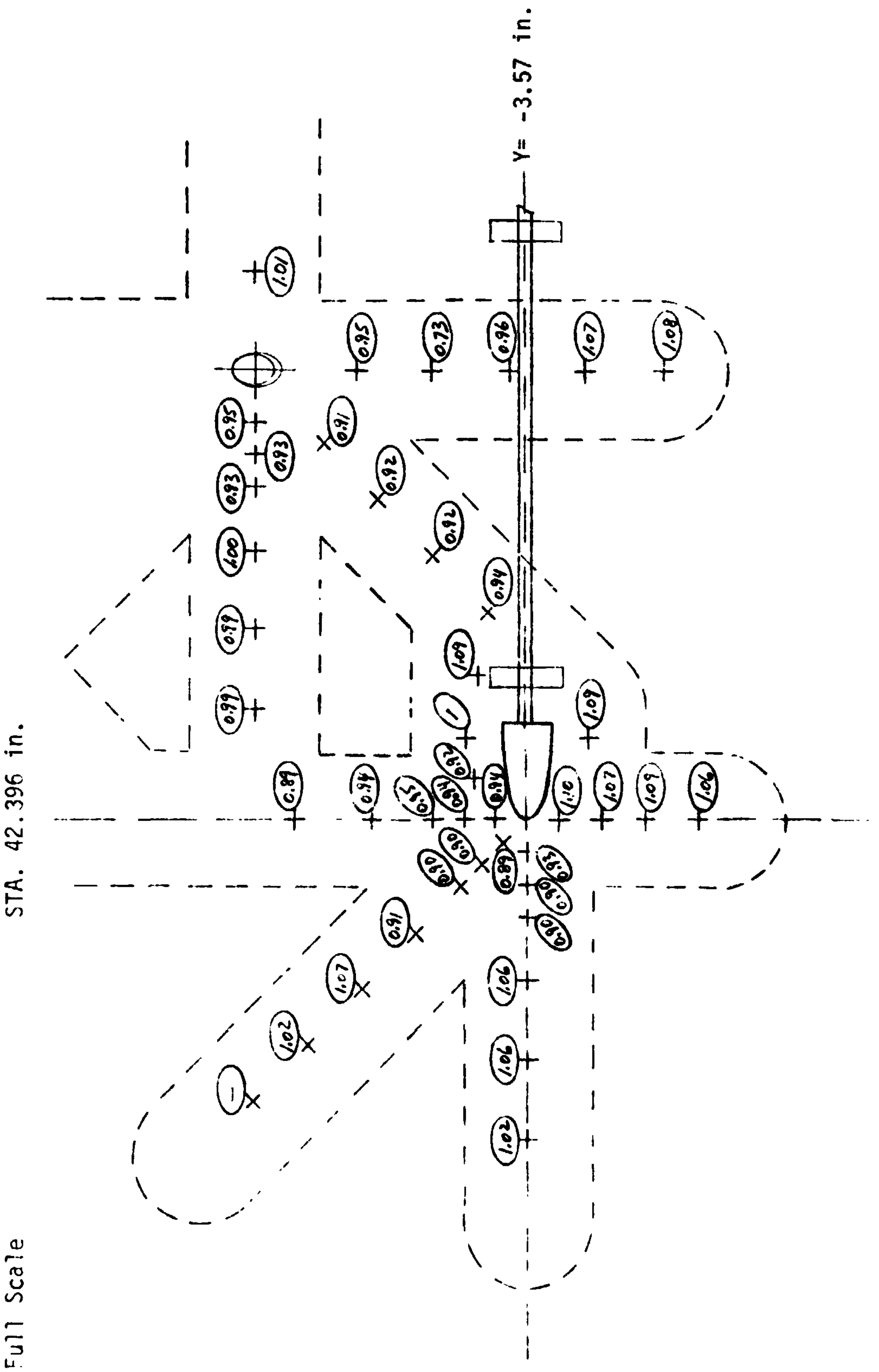

Fig. 3.31 Region E Clean Skin Factors (Flat Plate, B Config.)

Full Scale

STA. 42.396 in.

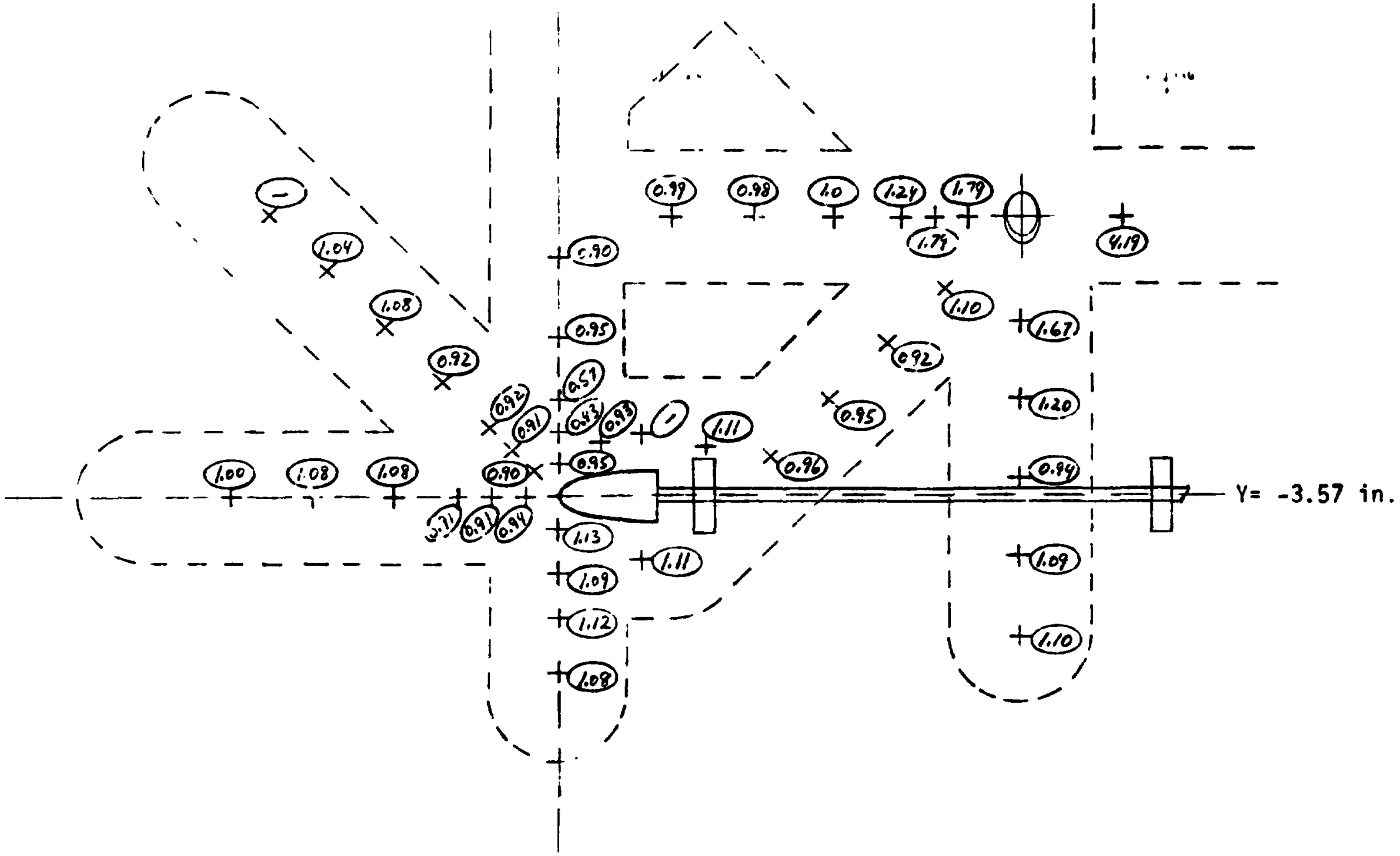

Fig. 3.32 Region E Orbiter Interference Factors (B Config.)

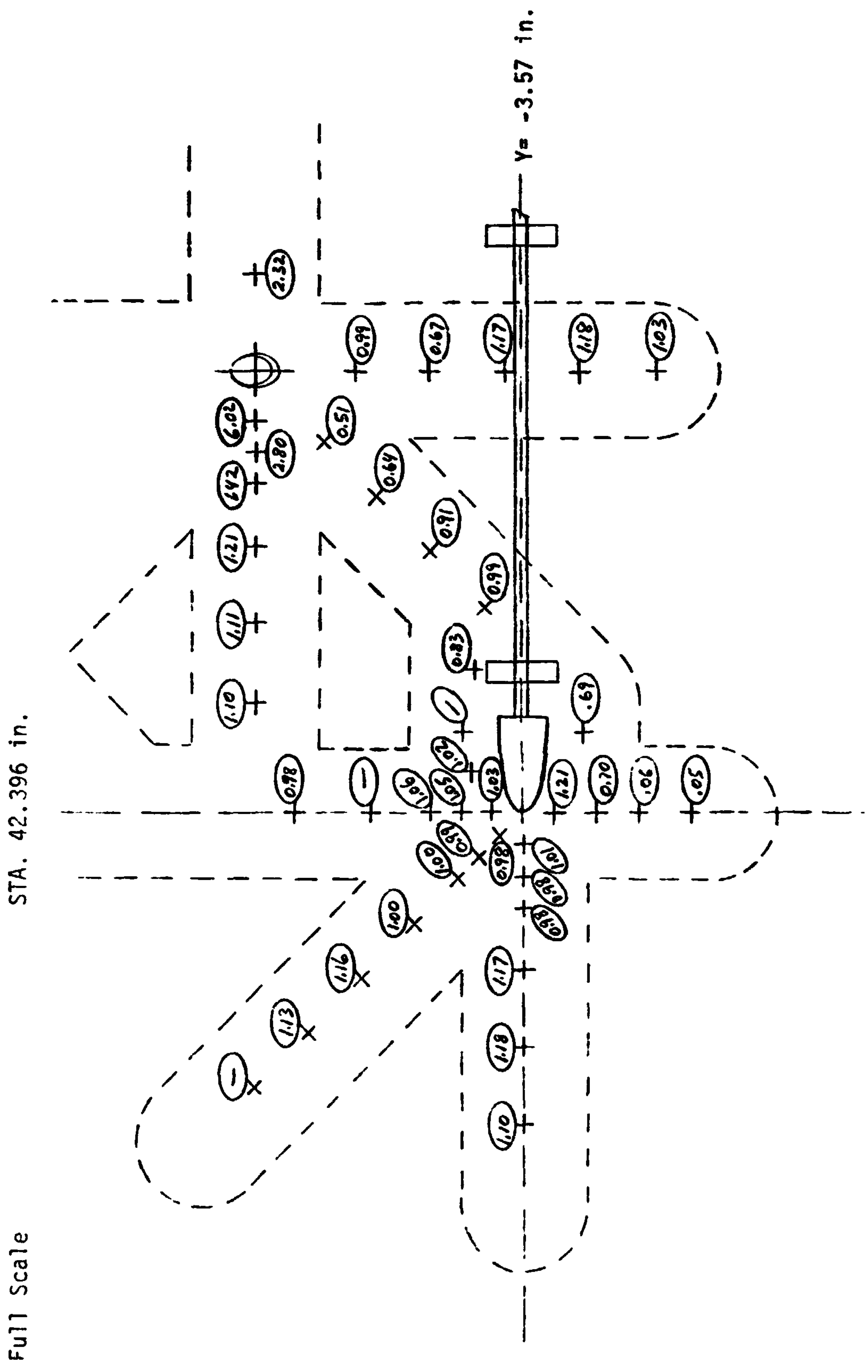

Fig. 3.33 Region E Tiedown Interference Factors (B Config.)

J.5

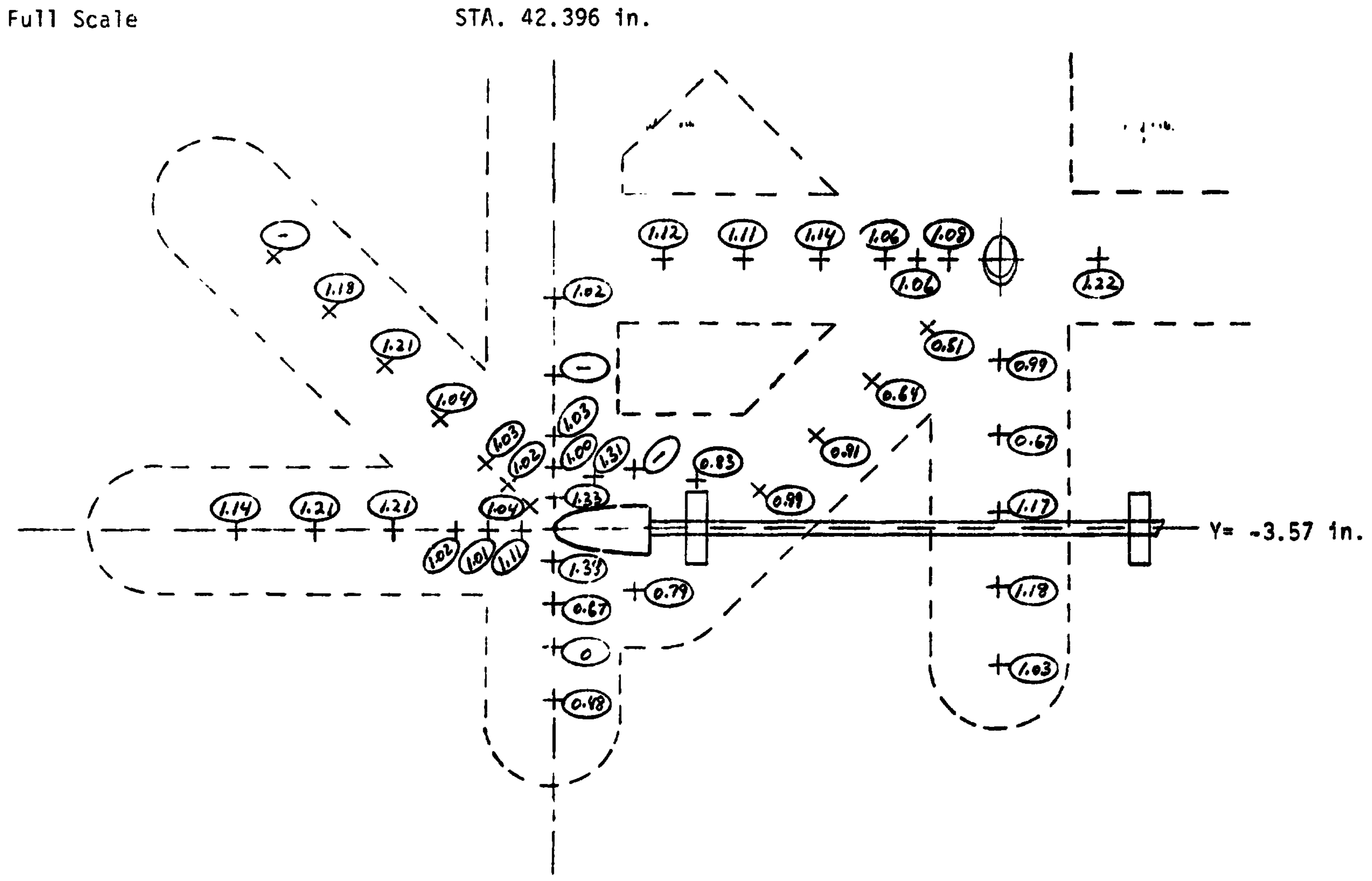

Fig. 3.34 Region E Tunnel Interference Factors (B Config.)

Full Scale

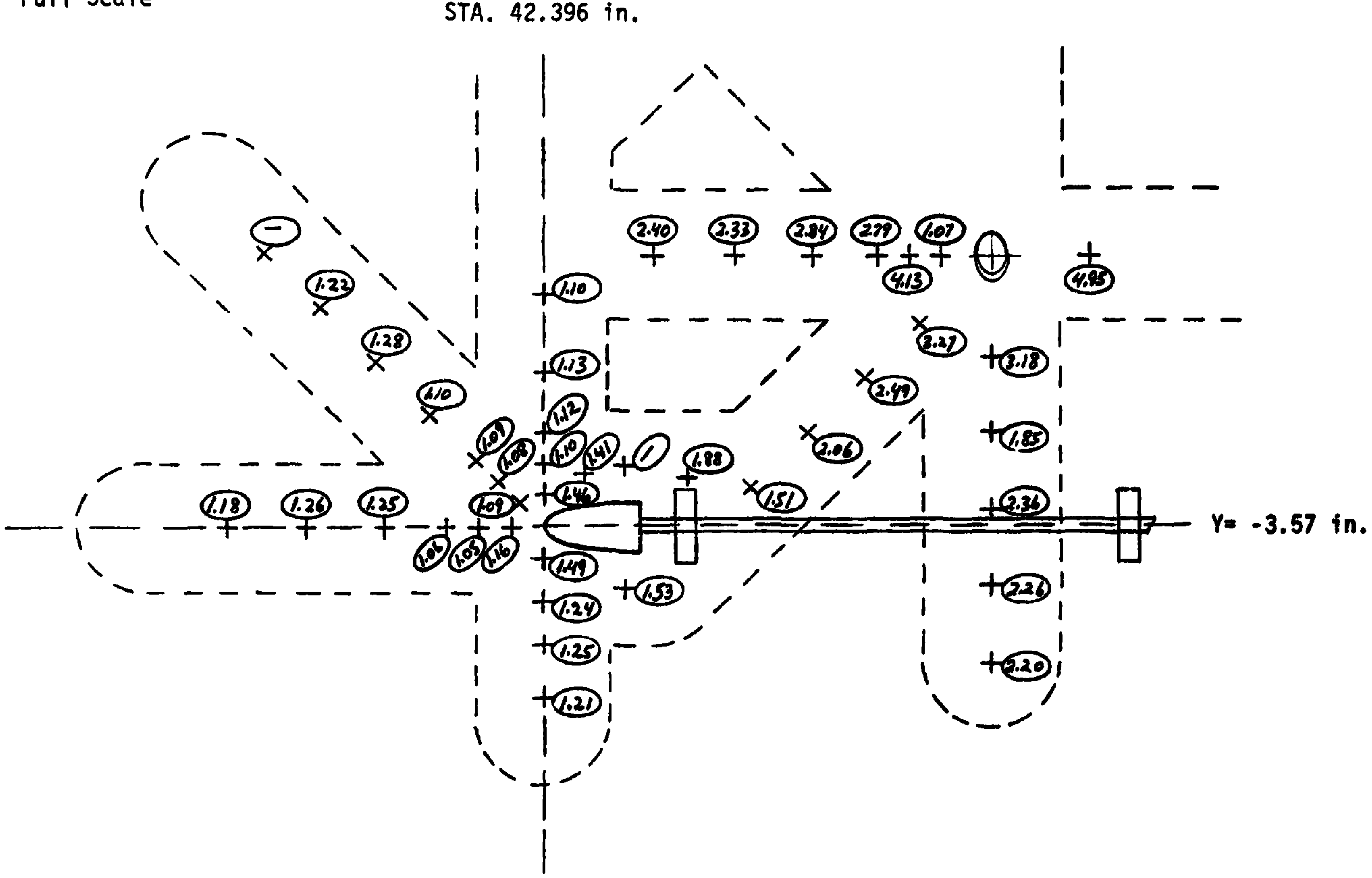

Fig. 3.35 Region E Total Interference Factors, Orbiter, Tiedown and Tunnels (B Config.)

T/C LOCATION TABLE
REGION F

T/C #	STA No.	B. P.	X (Inches)*	X_T (Inches)	Θ (Deg.)
135	45.796	-1.80	822.4	1144.9	344.91
136	46.796	↓	847.4	1169.9	↓
137	47.796	↓	872.4	1194.9	↓
138	49.796	↓	922.4	1244.9	↓
139	51.796	↓	972.4	1294.9	↓
177	47.886	-3.15	874.6	1197.2	333.59
178	↓	-3.37	↓	↓	331.75
179	↓	-3.82	↓	↓	327.97
180	↓	-4.02	↓	↓	326.30
181	48.236	-3.15	883.4	1205.9	333.59
182	↓	-4.02	↓	↓	326.30
183	47.586	-3.15	867.2	1189.6	333.59
184	↓	-3.35	↓	↓	331.92
185	↓	-3.83	↓		327.89
186	47.586	-4.02	867.2	1189.6	326.30
187	49.196	-2.43	907.4	1229.9	339.63
188	↓	-2.93	↓	↓	335.44
189	↓	-3.33	↓	↓	332.08
190	↓	-3.83	↓	↓	327.89
191	49.196	-4.23	907.4	1229.9	324.54
192	↓	-4.73	↓	↓	320.35

* $X = X_T - 322.5$ Equivalent Full Scale Axial Distance

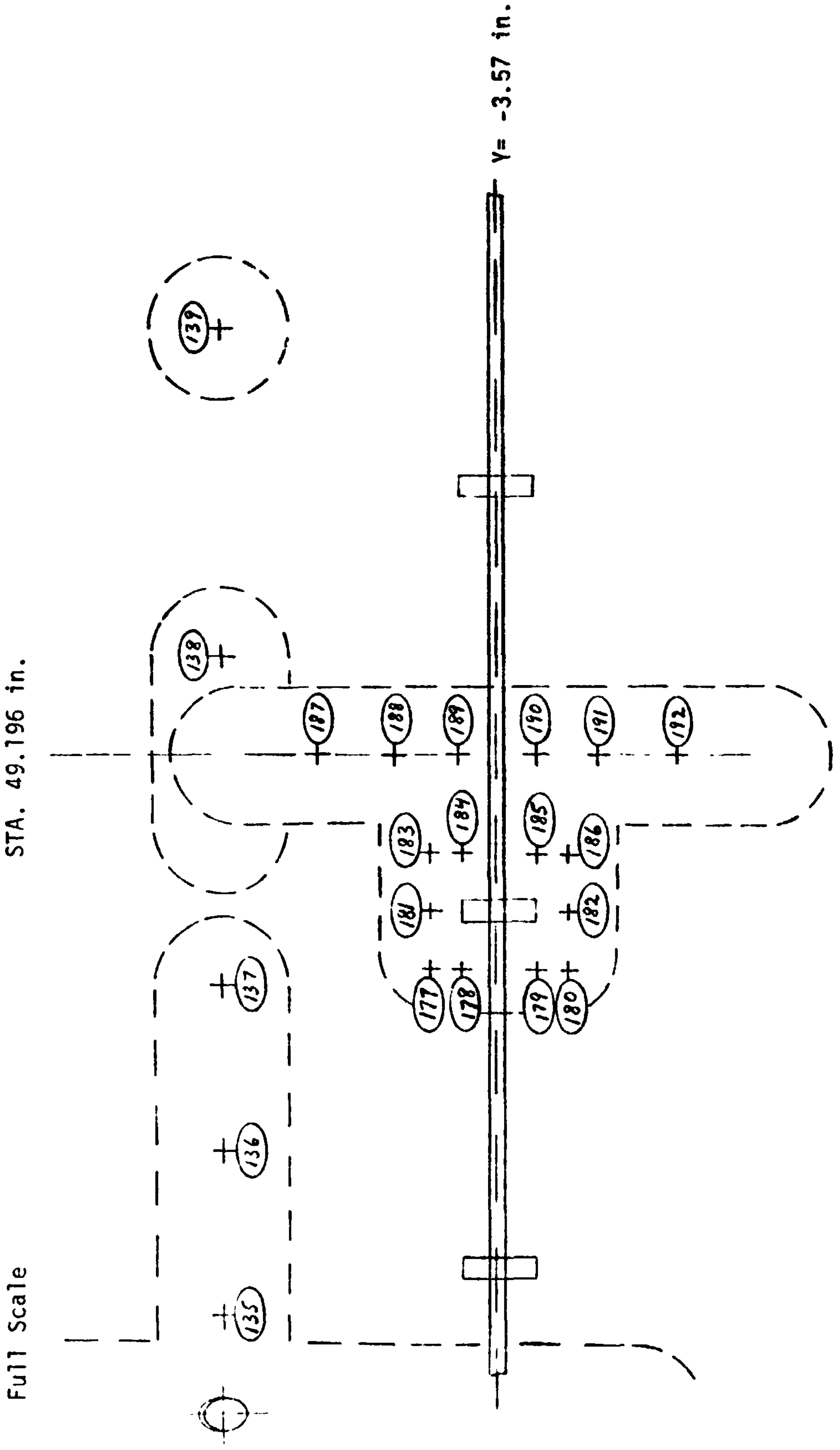

Fig. 3.36 Region F Skin Thermocouple Locations

Full Scale

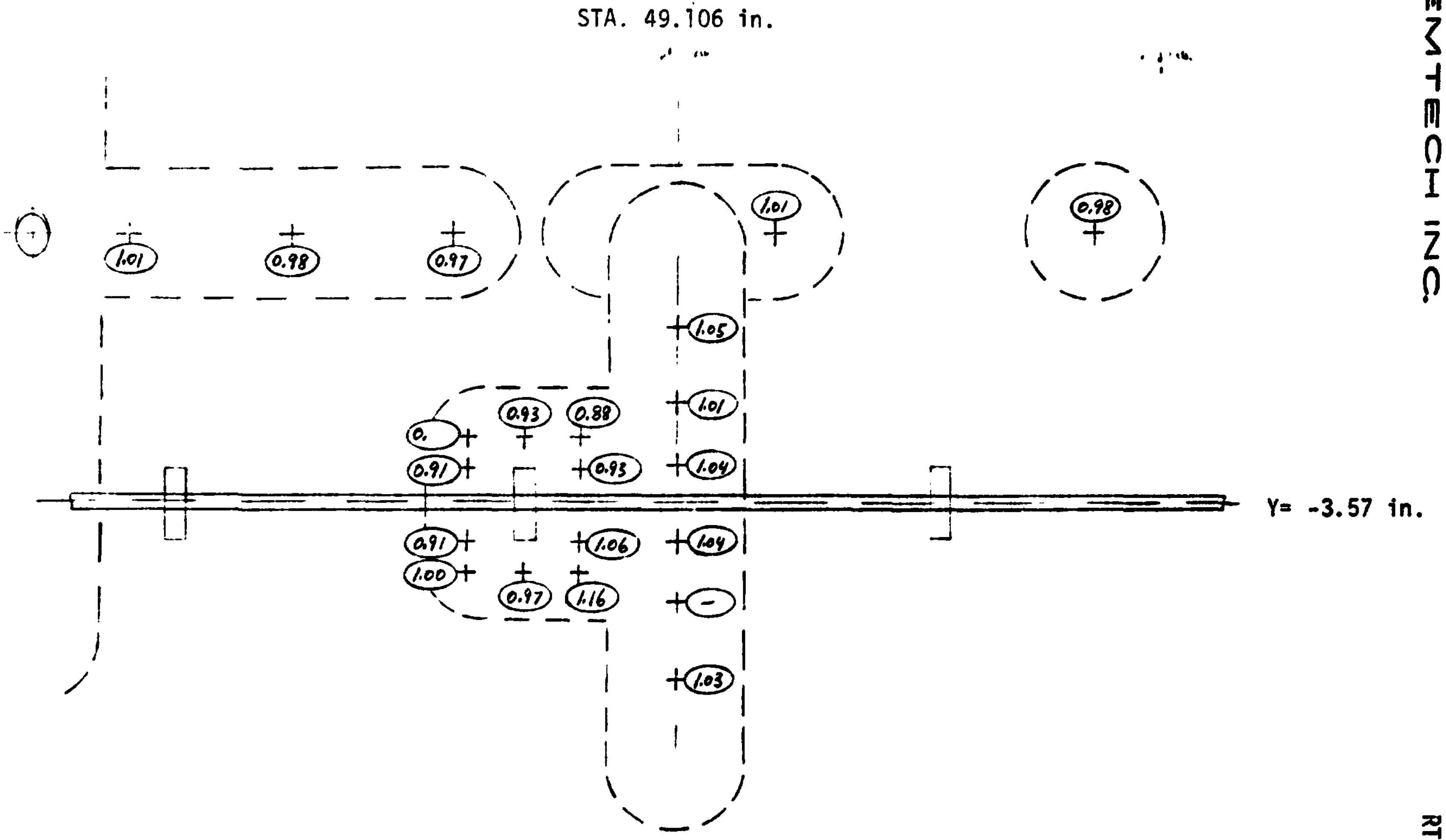

Fig. 3.37 Region F Clean Skin Factors (Flat Plate, B Config.)

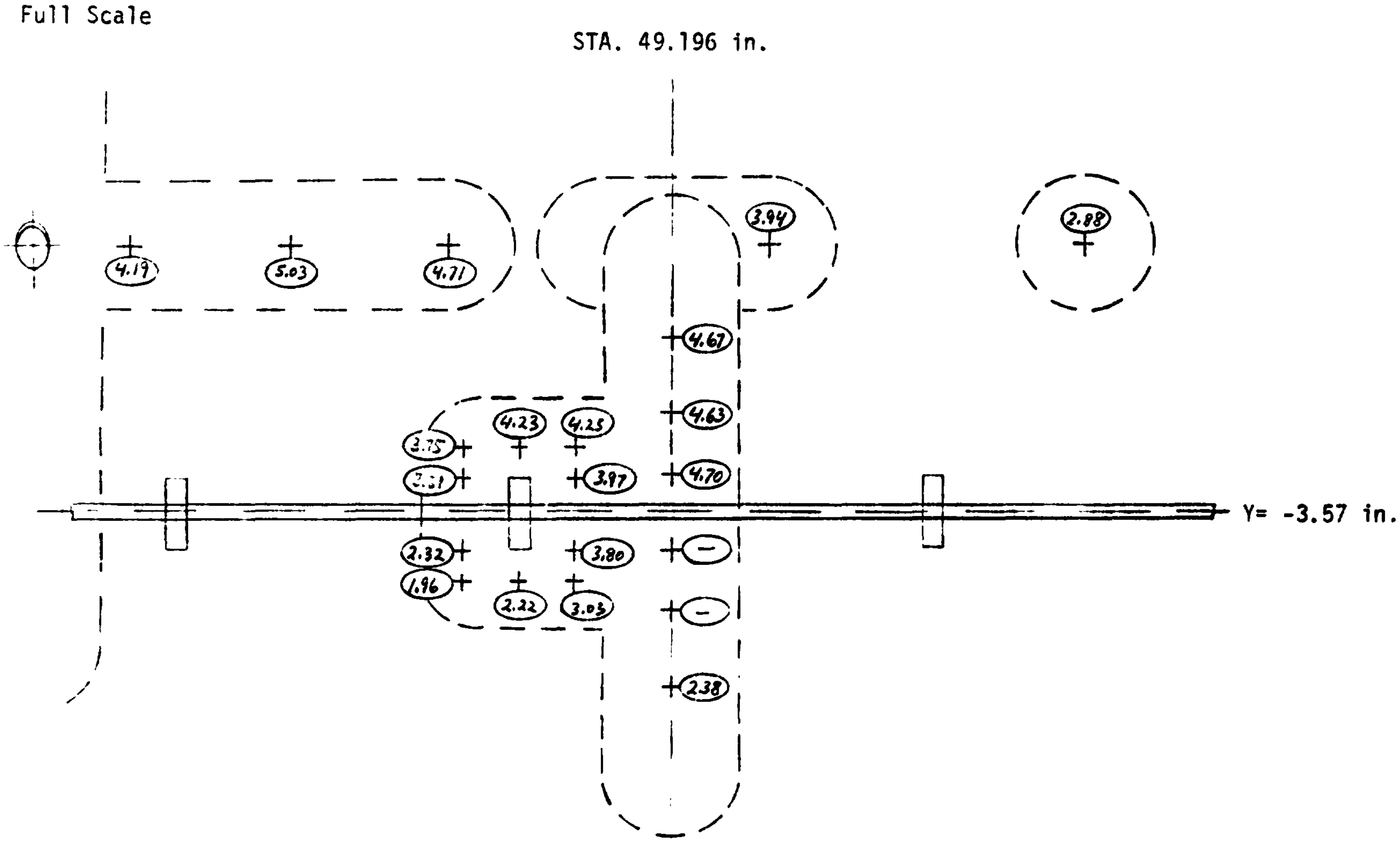

Fig. 3.38 Region F Orbiter Interference Factors (B Config.)

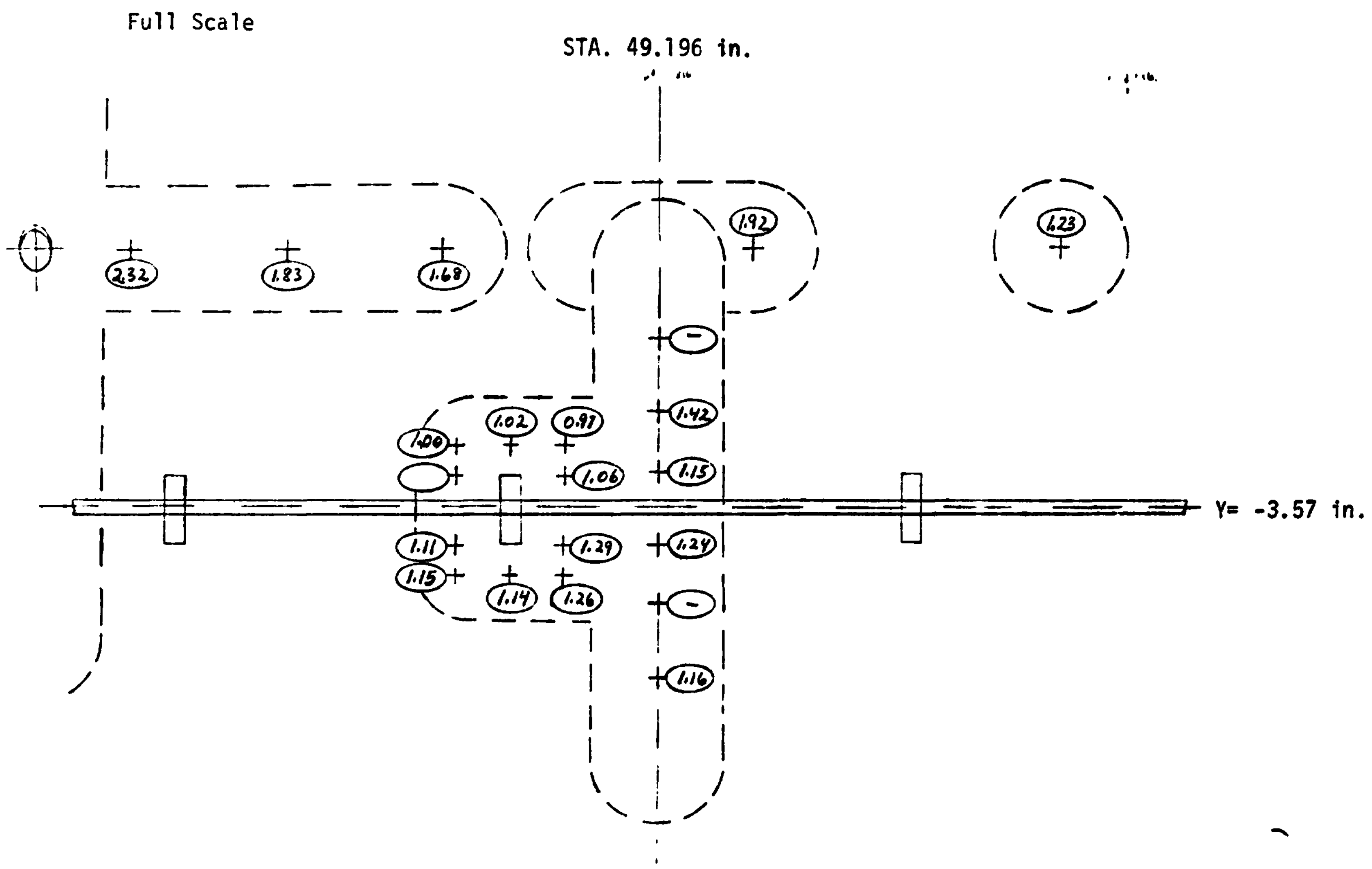

Fig. 3.39 Region F Tiedown Interference Factors (B Config.)

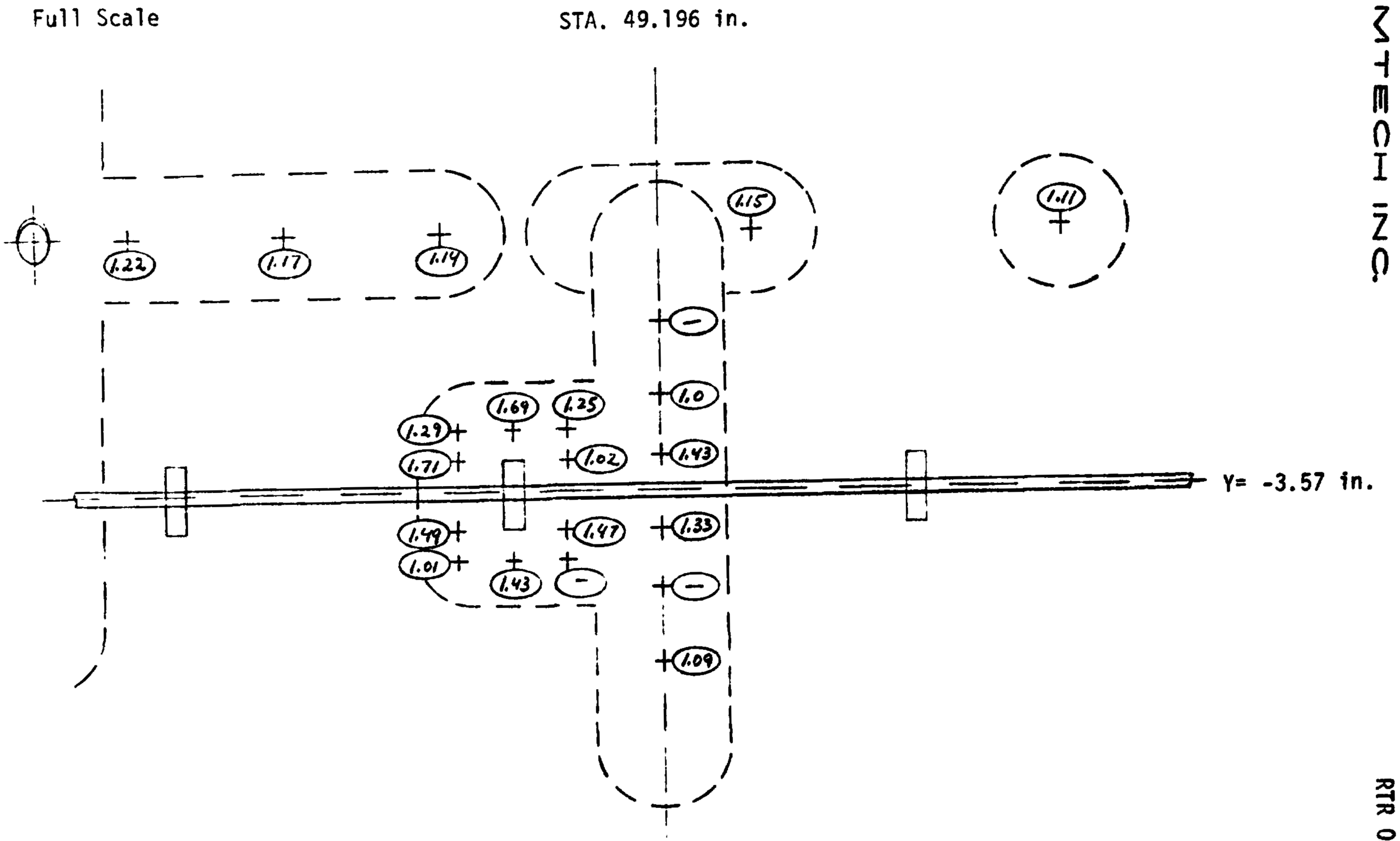

Fig. 3.40 Region F Tunnel Interference Factors (B Config.)

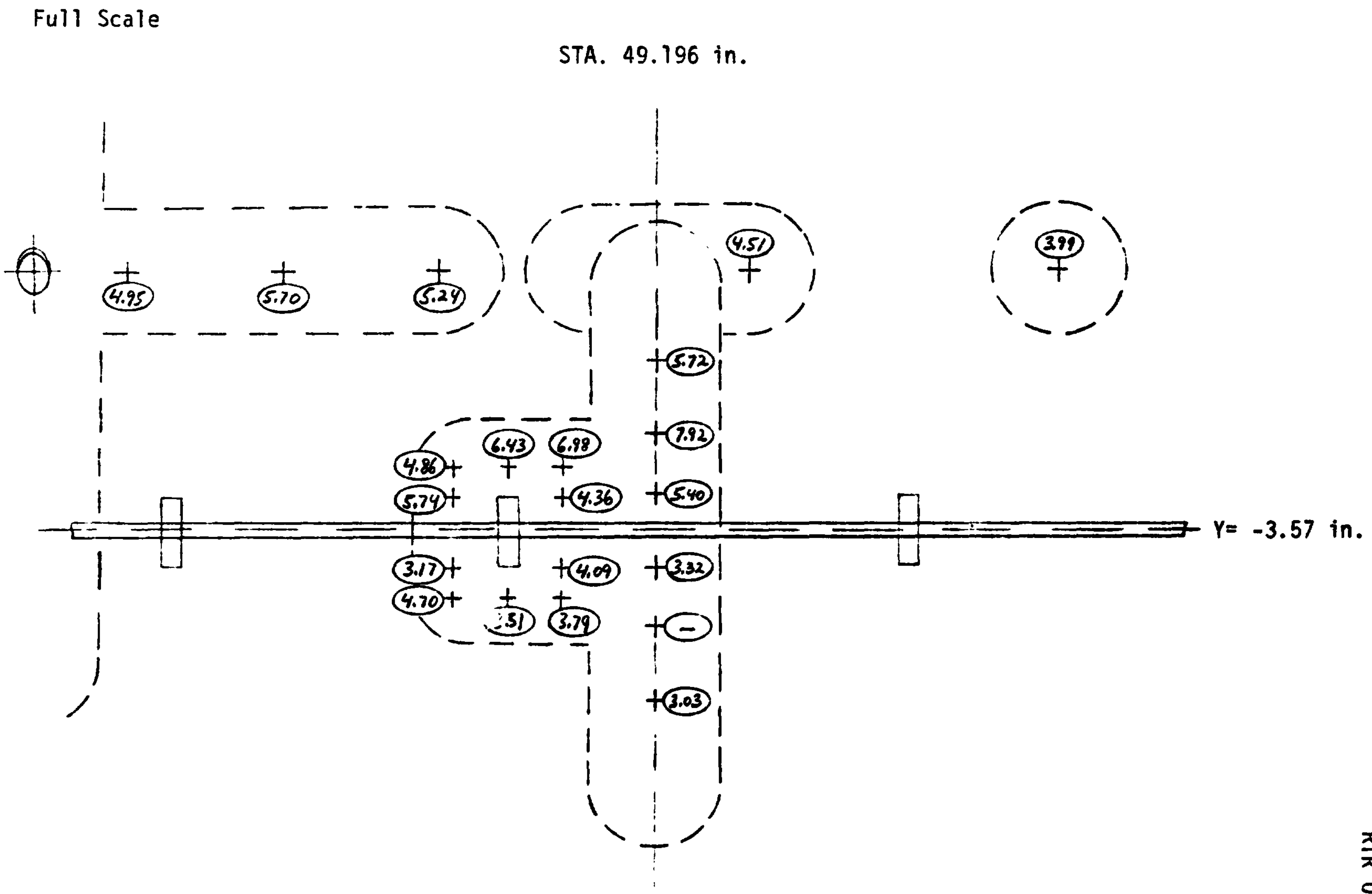

Fig. 3.41 Region F Total Interference Factors, Orbiter, Tiedown and Tunnels (B Config.)

TABLE 3.7
T/C LOCATION TABLE
REGION G

T/C	STA No.	B. P.	X (Inches)*	X_T (Inches)	(Deg.)
140	53.796	-1.80	1022.40	1344.90	344.90
141	55.796	-1.80	1072.40	1394.90	344.90
193	49.196	-2.43	907.40	1229.90	339.60
194	↓	-2.93	↓	↓	335.44
195	49.196	-3.33	907.40	1229.90	332.10
196	↓	-3.77	↓	↓	328.40
197		-4.17			325.00
198		-4.67			320.85

* $X = X_T - 322.5$ Equivalent Full Scale Axial Distance

Full Scale

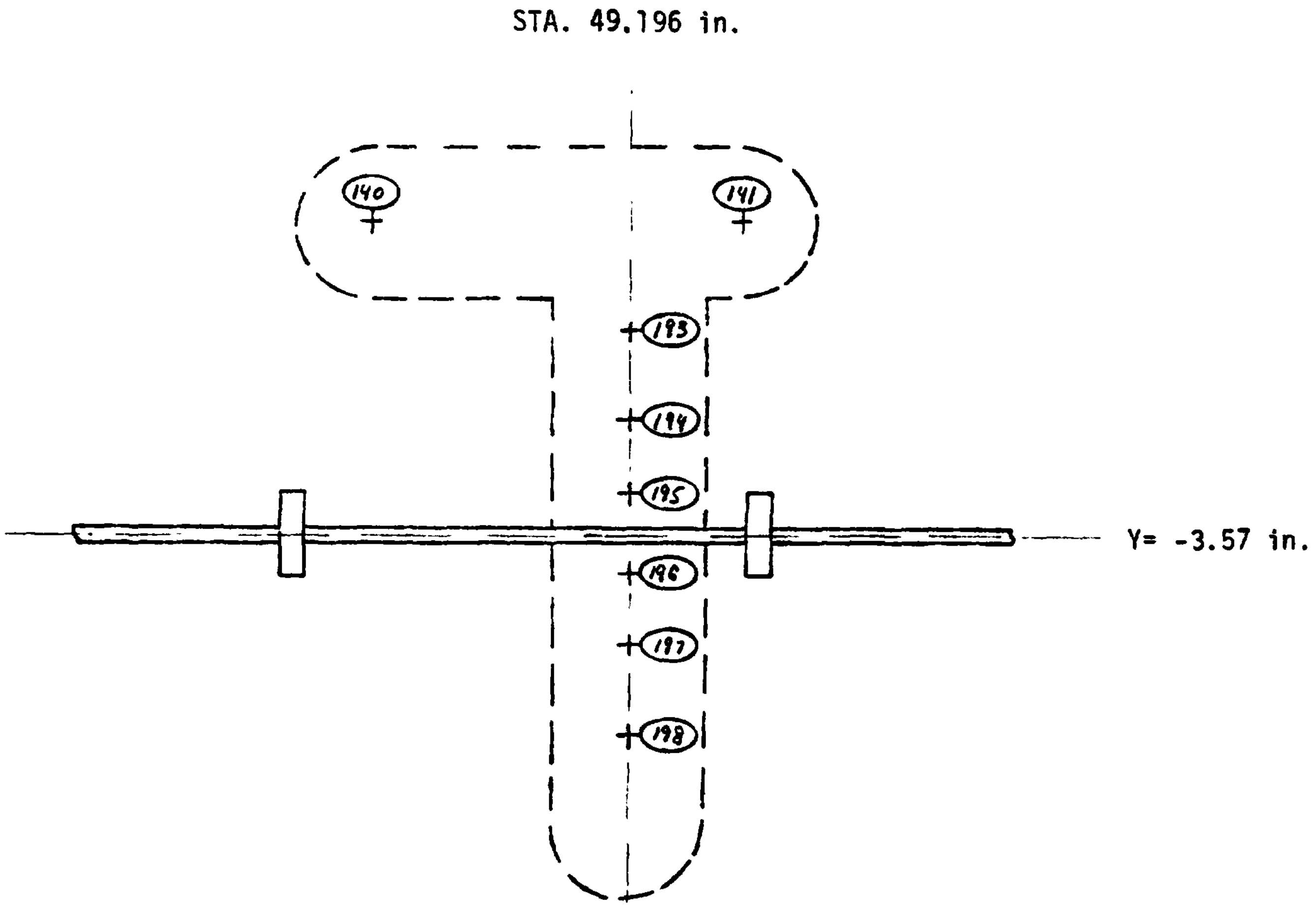

Fig. 3.42 Region G Skin Thermocouple Locations

Full Scale

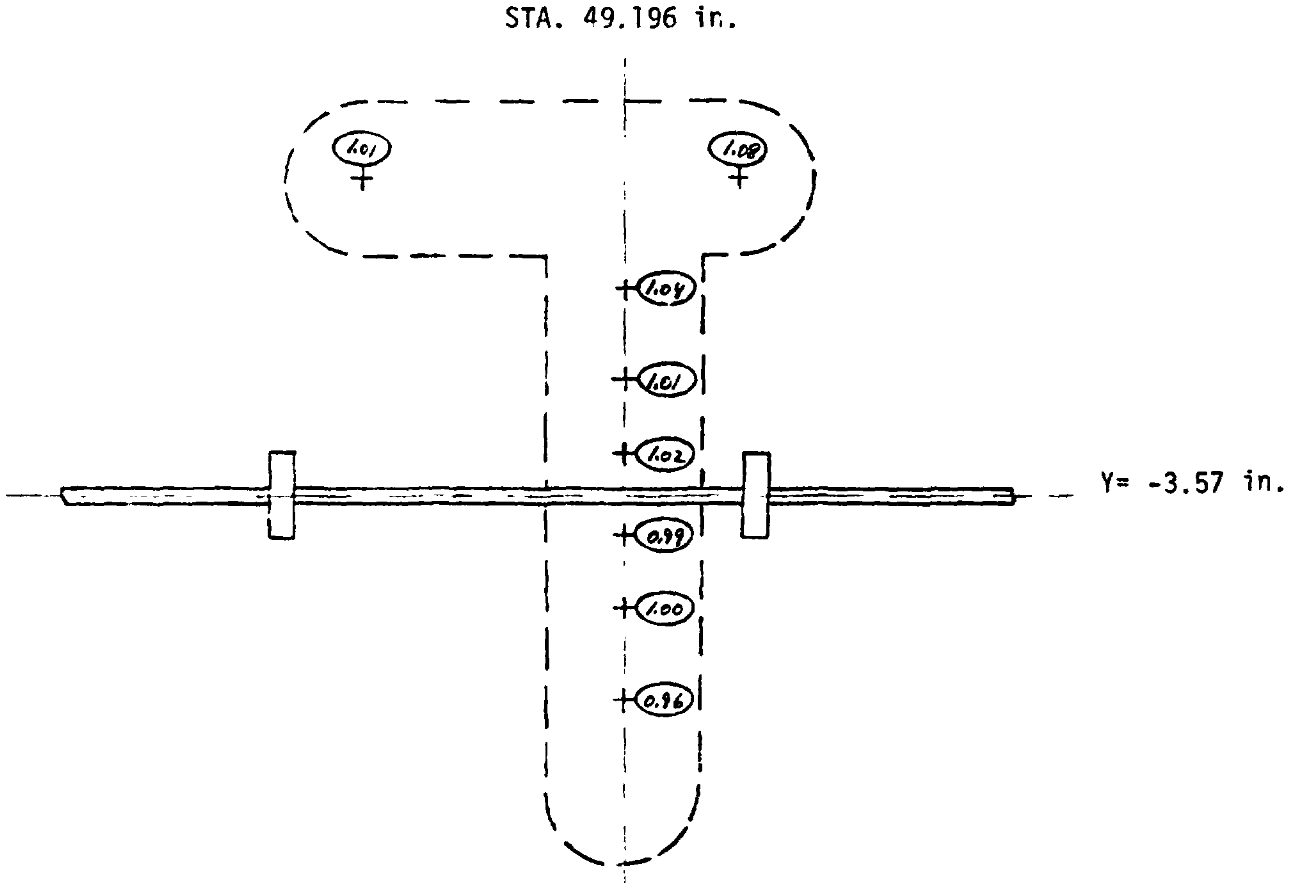

Fig. 3.43 Region G Clean Skin Factors (Flat Plate, B Ccnfig.)

Full Scale

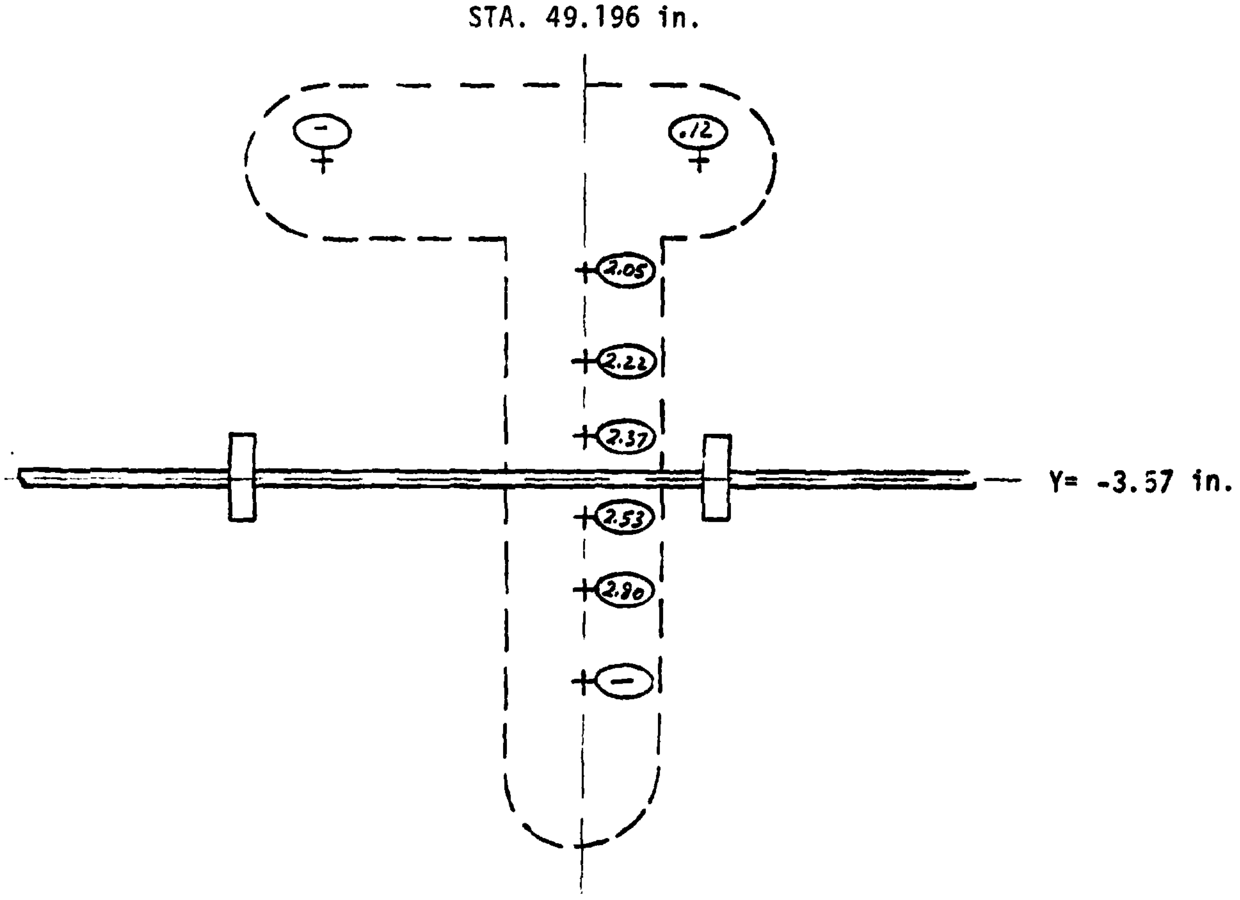

Fig. 3.44 Region G Orbiter Interference Factors (B Config.)

Full Scale

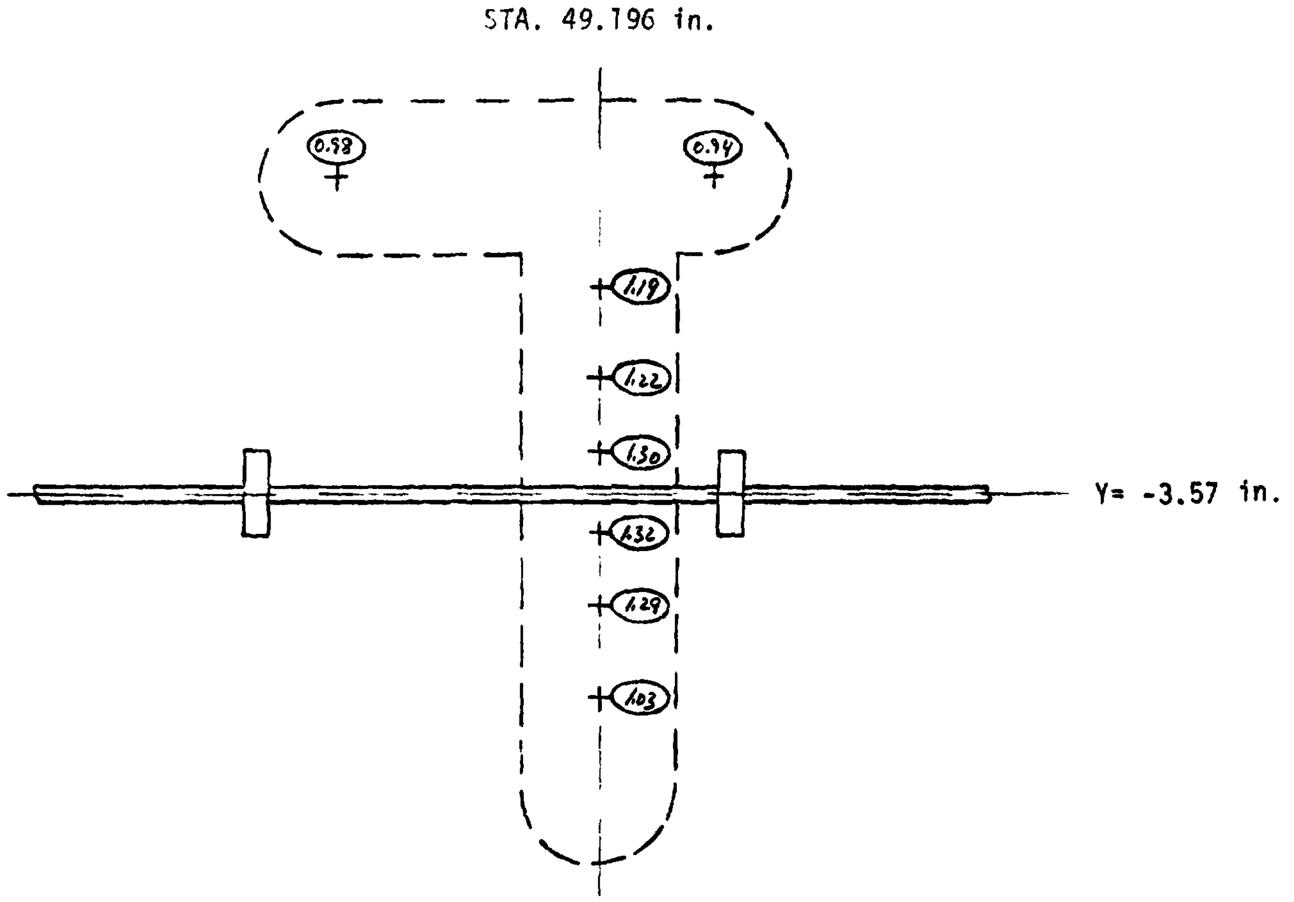

Fig. 3.45 Region G Tiedown Interference Factors (B Config.)

Full Scale

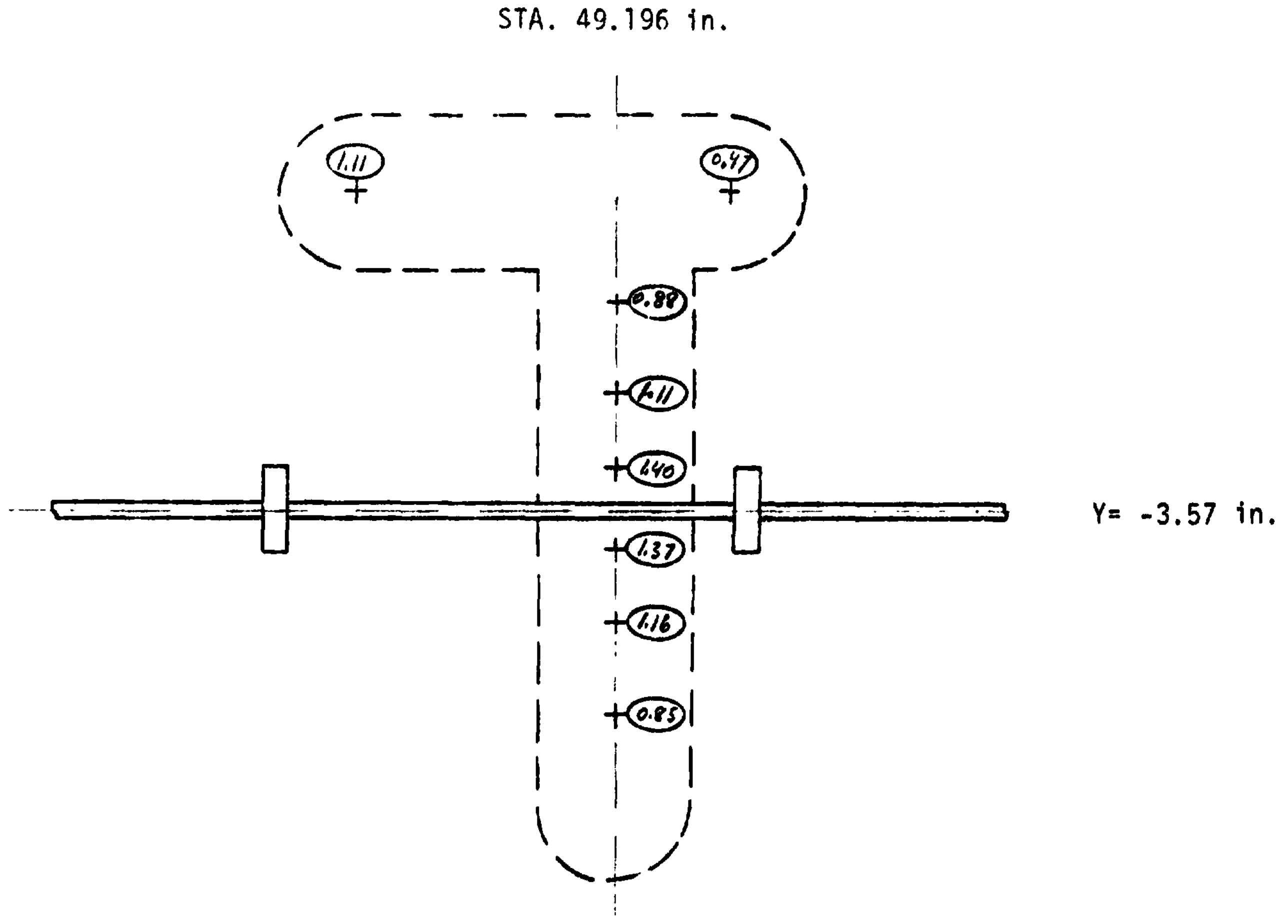

Fig. 3.46 Region G Tunnel Interference Factors (B Config.)

Full scale

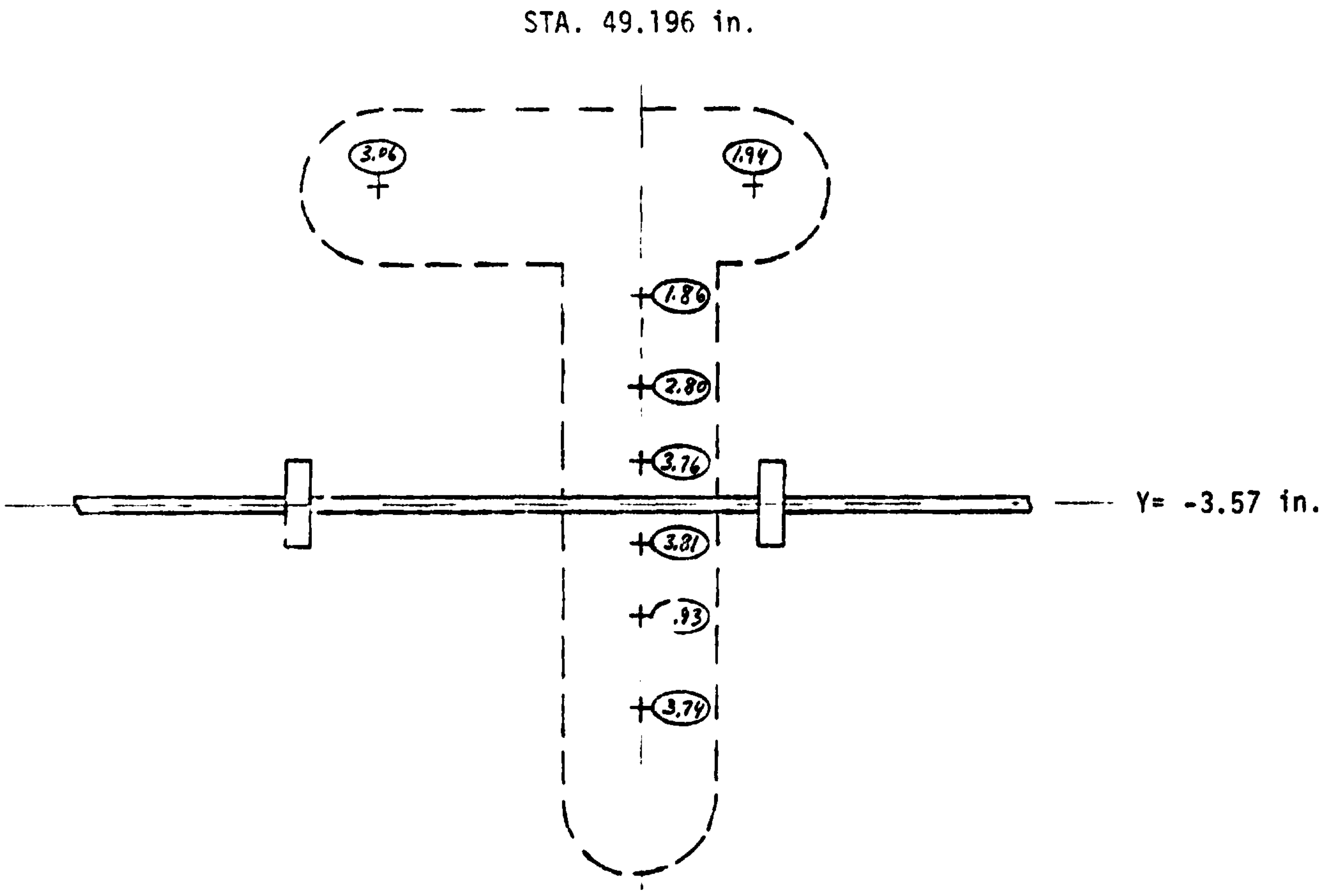

Fig. 3.47 Region G Total Interference Factors, Orbiter, Tiedown and Tunnels (B Config.)

TABLE 3.8

INTERFERENCE FACTORS ON PROTUBERANCES

				A Config.	B Config.			
	T/C	Station	X_T	Total	Orbiter	Tiedown	Tunnel	Total
LO_2 Feedline Fairing	1	39.457	986.42	13.34	1.0	1.0	8.32	9.30
	2	39.605	990.12	18.28	↓	↓	14.67	15.56
	3	39.910	997.75	10.89	↓	↓	10.81	11.32
	4	40.280	1007.00	5.07	↓	↓	5.64	6.05
	5	40.670	1016.75	2.08	↓	↓	2.29	2.44
	6	41.080	1027.00	.88	↓	↓	1.00	1.05
	7	39.580	989.50	3.04	1.11	↓	2.47	2.58
	8	39.770	994.25	2.30	1.12	↓	1.88	1.98
	9	40.145	1003.62	1.63	1.14	↓	1.38	1.56
	10	40.545	1013.62	1.05	1.10	↓	0.95	0.99
	11	40.945	1023.62	0.98	1.02	↓	0.80	0.82
	12	39.580	989.50	3.33	1.11	↓	3.02	3.15
	13	39.770	994.25	3.37	1.12	↓	3.15	3.30
	14	40.145	1003.62	2.88	1.14	↓	3.21	2.51
	15	40.545	1013.62	2.33	1.10	↓	1.71	1.81
	16	40.945	1023.62	----	1.01	↓	----	2.40
	17	44.821	1120.52	2.40	.829	.926	2.25	2.39
	18	44.821	1120.52	4.17	.838	.920	1.43	----
	19	44.821	1120.52	5.40	.860	.997	3.28	5.32
	20	44.821	1120.52	1.47	.838	.920	2.11	1.40
	21	4[illegible].116	1127.90	2.29	.829	.926	3.64	2.50
	22	49.196	1229.90	2.05	4.44	1.08	0.85	2.12
	23	49.196	1229.90	5.86	4.46	1.46	1.40	6.94
	24	49.196	1229.90	---	4.35	1.85	----	----
	25	49.196	1229.90	2.40	4.46	1.46	0.64	2.66
	26	54.726	1368.15	4.83	2.25	1.24	1.52	5.23
	27	54.726	1368.15	3.64	2.17	1.28	1.21	3.82
	28	54.726	1368.15	6.30	2.07	1.22	2.08	6.86
	29	54.726	1368.15	8.89	2.17	1.28	1.82	8.71
	30	55.00	1375.00	9.15	2.25	1.24	1.23	8.02

TABLE 3.8 (Cont.)

INTERFERENCE FACTOTS ON PROTUBERANCES

	T/C	Station	X_T	A Config. Total	B Config.			
					Orbiter	Tiedown	Tunnel	Total
LO_2 Antigeyser Line Fairing	31	39.61	990.25	9.87	1.0	1.0	8.22	8.27
	32	39.77	994.25	8.34	↓	↓	7.40	7.59
	33	40.12	1003.00	4.29	↓	↓	4.32	4.42
	34	40.55	1013.83	1.96	↓	↓	2.17	2.22
	35	40.93	1023.25	1.88	↓	↓	1.90	1.94
	36	41.34	1033.38	2.08	↓	↓	2.00	2.11
	37	39.78	994.50	3.40	↓	↓	3.42	3.27
	38	40.02	1000.50	2.94	↓	↓	2.93	3.07
	39	40.42	1010.50	3.10	↓	↓	3.06	3.23
	40	40.82	1020.50	----	↓	↓	----	----
	41	41.22	1030.50	1.98	↓	↓	1.86	1.99
	42	39.78	994.50	5.07	↓	↓	3.92	4.16
	43	40.02	1000.50	2.76	↓	↓	2.27	2.43
	44	40.42	1010.50	----	↓	↓	1.15	1.34
	45	40.82	1020.50	1.02	↓	↓	0.86	0.93
	46	42.92	1072.90	2.01	0.85	0.94	1.89	2.18
	47	42.92	1072.90	1.51	0.85	0.94	2.01	1.53
	48	53.05	1326.15	5.40	3.93	1.45	1.57	6.08
	49	53.05	1326.15	7.79	3.93	1.45	1.32	9.38
	50	55.82	1395.40	3.67	2.35	1.28	1.64	4.03
	51	55.82	1395.40	5.13	2.35	1.28	1.12	5.36
Electrical Conduit	52	42.960	1074.00	3.91	1.02	1.0	3.56	3.63
	53	52.846	1321.15	4.71	3.82	1.18	1.47	5.17
	54	52.846	1321.15	5.56	3.82	1.81	1.16	6.12
	55	53.046	1326.15	4.95	3.63	1.07	1.50	5.47
	56	53.046	1326.15	4.95	3.63	1.07	1.50	5.47
	57	55.816	1395.40	3.77	2.62	1.22	1.64	4.82
	58	55.816	1395.40	----	2.62	1.22	1.02	4.02
GH_2 Pressure Line Fairing	59	42.654	1066.35	----	1.0	1.0	2.98	2.53
	60	42.809	1070.22	----	1.0	1.0	2.98	3.11

3.3 Comparison of Additive and Multiplicative Methods

One of the objectives of the IH-51A test was to provide the data to determine what combination methods could be used to predict the total interference factor. The two methods hypothesized prior to the test were the additive and multiplicative methods. The additive method can be stated as

$$(h_i/h_u)_{total} = \underbrace{(h_i/h_u)_{prox}}_{\substack{\text{Proximity}\\ \text{Alone}}} + \underbrace{(h_i/h_u)_{prot}}_{\substack{\text{Protuberance}\\ \text{Alone}}} - 1$$

and the multiplicative method can be stated as

$$(h_i/h_u)_{total} = (h_i/h_u)_{prox} \times (h_i/h_u)_{prot}$$

These methods are compared with data on the protuberances and on the skin in this section. The data presented in Section 3.2 particularly Table 3.8, are used to make these comparisons.

The heating amplification due to the orbiter, tiedown and tunnels both separately and in total is shown in Fig. 3.42 for the centerline. The tunnels have negligible effect on the heating along the skin centerline. The effect of the tiedown and orbiter produce about the same magnitude amplification. The combined effect of tiedown and orbiter is significantly larger than for each component. A comparison of additive and multiplicative methods is shown in Fig. 3.43 for the data shown in Fig. 3.42. The data below the line of perfect agreement corresponds to an underprediction for that data point. The correlation using both methods is poor and over half of the data is underpredicted by each method. For a few points the multiplicative method substantially overpredicts.

Data were analyzed for three stations along the LO_2 feedline. The data are shown in three parts in Figs. 3.44, 3.45 and 3.46. Figure 3.44 presents the total interference factors for the LO_2 feedline and skin points below the line. The data at stations 44.8 and 54.7 are slightly upstream of the brackets (See Fig. 3.3). The filled in square is an exception which is for a thermocouple next to the bracket on the LO_2 line. The data show high amplification factors at station 54.7 where the bottom of the line and skin experience more heating than the top of the feedline. Figure 3.45 shows the separate effects of the orbiter and tunnels on the heating amplification for the tunnel. Note, proximity effects are measured on the skin, Fig. 3.46, whereas the final influence to be determined is on the protuberance above the skin. Figure 3.45 presents the separate effects on heating amplification for the skin below the tunnel. Note there is a definite effect of the tiedown on the skin data for the last two stations. This is most probably due to a vortex sheet and higher pressure region produced by the tiedown.

A comparison of the predictive methods and the measured results are given in Fig. 3.47 for the LO_2 feedline points. The proximity effect of the orbiter and the protuberance effects of the tunnel and tiedown were included. Both additive and multiplicative methods seriously underpredicted most of the data.

A comparison of the predictive methods and data for the skin below the LO_2 line is given in Fig. 3.48. The data which is significantly underpredicted is for the last station in front of the bracket.

The LO_2 feedline axial distribution of heating amplification is shown in Figs. 3.49, 3.50 and 3.51. The top centerline distribution is shown in Fig. 3.49. The heating amplification on the fairing is quite high and no significant proximity effect of the orbiter or other protuberances is evident. The inboard and outboard axial distributions on the LO_2 feedline are shown in Figs. 3.50 and 3.51 respectively. The heating amplification appears symmetrical on the fairing and substantially lower than for the top centerline.

Figure 3.52 presents the heating amplification data on the centerline of the antigeyser line. The heating on the bottom of the line is surprisingly high. The comparison of the additive and multiplicative methods for the top and bottom of the antigeyser line are shown in Figs. 3.53 and 3.54 respectively. Both methods underpredict for high amplification factors on the bottom of the line.

A schematic of the cable tray along with tabulated interference factors are given in Fig. 3.55. The orbiter produces the greatest influence on the interference factors. The multiplicative and additive methods are compared with data in Fig. 3.56 for the cable tray. The multiplicative method produces the best results while the additive method underpredicts.

Based on the analysis of the data presented in this section several conclusions may be drawn. Neither the additive nor multiplicative method predicts well for skin points influenced by a protuberance and the orbiter. Neither the additive or multiplicative method predicts well for protuberance points influenced by another protuberance and/or the orbiter. Neither method yields a conservative method of prediction. Thus, no acceptable method for combining protuberance and proximity data to yield the total interference has been identified. The only currently acceptable method for obtaining the total interference effects is by testing.

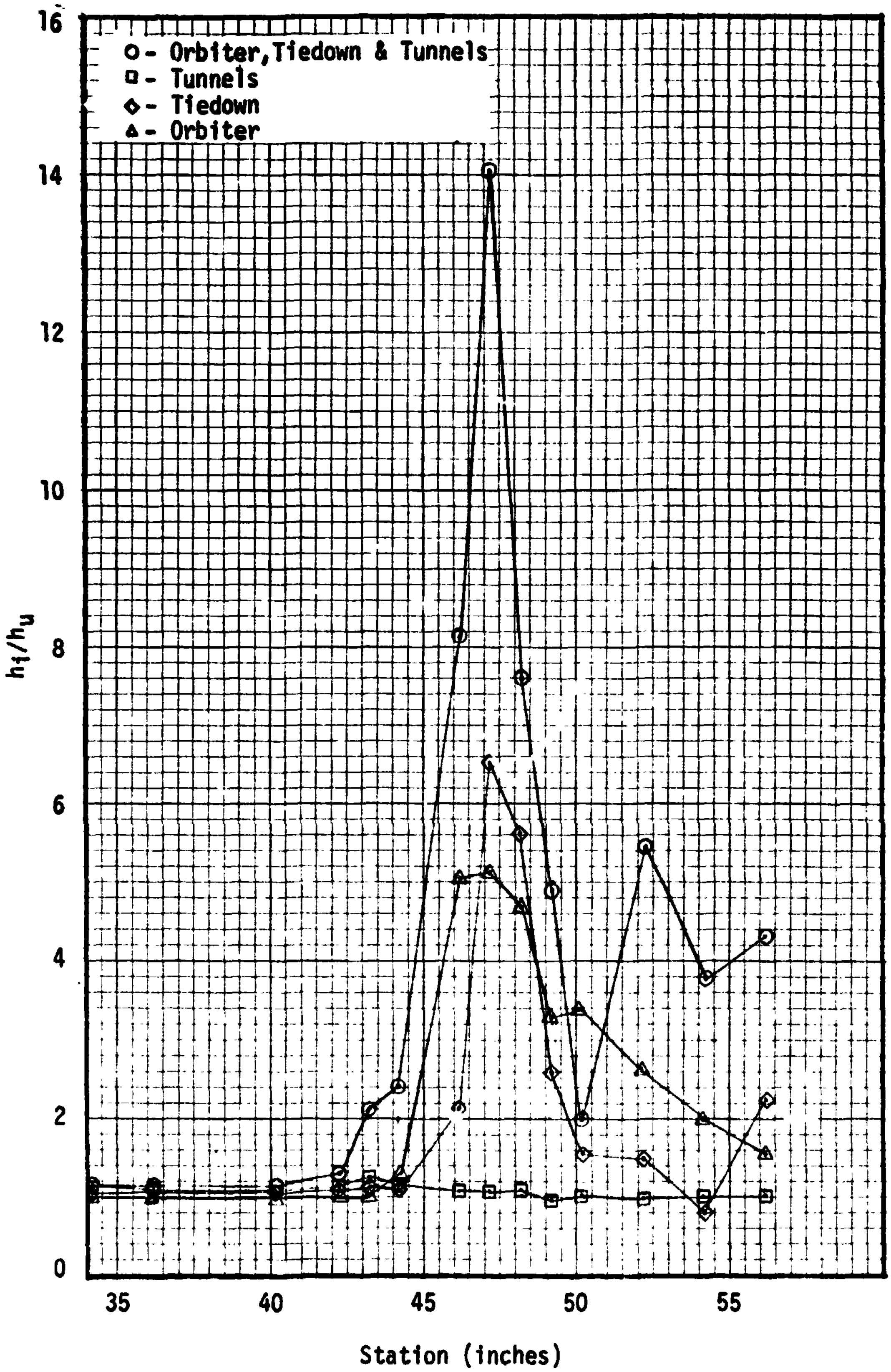

Fig. 3.42 Centerline (Θ_T=0) Data Distribution for the "B" Config.

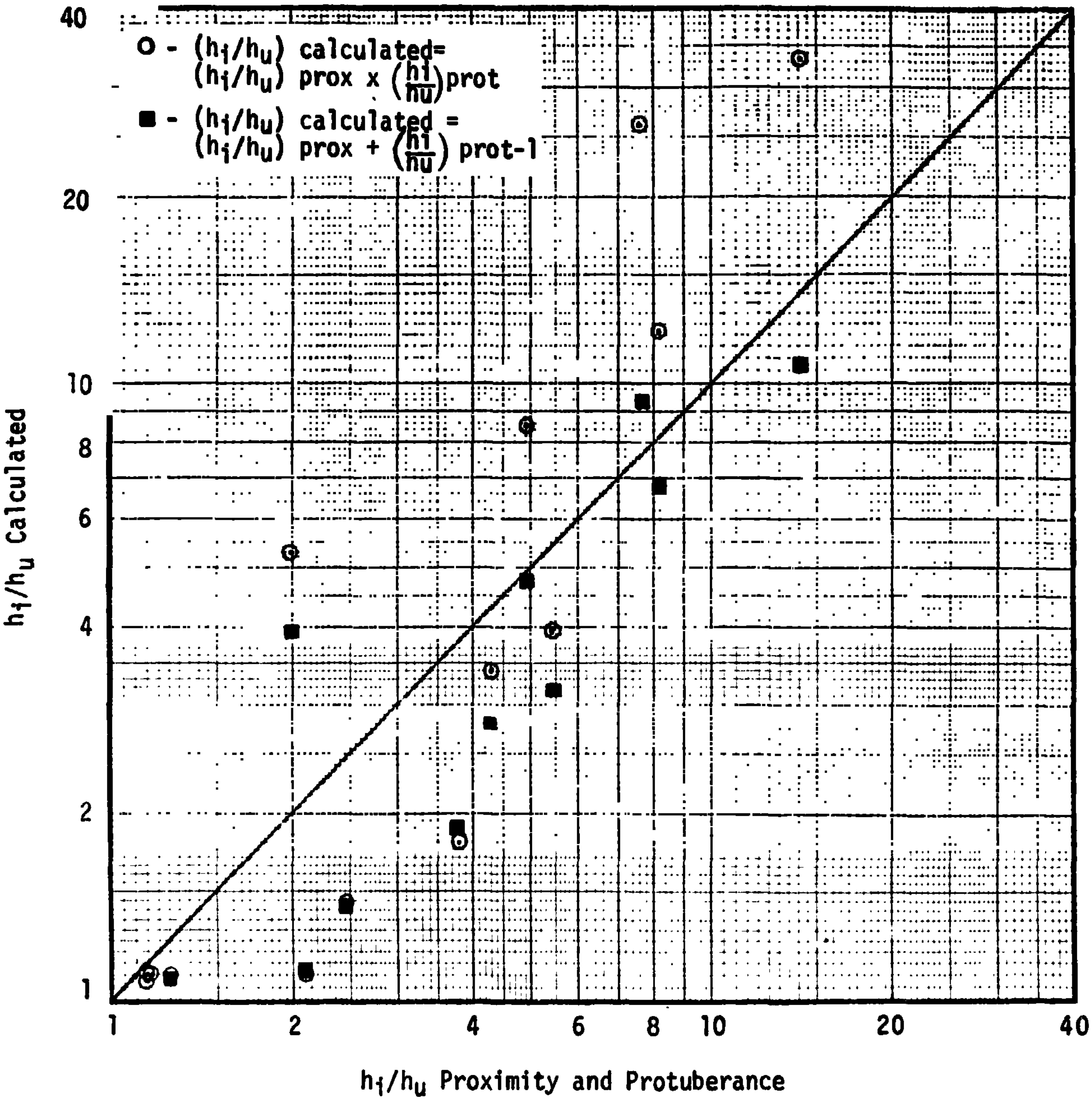

Fig. 3.43 Comparison of Additive and Multiplicative Methods Using the IH-51A Data Along the Centerline (B Config.)

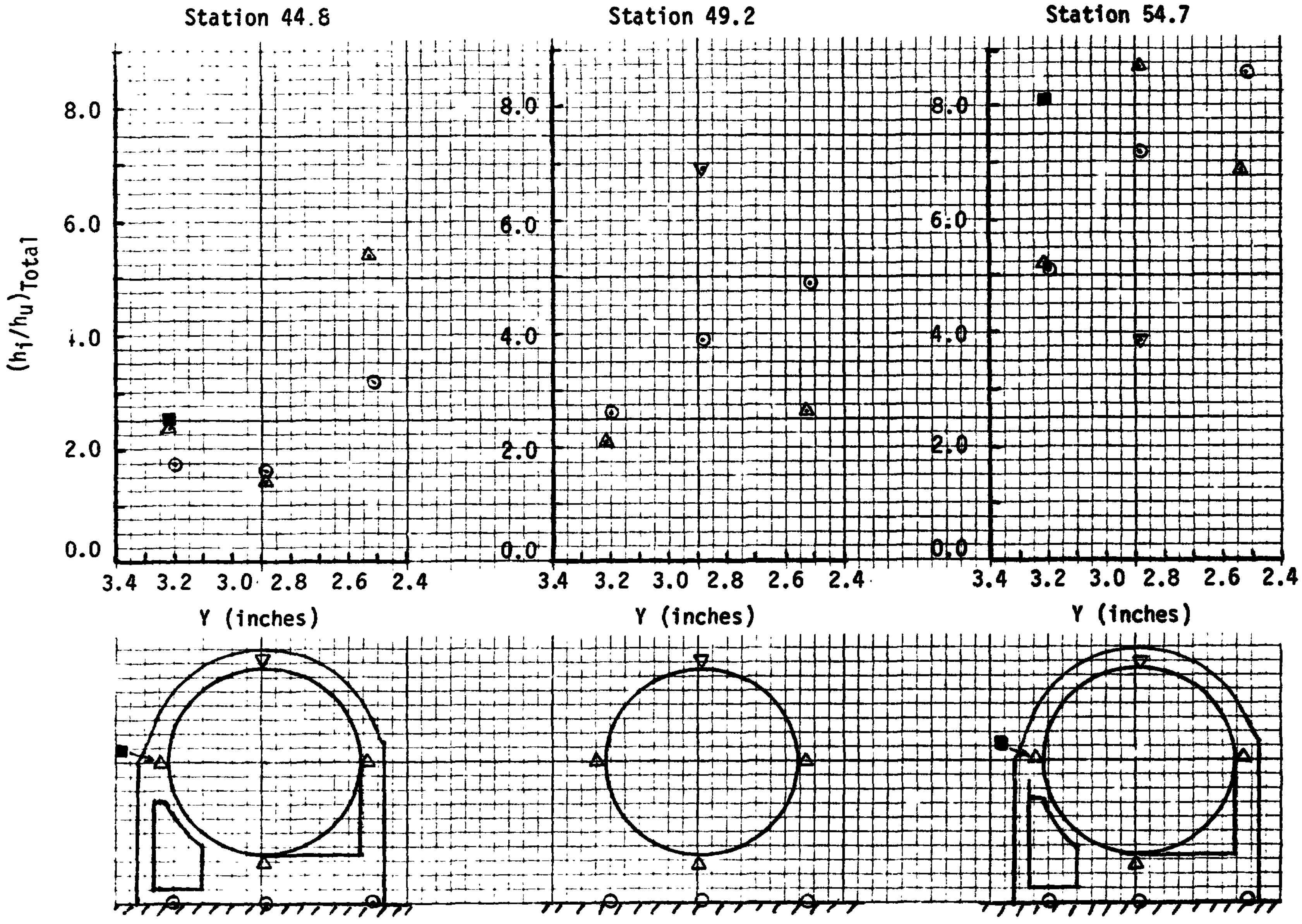

Fig. 3.44 Total Interference Heating Factors for the LO_2 Line and Skin Below the Line (B Config.)

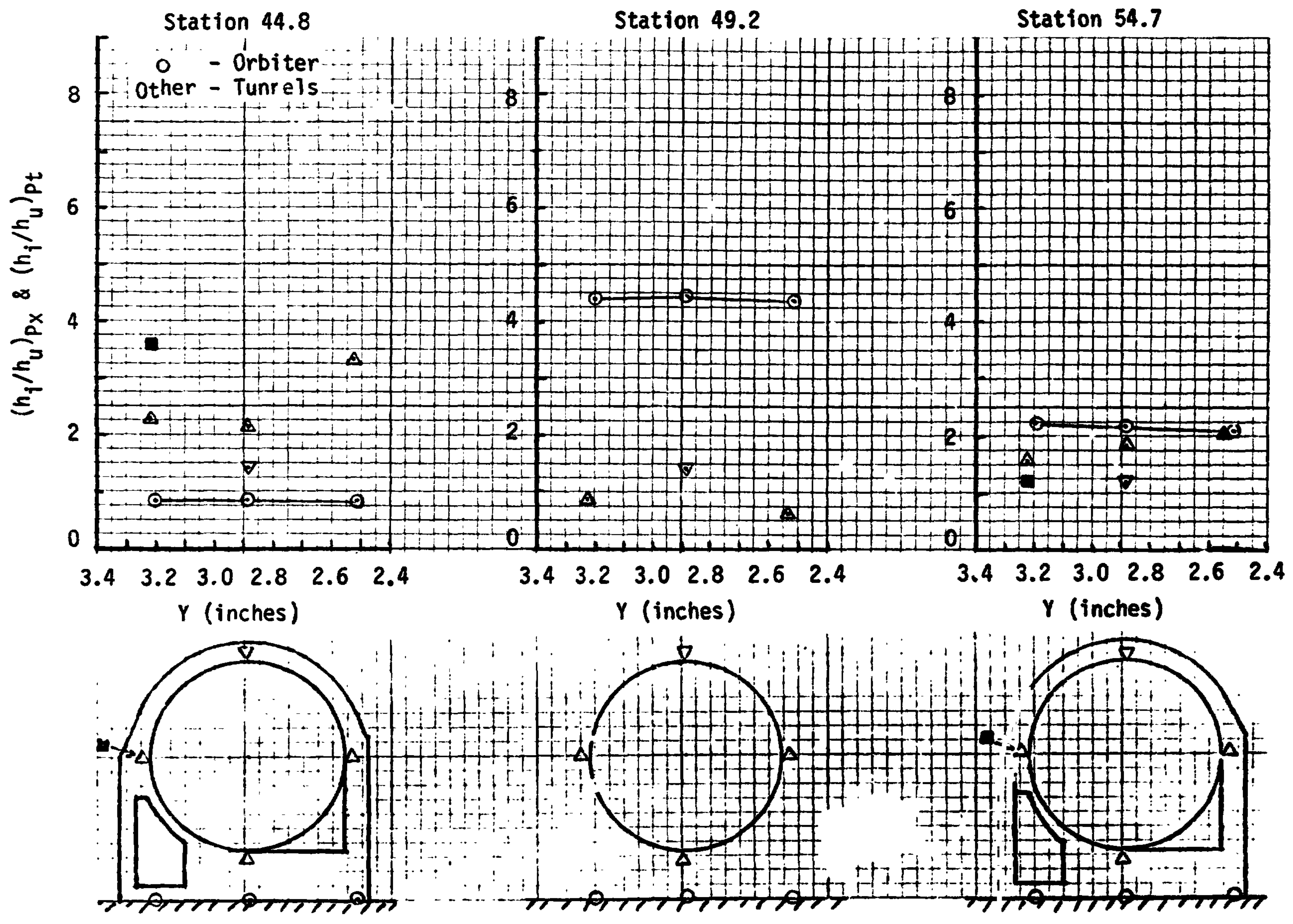

Fig. 3.45 Comparison of Proximity and Protuberance Heating on LO_2 Line (B config.)

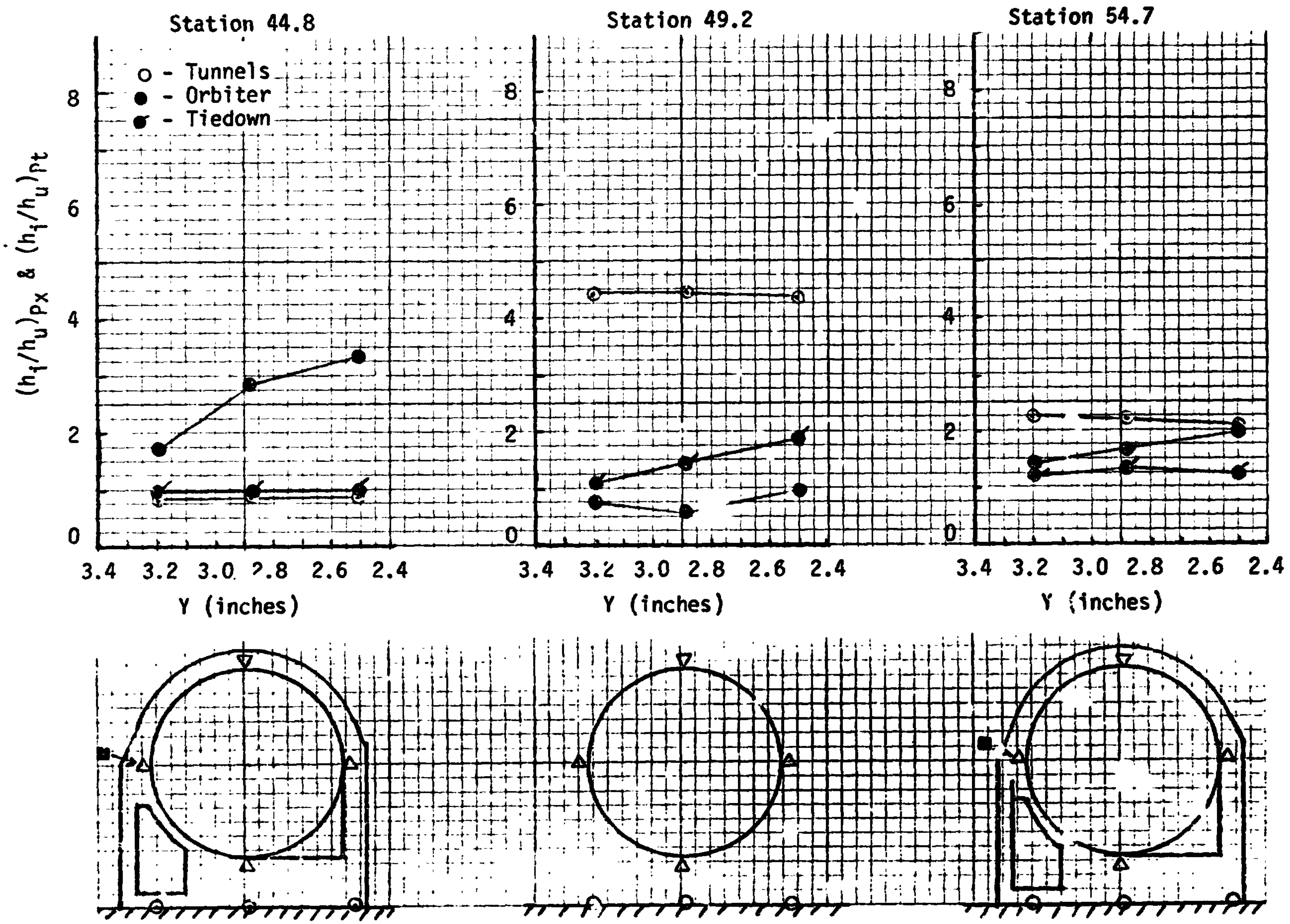

Fig. 3.46 Comparison o' Interference Components for Positions on the Skin Below the LO_2 Line (B Config.)

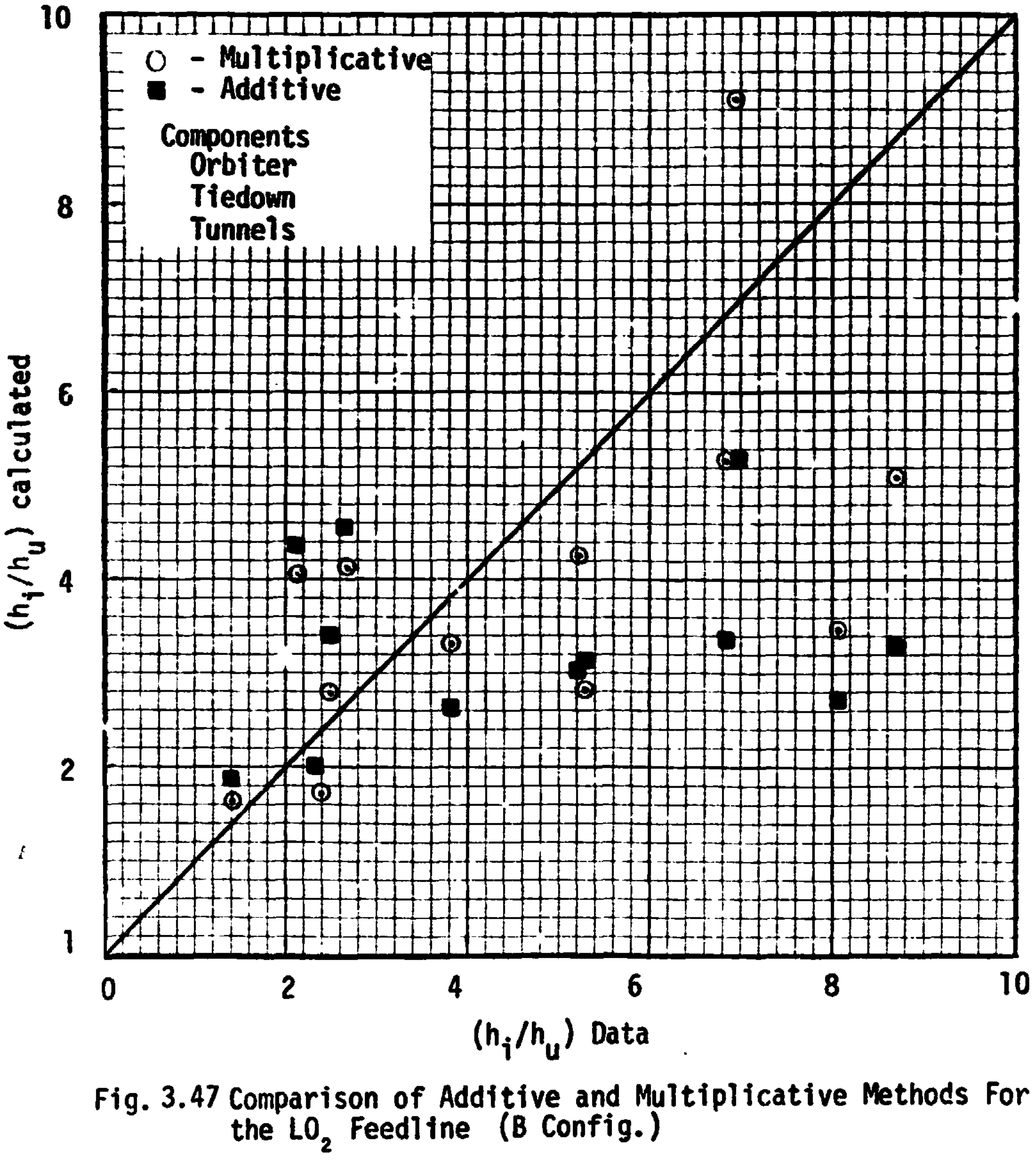

Fig. 3.47 Comparison of Additive and Multiplicative Methods For the LO_2 Feedline (B Config.)

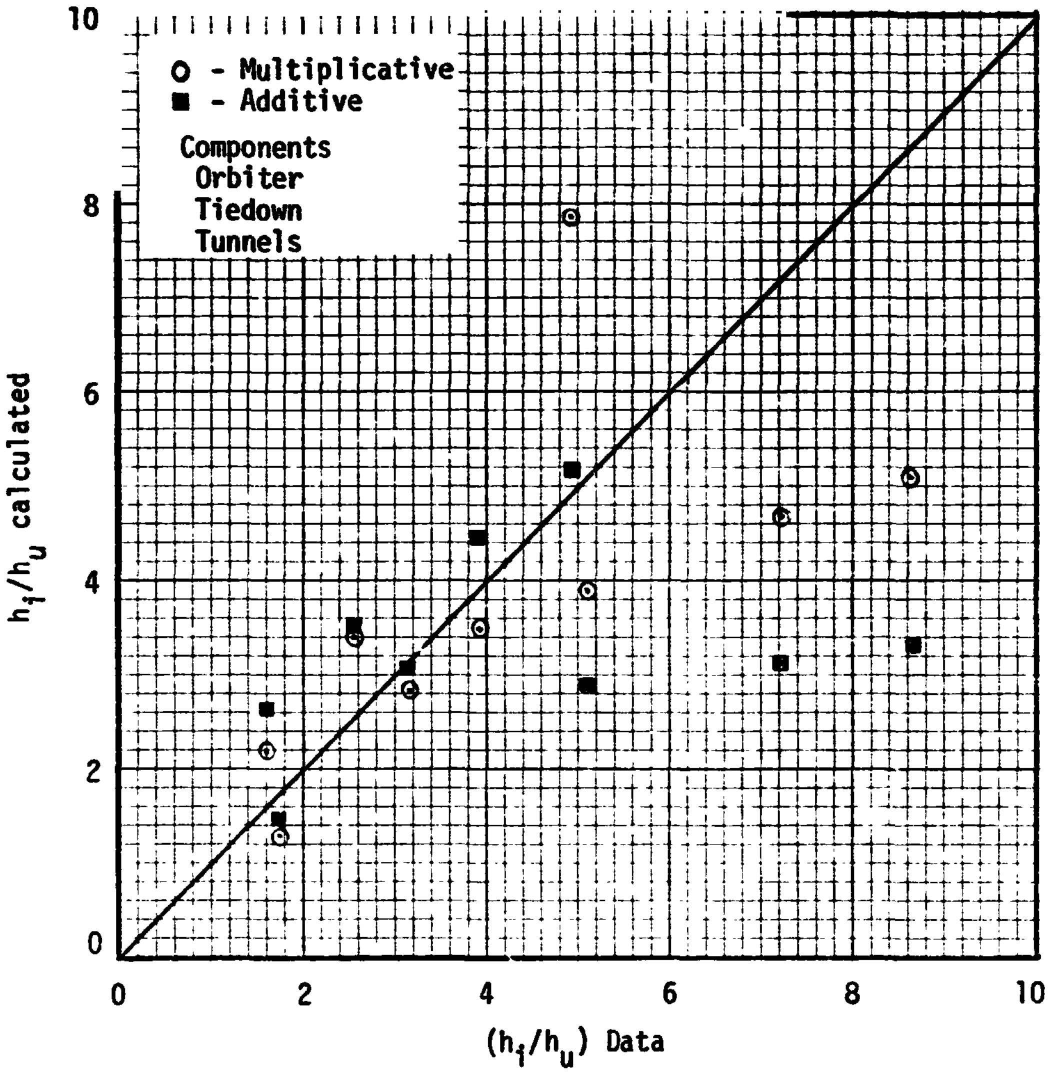

Fig.3.48 Comparison of Additive and Multiplicative Methods Using IH-51A Data of Skin Values Below the LO_2 Line (B Config.)

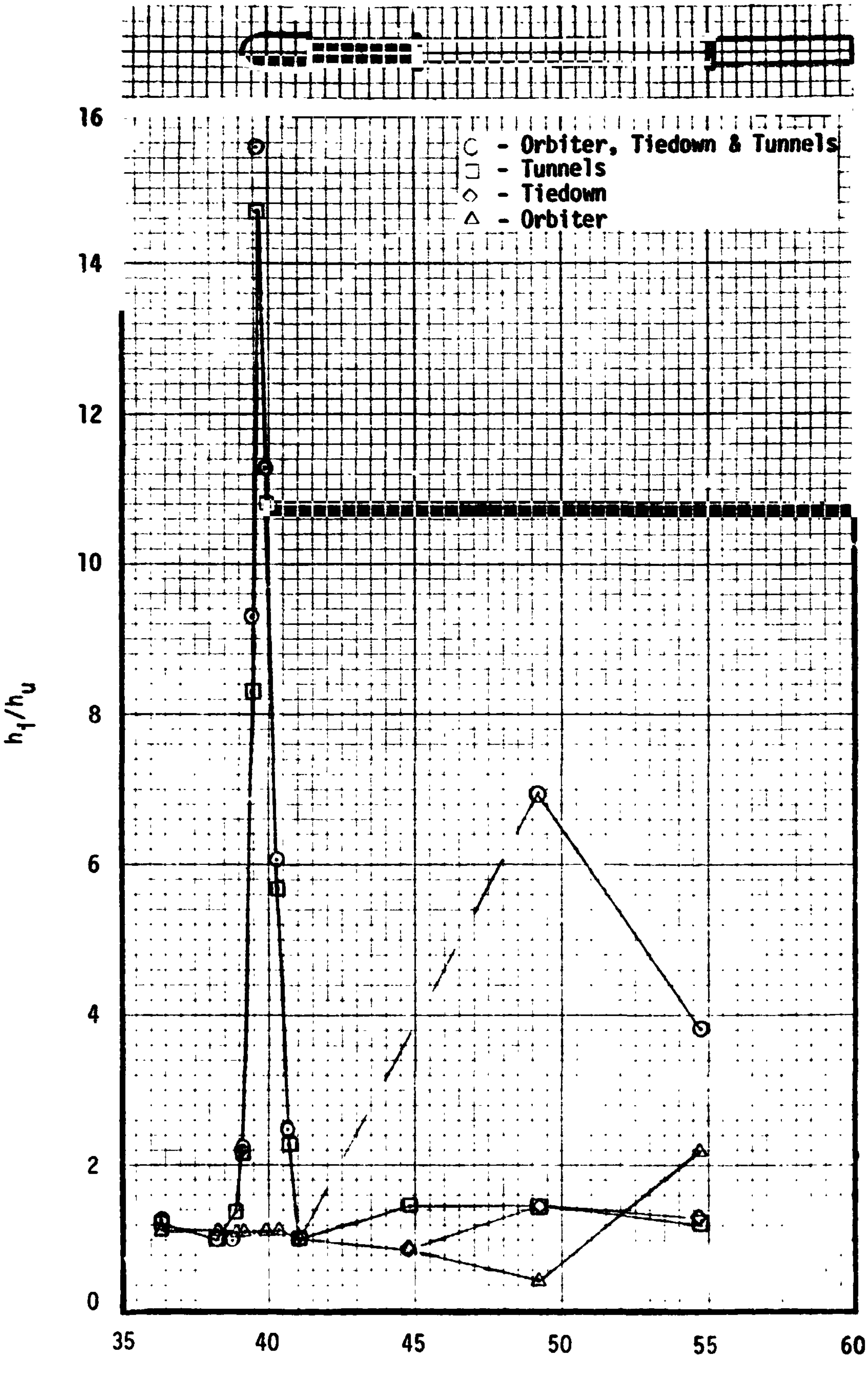

Fig.3.49 LO₂ Feedline Centerline Data Distribution for the "B" Configuration

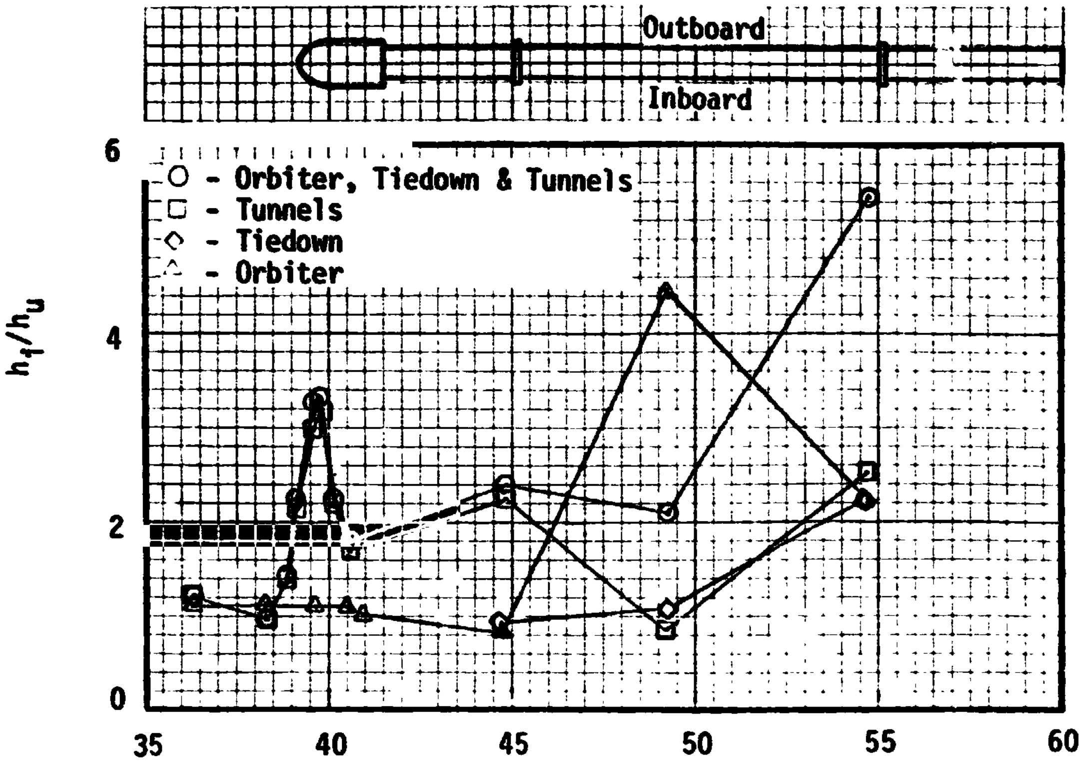

Fig. 3.50 LO_2 Feedline Outboard Data Distribution for the "B" Configuration.

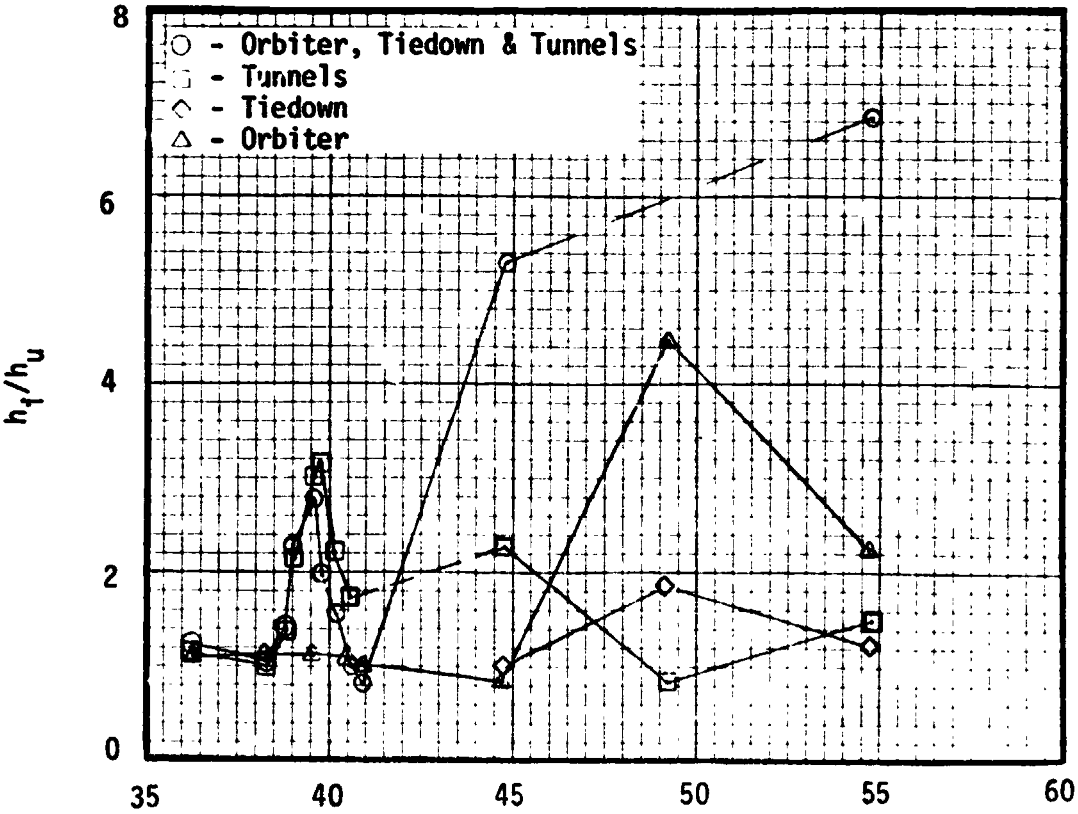

Fig. 3.51 LO_2 Feedline Inboard Data Distribution for the "B" Configuration.

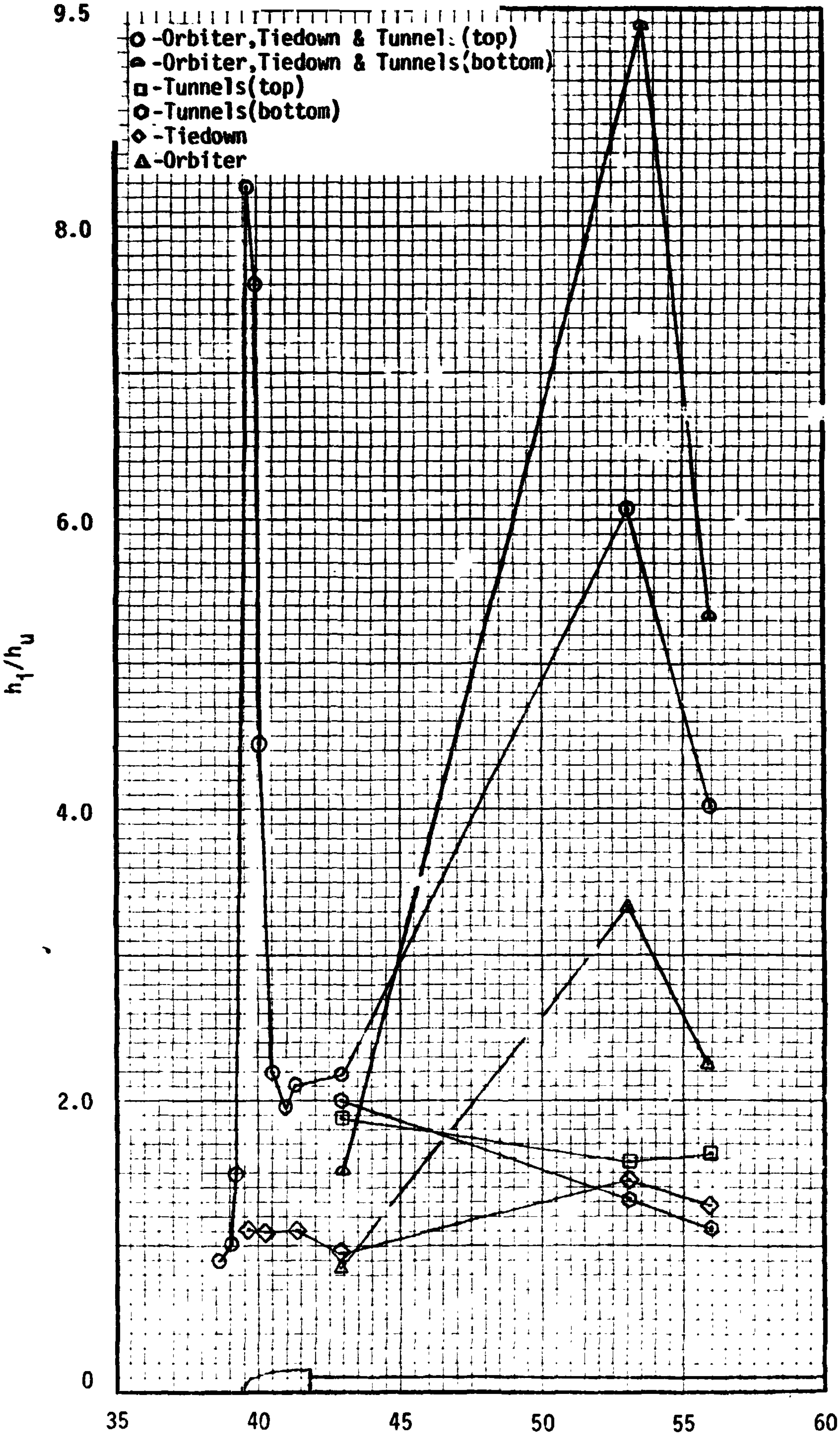

Fig.3.52 LO_2 Antigeyser ℄ Data Distribution for the "B" Configuration

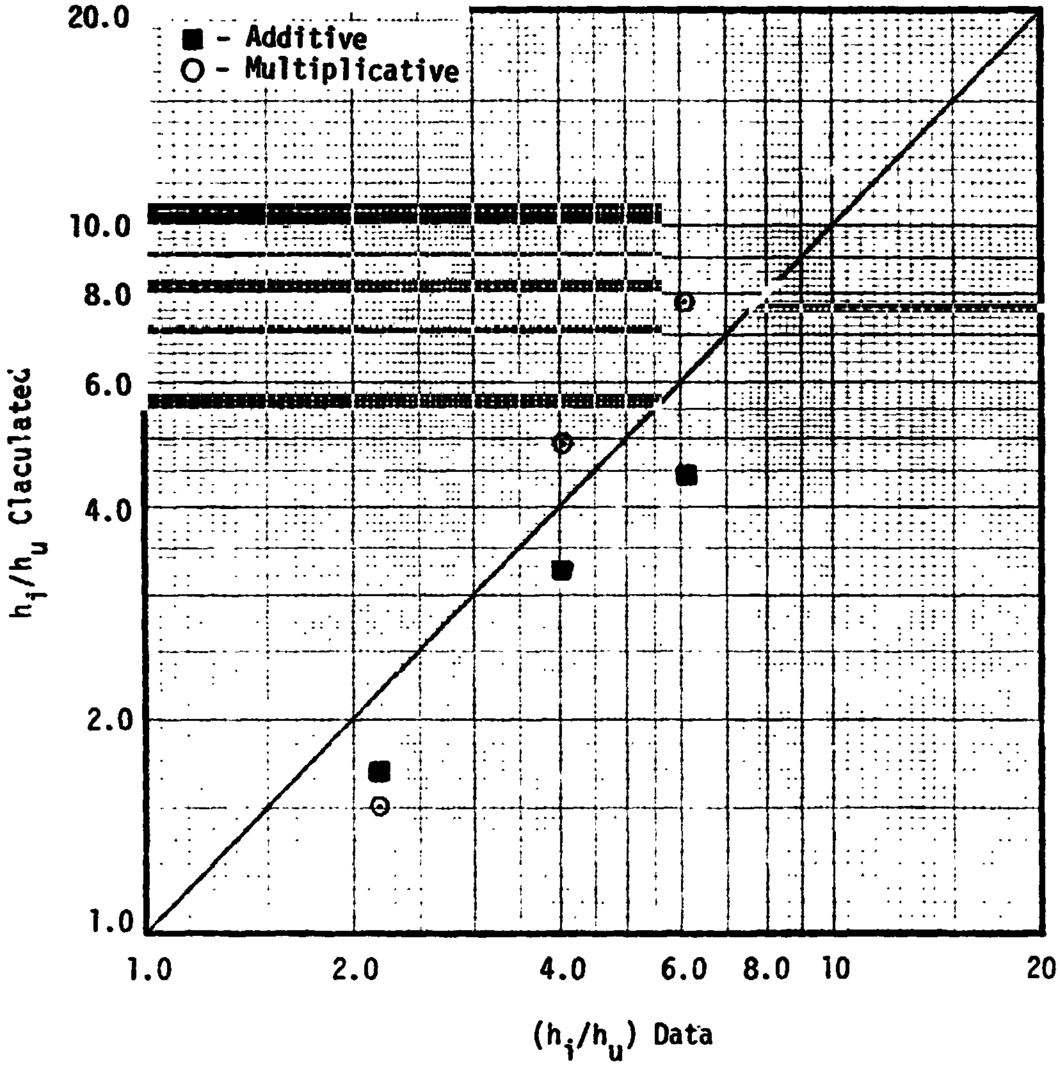

Fig. 3.53 Comparison of Additive and Multiplicative Methods for the Top of the LO_2 Antigeyser Line (B Configuration)

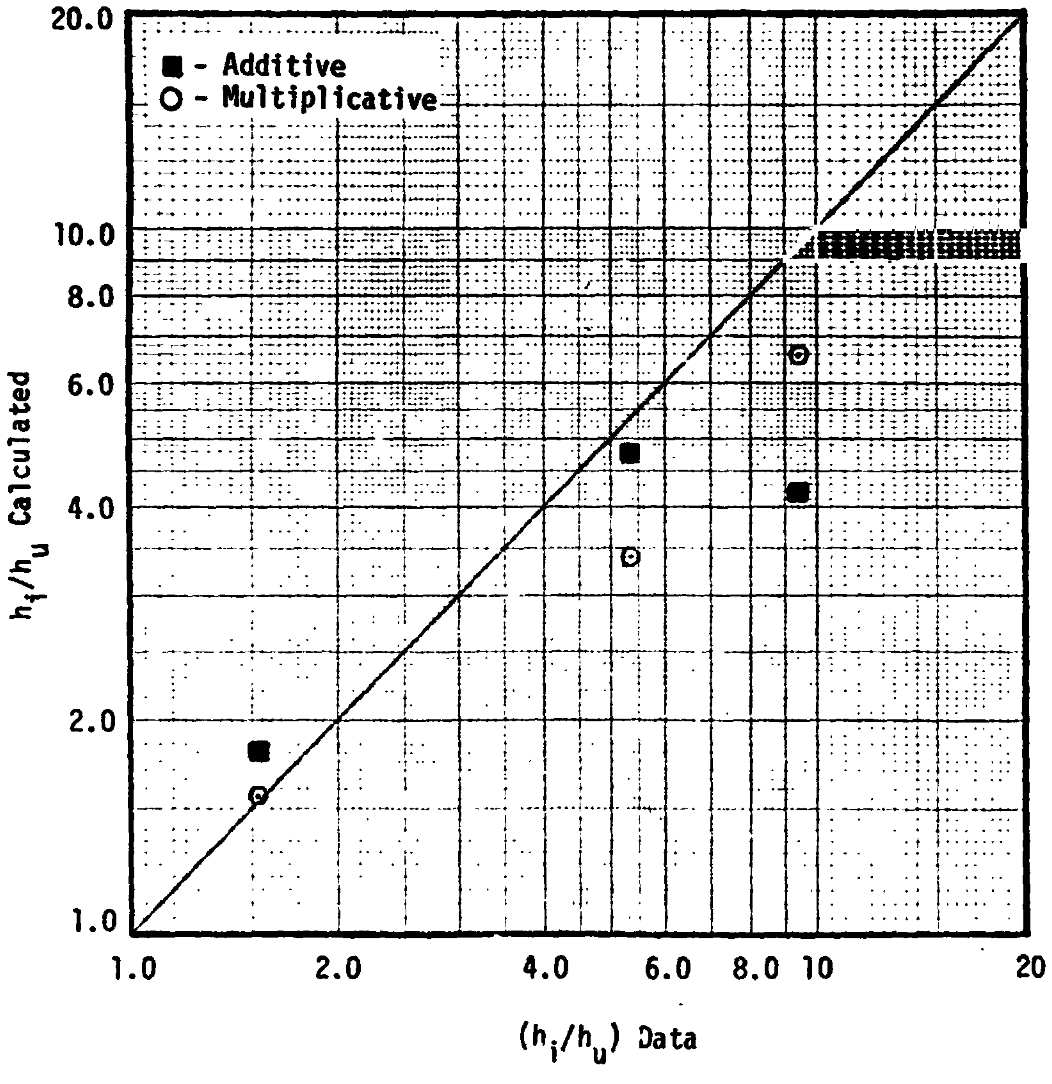

Fig. 3.54 Comparison of Additive and Multiplicative Methods for the Bottom of the LO_2 Antigeyser Line (B Configuration)

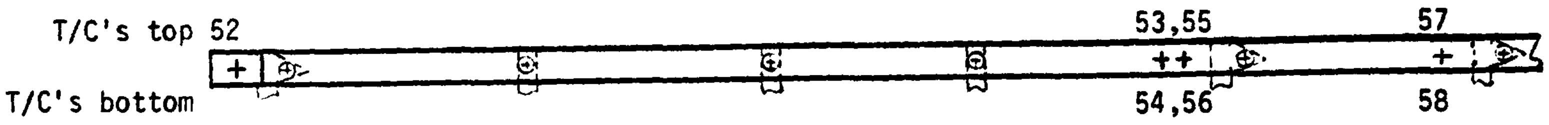

T/C No.	52	53	54	55	56	57	58
Orbiter, Tiedown & Tunnels	3.63	5.17	6.12	5.47	6.28	4.82	4.02
Tunnels	3.56	1.465	1.16	1.50	1.27	1.64	1.02
Tiedown (from skin data)	1.0	1.18	1.18	1.07	1.07	1.22	1.22
Orbiter (from skin data)	1.02	3.82	3.82	3.63	3.63	2.62	2.62
Station (Model)	42.960	52.846	52.846	53.046	53.046	55.816	55.816
X_T (in.)	1324.0	1321.15	1321.15	1326.15	1326.15	1395.40	1395.40

Fig. 3.55 Interference Factors for the Cable Tray

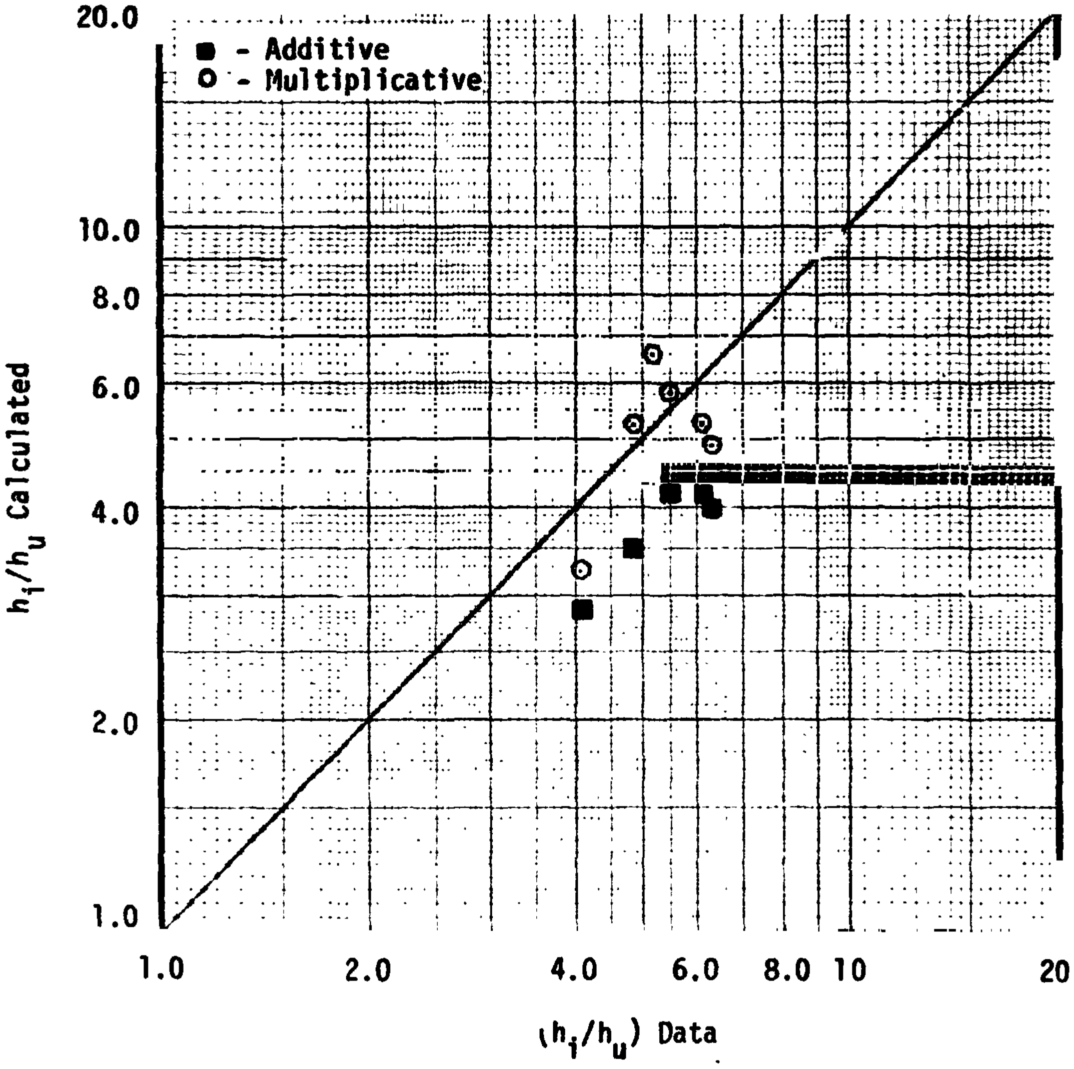

Fig. 3.56 Comparison of Multiplicative and Additive Methods for the ET Cable Tray (B Configuration)

3.4 Methods of Application to Flight

The previous section (3.3) results indicated that the effects of protuberances and body proximity can not be tested separately and combined to obtain the total interference. The IH-51A data for the total interference was obtained on a flat plate rather than an ET model. This was done in order to obtain the protuberance size large enough for detailed instrumentation. The problem of how to scale this data to flight remains. If a procedure can be developed to show that the IH-51A data can be scaled with ET model data, then the same scaling procedure used for ET model data can be used for the IH-51A data. This section addresses the development of a scaling procedure for the IH-51A data.

To determine how the IH-51A data fits in with model OT or OTS data, the local flow-field must be examined. The local surface Mach number on the ET at the same axial position of the orbiter nose was examined using the method of characteristics (MOC). These results are given in Fig. 3.57 as a function of angle of attack. Simple flow-field options are compared with the MOC results for $\alpha = 0$ in Fig. 3.58. These results support other evidence indicating that the 40° cone shock and tangent cone pressure option is the best simple flow-field option to use.

The centerline data from IH-51A was plotted and compared with the data of IH-48. Both tests have free-stream Mach numbers of 5.3. The IH-51A data distribution was found to be higher and shifted to higher X/L values than the IH-48 data. This was initially thought to be a result of the higher oncoming Mach number at the orbiter nose for IH-51A than IH-48. From Fig. 3.57 the Mach number for IH-51A to have the same oncoming Mach number as the IH-48 test is $M_\infty = 3.9$. The $M_\infty = 5.3$ data was scaled down on a log-log plot of h_i/h_u versus M_∞ to $M_\infty = 3.9$. These results are shown in Fig. 3.59 and the magnitude is in better agreement with the IH-48 data. The peak heating was probably missed because of the thermocouple spacing.

A plot comparing IH-51A data off of the centerline with model data is shown in Fig. 3.60. Unfortunately the model data is scarce and a conclusion is hard to draw. All other θ_T positions are just as bad or worse in terms of obtaining data for a comparison between IH-51A model and OT or OTS models. Consequently, it was not possible to obtain an indication of the 2D to 3D geometry effects.

In examining the ET flow-fields in Ref. 3.3, it was found that the Mach number varied radially from the ET surface. The Mach number at r/D = 0.7* is plotted versus M_∞ in Fig. 3.61 . This location is approximately halfway between the ET and orbiter nose. The Mach number at this location is used in the following analysis.

The interference factor, h_i/h_u, is plotted versus Mach number for three X/L locations in Figs. 3.62, 3.63 and 3.64. The IH-51A is compared with IH-41B, IH-48, IH-41A and IH-43 data in these figures. The IH-41A data correlates the best using M_{local} evaluated at r/d = 0.70. Notice that the peak value in Fig. 3.63 is thought to be missed by the IH-51A thermocouple spacing. Also, notice the M_∞ = 8 data from IH43 is lower than the IH-51A data. This substantiates that the IH51A data can not be used directly for flight predictions since it is equivalent to using OT model data for a free-stream Mach number of 9.8.

To explore the effect of the local Mach number on the location of the peak heating and thus the distribution, shadowgraph data were analyzed. The approximate orbiter shock angle was measured from MSFC-140B data presented in Ref. 3.3 and IH-51A data. These data are shown in Fig. 3.65 and appear to be quite consistent. In addition to the shock angle, the shock impingement location

---

*Note: r = radius from ET centerline, D = ET diameter was obtained from shadowgraph data. The impingement location, $(X/L)_i$, is plotted as a function of local Mach number in Fig. 3.66. The peak heating location data from thermocouple readings are also plotted in Fig. 3.66. These data indicate that the peak heating location is displaced from the impingement location and that the movement of the peak heating location is proportional to the movement of the shock impingement location. Again the IH-51A data form a consistent pattern with the model data and the peak value was missed. The measured peak is indicated by the symbol and the bars indicate the possible spread due to T/C spacing.

The peak impingement heating has been correlated on simple shapes with the pressure rise across the reflected shock, $h_i/h_u = (p_3/p_1)^{0.8}$. The measured incident shock angle, Fig. 3.65, and the local Mach number was used to compute the pressure ratio and thus the peak h_i/h_u for the wind tunnel OTS and IH-51A data conditions. These results are in excellent agreement with the measured data as shown in Fig. 3.67. It should be noted that the computed value from shadowgraph data is slightly higher than the measured peak value for IH-51A. This also indicated the peak was missed because of the T/C spacing.

The results presented thus far indicate that the local Mach number, M_L, in front of the orbiter nose must be used to relate the IH-51A data with other model data. The proposed scaling procedure for interference factors, h_i/h_u, is shown in Fig. 3.68. $M_\infty = 5.3$ data on the flat plate in Test IH-51A corresponds to $M_\infty = 9.8$ data on an OT model. Thus, the IH-51A $M_L = 5.3$ data have to be corrected to a local Mach number of $M_L = 4.2$ so that the results correspond to $M_\infty = 5.3$ on an OT model. This correction is made by ramping down h_i/h_u vs. M_L linearly on a $\log_{10}$-$\log_{10}$ paper from its $M_L = 5.3$ value to the $M_L = 4.2$ value. This new value of h_i/h_u is then used as the value of $M_\infty = 5.3$ for the

OT model. Using such an approach, comparisons were made on the ET centerline ($\Theta_T = 0$) between IH-51A reduced data and Test IH-41B and IH-48 data in Figs 3.69 and 3.70. It should be noted here that the reduced value of h_i/h_u at $M_\infty = 5.3$ in Test IH-51A was further ramped down to $M_\infty = 4$ to compare with $M_\infty = 4$ data from Test IH-41B. The magnitudes of the h_i/h_u peaks are comparable, but the IH-51A data peaks are behind those from Tests IH-41B and IH-48. The reason for such discrepancies is that no Mach number corrections were made for the peak locations.

No data are available to make similar comparisons on protuberances using this scaling method. The assumption made here is that the scaling procedure is the same. Accordingly, the configuration A data in Table 3.8 has been scaled and are presented in Table 3.9 to 3.12. Three columns of data are given:

$$\left.\begin{array}{l} h_i/h_u \\ M_\infty = 5.3 \\ M_L = 5.3 \end{array}\right\} \text{IH-51A data without adjustment}$$

$$\left.\begin{array}{l} h_i/h_u \\ M_\infty = 5.3 \\ M_L = 4.2 \end{array}\right\} \text{IH-51A data scaled to an ET model at } M_\infty = 5.3$$

$$\left.\begin{array}{l} h_i/h_u \\ M_\infty = 4.0 \\ M_L = 3.55 \end{array}\right\} \text{IH-51A data scaled to an ET model at } M_\infty = 4.0$$

These scaled data may be used in producing a flight math model for the turbulent flow regime.

Conclusions drawn from the results presented in this section are:

1. Interference data, shadowgraph, and peak heating location data indicate that the IH51A data is equivalent to running an OT model at $M_\infty = 9.8$.

(2) The local Mach number at r/D = 0.7 in front of the orbiter nose should be used for analysis and comparison of interference flow-field on the top centerline.

(3) The 2D effect in IH-51A cannot be separated from Mach number shift effects. The IH-51A and other model T/C locations are not consistent enough for $\Theta_T \neq 0$ analysis. Thus, the 2D to 3D effects can not be determinedusing the preceeding procedures.

(4) The IH-51A peak value and entire heating distribution is translated from other model data in X/L because of the oncoming Mach number effect.

(5) A scaling method for IH-51A data has been developed and the scaled IH-51A data agrees well with FT model data.

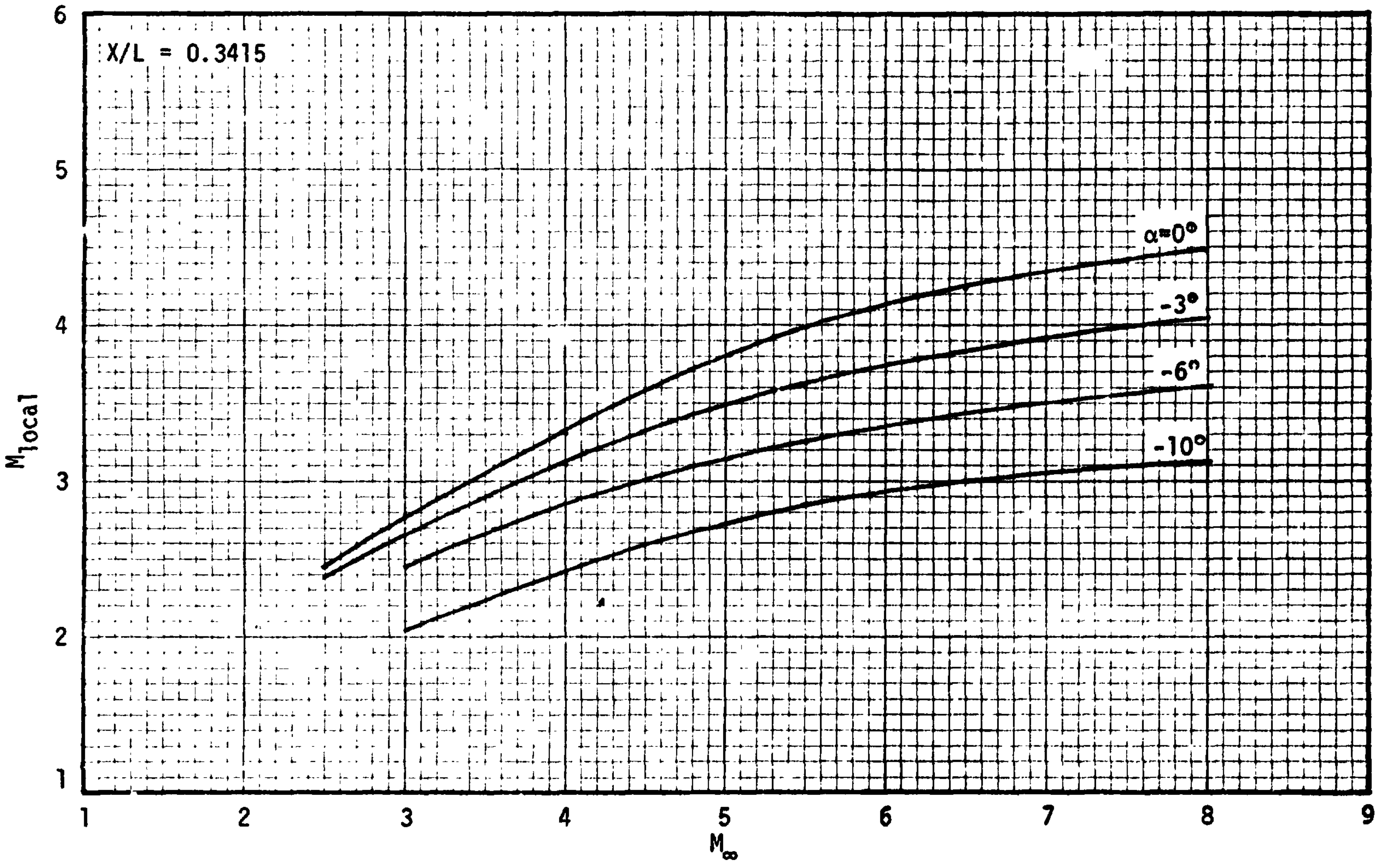

Fig.3.57 MOC Predicted Local Surface Mach Numbers for the ET

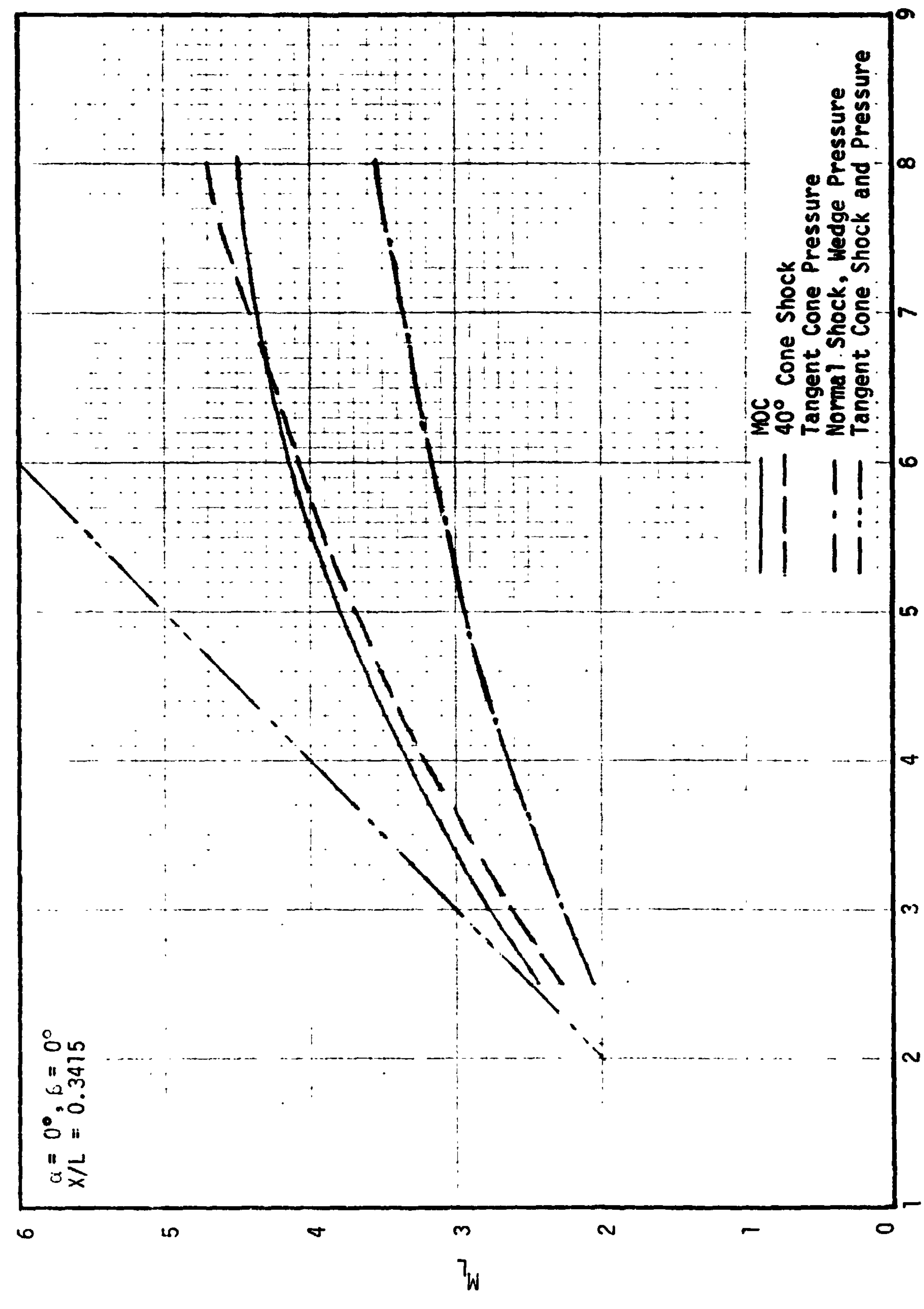

Fig. 3.58 Effect of Flow-Field Options on Local Mach Number, M_L, on the ET

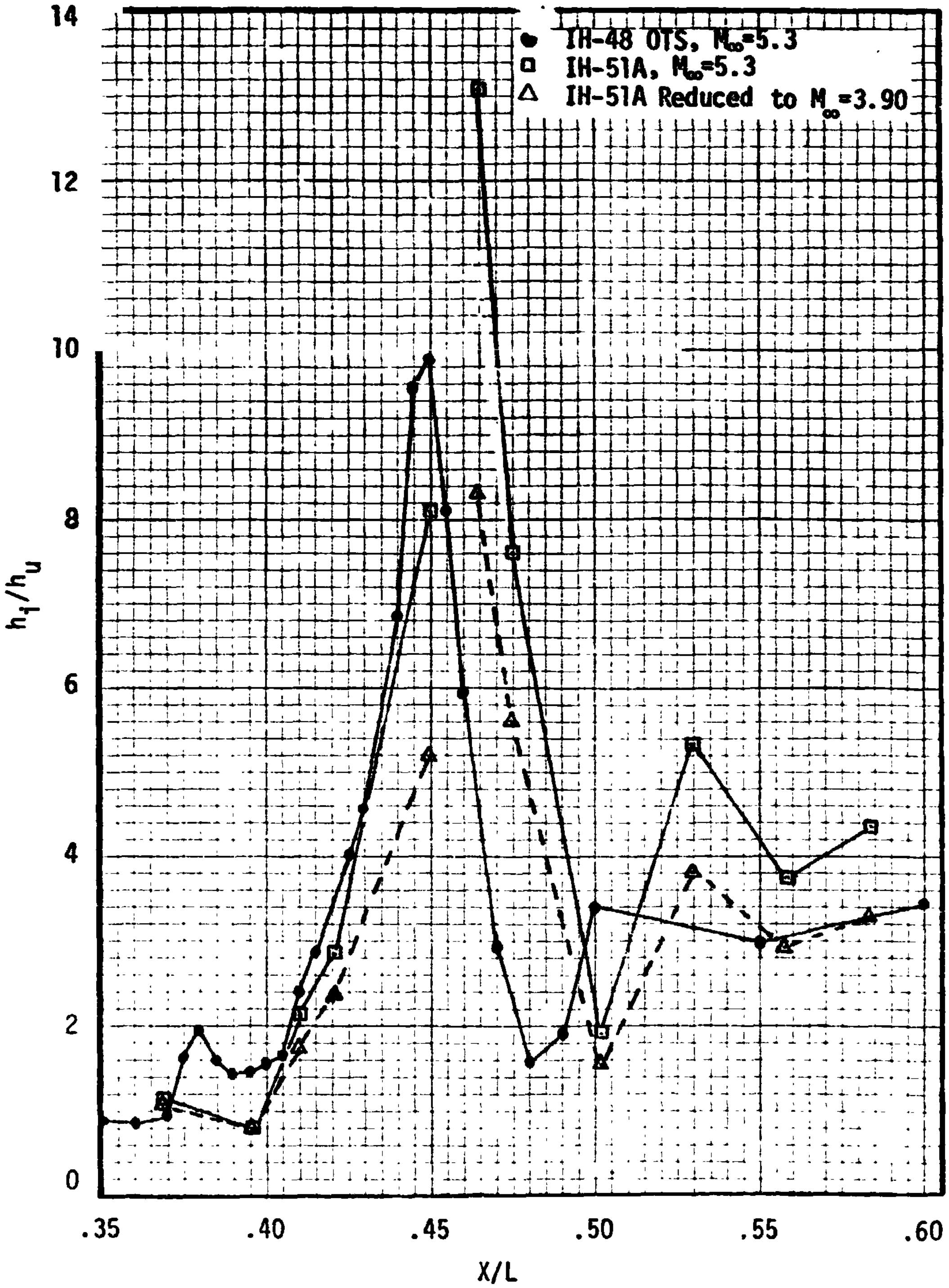

Fig. 3.59 Comparison of IH-48 and IH-51A Centerline Interference Data (θ_T=0°)

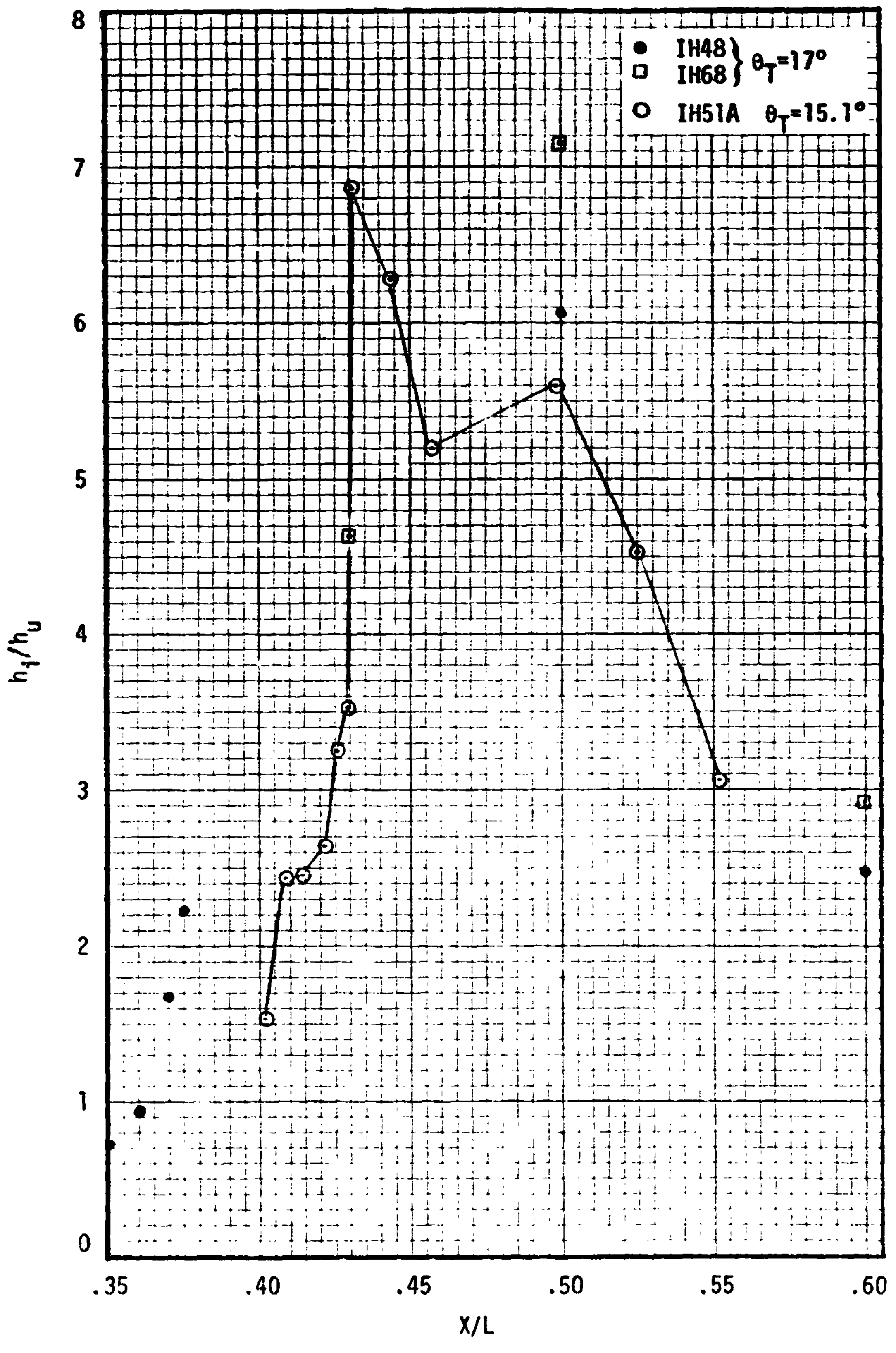

Fig. 3.60 Comparison of IH-51A Data with IH-68 and IH-48 Data at $\theta_T \approx 17°$

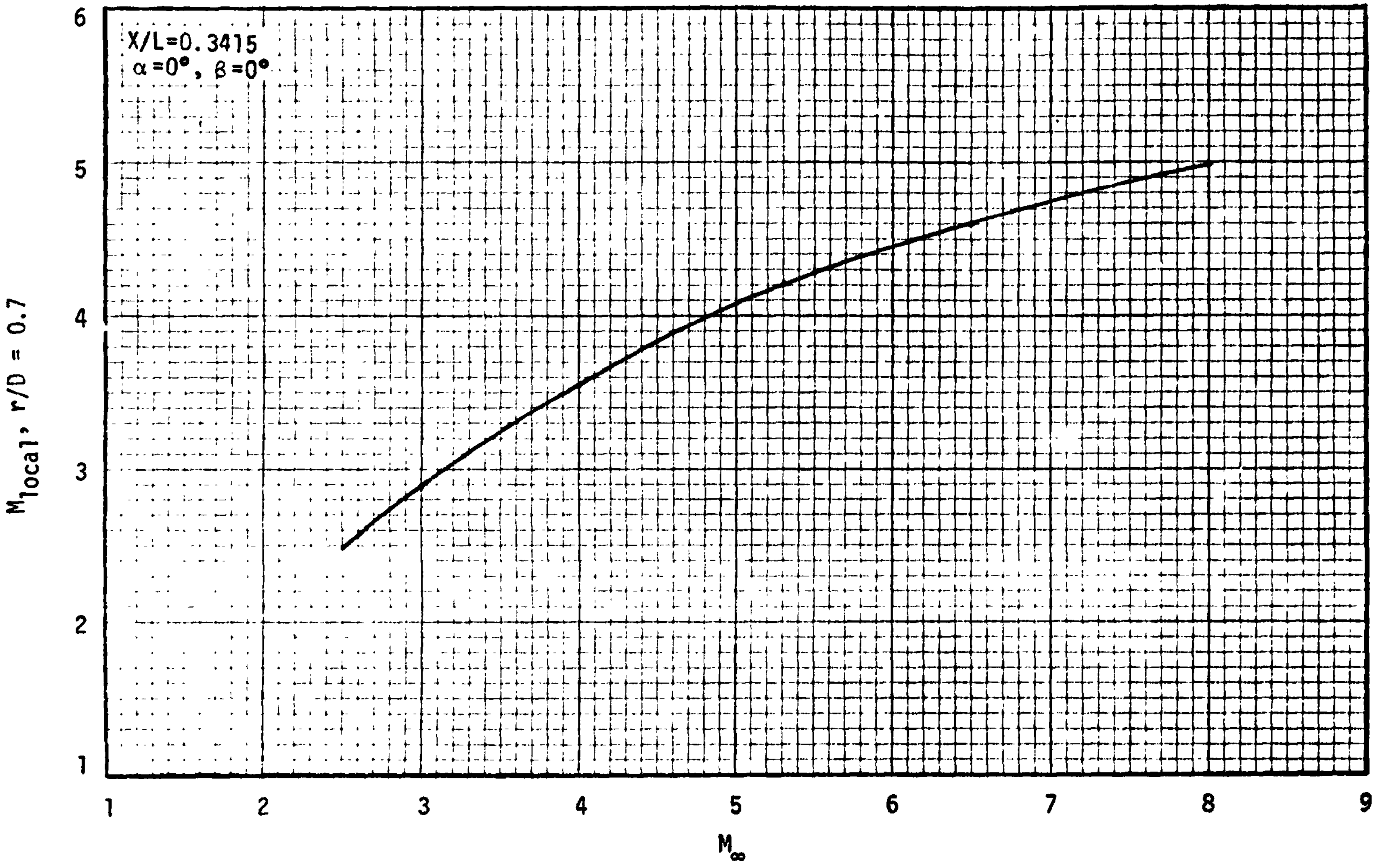

Fig. 3.61 MOC Predicted Local Mach Number Between the ET and Orbiter Nose

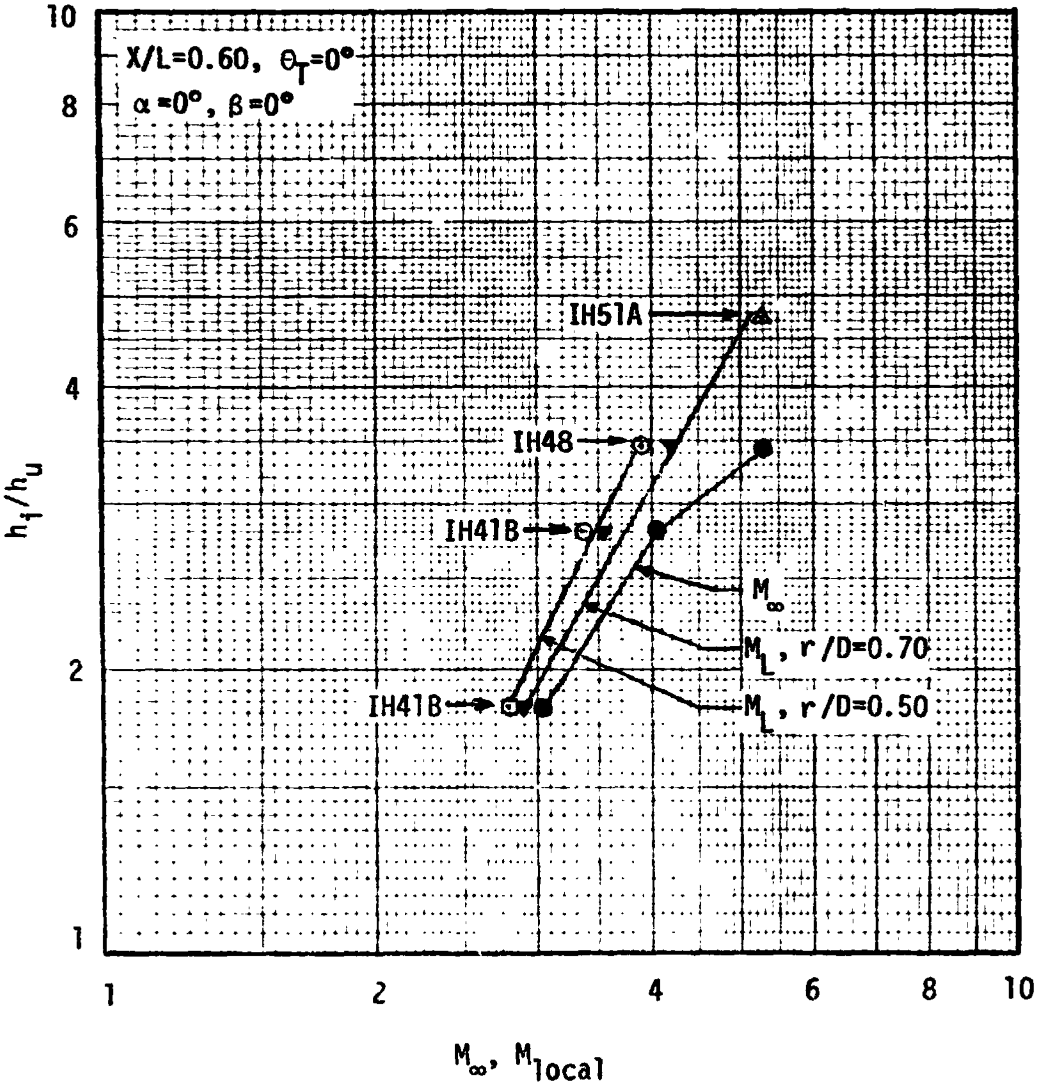

Fig. 3.62 Comparison of IH-51A Data with ET Model Data at X/L = 0.60

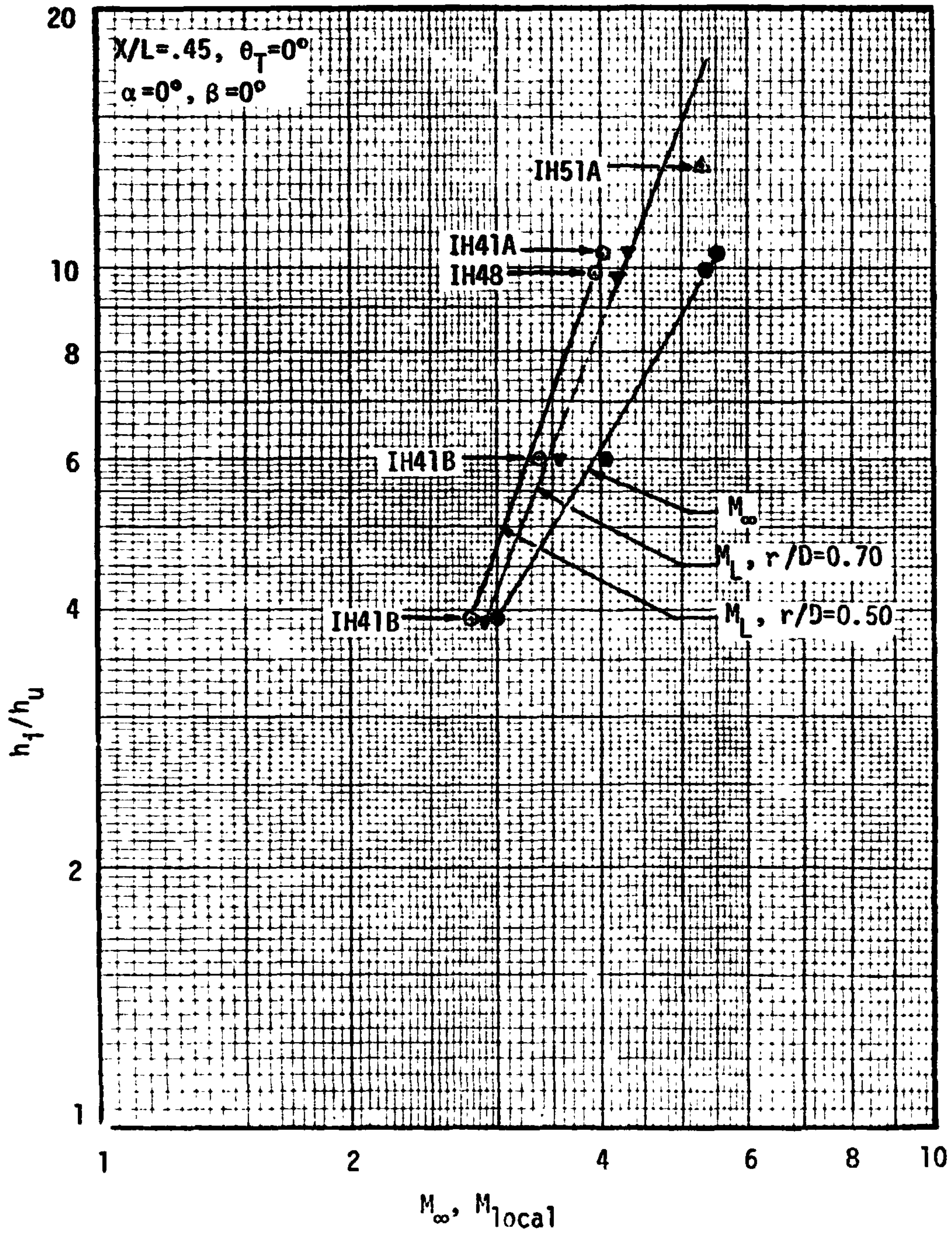

Fig.3.63 Comparison of IH-51A Data with ET Model Data at X/L = 0.45

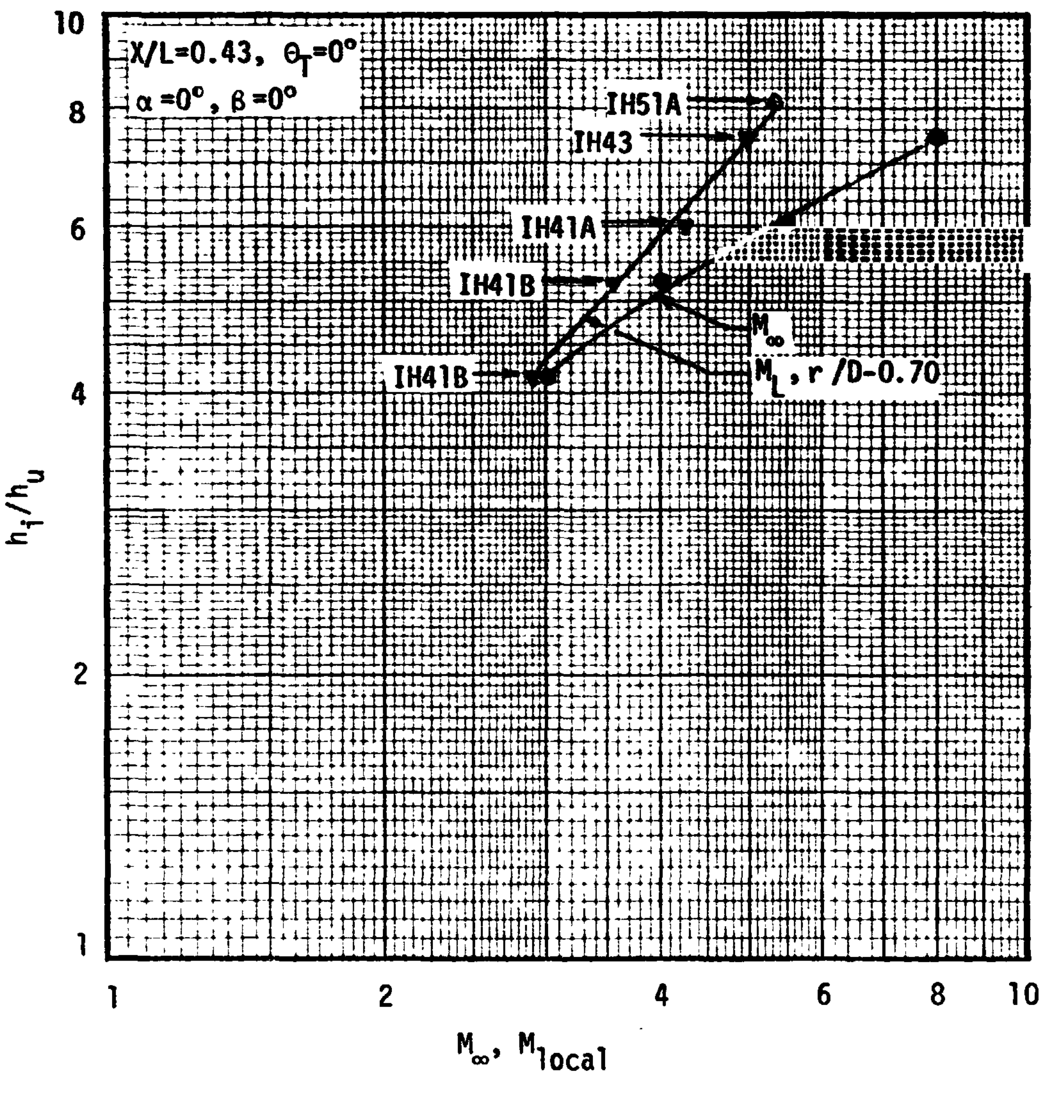

Fig. 3.64 Comparison of IH-51A Data with ET Model Data at X/L = 0.43

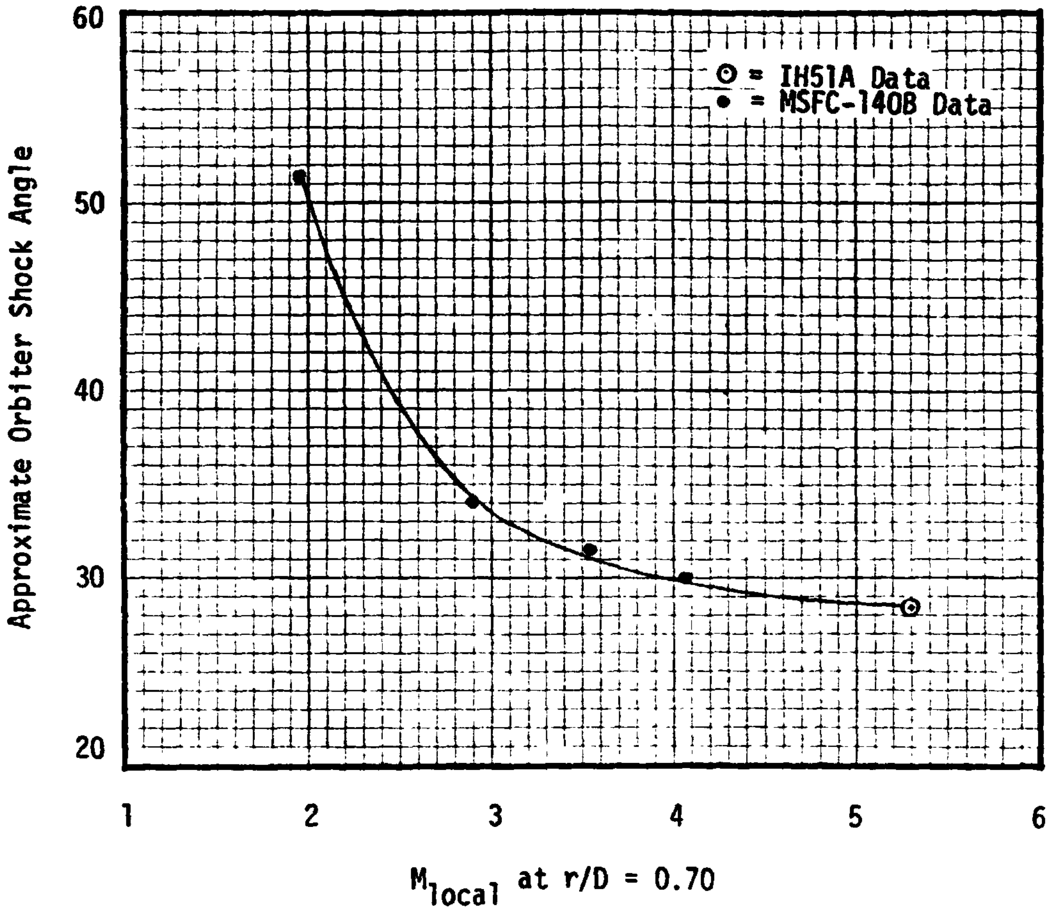

Fig. 3.65 Approximate Orbiter Nose Shock Angle Between Orbiter and ET

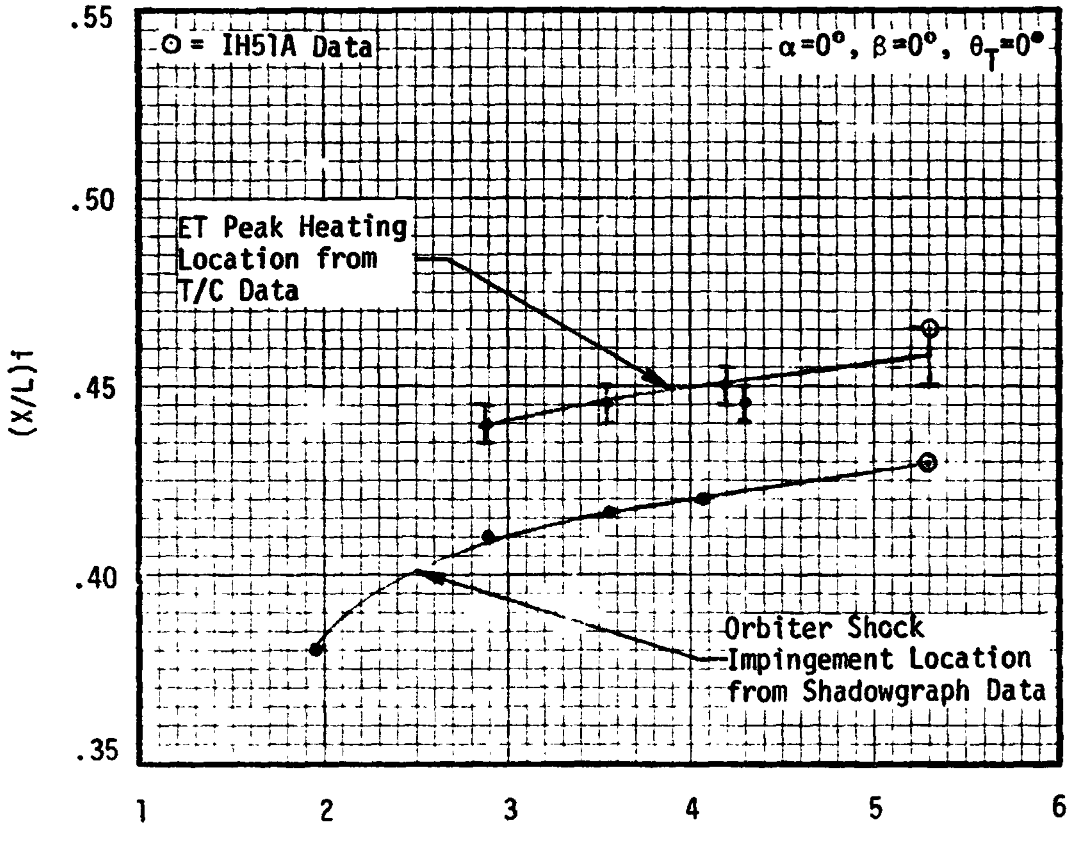

Fig. 3.66 Local Mach Number Effect on Shock Impingement and Peak Heating Locations

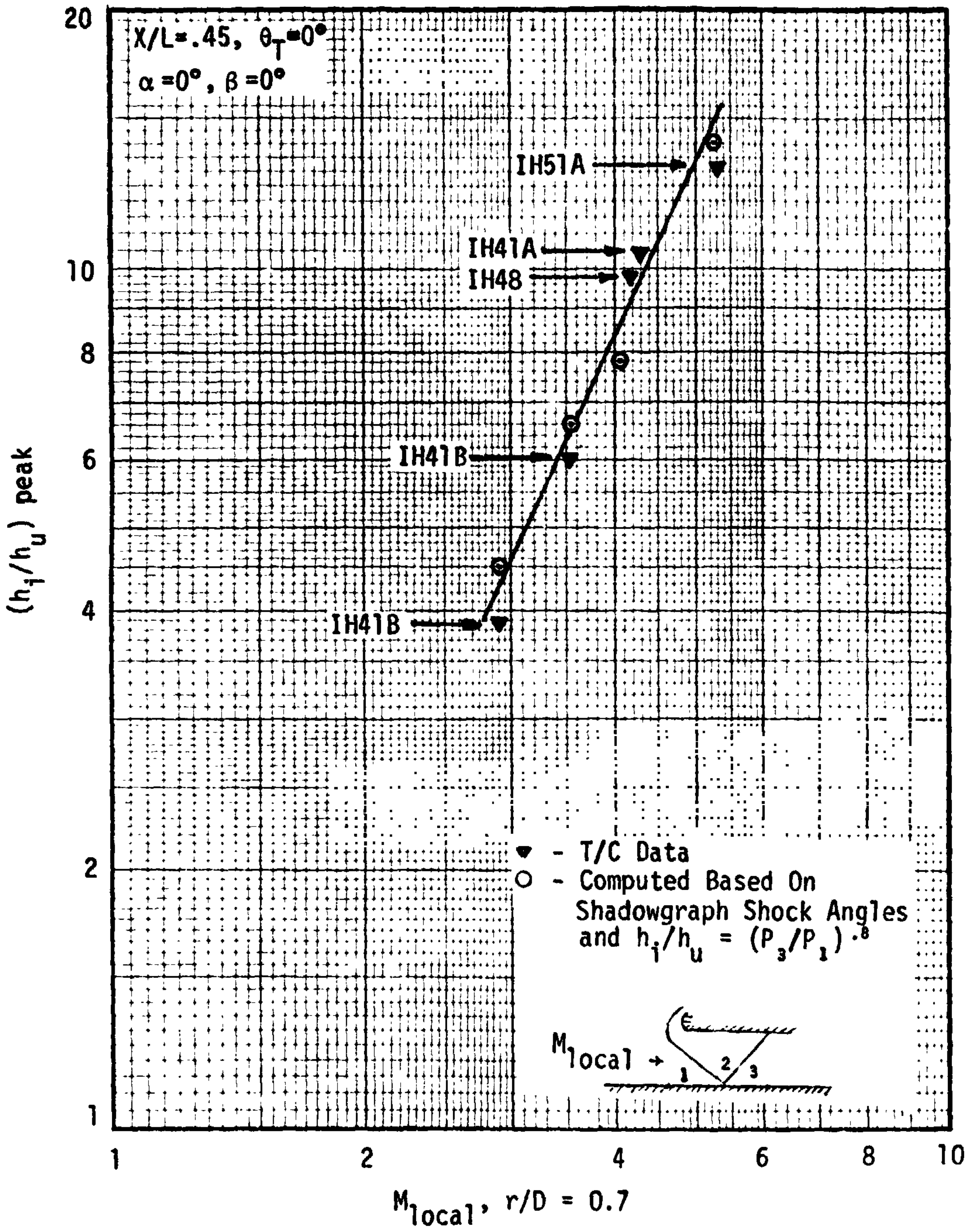

Fig. 3.67 Comparison of Measured Peak Heating and Computed Values Using Measured Incident Shock Angles

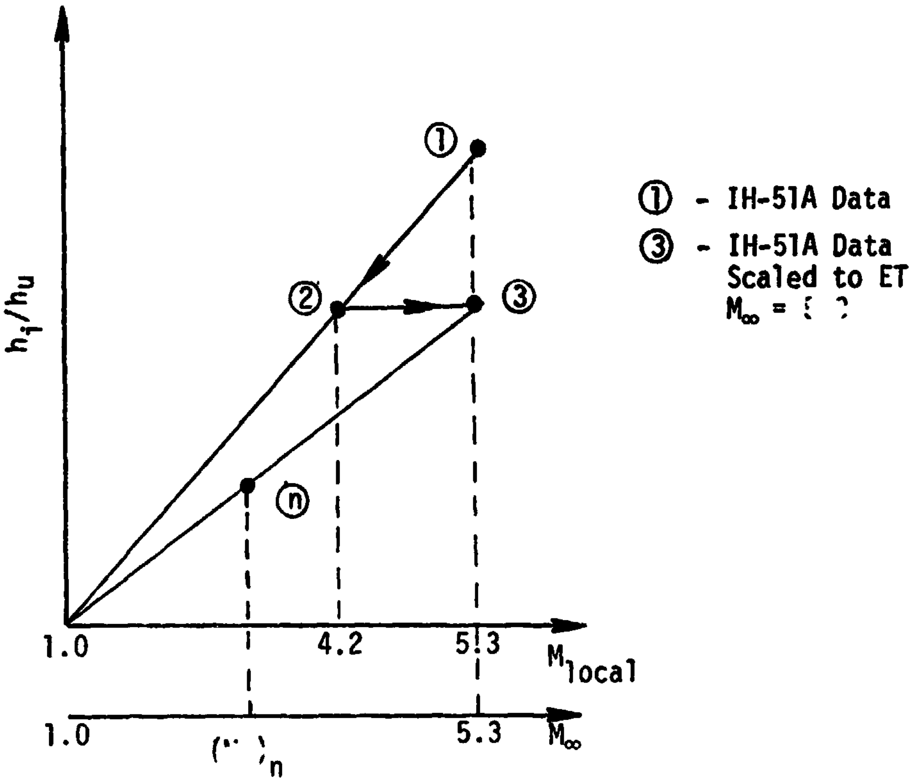

In general, $\log (h_i/h_u) = \log (h_i/h_u)_1 \dfrac{\log M_L}{\log M_1}$

② = ③ $\log (h_i/h_u)_3 = \log (h_i/h_u)_1 \dfrac{\log 4.2}{\log 5.3}$

or $(h_i/h_u)_3 = 10^{(0.860613 \log (h_i/h_u)_1)}$

and $(h_i/h_u)_n = 10^{(1.38069 \log (h_i/h_u)_3 \log (M_\infty)_n)}$

or $(h_i/h_u)_n = 10^{(1.18810 \log (h_i/h_u)_1 \log (M_\infty)_n)}$

Fig. 3.68 Local Mach Number Scaling Procedure for IH-51A Data

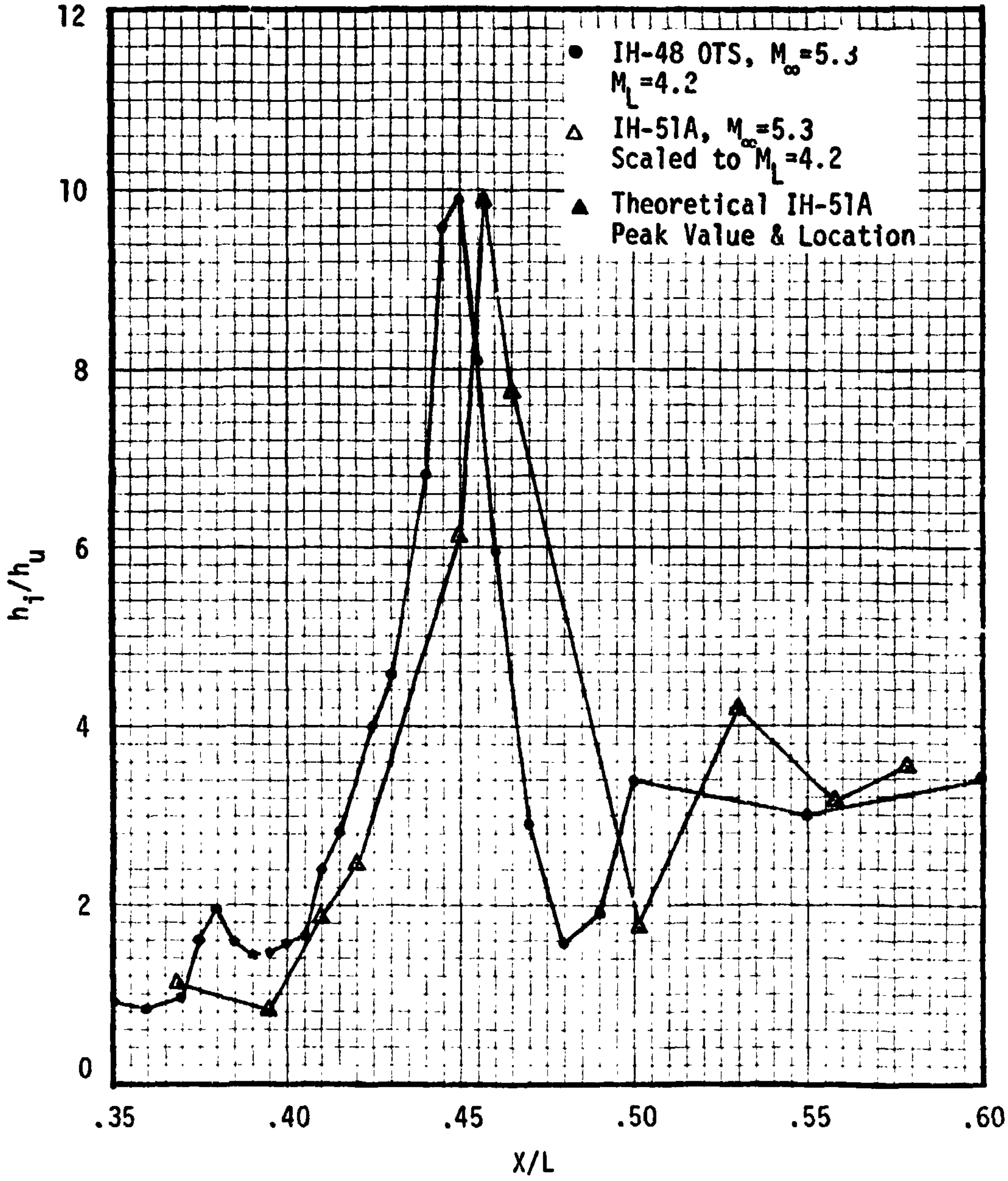

Fig. 3.69 Comparison of IH-48 and Scaled IH-51A Data Along the Centerline (θ_T = 0°)

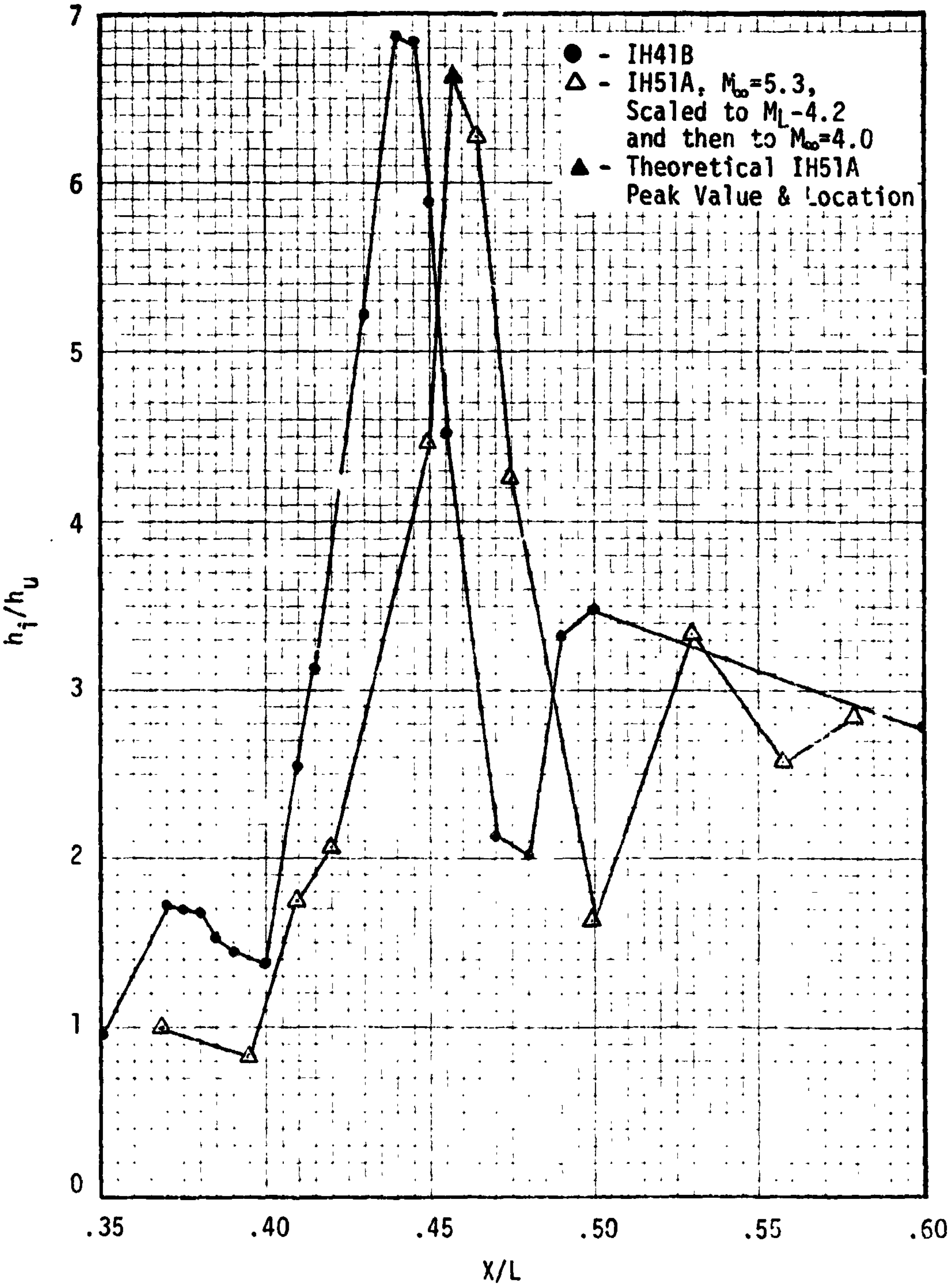

Fig. 3.70 Comparison of IH-41B and Scaled IH-51A Data Along the Centerline (θ_T = 0°)

TABLE 3.9
LO_2 FEEDLINE (IH-61A DATA)
$\Theta_T = 23.5°$

T/C	STA. NO.	X_T (Inches)	h_i/h_u $M_\infty=5.3$ $M_L=5.3$	h_i/h_u $M_\infty=5.3$ $M_L=4.2$	h_i/h_u $M_\infty=4.0$ $M_L=3.55$	COMMENTS			
1	39.457	986.42	13.34	9.29	6.38	Top ℄ Fairing ↓			
2	39.605	990.12	18.28	12.19	7.99				
3	39.910	997.75	10.89	7.81	5.52				
4	40.280	1007.00	5.07	4.04	3.19				
5	40.670	1016.75	2.08	1.88	1.69				
6	41.080	1027.00	.88	.90	.91				
7	39.580	989.50	3.04	2.60	2.22	Fairing Mid-Side Inboard ↓			
8	39.770	994.25	2.30	2.05	1.81				
9	40.145	1003.62	1.63	1.52	1.42				
10	40.545	1013.62	1.05	1.04	1.04				
11	40.945	1023.62	.93	.94	.95				
12	39.580	989.50	3.33	2.82	2.36	Fairing Mid-Side Outboard ↓			
13	39.770	994.25	3.37	2.84	2.38				
14	40.145	1003.62	2.88	2.48	2.13				
15	40.545	1013.62	2.33	2.07	1.83				
16	40.945	1023.62	2.16	1.94	1.73				
17	44.821	1120.52	2.40	2.12	1.87	Side Outboard			
18	44.821	1120.52	4.17	3.42	2.78	Top ℄			
19	44.821	1120.52	5.40	4.27	3.34	Side Inboard			
20	44.821	1120.52	1.47	1.39	1.32	Bottom ℄			
21	45.116	1127.90	2.29	2.04	1.81	Side Outboard			
22	49.196	1229.90	2.04	1.85	1.67	" "			
23	49.196	1229.90	5.86	4.58	3.54	Top ℄			
24	49.196	1229.90	--	--	--	Side Inboard			
25	49.196	1229.90	2.40	2.12	1.87	Bottom ℄			
26	54.726	1368.15	4.83	3.88	3.08	Side Outboard			
27	54.726	1368.15	3.64	3.04	2.52	Top ℄			

-- No Data Available

TABLE 3.9

LO_2 FEEDLINE (Cont.)

T/C	STA. NO.	X_T (Inches)	h_i/h_u $M_\infty=5.3$ $M_L=5.3$	h_i/h_u $M_\infty=5.3$ $M_L=4.2$	h_i/h_u $M_\infty=4.0$ $M_L=3.55$	COMMENTS		
28	54.726	1368.15	6.30	4.37	3.73	Side Inboard		
29	54.726	1368.15	8.89	6.55	4.77	Bottom ℄		
30	55.00	1375.00	9.15	6.72	4.87	Side Outboard		

Table 3.10

LO₂ ANTIGEYSER LINE (IH-51A DATA)

Θ_T = 34°

T/C	STA. NO.	X_T (Inches)	h_i/h_u M_∞=5.3 M_L=5.3	h_i/h_u M_∞=5.3 M_L=4.2	h_i/h_u M_∞=4.0 M_L=3.55	COMMENTS			
31	39.61	990.25	9.87	7.17	5.14	Top ℄ Fairing			
32	39.77	994.25	8.34	6.20	4.56	↓			
33	40.12	1003.00	4.29	3.50	2.83				
34	40.55	1013.83	1.96	1.78	1.62				
35	40.93	1023.25	1.88	1.72	1.57				
36	41.34	1033.38	2.08	1.88	1.69				
37	39.78	994.50	3.40	2.87	2.40	Fairing Mid-Side Inboard			
38	40.02	1000.50	2.94	2.53	2.16	↓			
39	40.42	1010.50	3.10	2.65	2.25				
40	40.82	1020.50	.11	.15	.21				
41	41.22	1030.50	1.98	1.80	1.63				
42	39.78	994.50	5.07	4.04	3.19	Fairing Mid-Side Outboard			
43	40.02	1000.50	2.70	2.35	2.04	↓			
44	40.42	1010.50	--	--	--				
45	40.82	1020.50	1.02	1.02	1.01				
46	42.92	1072.90	2.01	1.82	1.65	Top ℄ Line			
47	42.92	1072.90	1.51	1.43	1.34	Bottom ℄ Line			
48	53.05	1326.15	5.40	4.27	3.34	Top ℄ Line			
49	53.05	1326.15	7.79	5.85	4.34	Bottom ℄ Line			
50	55.82	1395.40	3.67	3.06	2.53	Top ℄ Line			
51	55.82	1395.40	5.13	4.08	3.22	Bottom ℄ Line			

-- No Data Available

TABLE 3.11
ELECTRICAL CONDUIT (IH-51A DATA)
$\Theta_T = 37.7°$

T/C	STA. NO.	X_T (Inches)	h_f/h_u $M_\infty=5.3$ $M_L=5.3$	h_f/h_u $M_\infty=5.3$ $M_L=4.2$	h_f/h_u $M_\infty=4.0$ $M_L=3.55$	COMMENTS			
52	42.960	1074.00	3.91	3.23	2.65	Top ℄ Cable			
53	52.846	1321.15	4.71	3.79	3.03	↓			
54	52.846	1321.15	5.56	4.38	3.41	Bottom ℄ Cable			
55	53.046	1326.15	4.95	3.96	3.14	Top ℄ Cable			
56	53.046	1326.15	4.35	3.54	2.86	Bottom ℄ Cable			
57	55.816	1395.40	3.77	3.13	2.58	Top ℄ Cable			
58	55.816	1395.40	--	--	--	Bottom ℄ Cable			

-- No Data Available

TABLE 3.12

GH_2 PRESSURE LINE (IH-51A DATA)

Θ_T = 330°

T/C	STA. NO.	X_T (Inches)	h_i/h_u M_∞=5.3 M_L=5.3	h_i/h_u M_∞=5.3 M_L=4.2	h_i/h_u M_∞=4.0 M_L=3.55	COMMENTS		
59	42.654	1066.35	4.55	3.68	2.96	Top ℄ Fairing		
60	42.809	1070.22	3.56	2.98	2.48	↓		

3.5 References

1. Berthold, C. L., "Pretest Information for 0.04-Scale SSV Interference Heating Tests on a Thin-Skin Thermocouple Model (58-OT) Utilizing a Simulated External Tank and Orbiter Forebody in the NASA/ARC 3.5-foot Hypersonic Wind Tunnel, Test IH-51A", Rockwell Report SD 77-SH-0156, June 6, 1977.

2. Dirling, Jr., R. B., "A Method for Computing Rough Wall Heat Transfer Rates on Reentry Nosetips," AIAA Paper No. 73-763, July 1973.

3. Engel, C. D., Rosner, H. R., "Method of Characteristic Flow Fields For The External Tank (M_∞ = 2.5 To 8.0)", REMTECH Report RM 022-2, March 1977.

SECTION 4

FH-15 AND FH-16 DATA

Data obtained from the Heat Transfer Test (FH-15) and the Heat Transfer Test (FH-16) are described in this section. FH-15 was conducted at the Arnold Engineering Development Center, Von Karman Gas Dynamics Facility (AEDC/VKF) Supersonic Tunnel A, and FH-16 was conducted at the NASA-Ames 3.5 Foot Hypersonic Windtunnel Facility. Both tests used a .0275 scale thin-skin model of the 30°/10°/40° Cone-Ogive External Tank Forebody. The FH-14 10°/40° Cone-Ogive .0275 scale thin-skin ET forebody heat transfer model was modified by truncating the 10° and 5.2 inches full scale with a 30° cone. Instrumentation was refurbished and 100 new T/C's added to obtain more detailed protuberance heating data. The data in this analysis was obtained from a facility printout. This section provides a test discription, reduced data, and plots to show interference factors for the nose, the forward fairing and fairing sides of the forward electrical conduit, the T/C's infront of the attachment fittings, and the T/C's beside the attachment fittings.

4.1 Test Description

The Heat Transfer Test (FH-15) and the Heat Transfer Test (FH-16) were conducted using a 0.0275 scale thin skin model of the 30°/10°/40° Cone-Ogive External Tank Forebody. The model consists of a modification to the 10°/40° cone ogive 0.0275 scale thin skin ET forebody (Fig. 4.1). The design change was to truncate the 10° cone 5.2 inches full scale with a 30° cone to increase the differential pressure and sensitivity for the Ascent Air Data System (AADS) for angle-of-attack and sideslip flight evaluation (Fig. 4.2).

The model was instrumented with the refurbished original 150 thermocouples (T/C's) used in FH-14 and with 100 new T/C's that were added to obtain more detailed protuberance heating data. The 100 additional T/C's, 151 through 250, are shown on Figs. 4.3a and b. Figures 4.4a and b show the T/C's on and around the protuberances. The tests conditions were repeated with protuberances on and off to provide a matrix of heating interference factors around all perturbed flow areas. The objectives of the tests as stated in Refs. 4.1 and 4.2 were:

To measure the change in heating due to the small change in the baseline nose spike.

To obtain heating and location of shock impingement areas.

To obtain increased interference heating (h_i) details on the skin around the forward fairing, trays, and GO_2 pressurization line mounting brackets to be ratioed to the clean heating (h_u) at the same location.

The tests were conducted under the following nominal conditions:

FH-15

M_∞	$Re_\infty/ft \times 10^{-6}$	P_0 (psia)	T_0 (°R)
3.01	3.7	36.0 ± .2	720 ± .5
4.01	↓	65, 63 ± .2	740, 720 ± .5
5.5	↓	127.0 ± .2	720 ± .5
5.5	5.0	174, 172 ± .2	730, 720 ± .5

FH-16

M_∞	$Re_\infty/ft \times 10^{-6}$	P_0 (psia)	T_0 (°R)
5.3	5.0	405.	1300.

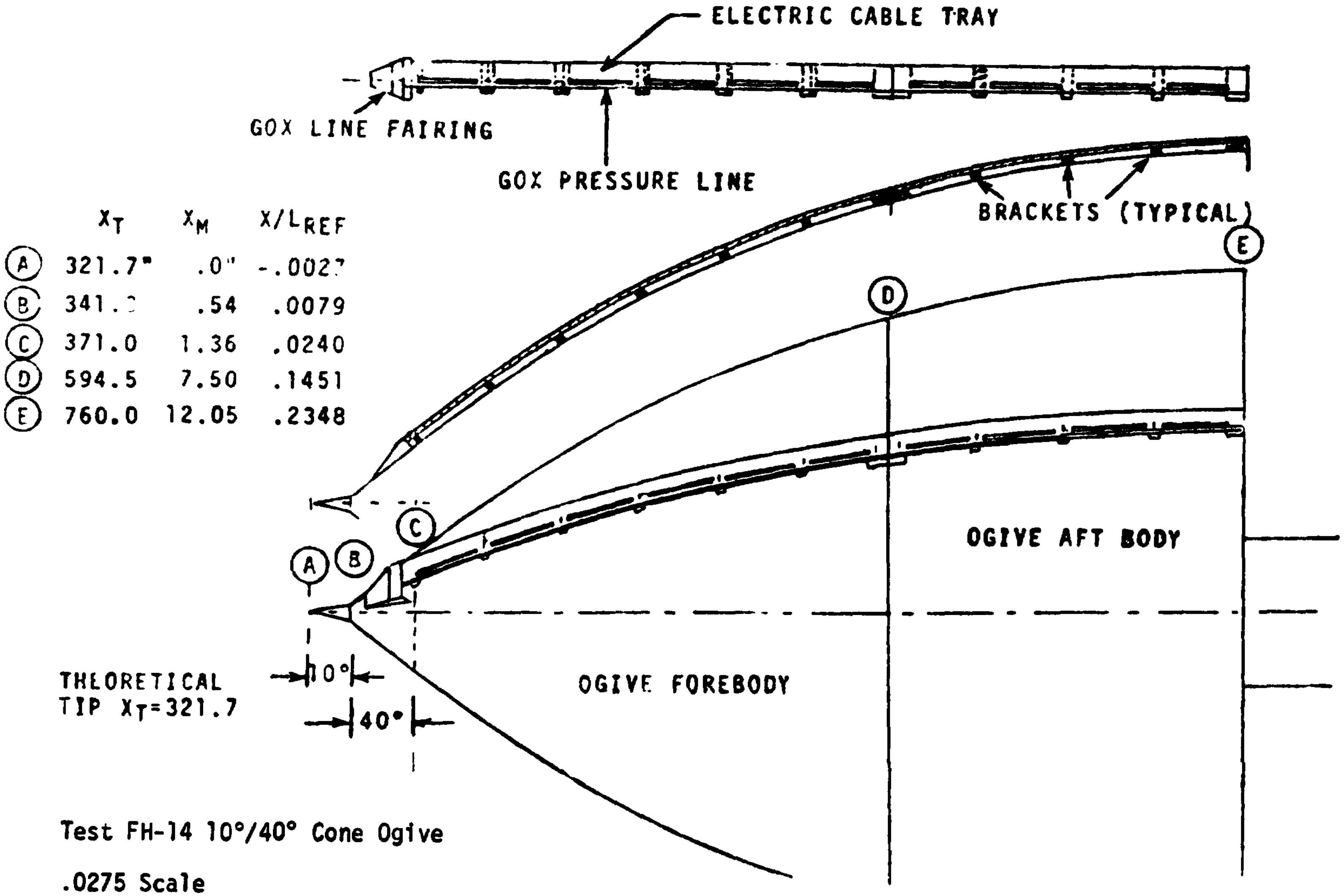

	X_T	X_M	X/L_{REF}
Ⓐ	321.7"	.0"	-.0027
Ⓑ	341.0	.54	.0079
Ⓒ	371.0	1.36	.0240
Ⓓ	594.5	7.50	.1451
Ⓔ	760.0	12.05	.2348

Test FH-14 10°/40° Cone Ogive

.0275 Scale

Note: Full scale body stations are shown with corresponding model scale dimensions.

Fig. 4.1 Basic Forebody of the External Tank 10° AADS/Lightning Rod, 40° Vent Cap, Ogive with External Hardware, Forward Fairing, Electrical Trays, GO_X Line in Supporting Brackets (Ref. 4.2)

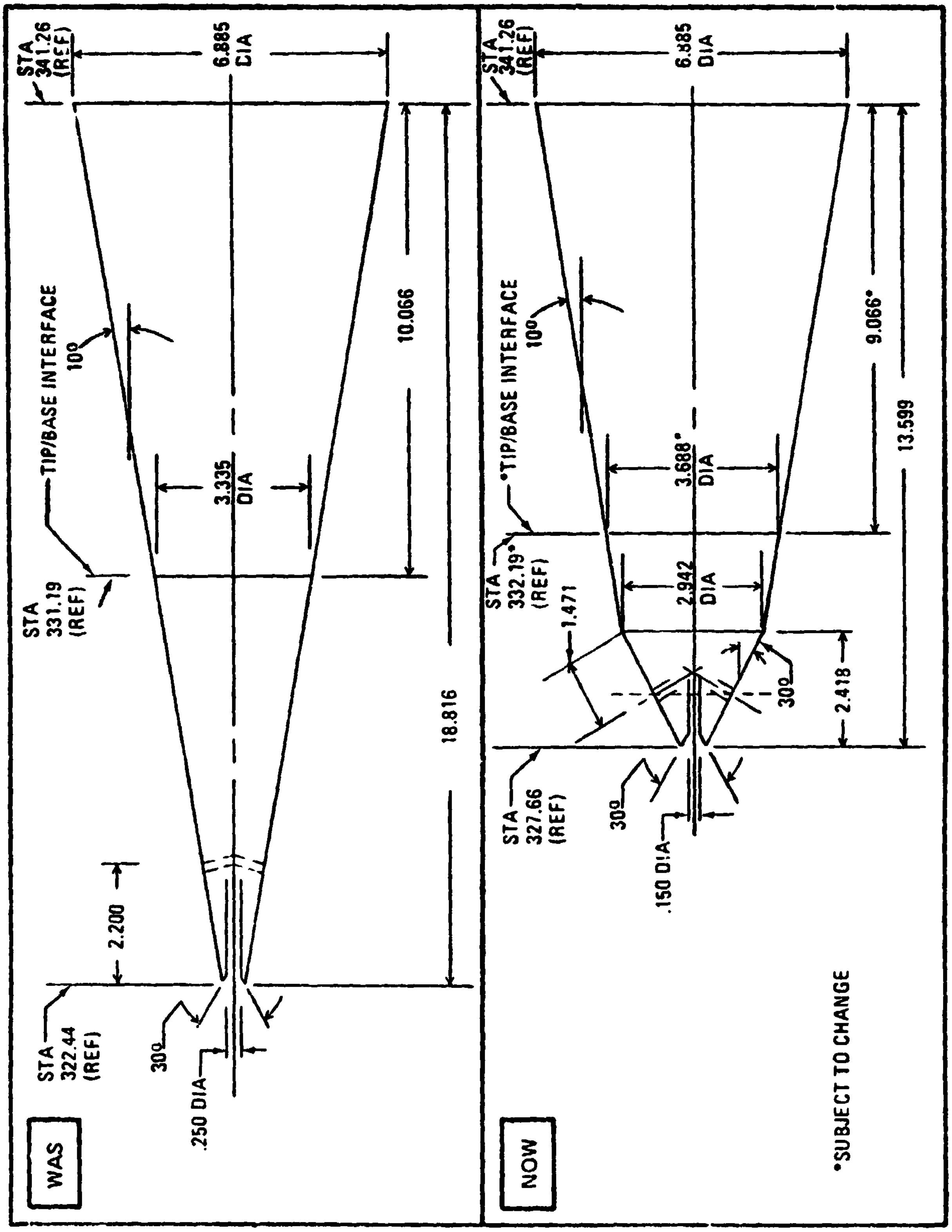

Fig. 4.2 Full Scale Change to 10° Nose Spike to Obtain a 30° Cone Face (AADS Change) (Ref. 4.2)

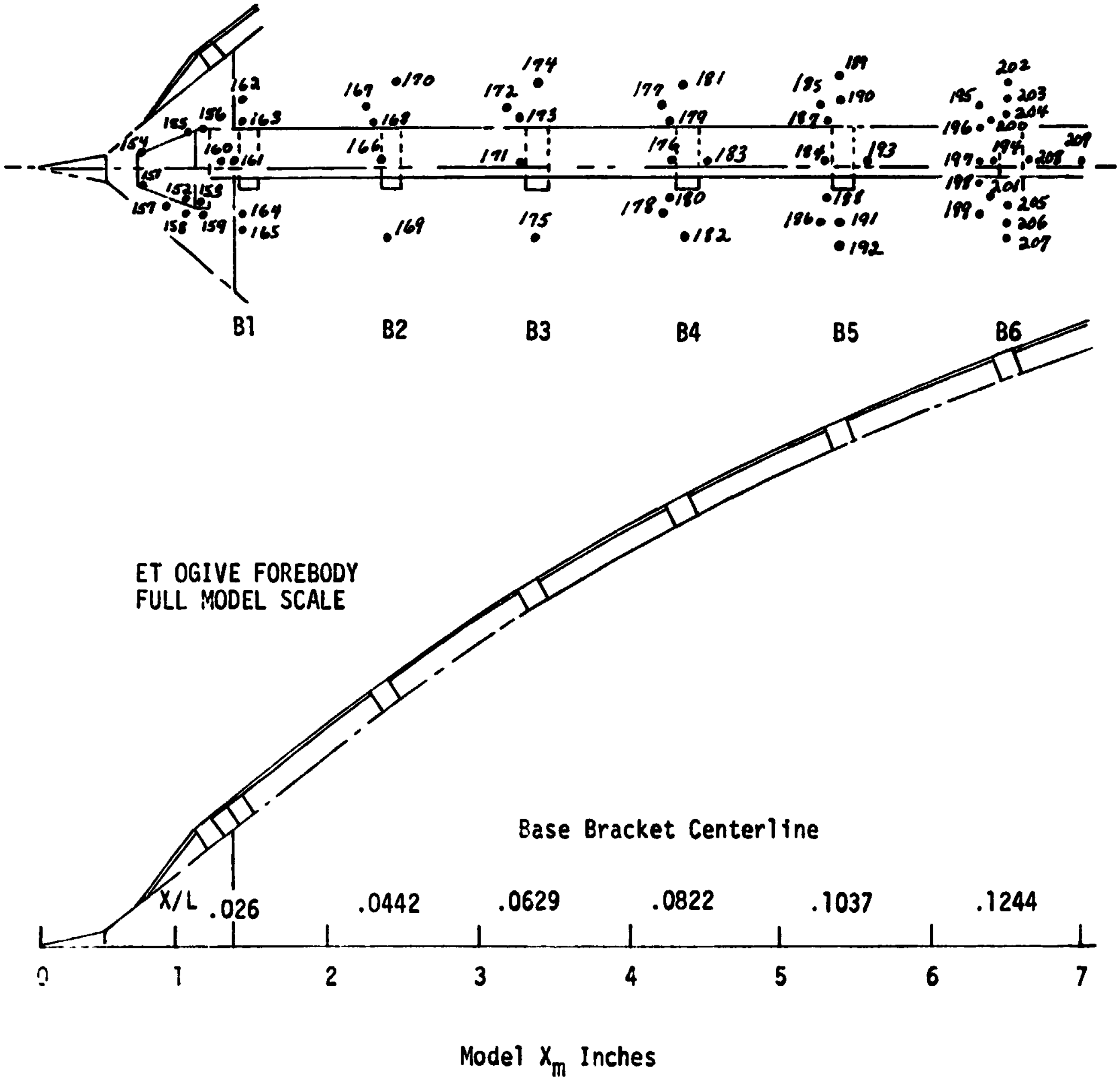

Fig. 4.3a New Instrumentation Locations .0275 Scale ET Forebody FH-15 and 16 (Ref. 4.1)

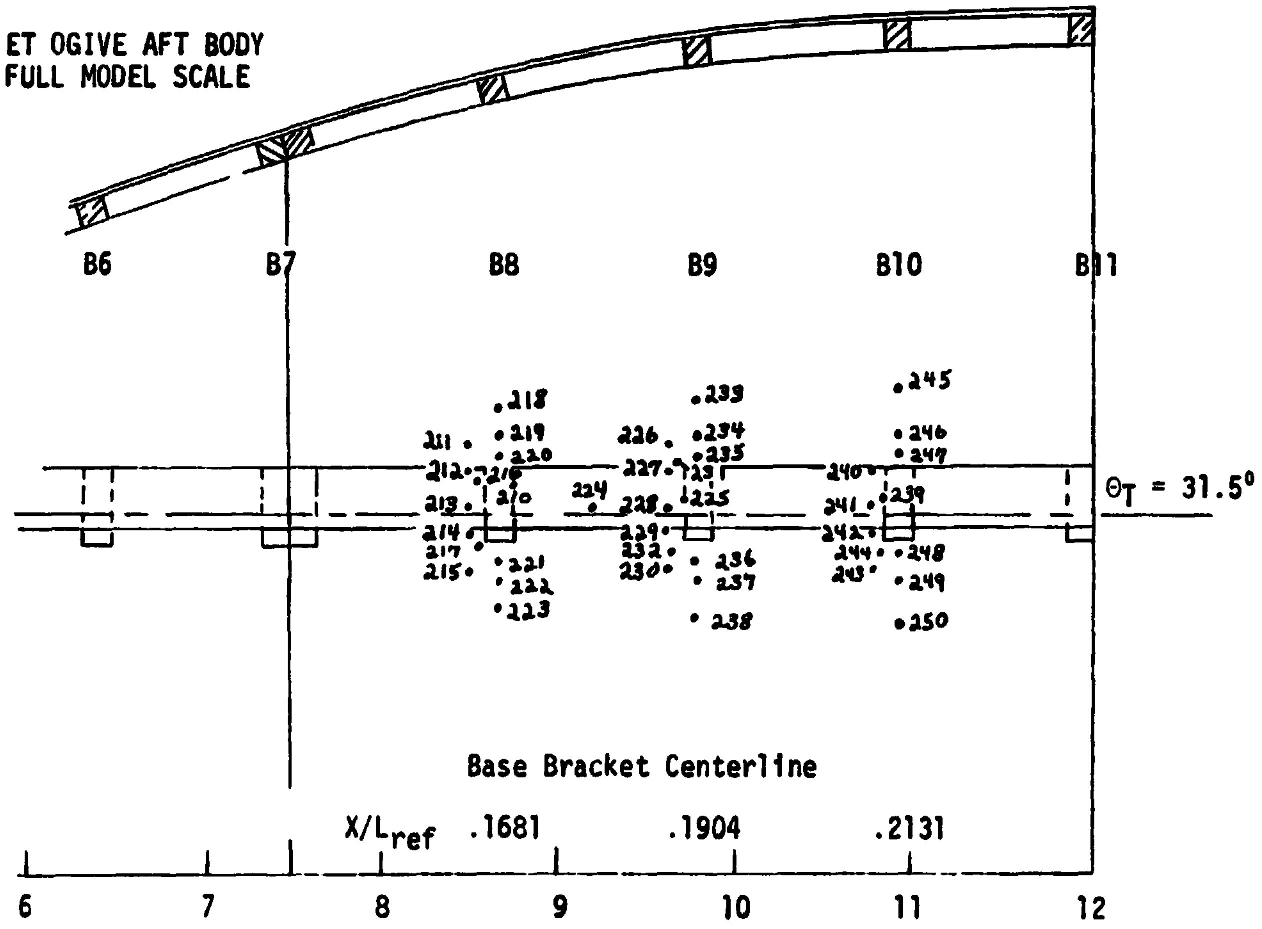

Fig. 4.3b New Instrumentation Locations .0275 Scale ET Forebody FH-15 and 16 (Ref. 4.2)

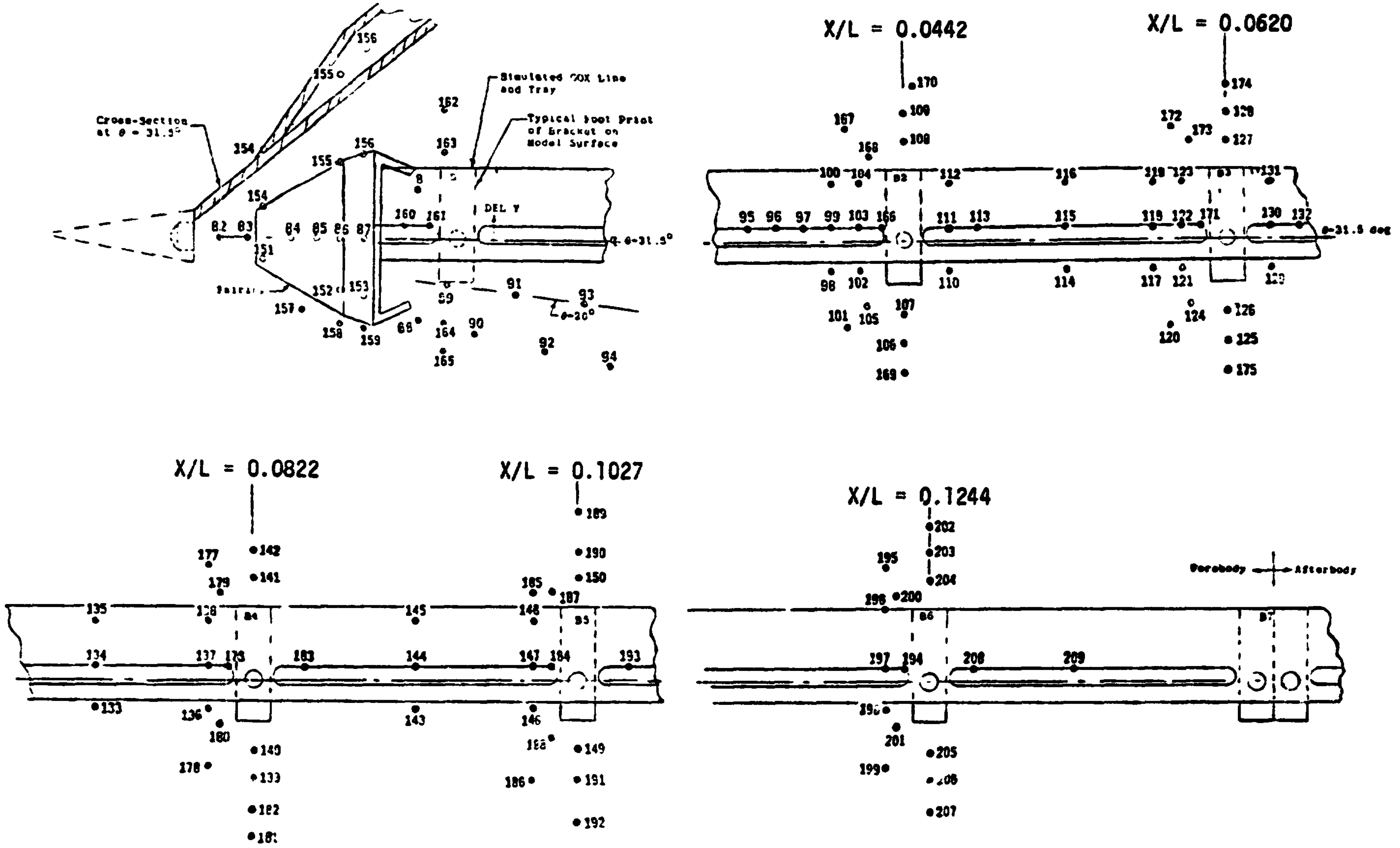

Fig. 4.4a 2X Enlargement of T/C Locations on the ET .0275 Scale Heat Transfer Model (Ref. 4.1)

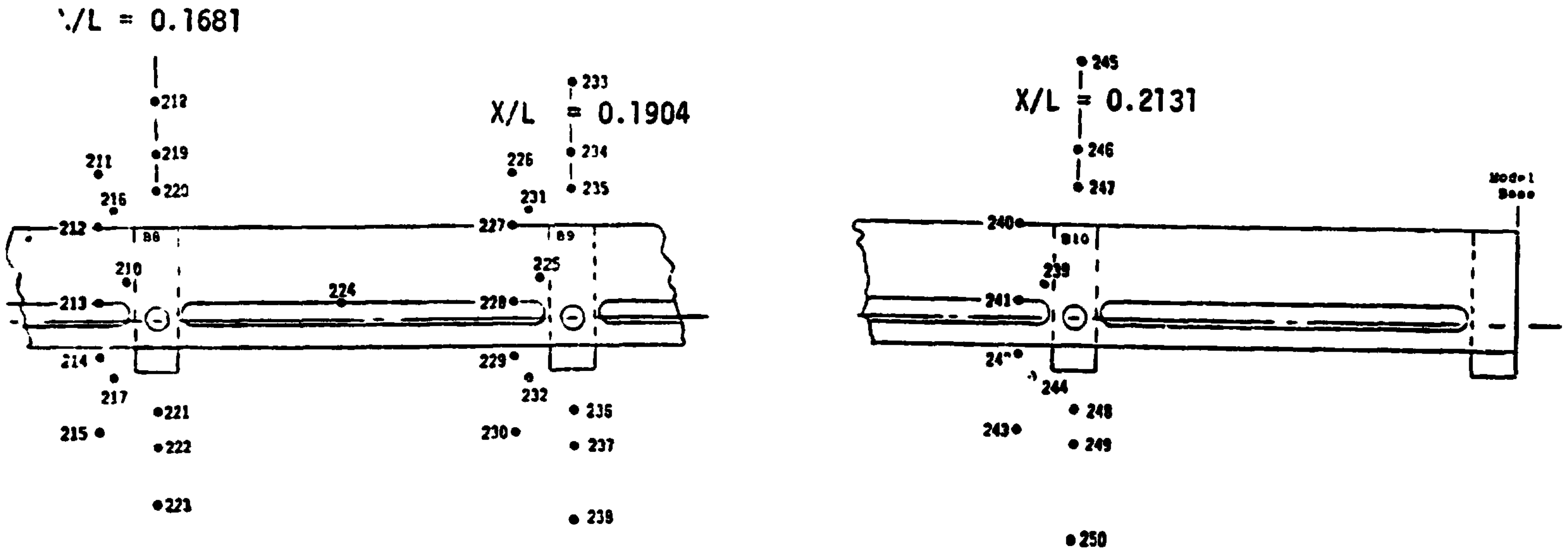

Fig. 4.4b 2X Enlargement of T/C Locations on the ET .0275 Scale Heat Transfer Model (Ref. 4.1)

4.2 Data Reduction

FH-15 and FH-16 heating data were reduced by nondimensionalizing the heat transfer coefficient data with the calculated undisturbed data h_u/h_{ref}.

The heat-transfer coefficient ratios h_u/h_{ref} are calculated by the modified MINIVER program called MINETT (MINIVER ET Tunnel).

The MINETT Computer program was used to calculate the heat-transfer rates on the ET model by the math model described in Ref. 4.3. MINETT was run by using the following options:

- 39.38 Deg. Cone Shock Entropy
- MOC Correlated Pressures
- Spalding-Chi skin friction correlation
- Reynolds number correction factor (Ref. 4.3)
- Von Karman Reynolds Analogy

FH-15 and FH-16 heating data were reduced to $(h_i)_{Data}/(h_u)_{Theory}$ for all thermocouple (T/C) locations for all runs of the tests. For FH-15 the undisturbed heat-transfer coefficient is calculated from the measurement of heat-transfer rate, total temperature, and wall temperature by using the heat transfer coefficient and $\overline{Ru}$ Waiter Calculations based on the discussion in Ref. 4.4 in the following manner:

$$h_u = \dot{q}_u/(\overline{Ru}\ T_0 - T_w) \tag{1}$$

where $\overline{Ru}$ is defined by

$$\overline{Ru} = \frac{T_{aw}}{T_0} = \frac{1 + r_f(\gamma-1)\ M_e^2/2}{1 + (\gamma-1)\ M_e^2/2} \tag{2}$$

and $r_f = 0.90$ for turbulent fl

The heat-transfer coefficient ratios h_u/h_{ref} were calculated with the same value of the undisturbed temperature efficiency $\overline{Ru}$ as used in the data reduction.

In FH-16 because the total temperature becomes so high that Cp becomes dependent on temperature, the heat-transfer coefficient is calculated based on enthalpy instead of temperature. The temperature dependence is factored out of the measured heat-transfer rates to make the data independent of wall temperature which could vary from point to point on the body. For FH-16 the heat transfer coefficient is calculated by using

$$h_u = \dot{q}_u/(\overline{Ru}\ H_t - H_w) \tag{3}$$

In order to reduce the heat-transfer data using Eq. (1) and (3), $\overline{Ru}$ has to be supplied from Eq. (2). M_e in Eq. (2) was calculated by using tangent-cone approximations to provide a correlation given by

$$\begin{aligned} \overline{Ru} &= a_1 + a_2 (\text{Sin } \alpha_L)a_3 \quad \text{for } \alpha_L > 0 \\ &= a_1 \qquad\qquad\qquad\quad \text{for } \alpha_L \leq 0 \end{aligned} \tag{4}$$

where α_L at any point on the ET body is the local angle of attack related to α, β, Θ_T, and δ_b by (for small α, β)

$$\alpha_L = -\alpha \text{ Cos } \Theta_T + \beta \text{ Sin } \Theta_T + \delta_b \tag{5}$$

The constants a_1, a_2, and a_3 are given in Table 4.1

Table 4.1

TEMPERATURE EFFICIENCY FACTOR CONSTANTS

M_∞	a_1	a_2	a_3
3	0.9345	0.1004	2.17
4	0.922	0.1004	1.967
5.3	0.914	0.1004	1.73
5.5	0.913	0.1004	1.695

The body angle δ_b on various portions of the ET surface is given by

$$
\begin{aligned}
\delta_b &= 30^\circ && \text{for } 0 \leq X/L \leq 0.00131 \\
&= 10^\circ && \text{for } 0.00131 \leq X/L \leq 0.00737 \\
&= 39.38^\circ && \text{for } 0.00737 \leq X/L \leq 0.0235 \\
&= \tan^{-1}\left[\frac{(0.2339 - X/L)}{[0.11 - (0.2339 - X/L)^2]^{0.5}}\right] && \qquad (6) \\
& && \text{for } 0.0235 \leq X/L \leq 0.2339 \\
&= 0^\circ && \text{for } 0.2339 \leq X/L \leq 0.93
\end{aligned}
$$

This work has all been calculated with reference to the new 30°/10°/40° nose. To translate back into the 10°/40° configuration use the following relationship

$$X/L_{10^\circ/40^\circ} = X/L_{30^\circ/10^\circ/40^\circ} + 0.0027$$

To find the effective value of angle of attack at the individual thermocouples use

$$\alpha_{eff} = -\alpha \operatorname{Cos} \Theta_T + \beta \operatorname{Sin} \Theta_T \qquad (7)$$

Tables 4.2 and 4.3 lists the h_u/h_{ref} values for the tests conditions. These values were used to reduce the heating data by nondimensionalizing the heat transfer rate with the undisturbed interpolated heat transfer coefficient in the following manner:

$$(h_i/h_{ref})/(h_u/h_{ref})$$

The h_u/h_{ref} values for X/L and angle of attack of the T/C are calculated by a double interpolation using the parameters in Tables 4.2 and 4.3. A semi-log interpolation was performed to calculate the corresponding h_u/h_{ref} for the X/L for each of the thermocouples. The linear interpolation computes the α_{eff} h_u/h_{ref} value. This final h_u/h_{ref} value is used to nondimensionalize the heat transfer coefficient. Plots of the reduced data from Ref. 4.5 are presented in the next subsection.

Table 4.2

FH-15 THEORETICAL HEATING PARAMETERS

M_∞ —	3.01	.13601 — P_∞(psia)				
h_u/h_{ref} —	.8594	.8616	.8496	.8228	.7752	.6936
	.7237	.7254	.7150	.6920	.6515	.5810
	.69967	.7024	.6937	.6729	.6351	.5700
	.51001	.5245	.5269	.5220	.5084	.4809
	.43277	.4520	.4591	.4607	.4560	.4422
	.40558	.4265	.4352	.4388	.4371	.4278
	.32309	.3490	.3620	.3717	.3782	.3805
	.20197	.2327	.2495	.2643	.2780	.2908
	.12380	.1504	.1651	.1790	.1920	.2048
	.10662	.1247	.1348	.1443	.1534	.1624
M_∞ —	4.02	.13681 — P_∞(psia)				
h_u/h_{ref} —	.83013	.8431	.8431	.8332	.8178	.7768
	.69684	.7080	.7080	.6999	.6820	.6510
	.67204	.6838	.6844	.6776	.6615	.6324
	.47557	.4954	.5032	.5060	.5026	.4919
	.39531	.4190	.4300	.4369	.4390	.4355
	.36795	.3923	.4043	.4126	.4166	.4156
	.28338	.3115	.3267	.3390	.3483	.3542
	.16262	.1929	.2111	.2270	.2411	.2539
	.08785	.1136	.1283	.1420	.1552	.1685
	.07173	.0689	.0991	.1093	.1192	.1293
M_∞ —	5.3	.13681 — P_∞(psia)				
h_u/h_{ref} —	.9245	.9407	.9423	.9326	.9105	
	.7905	.8048	.8060	.7978	.7785	
	.7630	.7781	.7805	.7734	.7436	
	.5407	.5651	.5759	.5798	.5759	
	.4477	.4760	.4903	.4992	.5051	
	.4148	.4446	.4601	.4706	.4748	
	.3143	.3481	.3669	.3820	.3931	
	.1712	.2074	.2286	.2475	.2642	
	.0827	.1127	.1301	.1468	.1628	
	.0639	.0836	.0957	.1079	.1203	
M_∞ —	5.501	.13681 — P_∞(psia)				
h_u/h_{ref} —	.7587	.7777	.7819	.7779	.7635	.7369
	.6314	.6475	.6512	.6476	.6353	.6126
	.6073	.6240	.6283	.6256	.6145	.5933
	.4190	.4410	.4506	.4553	.4543	.4464
	.3433	.3678	.3798	.3877	.3910	.3887
	.3170	.3422	.3551	.3641	.3451	.3686
	.2378	.2643	.2808	.2932	.3021	.3075
	.1282	.1561	.1722	.1877	.2008	.2121
	.0556	.0838	.0971	.1103	.1226	.1344
	.0468	.0610	.0709	.0806	.0902	.0999
M_∞ —	5.501	.18651 — P_∞(psia)				
h_u/h_{ref} —	.8266	.8469	.8509	.8462	.8299	.8015
	.6924	.7093	.7134	.7087	.6951	.6709
	.6663	.6843	.6883	.6850	.6730	.6503
	.4619	.4860	.4963	.5014	.5002	.4920
	.3790	.4060	.4190	.4276	.4312	.4291
	.3501	.3778	.3919	.4018	.4070	.4070
	.2631	.2934	.3102	.3238	.3338	.3400
	.1413	.1772	.1901	.2063	.2218	.2345
	.0672	.0923	.1071	.1213	.1349	.1484
	.0514	.0679	.0781	.0886	.0992	.1103
α_{eff} —	0.0	3.0	5.0	7.0	9.0	11.0
X/L —	0.0145	0.02348	0.02572	0.05069	.06815	
	0.07560	0.10057	0.15050	0.20022	.22913	

Table 4.3

FH-16 THEORETICAL HEATING PARAMETERS

M_∞ —	5.3	.13681 — P_∞(psia)			
h_u/h_{ref} —	.9245	.9430	.9423	.9325	.9105
	.7905	.8048	.8050	.7979	.7785
	.[illegible]630	.7791	.7805	.7734	.7436
	.5407	.5651	.5759	.5793	.5759
	.4477	.4750	.4903	.4992	.5051
	.4143	.4446	.4601	.4706	.4748
	.3143	.3491	.3659	.3820	.3931
	.1712	.2074	.2295	.2475	.2642
	.0827	.1127	.1301	.1459	.1628
	.0639	.0835	.0957	.1079	.1203
α_{eff} —	0.0	3.0	5.0	7.0	9.0
X/L —	0.0145	0.02348	0.02572	0.05069	.06915
	0.07556	0.10057	0.15050	0.20022	.22913

ORIGINAL PAGE IS
OF POOR QUALITY

4.3 Data Analysis

Several features of the FH-15 and 16 data are examined in this section. The data is examined in interference factor (h_i/h_u) form where h_u is theoretical. A theoretical undisturbed value was used such that the interference factors will be compatible with theory in flight application work. The features of the data which were examined were:

- Comparison of undisturbed data and theory
- New nose interference on a clean tank
- Interference on the top of the forward fairing of the electrical conduit
- Interference on the side of the forward fairing of the electrical conduit
- Interference on the skin beside the electrical conduit attachment fittings
- Interference on the skin in front of the electrical conduit attachment fittings

Comparisons of undisturbed data and theory were made in the following manner. The undisturbed data to theory ratio (h_d/h_t) was calculated for each thermocouple. The following average was then computed

$$\left(\frac{h_d}{h_t}\right)_{avg} = \frac{\sum\limits_{i=1}^{n} (h_d/h_t)_i}{n} \qquad n = \text{total no. of Thermocouples}$$

where the thermocouples considered were either all thermocouples or only thermocouples along $\Theta_T = 0°$. The X/L range was restricted to 0.03 to 0.2131 to eliminate 30°/10° nose effects. The average values were then plotted versus β as shown in Figs. 4.5 to 4.9. This data indicates that theory and data compare quite well for all Mach numbers and $-6 \leq \beta \leq 6$ degrees. The theory is conservative for $\beta < -6$ degrees.

The influence of the 30°/10° cone on the 40° cone heating is shown in Figs. 4.10 to 4.29. The maximum interference factor occurs at $\alpha = 0$ for all Mach numbers and β's at $\Theta_T = 270°$. The interference is lower than 1.2 for $.019 < X/L \leq .0235$ which is the last 28 percent of the 40 degree cone. The effect of increasing α_{eff} is to decrease the interference factor for windward surfaces. Leeward interference factors are higher than windward for $\beta > 0$ but are lower than for $\beta = 0$ (see Fig. 4.17).

Interference factors on the top centerline of the forward fairing of the electrical conduit are shown in Figs. 4.30 to 4.34. The effect of increasing α_{eff} is to decrease the interference factors for the first three T/C stations at all Mach numbers. The interference factors for the last three stations are much less sensitive to α_{eff} than the first three stations and the interference factor is not a monotonic function of the effective angle of attack.

The interference factors on the side of the forward fairing of the electrical conduit are shown in Fig. 4.35 for a Mach number of 4.02. The angle of attack, α, has a large effect on the heating amplification. The forward T/C location registered large amplifications while the two further back on the fairing registered nominal to smaller values. In fact for $\alpha = -5$ degrees no amplification was measured at the two T/C locations aft of the tip.

The interference factors on the skin beside the electrical conduit attachment fittings are shown in Figs. 4.36 and 4.37 for $M_\infty = 4.02$. The interference factor starts out well below 1.0 and exhibits an increasing trend with increasing X/L. The double bracket at X/L = 0.145 may be the cause in the larger than expected increase at T/C number 221. The effect of β is not the same for each X/L although the magnitude of the change due to changing β is not large.

The interference factors on the skin in front of the electrical conduit attachment fittings are shown in two sets of figures. Figures 4.38 and 4.39 illustrate that the interference in front of the attachment fitting is larger than beside the fittings as was shown in Figs. 4.36 and 4.37. The effect of β on the interference factor is too complex for any general statement. Consequently, "β - plots" were developed for each T/C in front of attachment fittings for four Mach numbers. These plots are given in Figs. 4.40 to 4.44 for three angles of attack. Each fitting has its own behavior. The combination $\alpha = \beta = 0$ yields the highest interference factor in most but certainly not all cases. The highest interference factor measured in front of a fitting was 2.35 which occurred at $M_\infty = 5.3$ on Fig. 4.42.

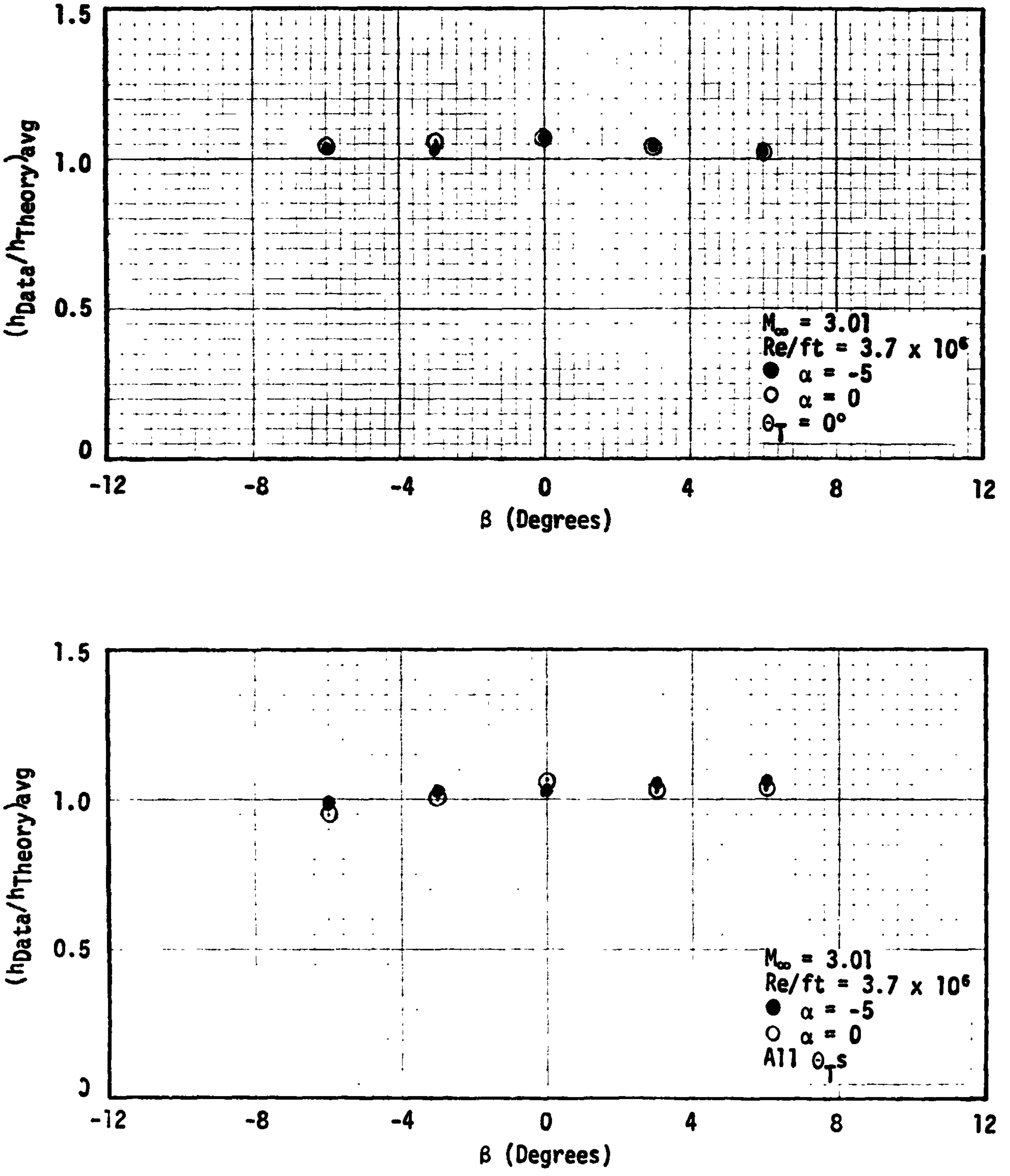

Fig. 4.5 Clean ET Ogive FH-15 Data Divided by Theory and Averaged Over $0.03 \leq X/L \leq 0.2131$ Versus Beta at M_∞ = 3.01 and Re/ft = 3.7 x 10^6

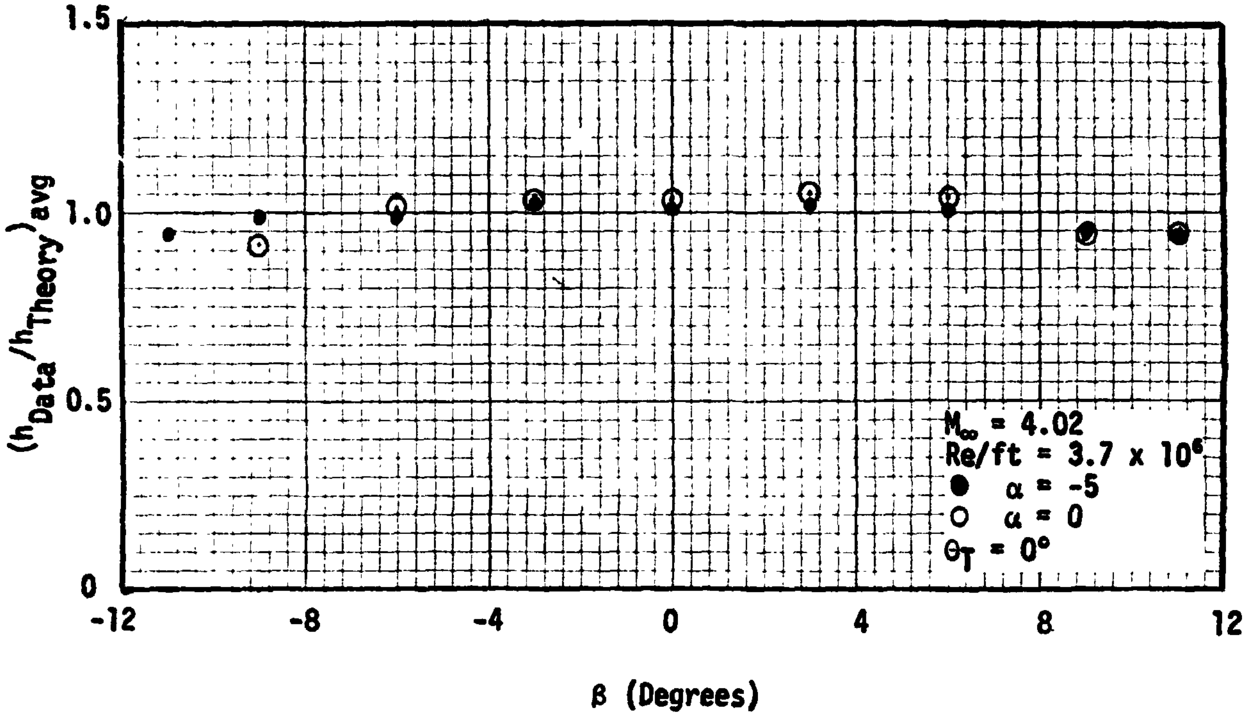

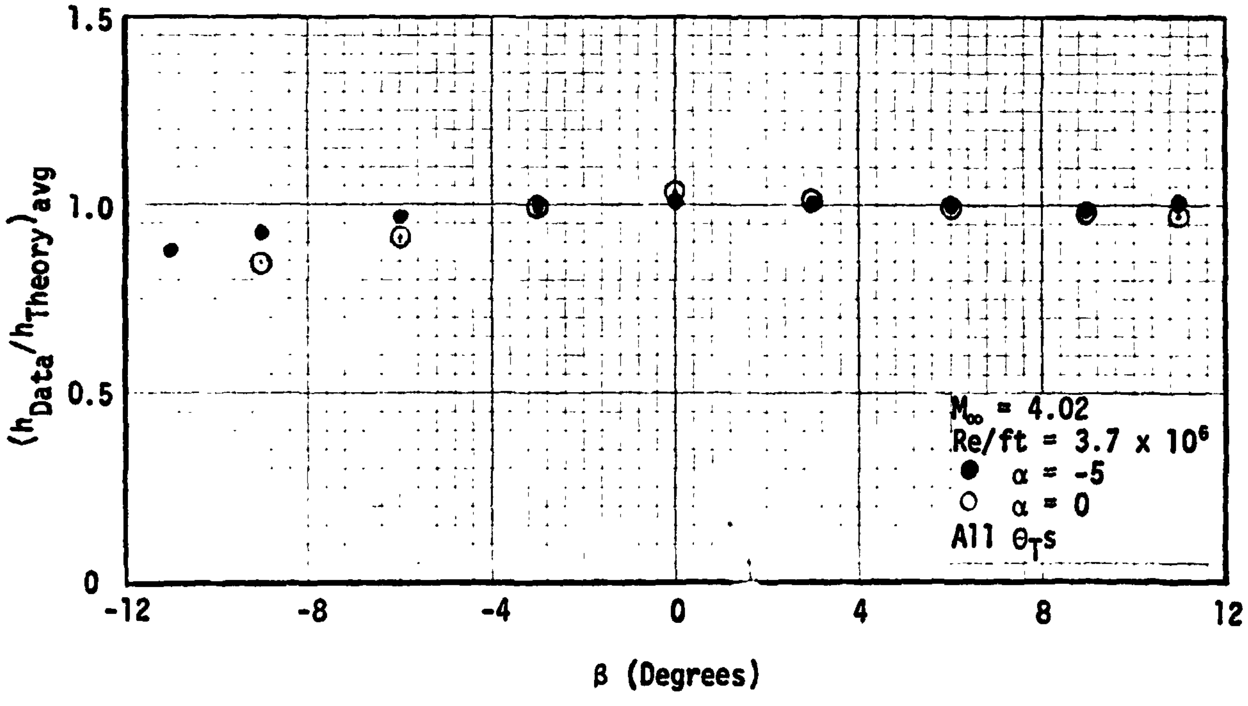

Fig. 4.6 Clean ET Ogive FH-15 Data Divided by Theory and Averaged Over $0.3 \leq X/L \leq 0.2131$ Versus Beta at M_∞ = 4.02 and Re/ft = 3.7 x 10^6

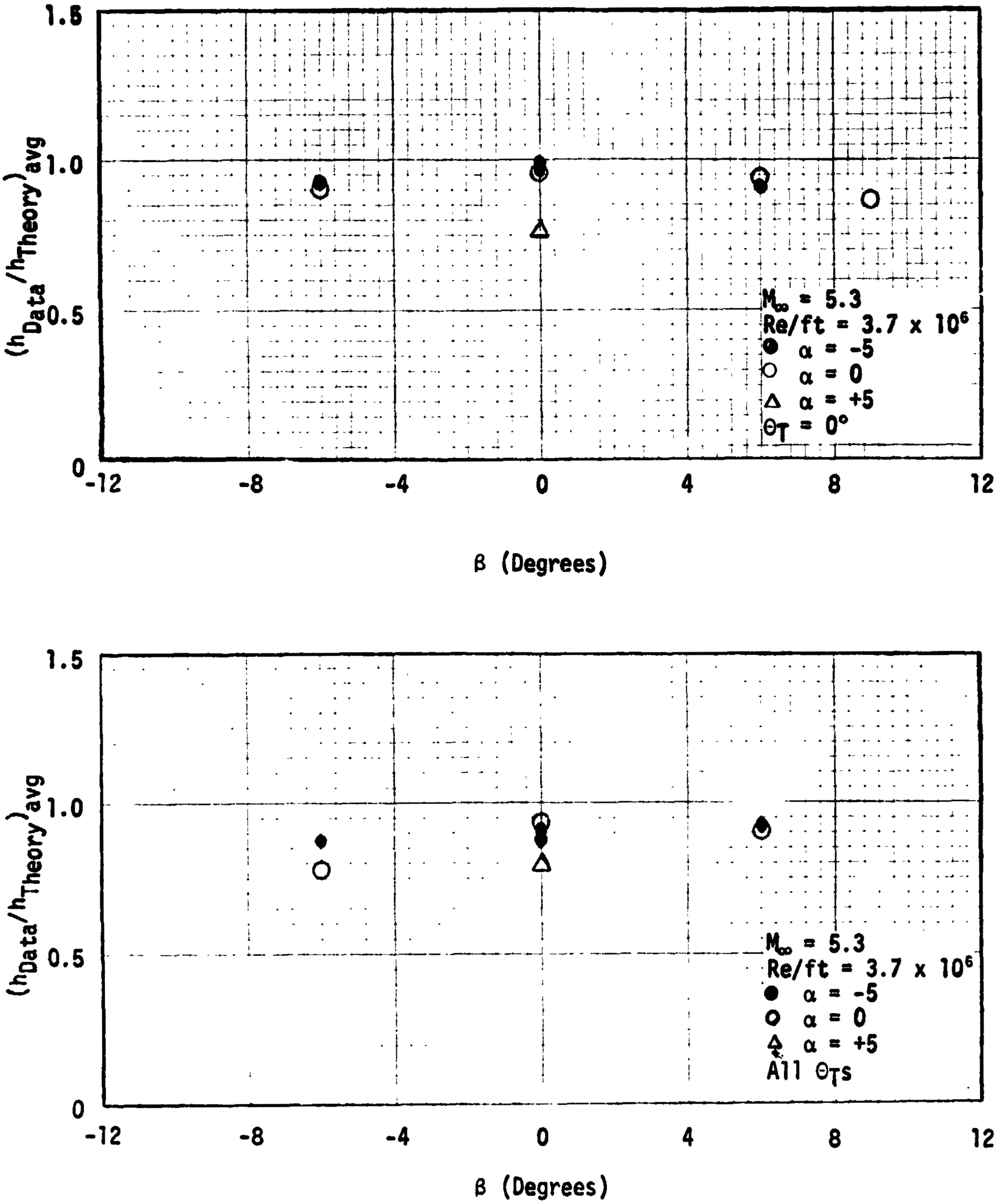

Fig. 4.7 Clean ET Ogive FH-16 Data Divided by Theory and Averaged Over $0.03 \leq X/L \leq 0.2131$ Versus Beta at M_∞ = 5.3 and Re/ft = 3.7 x 10^6

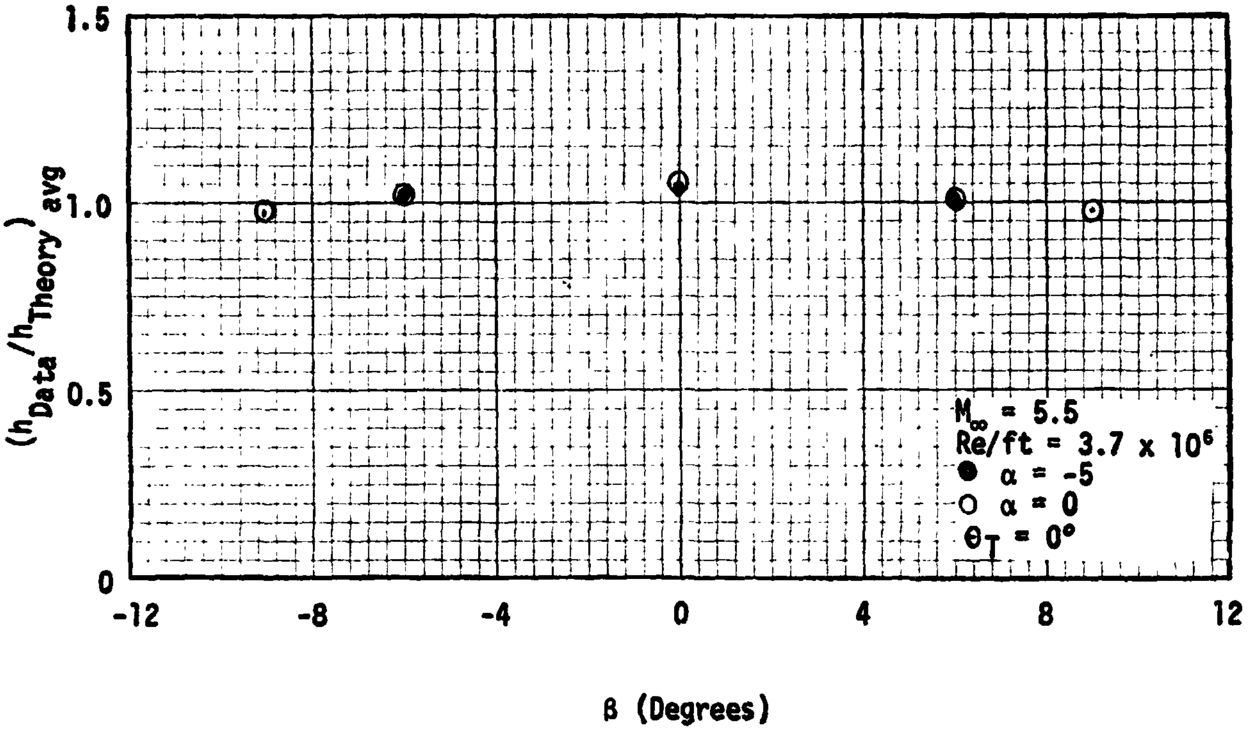

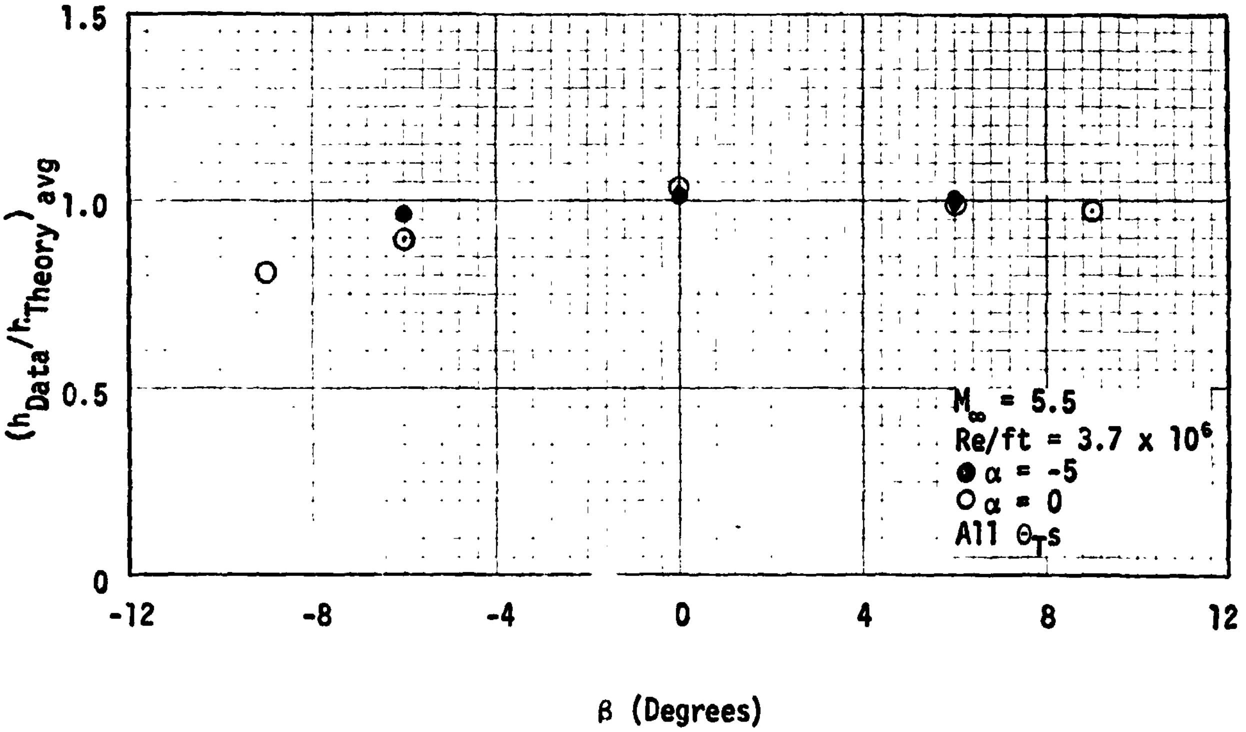

Fig. 4.8 Clean ET Ogive FH-15 Data Divided by Theory and Averaged Over $0.03 \leq X/L \leq 0.2131$ Versus Beta at M_∞ = 5.5 and Re/ft -3.7 x 10^6

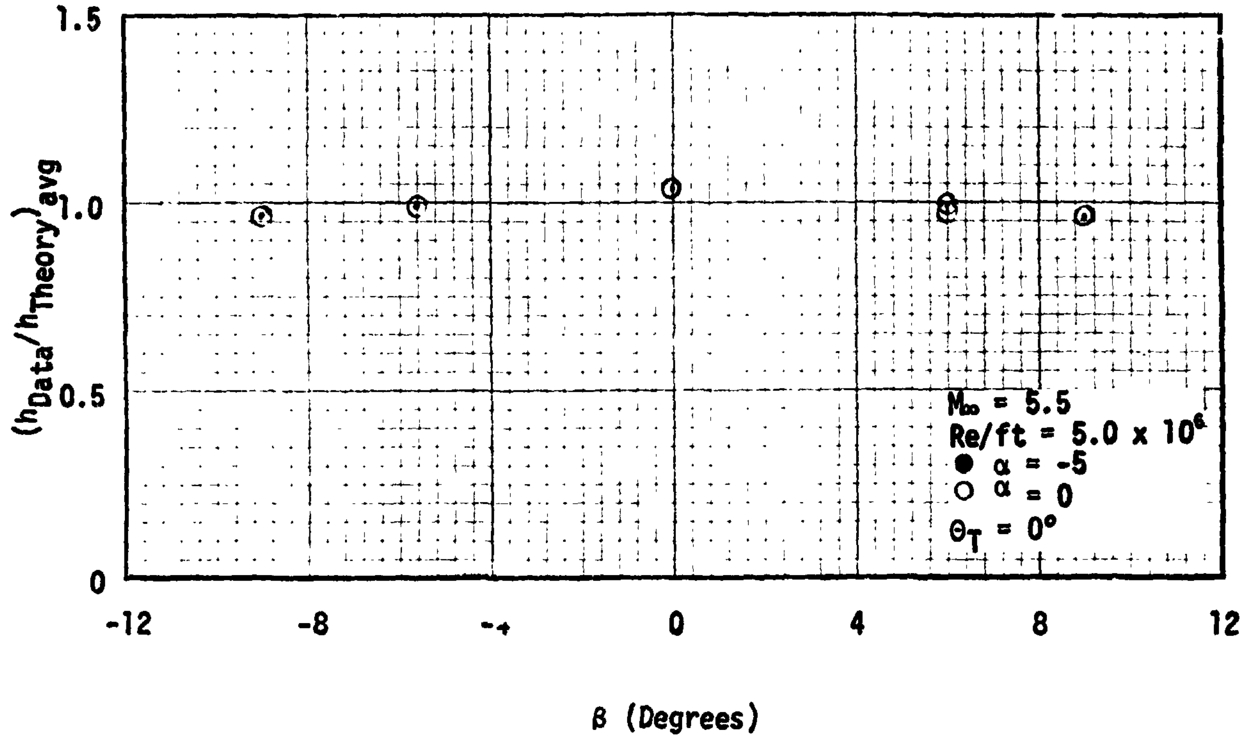

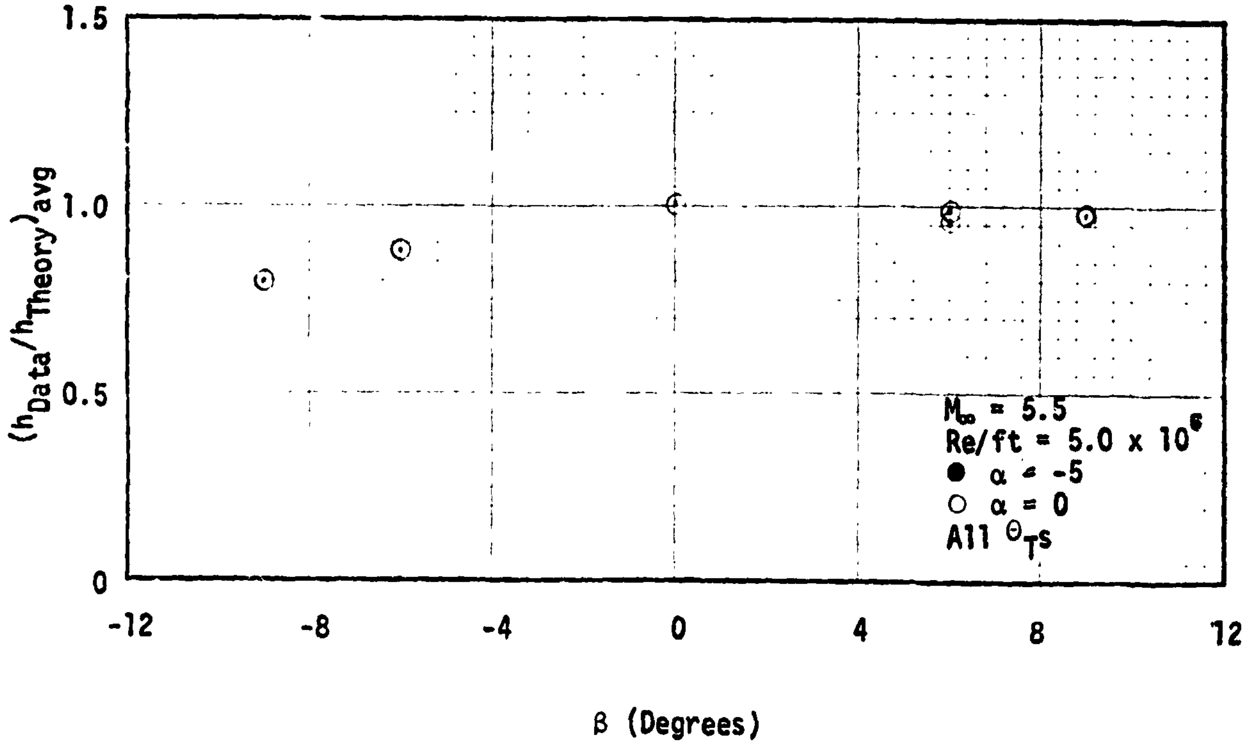

Fig. 4.9 Clean ET Ogive FH-15 Data Divided by Theory and Averaged Over $0.03 \leq X/L \leq 0.2131$ Versus Beta at M_∞ = 5.5 and Re/ft =5.5 x 10^6

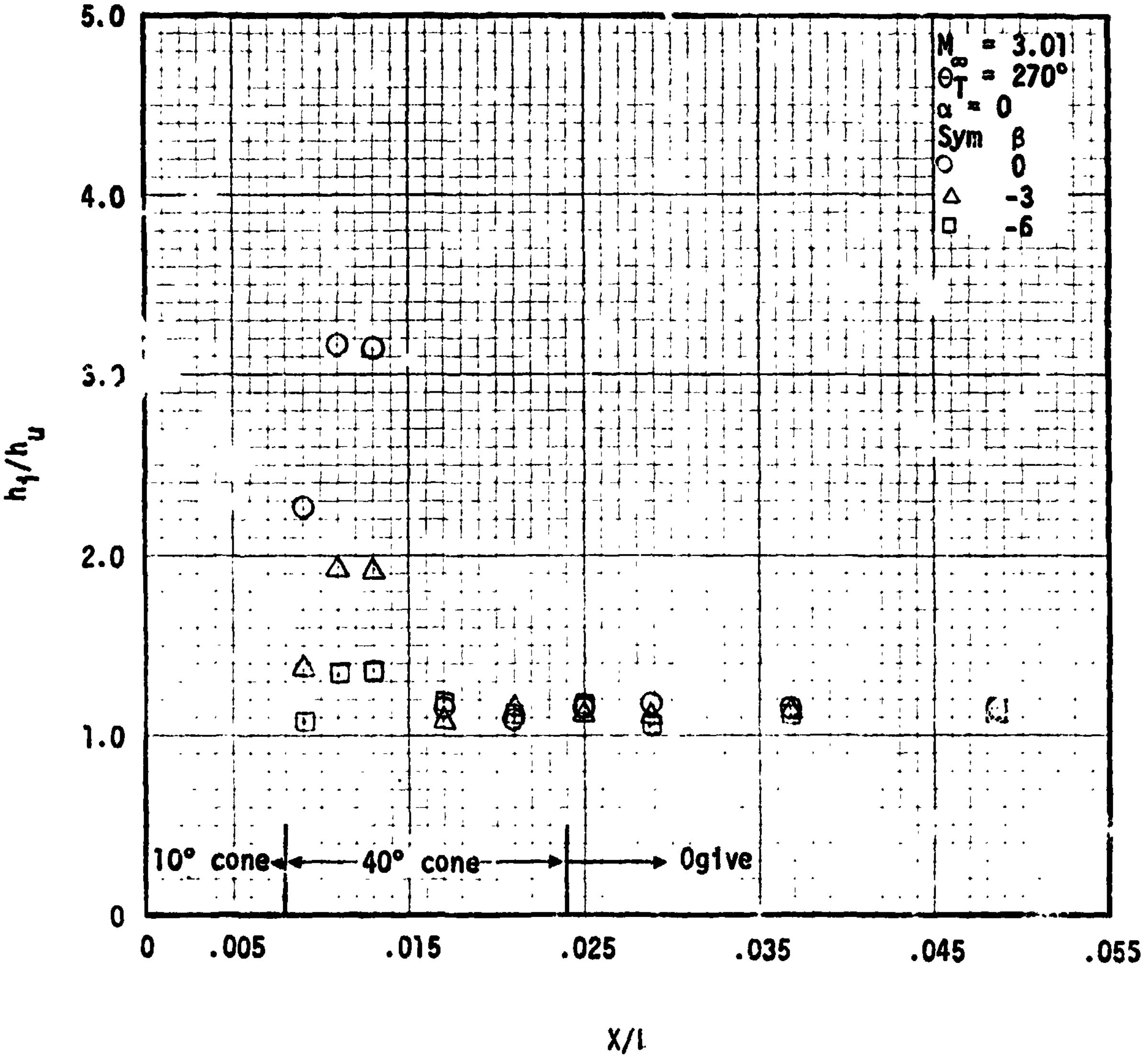

Fig. 4.10 ET AADS Nose Interference Effects from Clean FH-15 Data and Theory at M_∞ = 3.01 and Re/ft = 3.7 x 10^6

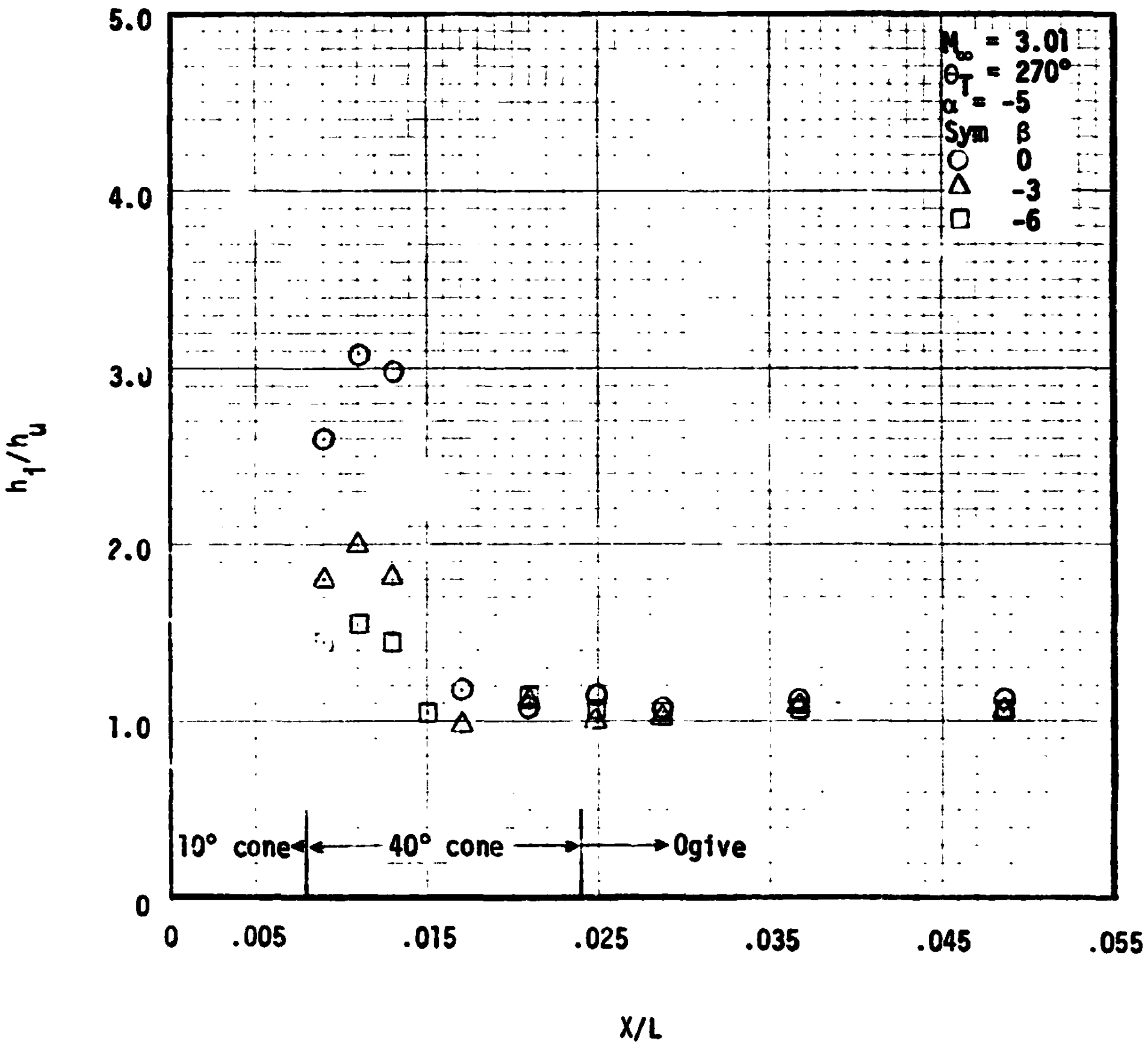

Fig. 4.11 ET AADS Nose Interference Effects from Clean FH-15 Data and Theory at M_∞ = 3.01 and Re/ft = 3.7 x 10^6

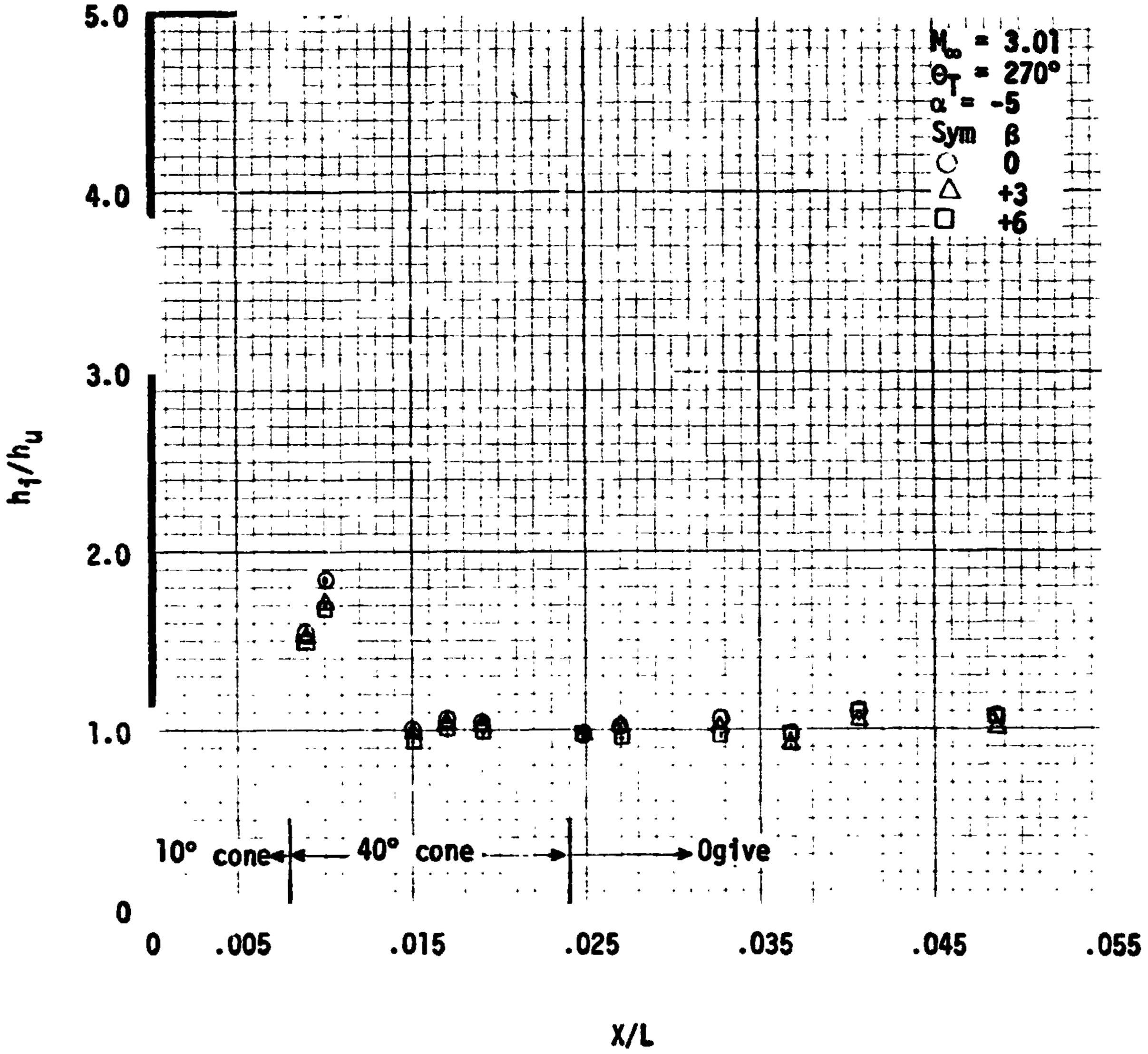

Fig. 4.12 ET AADS Nose Interference Effects from Clean FH-15 Data and Theory at M_∞ = 3.01 and Re/ft = 3.7 x 10^6

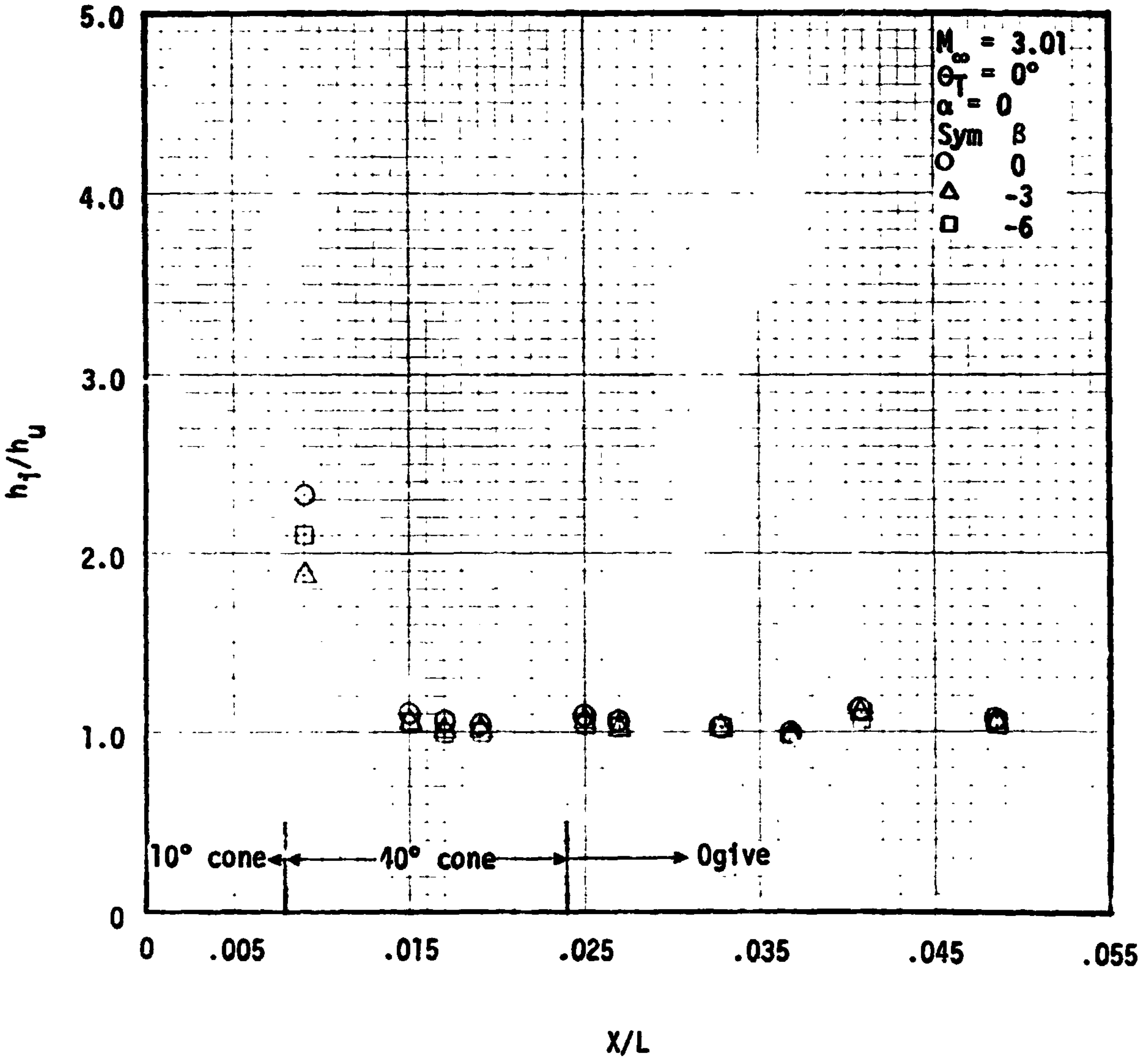

Fig. 4.13 ET AADS Nose Interference Effects from Clean FH-15 Data and Theory at M_∞ = 3.01 and Re/ft = 3.7 x 10^6

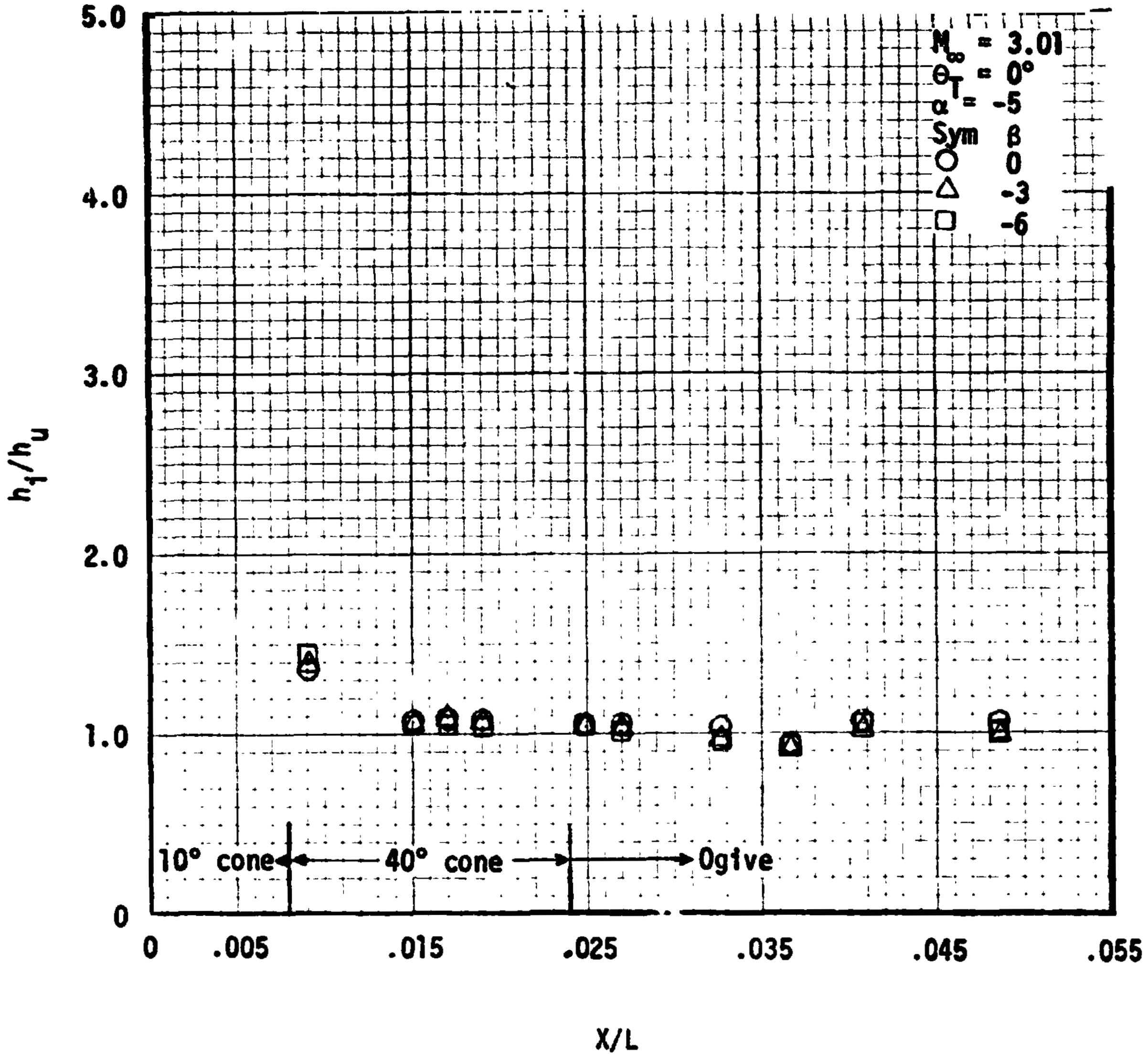

Fig. 4.14 ET AADS Nose Interference Effects from Clean FH-15 Data and Theory at M_∞ = 3.01 and Re/ft = 3.7 x 10^6

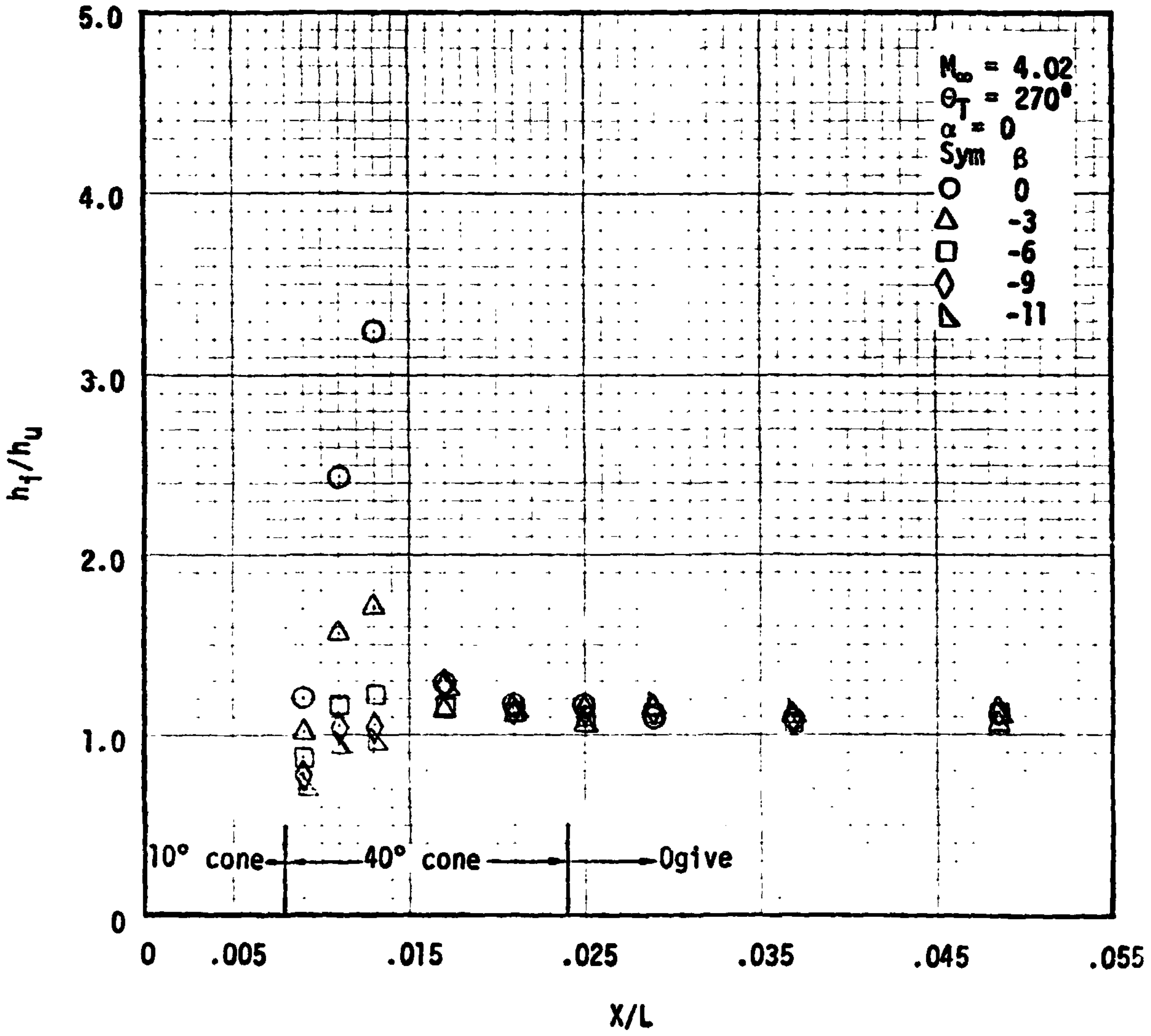

Fig. 4.15 ET AADS Nose Interference Effects from Clean FH-15 Data and Theory at M_∞ = 4.02 and Re/ft = 3.7 x 10^6

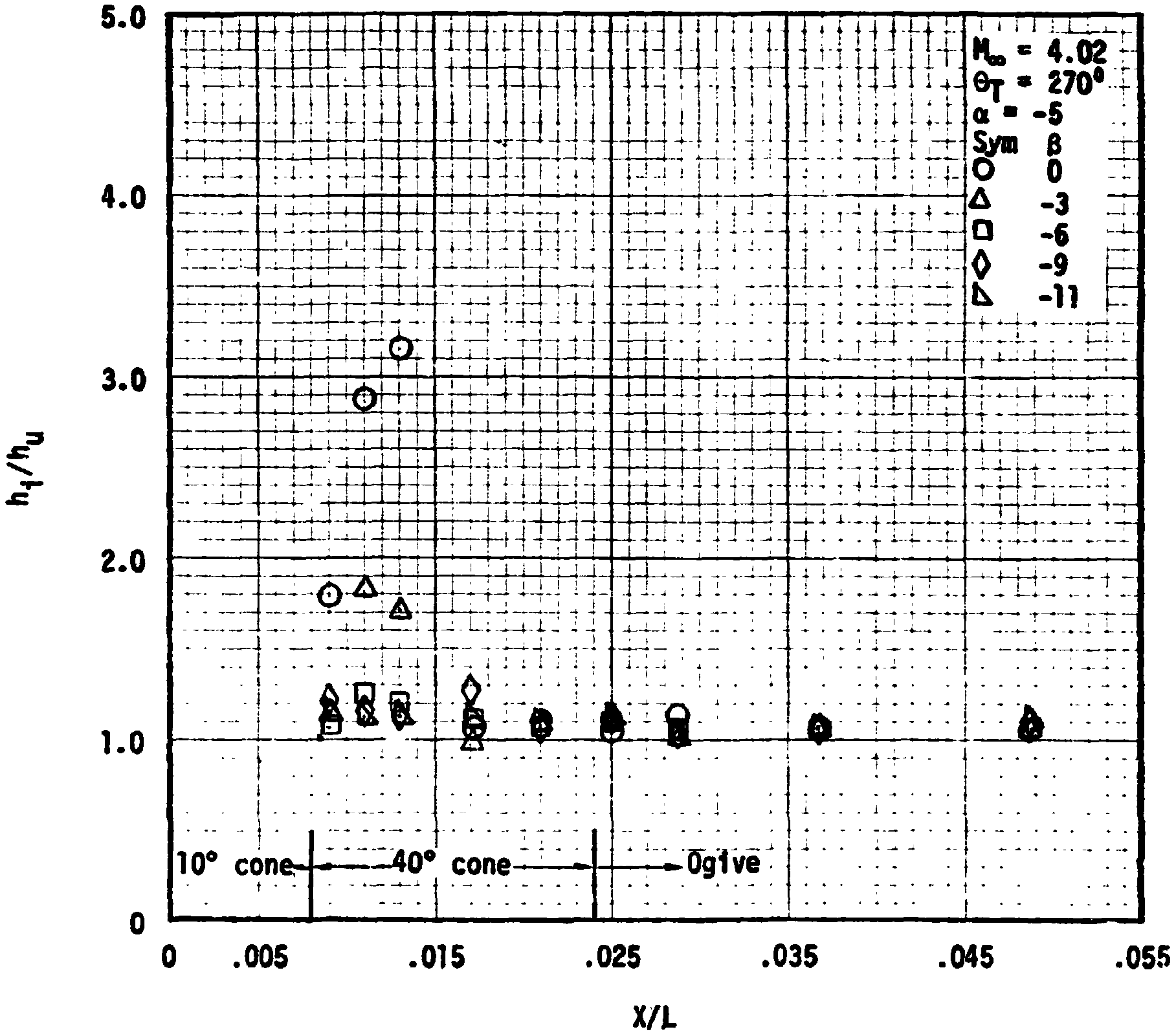

Fig. 4.16 ET AADS Nose Interference Effects from Clean FH-15 Data and Theory at M_∞ = 4.02 and Re/ft = 3.7 x 10^6

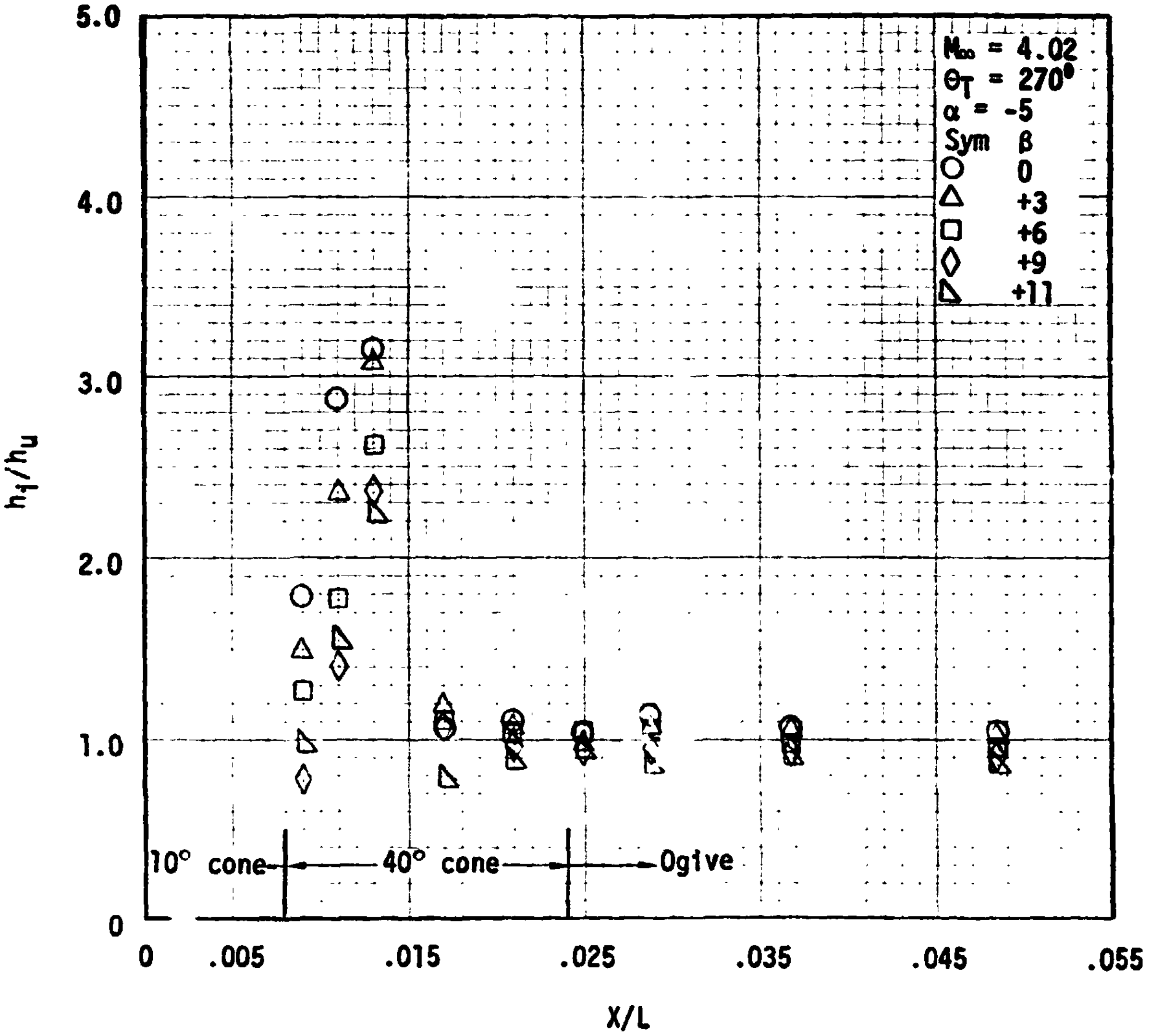

Fig. 4.17 ET AADS Nose Interference Effects from Clean FH-15 Data and Theory at M_∞ = 4.02 and Re/ft = 3.7 x 10^6

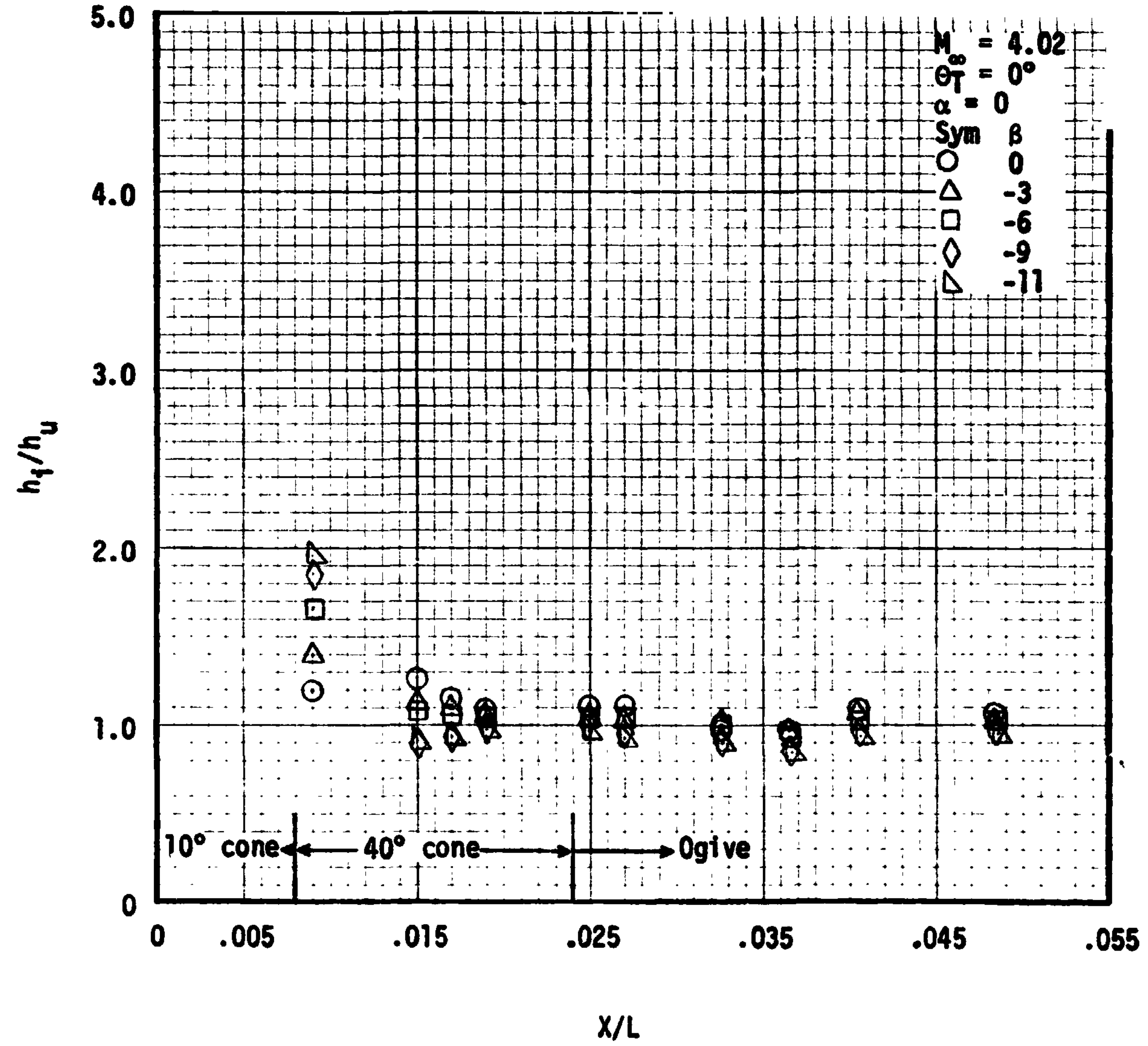

Fig. 4.18 ET AA[illegible] [illegible]e Interference Effects from Clean FH-15 Data and Theory [illegible] M_∞ = 4.02 and Re/ft = 3.7 x 10^6

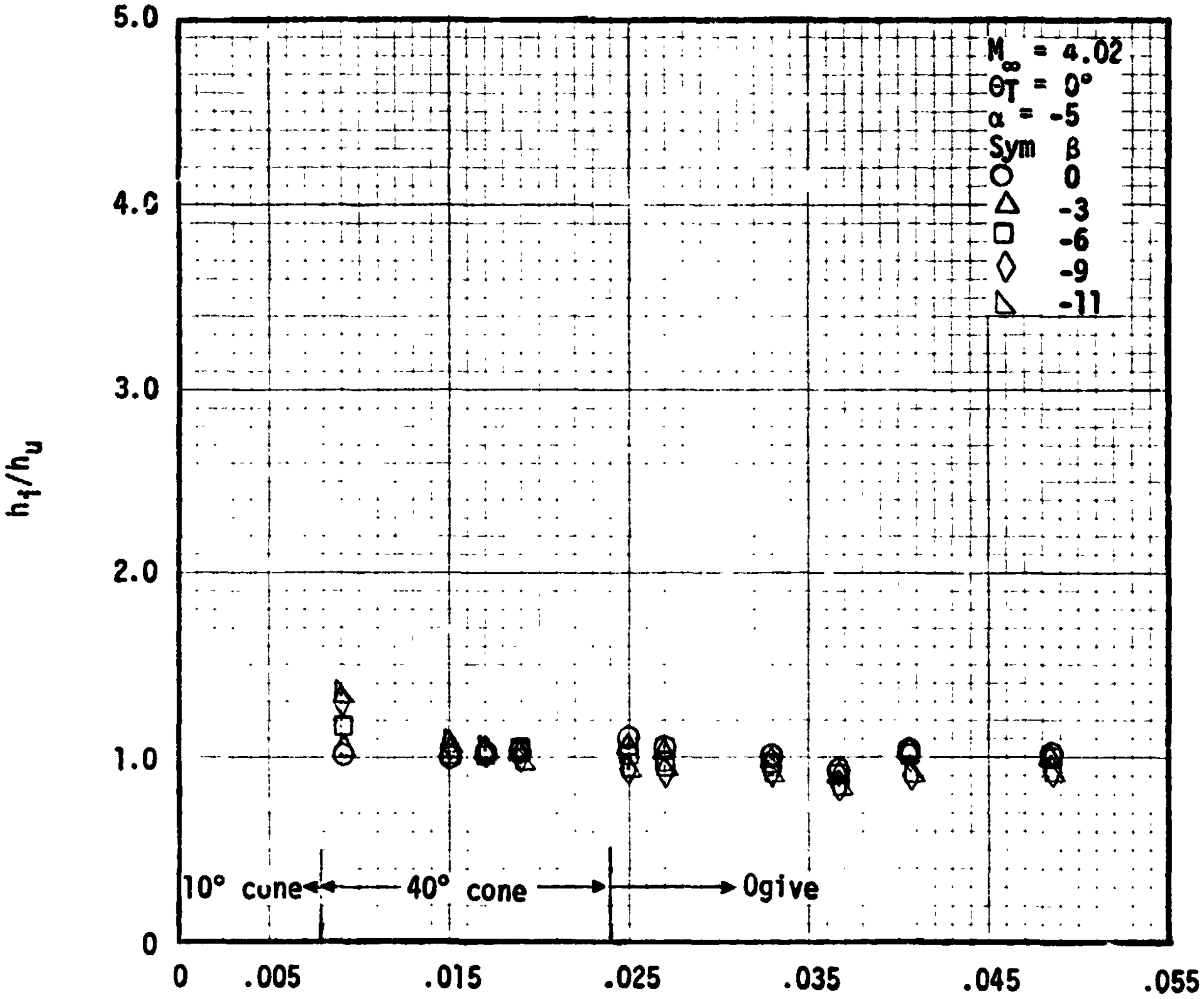

X/L

Fig. 4.19 ET AADS Nose Interference Effects from Clean FH-15 Data and Theory at M_∞ = 4.02 and Re/ft = 3.7 x 10^5

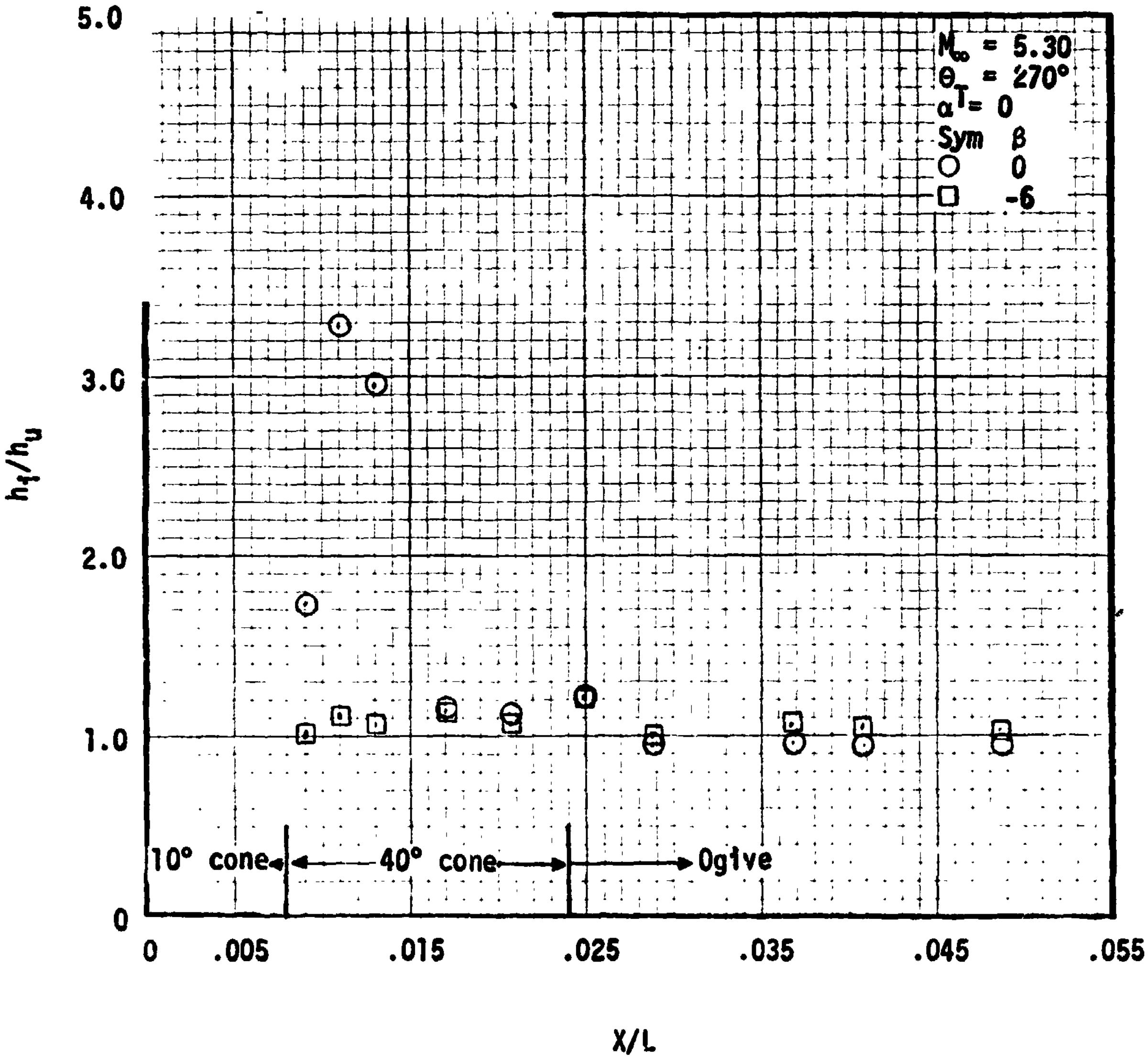

Fig. 4.20 ET AADS Nose Interference Effects from Clean FH-16 Data and Theory at M_∞ = 5.30 and Re/ft = 3.7 x 10^6

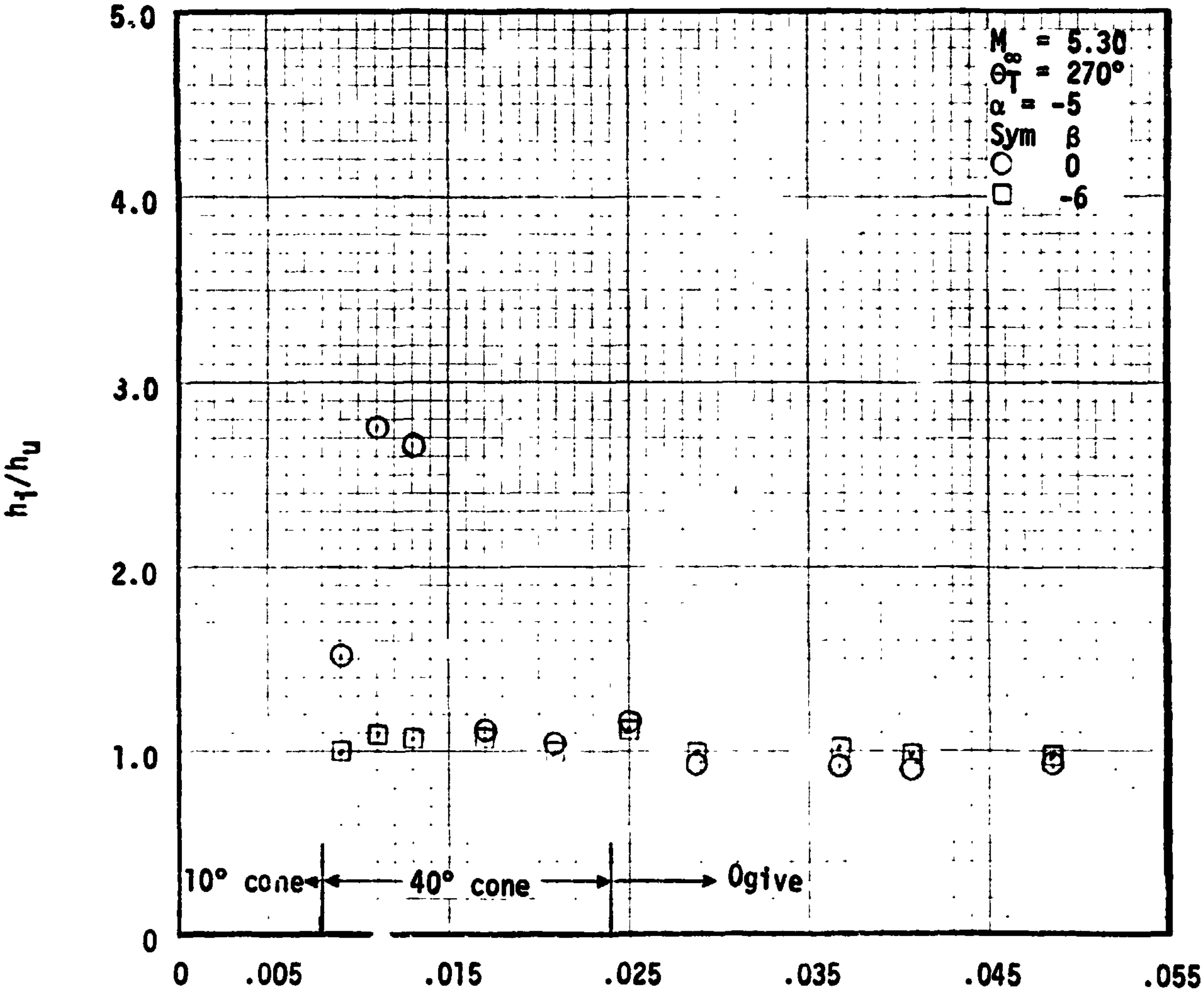

Fig. 4.21 ET AADS Nose Interference Effects from Clean FH-16 Data and Theory at M_∞ = 5.30 and Re/ft = 3.7 x 10^6

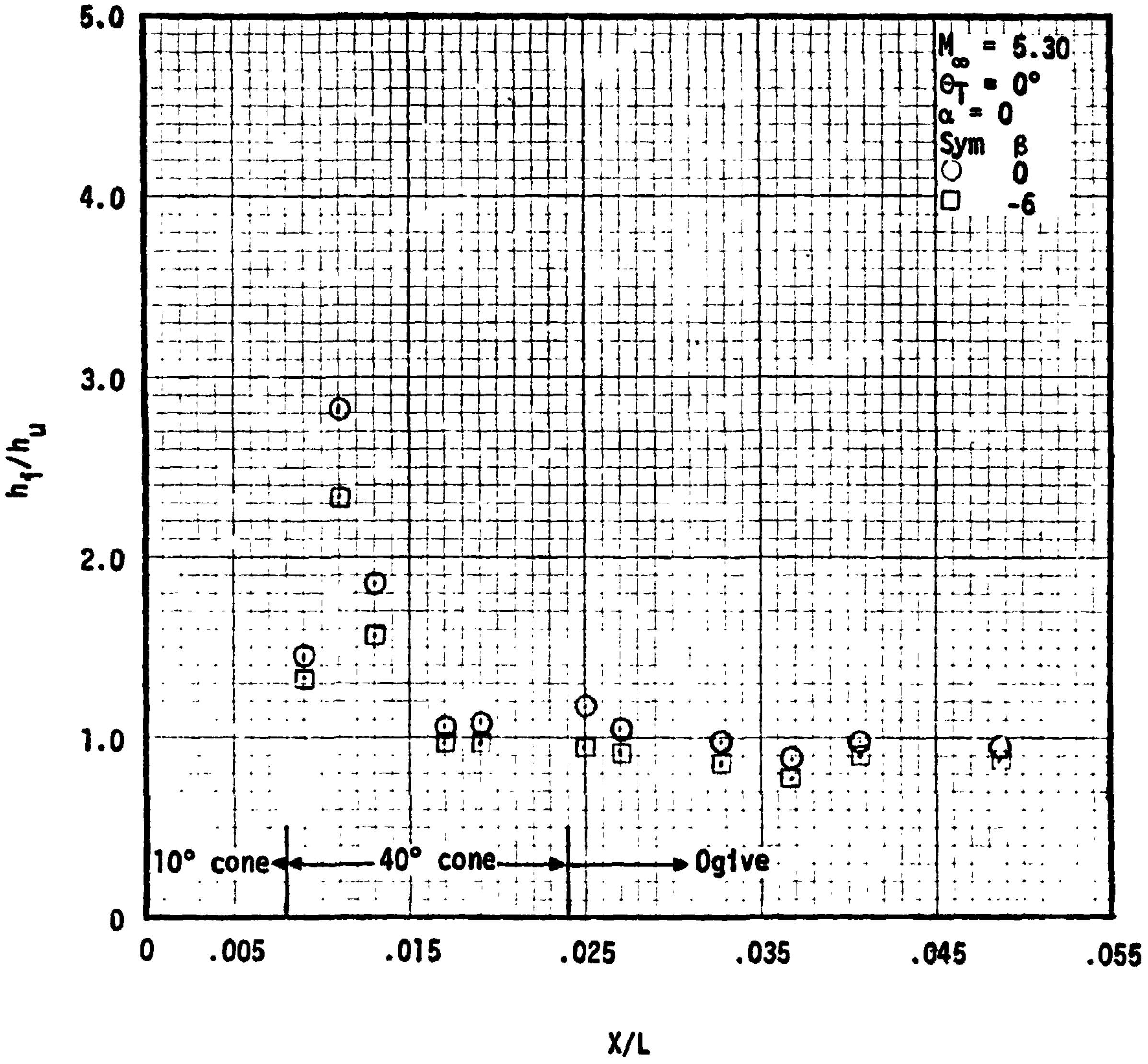

Fig. 4.22 ET AADS Nose Interference Effects from Clean ··16 Data and Theory at M_∞ = 5.30 and Re/ft = 3.7 x 10^6

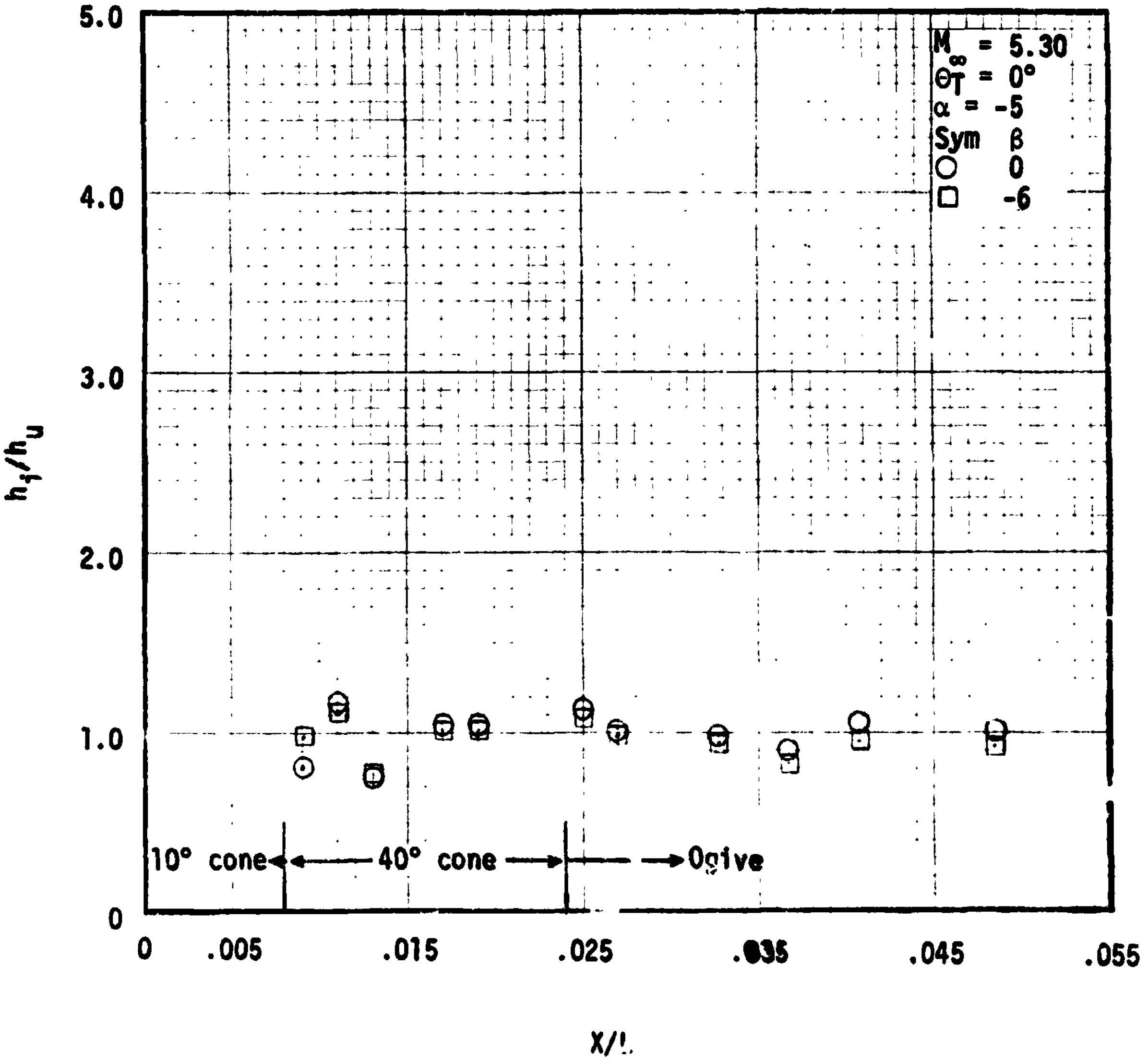

Fig. 4.23 ET AADS Nose Interference Effects from Clean FH-3 Data and Theory at M_∞ = 5.30 and Re/ft = 3.7 x 10^6

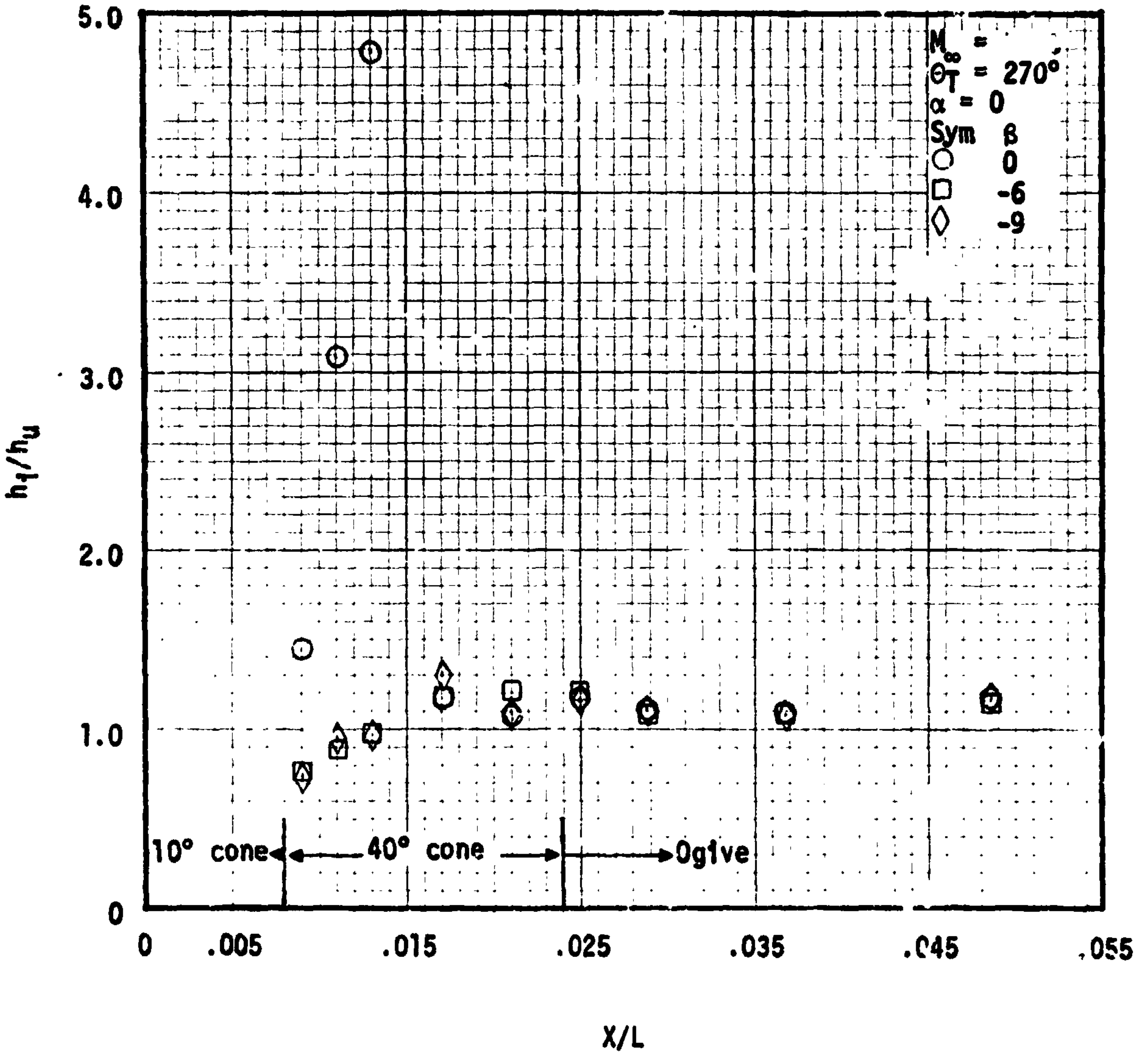

Fig. 4.24 F^T AADS Nose Interference Effects from Clean FH-15 Data and Theory at M_∞ = 5.50 and Re/ft = 3.7 x 10^6

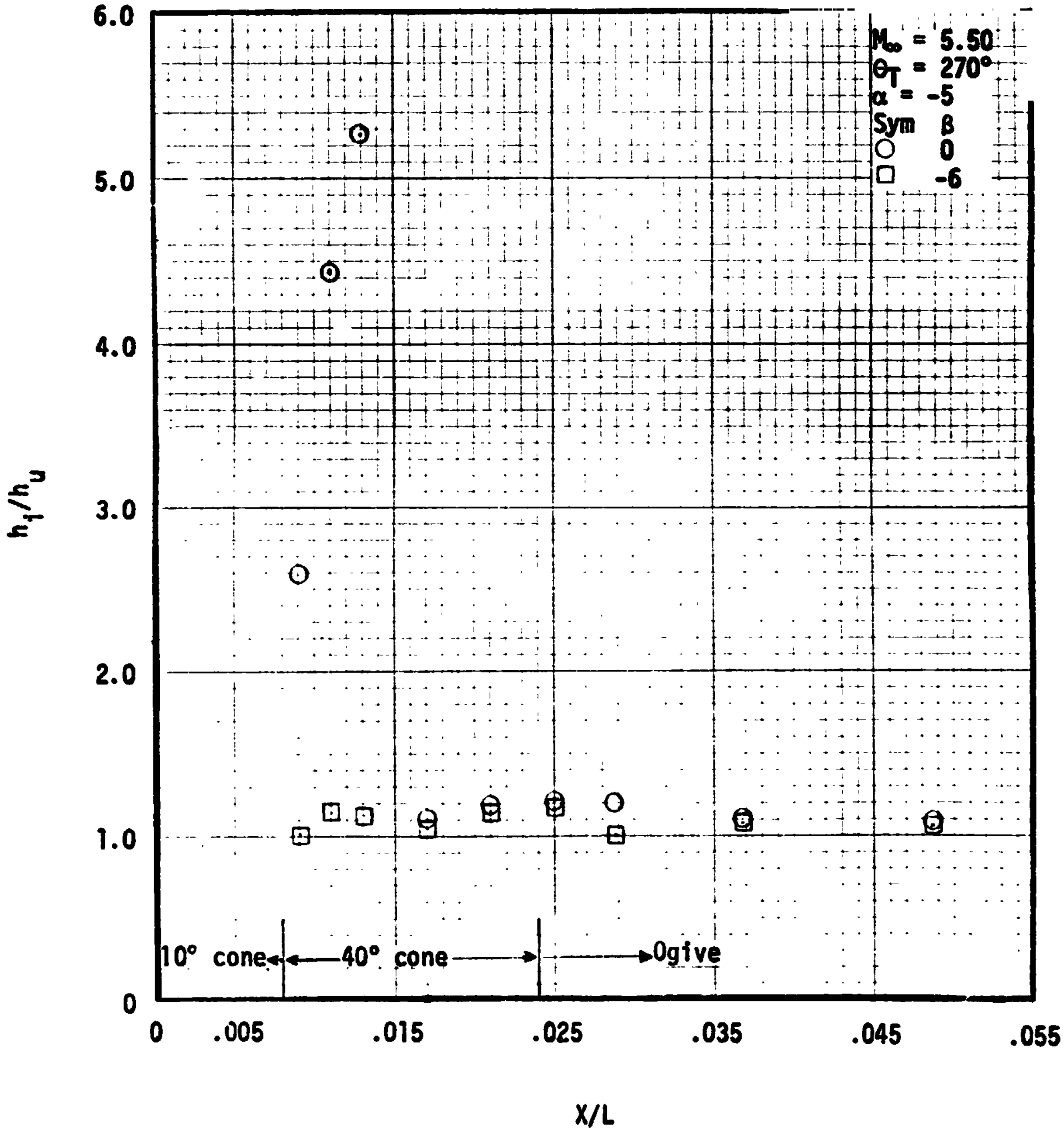

Fig. 4.25 ET AADS Nose Interference Effects from Clean FH-15 Data and Theory at M_∞ = 5.50 and Re/ft = 3.7 x 10^6

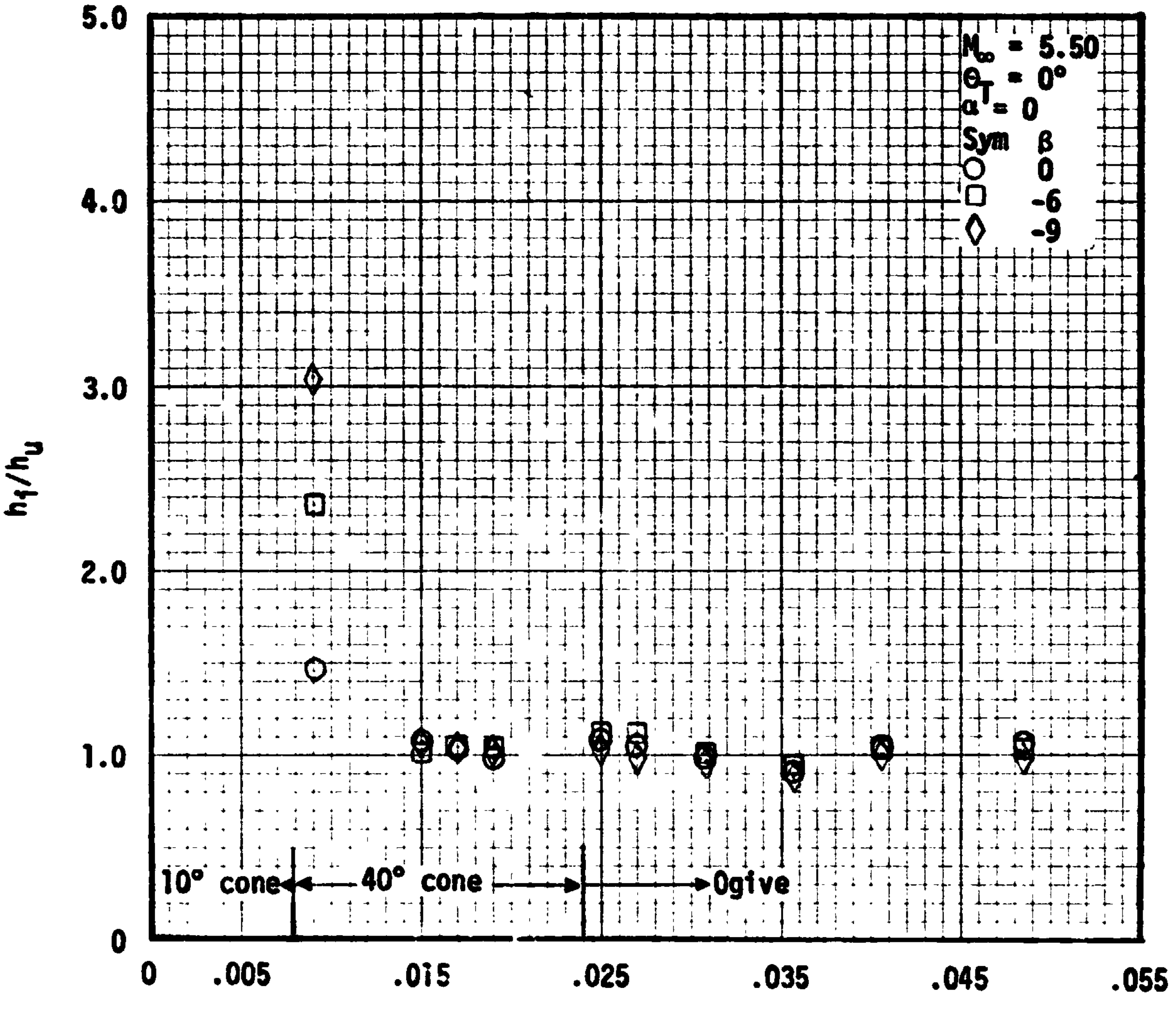

Fig. 4.26 ET AADS Nose Interference Effects from Clean FH-15 Data and Theory at M_∞ = 5.F0 and Re/ft = 3.7 x 10^6

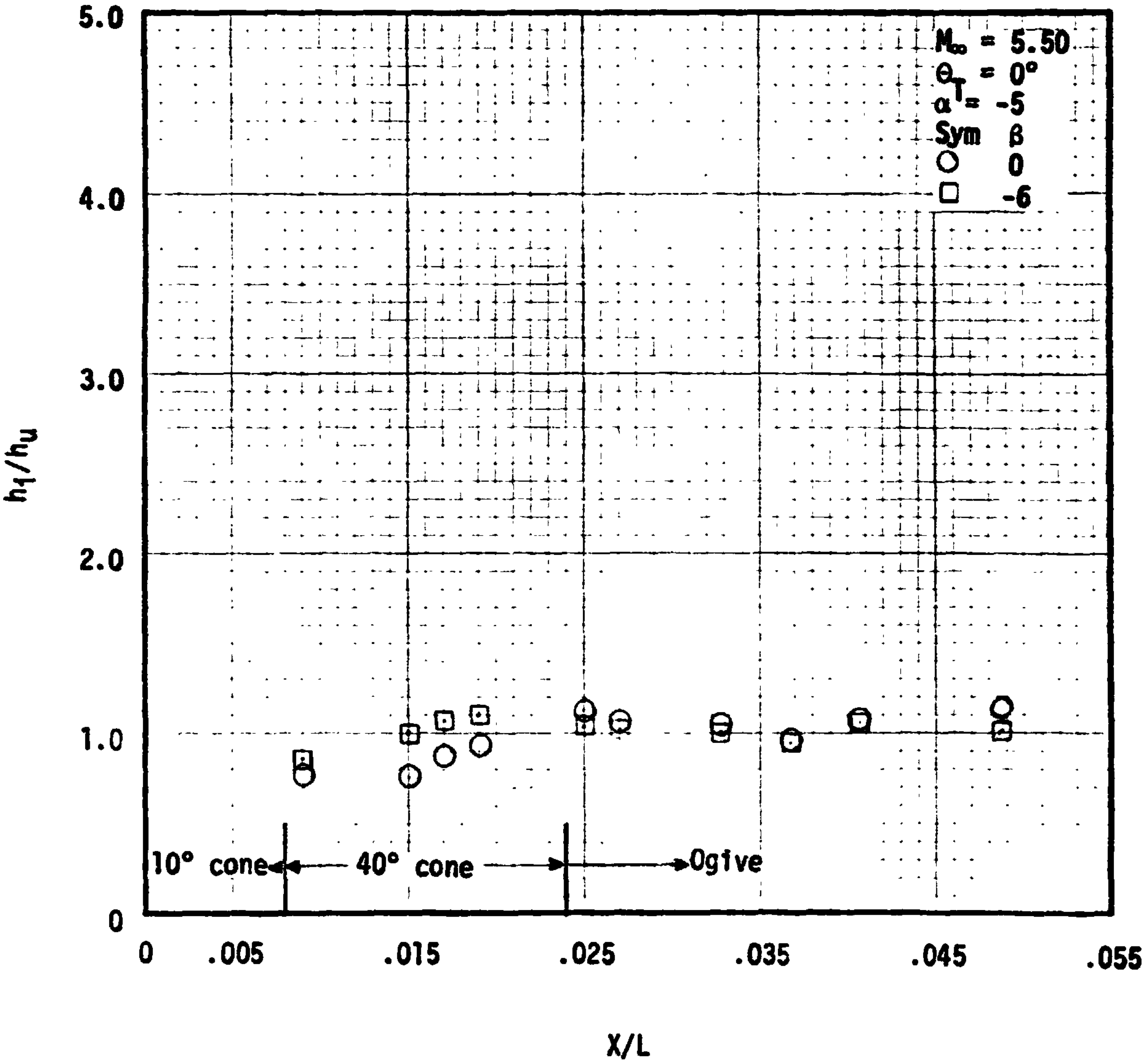

Fig. 4 27 ET AADS Nose Interference Effects from Clean FH-15 Data and Theory at M_∞ = 5.50 and Re/ft = 3.7 x 10^6

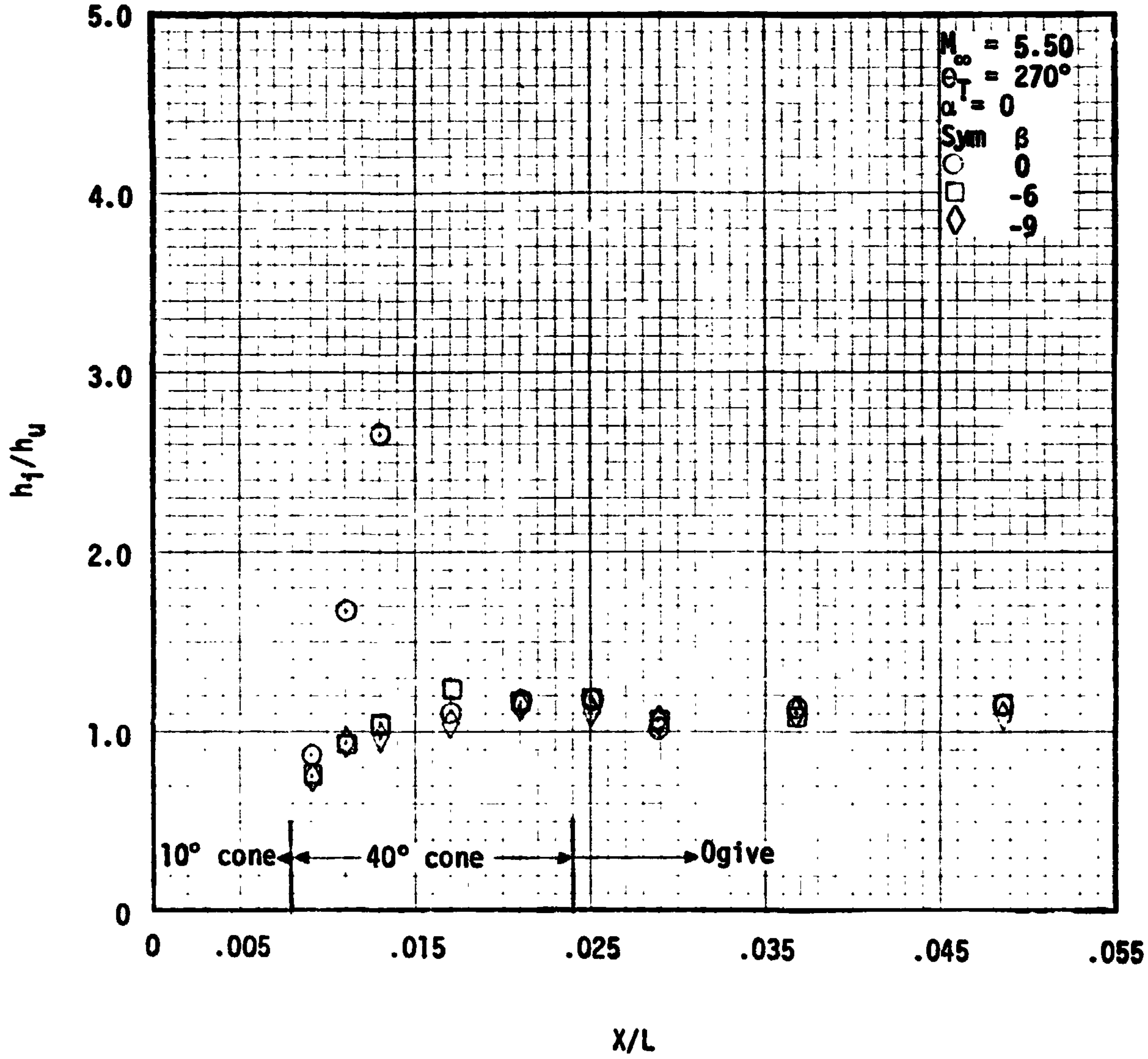

Fig. 4.28 ET AADS Nose Interference Effects from Clean FH-15 Data and Theory at M_∞ = 5.50 and Re/ft = 5.0 x 10^6

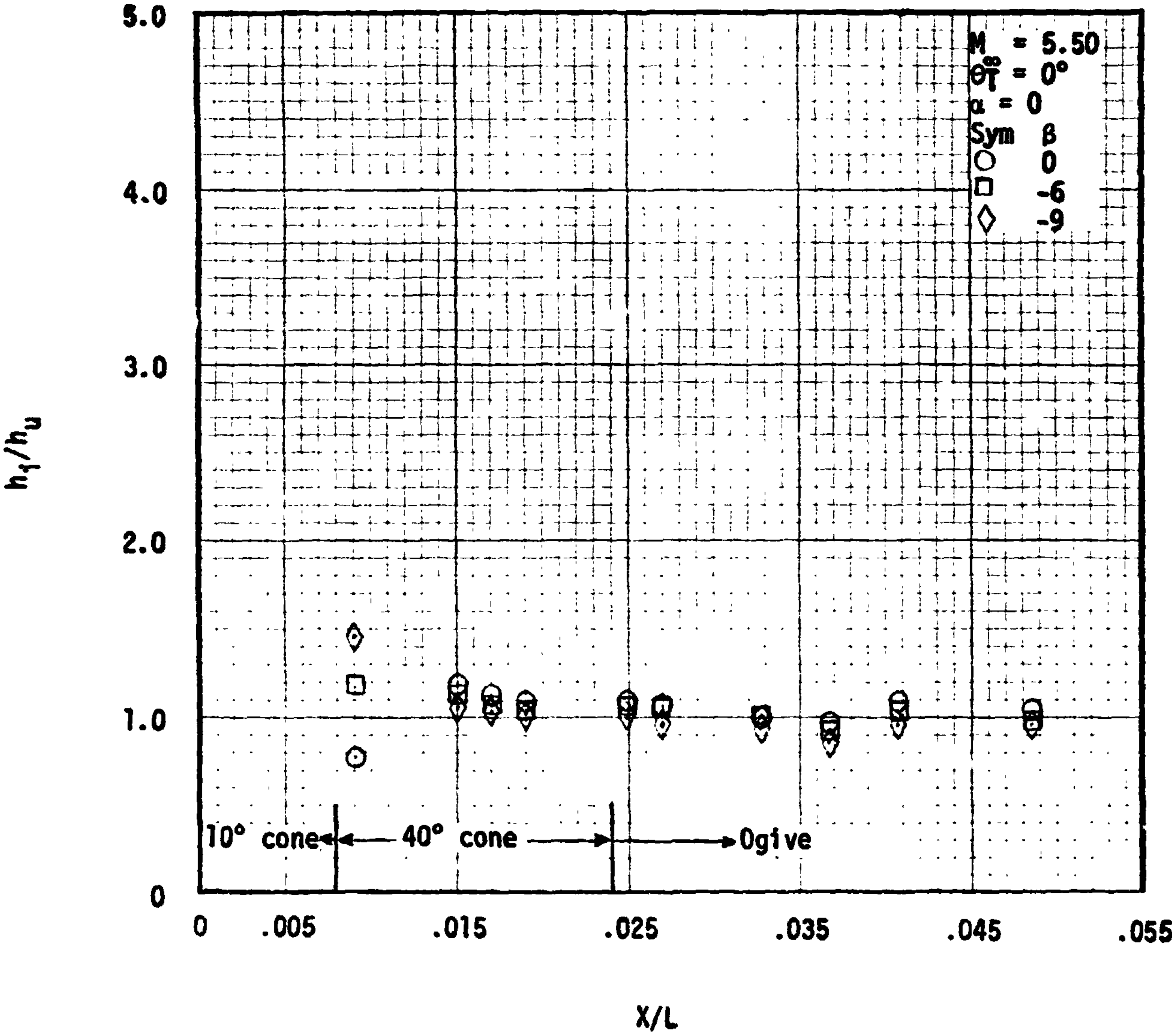

Fig. 4.29 ET AADS Nose Interference Effects from Clean FH-15 Data and Theory at M_∞ = 5.5 and Re/ft = 5.0 x 10^6

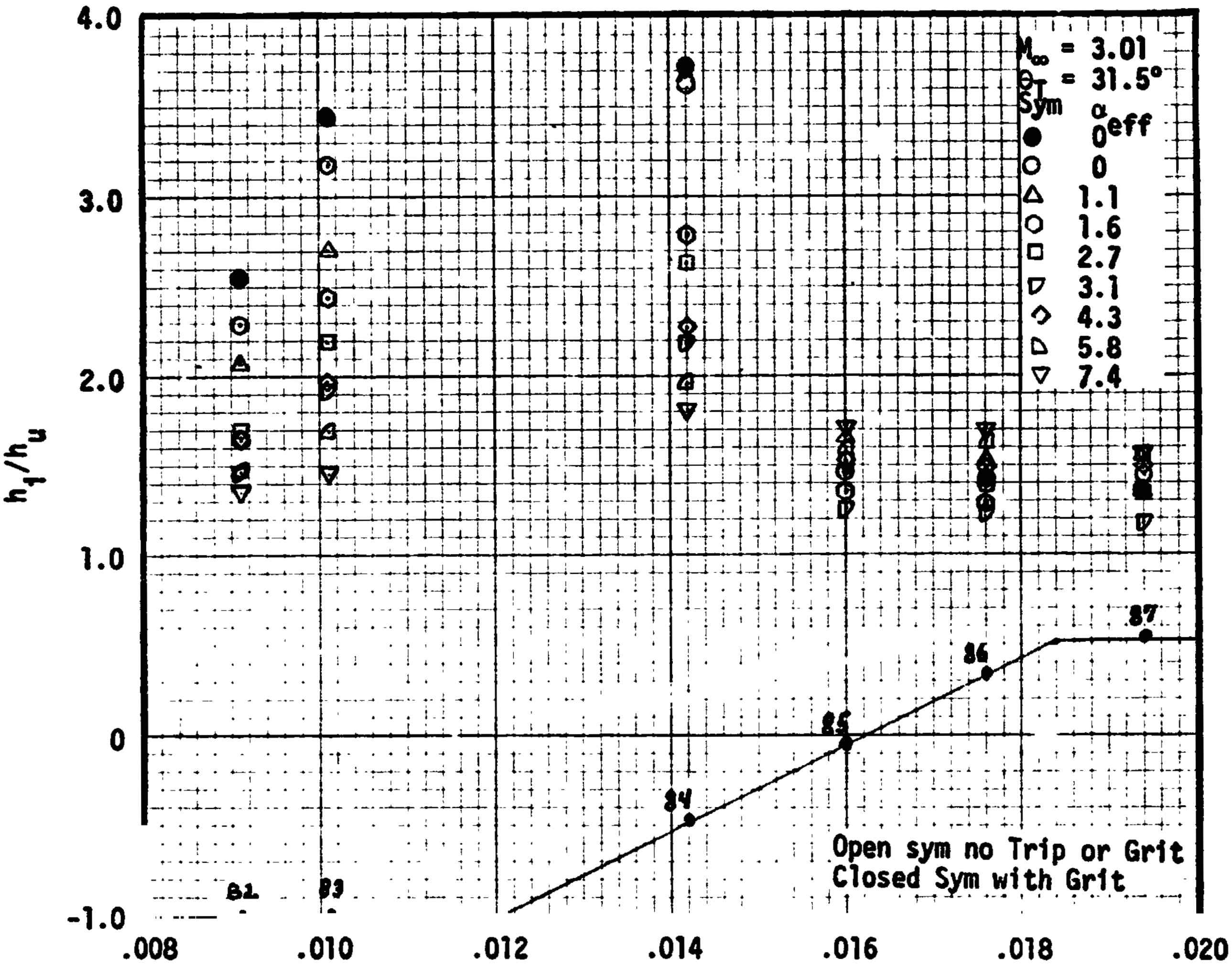

Fig. 4.30 Interference Effects from FH-15 Data and Theory at M_∞ = 3.01 and Re/ft = 3.7 x 10^6 for Thermocouples Located on the Top Centerline of the Forward Fairing of the Forward Electrical Conduit

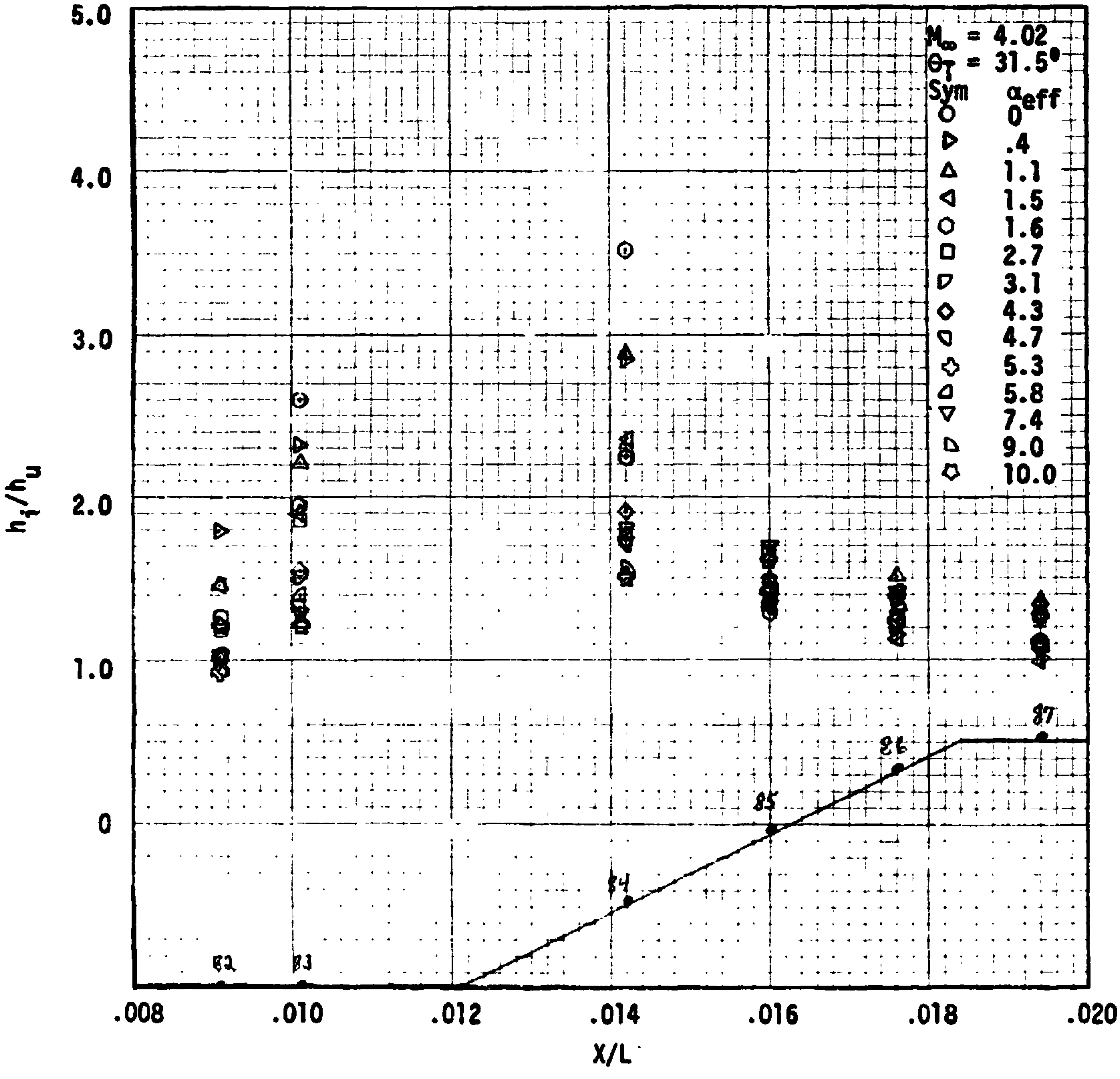

Fig. 4.31 Interference Effects from FH-15 Data and Theory at M_∞ = 4.02 and Re/ft = 3.7 x 10^6 for Thermocouples Located on the Top Centerline of the Forward Fairing of the Forward Electrical Conduit

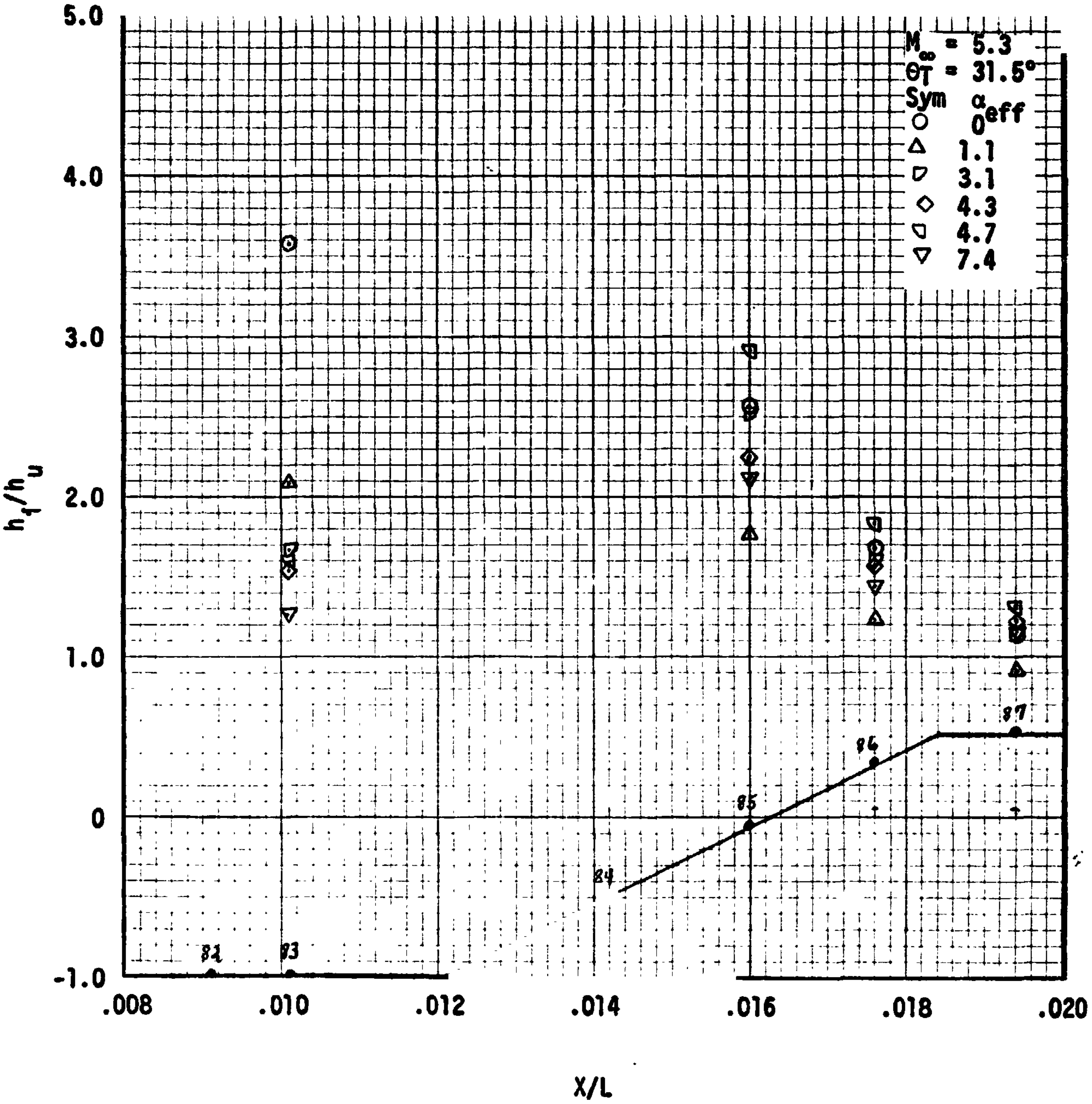

Fig. 4.32 Interference Effects from FH-16 Data and Theory at M_∞ = 5.3 and Re/ft = 3.7 x 10^6 for Thermocouples Located on the Top Centerline of the Forward Fairing of the Forward Electrical Conduit

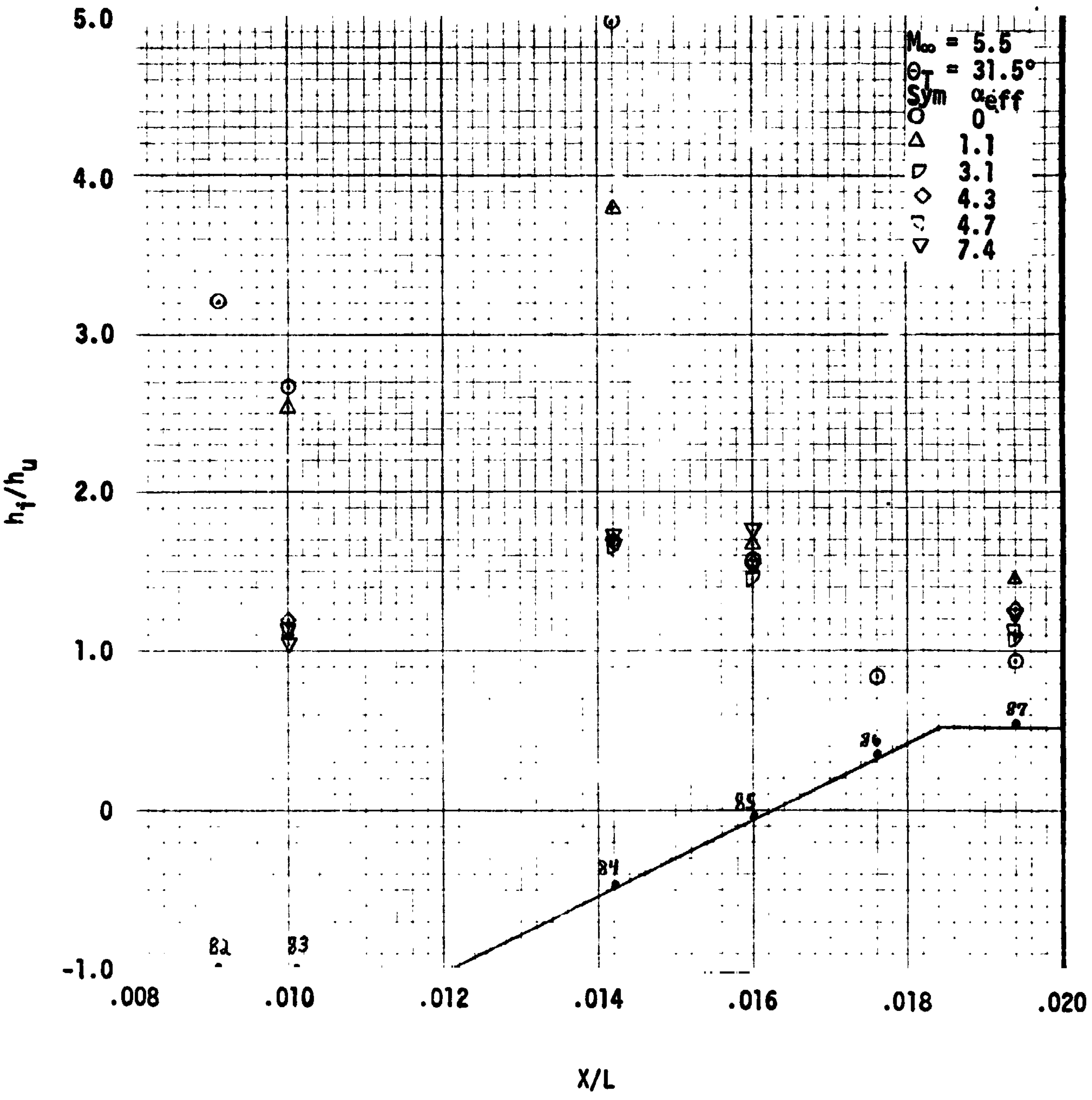

Fig. 4.33 Interference Effects from FH-15 Data and Theory at M_∞ = 5.5 and Re/ft = 3.7 x 10^6 for Thermocouples Located on the Top Centerline of the Forward Fairing of the Forward Electrical Conduit

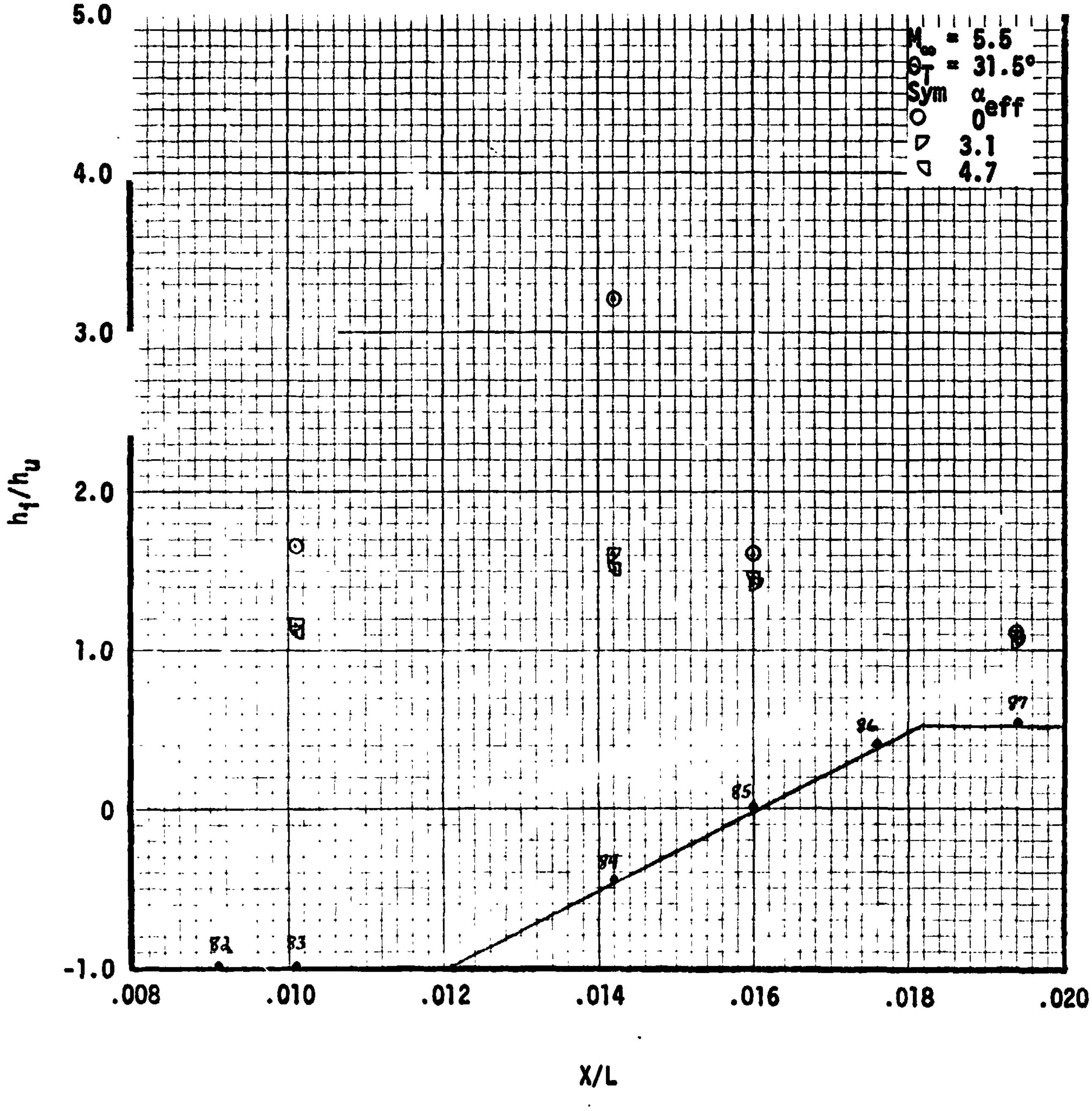

Fig. 4.34 Interference Effects from FH-15 Data and Theory at M_∞ = 5.5 and Re/ft = 5.0 x 10^6 for Thermocouples Located on the Top Centerline of the Forward Fairing of the Forward Electrical Conduit

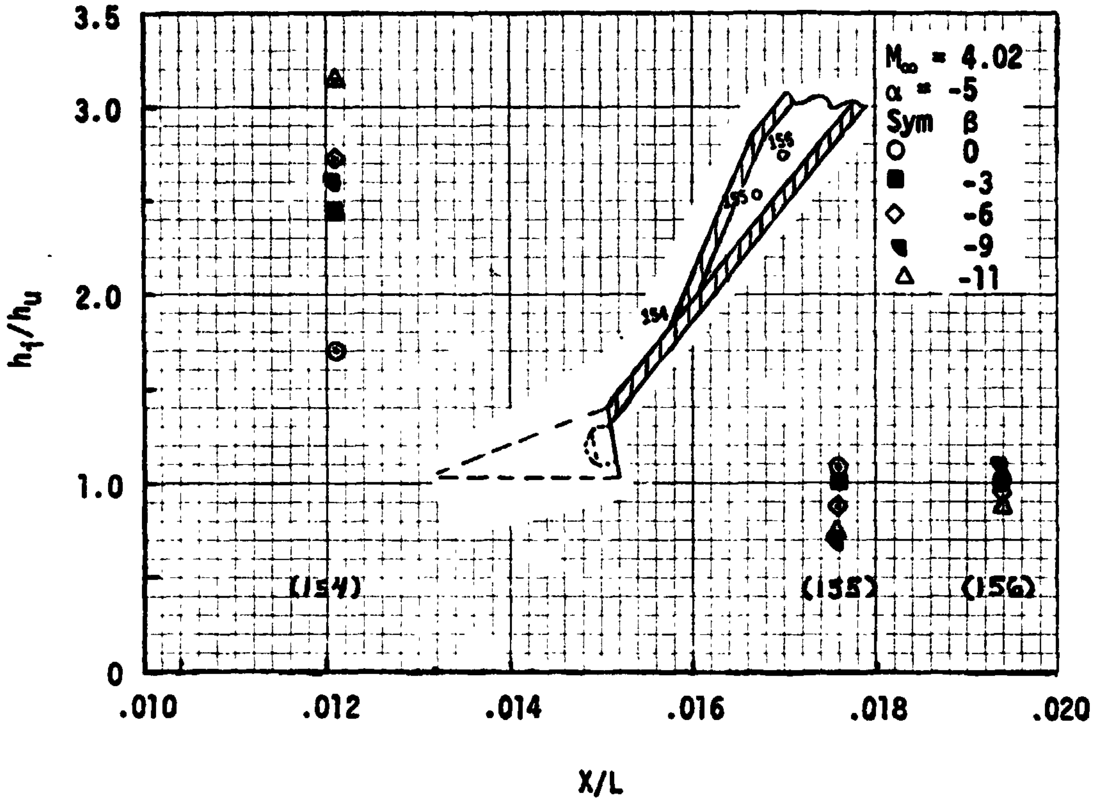

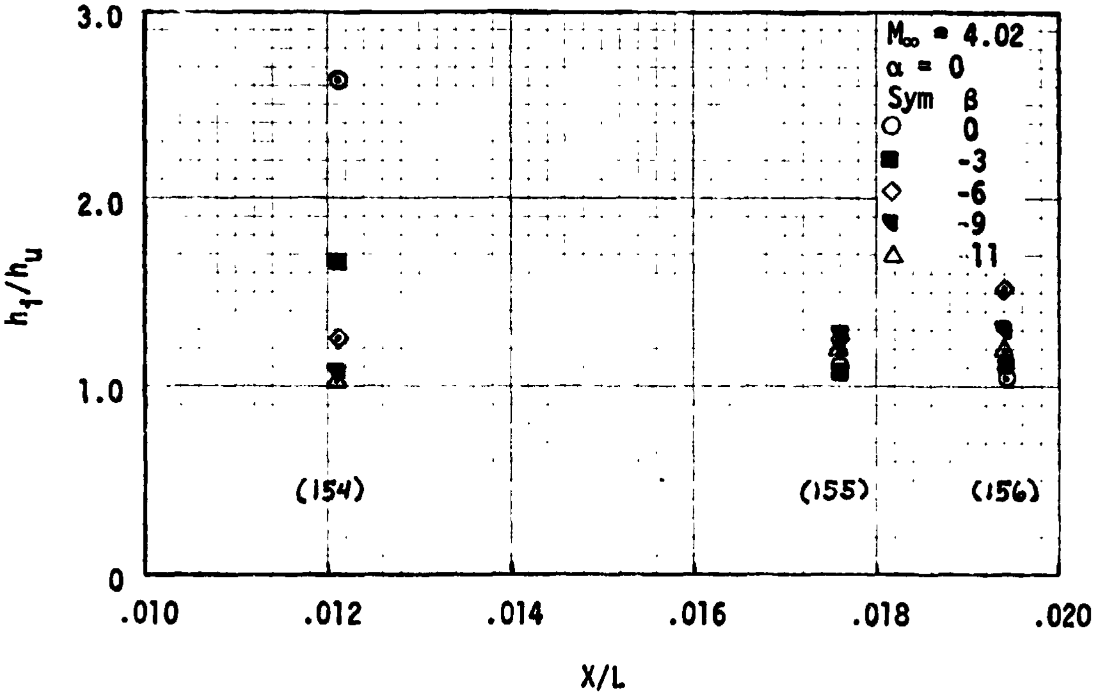

Fig. 4.35 Interference Effects from FH-15 Theory and Data at M_∞ = 4.02 and Re/ft = 3.7 x 10^6 for the T/C's Located on the Forward Fairing Side of the Forward Electrical Conduit

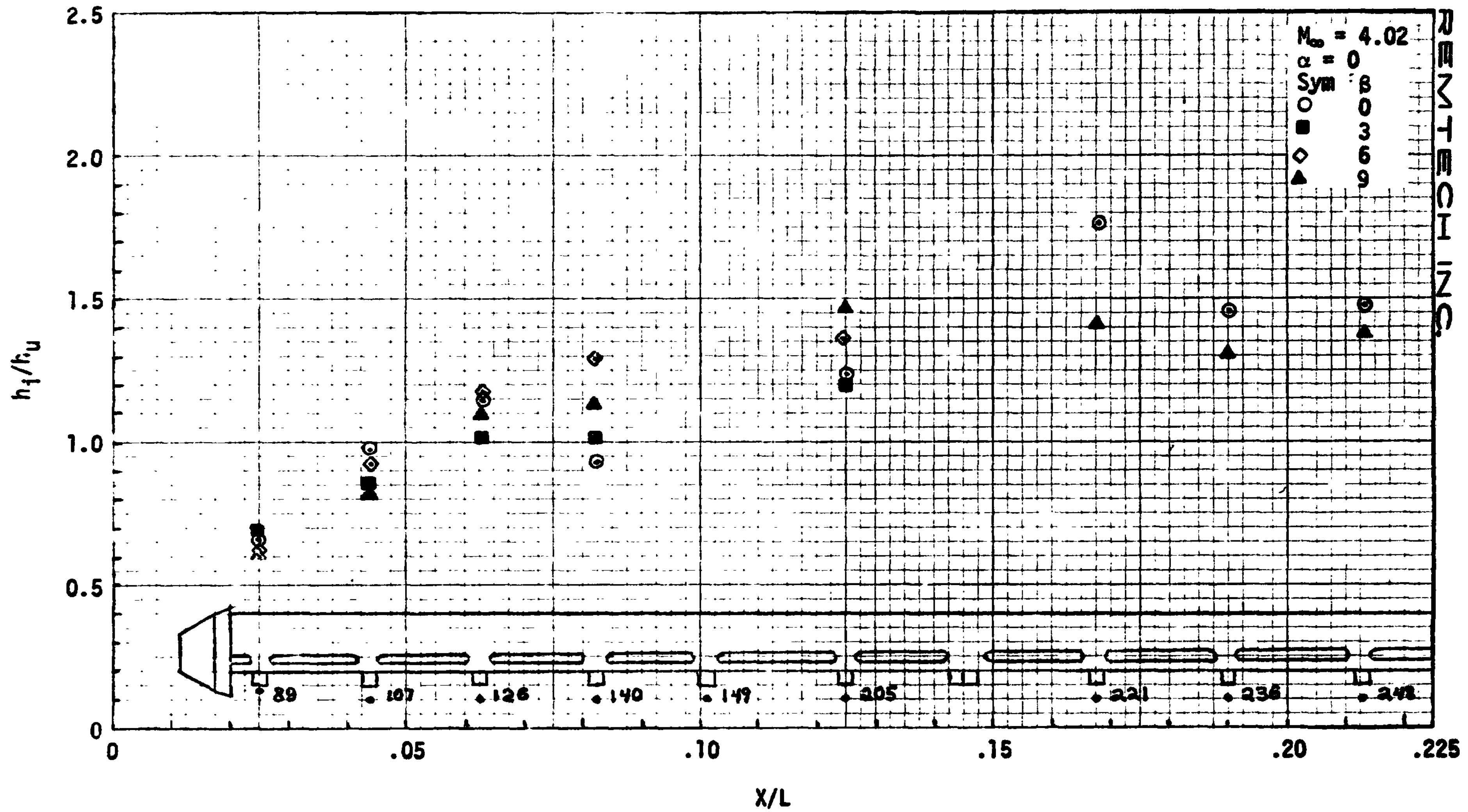

Fig. 4.36 Interference Effects for T/C's Located Beside the Attachment Fittings from Disturbed FH-15 Data and Theory for M_∞ = 4.02 and Re/ft = 3.7 x 10^6

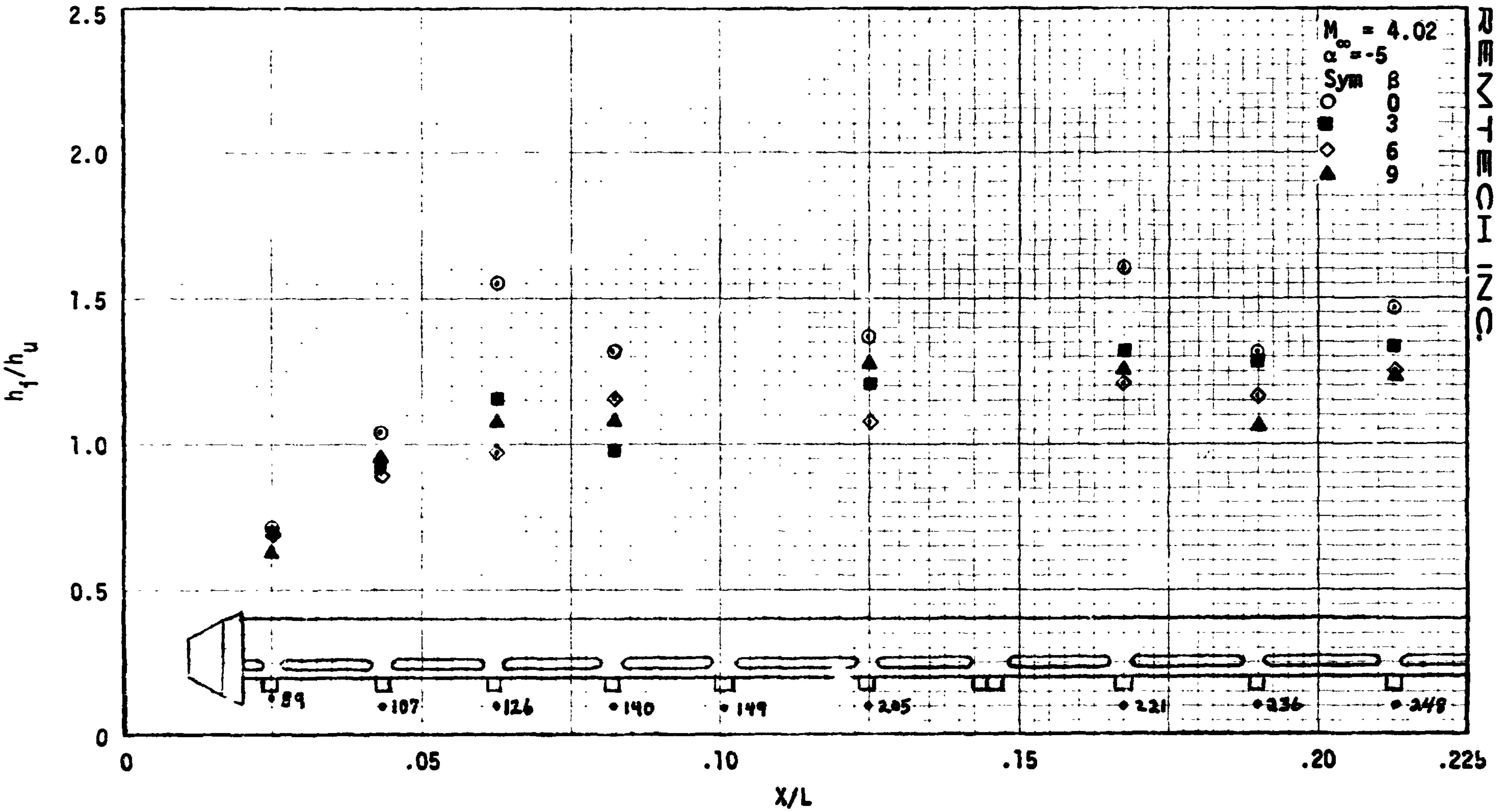

Fig. 4.37 Interference Effects for T/C's Located Beside the Attachment Fittings from Disturbed FH-15 Data and Theory for M_∞ = 4.02 and Re/ft = 3.7 x 10^6

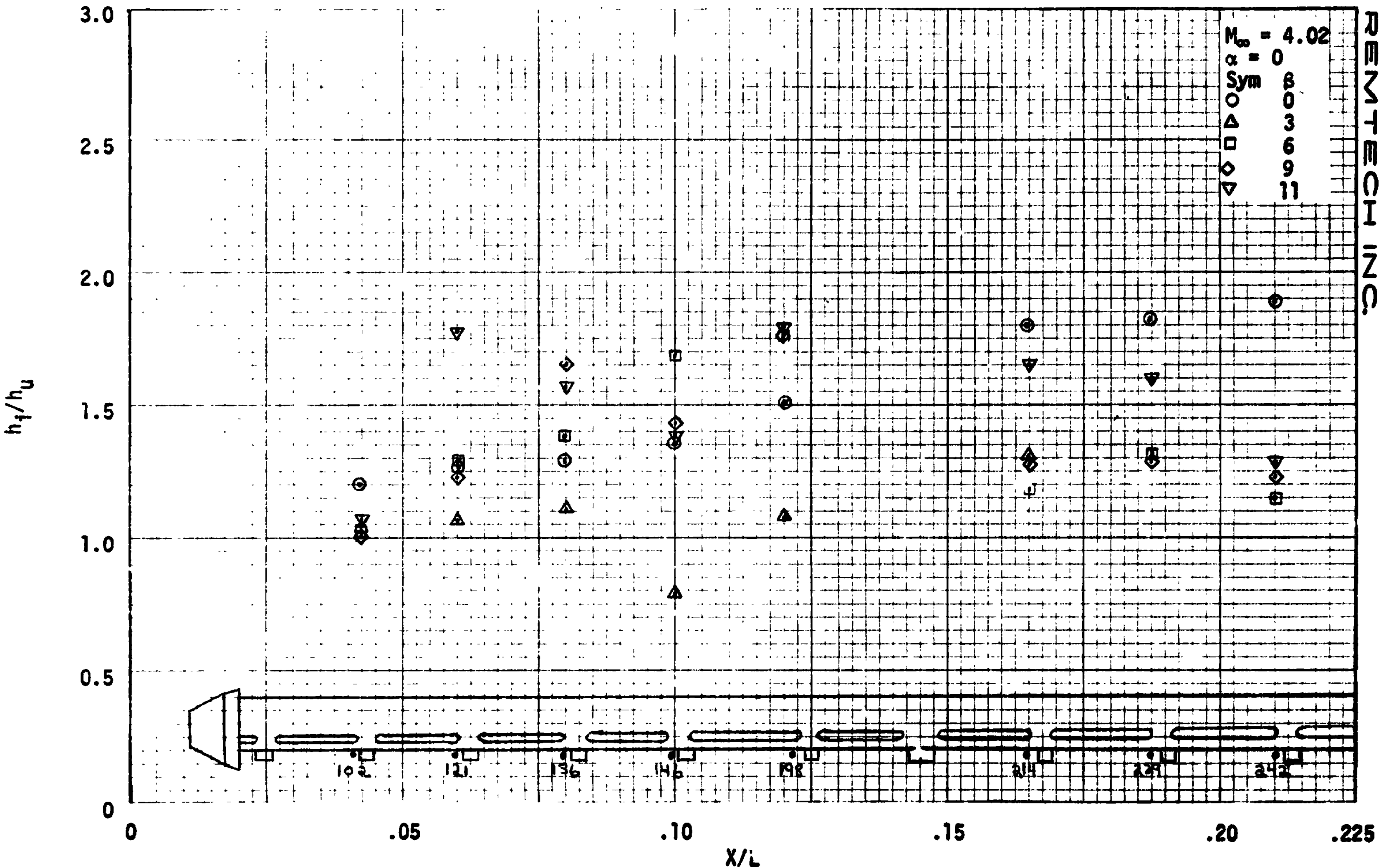

Fig. 4.38 Interference Effects from FH-15 Data and Theory for T/C Locations in Front of Attachment Fittings on the ET AADS Forebody for M_∞ = 4.02 and Re/ft = 3.7 x 10^6

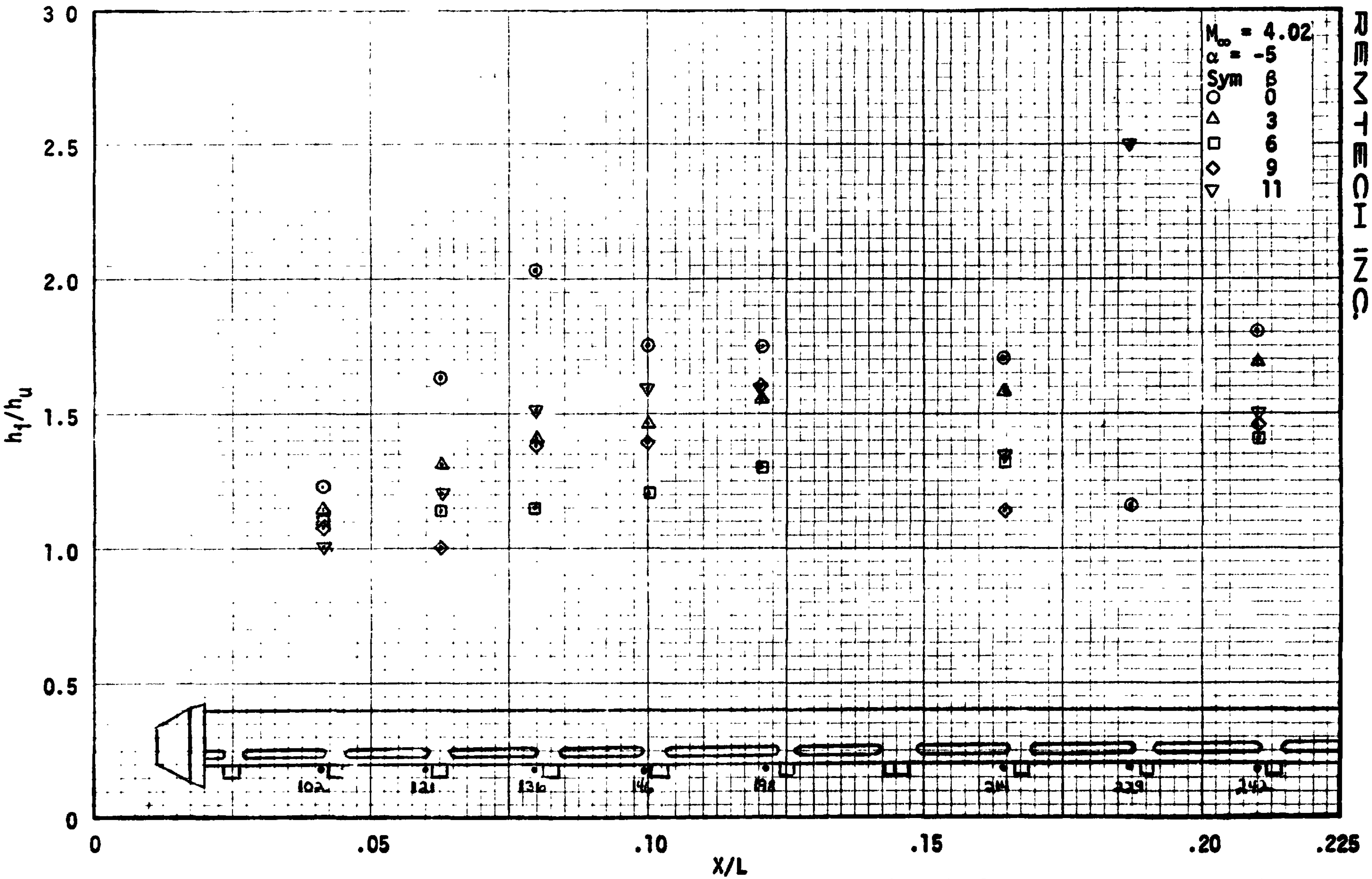

Fig. 4.39 Interference Effects from FH-15 Data and Theory for T/C Locations in Front of Attachment Fittings on the ET AADS Forebody for M_∞ = 4.02 and Re/ft = 3.7 x 10^6

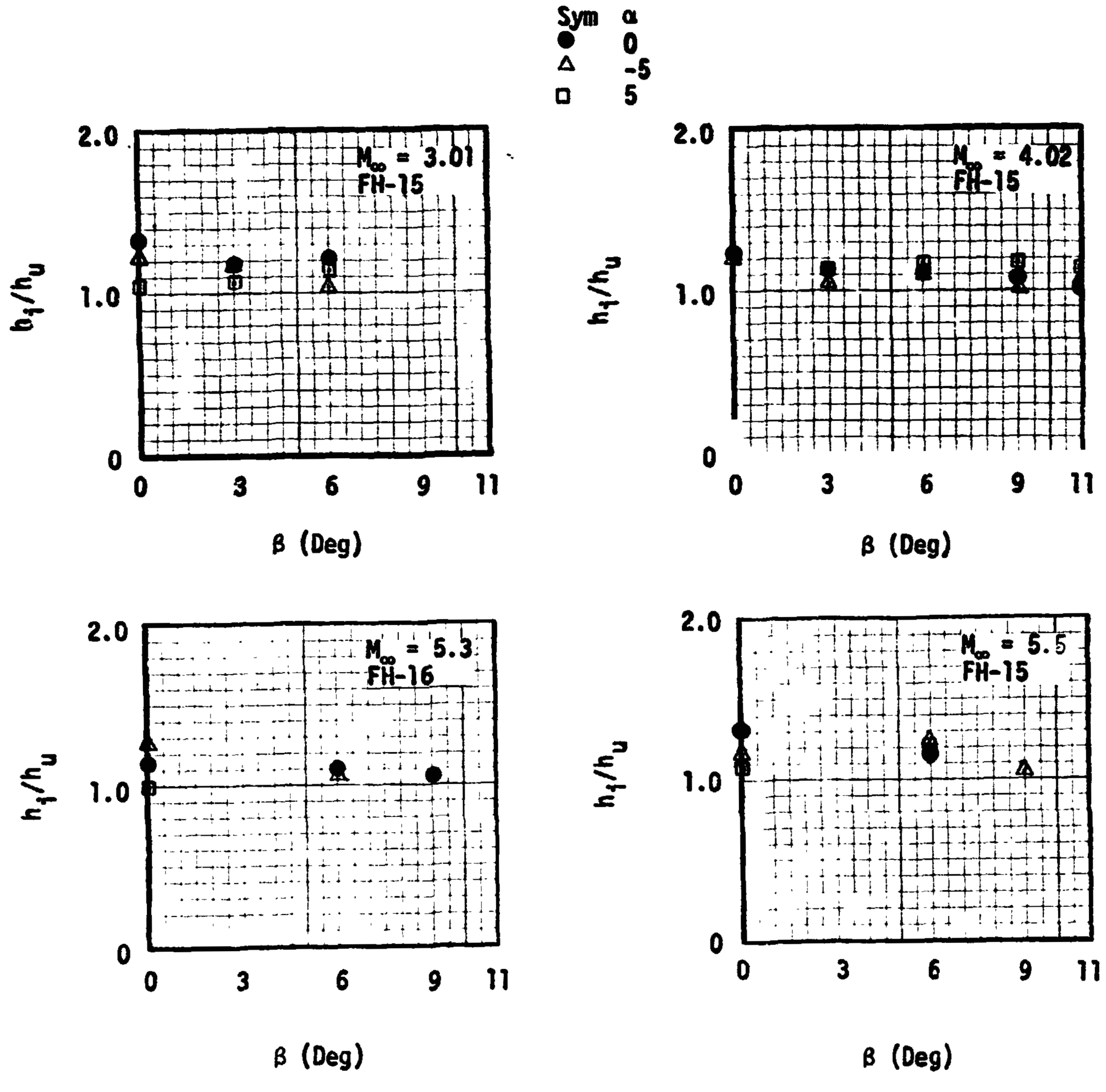

Fig. 4.40 Peak Heating Values of T/C 102 Located in Front of Attachment Fitting on ET AADS Forebody at Θ_T = 27.6° and X/L = 0.0416

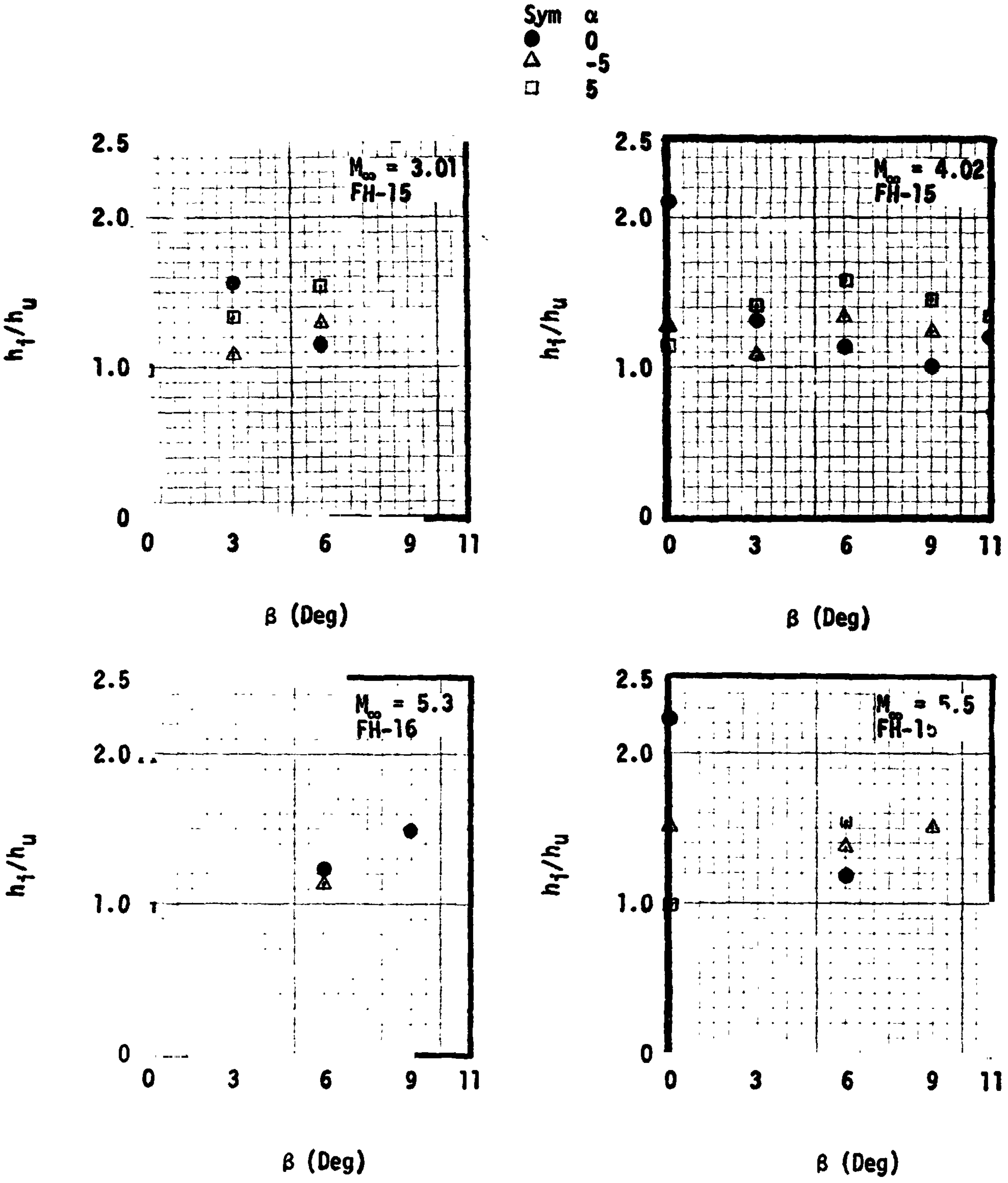

Fig. 4.41 Peak Heating Values of T/C 121 Located in Front of Attachment Fitting on ET AADS Forebody at Θ_T = 28.8° and X/L = 0.0604

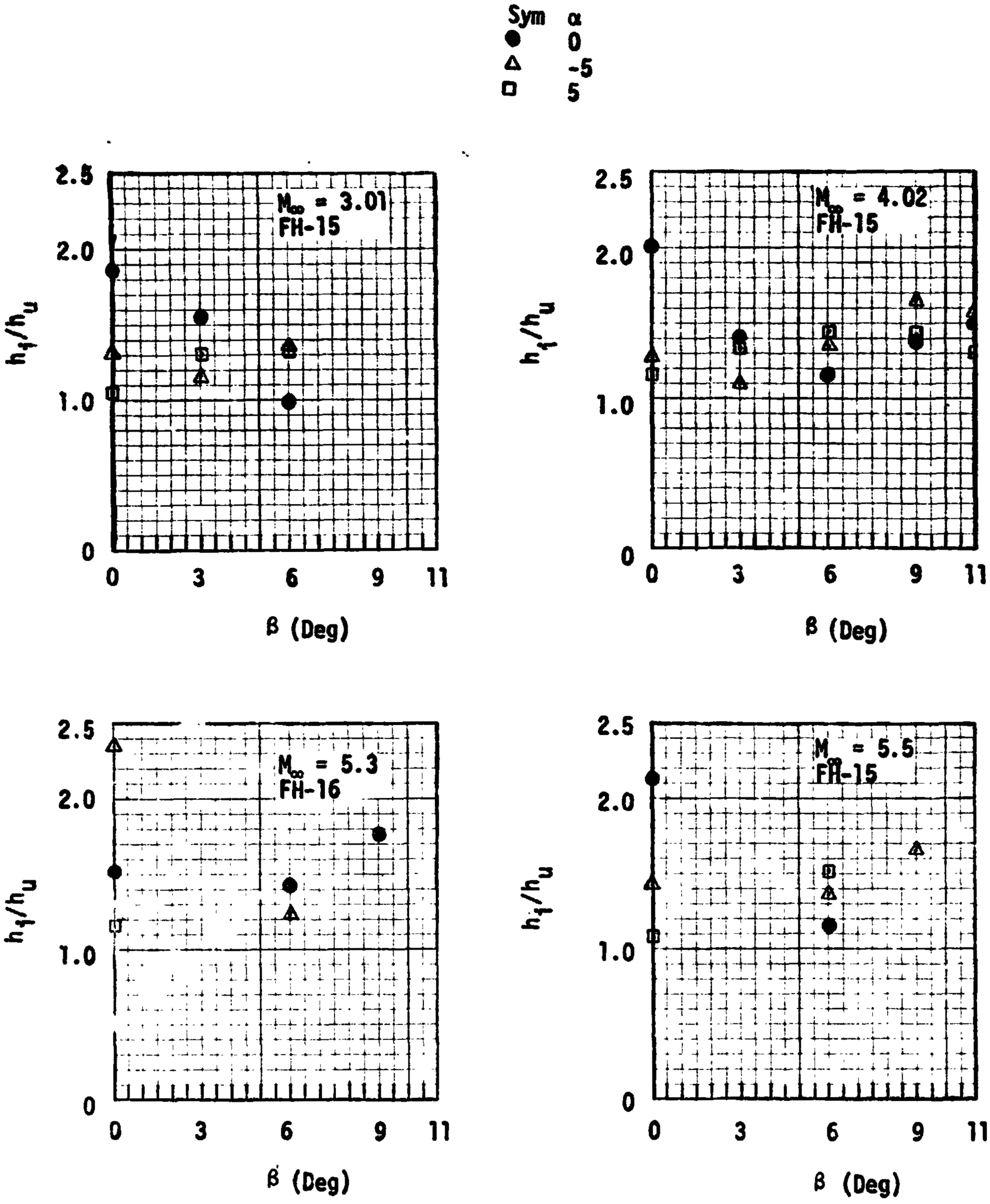

Fig. 4.42 Peak Heating Values of T/C 136 Located in Front of Attachment Fitting on ET AADS Forebody at $\Theta_T = 29.3^\circ$ and X/L = .0795

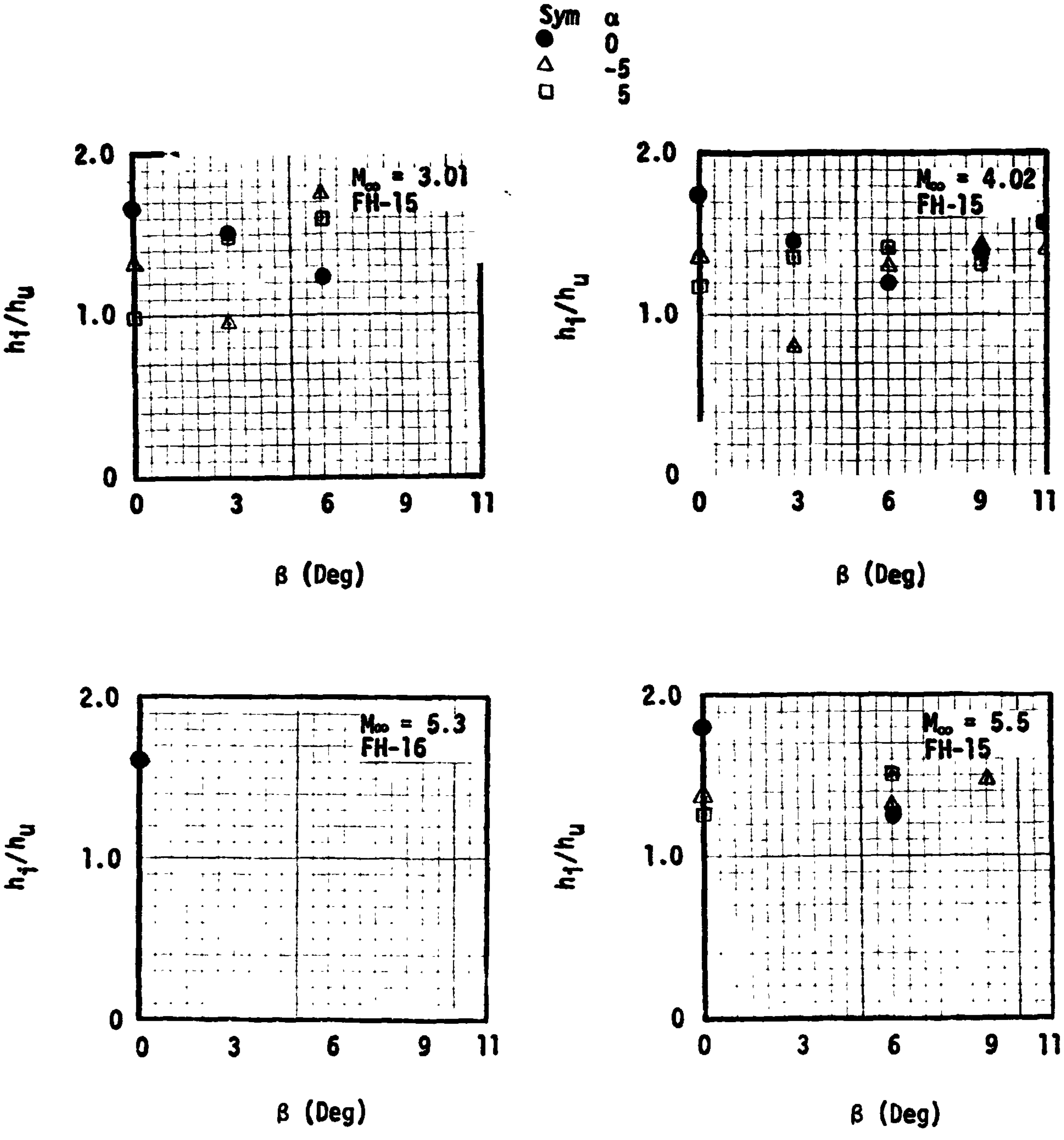

Fig. 4.43 Peak Heating Values of T/C 146 Located in Front of Attachment Fitting on ET AADS Forebody at Θ_T = 29.7° and X/L = 0.100

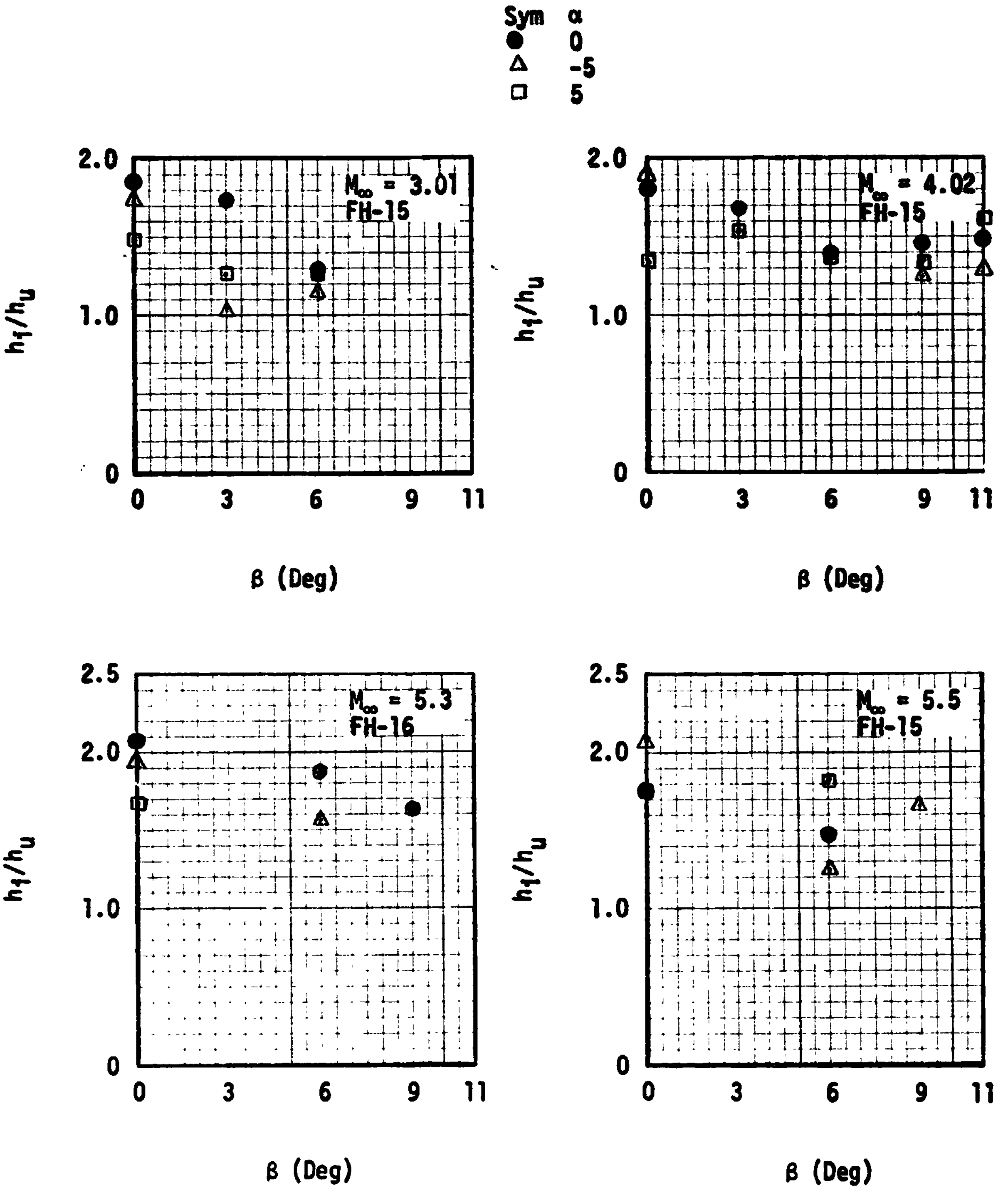

Fig. 4.44 Peak Heating Values of T/C 242 Located in Front of Attachment Fitting on ET AADS Forebody at Θ_T = 30.3° and X/L = 0.2101

4.4 References

4.1 Carroll, Harry R., "External Tank Data Report for the Supersonic Heat Transfer Test of the 30°/10°/40° Cone Ogive .0275 Scale ET Forebody in the AEDC-VKF Tunnel "A" Facility," Martin Marietta Report MMC-ET-SE05-82, July 1978.

4.2 Carroll, Harry R., "External Tank Data Report for Heat Transfer Test FH-16 on a .0275 Scale ET 30°/10°/40° Cone-Ogive in the NASA-Ames 3.5 Foot Hypersonic Wind Tunnel Facility," Martin Marietta Report MMC-ET-SE05-81, June 1978.

4.3 Praharaj, S. C., "Undisturbed Flowfield and Turbulent Heat-Transfer Analysis on the Space Shuttle External Tank," AIAA Paper 79-0378, New Orleans, La., Jan. 1979.

4.4 Waiter, S. A., "Determination of the Temperature Efficiency in Low Temperature Wind Tunnels - An Engineering Attempt," Rockwell International Internal Letter to C. A. Scottoline, IL-SAS-AA&T-76-0977, June 24, 1976.

4.5 Lapointe, Judy K., Powell, Robert T., and Engel, Carl D., "ET LO_2 Tank Heating From FH-15 and FH-16 Tests," REMTECH Report RM 029-1, January 1979.

Section 5

INDIVIDUAL PROTUBERANCE DATA

The purpose of this section is to present heat transfer data and correlations for protuberances which have been individually tested. The data were obtained from calibration runs made with accompanying material test runs. The data from the calibration runs provides a data base of interest in itself. The tests were conducted at AEDC Tunnel C at a nominal Mach number of 10. The protuberances tested were mounted on a wedge. The parameters varied were the wedge angle, total pressure, and protuberance geometry. The following subsections describe the heating data to the different protuberances tested.

5.1 SRB Systems Tunnel (Forward End)

All of the protuberance data were obtained by attaching the protuberance to a wedge fixture. In order to nondimensionalize the measured heating data to the undisturbed value, the proper wedge heating rates were required. The tests for all protuberances in subsections 5.1 to 5.5 were conducted using wedge angles between 0 and 25 degrees. The wedge Mach number for $M_\infty = 10.17$ is given in Fig. 5.1. Calibration data on the wedge were obtained for several run conditions. These data, along with theory, were used to establish the local undisturbed heating.

Wedge heating rate data are presented in Fig. 5.2. Unfortunately, some of the data is transitional. This required determining the virtual origin of the turbulent boundary layer as a function of wedge angle. The virtual origin was determined empirically using the Spaulding-Chi turbulent boundary layer theory as a basis. The virtual origins are marked in Fig. 5.2 and are plotted in Fig. 5.3. The data past 21 inches on the wedge could not be used since the flow was effected by separation due to the protuberance being tested.

Based on the results of Figs. 5.2 and 5.3, an equation was developed for nondimensionalizing the data presented in subsections 5.1 and 5.2.

$$q_u = q_{12}\left(\frac{12}{X-X_v}\right)^{0.2}$$

where

q_u = Undisturbed local heating rate at X

q_{12} = Undisturbed Spaulding-Chi heating rate at 12 inches running length.

X_v = Virtual origin location from leading edge of wedge

X = Distance of point of interest from leading edge of wedge.

The recovery factor on the wedge and protuberance are assumed equal, thus, making the heating rate and heat transfer coefficient ratios equal.

The protuberance model of the systems tunnel is shown schematically in Fig. 5.4. A side view of the model, along with the shock structure, is given by the shadowgraphs in Fig. 5.5. The effect of wedge angle on shock structure is also shown in Fig. 5.5. Enlarged shadowgraphs for wedge angles of 10 and 18 degrees are given in Figs. 5.6 and 5.7. Note that the wedge shock and forward face shock intersect and produce a weak shock impinging near the top leading edge of the tunnel.

The systems tunnel heating factor data are presented in tabular form in Table 5.1 . These data were obtained from Refs. 5.1 and 5.2. Data from Ref. 5.1 is denoted by a "D" in the run number and data from 5.2 by a "S" in the run number. The individual test conditions are listed below the associated heating amplification factors.

Plots of the systems tunnel centerline data for two tunnel total pressures are given in Figs. 5.8a and b. The small peak in heating on the forward face is a result of the forward face shock and wedge boundary layer interaction. The low heating on the aft end of cylindrical section is due to boundary layer separation. This is induced by the flow angle off of the front face and the reflected shock impingement near the forward end of the cylinder section.

The heating amplification over most of the forward face is nearly constant. This constant value is correlated with the theoretical wedge pressure values as shown in Fig. 5.9. The correlation with pressure ratio is quite good.

The heating distribution around the cylindrical section of the protuberance is shown in Fig. 5.10. The open symbols indicate a symmetrical distribution exists for no yaw. Further, the heating is highest on the side where flow is probably attached due to the presence of the wedge. The effect of yaw is illustrated by the solid symbols. Yaw produces a significant heating factor on the windward side of the tunnel.

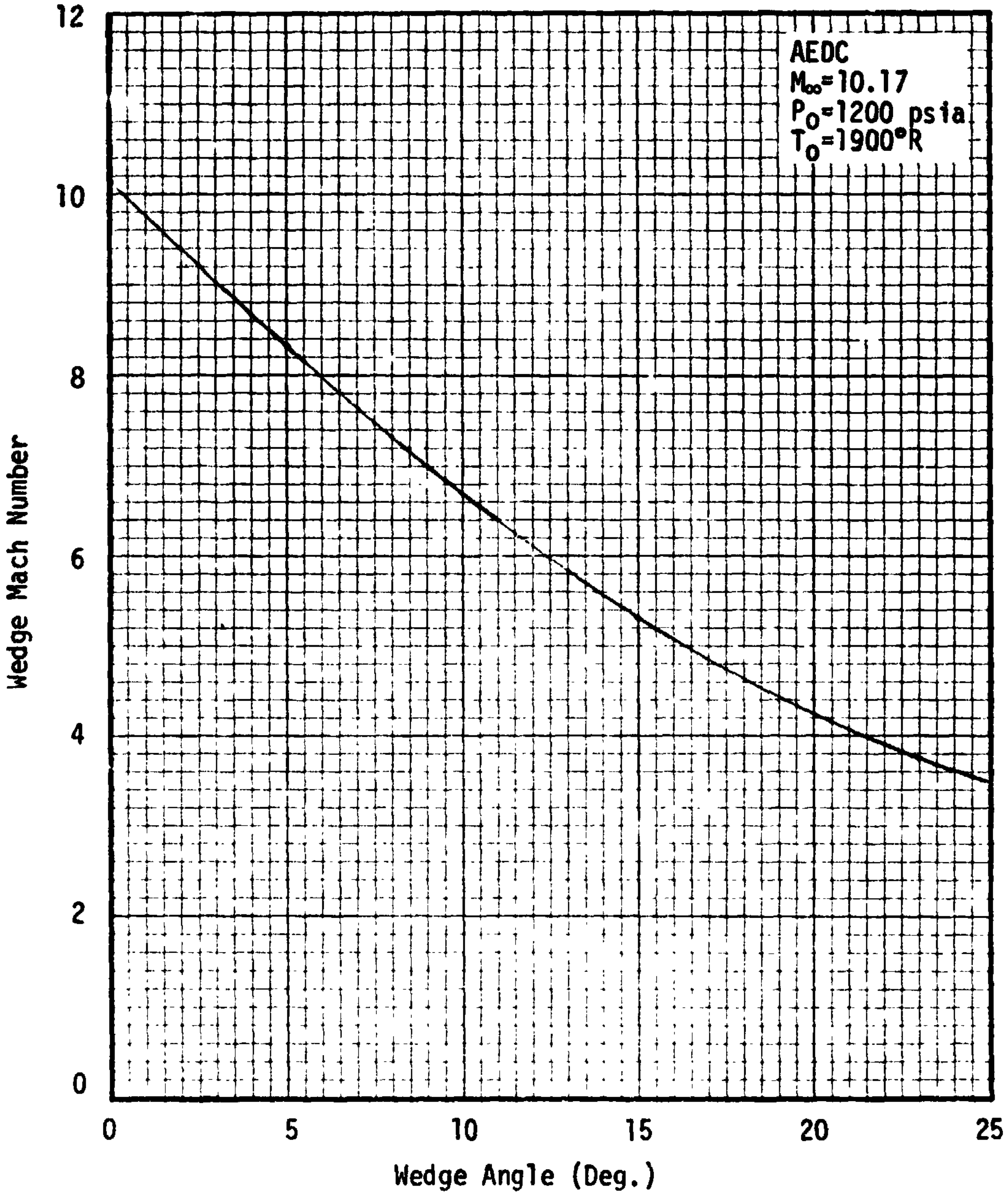

Fig. 5.1 Wedge Mach Number for Attach Ring Calibration Test

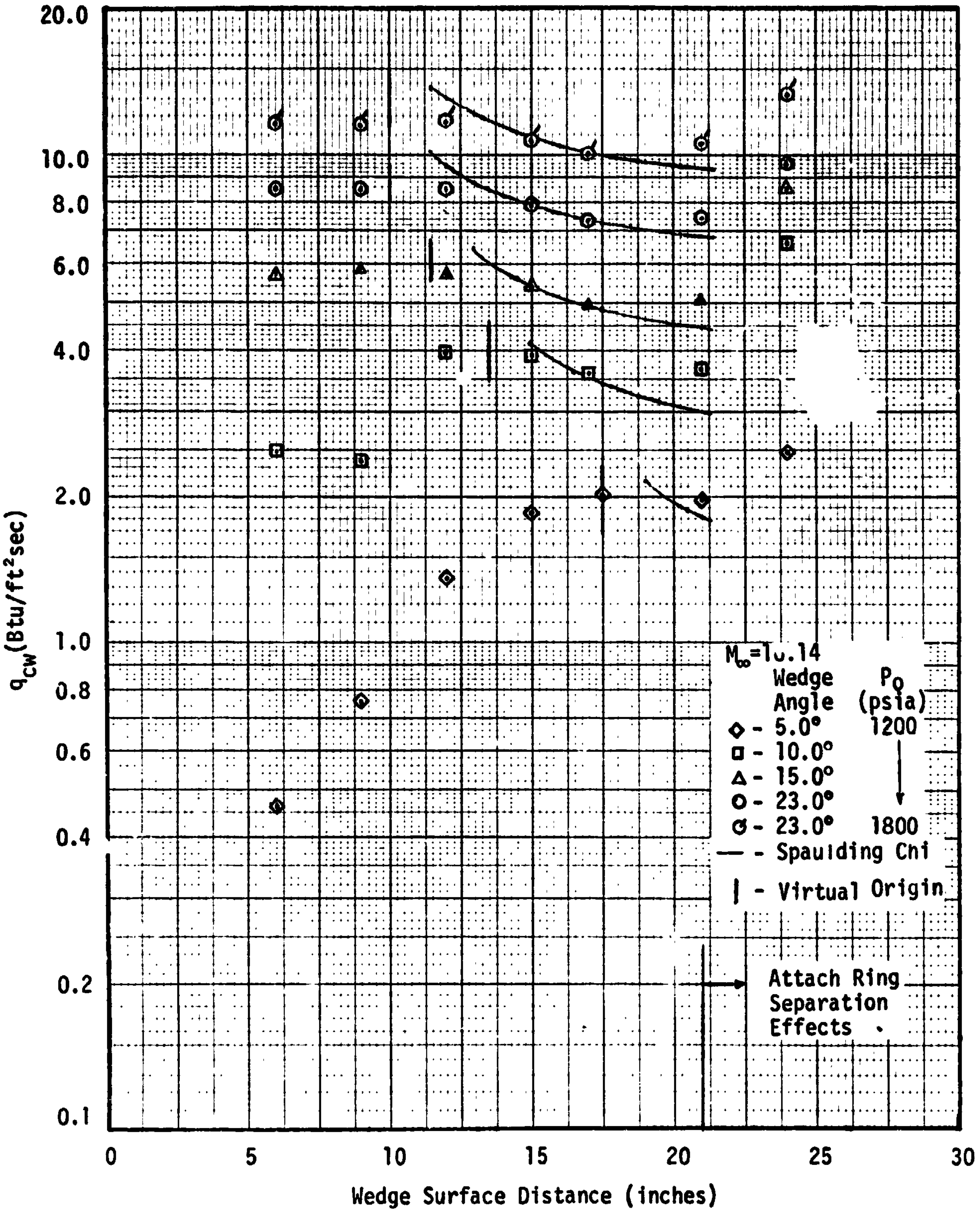

Fig. 5.2 Comparison of Wedge Heating Rates with Theory (T_w = 460°R)

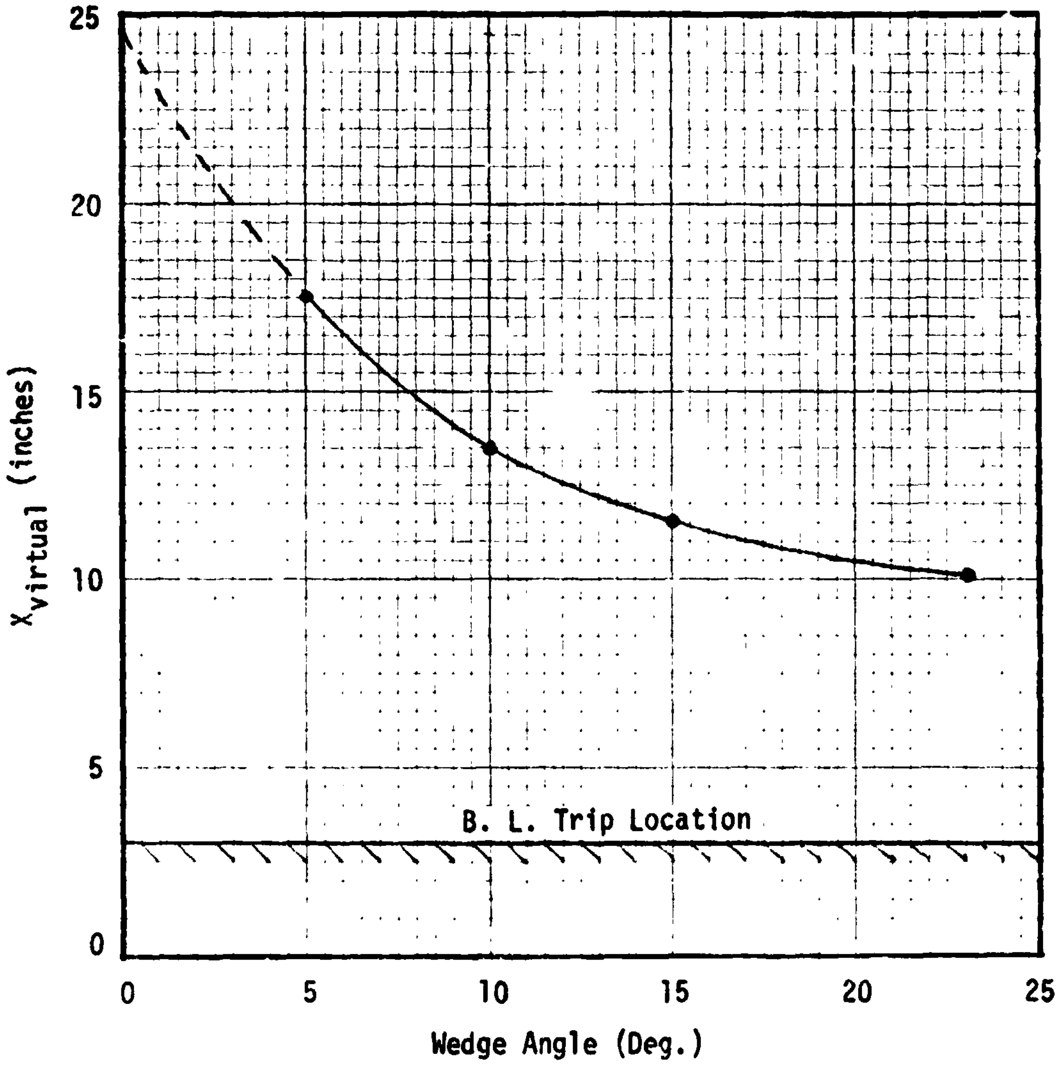

Fig. 5.3 Virtual Origin Correlation for AEDC Wedge Conditions

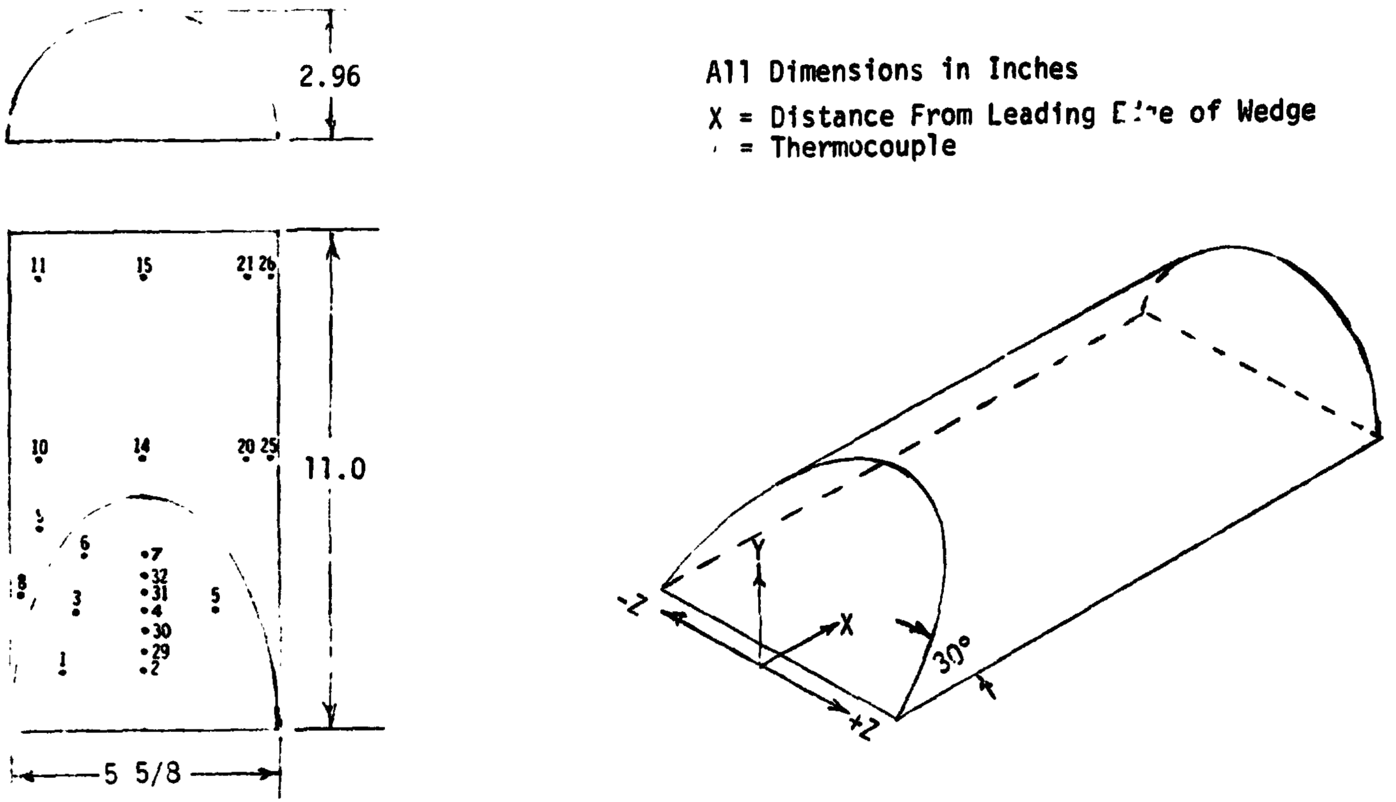

All Dimensions in Inches

X = Distance From Leading Edge of Wedge

• = Thermocouple

Fig. 5.4 SRB Systems Tunnel Protuberance Model

δ_w = 5 Deg.
M_∞ = 10.17
P_o = 1796 psia
T_o = 1996°R
Run 1S

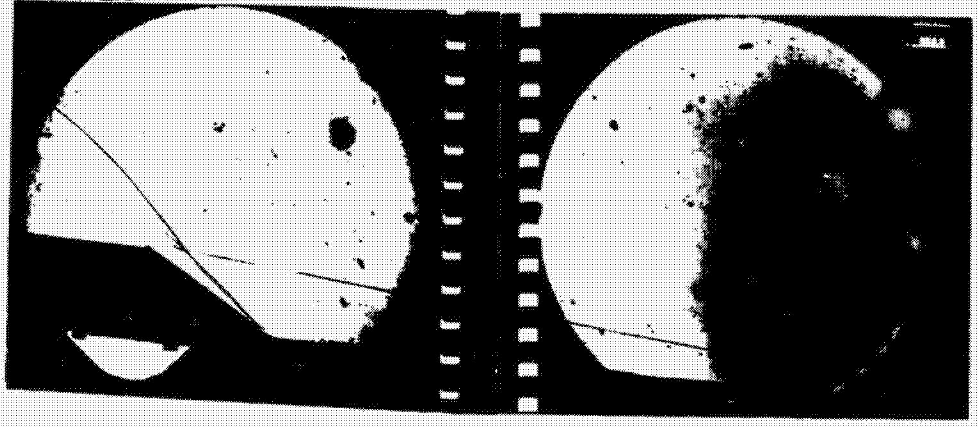

δ_w = 10 Deg.
M_∞ = 10.17
P_o = 1805 psia
T_o = 1996°R
Run 2S

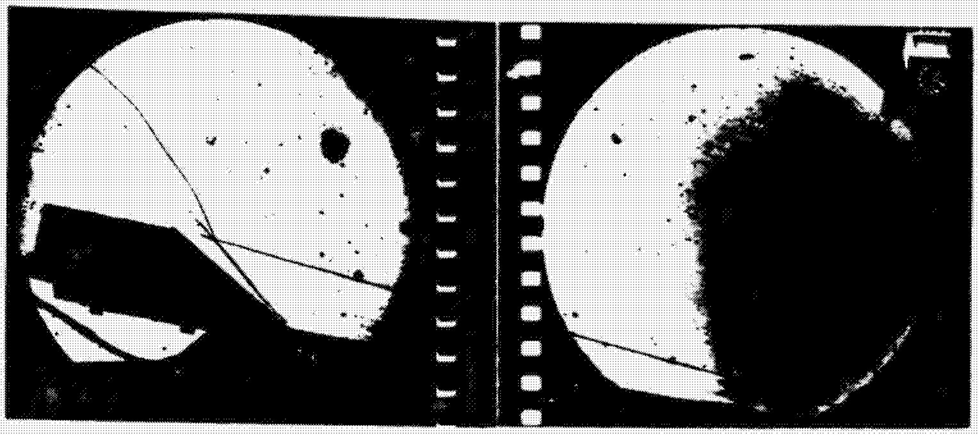

δ_w = 18 Deg.
M_∞ = 10.11
P_o = 800 psia
T_o = 1887°R
Run 25D

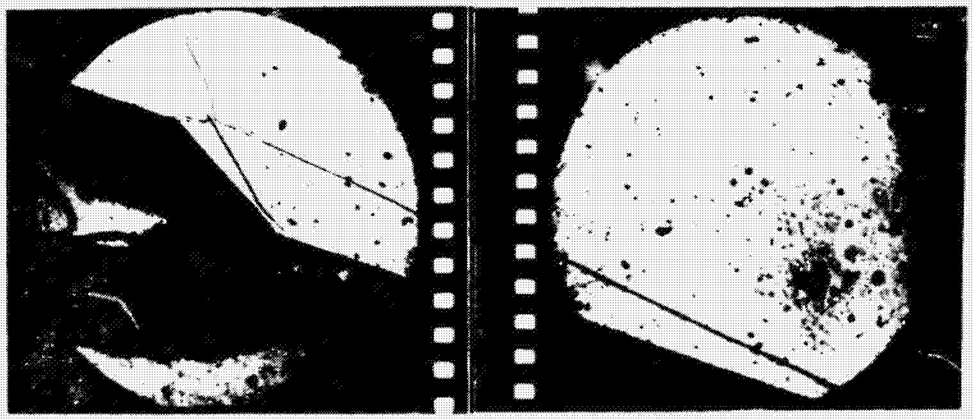

δ_w = 23 Deg.
M_∞ = 10.11
P_o = 799 psia
T_o = 1889°R
Run 26D

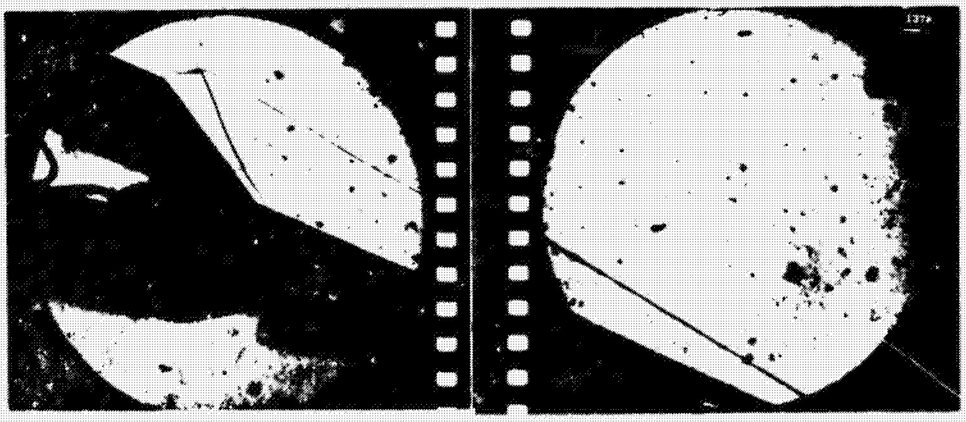

Fig. 5.5 System Tunnel Shadowgraph Series

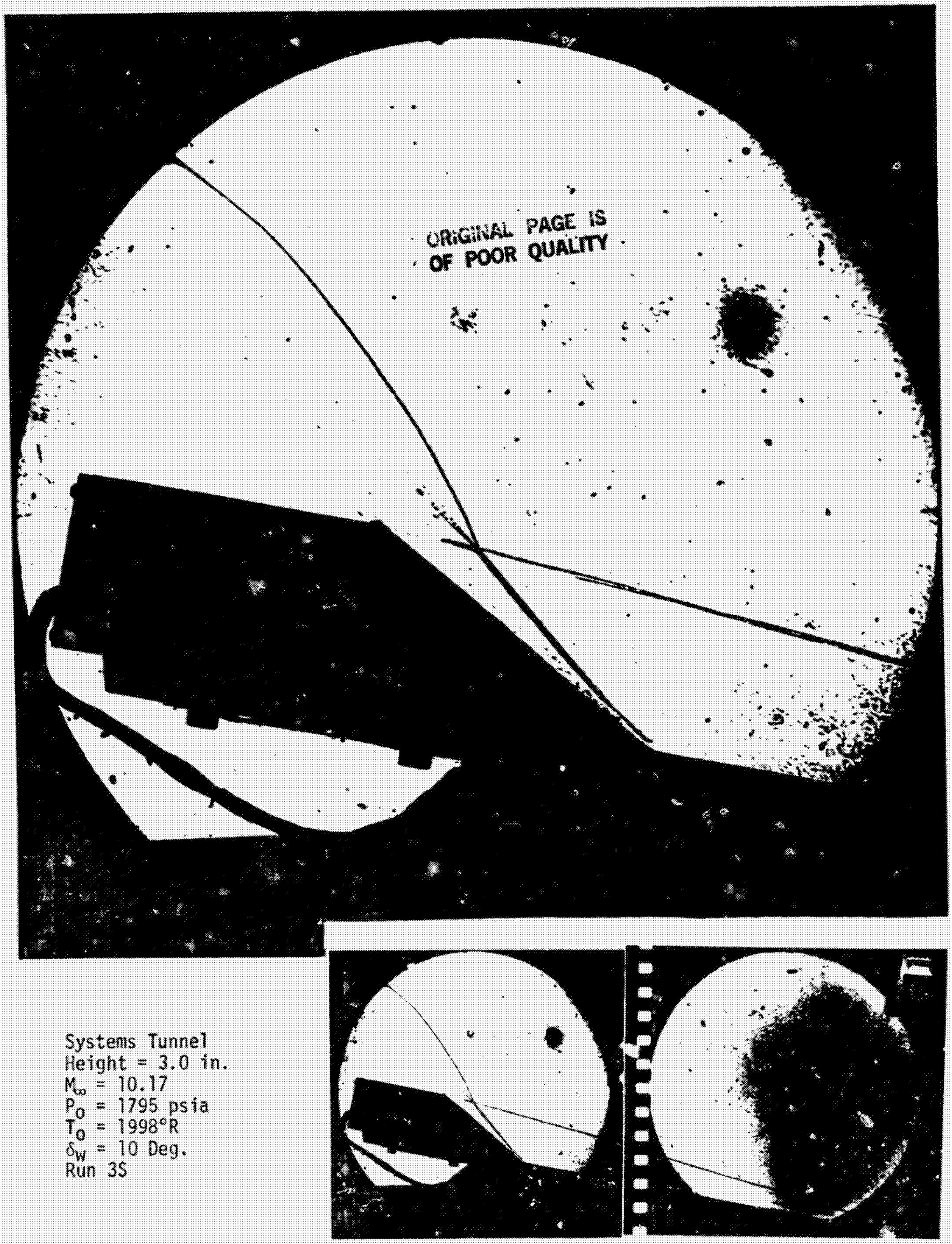

Systems Tunnel
Height = 3.0 in.
$M_\infty = 10.17$
$P_o = 1795$ psia
$T_o = 1998°R$
$\delta_w = 10$ Deg.
Run 3S

Fig. 5.6 Systems Tunnel Shadowgraph Enlargement for $\delta_w = 10$ deg.

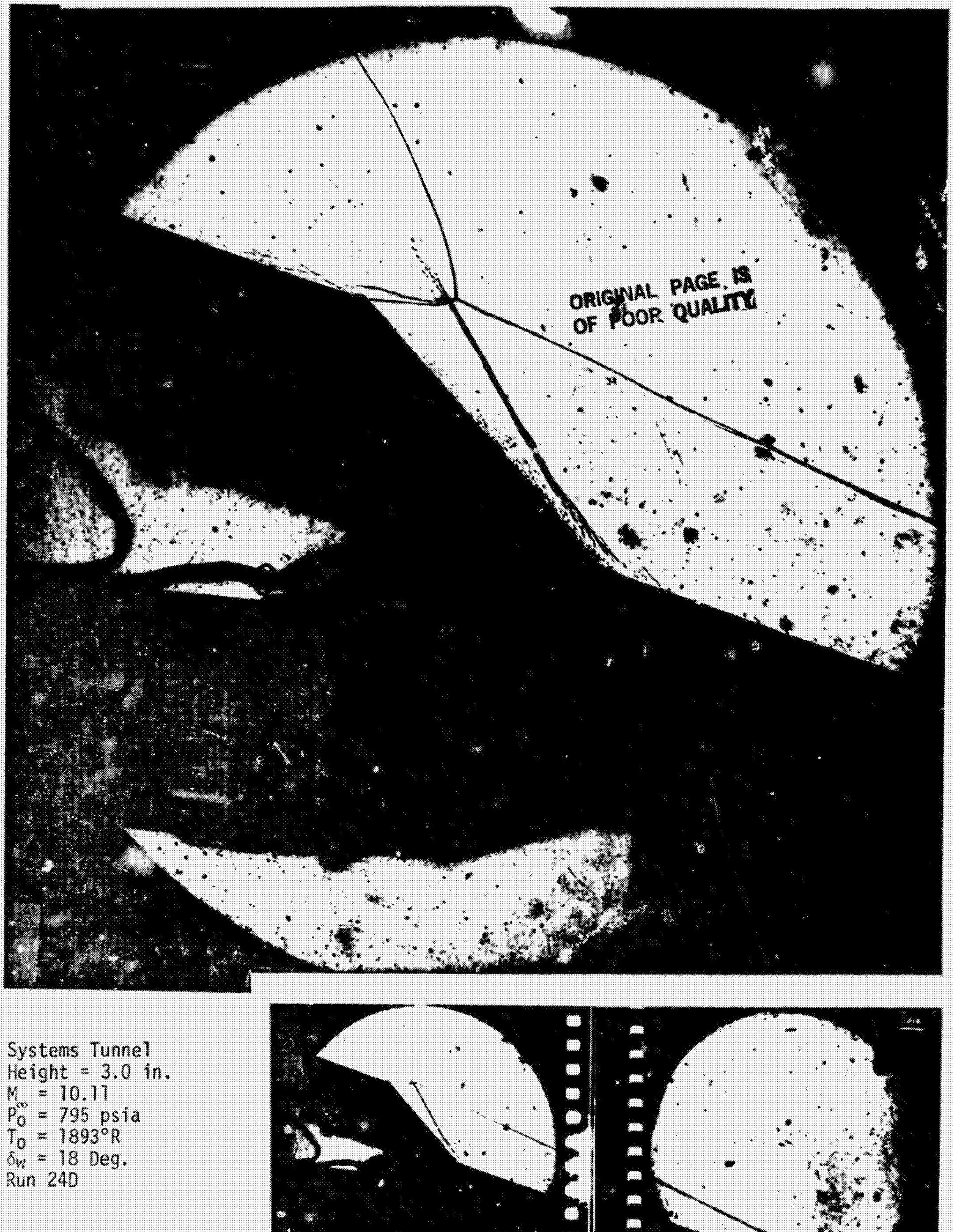

Systems Tunnel
Height = 3.0 in.
M_∞ = 10.11
P_0 = 795 psia
T_0 = 1893°R
δ_W = 18 Deg.
Run 24D

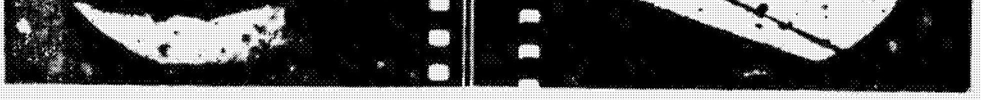

Fig. 5.7 Systems Tunnel Shadowgraph Enlargement for δ_W = 18 Deg.

Table 5.1
Systems Tunnel Heating Amplification Factors

TC NO.	X (IN)	Y (IN)	Z (IN)	h_i/h_u	h_i/h_u	h_i/h_u	h_i/h_u	h_i/h_u	h_i/h_u	h_i/h_u	h_i/h_u	h_i/h_u
1	32.80	0.75	-1.75	22.39	13.09	12.89	12.75	12.95	16.07	8.83	8.92	6.43
2	32.80	0.75	0.00	20.86	12.80	12.78	12.57	12.68	15.47	8.73	8.79	6.30
3	34.10	1.50	-1.50	18.42			11.82	11.79		7.99	8.07	5.79
4	34.10	1.50	0.00	17.40	11.82	11.86	11.38	11.56	12.72	7.95	8.13	5.73
5	34.10	1.50	1.50	17.23	12.03	11.99	11.70	11.81	13.26	7.99	8.01	5.78
6	35.40	2.25	-1.25	16.64	11.40	11.45	11.15	11.35	12.53	7.74	7.87	5.71
7	35.40	2.25	0.00	14.65	10.36	10.31	9.76	10.04	11.38	7.11	7.23	5.17
8	34.50	1.00	-2.75	1.22	0.83	0.76	0.27	0.28	0.83	0.57	0.59	0.54
9	36.00	2.00	-2.25	0.74	0.53	0.50	0.48	0.45	0.55	0.36	0.40	0.36
10	37.50	2.00	-2.25	0.36	0.32	0.35	0.37	0.39	0.36	0.21	0.22	0.20
11	41.50	2.00	-2.25	0.28	0.35	0.35	0.07	0.07	0.25	0.70	0.73	0.78
14	37.50	3.00	0.00	1.60	0.85	0.81	0.67	0.67	0.82	1.52	1.50	1.10
15	41.50	3.00	0.00	0.49	0.29	0.29	0.29	0.27	0.30	0.28	0.20	0.32
20	37.50	2.00	2.25	0.45	0.32	0.33	2.81	2.84	0.41	0.22	0.23	0.23
21	41.50	2.00	2.25	0.72	0.71	0.76	2.63	2.62	0.54	0.63	0.65	0.65
25	37.50	1.00	2.75	1.40	1.27	1.25	3.53	3.59	1.11	1.25	1.31	1.17
26	41.50	1.00	2.75	1.56	1.24	1.26	3.44	3.56	1.01	1.34	1.38	1.37
29	33.23	1.00	0.00	18.19	11.05	11.56	11.26	11.28	13.27	7.77	7.81	5.49
30	33.67	1.25	0.00	17.58	11.25	11.16	10.99	11.23	12.64	7.80	8.00	5.65
31	34.53	1.75	0.00	16.73	11.43	11.37	10.95	11.09	12.45	7.69	7.83	5.58
32	34.96	2.00	0.00	16.59	11.45	11.27	10.87	10.88	12.56	7.79	7.91	5.69
Run				1S	2S	3S	4S	5S	6S	24D	25D	26D
M_∞				10.17	10.17	10.17	10.17	10.17	10.08	10.11	10.11	10.11
P_o (psia)				1796.	1805.	1795.	1803.	1798.	802.	795.	800.	799.
T_o (°R)				1996.	1996.	1998.	1994.	1997.	2002.	1893.	1887.	1889.
Wedge Angle (Deg.)				5.02	10.04	10.05	10.04	10.06	10.04	18.00	18.02	23.01
Yaw Angle (Deg.)				0.00	0.00	0.00	11.00	11.00	0.00	0.00	0.00	0.00
q_{12} (Btu/ft^{2}sec) at X = 12"				1.986	3.864	3.864	3.864	3.864	2.052	3.568	3.568	4.574

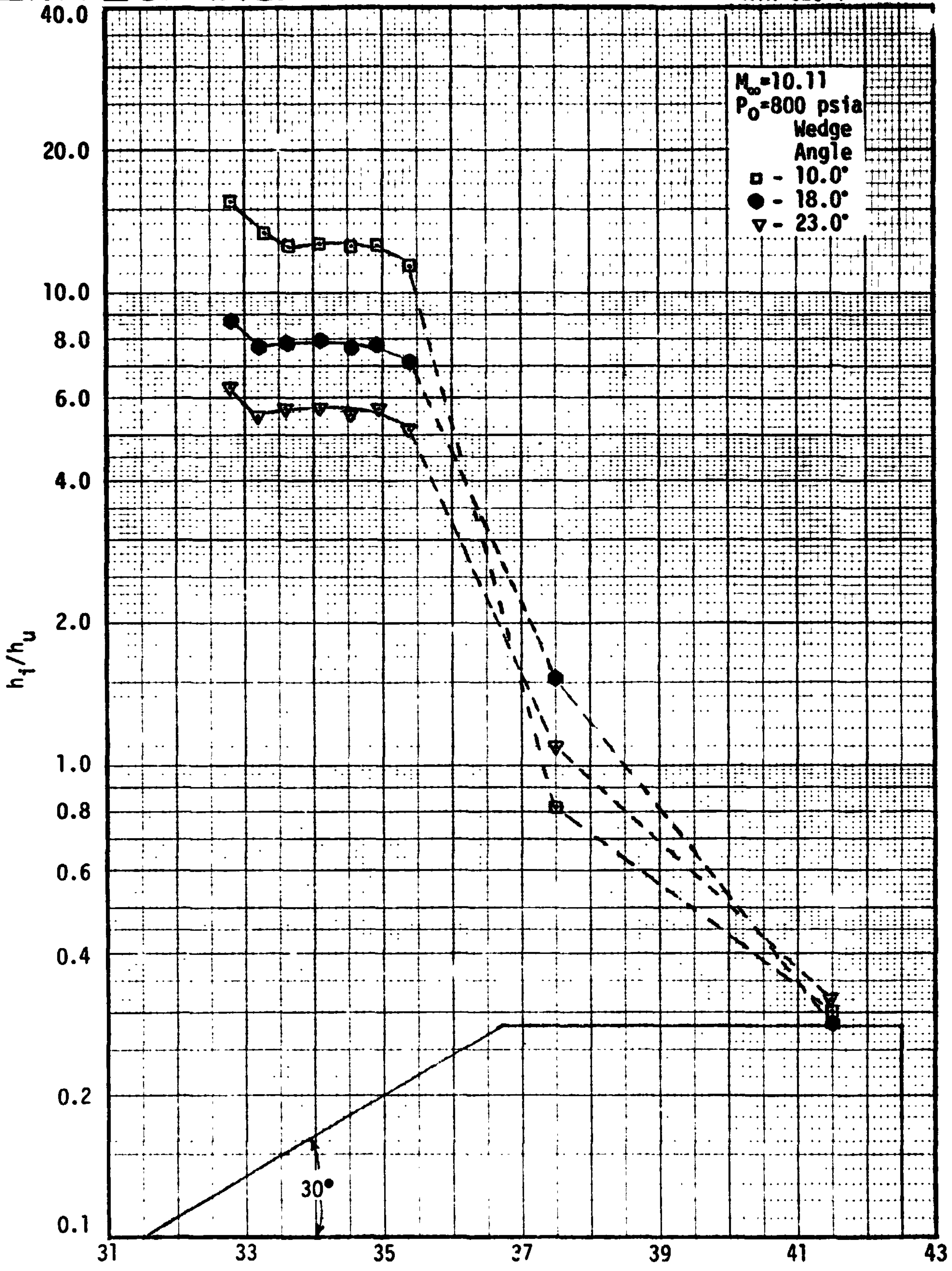

Fig. 5.8a Systems Tunnel Centerline Interference Factors at P_o = 800 psi

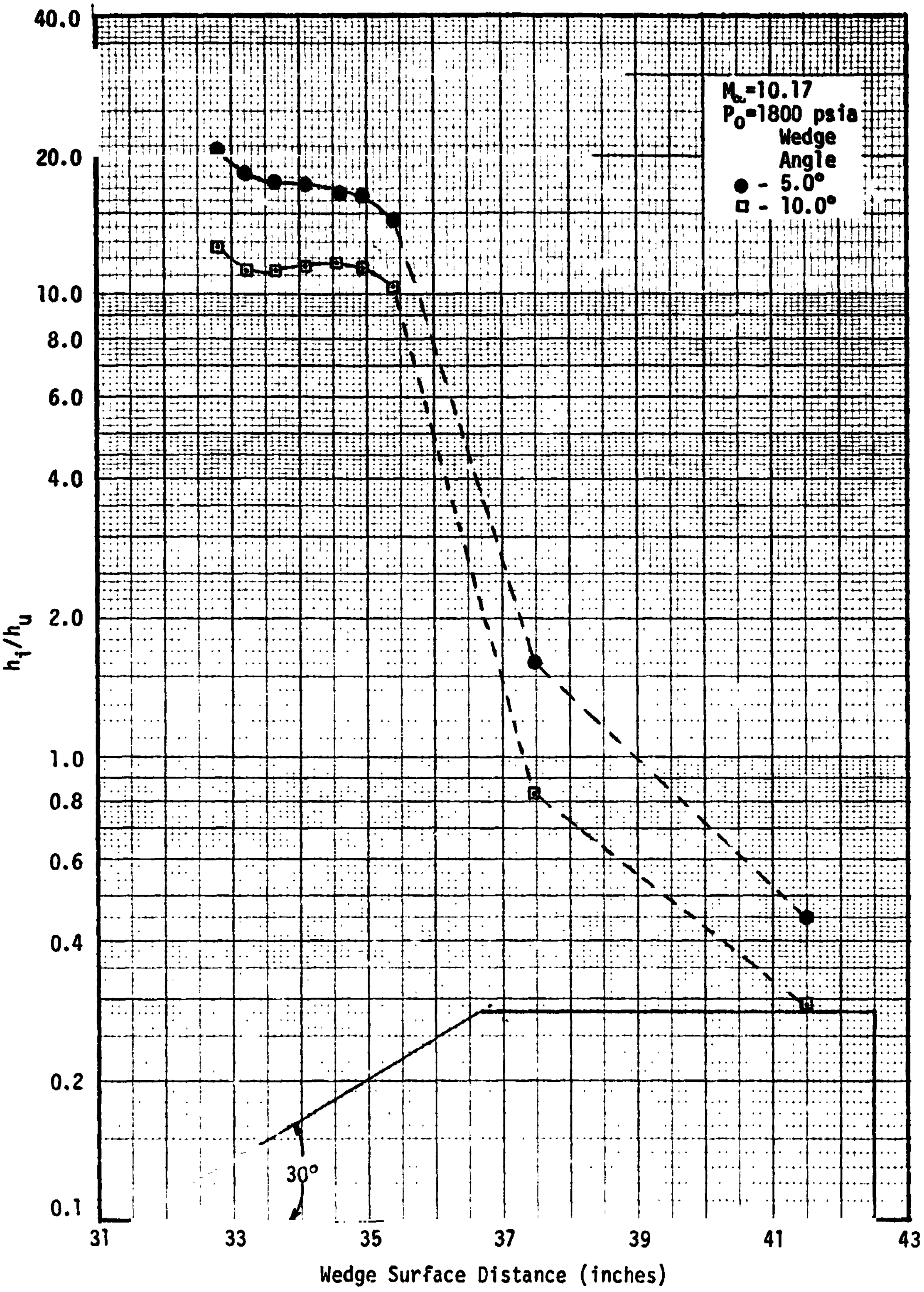

Fig. 5.8b Systems Tunnel Centerline Interference Factors at P_0 = 1800 psia

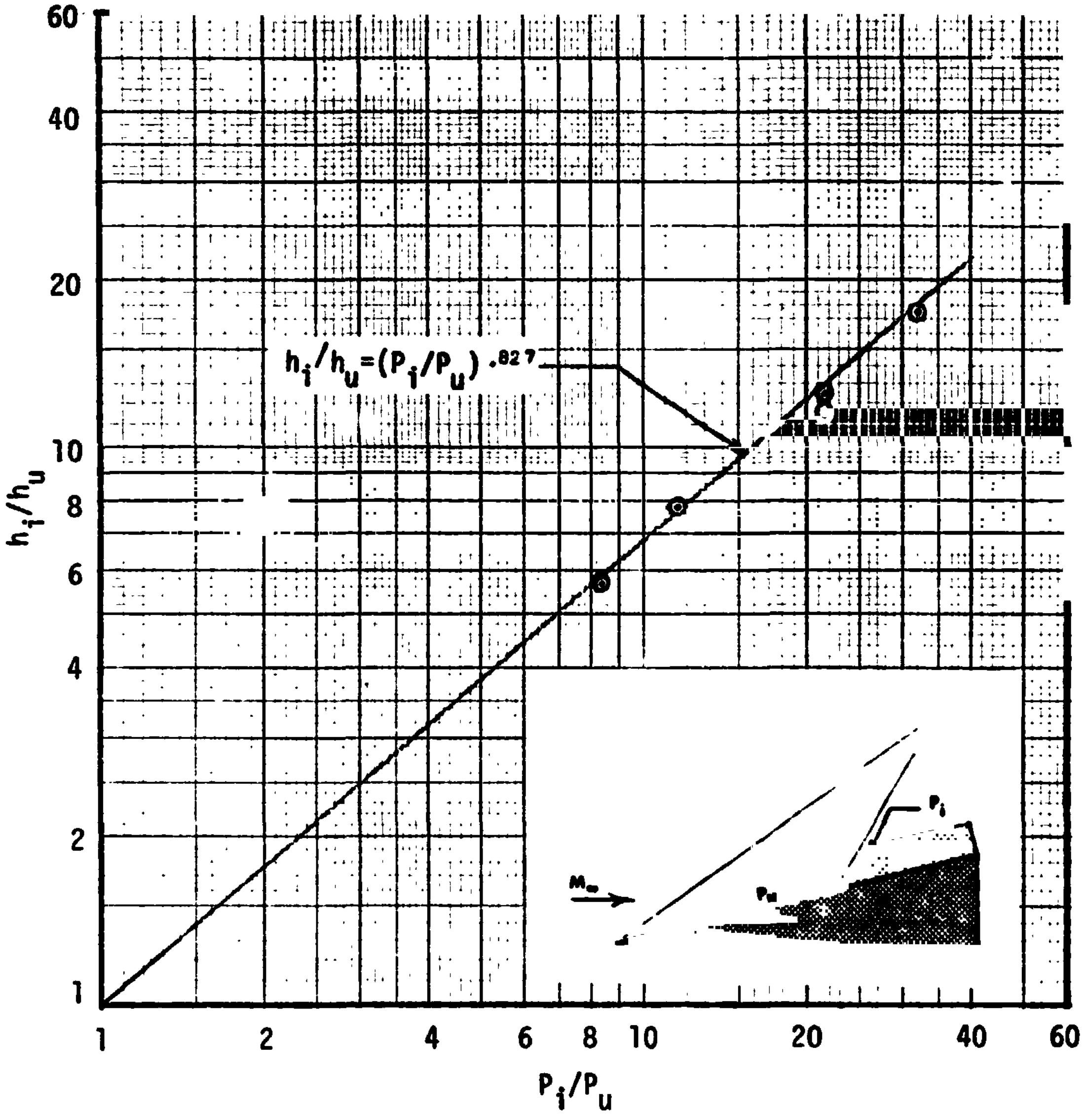

Fig. 5.9 SystemsTunnel Front Face Plateau Heating Amplification Correlated with Theoretical Wedge Pressures

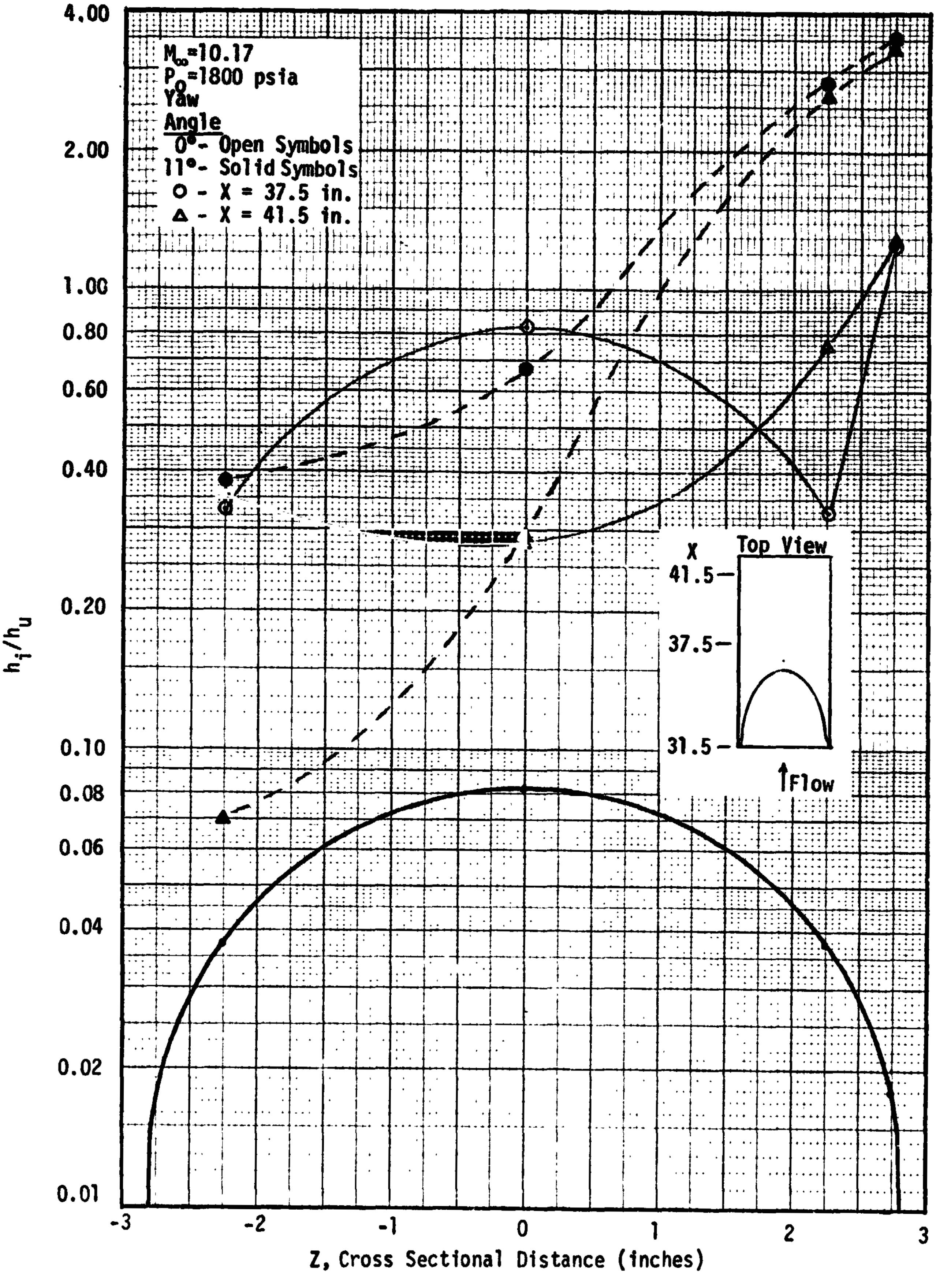

Fig. 5.10 Systems Tunnel Cross Flow Heating Factor Distributions for a Wedge Angle of 10 Degrees.

5.2 SRB Command Destruct Anten. a

The geometry and thermocouple locations for the SRB command destruct antenna are shown in Fig. 5.11. This configuration was run for a series of wedge angles and two total pressures. A series of shadowgraphs for one total pressure level is shown in Fig. 5.12. The double wedge geometry placed on the main wedge fixture produces a complex triple shock interaction.

Shadowgraph enlargements for two total pressure levels for a wedge angle of 5.0 degrees are shown in Fig. 5.13. The shock from the small wedge interacts with the second wedge shock of the protuberance in a different manner at low pressure than at high pressure. This is a result of the different boundary layer thickness. The shadowgraphs in Fig. 5.14 for the same pressure level and two wedge angles also show that the first and second protuberance shock interact differently as a function of wedge angle.

The heating amplification data derived from Ref. 5.1 is presented in Table 5.2. The heating data from Ref. 5.1 was nondimensionalized using the methods described in subsection 5.1.

Centerline interference factors are plotted in Figs. 5.15 and 5.16 for two tunnel total pressures. Near the end of the second wedge section the heating reaches a plateau value. The peak heating which occurs on the leading end of the second wedge is a result of the shock interactions discussed with the shadowgraphs. The highest peaks on the second wedge are accompanied by the lowest factors on the first wedge. Separation occurs on the top surface for all wedge angles greater than zero for $P_0 = 1800$ psia, whereas, separation and reattachment occurs for $\delta_W = 5$ and 10 degrees for $P_0 = 300$ psia.

The plateau heating factors on the second wedge of the protuberance were correlated with the theoretical pressure rise across a single wedge shock.

The results are shown in Fig. 5.17. This correlation shown is the same as that developed for the wedge section of the systems tunnel. The agreement is reasonably good considering the additional flow complexity caused by the small leading wedge of the protuberance. The peak heating amplification was correlated in the same manner and is shown in Fig. 5.18. The peak values for P_o = 300 psia correlate with the line given in the figure. However, the data for P_o = 1800 has two characteristics. At low P_i/P_u the data agrees with the plateau values. Then, a transition in character occurs at a wedge angle of 5 degrees and at zero degree wedge angle the data is in agreement with the P_o = 300 psia data. This behavior is a result of the effect of the boundary layer on the shock structure produced by the first wedge of the protuberance.

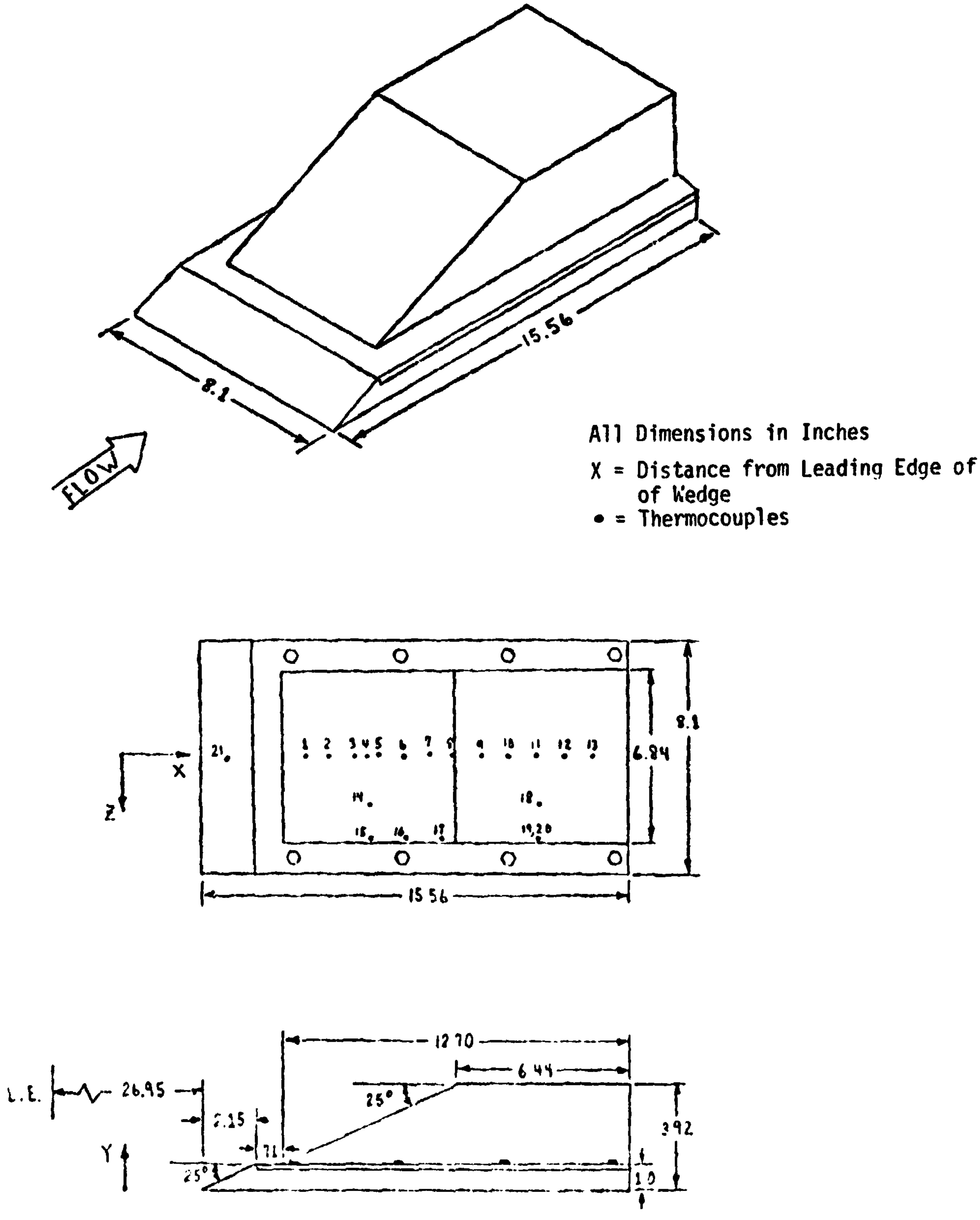

All Dimensions in Inches

X = Distance from Leading Edge of of Wedge

● = Thermocouples

Fig. 5.11 SRB Command Destruct Antenna Protuberance Model

δ_w = 0 Deg.
Run 38D

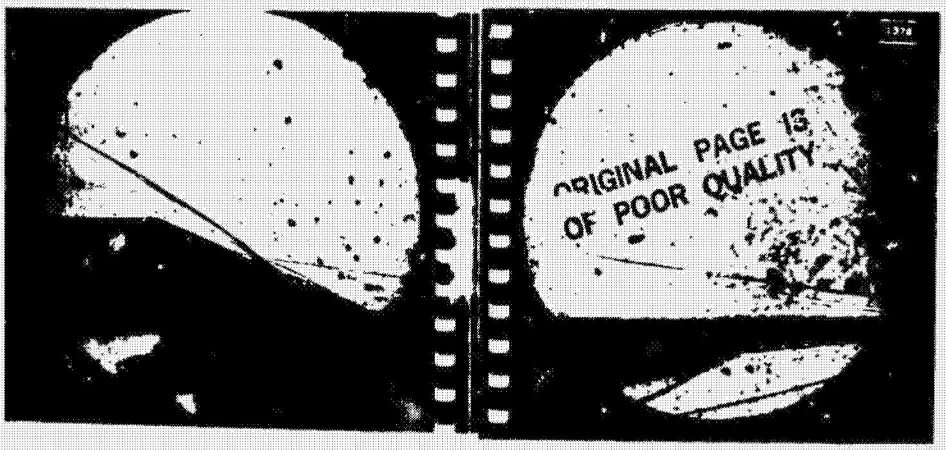

δ_w = 5 Deg.
Run 39D

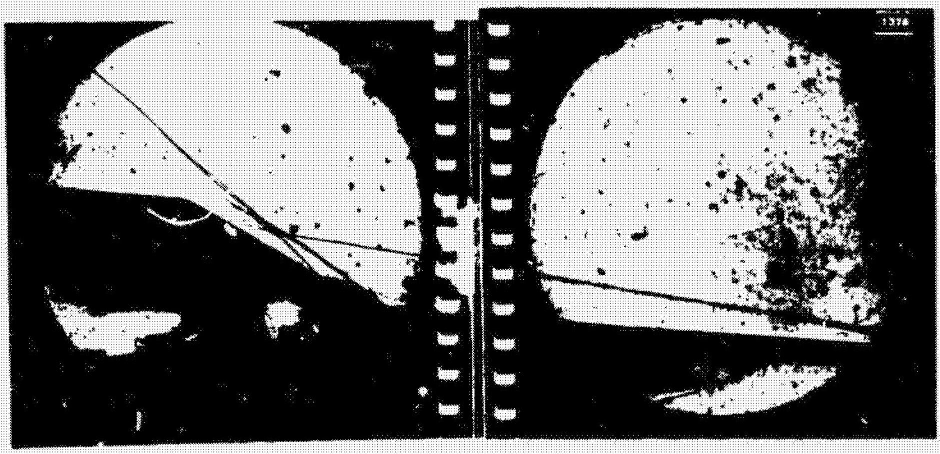

δ_w = 10 Deg.
Run 40D

All Runs at
M_∞ = 10.17
P_o = 1800 psia
T_o = 1900°R

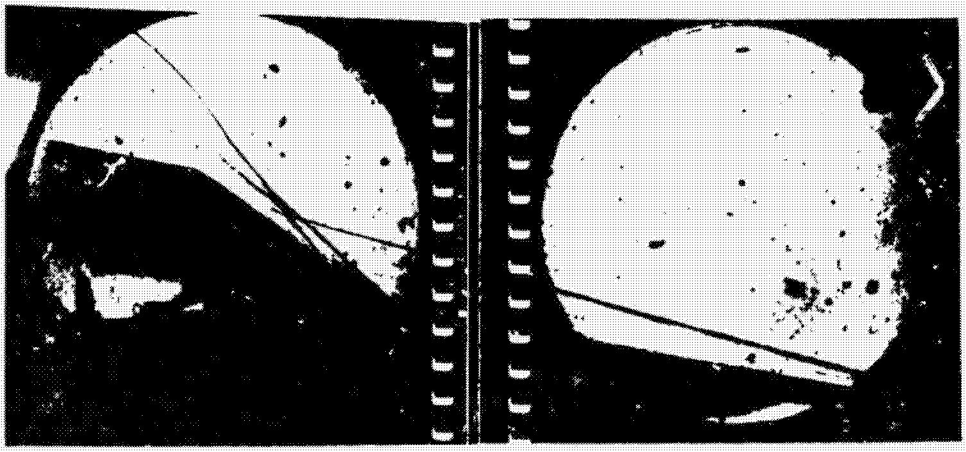

Fig. 5.12a C. D. Antenna Shadowgraph Series

δ_w = 15 Deg.
Run 41D

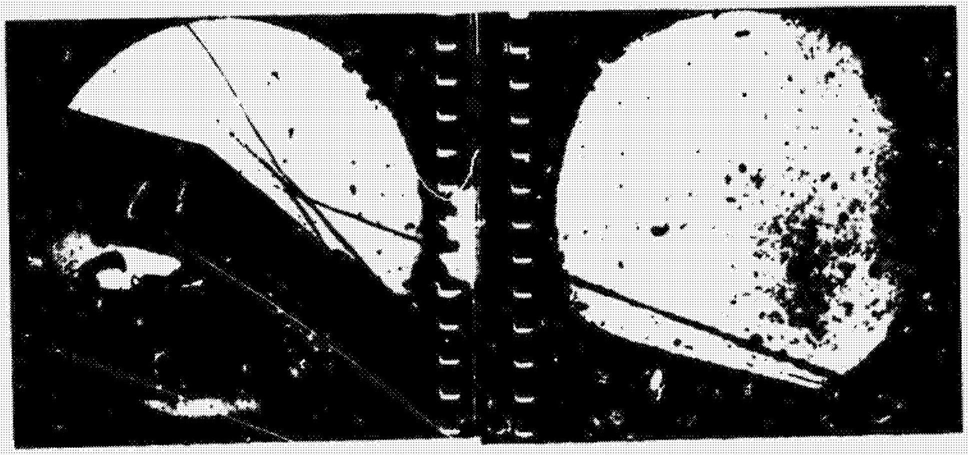

δ_w = 20 Deg.
Run 42D

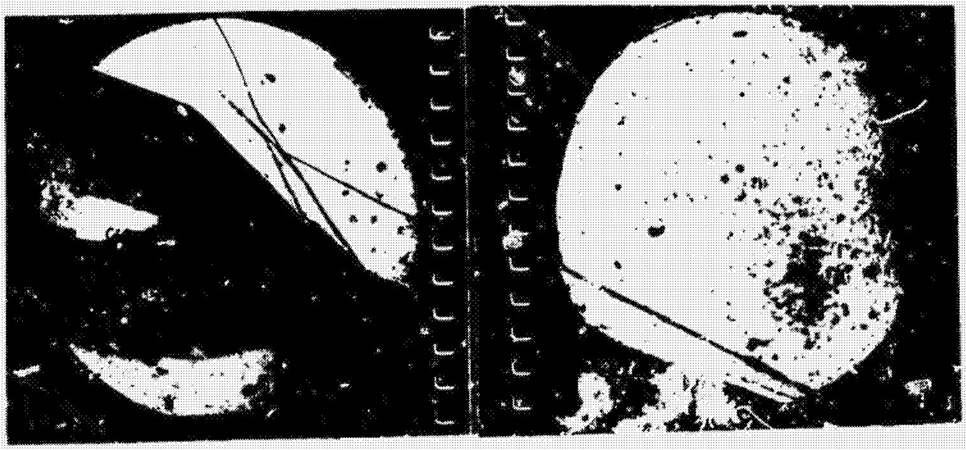

δ_w = 24.5 Deg.
Run 43D

All Runs at
M_∞ = 10.17
P_o = 1800 psia
T_o = 1900°R

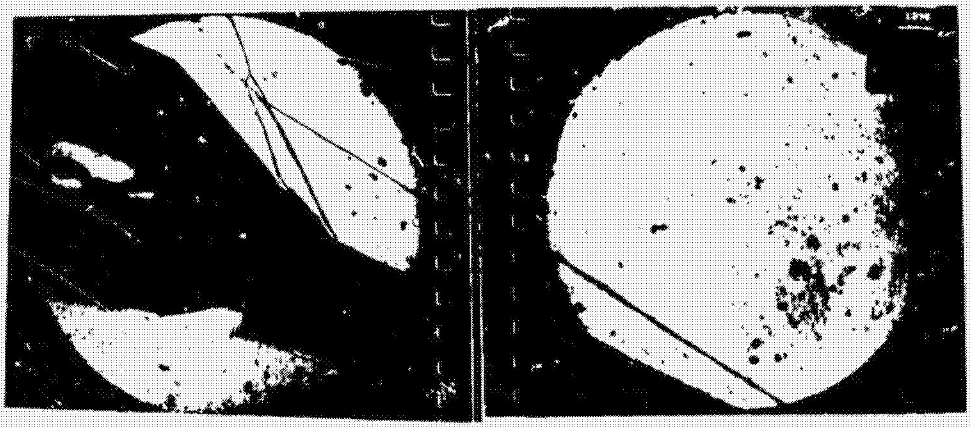

Fig. 5.12b C. D. Antenna Shadowgraph Series

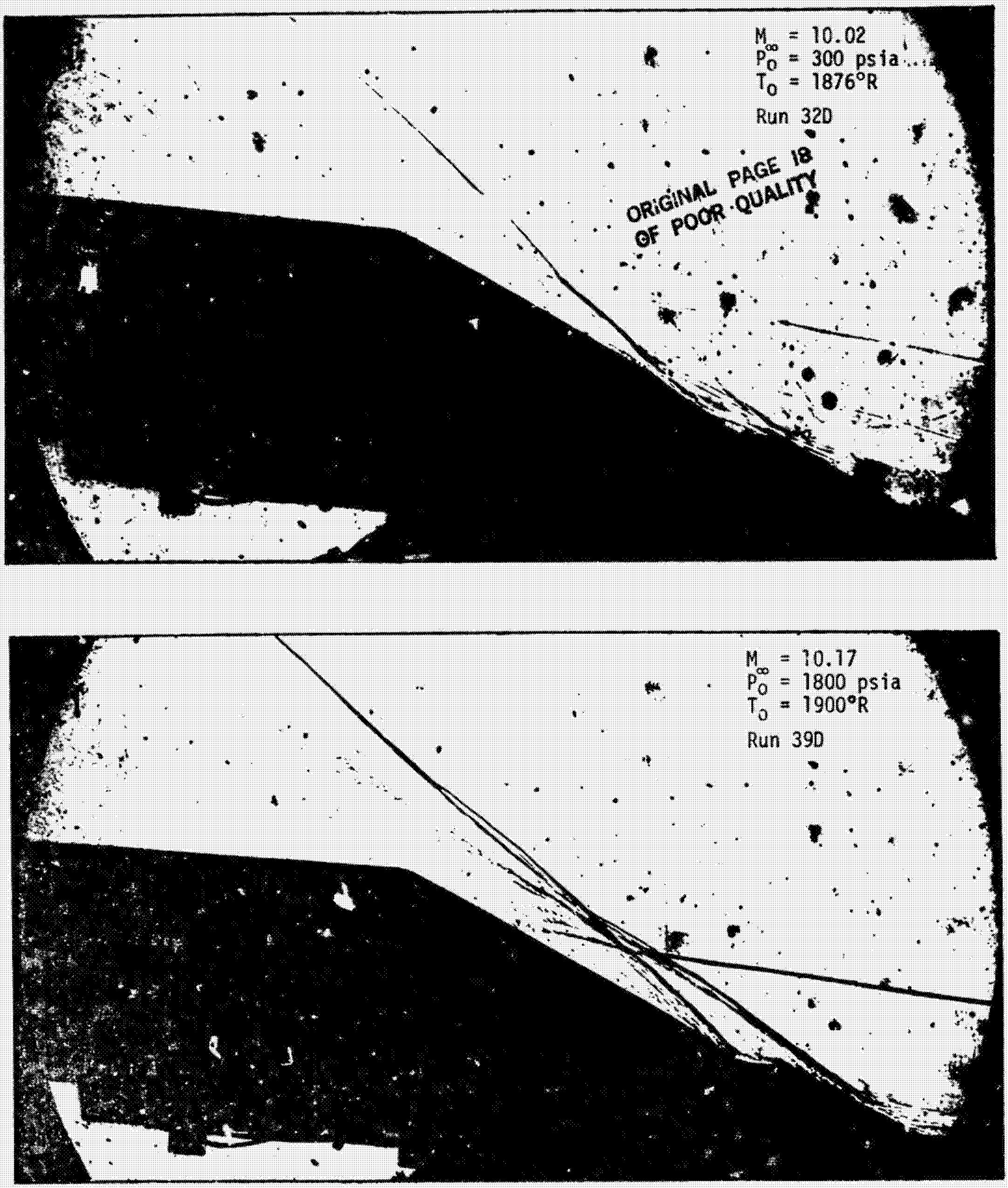

Fig. 5.13 C. D. Antenna Shadowgraph Enlargements for Two Total Pressures at δ_w = 5.0 Deg.

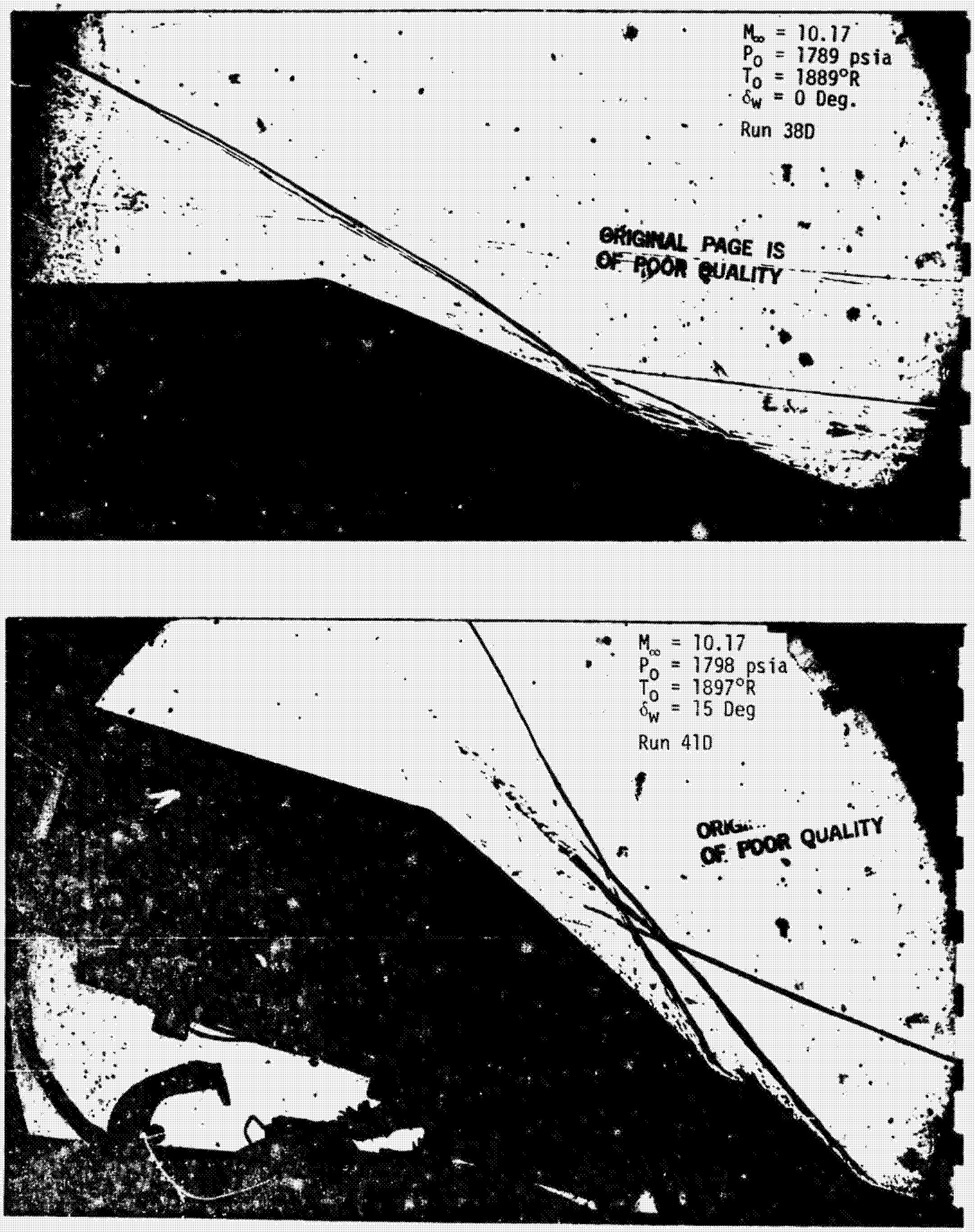

Fig. 5.14 C. D. Antenna Shadowgraph Enlargements for Two Wedge Angles

Table 5.2

Command Destruct Antenna Heating Amplification Factors

TC NO.	X (IN)	Y (IN)	Z (IN)	h_i/h_u	h_i/h_u	h_i/h_u	h_i/h_u	h_i/h_u
1	30.710	1.42	0.00	26.22	20.13	11.94	7.07	5.68
2	31.610	1.84	0.00	27.08	15.72	9.31	5.60	4.44
3	32.520	2.27	0.00	20.69	14.18	8.58	5.31	4.05
4	32.970	2.48	0.00	17.26	13.52	8.18	5.23	3.97
5	33.430	2.69	0.00	15.44	12.87	8.30	5.32	3.98
6	34.330	3.11	0.00	14.91	10.28	7.85	5.07	3.93
7	35.240	3.54	0.00	13.40	4.49	4.54	3.31	3.54
8	36.140	3.92	0.00	4.35	2.29	2.04	1.81	1.93
9	37.140	3.92	0.00	0.89	0.59	0.52	0.56	0.57
10	38.140	3.92	0.00	8.98	0.44	0.43	0.45	0.40
11	39.140	3.92	0.00	9.04	0.40	0.37	0.34	0.33
12	40.140	3.92	0.00	9.12	4.82	0.34	0.22	0.28
13	41.140	3.92	0.00	9.21	4.88	0.31	0.23	0.23
14	32.970	2.48	2.00	16.52	13.09	7.98	4.92	3.83
15	32.970	2.48	3.38	11.66	6.78	4.12	2.77	2.32
16	34.330	3.32	3.38	1.48	0.67	0.32	0.56	0.47
17	35.690	3.54	3.38	8.02	2.38	2.20	1.65	1.57
18	39.140	3.92	2.00	9.05	4.72	0.30	0.32	0.34
19	39.140	3.92	3.38	1.01	4.84	2.99	0.26	0.29
20	39.140	2.45	3.38	9.14	0.50	0.62	0.55	0.59
21	27.860	0.51	0.00	3.06	6.47	9.28	5.54	4.19
Run				32D	33D	34D	35D	36D
M_∞				10.02	10.02	10.02	10.02	10.02
P_o(psia)				301.0	305.0	306.0	301.0	300.0
T_o(°R)				1876.0	1879.0	1883.0	1887.0	1890.0
Wedge Angle (Deg.)				4.99	10.01	15.05	19.98	24.65
q_{12} (Btu/ft^{2}sec) at X = 12 in.				0.4565	0.8709	1.350	1.856	2.239

Table 5.2 (Cont.)

Command Destruct Antenna Heating Amplification Factors

TC NO.	X (IN)	Y (IN)	Z (IN)	h_i/h_u	h_i/h_u	h_i/h_u	h_i/h_u	h_i/h_u	h_i/h_u
1	30.710	1.42	0.00	37.06	15.40	8.15	5.88	4.26	3.46
2	31.610	1.84	0.00	29.01	11.92	7.61	5.64	4.13	3.25
3	32.520	2.27	0.00	22.65	12.33	8.11	5.84	4.31	3.31
4	32.970	2.48	0.00	19.19	12.36	8.09	5.71	4.18	3.23
5	33.430	2.69	0.00	16.93	12.31	8.13	5.74	4.26	3.33
6	34.330	3.11	0.00	18.89	11.72	5.60	5.18	4.20	3.28
7	35.240	3.54	0.00	15.20	9.84	6.01	4.15	3.65	3.32
8	36.140	3.92	0.00	7.73	4.33	2.90	2.26	2.17	1.80
9	37.140	3.92	0.00	1.52	0.94	0.60	0.45	0.37	0.46
10	38.140	3.92	0.00	1.06	0.67	0.43	0.33	0.29	0.31
11	39.140	3.92	0.00	0.96	0.58	0.34	0.26	0.26	0.24
12	40.140	3.92	0.00	0.97	0.51	0.31	0.24	0.22	0.22
13	41.140	3.92	0.00	1.03	0.50	0.28	0.21	0.20	0.19
14	32.970	2.48	2.00	19.56	11.19	7.29	5.08	3.81	3.11
15	32.970	2.48	3.38	10.43	6.15	4.26	3.05	2.24	1.86
16	34.330	3.32	3.38	1.27	0.44	0.36	0.52	0.52	0.47
17	35.690	3.54	3.38	10.24	4.47	2.32	1.77	1.43	1.22
18	39.140	3.92	2.00	0.76	0.45	0.31	0.27	0.26	0.36
19	39.140	3.92	3.38	2.64	0.34	0.21	0.16	0.18	0.25
20	39.140	2.45	3.38	0.41	0.58	0.81	0.64	0.56	0.54
21	27.860	0.51	0.00	2.22	15.23	7.64	5.05	3.55	2.75
Run				38D	39D	40D	41D	42D	43D
M_∞				10.17	10.17	10.17	10.17	10.17	10.17
P_o(psia)				1789.	1800.	1797.	1798.	1796.	1794.
T_o(°R)				1889.	1900.	1893.	1897.	1898.	1901.
Wedge Angle (Deg.)				-0.01	5.01	10.01	15.01	20.00	24.52
q_{12} (Btu/ft^{2}sec) at X = 12 in.				.7372	1.868	3.612	5.642	7.816	9.388

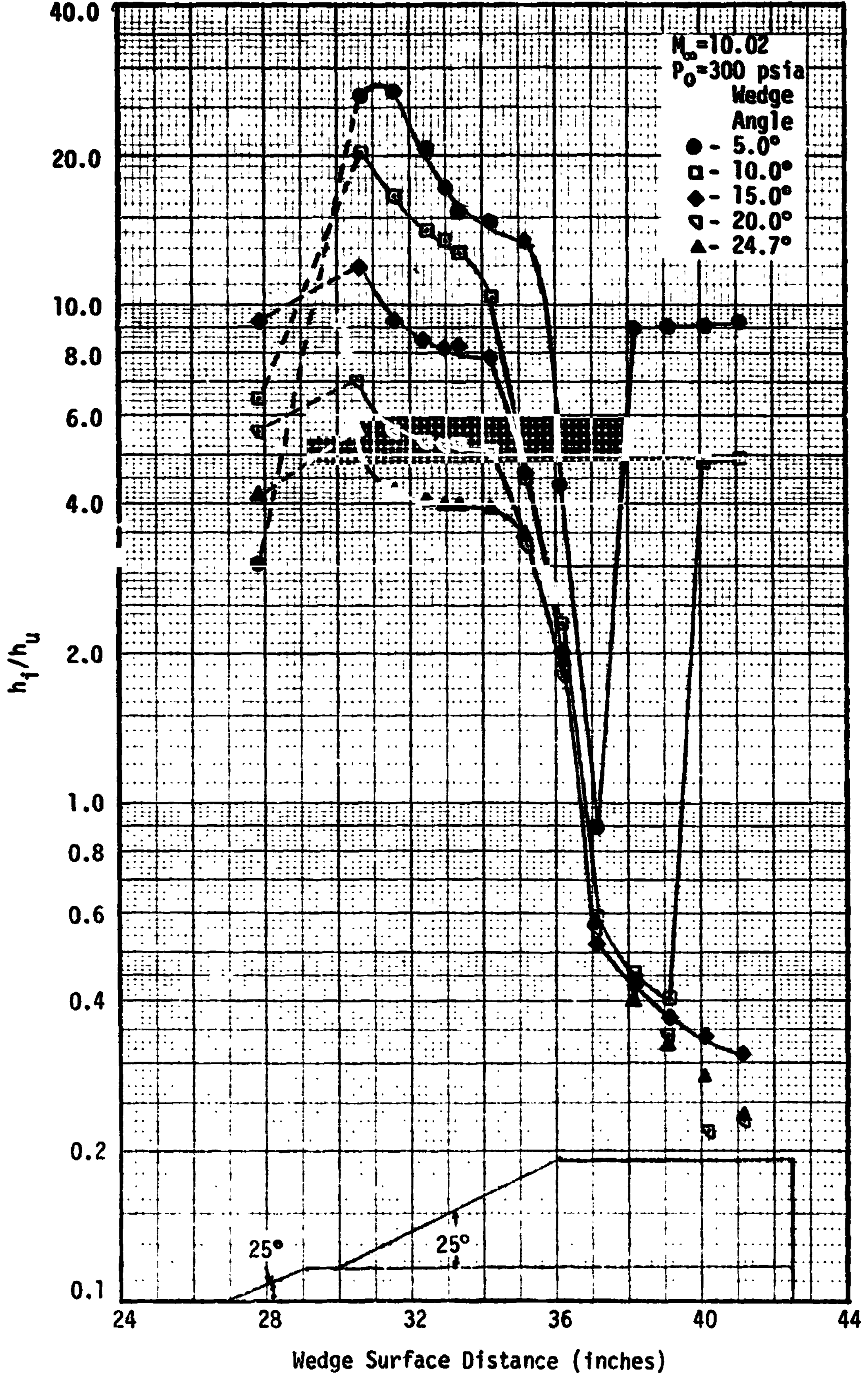

Fig. 5.15 Command Destruct Antenna Centerline Interference Factors at P_o = 300 psia

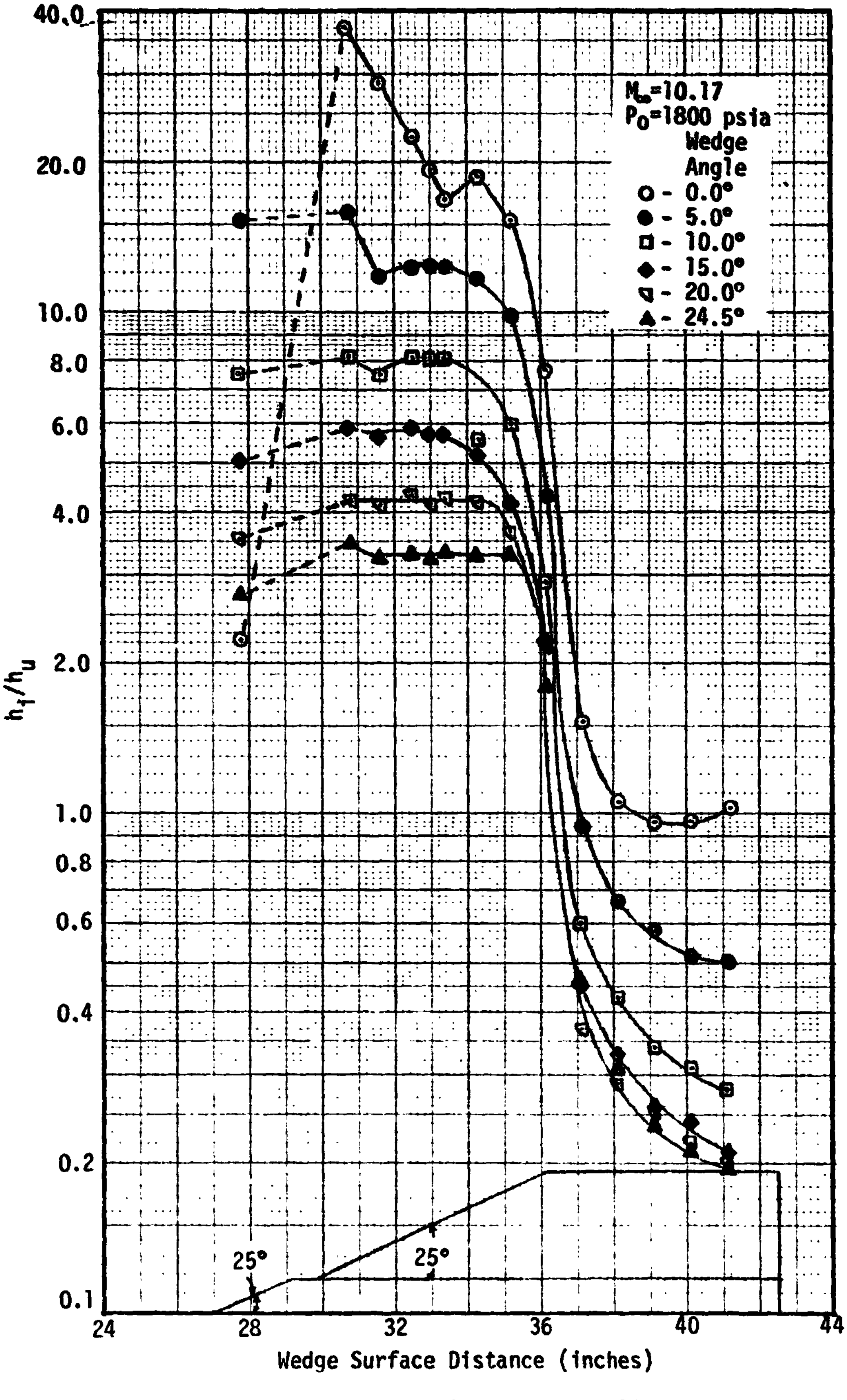

Fig. 5.16 Command Destruct Antenna Centerline Interference Factors at P_0 = 1800 psia.

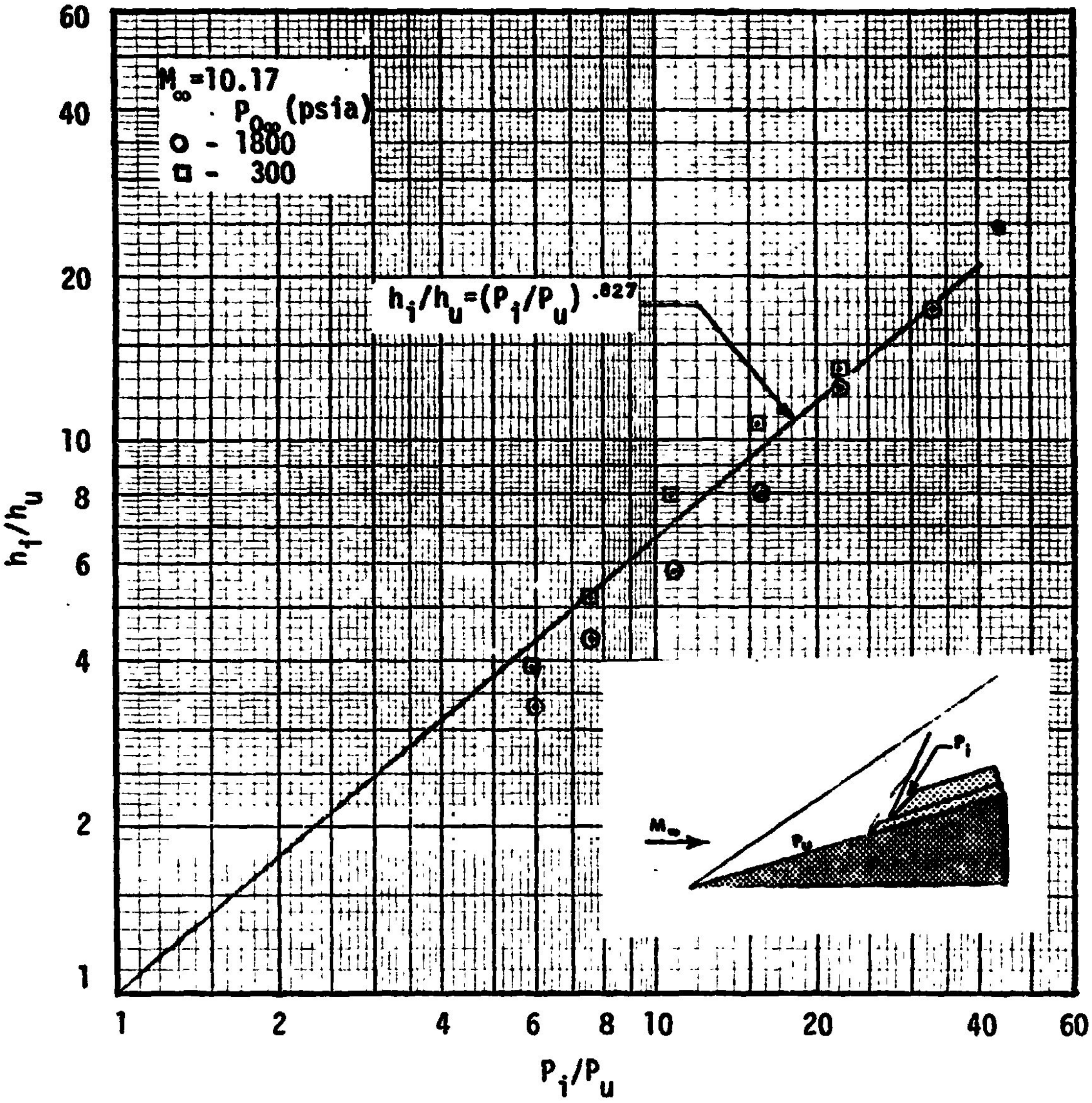

Fig. 5.17 Command Destruct Antenna Forward Face Plateau Heating Amplification Correlated With Theoretical Wedge Pressures

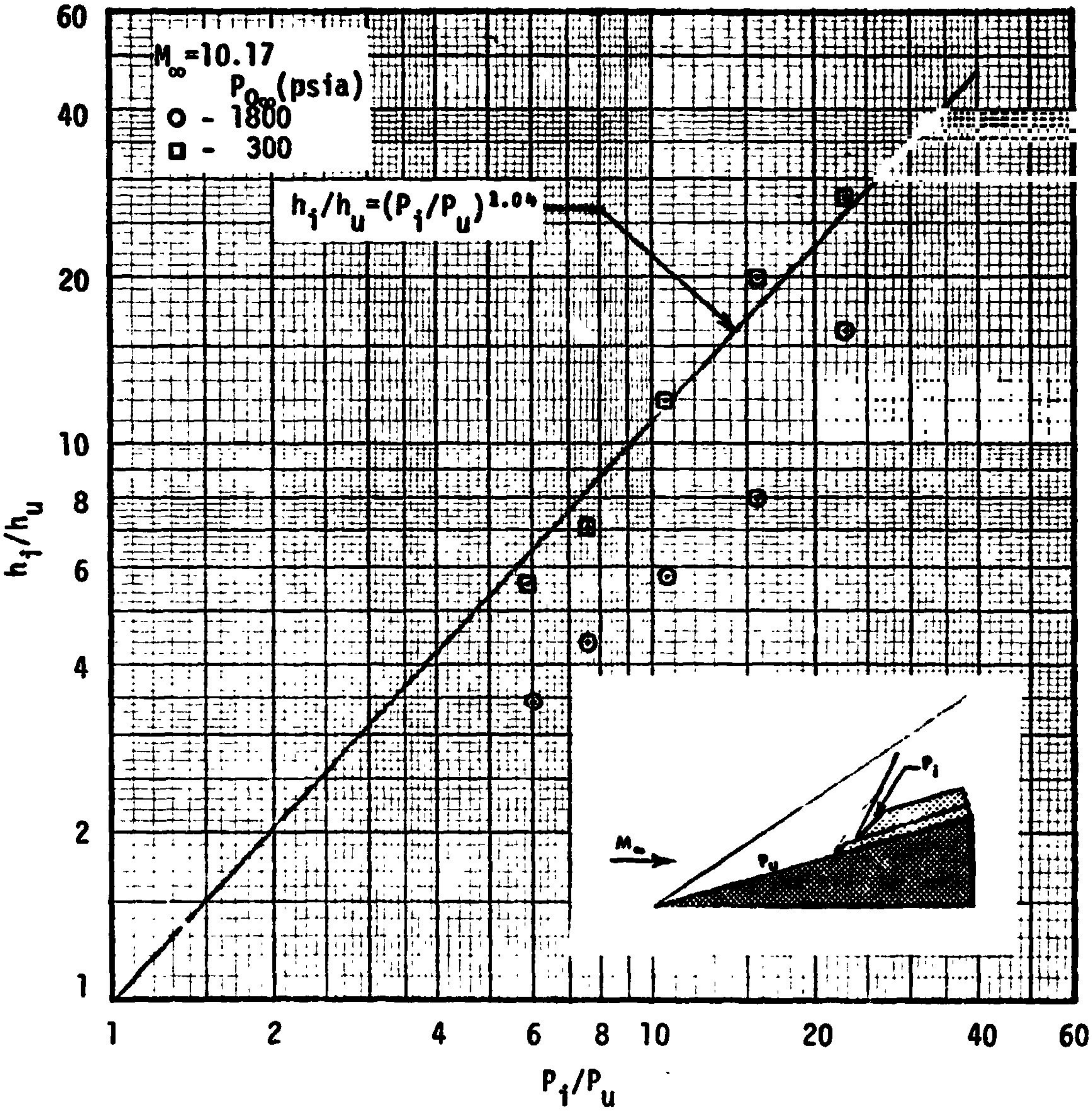

Fig. 5.18 Command Destruct Antenna Forward Face Peak Heating Amplification Correlated with Theoretical Wedge Pressures

5.3 SRB Attach Ring

Data was obtained during two tests (Refs. 5.1 and 5.2) for the SRB attach ring geometry shown in Fig. 5.19. The flow field and type of heating on this geometry is different than observed for the protuberances described in the previous section. Accordingly, a different approach for analysis was taken.

A series of shadowgraphs for four wedge angles are shown in Fig. 5.20. The flow on the front face of the protuberance is processed by the wedge shock and a strong separation shock. The separation shock does not impinge on the protuberance. The flow over the forward lip of the protuberance is, in addition, processed by a normal shock. Figure 5.21 provides an enlarged view of this shock for a wedge angle of 23 degrees.

Data on the wedge surface upstream of the protuberance were obtained and are shown in Fig. 5.2. The data at X = 21 inches was found to be undisturbed. The measured values of wedge heating at X = 21 inches, pre-separation values, were used to nondimensionalize the data on the protuberance. These data are given in Table 5.3.

The effect of separation on the heating upstream of the front face on the wedge is shown in Fig. 5.22 for four wedge angles. Other data in front of forward facing steps (Ref. 5.4) shows an increasing amplification with increasing Mach number. The current data does not have this trend. Decreasing the wedge angle increases the wedge Mach number (See Fig. 5.1). The 5 degree data is lower than the other data, even though it is for the highest Mach number. One possible cause is the flow may be transitional rather than fully turbulent. Alternately, the wedge flow-step interaction process is different than a flat plate-step process.

Typical data on the protuberance forward lip are plotted in Fig. 5.23. The scatter in the data is probably due to inaccuracies in placement of the thermocouples in the corner of the lip. The data shows an increasing trend with decreasing Mach number. Interference factors have been correlated with Mach number on a log-log plot by many investigators. This has been done with the present data for a few representative thermocouple locations in Fig. 5.24. Thermocouple 5 and 1 data correlate quite well with Mach number, whereas, thermocouple 10 and 6 data are in poor agreement at high Mach number.

An alternate method of analysis was developed for the forward lip of the attach ring. The flow is processed by the wedge shock, separation shock, and lip normal shock. In order to make flow field, and subsequently heating calculations, the separation shock angle must be known. Using shadowgraphs typified by Fig. 5.20, the separation shock angle was measured and correlated with wedge angle as shown in Fig. 5.25. The flow properties through the shock system were then computed.

Based on the conditions behind the normal shock of the lip, the heating was computed as follows.

$$q_{lip} = q_{FR} \times \underset{(a)}{\left(\frac{1}{\sqrt{2}}\right)} \underset{(b)}{\left(\frac{q_{Bcyl}}{q_{FR}}\right)} \underset{(c)}{\left(\frac{1}{\sqrt{2}}\right)}$$

(a) $\frac{q_{2D\ cyl}}{q_{B\ cyl}} = \frac{1}{\sqrt{2}}$, $\frac{\text{2D cylinder}}{\text{axisymmetric blunt face cylinder}}$

(b) $\frac{q_{B\ cyl}}{q_{FR}} = 0.46628\, e^{.4471/M_\infty}$, from Boison & Curtis (Ref. 5.5) M_∞ evaluated just upstream of the normal shock

(c) $\frac{1}{\sqrt{2}}$, velocity gradient correction from a blunt 2D flat face to account for flow relief only on one side of the lip

where

q_{FR} = Fay and Riddell stagnation point heating to a hemisphere of radius 1/2 the lip thickness (computed using the MINIVER computer program, Ref. 5.6).

The results of these calculations are compared with data in Fig. 5.26. The theory and data are in agreement in trend, but the theory is slightly lower than the data. This is probably due to the velocity gradient correction (c) being too large since there is some relief of the flow toward the wedge from the center of the lip. The flagged symbols in Fig. 5.26 were derived using the ratio of TC 21/5 data at 5 degrees wedge angle and the TC No. 5 data at wedge angles greater than 5.

All Dimensions in Inches

X = Distance from Leading Edge of Wedge

• = Thermocouples

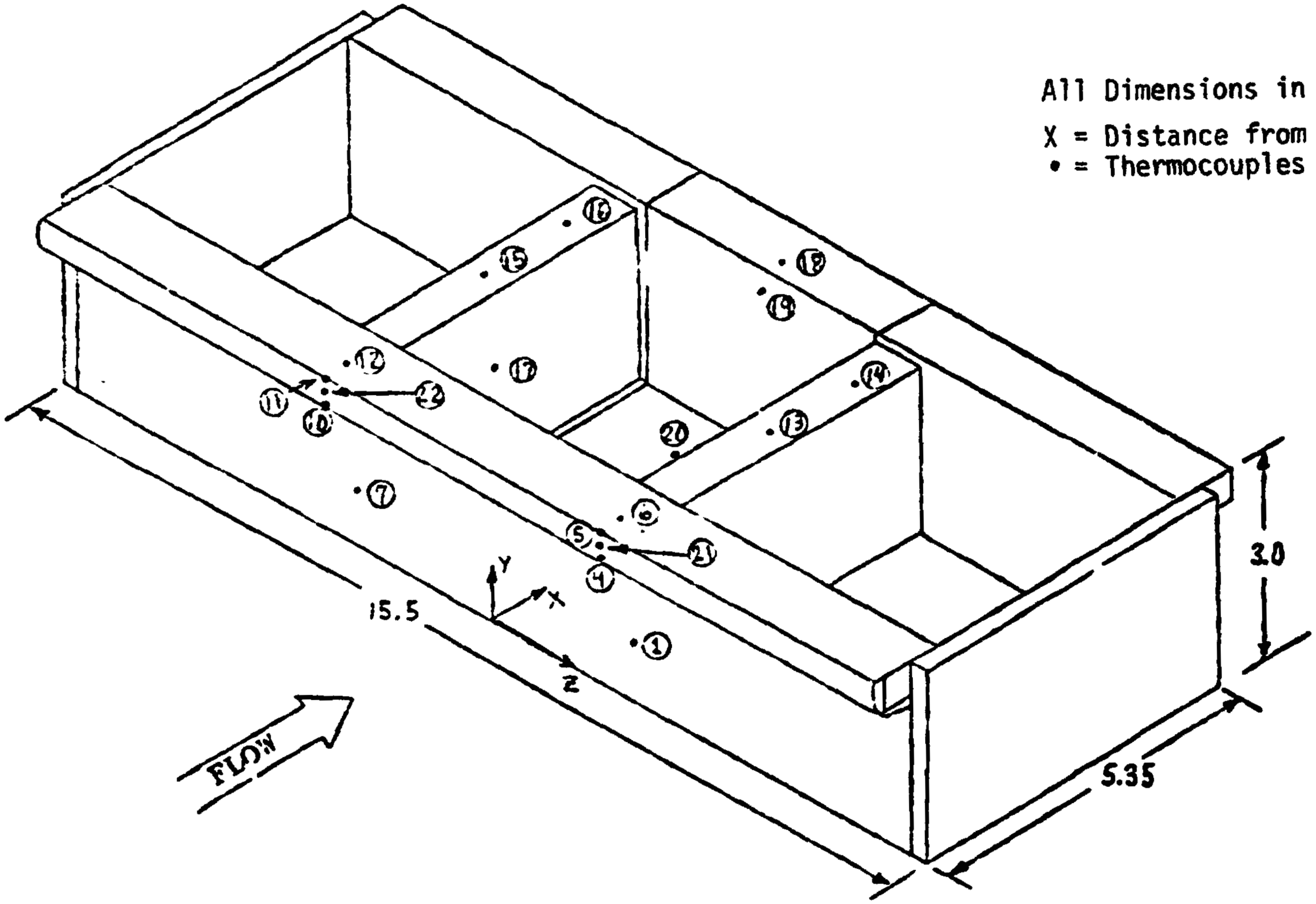

Fig. 5.19 SRB Attach Ring Protuberance Model

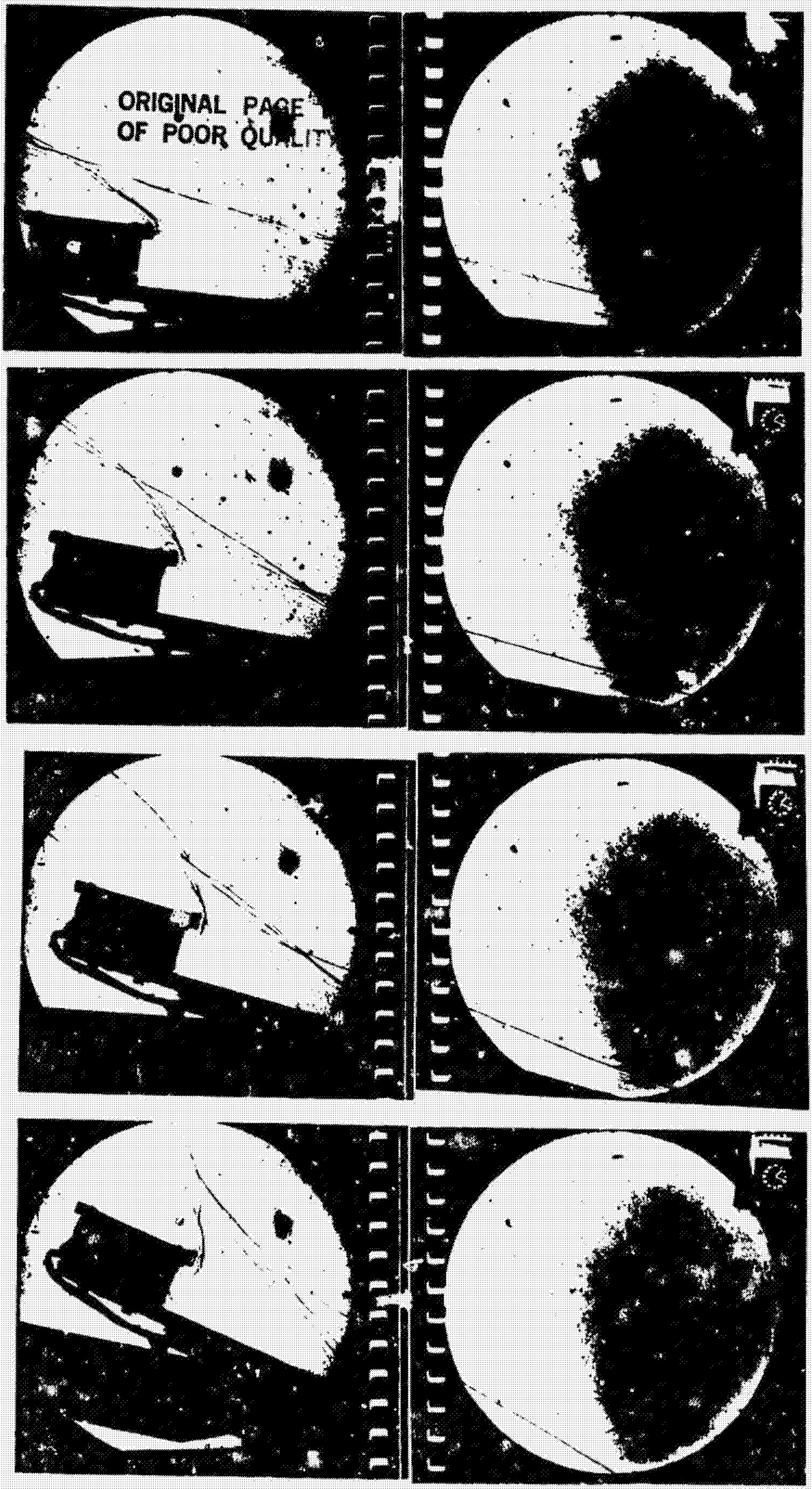

δ_w = 5 Deg.
Run 7S

δ_w = 10 Deg.
Run 8S

δ_w = 15 Deg.
Run 9S

δ_w = 23 Deg.
Run 10 S

All Runs At
M_∞ = 10.13
P_o = 1200 psia
T_o = 2000°R

Fig. 5.20 Attach Ring Shadowgraph Series

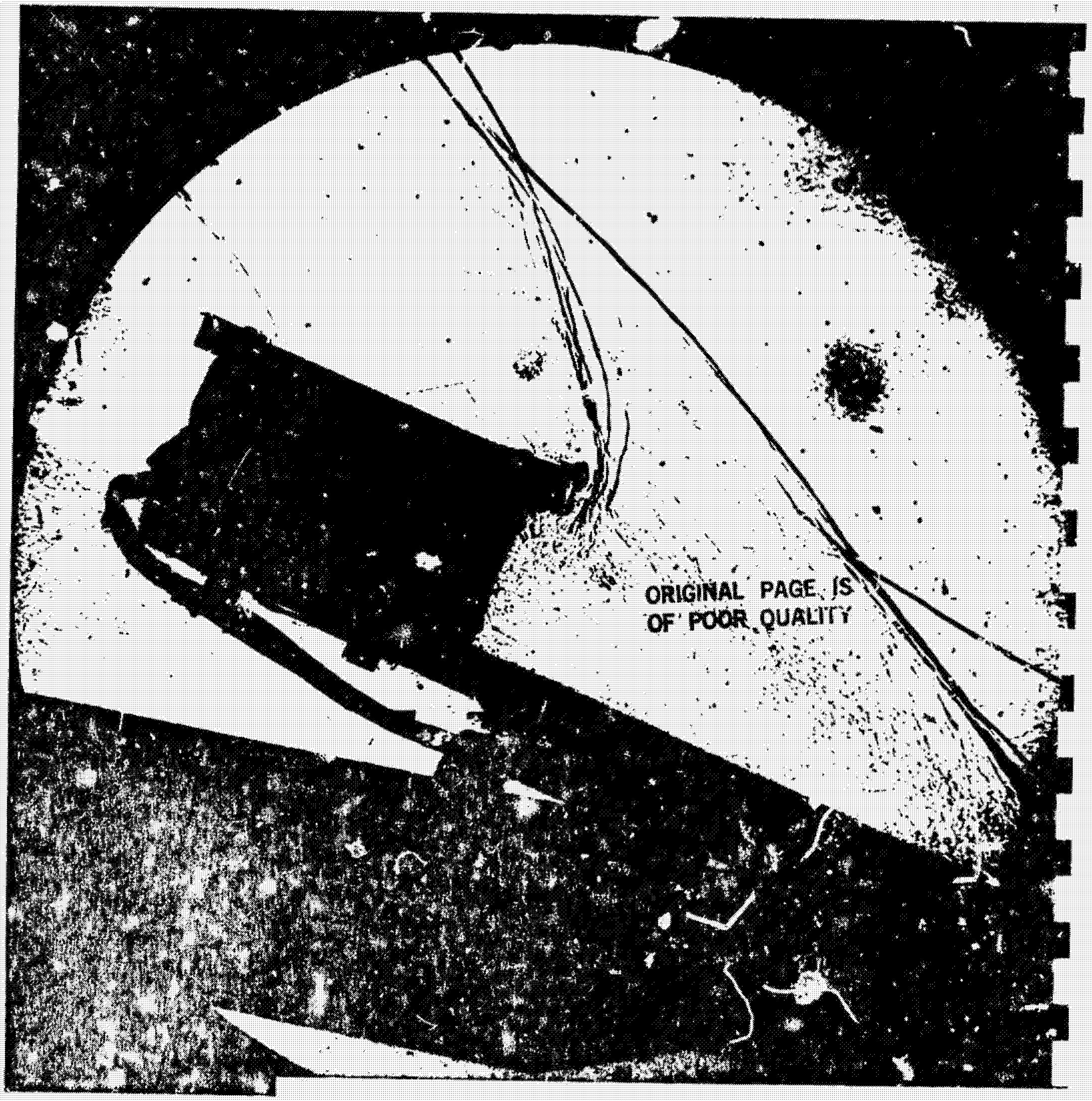

Attach Ring
Height = 3.0 in.
M_∞ = 10.17
P_o = 1800 psia
T_o = 2000 °R
δ_W = 23 Deg.
Run 12S

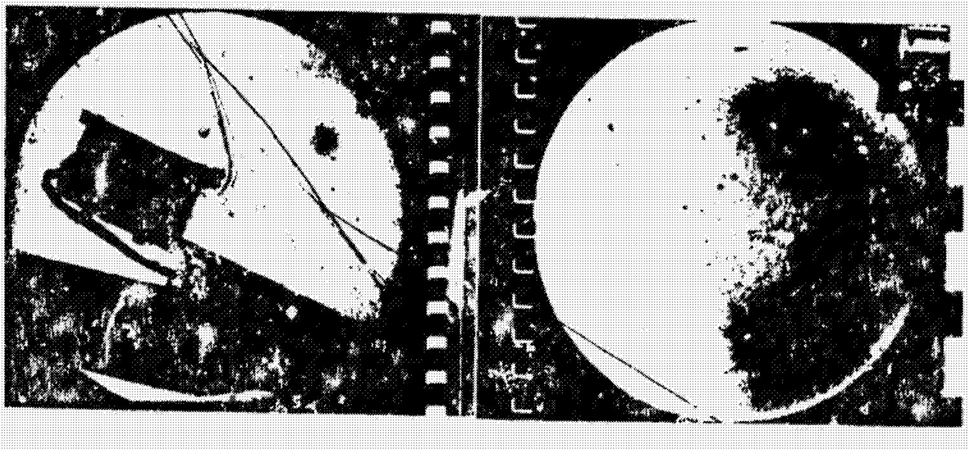

Fig. 5.21 Attach Ring Shadowgraph Enlargement for δ_W = 23 Deg.

Table 5.3

Attach Ring Heating Amplification Factors

TC NO.	X (IN)	Y (IN)	Z (IN)	h_i/h_u	h_i/h_u	h_i/h_u	h_i/h_u	h_i/h_u	h_i/h_u	h_i/h_u	h_i/h_u	h_i/h_u
1	35.810	0.88	2.50	3.69	3.35	3.18	2.57	2.42	2.55	3.90	3.94	3.95
2	35.810	2.06	2.50	5.78	6.92	6.42	4.48	4.00	1.69	7.48	3.37	3.18
3	35.810	2.50	2.50	----	----	----	----	----	----	4.61	4.80	4.75
4	35.185	2.50	2.50	8.62	8.14	7.19	4.86	4.32	4.28	----	----	----
5	35.185	3.00	2.50	20.23	13.80	10.40	6.64	5.71	5.88	23.23	23.69	23.85
6	35.560	3.00	2.50	2.91	6.24	5.60	4.09	3.65	3.78	5.13	5.04	5.05
7	35.810	0.88	-2.50	2.80	3.51	3.83	2.61	2.60	2.56	2.74	2.78	2.78
8	35.810	2.06	-2.50	4.32	8.52	7.68	5.35	4.64	4.89	5.24	5.55	5.70
9	35.810	2.50	-2.50	5.69	3.32	2.46	1.65	1.54	1.50	3.19	3.29	3.33
10	35.185	2.50	-2.50	6.52	10.12	8.53	5.66	4.82	----	10.46	10.85	10.54
11	35.185	3.00	-2.50	7.85	8.06	5.90	3.75	3.13	3.09	15.77	16.38	15.85
12	35.560	3.00	-2.50	4.65	3.30	2.48	1.64	1.46	1.48	2.42	2.13	2.06
13	38.310	.88	2.50	2.24	1.56	1.30	0.93	0.88	0.86	2.16	2.18	2.20
14	39.810	2.88	2.50	1.59	1.13	0.98	0.85	0.81	0.80	1.48	1.53	1.51
15	38.310	2.88	-2.50	1.77	1.59	1.40	1.02	0.93	0.92	1.88	1.93	1.92
16	39.810	2.88	-2.50	1.52	1.10	1.01	0.89	0.85	0.85	1.40	1.48	1.49
17	38.310	1.50	-2.50	0.89	0.50	0.45	0.38	0.38	0.38	0.83	0.85	0.85
18	40.810	3.00	0.00	3.05	2.22	2.00	1.70	1.59	1.53	2.93	2.98	3.05
19	40.560	2.75	0.00	6.31	4.85	4.16	2.86	2.47	2.47	7.09	7.26	7.13
20	38.310	0.38	0.00	0.79	0.56	0.54	0.43	0.43	0.42	----	----	----
21	35.185	2.50	0.00	----	----	----	----	----	----	30.46	25.62	26.23
22	35.185	2.50	-2.50	----	----	----	----	----	----	----	20.23	19.92
Run				7S	8S	9S	10S	11S	12S	12D	13D	140
M_∞				10.13	10.13	10.13	10.13	10.17	10.17	10.14	10.14	10.14
P_o (psia)				1203.	1202.	1198.	1200.	1797.	1800.	1197.	1198.	1200.
T_o (°R)				1993.	1999.	1997.	1997.	1995.	1993.	1898.	1885.	1898.
Wedge Angle (Deg.)				5.00	10.01	15.01	23.0	22.96	23.0	5.00	5.01	5.05
h_{uo} (Btu/ft^{2}sec°R) at X = 21"				.0013	.00237	.00327	.00482	.00687	.00687	.0013	.0013	.0013

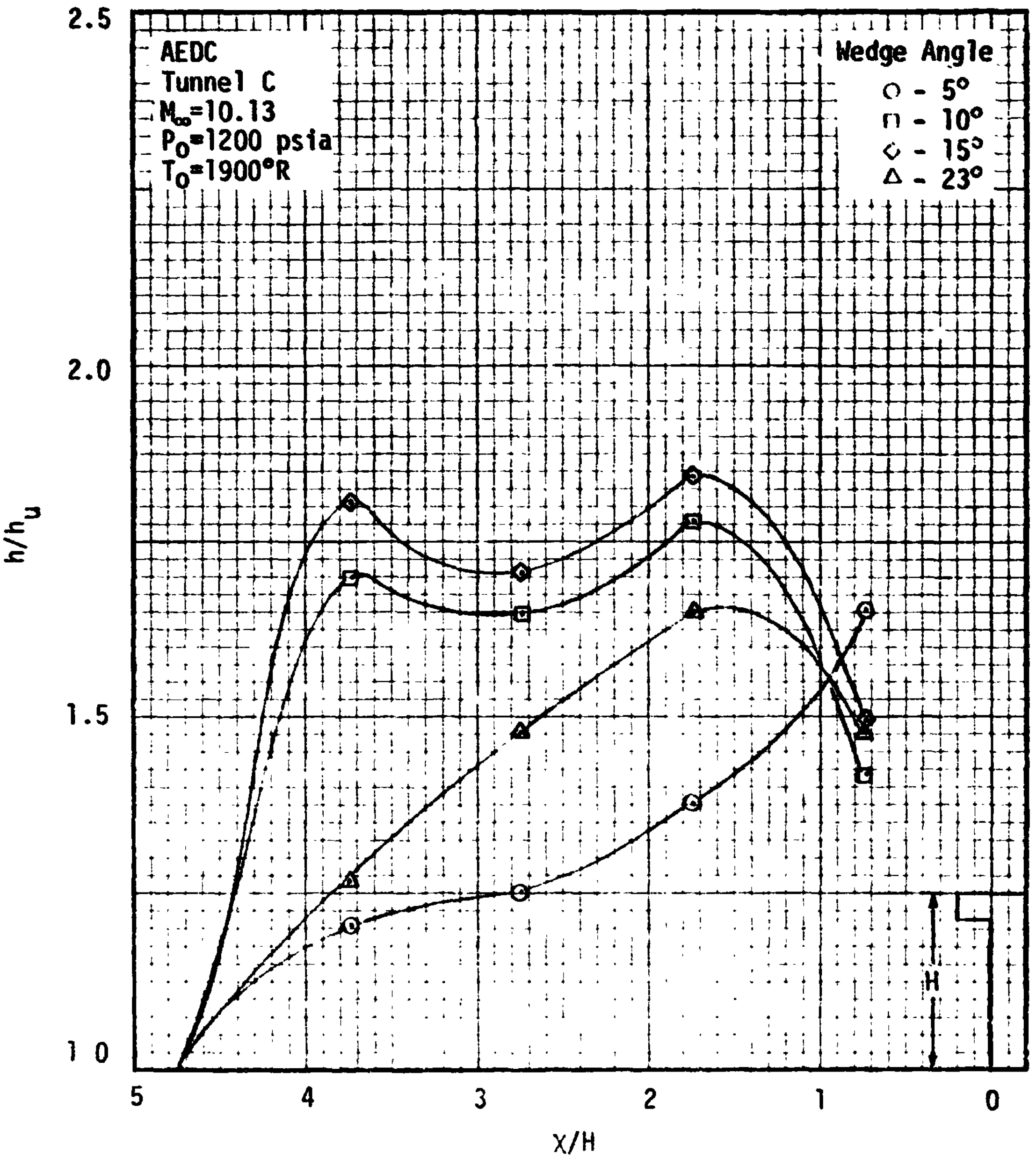

Fig. 5.22 Upstream Interference Factors for the 2D SRB Attachment Ring on a Wedge

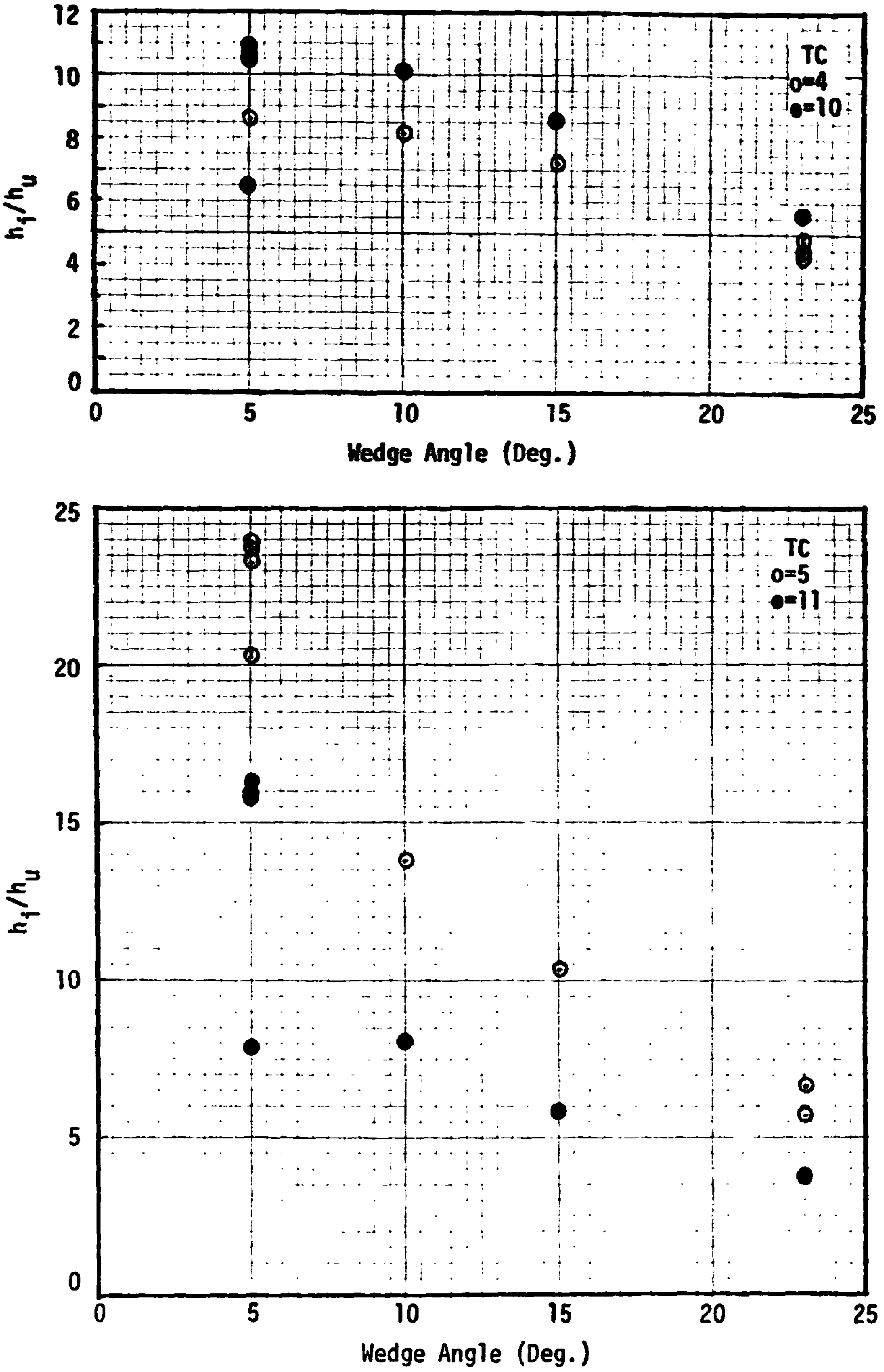

Fig. 5.23 Attach Ring Forward Lip Heating Amplification Versus Wedge Angle

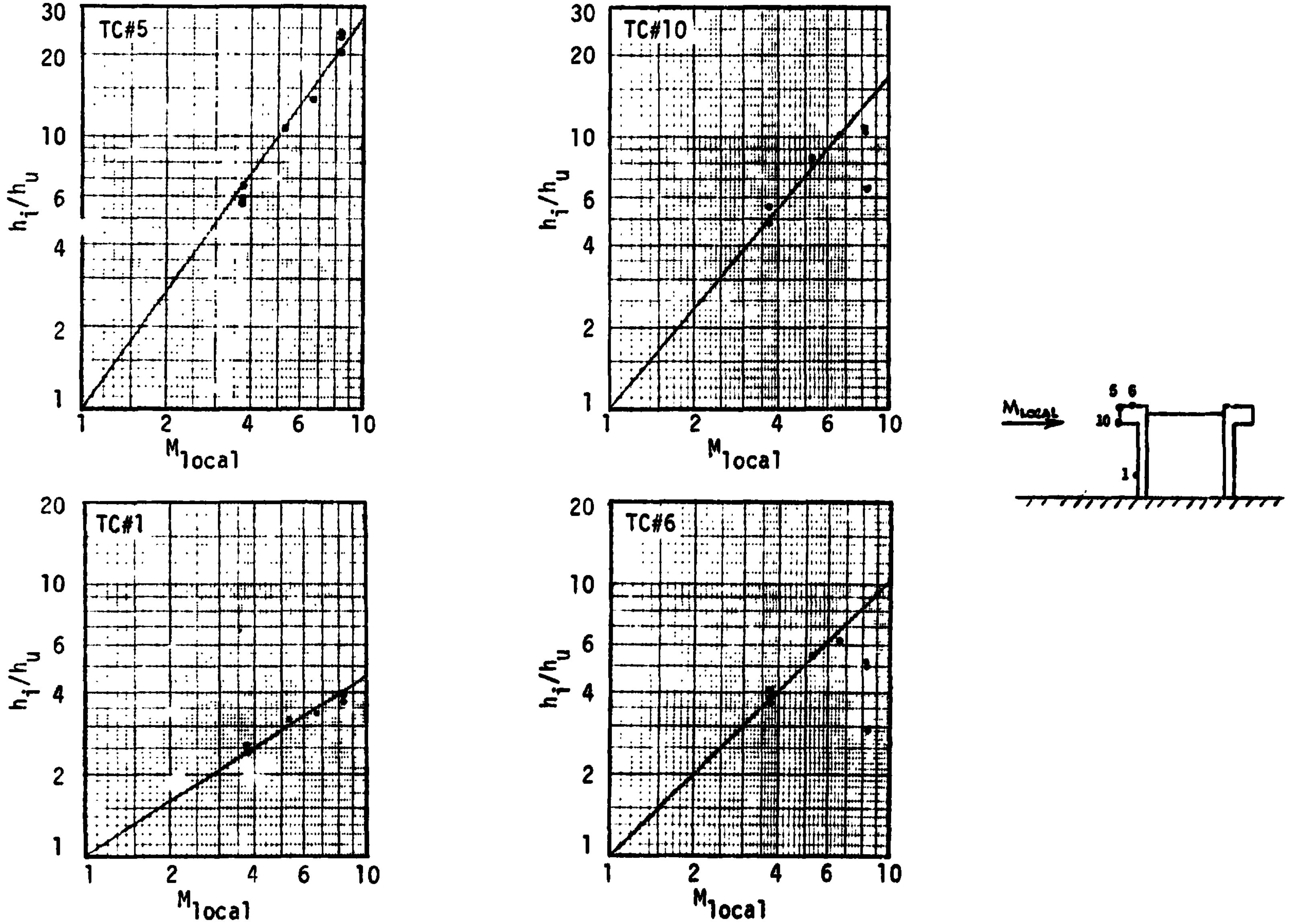

Fig. 5.24 Representative Plots of h_i/h_u Versus Local Mach Number

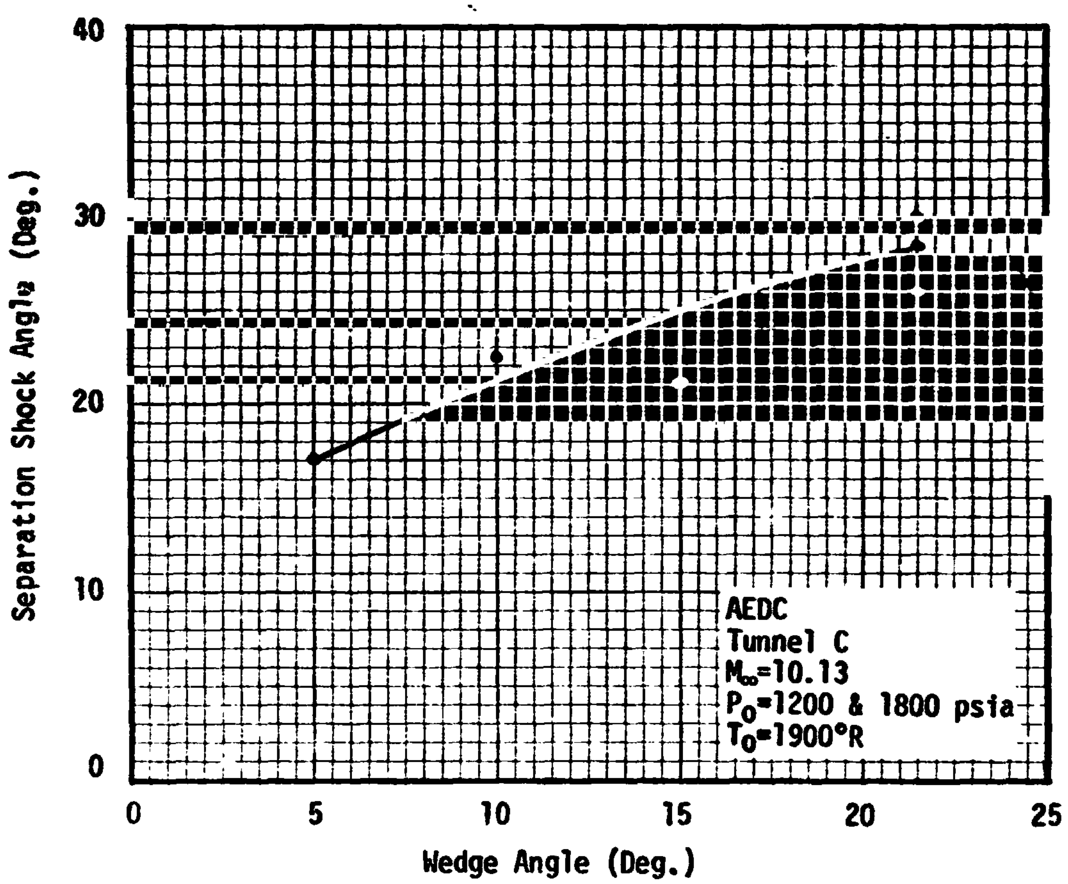

Fig. 5.25 2D Attachment Ring Separation Shock Angles from Shadowgraph Data

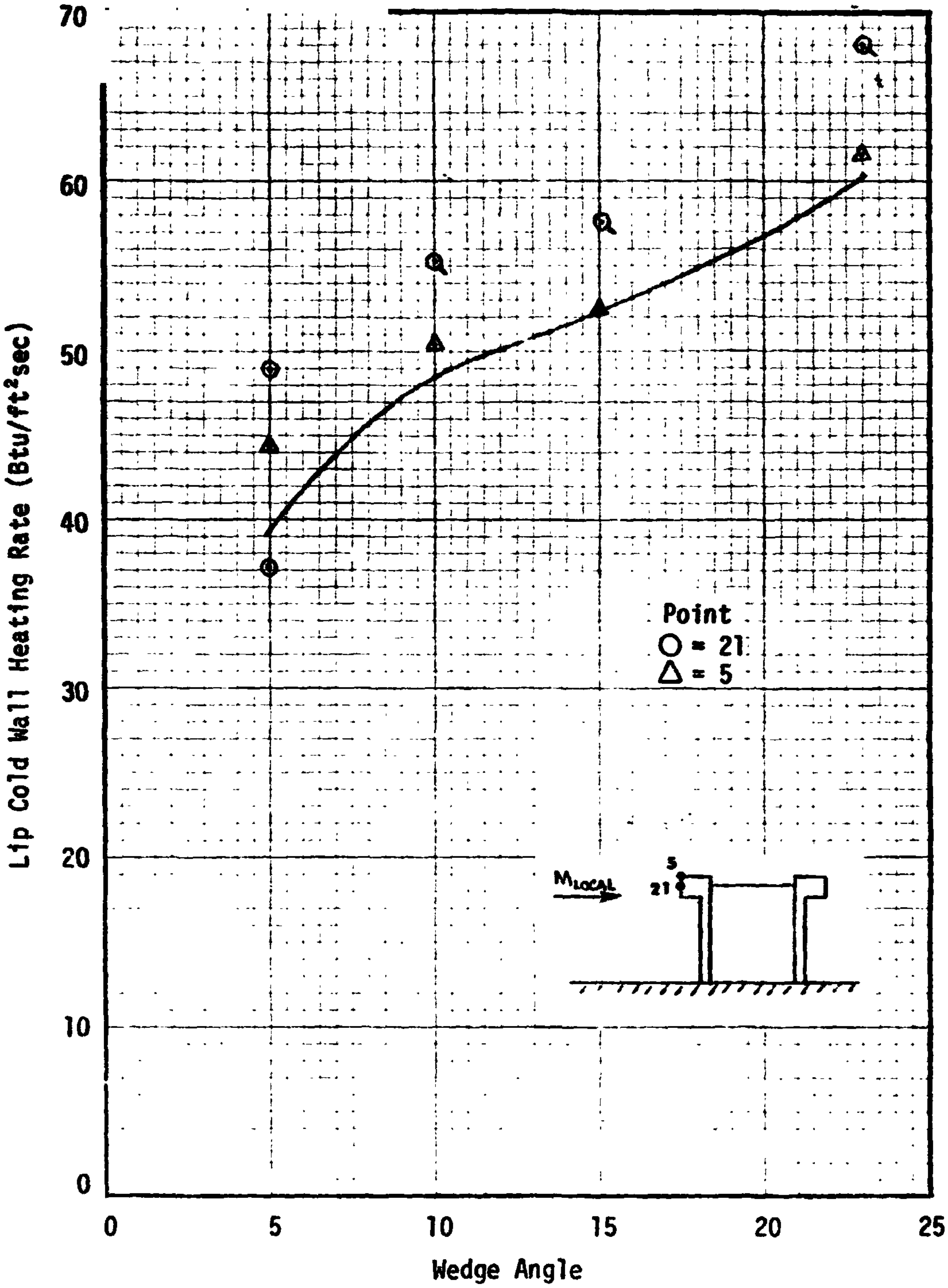

Fig. 5.26 Comparison of Attach Ring Lip Data and Theory

5.4 SRB Kick Ring

Data was obtained for the SRB kick ring as shown in Fig. 5.27 from one test (Ref. 5.1).The flow field and type of heating is nearly the same as that observed for the attach ring forward face.

A shadowgraph of the flow is given in Fig. 5.28 for a wedge angle of 5 degrees. This protuberance was tested only at a 5 degree wedge angle. The heating amplifications for the runs made are given in Table 5.4. The heating data were nondimensionalized using the same method as was used for the attach ring.

The heating amplifications averaged from the two runs in Table 5.4 are shown on scaled cross sections of the kick ring in Fig. 5.29. The different heating factors at the three cross sections indicate a nonuniformity across the front face of the model. Material test photographs revealed that the model probably had a slignt yaw which also introduced additional end effects. Thus, the centerline data is thought to be more representative of the two dimensional flow conditions.

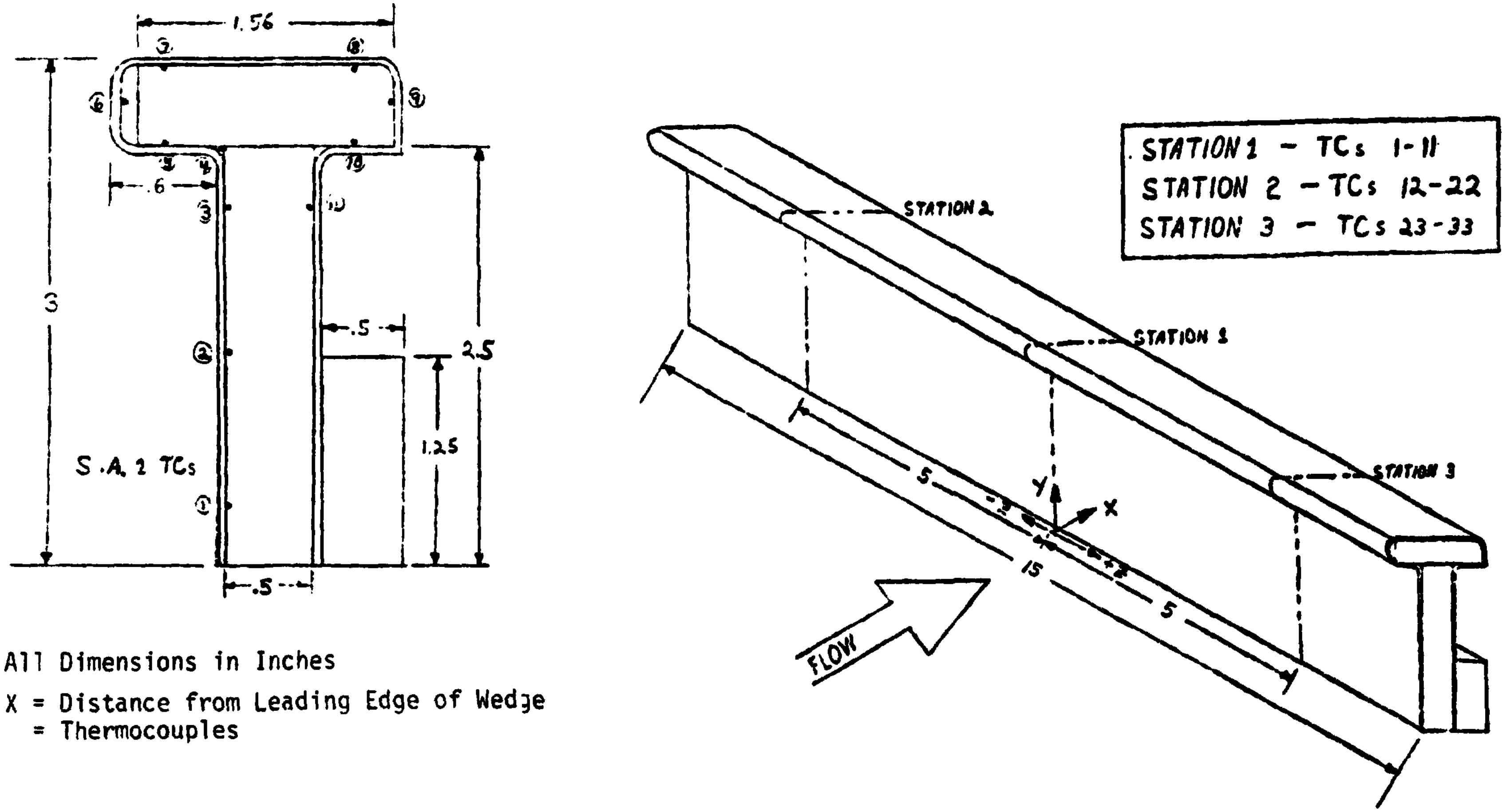

All Dimensions in Inches

X = Distance from Leading Edge of Wedge
  = Thermocouples

Fig. 5.27 SRB Kick Ring Protuberance Model

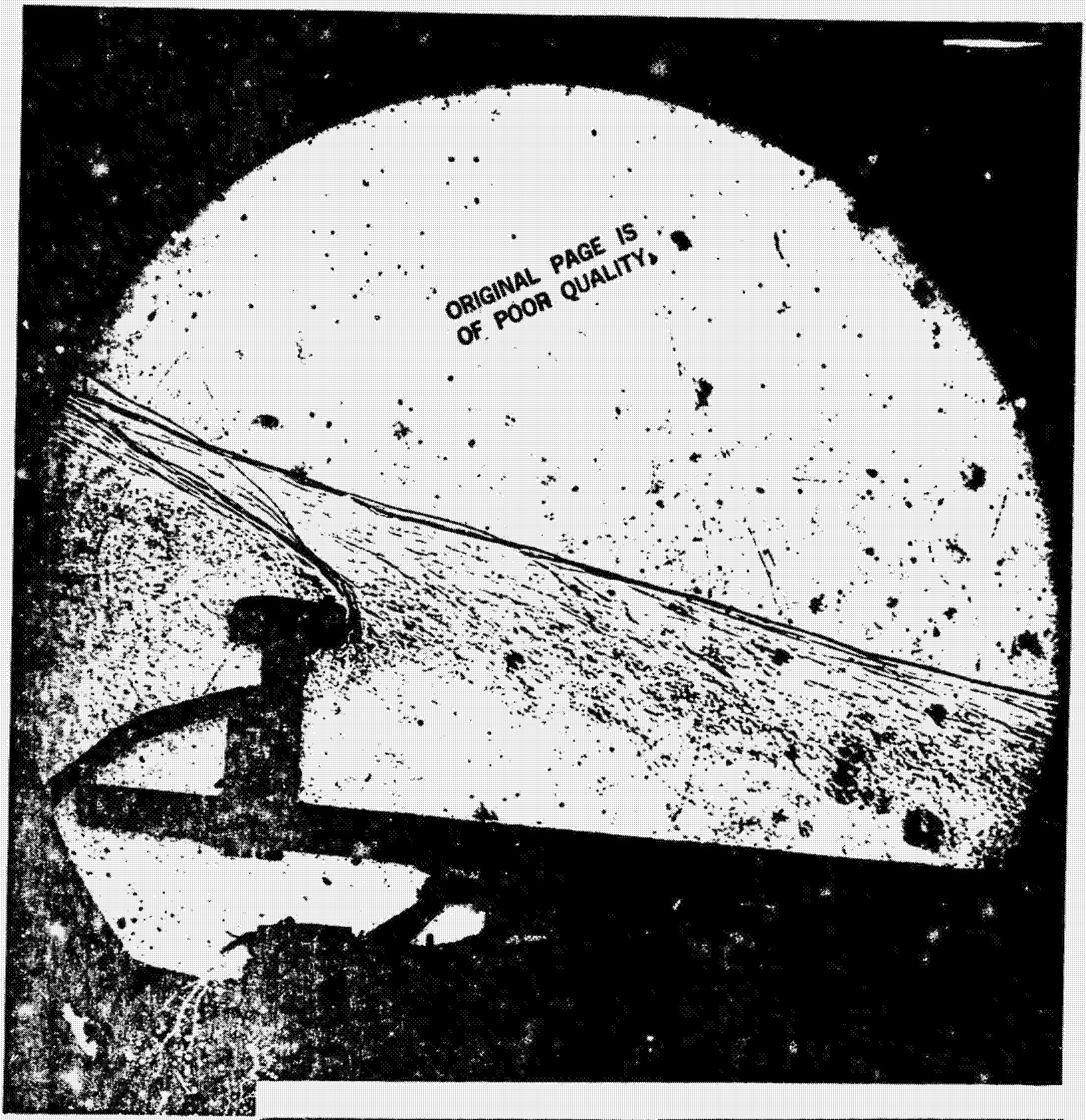

SRB Kick Ring
Height = 3 inches
M_∞ = 10.14
P_o = 1198 psia
T_o = 1894°R
δ_W = 5 Deg.
Run 17D

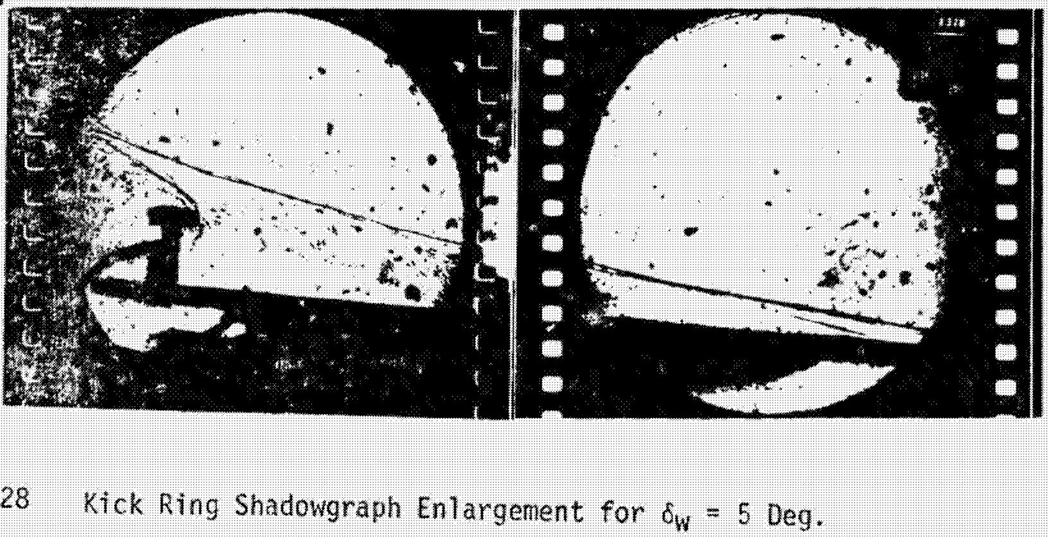

Fig. 5.28 Kick Ring Shadowgraph Enlargement for δ_W = 5 Deg.

Table 5.4

SRB Kick Ring Heating Amplification Factors

TC NO.	X (IN)	Y (IN)	Z (IN)	h_i/h_u	h_i/h_u
2	37.970	1.25	0	4.45	4.50
3	37.970	2.13		7.19	7.30
4	34.970	2.50		4.65	4.53
5	37.720	2.50		4.12	4.09
6	37.370	2.75		17.85	17.77
7	37.720	3.00		4.51	4.51
8	38.720	3.00		2.38	2.42
9	38.970	2.75		0.48	0.47
13	37.970	1.25	-5.00	4.06	4.04
14	37.970	2.13		5.87	5.79
15	37.970	2.50		4.14	4.14
16	37.720	2.50		3.45	3.42
17	37.370	2.75		19.23	19.30
18	37.720	3.00		4.56	4.48
19	38.720	3.00		2.62	2.54
20	38.970	2.75		0.43	0.42
21	38.720	2.50		----	5.98
24	37.970	1.25	5.00	7.06	6.99
25	37.970	2.13		----	10.38
26	37.970	2.50		9.77	9.08
27	37.720	2.50		8.62	8.23
28	37.370	2.75		42.00	39.84
29	37.720	3.00		3.05	2.92

Group	17D	16D
M_∞	10.14	10.14
P_0 (psia)	1198.0	1198.0
T_0 (°R)	1894.0	1897.0
Wedge Angle (Deg.)	5.02	5.07
h_{uo} (Btu/ft^{2}sec°R) at X = 21 in.	.00130	.00130

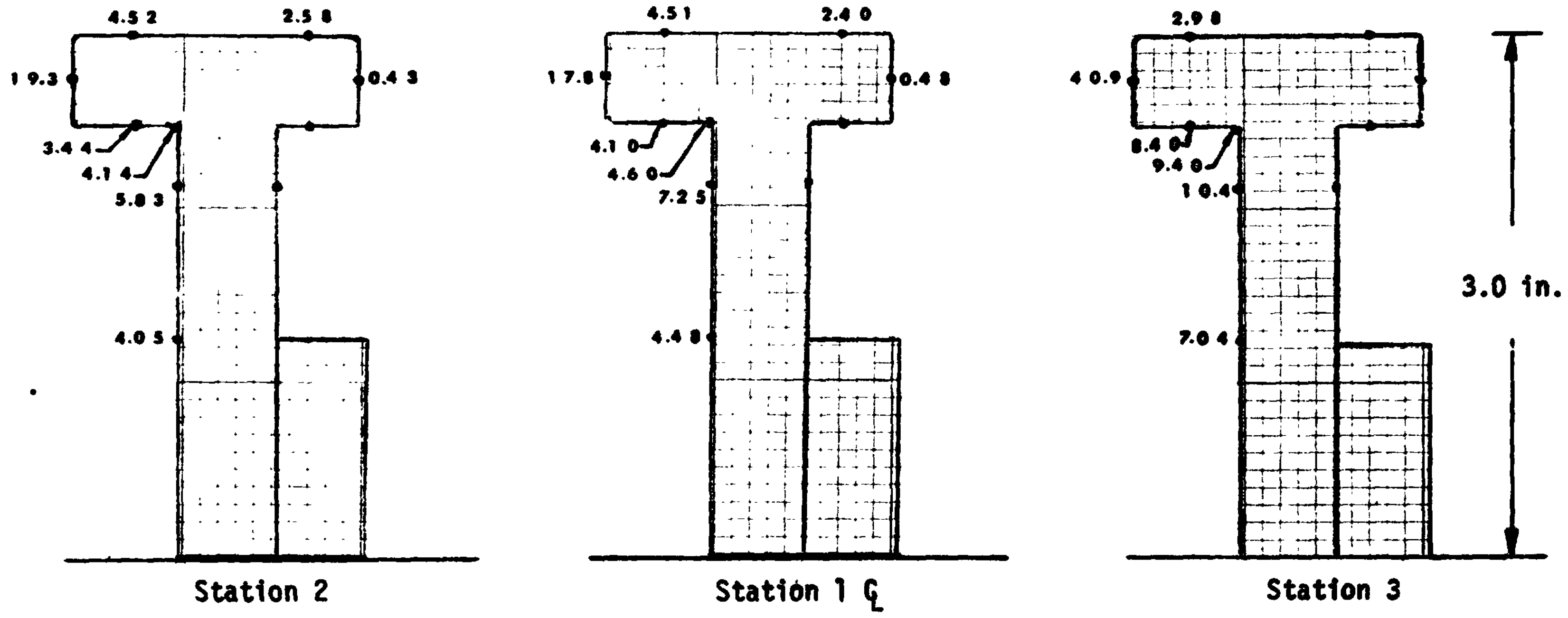

Fig. 5.29 Heating Amplification Factors for the Kick Ring

5.5 Cylinder-Shock Impingement Heating

Two tests were conducted in which shock impingement heating on a cylinder was measured (Ref. 5.1 and 5.3). In both situations, the cylinder was mounted on a wedge with its axis normal to the wedge. The cylinder protuberance was used to simulate either the ET-orbiter forward attach strut, or the SRB-ET aft attach strut. The geometries for the two tests are nearly the same as shown in Figs. 5.30 and 5.31 . The major difference being the axial placement of the cylinder on the wedge. In the test of Ref. 5.1, the front of the cylinder was 34.5 inches from the leading edge, whereas, the Ref. 5.3 test placed the cylinder 13.5 inches from the leading edge.

A shadowgraph of the flow field from Ref. 5.1 is shown in Fig. 5.32. Note that the wedge shock and separation shock intersect before either reaches the bow shock of the cylinder. Shadowgraph from Ref. 5.3, not included here, indicate that the wedge and separation shock coalesce very near the bow shock causing a stronger shock impingement.

The nondimensionalized data from Ref. 5.1 is given in Table 5.5 and the data from Ref. 5.3 is given in Table 5.6. The h_i/h_u values were computed by dividing the measured heating rate by $q_{cyl,\infty}$. The value of $q_{cyl,\infty}$ is the stagnation line heating rate to a cylinder normal to the free stream flow based on the theory of Fay and Riddell. The value of $q_{cyl,w}$ is also given in the tables. This is the value of the stagnation line heating to a cylinder normal to the post wedge shock flow.

The peak heating rate on the stagnation line normalized with the free stream cylinder heating rate is presented in Fig. 5.33. The data for $X_w = 34.5$ in, cylinder distance from leading edge, forms a peak near 12 to 13 degrees wedge angle. The two total pressures yield the same heating amplification factors except at 5 degrees, where the higher total pressure yields the smallest factor. The effect of the cylinders distance from the leading edge is dramatic in terms of heating amplification. The shadowgraph data indicated a single shock impingement when X_w = 13.5 in., whereas, the wedge shock is dispersed by the separation shock when X_w = 34.5 inches. The effect of this distance on the stagnation line distribution is shown in Fig. 5.34. The cylinder located further downstream of the leading edge exhibits a double peak behavior corresponding to the separation shock and deflected wedge shock locations.

The peak stagnation line heating was normalized by $q_{cyl,w}$ and plotted in Fig. 5.35a. This distribution shows less of a peak than in Fig. 5.33. The average stagnation line heating was evaluated and plotted in Fig. 5.35b. Here the lower total pressure data, X_w = 13.5 inches, is amplified slightly more than the higher pressure data. Again, the data for X_w = 34.5 inches is lower than the X_w = 13.5 inch data.

The effect of wedge angle on the stagnation line heating amplification is shown in Fig. 5.36a and b for two total pressure conditions. The 5 degree wedge data in Fig. 5.36 b shows a double peak like the X_w = 34.5 inch data. The heating amplification at two circumferential locations are compared to the stagnation line distribution in Fig. 5.37. At Θ = 90 degrees, the heating factor is nearly constant and equal to 0.40 times the free stream stagnation line value. The effect of wedge angle on the heating amplification distribution is shown in Fig. 5.38 and Fig. 5.39 for Θ = 45° and 90° respectively. The trend of increasing amplification going to the wall from 1.0 inch above the surface occurs in both Θ locations and all wedge angles.

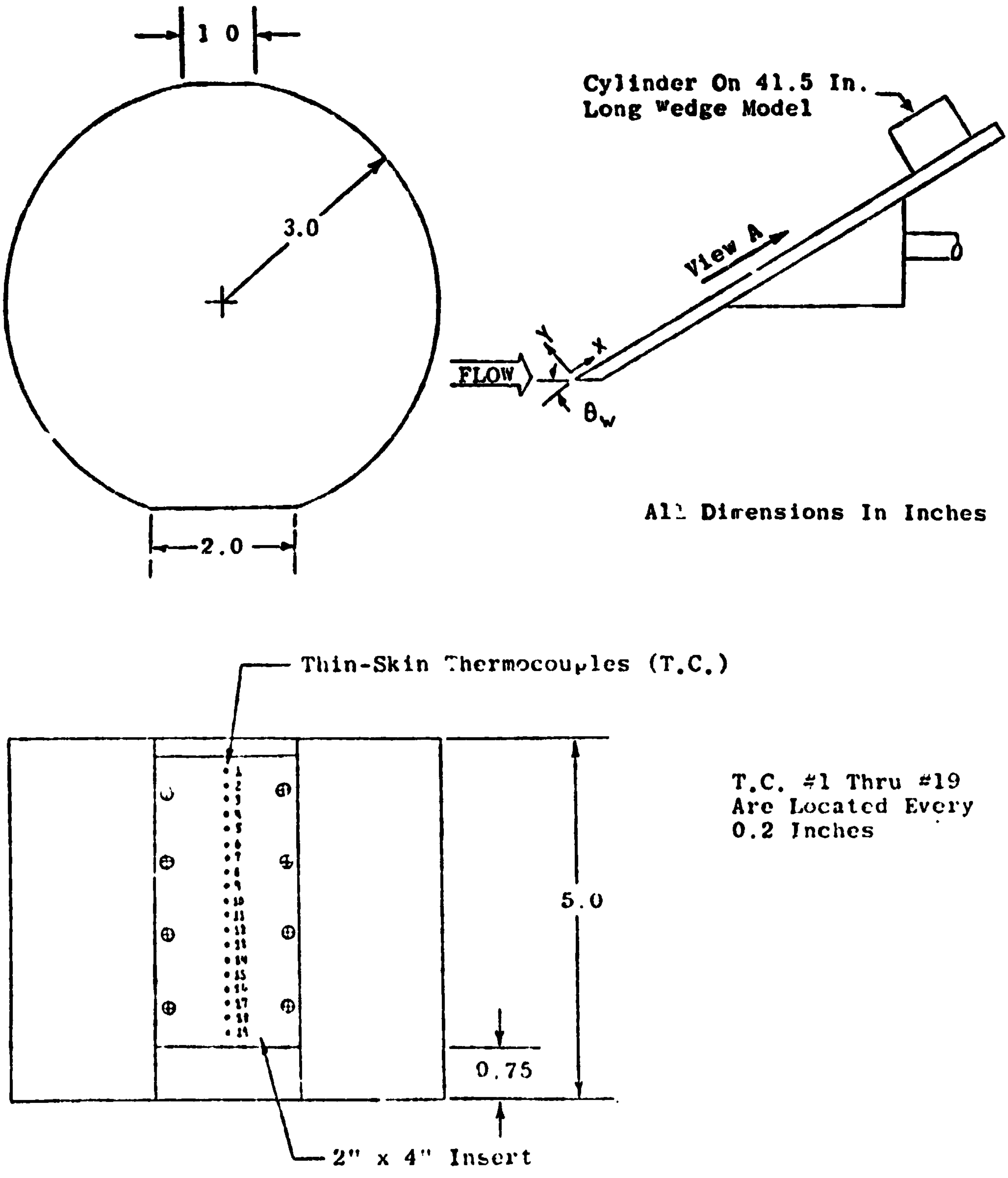

All Dimensions In Inches

T.C. #1 Thru #19
Are Located Every
0.2 Inches

View A - Half Scale

Fig. 5.30 Cylinder Protuberance Model (Ref. 5.1)

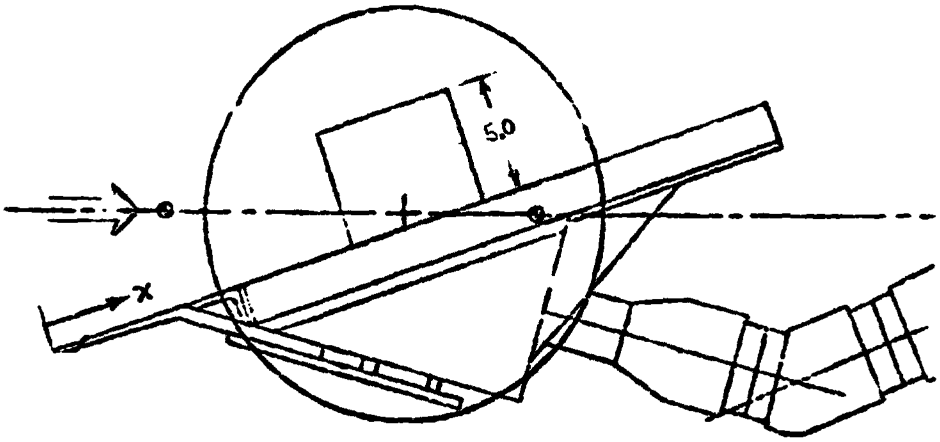

All Dimensions in Inches

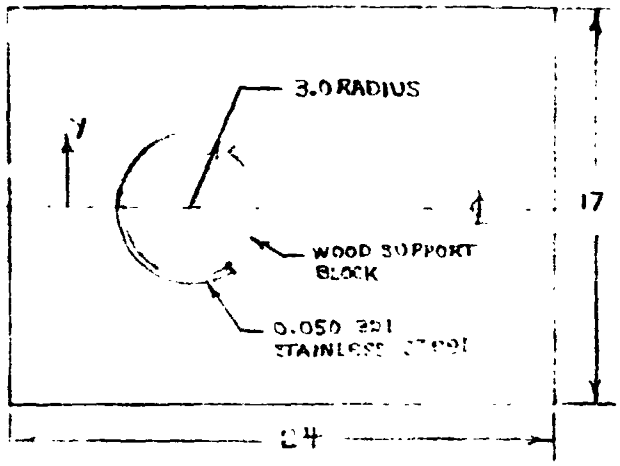

Fig. 5.31 Cylinder Protuberance Model (Ref. 5.3)

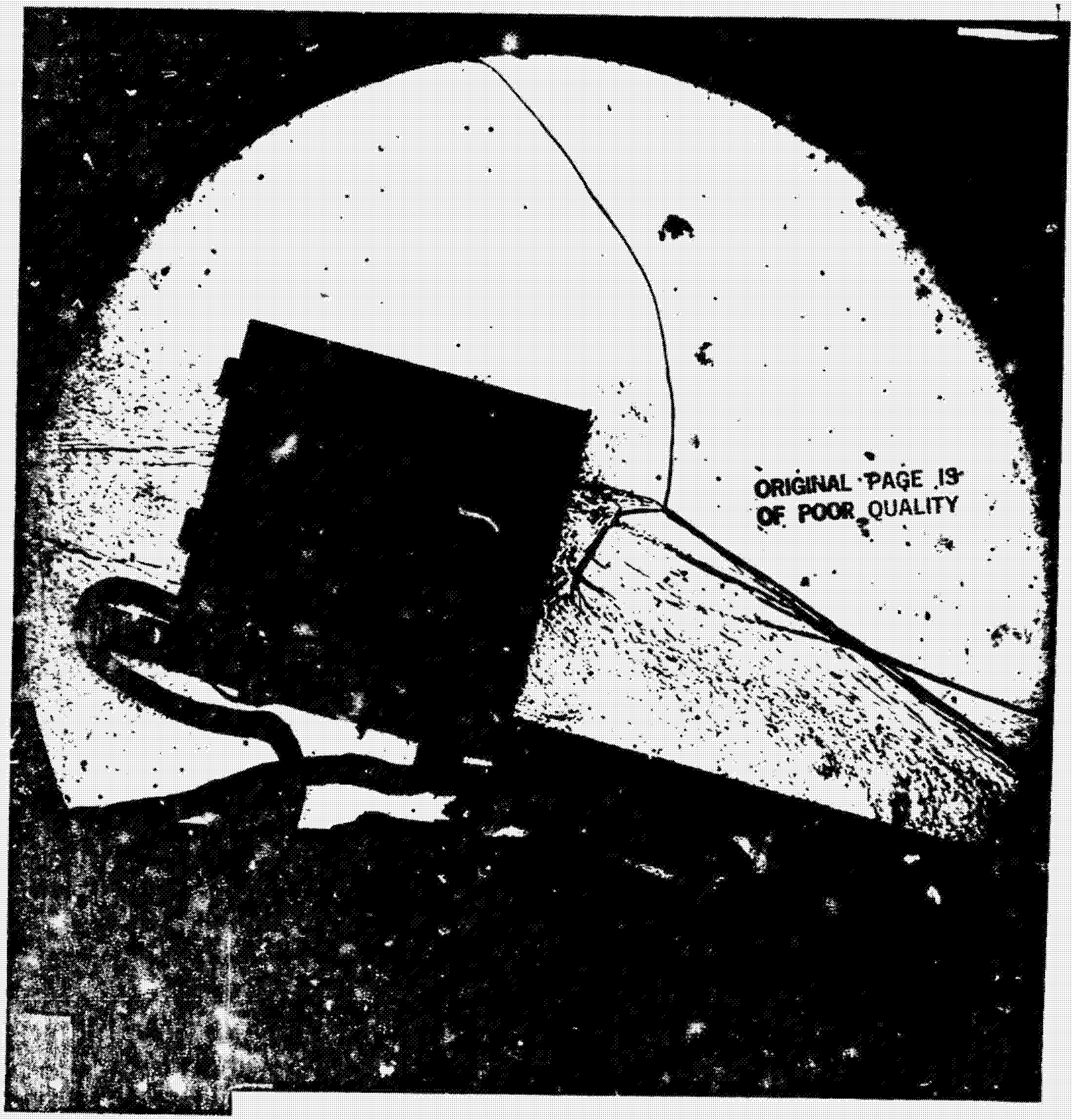

Cylinder
Dia. = 6 inches
Height = 5 inches
M_∞ = 10.17
P_o = 1796 psia
T_o = 1898°R
δ_w = 12 Deg.
Run 46D

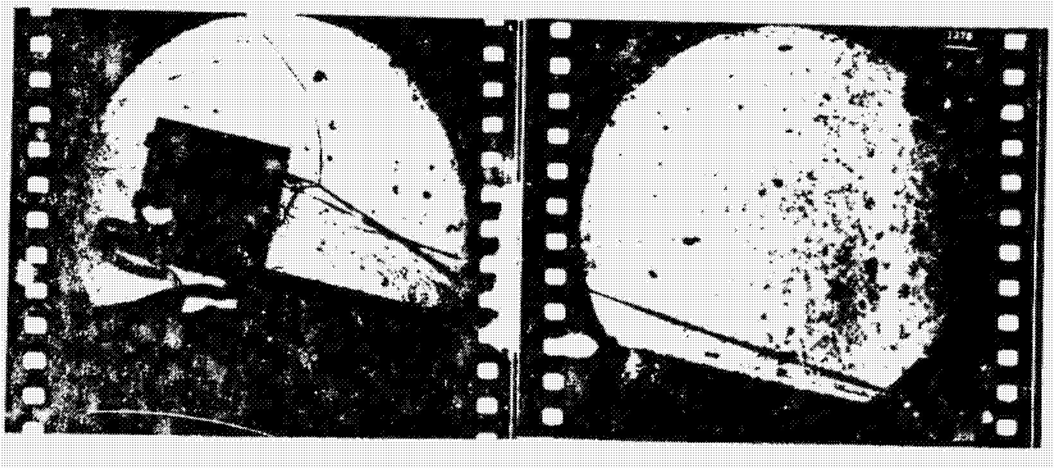

Fig. 5.32 Cylinder Shadowgraph Enlargement for δ_w = 12 Deg.

Table 5.5

Cylinder Heating Amplification Factors for X_w = 34.5 in.

TC NO.	X (IN)	Y (IN)	Z (IN)	h_i/h_u
1	34.500	4.63	0	1.44
2	↓	4.43	↓	1.73
3		4.23		2.91
4		4.02		4.35
5		3.82		5.74
6		3.63		7.21
7		3.43		7.93
8		3.22		7.72
9		3.03		6.89
10		2.82		6.13
11		2.63		6.17
12		2.43		6.45
13		2.22		7.25
14		2.03		7.19
15		1.83		6.23
16		1.63		4.63
17		1.42		3.38
18		1.22		2.49
19		1.03		2.55

Run	46D
M_∞	10.17
P_0(psia)	1796
T_0(°R)	1898
Wedge Angle (Deg.)	12.03
$q_{cyl,\infty}$(Btu/ft^{2}sec)	12.26
$q_{cyl,w}$(Btu/ft^{2}sec)	22.51

Table 5.6

Cylinder Heating Amplification Factors for X_w = 13.5 in.

TC NO.	X (IN)	Y (IN)	Z (IN)	h_i/h_u	h_i/h_u	h_i/h_u	h_i/h_u	h_i/h_u	h_i/h_u	h_i/h_u
1	13.50	0	4.50	5.34	3.15	2.68	4.39	4.16	5.28	5.45
2			4.00	5.63	2.55	2.45	4.78	4.51	5.38	5.58
3			3.80	5.33	3.11	2.36	5.01	4.73	4.69	5.01
4			3.60	4.82	5.77	2.46	5.30	5.18	4.09	4.62
5			3.40	4.59	8.36	2.70	5.71	5.95	4.14	4.70
6			3.20	5.50	7.85	2.96	5.94	7.15	5.21	5.69
7			3.00	7.40	5.63	3.60	6.24	8.43	7.35	7.54
8			2.90	8.30	5.05	3.95	6.34	8.92	9.30	8.92
9			2.80	10.55	5.00	4.36	6.47	9.59	10.59	10.84
10			2.70	11.81	5.11	4.80	6.61	10.02	12.15	11.96
11			2.60	13.37	5.47	5.32	6.60	10.35	13.59	13.41
12			2.50	14.11	5.72	5.83	6.56	10.49	14.40	14.03
13			2.40	14.30	6.04	6.18	6.58	10.58	14.61	14.66
14			2.30	14.73	6.33	6.68	6.71	10.76	14.50	14.82
15			2.20	13.47	6.36	6.93	6.68	10.95	14.40	14.93
16			2.10	13.26	6.17	6.91	6.85	10.97	13.19	14.23
17			2.00	12.52	5.67	7.02	6.65	10.83	12.54	13.80
18			1.90	11.94	4.71	7.14	6.55	10.57	12.03	13.26
19			1.80	11.70	3.99	7.07	6.50	10.07	11.78	12.72
20			1.70	11.25	3.28	6.95	6.33	9.40	11.51	12.33
21			1.60	10.60	2.50	6.87	6.10	8.47	11.09	11.62
22			1.50	10.00	2.04	6.82	5.52	7	11.10	11.62
23			1.40	9.12	1.67	6.72	5.71	6	9.94	10.40
24			1.30	7.93	1.22	6.52	5.18	5.22	8.91	9.08
25			1.20	6.95	.95	6.15	5.07	4.53	7.82	7.83
26			1.10	5.72	.84	5.72	4.73	3.65	6.58	6.50
27			1.00	4.77	.68	5.24	4.53	3.13	6.08	5.97
28			.90	4.19	.65	5.10	4.50	2.61	4.74	4.81
29			.80	3.63	.70	4.47	4.11	2.30	4.31	4.28
30			.70	3.56	.77	4.22	4.13	2.21	3.61	3.55
31			.60	3.88	.85	3.81	4.00	2.25	3.88	3.68
32			.50	3.91	.90	3.63	4.17	2.42	4.10	4.01
33			.40	4.36	.95	4.02	4.50	2.65	4.61	4.45
34			.30	4.45	.98	4.60	4.51	2.73	4.94	4.85
35			.20	4.15	.86	4.06	4.07	2.72	4.92	5.00
36	↓	↓	.10	3.39	.92	3.03	3.20	2.27	3.83	3.76
Group				4MD	6MD	7MD	11MD	12MD	16MD	20MD

Table 5.6 (Cont.)

TC NO.	X (IN)	Y (IN)	Z (IN)	h_i/h_u	h_i/h_u	h_i/h_u	h_i/h_u	h_i/h_u	h_i/h_u	h_i/h_u
37	14.38	2.12	4.50	2.99	1.59	1.63	2.36	2.01	2.77	2.85
38			4.00	2.85	1.52	1.53	2.56	2.17	2.29	2.54
39			3.80	2.52	2.18	1.52	2.51	2.28	2.05	2.36
40			3.60	2.32	2.90	1.82	2.29	2.41	2.18	2.53
41			3.40	2.70	3.38	1.93	2.84	3.16	2.72	2.63
42			3.20	3.28	2.80	1.99	2.71	3.41	3.40	3.16
43			3.00	3.57	1.80	1.82	2.22	2.93	3.19	3.36
44			2.80	4.92	2.02	2.41	2.70	3.97	5.08	4.65
45			2.60	5.83	2.14	2.73	2.99	4.27	5.95	5.23
46			2.40	6.43	2.39	3.06	2.91	4.43	6.06	5.86
47			2.20	5.97	2.27	3.05	2.75	4.22	5.55	5.58
48			2.00	5.41	1.99	2.99	2.59	3.93	5.15	5.27
49			1.80	5.51	1.64	3.29	2.80	3.96	5.20	5.35
50			1.60	4.65	1.16	3.03	2.40	3.30	4.60	4.76
51			1.40	4.18	.78	3.03	2.47	2.76	4.28	4.33
52			1.20	3.42	.53	2.81	2.34	2.10	3.62	3.56
53			1.00	2.62	.49	2.53	2.23	1.51	2.73	2.72
54			.80	2.31	.58	2.31	2.18	1.27	2.18	2.15
55			.60	2.63	.65	2.25	2.35	1.51	2.57	2.56
56			.40	2.97	.72	2.89	2.66	1.60	3.00	2.94
58	16.50	3.00	4.50	.33	.14	.50	.39	.23	.29	.30
59			4.00	.25	.22	.38	.36	.26	.27	.28
60			3.50	.28	.23	.35	.37	.34	.30	.36
61			3.00	.37	.19	.33	.34	.34	.41	.42
62			2.50	.40	.19	.36	.33	.35	.46	.44
63			2.00	.39	.18	.40	.34	.35	.46	.43
64			1.50	.32	.12	.42	.34	.27	.33	.33
65			1.00	.45	.19	.42	.41	.32	.46	.45
66			.50	.63	.20	.70	.56	.38	.62	.59

Run	4MD	6MD	7MD	11MD	12MD	16MD	20MD
M_∞	10.05	10.05	10.05	10.02	10.02	10.02	10.02
P_0 (psia)	502	501	496	204	201	202	203
T_0 (°R)	1897	1896	1898	1779	2049	1904	1902
Wedge Angle (Deg.)	11.96	5.00	24.01	24.01	5.02	13.29	12.04
$q_{cyl,\infty}$(Btu/ft²sec)	6.673	6.680	6.687	3.989	4.888	4.410	4.402
$q_{cyl,w}$(Btu/ft²sec)	12.08	9.582	12.72	7.500	6.990	8.133	7.999

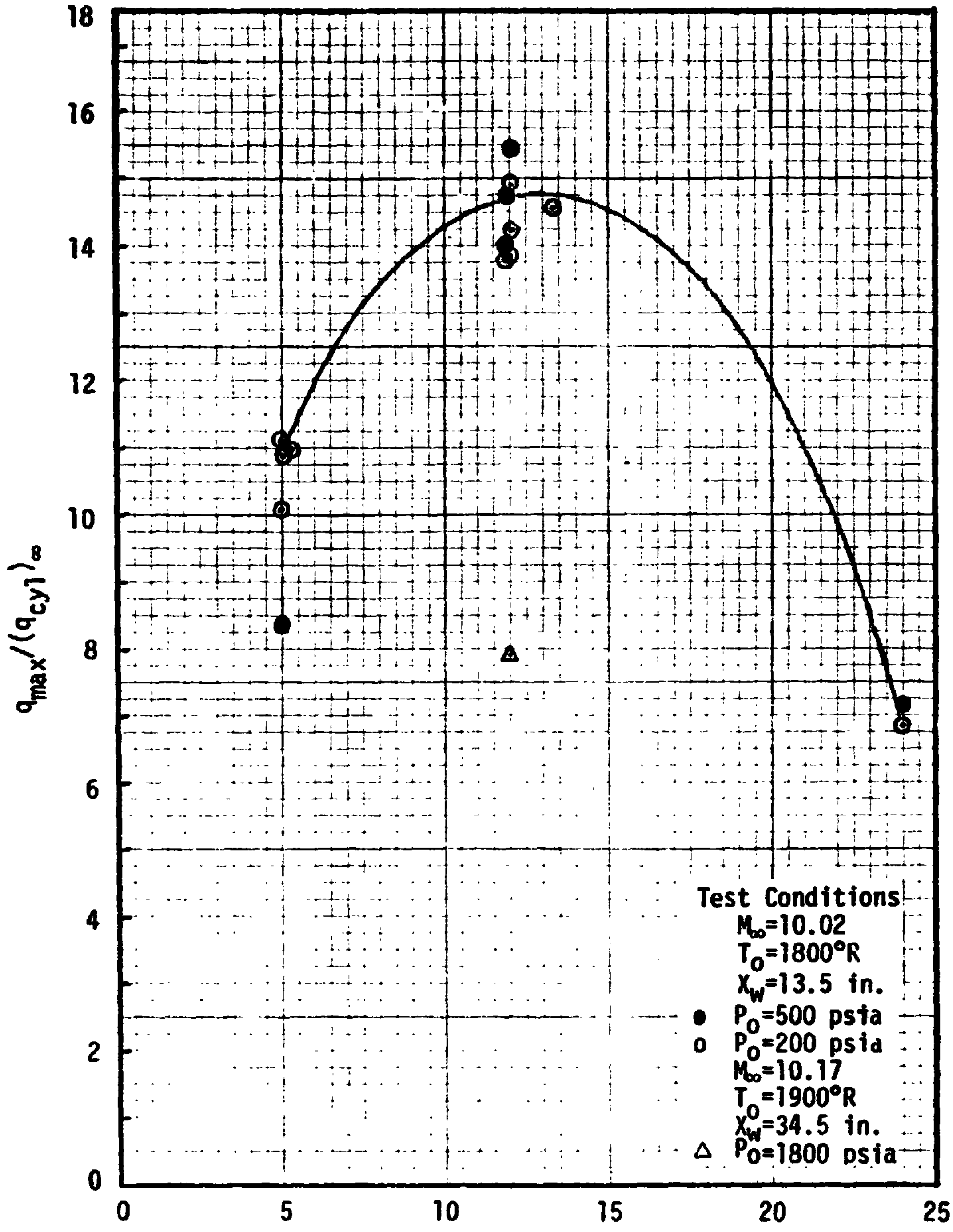

Fig. 5.33 Maximum Heating Rate Amplification on a Cylinder Due to a Wedge Flow-Field Interaction

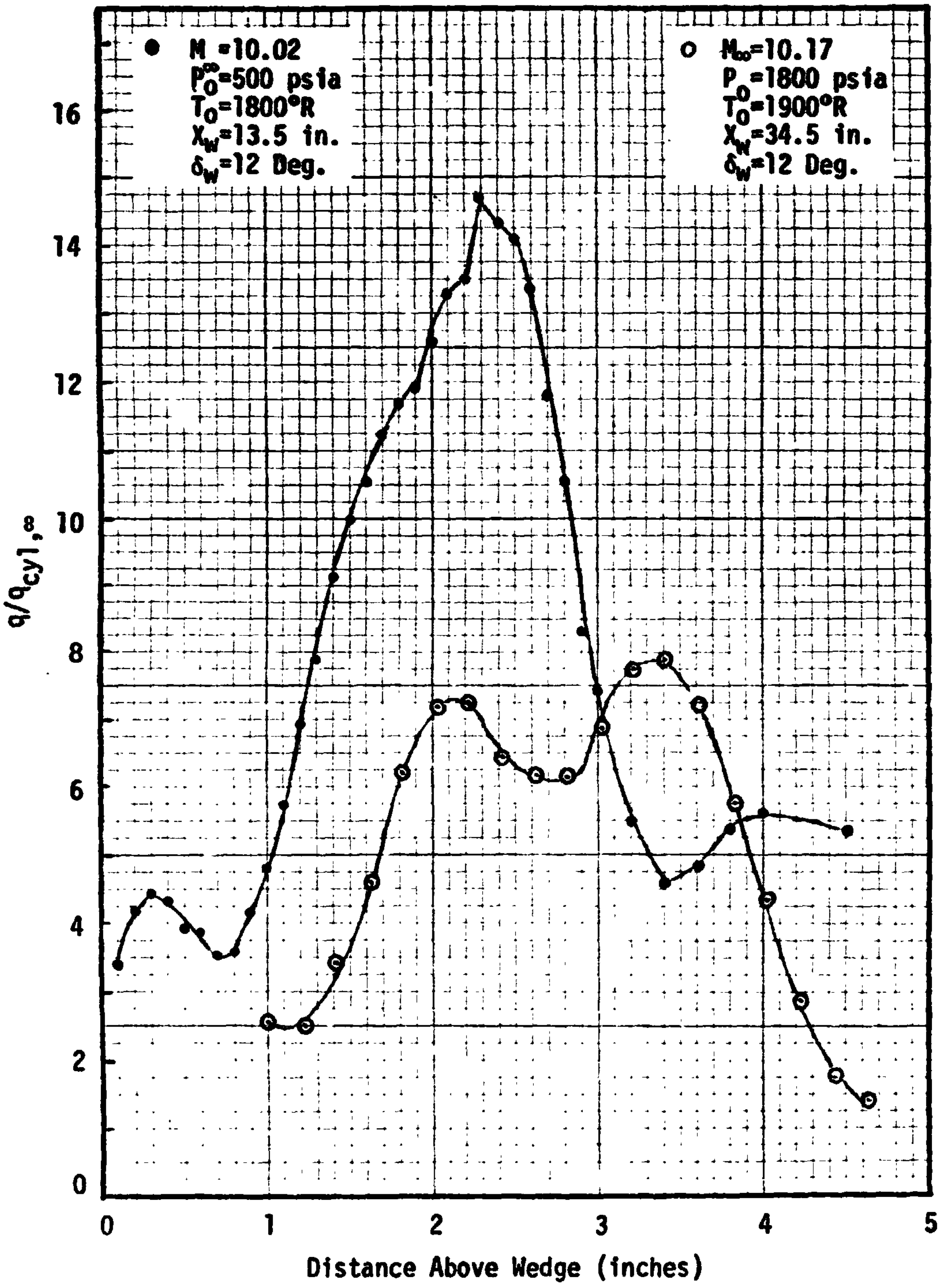

Fig. 5.34 Stagnation Line Interference Factors for Cylinders with Different Length Wedges

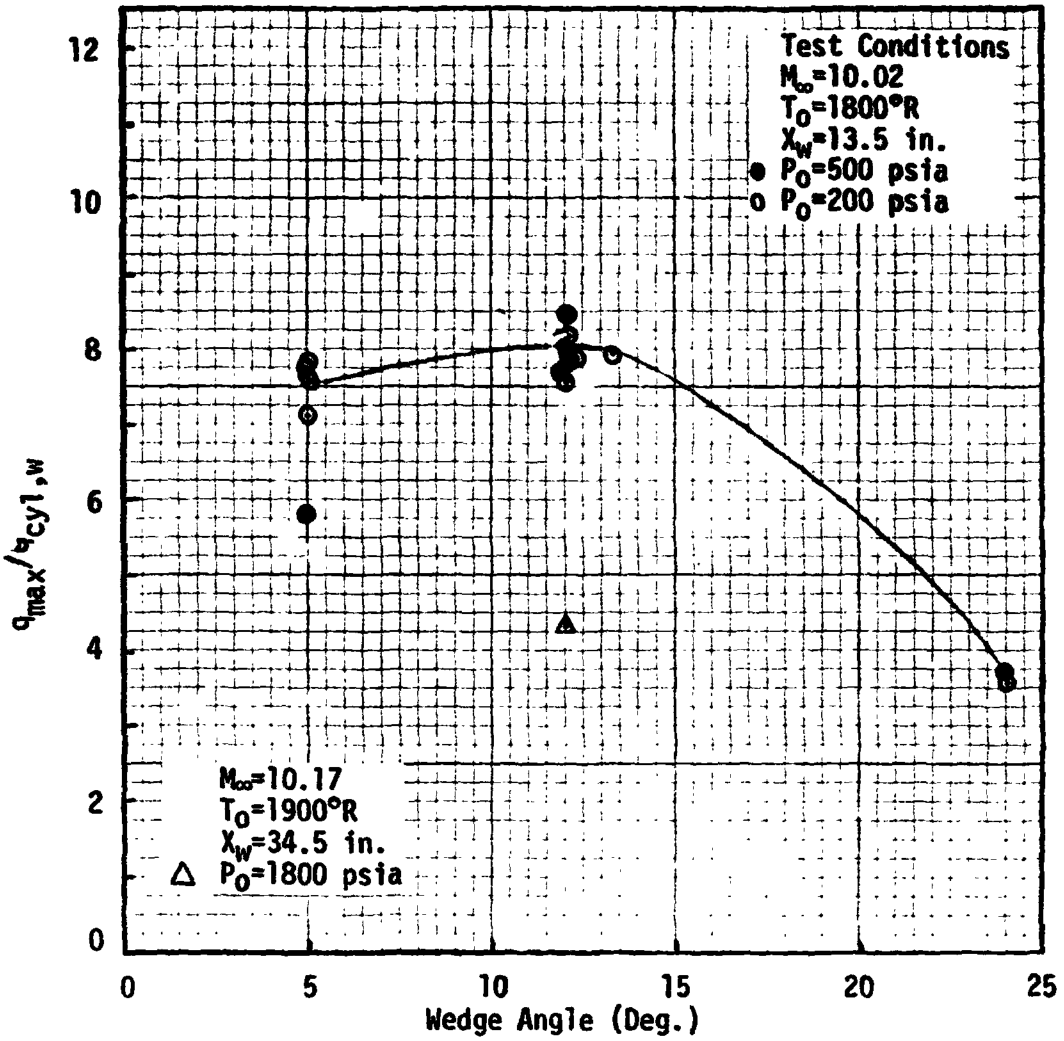

Fig. 5.35a Stagnation Line Heating Normalized with Post Wedge Shock Heating.

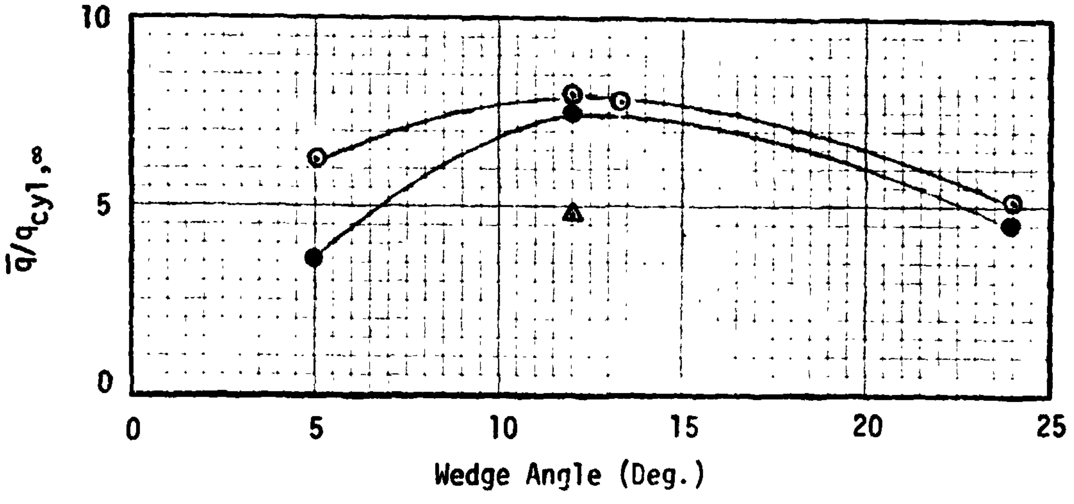

Fig. 5.35b Stagnation Line Averaged Heatings Versus Wedge Angle

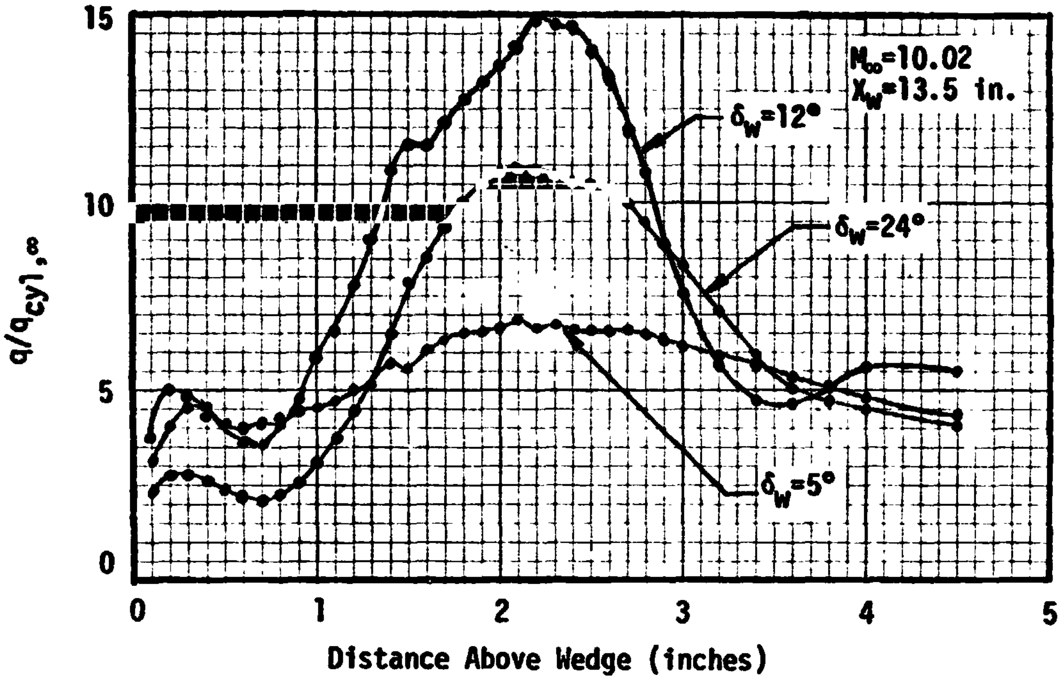

Fig. 5.36a Stagnation Line Interference Factors for P_0 = 200 psia

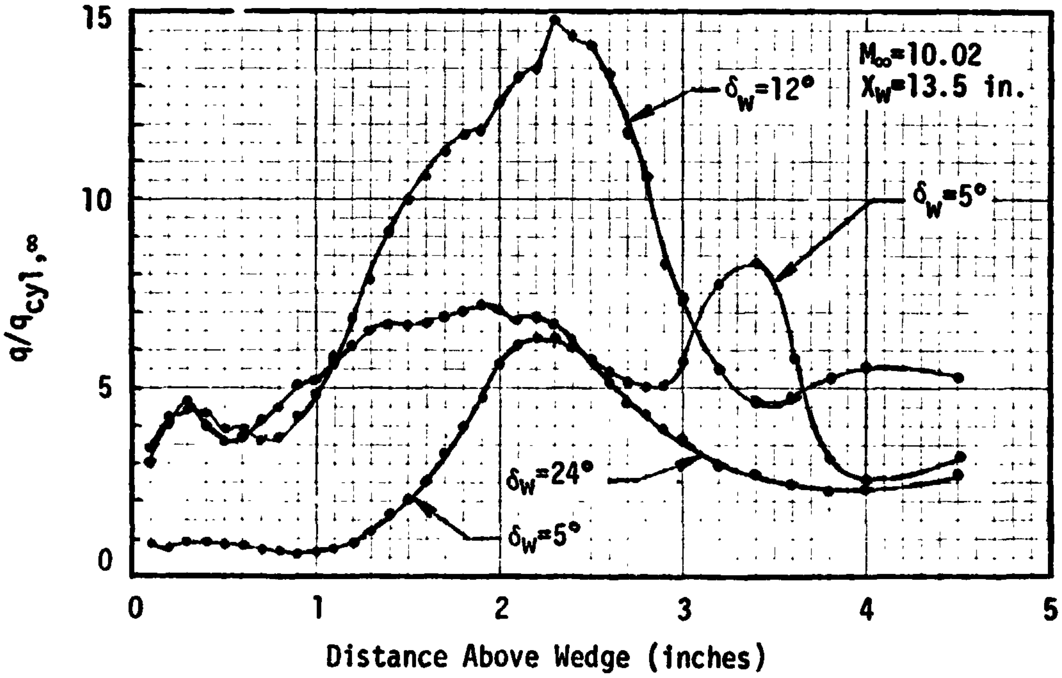

Fig. 5.36b Stagnation Line Interference Factors for P_0 = 500 psia

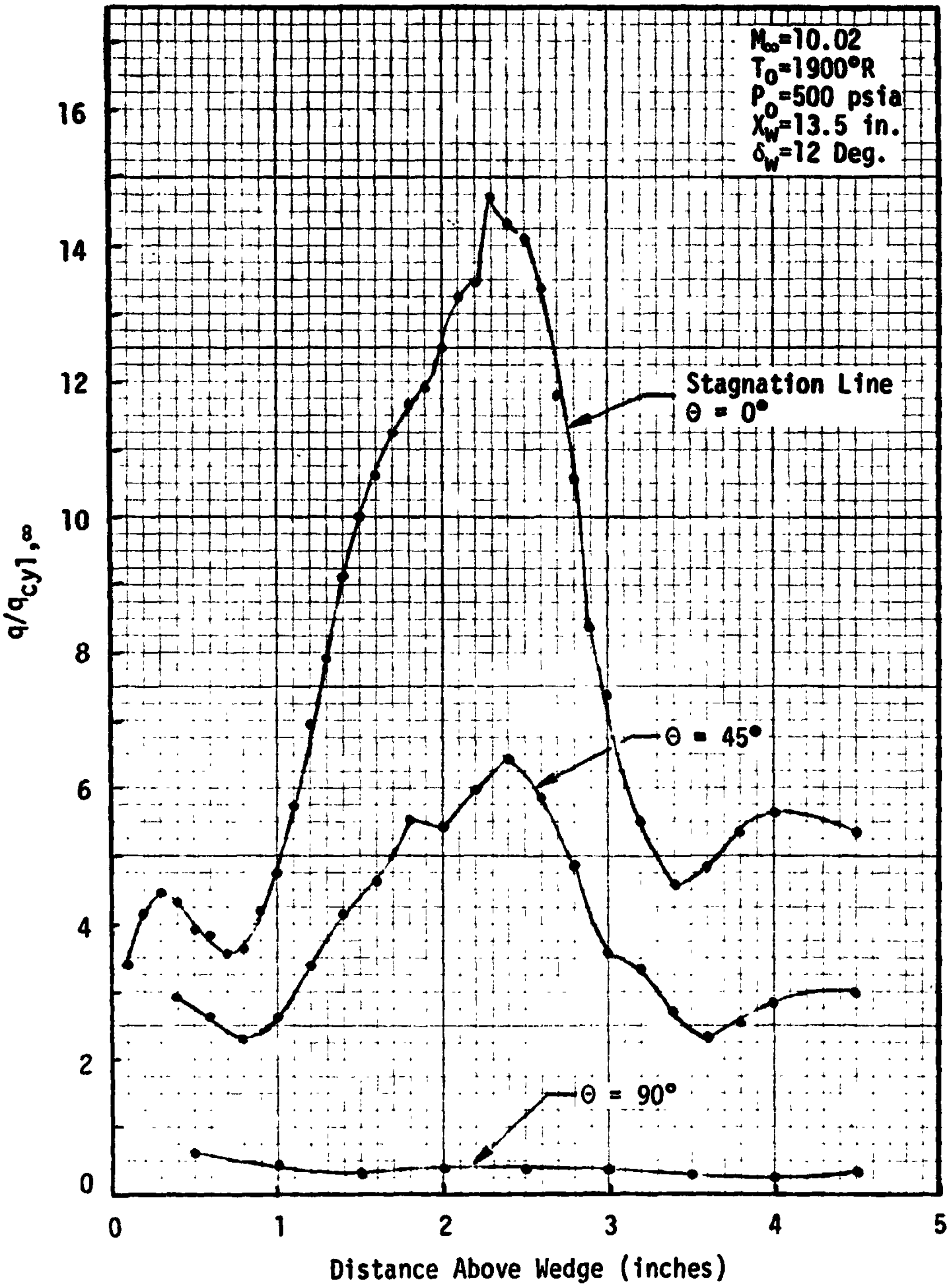

Fig. 5.37 Interference Heating Distributions Around the Cylinder

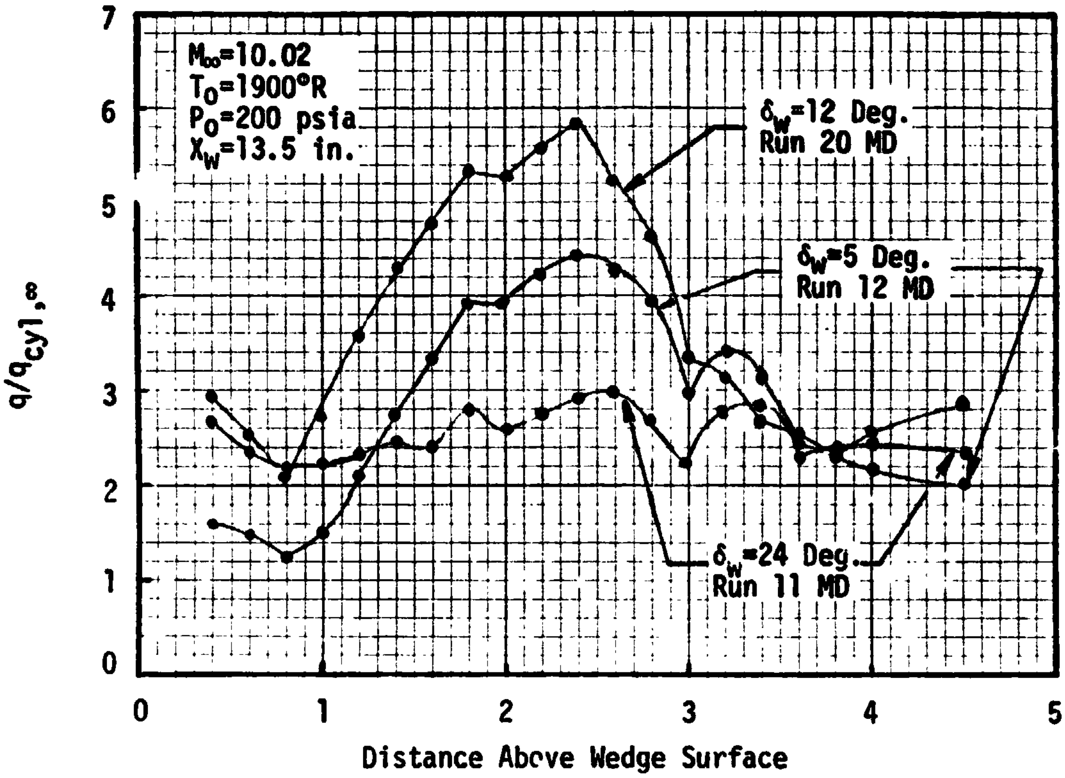

Fig. 5.38 Cylinder Interference Heating Distributions at Θ = 45 Deg.

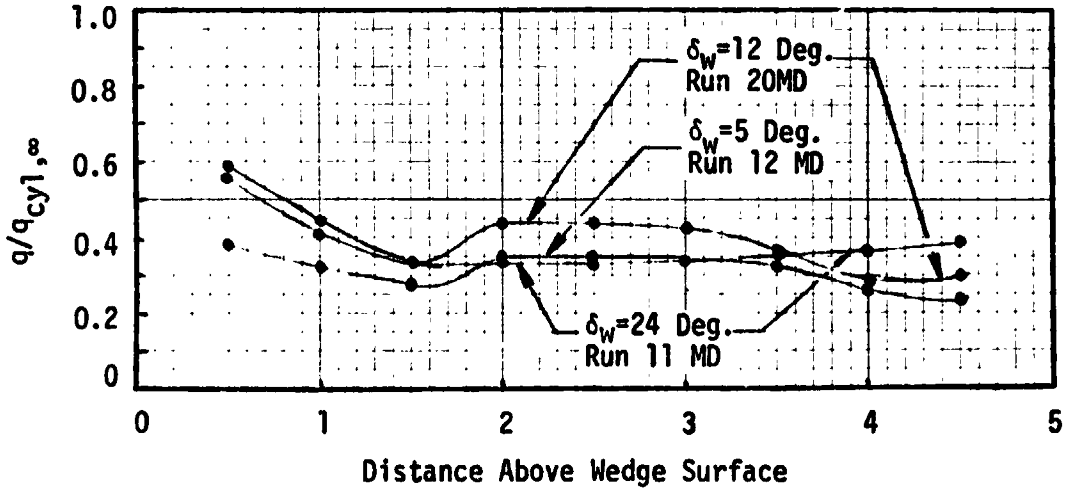

Fig. 5.39 Cylinder Interference Heating Distributions at Θ = 90 Deg.

5.6 References

5.1 Spencer, D., "NASA/LMSC SRB TPS Test, Final Data Package," ARO, Inc. V41C-V9A, December 1977.

5.2 Spencer, S., "NASA/LMSC SRB TPS Test, Final Data Package," ARO, Inc. V41C-L1A, September 1977.

5.3 Stallings, D., "NASA/MM ET Materials Test Final Data Package," ARO, Inc. V41C-N1A, December 1976.

5.4 Nestler, D. E., Saydah, A. R., Auxer, W. L., "Heat Transfer to Steps and Cavities in Hypersonic Turbulent Flow", AIAA Journal Vol. 7, No. 7, January 1969.

5.5 Boison, J. C., Curtiss, H. A., "An Experimental Investigation of Blunt Body Stagnation Point Velocity Gradient," ARS Journal, pp. 130-135, February 1959.

5.6 Hender, D., "A Miniature Version of the JA70 Aerodynamic Heating Computer Program, H800 (MINIVER), MDC Report No. G0462, June 1970 (Revised January 1972).

SECTION 6

IH-42 PAINT DATA

This section contains a description of the IH-42 Space Shuttle launch configuration test. The model used was a cast model for phase change testing. A calibration of the phase change paint lines is given. A procedure to calculate the h_i/h_u values from the calibrated data is given and compared with thermocouple data.

6.1 Test Description

The IH-42 phase change paint test was conducted by Rockwell International in the Ames 3.5 foot hypersonic wind tunnel. The nominal test conditions were $M_\infty = 5.3$, $P_0 = 410$ psia and $T_0 = 1300°R$. The model used was a cast of the orbiter, tank and SRB's using the same contours as the 60-0 thermocouple model. This 1.75 percent scaled model was used with four paint temperatures given below

Paint Temperature °F	$\sqrt{\rho c k}$ Btu/ft² sec·⁵ °F
300	.05619
350	.05669
400	.05686
500	.05602

The material properties for transient heat conduction analysis are given in the preceding tables for each paint temperature.

The objective of the test was to obtain interference heating contours on and around protuberances on the ET which could not be obtained using thermocouple models. The data analyzed are taken from facility printouts and model photos taken during the test.

6.2 Paint Calibration

The timed sequenced photos taken during the test were by and large found to be unusable. Many post-run photos were taken of each component of the model. These photos show the paint melt lines at the end of the run and constitute the usable data of the test. A typical set of photos for one run are shown in Fig. 6.1 to 6.5. These photos show the melted areas corresponding to temperatures above the melt temperature quite clearly. The figures shown are black and white although the set of photos for the test are in color giving additional detail. The primary objective of this subsection is to provide the calibration of these photos so that they may be used in determining heating levels.

The concept of calibrating the paint data by using thermocouple data from IH-68 on the ogive was provided by Dr. Frank Hung of Rockwell International. The ogive is a continuous curved surface on which melt lines of all of the paint temperatures occurred. The ogive heating is nearly all undisturbed flow. The IH-68 thermocouple test used the same scaled model in the same wind tunnel at the same free stream conditions. Thus, the paint and thermocouple data should be consistent.

The procedure used is as follows:

(1) The IH-42 pictures are inspected to determine for what Θ_T line both thermocouple and paint data are available for the ogive. This is done for each paint test run.

(2) A plot of the thermocouple data, h/h_{ref}, on the ogive versus X/L is made for the selected Θ_T. (See Fig. 5.6)*

(3) The X/L station where melt occurs for the selected Θ_T is determined from the pictures.

(4) The X/L station where melt occurs is plotted on the plot of thermocouple data. (See Fig. 6.6)

---

*$h_{ref} = h_s$, stagnation point heating reference throughout this section.

P. 61

(5) The value of h/h_{ref} is read from this plot for the paint measurement. This value of h/h_{ref} is assigned to all melt lines on the run so analyzed.

This procedure was applied to all the runs of IH-42 and the results are given in Table 6.1.

To check the consistency of the data the following analysis was performed from semi-infinite slab conduction theory

$$\bar{T} = \frac{T_s - T_{aw}}{T_i - T_{aw}} = e^{H^2} \text{ erfc } (H)$$

where

T_s = Surface or paint temperature
T_{aw} = Adiabatic wall temperature
T_i = Initial material temperature
H = $h \sqrt{\Delta t} / \sqrt{\rho c k}$
h = Heat transfer coefficient
Δt = Time duration of step function in h
ρ = Material density
c = Material heat capacity
k = Material thermal conductivity

Since all of the test for IH-42 were conducted at nearly the same tunnel conditions, the value of $\bar{T}$ is approximately constant. This implies that H is constant. For a given paint temperature $\sqrt{\rho c k}$ can be considered constant. Thus, $h \sqrt{\Delta t}$ could be considered constant. Accordingly, the value of $h \sqrt{\Delta t}/h_s$ was computed and plotted as shown in Fig. 6.7 for two recovery factors. (Note the figure contains two scales.) The value for t was obtained form the last printout frame of the paint test and h/h_s from the thermocouple calibration procedure.

The statistical information for the data shown in Fig. 6.7 is given in Table 6.2. The overall agreement is acceptable in that there is a significant uncertainty in Δt. The starred,"*",values given in Table 6.1 were determined using the mean value of $h \sqrt{\Delta t}/h_s$ for the appropriate paint temperature.

From the photos, lines of constant h/h_{ref} may be plotted. An example is shown in Fig. 6.8. The values of h/h_{ref} for the paint are obtained from Table 6.1 and the h/h_{ref} value for thermocouples are from the IH-68 test. The two sets of data appear to be in reasonable agreement although a quantitative assessment is difficult.

6.3 Calculation of h_i/h_u

This subsection addresses the problem of converting the h_i/h_s data into h_i/h_u data for comparison with thermocouple data. The calculation algorithm presented here is based on the work of Ref. 6.1 and 6.2. The step by step process is as follows:

(1) Compute the effective angle of attack of the ray line of interest

$$\alpha_{eff} = -\alpha\cos\Theta_T + \beta\sin\Theta_T$$

α = model angle of attack
β = model side slip angle
Θ_T = ET body angle

(2) Compute the recovery factor

$$\overline{R}_{\alpha,\beta} = a_1 + a_2\sin(\alpha_{eff})^{a_3}$$

$$\left.\begin{aligned} a_1 &= 0.9140 \\ a_2 &= -0.1004 \\ a_3 &= 1.73 \end{aligned}\right\}\ \text{for IH-68 and IH-42 Test Conditions}$$

(3) Compute the undisturbed to reference heat transfer coefficient ratio at zero angle of attack

$$(h_{u_{0,0}}/h_S) = A\ (X/L)^B$$

$$\left.\begin{aligned} A &= 0.03885 \\ B &= -0.11930 \end{aligned}\right\}\ \text{for IH-68 and IH-42 Test Conditions}$$

X/L = nondimensional axial distance

(4) Compute the undisturbed to reference heat transfer coefficient ratio at angle of attack

$$h_{u_{\alpha,\beta}}/h_S = (h_{u_{0,0}}/h_S)(1+k\alpha_{eff})$$

where $k = 0.02402 + 0.01246M_\infty$

$= 0.09008$ **for** $M_\infty = 5.3$

(5) Calculate the recovery factor adjustment term for the paint data

$$f = \frac{T_o - T_{paint}}{R_{\alpha,\beta}T_o - T_{paint}}$$

T_o **= Tunnel total temperature**

T_{paint} **= Paint temperature**

(6) Calculate the paint line heat transfer coefficient value ratioed to the undisturbed

$$\left(\frac{h_i}{h_u}\right)_{\alpha,\beta} = \frac{f(h_i/h_s)_{paint}}{(h_{u_{\alpha,\beta}}/h_s)}$$

where $\left(\frac{h_i}{h_s}\right)_{paint}$ is provided in Table 6.3 for $\bar{R} = 1.0$.

Thus given the photos for a particular run, the heating interference factor may be calculated using the preceding algorithm with the data in Table 6.3.

An example case has been worked and is presented in Table 6.4 for the ET top centerline near the forward attach point. Three runs for three paint temperatures at the same angle of attack and yaw were selected. The recovery factor is invariant for the three runs. The X/L locations are the measured paint line locations from the IH-42 photos. The h_i/h_u values are the final results using the preceding algorithm.

The interference factors from the preceding example are compared with thermocouple data from IH-48 in Fig. 6.9 for the same flow conditions. The paint data indicates a higher interference than the thermocouple data. The reading accuracy in X/L was questioned to explain this difference. This accuracy is approximately ± 0.01 X/L. Thus, this does not explain why the paint data is higher. The paint data has the same shape distribution but is broader. The high values of the paint data are thought to be due to the testing technique. That is, the data was obtained from post test photos. At the end of the test the regions which were at higher temperature than the paint lost their heat through conduction to the regions slightly below the paint temperature. This would raise the temperature in the regions near the paint melt line and thus enlarge the melt regions. This effect could be substantiated by a transient heat conduction analysis.

It can be concluded that the IH-42 data must be used with care since post-run conduction effects in regions of high heating gradients can yield heating interference factors which are higher than the actual values.

6.4 References

6.1 Hurst, C. W., "Least Squares Correlation of External Tank Barrel Section Undisturbed Heat Transfer Data at Angle of Attack", NSI Memorandum No. M-9230-76-71, Northrop Services, Incorporated, Huntsville, Alabama, December 2, 1976.

6.2 Praharaj, S. C., "Methodology for Evaluating Thermal Environments of the Space Shuttle External Tank Barrel Section", NSI Technical Report TN-224-1794, Northrop Services Incorporated, Huntsville, Alabama, May, 1977.

TABLE 6.1

CALIBRATED IH-42 PAINT LINES

USING IH-68 THERMOCOUPLE ET OGIVE DATA

Run No.	α (Deg.)	β (Deg.)	T/C Interpreted		Last Frame Paint		T_{paint} (°F)	h_s LBM/FT^2-SEC	Config.
			h/h_s R=1.0	h/h_s R=0.9	h/h_s R=1.0	h/h_s R=0.9			
5	0	0	.194	.227	.162	.221	400	.3202	OTS
6	0	0	.138	.172	.131	.176	350	.3200	OTS
7	0	0	.109	.129	.085	.110	300	.3212	OTS
8	-5	0	.196	.235	.167	.236	400	.3216	OTS
9	-5	0	.120	.145	.098	.131	350	.3216	OTS
10	0	0	.292	.360	.292	.483	500	.3194	OTS
11	+5	0	.185	.221	.151	.203	400	.3222	OTS
12	+5	0	.108	.132	.086	.111	300	.3238	OTS
13*	+5	+5	.192	.230	.160	.220	400	.3215	OTS
14*	+5	+5	.106	.128	.103	.136	300	.3218	OTS
15*	0	+5	.192	.230	.199	.291	400	.3201	OTS
16*	0	+5	.105	.127	.112	.152	300	.3215	OTS
17	-5	+5	.194	.186	.130	.171	400	.3240	OTS
18	-5	+5	.096	.119	.089	.114	300	.3237	OTS
19*	0	+5	.293	.355	.225	.328	500	.3217	OTS
20*	+5	+5	.293	.355	.242	.362	500	.3217	OTS
21	0	-5	.224	.266	.185	.262	400	.3210	OTS
22	0	-5	.109	.129	.098	.127	300	.3227	OTS
23	+5	-5	.165	.198	.149	.200	400	.3228	OTS
24	+5	-5	.095	.114	.087	.112	300	.3241	OTS
25	-5	-5	.202	.241	.170	.239	400	.3210	OTS
26	-5	-5	.121	.144	.097	.127	300	.3221	OTS
27	+5	0	.302	.360	.242	.364	500	.3206	OTS
28*	0	0	.287	.348	.254	.390	500	.3204	OT
29	0	0	.095	.115	.084	.108	300	.3234	OT
30*	-5	0	.285	.345	.265	.419	500	.3203	OT

TABLE 6.1 (Cont.)

CALIBRATED IH-42 PAINT LINES USING IH-68 THERMOCOUPLE ET OGIVE DATA

Run No.	α (Deg.)	β (Deg.)	T/C Interpreted		Last Frame Paint		T_{paint} (°F)	h_s LBM/FT^2-SEC	Config.
			h/h_s R=1.0	h/h_s R=0.9	h/h_s R=1.0	h/h_s R=0.9			
31	-5	+5	.265	.320	.268	.425	500	.3202	OT
32*	0	+5	.282	.342	.248	.382	500	.3207	OT
33*	0	+5	.190	.228	.166	.230	400	.3213	OT
34*	0	+5	.220	.266	.183	.235	300	.3234	OT
35*	0	+5	.103	.125	.085	.110	300	.3233	OT
36	-5	+5	.184	.218	.152	.209	400	.3217	OT
37	-5	+5	.118	.146	.091	.119	300	.3223	OT
38*	+5	+5	.186	.225	.162	.227	400	.3212	OT
39*	+5	+5	.103	.125	.093	.122	300	.3224	OT
40	0	0	.159	.198	.146	.201	400	.3221	OT
41	-5	0	.168	.230	.165	.232	400	.3211	OT
42	-5	0	.095	.119	.092	.119	300	.3235	OT
43	+5	0	.209	.249	.155	.212	400	.3218	OT
44	+5	0	.097	.119	.087	.118	300	.3226	OT
45	0	-5	.178	.212	ND	ND	400	ND	OT
46	0	-5	.094	.113	.087	.118	300	.3233	OT
47	-5	-5	.185	.223	.165	.231	400	.3211	OT
48	-5	-5	.103	.124	.096	.126	300	.3223	OT
49	+5	-5	.222	.272	.182	.261	400	.3205	OT
50	+5	-5	.118	.142	.089	.115	300	.3229	OT
51*	-5	+5	.189	.226	.183	.264	400	.3203	OTS

* Direct T/C data was not available for these runs. The h/h_s values were computed using the mean value of $h\sqrt{\Delta t}/h_s$ derived from the remainder of the data for the respective paint temperature.

TABLE 6.2

Calibration Statistics for IH-42 Paint Data
Using IH-68 ET Ogive Thermocouple Data

Paint Temp. (°F)	R = 0.9 $h\sqrt{\Delta T}/h_s$ (mean)	σ	% for 1 σ	Max % Dev.	R = 1.0 $h\sqrt{\Delta T}/h_s$ (mean)	σ	% for 1 σ	Max % Dev.
300	.2918	± 0.0267	9.15%	+16.83%	.2407	± 0.0233	9.68%	+17.91%
350	.3642	± 0.0450	12.36%	- 8.76%	.2964	± 0.0302	10.19%	- 7.22%
400	.5253	± 0.0593	11.29%	+20.69%	.4381	±0.0518	11.99%	-21.80%
500	.805	± 0.0507	6.30%	- 7.20%	.6650	±0.0436	6.56%	- 6.96%

TABLE 6.3
BASIC IH-42 PAINT DATA

Run	T_o (°R)	T_{paint} °R	h_i/h_s ($\bar{R}$=1.0)	α (Deg)	β (Deg)
5	1342.6	860	.194	0	0
6	1293.9	810	.138	0	0
7	1334.7	760	.109	0	0
8	1286.2	860	.196	-5	0
9	1254.4	810	.120	-5	0
10	1264.5	960	.292	0	0
11	1372.2	860	.185	+5	0
12	1372.4	760	.108	+5	0
13	1333.4	860	.192	+5	+5
14	1272.5	760	.106	+5	+5
15	1239.2	860	.192	0	+5
16	1215.3	760	.105	0	+5
17	1454.4	860	.194	-5	+5
18	1381.0	760	.096	-5	+5
19	1378.2	960	.293	0	+5
20	1356.9	960	.293	+5	+5
21	1277.7	860	.224	0	-5
22	1320.0	760	.109	0	-5
23	1378.0	860	.165	+5	-5
24	1353.0	760	.095	+5	-5
25	1290.5	860	.202	-5	-5
26	1291.5	760	.121	-5	-5
27	1341.9	960	.302	+5	0
28	1320.8	960	.287	0	0
29	1358.6	760	.095	0	0
30	1297.7	960	.285	-5	0
31	1293.3	960	.265	-5	+5
32	1317.3	960	.282	0	+5
33	1320.3	860	.190	0	+5
34	1352.5	760	.220	0	+5
35	1338.3	760	.103	0	+5
36	1325.6	860	.184	-5	+5
37	1297.3	760	.118	-5	+5
38	1300.2	860	.136	+5	+5
39	1291.9	760	.103	+5	+5
40	1343.4	860	.159	0	0
41	1288.5	860	.188	-5	0
42	1343.7	760	.095	-5	0
43	1350.2	860	.209	+5	0
44	1329.6	760	.097	+5	0
45	ND	860	.178	0	-5
46	1336.1	760	.094	0	-5
47	1298.6	860	.185	-5	-5
48	1291.2	760	.103	-5	-5
49	1262.1	860	.222	+5	-5
50	1323.1	760	.118	+5	-5
51	1260.6	860	.189	-5	+5

TABLE 6.4

h_l/h_u SAMPLE CASE

ET TOP CENTERLINE

Run ı h/h_s	5 1.314 0.194	6 1.299 0.138	7 1.250 0.109		
	X/L Paint Melt	X/L Paint Melt	X/L Paint Melt	h_u/h_s	h_l/h_u
			0.400	.04333	3.139
		0.4026		.04330	4.139
	0.421			.04307	5.921
	0.468			.04253	5.996
		0.4705		.04251	4.210
			0.4797	.04241	3.207
			0.495	.04225	3.219
		0.496		.04224	4.238
	0.499			.04220	6.043
	0.521			.04199	6.073
		0.547		.04175	4.287

$\overline{R} = 0.914$

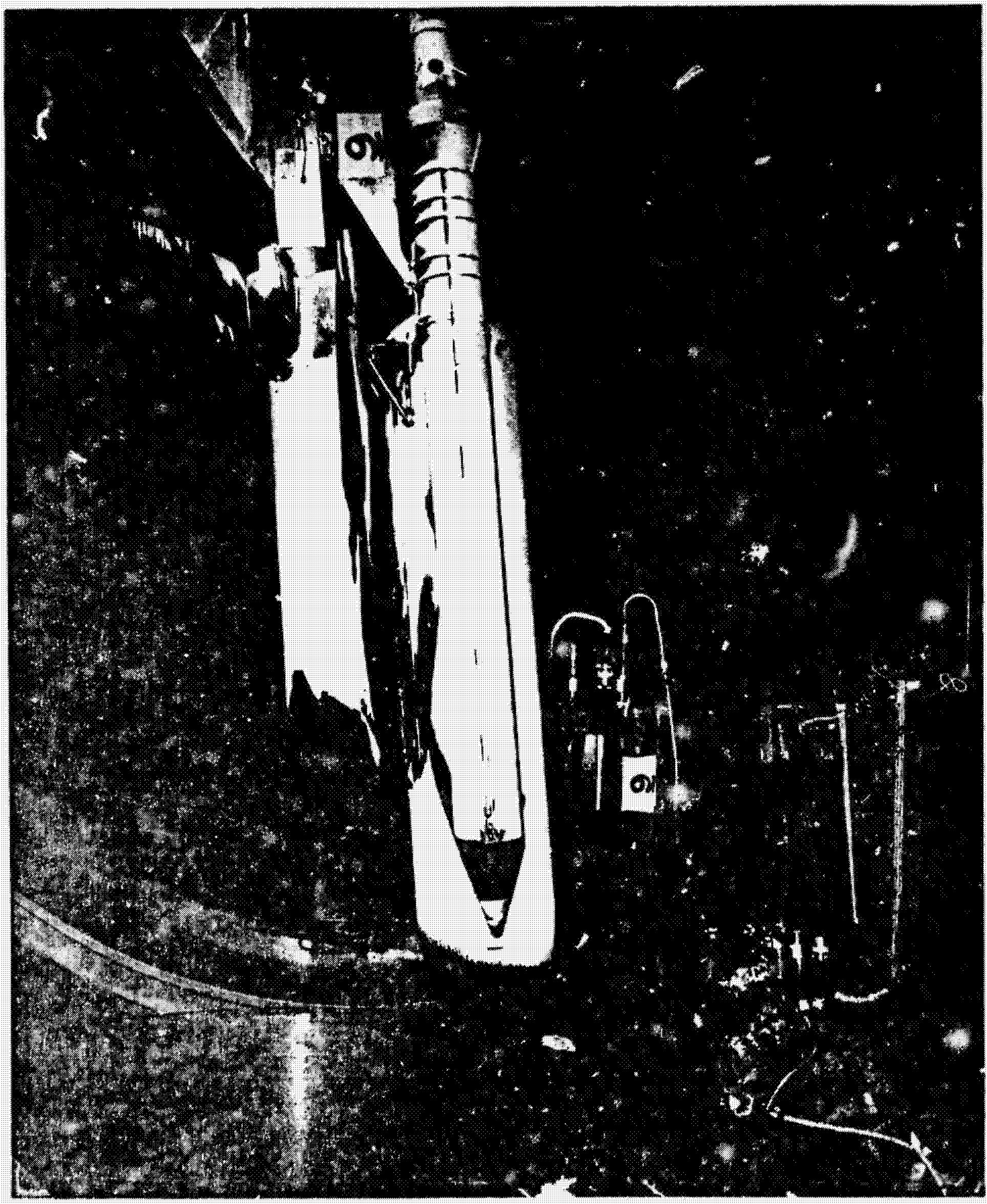

A760513 D-24 C

Fig. 6.1 Matted Configuration, Run 9

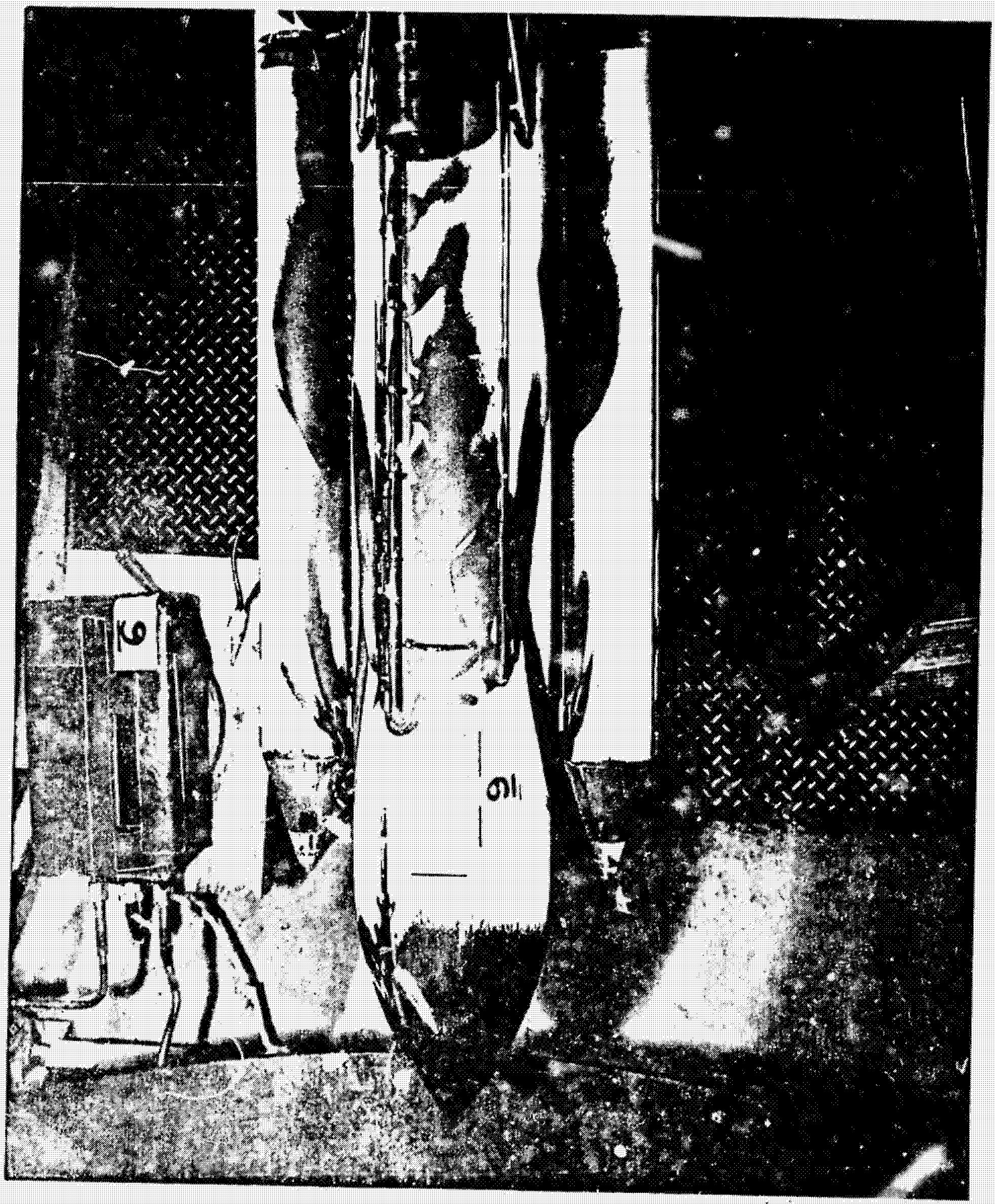

A760513 D-25 C

Fig. 6.2 ET-SRB Top View, Run 9

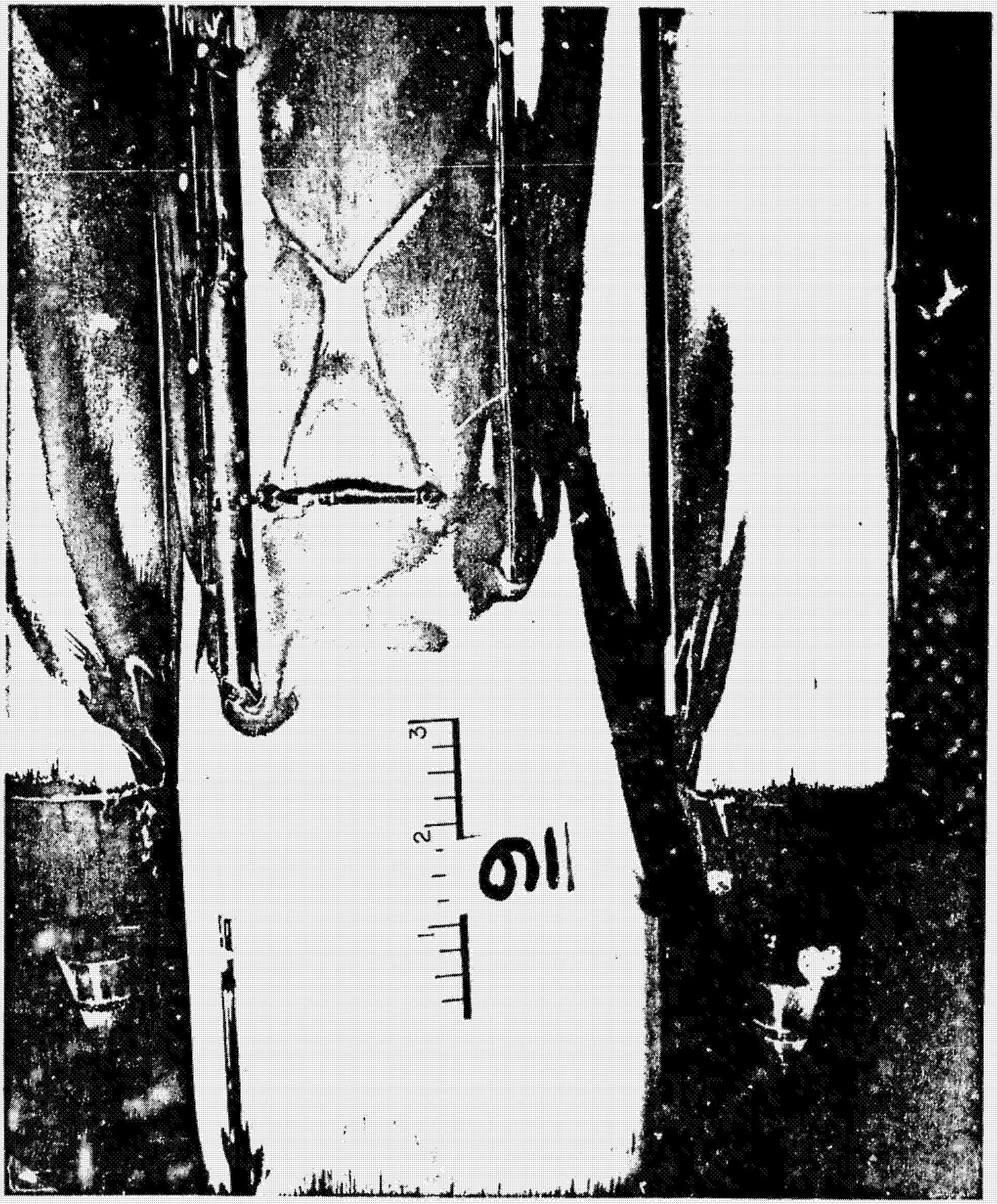

A760513 D-26 C

Fig. 6.3 ET Top View Enlargement, Run 9

ORIGINAL PAGE IS
OF POOR QUALITY

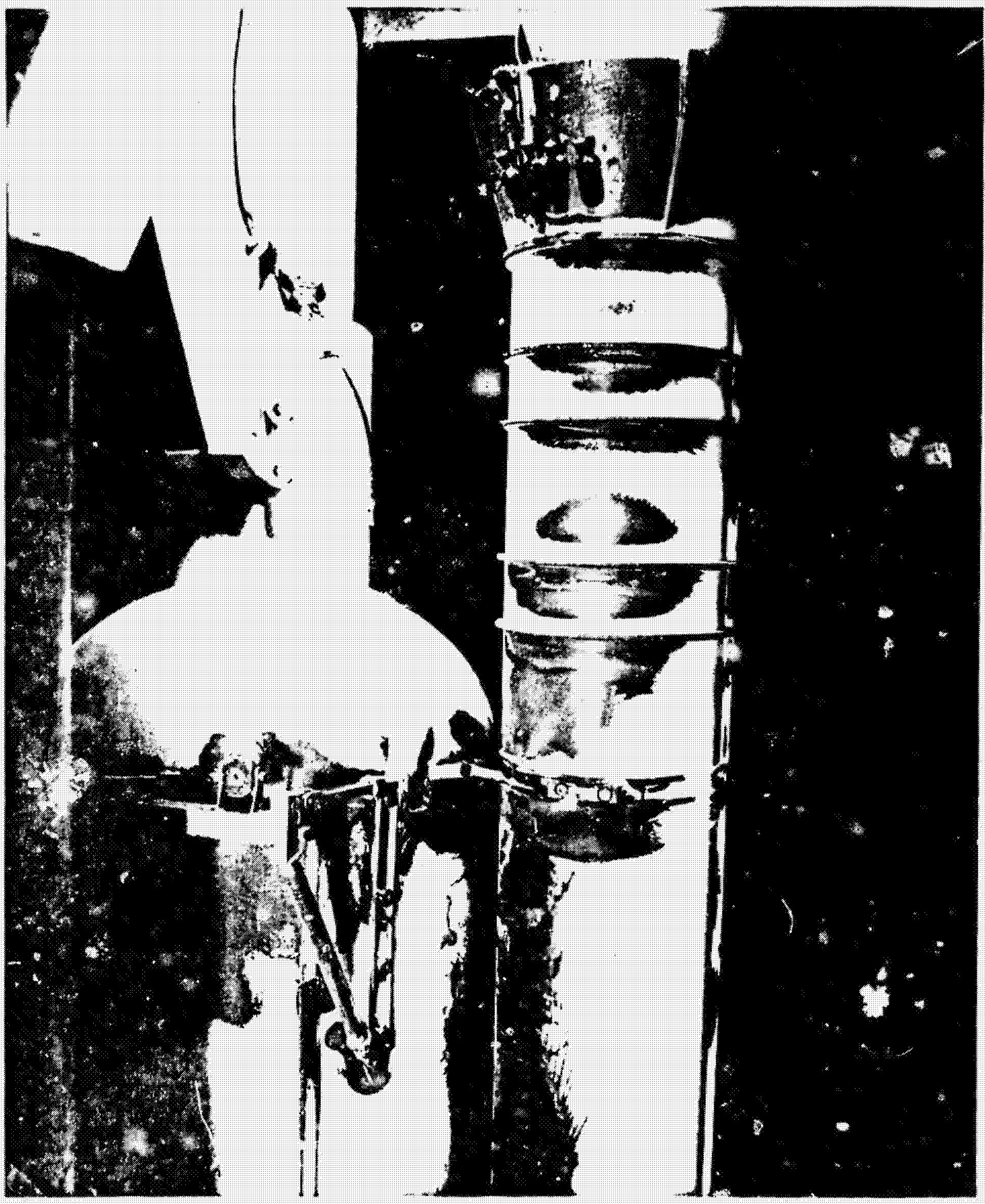

A760513 D-27 C

Fig. 6.4 ET-SRB Aft End Top View, Run 9

A/E0513 D-28 C

Fig. 6.5 ET-SRB Side View of Top Section, Run 9

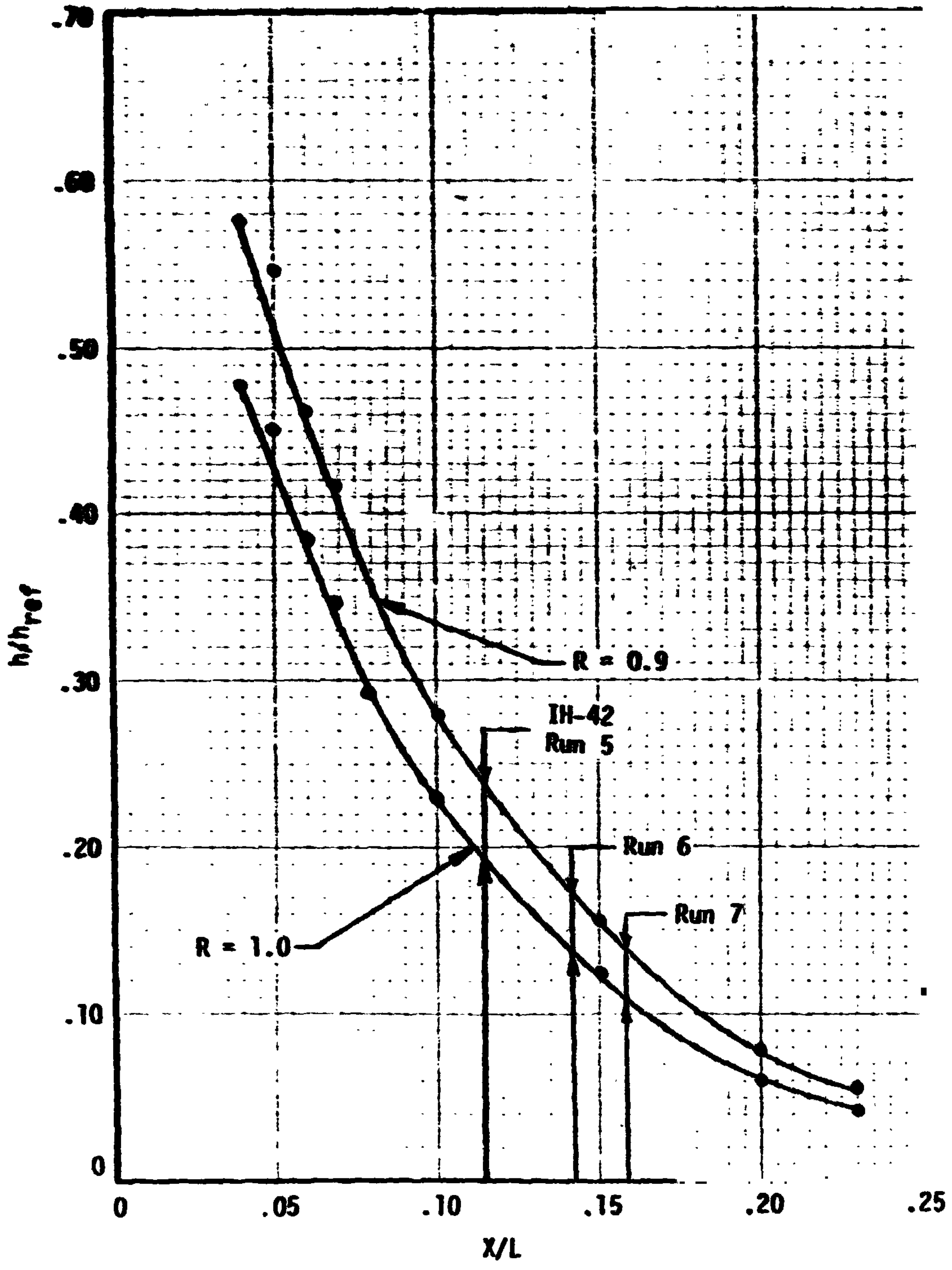

Fig. 6.6 IH-68 T/C Data on the ET Ogive (α=0°, β=0°, θ_T=270°)

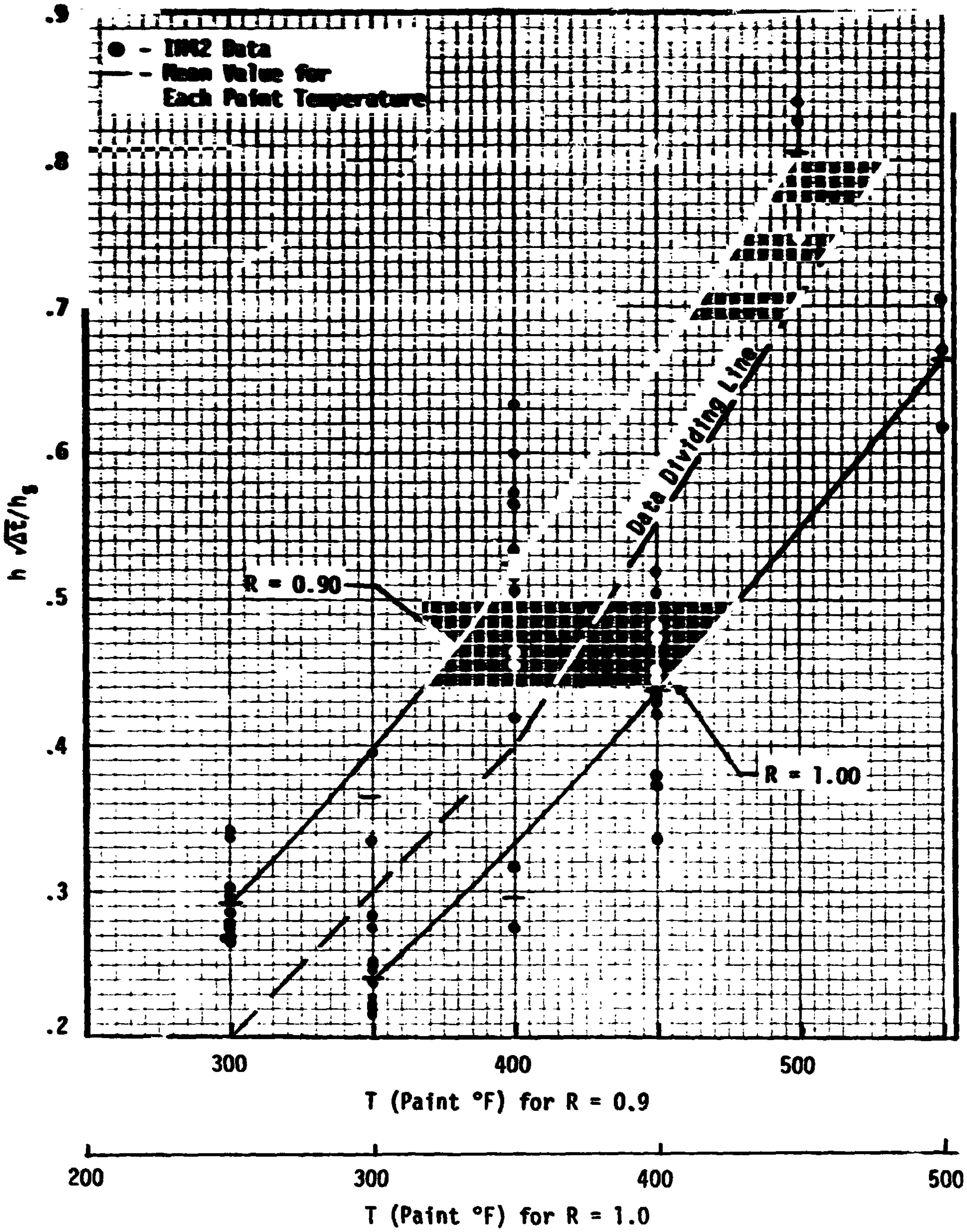

Fig. 6.7 IH-42 Paint Line Values of Heat Transfer Coefficient Ratio Data

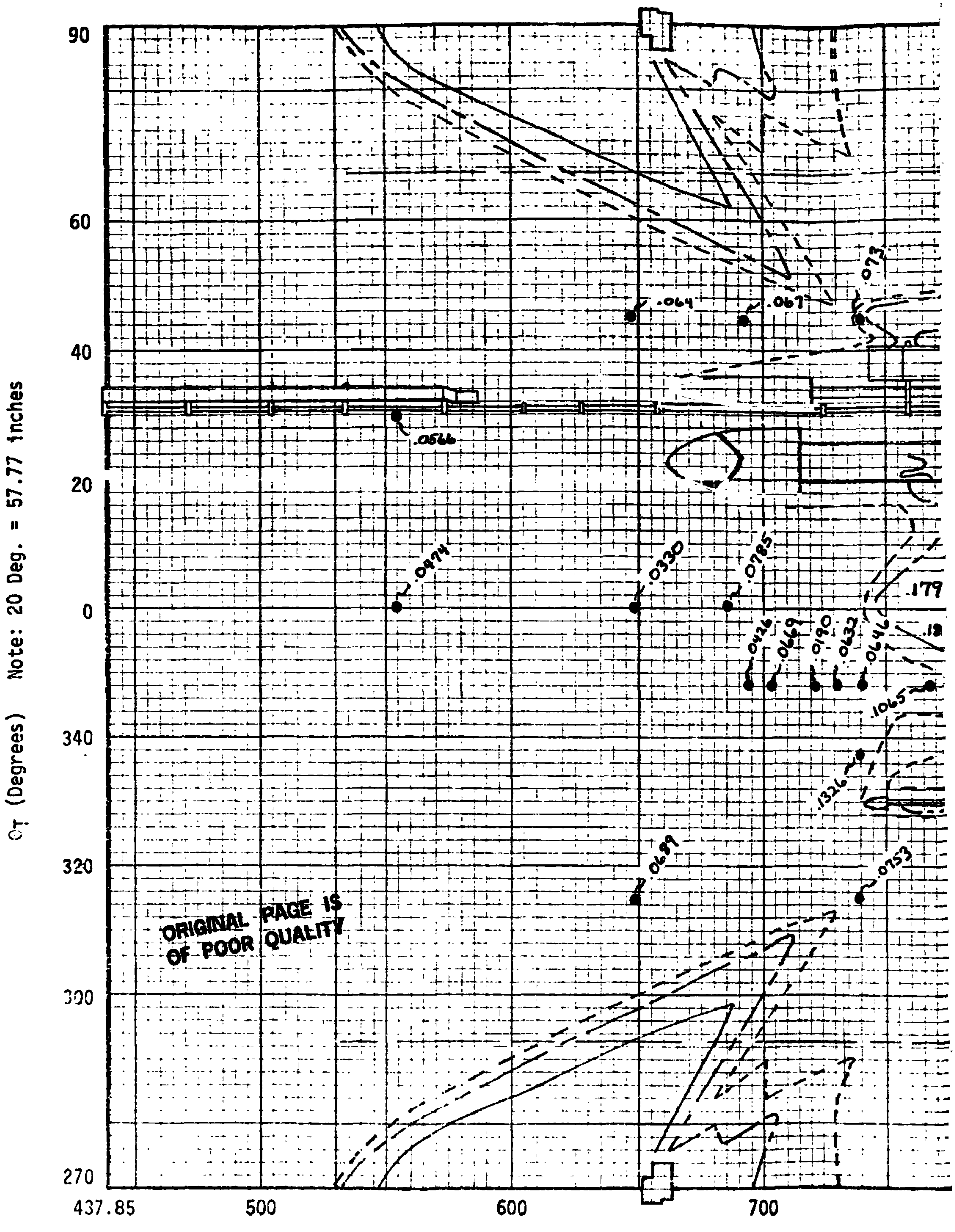

Fig.6.8 Zone 4 Skin Paint Contours and Thermocouple Dat

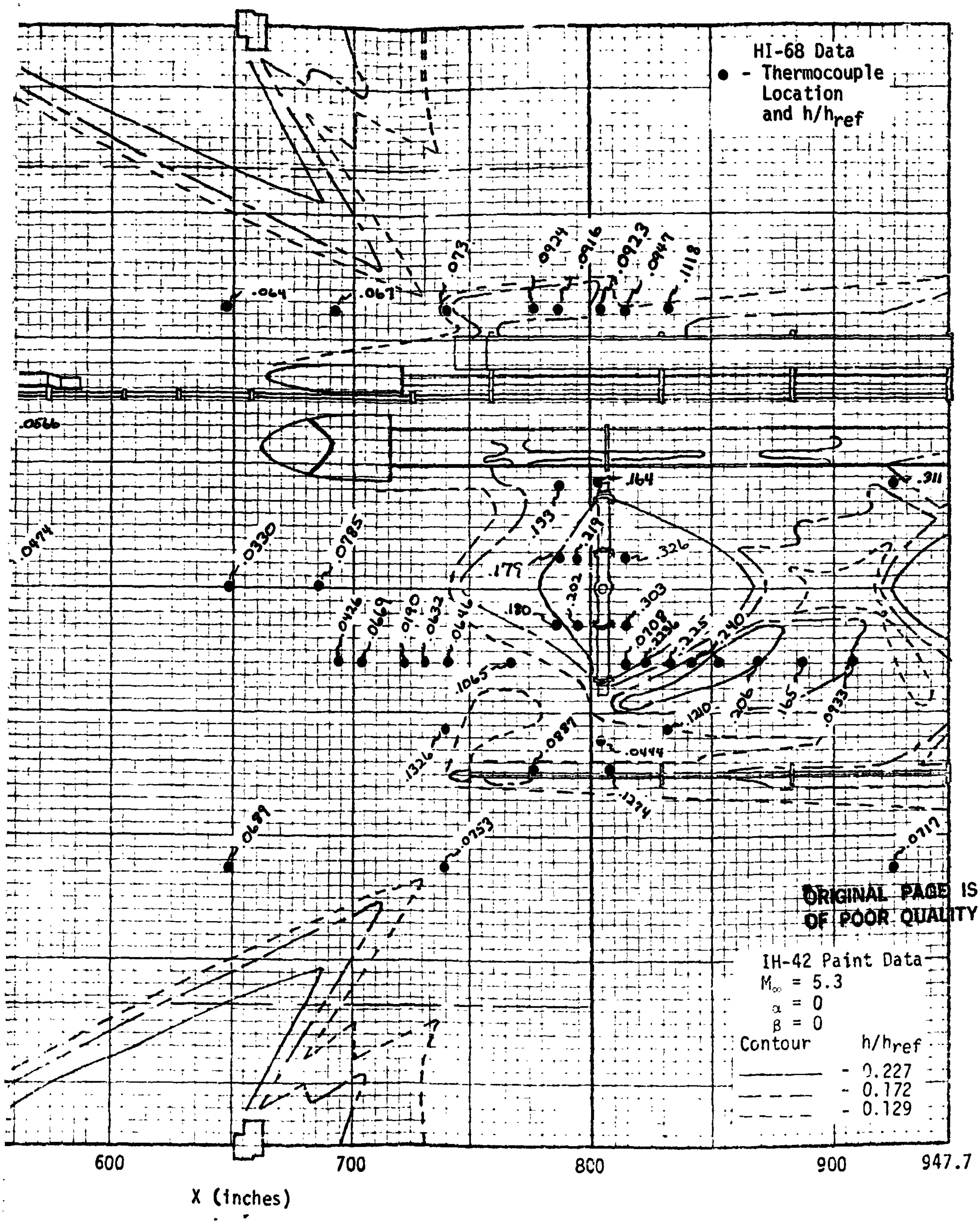

6.8 Zone 4 Skin Paint Contours and Thermocouple Data

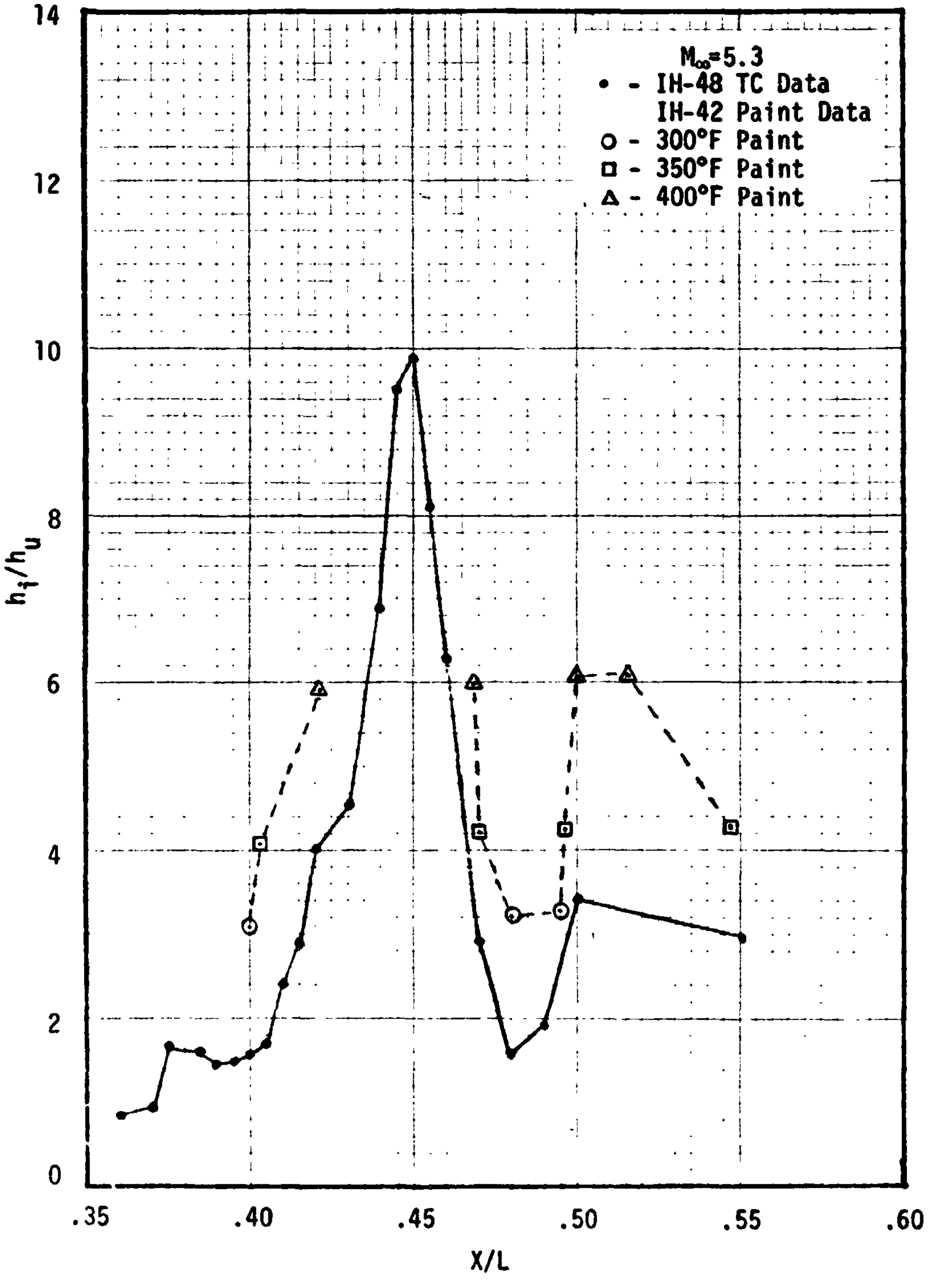

Fig. 6.9 ET Top Centerline Interference Factors from IH-42 and IH-48 Tests (α=0,β =0)